THE IMPLICATIONS OF FOSSIL FUEL COMBUSTION ON GLOBAL CLIMATE CHANGE: AN OVERVIEW

Charles W. Garrett

Office of Technical Coordination
Fossil Energy
U.S. Department of Energy
Washington, DC 20585

Keywords: Global Climate Change; Carbon Dioxide; Fossil Fuels

INTRODUCTION

The potential for future global climate change (GCC) and its implications for fossil fuels (FF) currently are hot issues. They are the subject of much ongoing research and scientific debate and they have policy ramifications with international repercussions. The recently completed environmental conference in Rio de Janeiro is a case in point, testifying to the encompassing importance of the topic.

GCC is very complicated and our understanding is far from adequate, hindering our ability to deal effectively with it from either the technical or the policy standpoint. Uncertainties and controversies abound. To highlight the subject for those of us who must deal with it in our daily tasks, the Fuel Chemistry Division of the American Chemical Society is conducting this one-day "pedagogical" symposium. The purpose is not to put forth any specific policy or to advocate any particular scientific position. Rather, it is to provide information on the current state-of-the-science so that as we return to our continuing responsibilities we might be better able to formulate our own decisions regarding both the conduct of our profession and policy alternatives which, as knowledgeable representatives of the scientific and engineering communities, we will be asked to explain and support.

The topic can be divided into two major areas: atmospheric science and fossil fuel implications. This symposium will focus on both. At the conclusion, two papers on policy underpinnings will suggest some techniques that can aid in policy determinations, but policies *per se* are beyond our horizon. We leave them for your personal consideration upon departure this afternoon.

ATMOSPHERIC SCIENCE

There are some things concerning GCC that are well known and beyond serious debate. Among them is the "greenhouse effect" (GHE) which has an unquestioned scientific basis. It is, for example, a major cause of the earth's average surface temperature of 15°C, Mars' -47°C and Venus' 477°C. Figure 1

illustrates the GHE. The GHE and the characteristics of the six principal greenhouse gases will be examined in our first paper.

Essential to our analysis of the present is an understanding of what has happened in the past. One GH gas of great importance to fossil fuel is, of course, CO_2, a major product of combustion. CO_2 enters the globe's carbon cycle which, although generically illustrated on figure 2, is not fully understood. The material balance, for example, cannot be closed. The atmospheric concentration of CO_2 has undergone significant variation over the earth's history and some of those variations have been correlated with climatic changes. Those of the ice ages are an example. Most variations were before man and thus stemmed from natural causes. But over the industrial revolution of the last 150 years, anthropogenic (i.e. man-produced) carbon emissions have caused the atmospheric CO_2 concentration to increase some 25 percent, and this is one basis of the present concern. The world's carbon emissions and resulting atmospheric concentrations of CO_2 over the industrial revolution are shown on figures 3 and 4.

The earth's climate, characterized by such things as temperature, precipitation and soil moisture, has varied considerably over its billion-year history. I show on figure 5 temperature variations over a million-year period. That significant variations have occurred over these long time intervals is not disputed. What has happened over the past 150 years, however, is. Some conclude the earth has warmed perhaps a half degree C during that period; others aren't so sure. Our second paper will address these data of our climatic record.

Large mathematical climate simulations, performed by "General Circulation Models" (GCMs), are essential to both analyze collected raw data and to predict the future. While necessary and useful, they are lacking in several ways. First, present computing hardware and algorithms that solve the huge but necessary multi-dimensional partial differential equation sets are not yet fully up to the task, at least when the cost of calculation is considered. Second, our knowledge of the fundamental processes involved (including complicated and significant climatic feedback mechanisms) is not sufficient even if they were. Third, the data presently available are not complete enough nor understood well enough to enable full validation of our models. Nevertheless, GCMs are a major tool in our armamentarium. Two papers will focus on GCMs, the first on the characteristics of the models, and the second on differences among the computed results (testifying, thereby, to the present state of affairs).

As is now clear, there is a great deal of uncertainty in our present ability to draw causal relationships between the GHE and GCC. Research results are reported almost daily that affect them; a recent example being new data on the role of atmospheric aerosols. Significant scientific controversies remain. These ambiguities are bases for differing policy alternatives as well as food for future research. Wrapping up our morning will be a paper directly focusing on these uncertainties and controversies.

FOSSIL FUEL IMPLICATIONS

The fossil fuels of interest are natural gas, petroleum, and coal. The fuels have different properties that cause them to produce different amounts of CO_2 as one of their combustion products. To release equal amounts of energy from combustion (assuming 100 percent efficiency) and normalized to natural gas, these three fuels create approximately the following ratios of CO_2 (on a weight basis):[5]

Natural gas -- 1.0 Petroleum -- 1.4 Bituminous Coal -- 1.8

The differences are significant enough to make fuel selection an important determinant. But even the lowest, natural gas, creates sufficient CO_2 to itself be a concern. Thus ways of minimizing CO_2 releases from fossil fuel combustion have received considerable attention.[6] In the first of two papers this afternoon, we will learn more details of the fuel's chemical and physical properties and how, through better combustion efficiencies and fuel switching, we can mitigate the problem. The second paper will deal specifically with the post-combustion capture and sequestration of CO_2, a technology presently in its infancy.

POLICY FORMULATION

While this symposium will not address or analyze specific policy proposals, either those already on the table or those lingering in the background, their existence and importance cannot be ignored. Science plays a part in policy formation. In addition to developing better means of climatic prediction and CO_2 control, there are other ways in which science can help. Closing out our symposium will be two papers that suggest ways in which objective analysis can contribute to the elucidation of crucial factors surrounding these policies. The first will deal with a unified economic analytical framework. The second will demonstrate a way in which uncertainties quantitatively can be dealt with in GCMs, significantly reducing the spread of possible outcomes.

Finally, we will round out our day in a panel session with all authors fielding questions from the audience.

SOME OTHER IMPORTANT ASPECTS

There are additional factors that are now and will remain major determinants of future events. As important to an understanding of the issue as the science of GCC and FF combustion *per* se, they include, for example:

- -- *International differences* as represented by differing aspirations and priorities among the developed and the lesser developed nations.
- -- *Political differences* as represented by the various positions taken by environmental protectionists and CO_2-producing industries.

-- *Philosophical and moral issues* as represented by population and its control.

We do not have the time to delve into these matters in detail. But do not take their limited mention as an indication of relative influence. It is only time, not importance, that forces us to deal primarily with other things; in the end, these issues may well prove to have the greatest influence of all on the world's response to the threat of GCC from the GHE. It is important that we technologists also appreciate them and I'll finish this overview with a very inadequate coverage of a few of the most important . . .

GH gases are worldwide, and dealing with them will, of necessity, require a coordinated, international approach. But not all nations are involved equally. First, the predicted climate changes vary; some nations may even benefit as the agricultural environment of their country is bettered at the expense of another nation's loss. Second, many of the developing countries are wrestling with horrendous health and economic woes; their priorities are on the present and not on what might (or might not) be done to affect GCC many years hence. Relatively poor and technically primitive, whatever they do will require both technological and economic aid. (I note in passing that the Montreal Protocol on CFC control was first rejected by these countries who joined in only after the developed nations offered economic assistance.) And third is the question of equity these struggling nations raise: "It is the rich nations of the world that have polluted the global nest while achieving their status of well-being; they should pay for it, not us," one hears them exclaim, adding, "The well-off nations should now help us reach equal wealth."

One cannot escape the economic consequences of the moment, as policy discussions in the U.S. reveal. It is no simple matter to suggest the present economic base of this country, which is highly dependent upon fossil fuel combustion, should be quickly altered. At the same time, there are those with a genuine concern for long-term environmental consequences who auger for immediate constraints on CO_2. Feeling we cannot afford the time it will take to obtain a better scientific basis for policy, they believe the downside risk is too large to wait. So even in a single nation, legitimate differences of perspective lead to radically different political positions.

Finally, there are some moral factors that cannot be escaped. One major determinant of the magnitude of future CO_2 emissions will be the number of people generating it -- the world's population, which is rapidly rising. If the trend continues as predicted, it will swamp CO_2 emission controls. That, in turn, suggests population control, a highly emotional and contested factor but nonetheless a very important determinant.

SUMMARY

To illustrate how factors affected by technology and those that are not are interminably intertwined, I use an identity proposed by Gibbons[6] several years ago. One can estimate CO_2 emissions at some time, T, by:

CO_2 Emitted @ time t=T = CO_2 Emitted per Unit of Consumed Energy @ t=T (1)

x Energy Consumed per Unit of Gross Domestic Product @ t=T (2)

x Gross Domestic Product (GDP) per person @ t=T (3)

x Population @ t=T (4)

Letting E represent consumed energy, we rearrange and define four quantities, A, B, C, and D, in the process:

$$\frac{CO_2 \text{ Emitted @ Time T}}{} = A \frac{(CO_2 \text{ emitted/E}) @ t=T}{(CO_2 \text{ emitted/E}) @ t=0} \times \frac{CO_2 \text{ emitted @ t=0}}{E @ t=0}$$

$$\times B \frac{(E/GDP) @ t=T}{(E/GDP) @ t=0} \times \frac{E @ t=0}{GDP @ t=0}$$

$$\times C \frac{(GDP/person) @ t=T}{(GDP/person) @ t=0} \times \frac{GDP @ t=0}{person @ t=0}$$

$$\times D \frac{(population @ t=T)}{(population @ t=0)} \times population @ t=0$$

The beauty of this representation is that the four quantities on the left are merely ratios of the future (t = T) to the present (t = 0), while the right-hand quantities contain information only on the present. Further, it separates effects of energy technology (A & B) from other determinants (C & D). "A" reflects emissions from the generation of such useful energy forms as heat, electricity and motion; improving system efficiencies and fuel switching can lower it. "B" measures "energy efficiency" changes -- how we use that energy -- and reflects (among other things) end-use conservation. These first two terms embody just about all that energy technology can do. "C" is a measure of the change in productivity of a people. It goes up with an improved standard of living and the objective is to *increase* this parameter. "D" invokes all kinds of controversial considerations if there is an attempt to control it.

Relative to the present, one can estimate future emissions of CO_2 for a local region, a nation or, indeed, the world by insertion of the proper values for A, B, C, and D. If their product is lower than one, emissions at T are less than those at present; if it is greater than one, they will be more. As we shall see, all four are important and each must be appreciated.

Using available data and predictions of the experts, I have estimated the values of the four quantities, updating similar values computed earlier[7] for the 35-year period ending in the year 2025 for three different regions; the U.S., Africa, and the world. Assuming the percentage of useful energy generated by all fossil fuels remains constant, my predictions of improved

efficiencies and fuel switching were optimistic; for example, in the U.S. average overall system efficiency improves some 38%, coal use drops 30% and oil use drops 20% (both replaced by natural gas) over that time. The results were:

	A	B	C	D	AxBxCxD
United States	0.67	0.71	1.74	1.21	1.00
Africa	0.76	1.91	0.73	2.44	2.58
World	0.71	0.74	1.67	1.60	1.40

The implications are clear. Under these high-efficiency, high-gas, low-coal assumptions, CO_2 emissions stay the same only in an advanced-technology nation where population growth is simultaneously limited. They increase elsewhere despite what technology can do. To control worldwide emissions, non-energy technology factors (e.g. productivity, population) also must be dealt with, with significant international and moral implications. It should be noted, however, that without technology providing large reductions in A and B, the situation would be far worse -- technology is doing its part!

Our symposium today focuses only on the first parameter, A, which deals with energy generation by fossil fuel combustion. That in itself will be difficult to do in only a few hours' time. The impacts of the others should not be minimized, however. For they also have a critical importance in matters concerning global climate change.

1. Adapted from Schneider, S. H., *Science* **243**, 772 (1989). Copyrighted by the AAAS; reprinted by permission.

2. *Changing By Degrees: Steps to Reduce Greenhouse Gases*, U.S. Office of Technology Assessment report OTA-O-482, U.S. Government Printing Office, Washington, DC (Feb. 1991).

3. *Trends '90*, Carbon Dioxide Information Analysis Center report ORNL/CDIAC-36 (1990).

4. Intergovernmental Panel on Climate Change, *Climate Change - The IPCC Scientific Assessment*, Cambridge Univ. Press (1990). Copyrighted by the IPCC; reprinted by permission.

5. Garrett, C. W., On Global Climate Change, Carbon Dioxide, and Fossil Fuel Combustion, *Progress in Energy and Combustion Science*, in press.

6. Gibbons, J. H., The Interface of Environmental Science and Policy, in *Energy and the Environment in the 21st Century*, Tester, J. W., Wood, D. O. and Ferrari, N. A., eds.; MIT Press, Cambridge, MA (1991).

7. *Op. Cit.* 5.

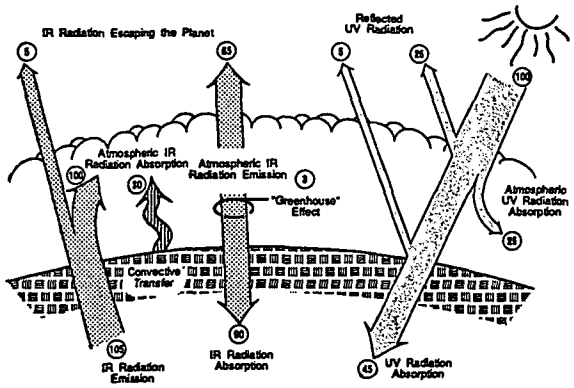

Figure 1

THE GREENHOUSE EFFECT

Source: Ref. 1

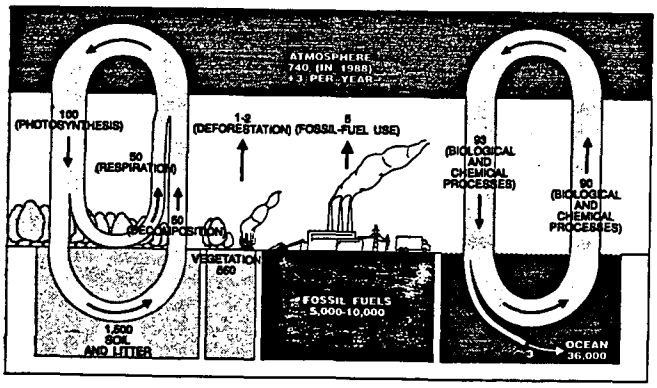

Figure 2

GLOBAL CARBON CYCLE

Source: Ref. 2

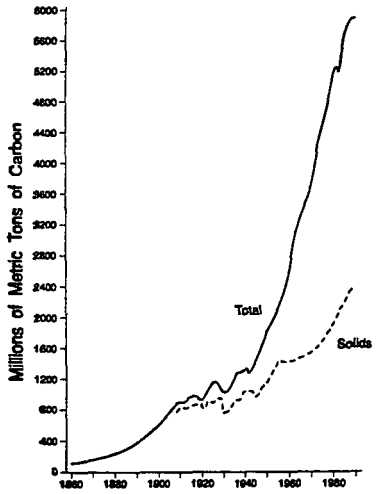

Figure 3

GLOBAL CARBON EMISSIONS

Source: Ref. 3

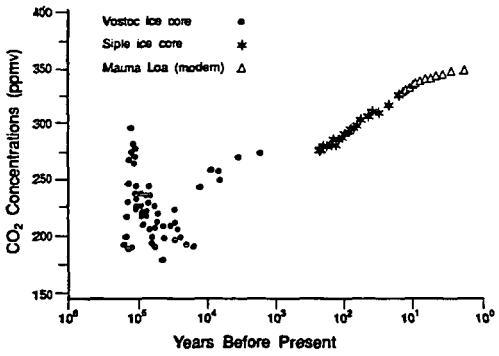

Figure 4

CO_2 ATMOSPHERIC CONCENTRATIONS

Source: Ref. 3

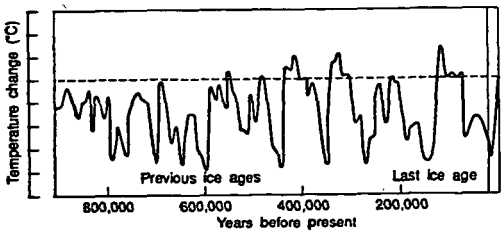

Figure 5

HISTORIC TEMPERATURE VARIATIONS

(dashed line = 1900)

Source: Ref. 4

THE BASICS OF THE GREENHOUSE EFFECT: The Role of Greenhouse Gases and Aerosols

R. T. Watson

Introduction:

Although there have been no major changes in our understanding of the sources and sinks of greenhouse gases and aerosols during the last two years, i.e., since the 1990 Intergovernmental Panel on Climate Change (IPCC) Scientific Assessment, there have been a number of important advances. These advances include an improved quantitative understanding of the atmospheric distributions, trends, sources and sinks of greenhouse gases, their precursors and aerosols, and an improved understanding of the processes controlling their global budgets. In addition, there have been significant advances in our understanding of the impact of ozone depletion and sulphate aerosols on radiative forcing and of the limitations of the concept of the Global Warming Potential (GWP). The contents of this paper are taken from the 1992 IPCC Scientific Assessment.

The role of greenhouse gases and aerosols in changing the Earth's climate:

Increases in the concentration of the greenhouse gases reduce the efficiency with which the Earth cools to space and tend to warm the lower atmosphere and surface. The amount of warming depends on the size of the increase in concentration of each greenhouse gas, the radiative properties of the gases involved, and the concentration of other greenhouse gases already present in the atmosphere. It also can depend on local effects such as the variation with height of the concentration of the greenhouse gas, a consideration that may be particularly germane to water vapour which is not uniformly mixed throughout the atmosphere.

Aerosols (small particles) from volcanoes, natural and industrial emissions of sulfur containing gases, and biomass burning can absorb and reflect radiation. Moreover, changes in aerosol concentrations can alter cloud reflectivity through their effect on cloud properties. In most cases increases in the atmospheric abundance of aerosols tend to cool climate. In general, they have a much shorter lifetime than greenhouse gases so they are not uniformly distributed and their concentrations respond much more quickly to changes in emissions.

A necessary starting point for the prediction of changes in climate due to increases in greenhouse gases and aerosols is an estimate of their future concentrations. This requires a knowledge of both the strengths of their sources (natural and man-made) and also the mechanisms of their eventual removal from the atmosphere (their sinks). The projections of future concentrations can then be used in climate models to estimate the climatic response.

Recent Improvements in Scientific Understanding of the Sources and Sinks of Greenhouse Gases and Aerosols:

Atmospheric Concentrations and Trends of Long-lived Greenhouse Gases:

The atmospheric concentrations of the major long-lived greenhouse gases, carbon dioxide (CO_2), methane (CH_4), nitrous oxide (N_2O), chlorofluorocarbons (CFCs), and carbon tetrachloride (CCl_4), continue to increase because of human activities. While the growth rates of most of these gases have been steady or increasing over the past decade, that of CH_4 and some of the halocarbons has been decreasing. The rate for CH_4 has declined from about 20 ppbv/yr in the late 1970s to possibly as low

as 10 ppbv/yr in 1989. While a number of hypotheses have been forwarded to explain these observations, none is completely satisfactory.

Sources and Sinks of Carbon Dioxide:

The two primary sources of the observed increase in atmospheric CO_2 are combustion of fossil fuels and land-use changes; cement production is a further important source.

The emission of CO_2 from the combustion of fossil fuels grew between 1987 and 1989. Preliminary data for 1990 indicate similar emissions to 1989. The best estimate for global fossil fuel emissions in 1989 and 1990 is 6.0±0.5 GtC (1 GtC (gigatonne of carbon) equals one billion [one thousand million (10^9)] tonnes of carbon), compared to 5.7±0.5 GtC in 1987 (IPCC, 1990). The estimated total release of carbon in the form of CO_2 from oil well fires in Kuwait during 1991 was 0.065 GtC, about one percent of total annual anthropogenic emissions.

The direct net flux of CO_2 from land use changes (primarily deforestation), integrated over time, depends upon the area of land deforested, the rate of reforestation and afforestation, the carbon density of the original and replacement forests, and the fate of above-ground and soil carbon. These and other factors are needed to estimate annual net emissions but significant uncertainties exist in our quantitative knowledge of them. Since IPCC (1990) some progress has been made in reducing the uncertainties associated with the rate of deforestation, at least in Brazil. A comprehensive, multi-year, high spatial resolution satellite data set has been used to to estimate that the average rate of deforestation in the Brazilian Amazonian forest between 1978 and 1989 was 2.1 million hectares (Mha) per year. The rate increased between 1978 and the mid-1980s, and has decreased to 1.4 Mha/yr in 1990. The Food and Agriculture Organization (FAO), using information supplied by individual countries, recently estimated that the rate of global tropical deforestation in closed and open canopy forests for the period 1981-1990 was about 17 Mha/yr, approximately 50% higher than in the period 1976-1980.

Despite the new information regarding rates of deforestation, the uncertainties in estimating CO_2 emissions are so large that there is no strong reason to revise the IPCC 1990 estimate of annual average net flux to the atmosphere of 1.6±1.0 GtC from land-use change during the decade of the 1980s.

Since IPCC (1990) particular attention has focussed on understanding the processes controlling the release and uptake of CO_2 from both the terrestrial biosphere and the oceans, and on the quantification of the fluxes. Based on models and the atmospheric distribution of CO_2, it appears that there is a small net addition of carbon to the atmosphere from the equatorial region, a combination of outgassing of CO_2 from warm tropical waters and a terrestrial biospheric component that is the residual between large sources (including deforestation) and sinks. There appears to be a strong Northern Hemisphere sink, containing both oceanic and terrestrial biospheric components, and a weak Southern Hemisphere (SH) sink. The previous IPCC global estimate for an ocean sink of 2.0±0.8 GtC per year is still a reasonable one. The terrestrial biospheric processes which are suggested as contributing to the sinks are sequestration due to forest regeneration, and fertilization arising from the effects of both CO_2 and nitrogen (N), but none of these can be adequately quantified. This implies that the imbalance (of order 1-2 GtC/yr) between sources and sinks, i.e., "the missing sink", has not yet been resolved. This fact has significant consequences for estimates of future atmospheric CO_2 concentrations and the analysis of the concept of the Greenhouse Warming Potential.

Sources and Sinks of Methane:

A total (anthropogenic plus natural) annual emission of CH_4 of about 500Tg can be deduced from the magnitude of its sinks combined with its rate of accumulation in the atmosphere. While the sum of the individual sources is consistent with a total of 500Tg CH_4, there are still many uncertainties in accurately quantifying the magnitude of emissions from individual sources. Significant new information includes a revised rate of removal of CH_4 by atmospheric hydroxyl (OH) radicals (because of a lower rate constant), a new evaluation of some of the sources (e.g., from rice fields) and the addition of new sources (e.g., animal and domestic waste). Recent CH_4 isotopic studies suggest that approximately 100Tg CH_4 (20% of the total CH_4 source) is of fossil origin, largely from the coal, oil, and natural gas industries. Recent studies of CH_4 emissions from rice agriculture, in particular Japan, India, Australia, Thailand and China, show that the emissions depend on growing conditions, particularly soil characteristics, and vary significantly. While the overall uncertainty in the magnitude of global emissions from rice agriculture remains large, a detailed analysis now suggests significantly lower annual emissions than reported in IPCC 1990. The latest estimate of the atmospheric lifetime of CH_4 is about 11 years.

Sources and Sinks of Nitrous Oxide:

Adipic acid (nylon) production, nitric acid production and automobiles with three-way catalysts have been identified as possibly significant anthropogenic global sources of nitrous oxide. However, the sum of all known anthropogenic and natural sources is still barely sufficient to balance the calculated atmospheric sink (stratospheric photolysis) or to explain the observed increase in the atmospheric abundance of N_2O.

Sources of Halogenated Species:

The worldwide consumption of CFCs 11, 12, and 113 is now 40% below 1986 levels, substantially below the amounts permitted under the Montreal Protocol. Further reductions are mandated by the 1990 London Amendments to the Montreal Protocol. As CFCs are phased out, HCFCs and HFCs will substitute, but at lower emission rates.

Atmospheric Concentrations and Trends of Other Gases that Influence the Radiative Budget:

Ozone (O_3) is an effective greenhouse gas both in the stratosphere and in the troposphere. Significant decreases have been observed during the last one to two decades in total column O_3 at all latitudes - except the tropics - in spring, summer and winter. The downward trends were larger during the 1980s than in the 1970s. These decreases have occurred predominantly in the lower stratosphere (below 25km), where the rate of decrease has been up to 10% per decade depending on altitude. In addition, there is evidence to indicate that O_3 levels in the troposphere up to 10km altitude above the few existing ozonesonde stations at northern middle latitudes have increased by about 10% per decade over the past two decades. Also, the abundance of carbon monoxide (CO) appears to be increasing in the NH at about 1% per year. However, there is little new information on the global trends of other tropospheric O_3 precursors, (non-methane hydrocarbons (NMHC) and oxides of nitrogen (NO_x)).

Stratospheric Ozone Depletion:

Even if the control measures of the 1990 London amendments to the Montreal Protocol were to be implemented by all nations, the abundance of stratospheric chlorine and bromine will increase over the next several years. The Antarctic ozone hole, caused by industrial halocarbons, will therefore recur

each spring. In addition, as the weight of evidence suggests that these gases are also responsible for the observed reductions in middle- and high latitude stratospheric O_3, the depletion at these latitudes is predicted to continue unabated through the 1990s.

Sources of Precursors of Tropospheric Ozone:

Little new information is available regarding the tropospheric ozone precursors (CO, NMHC, and NO_X), all of which have significant natural and anthropogenic sources. Their detailed budgets therefore remain uncertain.

Source of Aerosols:

Industrial activity, biomass burning, volcanic eruptions, and sub-sonic aircraft contribute substantially to the formation of tropospheric and stratospheric aerosols. Industrial activities are concentrated in the Northern Hemisphere where their impact on tropospheric sulphate aerosols is greatest. Sulphur emissions, which are due in large part to combustion effluents, have a similar emissions history to that of anthropogenic CO_2. Estimates of emissions of natural sulphur compounds have been reduced from previous figures, thereby placing more emphasis on the anthropogenic contribution.

Scenarios of Future Emissions of Greenhouse Gases, Greenhouse Gas Precursors, and Aerosol Precursors

Scenarios of net greenhouse gas and aerosol precursor emissions for the next 100 years or more are necessary to support study of potential anthropogenic impacts on the climate system. The scenarios provide inputs to climate models and assist in the examination of the relative importance of relevant trace gases and aerosol precursors in changing atmospheric composition and climate. Scenarios can also help in improving the understanding of key relationships among factors that drive future emissions.

Scenario outputs are not predictions of the future, and should not be used as such; they illustrate the effect of a wide range of economic, demographic and policy assumptions. They are inherently controversial because they reflect different views of the future. The results of scenarios can vary considerably from actual outcomes even over short time horizons. Confidence in scenario outputs decreases as the time horizon increases, because the basis for the underlying assumptions becomes increasingly speculative. Considerable uncertainties surround the evolution of the types and levels of human activities (including economic growth and structure), technological advances, and human responses to possible environmental, economic and institutional constraints. Consequently, emission scenarios must be constructed carefully and used with great caution.

Since completion of the 1990 IPCC Scenario A (SA90) events and new information have emerged which relate to that scenario's underlying assumptions. These developments include: the London Amendments to the Montreal Protocol; revision of population forecasts by the World Bank and United Nations; publication of the IPCC Energy and Industry Sub-group scenario of greenhouse gas emissions to 2025; political events and economic changes in the former USSR, Eastern Europe and the Middle East; re-estimation of sources and sinks of greenhouse gases (reviewed in this Assessment); revision of preliminary FAO data on tropical deforestation; and new scientific studies on forest biomass. There has also been recognition of considerable uncertainty regarding other important factors that drive future emissions.

These factors have led to an update of the SA90. Six alternative IPCC Scenarios (IS92 a-f) now embody a wide array of assumptions (population growth, economic growth, role of nuclear power, renewable energy costs), that affect how future greenhouse gas emissions might evolve in the absence

of climate policies beyond those already adopted. This constitutes a significant improvement over the previous methodology. However, the probability of any of the resulting emission paths has not been analyzed. IPCC WGI does not prefer any individual scenario. Other combinations of assumptions could illustrate a broader variety of emission trajectories. The different worlds which the new scenarios imply, in terms of economic, social and environmental conditions, vary widely. The current exercise provides an interim view and lays a basis for a more complete study of future emissions of greenhouse gas and aerosol precursors.

Scenario Results:

The range of possible annual emissions of greenhouse gases is very wide as shown by the selected results of six IPCC Greenhouse gas scenarios below:

Scenario	Year	CO_2 (GtC)	CH_4 (Tg)	N_2O (TgN)	CFCs (kt)	SO_x (TgS)
IS92a	1990	7.4	506	12.9	827	98
	2025	12.2	659	15.8	217	141
	2100	20.3	917	17.0	3	169
IS92b	2025	11.8	659	15.7	36	140
	2100	19.1	917	16.9	0	164
IS92c	2025	8.8	589	15.0	217	115
	2100	4.6	546	13.7	3	77
IS92d	2025	9.3	584	15.1	24	104
	2100	10.3	567	14.5	0	87
IS92e	2025	15.1	692	16.3	24	163
	2100	35.8	1072	19.1	0	254
IS92e	2025	14.4	697	16.2	217	151
	2100	26.6	1168	19.0	3	204

All six scenarios can be compared to SA90. IS92a is slightly lower than SA90 due to modest and largely offsetting changes in the underlying assumptions. (For example, compared to SA90, higher population forecasts increase the emission estimates, while phaseout of halocarbons and more optimistic renewable energy costs reduce them.) The highest greenhouse gas levels result from the new scenario IS92e which combines, among other assumptions, moderate population growth, high economic growth, high fossil fuel availability and eventual hypothetical phaseout of nuclear power. The lowest greenhouse gas levels result from IS92c which assumes that population grows, then declines by the middle of the next century, that economic growth is low and that there are severe constraints on fossil fuel supplies. Overall, the scenarios indicate that greenhouse gas emissions could rise substantially over the coming century in the absence of new measures explicitly intended to reduce their emission. However, IS92c has a CO_2 emission path which eventually falls below its starting 1990 level. IS92b, a modification of IS92a, suggests that current commitments by many OECD Member countries to stabilize or reduce CO_2 might have a small impact on greenhouse gas emissions over the next few decades, but would not offset substantial growth in possible emissions in the long run. IS92b does not take into account that such commitments could accelerate development and diffusion of low greenhouse gas technologies, nor possible resulting shifts in industrial mix.

Carbon Dioxide:

The new emissions scenarios for CO_2 from the energy sector span a broad range of futures Population and economic growth, structural changes in economies, energy prices, technological advance, fossil fuel supplies, nuclear and renewable energy availability are among the factors which could exert major influence on future levels of CO_2 emissions. Developments such as those in the republics of the former Soviet Union and in Eastern Europe, now incorporated into all the scenarios, have important implications for future fossil fuel carbon emissions, by affecting the levels of economic activities and the efficiency of energy production and use. Biotic carbon emissions in the early decades of the scenarios are higher than SA90, reflecting higher preliminary FAO estimates of current rates of deforestation in many - though not all - parts of the world, and higher estimates of forest biomass.

Halocarbons:

The revised scenarios for CFCs and other substances which deplete stratospheric ozone are much lower than in SA90. This is consistent with wide participation in the controls under the 1990 London Amendments to the Montreal Protocol. However, the future production and composition of CFC substitutes (HCFCs and HFCs) could significantly affect the levels of radiative forcing from these compounds.

Methane, Nitrous Oxide, Ozone Precursors and Sulphur Gases:

The distribution of CH_4 and N_2O emissions from the different sources has changed from the SA90 case. Methane from rice paddies are lower, and emissions from animal waste and domestic sewage have been added. N_2O emission factors for stationary sources and biomass burning have been revised downwards. Adipic and nitric acid have been included as additional sources of N_2O. Preliminary analysis of the emissions of volatile organic compounds and sulphur dioxide suggests that the global emissions of these substances are likely to grow in the coming century if no new limitation strategies are implemented.

Relationship Between Emissions and Atmospheric Concentrations and the Influence on the Radiative Budget

A key issue is to relate emissions of greenhouse gases, greenhouse gas precursors and aerosol precursors to future concentrations of greenhouse gases and aerosols in order to assess their impact on the radiative balance. A number of different types of model have been developed.

Carbon Cycle Models:

While there is a variety of carbon cycle models (including 3-D ocean-atmosphere models, 1-D ocean-atmosphere box-diffusion models, and box models that incorporate a terrestrial biospheric sink) all such models are subject to considerable uncertainty because of an inadequate understanding of the processes controlling the uptake and release of CO_2 from the oceans and terrestrial ecosystems. Some models assume a net neutral terrestrial biosphere, balancing fossil fuel emissions of CO_2 by oceanic uptake and atmospheric accumulation, others achieve balance by invoking additional assumptions regarding the effect of CO_2 fertilization on the different parts of the biosphere. However even models that balance the past and contemporary carbon cycle may not predict future atmospheric concentrations accurately because they do not necessarily represent the proper mix of processes on land and in the oceans. The differences in predicted changes in CO_2 concentrations are up to 30%. This does not represent the major uncertainty in the prediction of future climate change compared with uncertainties in estimating future patterns of trace gas emissions, and in quantifying climate feedback processes. A

simple empirical estimate can be based on the assumption that the fraction of emissions which remains in the atmosphere is the same as that observed over the last decade; i.e., 46±7%.

Atmospheric Gas Phase Chemistry Models:

Current tropospheric models exhibit substantial differences in their predictions of changes in O_3, in the hydroxyl radical (OH) and in other chemically active gases due to emissions of CH_4, non-methane hydrocarbons, CO and, in particular, NO_x. These arise from uncertainties in the knowledge of background chemical composition and our inability to represent small-scale processes occurring within the atmosphere. These deficiencies limit the accuracy of predicted changes in the abundance and distribution of tropospheric O_3, and in the lifetimes of a number of other greenhouse gases, including the HCFCs and HFCs, all of which depend upon the abundance of the OH radical. Increases in CH_4, NMHCs, and CO all lead to increases in O_3, and decreases in OH, thus leading to an increase in radiative forcing. On the other hand because increases in NO_x lead to an increase in both O_3 and OH, the net effect on radiative forcing is uncertain.

Atmospheric Sulphate Aerosol Models:

The atmospheric chemistry of sulphate aerosols and their precursors has been extensively studied in relation to the acid rain issue. While our understanding of processes related to chemical transformations has increased significantly in recent years, substantial uncertainties remain, especially regarding the microphysics of aerosol formation, interaction of aerosols with clouds, and the removal of aerosol particles by precipitation.

How has our Understanding of Changes in Radiative Forcing Changed?

Since IPCC (1990), there have been significant advances in our understanding of the impact of ozone depletion and sulphate aerosols on radiative forcing and of the limitations of the concept of the Global Warming Potential.

Radiative Forcing due to Changes in Stratospheric Ozone:

For the first time observed global depletions of O_3 in the lower stratosphere have been used to calculate changes in the radiative balance of the atmosphere. Although the results are sensitive to atmospheric adjustments, and no GCM studies of the implications of the O_3 changes on surface temperature have been performed, the radiative balance calculations indicate that the O_3 reductions observed during the 1980s have caused reductions in the radiative forcing of the surface-troposphere system at mid- and high- latitudes. This reduction in radiative forcing resulting from O_3 depletion could, averaged on a global scale and over the last decade, be approximately equal in magnitude and opposite in sign to the enhanced radiative forcing due to increased CFCs during the same time period. The effect at high latitudes is particularly pronounced and, because of these large variations with latitude and region, studies using GCMs are urgently required to further test these findings.

Radiative Forcing due to Changes in Tropospheric Ozone:

While there are consistent observations of an increase in tropospheric ozone (up to 10% per decade) at a limited number of locations in Europe, there is not an adequate global set of observations to quantify the magnitude of the increase in radiative forcing. However, it has been calculated that a 10% uniform global increase in tropospheric ozone would increase radiative forcing by about a tenth of a watt per square metre.

Radiative Effects of Sulphur Emissions:

Emissions of sulphur compounds from anthropogenic sources lead to the presence of sulphate aerosols which reflect solar radiation. This is likely to have a cooling influence on the Northern Hemisphere (there is negligible effect in the Southern Hemisphere). For clear-sky conditions alone, the cooling caused by current rates of emissions has been estimated to be about $1Wm^{-2}$ averaged over the Northern Hemisphere, a value which should be compared with the estimate of $2.5Wm^{-2}$ for the heating due to anthropogenic greenhouse gas emissions up to the present. The non-uniform distribution of anthropogenic sulphate aerosols coupled with their relatively short atmospheric residence time produce large regional variations in their effects. In addition, sulphate aerosols may affect the radiation budget through changes in cloud optical properties.

Global Warming Potentials:

Gases can exert a radiative forcing both directly and indirectly: direct forcing occurs when the gas itself is a greenhouse gas; indirect forcing occurs when chemical transformation of the original gas produces a gas or gases which themselves are greenhouse gases. The concept of the Global Warming Potential (GWP) has been developed for policymakers as a measure of the possible warming effect on the surface-troposphere system arising from the emission of each gas relative to CO_2. The indices are calculated for the contemporary atmosphere and do not take into account possible changes in chemical composition of the atmosphere. Changes in radiative forcing due to CO_2, on a kg basis, are non-linear with changes in the atmospheric CO_2 concentrations. Hence, as CO_2 levels increase from present values, the GWPs of the non-CO_2 gases would be higher than those evaluated here. For the concept to be most useful, both the direct and indirect components of the GWP need to be quantified.

Direct Global Warming Potentials:

The direct components of the Global Warming Potentials (GWPs) have been recalculated, taking into account revised estimated lifetimes, for a set of time horizons ranging from 20 to 500 years, with CO_2 as the reference gas. The same ocean-atmosphere carbon cycle model as in IPCC (1990) has been used to relate CO_2 emission to concentrations. Table 3 shows values for a selected set of key gases for the 100 year time horizon. While in most cases the values are similar to the previous IPCC (1990) values, the GWPs for some of the HCFCs and HFCs have increased by 20 to 50% because of revised estimates of their lifetimes. The direct GWP of CH_4 has been adjusted upward, correcting an error in the previous IPCC report. The carbon cycle model used in these calculations probably underestimates both the direct and indirect GWP values for all non-CO_2 gases. The magnitude of the bias depends on the atmospheric lifetime of the gas, and the GWP time horizon.

Indirect Global Warming Potentials:

Because of our incomplete understanding of chemical processes, most of the indirect GWPs reported in IPCC (1990) are likely to be in substantial error, and none of them can be recommended. Although we are not yet in a position to recommend revised numerical values, we know, however, that the indirect GWP for methane is positive and could be comparable in magnitude to its direct value. In contrast, based on the sub-section above, the indirect GWPs for chlorine and bromine halocarbons are likely to be negative. The concept of a GWP for short-lived, inhomogeneously distributed constituents, such as CO, NMHC, and NO_x may prove inapplicable, although, as noted above, we know that these constituents will affect the radiative balance of the atmosphere through changes in tropospheric ozone and OH. Similarly, a GWP for SO_2 is viewed to be inapplicable because of the non-uniform distribution of sulphate aerosols.

"GLOBAL WARMING": OBSERVED VARIATIONS AND CHANGES

Thomas R. Karl
National Climatic Data Center
NOAA/NESDIS/EIS
37 Battery Park Ave.
Federal Building
Asheville, NC 28801

Keywords: Greenhouse Effect, Variations and Changes, Observations

ABSTRACT

There are several parameters of fundamental importance with respect to understanding why the climate is or is not changing, especially as related to the "greenhouse effect". These parameters include integrated changes of temperature (horizontal and vertical), precipitation (horizontal) and water vapor (horizontal and vertical). It is also of fundamental importance however to determine how these parameters respond to an enhanced anthropic greenhouse. This includes knowledge about temporal and spatial the details of climate variations. The details of how they are expected to change is often of fundamental importance with respect to the impact on socio-economic, biochemical, and geophysical systems. This implies that we must understand both why and how the climate may change. Monitoring and analysis for why the climate is changing is not synonymous with having how the climate has or will change.

UNDERSTANDING WHY TEMPERATURES HAVE INCREASED

The most pervasive consequence of an enhanced greenhouse effect is the projected increase of global average temperatures. For this reason there has been considerable effort expended in obtaining accurate representations of the instrumented and proxy thermometric record (Jones et al., 1986a; Jones et al 1986b; Jones, 1988; Hansen and Lebedeff, 1987; Hansen and Lebedeff, 1988; Vinnikov et al., 1990; Cook et al., 1991; Bradley and Jones, 1992; Folland et al., 1990). At present, the best estimates of the observed change in global mean temperatures over the past 100 years is in the range of 0.3 to 0.6°C (IPCC, 1990, 1992). The rather wide confidence interval stems from a variety of monitoring problems including: 1) changes of observing methods, 2) incomplete global monitoring, and 3) the separation of local micro- and meso- scale climate variations (including urban heat island effects) from large-scale changes.

Over the past 100 years increases of anthropic greenhouse gases such as CO_2, N_2O, CH_4, O_3, and CFCs have lead to an enhanced greenhouse effect. This has resulted in increases in the radiative forcing at the top of the troposphere. Using the physics from radiative transfer models the IPCC (1990) estimates this increase close to 2 W/m^2 when averaged over the globe. This is equivalent to about a 1.5 increase in equivalent CO_2 forcing.

The sensitivity of the climate system to this forcing at the earth's surface is of critical importance. There are many indirect effects, such as ancillary changes in clouds and water vapor, that can occur with an increase of global mean temperature which affect the sensitivity of the climate system to increases in greenhouse gases. For this reason, comparison of actual changes of surface temperature with projected changes of temperature from General Circulation Models (GCMs) has taken on special importance. The GCMs include many, but not all, of the indirect forcing functions. Assuming all other forcing functions are near zero, such comparisons yield estimates of climate sensitivity to a doubling of equivalent CO_2 in the range of 1° to 2°C using an observed 100-year warming rate of 0.5°C. If a lower estimate of observed warming (0.3°C) is used the sensitivity is less than 1°C, but if the high end (0.6°C) is used the sensitivity is about 2°C.

It may be overly simplistic to simply compare the greenhouse induced climate change with the observed record. The instrumented climate record may be affected by other important forcing functions besides greenhouse forcings. For example, atmosphere/ocean GCMs (AOGCMs) have indicated that the climate system could have internal chaotic variations of the order of several tenths of °C over periods as short as a Century (Hansen et al., 1988; Manabe et al., 1991; Manabe et al., 1992). Proxy records of global temperature suggest that the climate has fluctuated by at least several tenths of degrees over the past several Centuries (Bradley and Jones, 1992). On shorter time-scales volcanic forcing will clearly lead to a cooling effect at the surface (Hansen et al., 1991). Additionally, recent evidence suggests that manmade sulfate aerosol forcing (Charlson et al., 1992) and biomass burning may have significantly altered the radiative balance (-1 W/m^2) of the planet, partially offsetting the greenhouse effect.

Some have argued (Madden and Ramanathan, 1980; Baker and Barnett, 1982; MacCracken and Moses, 1982) that the greenhouse forcings should leave a fingerprint in the climate record which could then be specifically attributed to the greenhouse effect. Such a strategy focuses around a multivariate selection of parameters to analyze. These parameter should posses high signal to noise ratios, reliable and "long" records, and appropriate time and space scales. Some of the simultaneous changes expected in the climate record include: 1) Increases of global mean temperature, 2) A reduction in the pole to equator temperature gradient in the Northern Hemisphere (primarily the cold half of the year), 3) Stratospheric cooling and tropospheric warming, 4) A Global increase of precipitation with mid-continent drying during summer, 5) Tropospheric water vapor increase, 6) A rise of sea-level, and 7) An increase of the land surface temperature relative to the sea-surface temperature. Some aspects of the observed climate record are consistent with these projected changes while others are problematic (Barnett and Schlesinger, 1987, IPCC, 1990). Nonetheless, there has been insufficient

research to separate out the signature or pattern of change which might arise due to a global warming from other causes, e.g. natural variability.

UNDERSTANDING HOW TEMPERATURES HAVE INCREASED

Knowing why the climate has changed is only part of the challenge of understanding the climate system. We must also be able to project how the climate will change as it relates to man-made and natural systems on earth. As a prerequisite this means documenting and understanding the interaction between relevant climate parameters as they may affect these systems. Several examples are presented to illustrate the challenge.

Changes in the frequency of extreme temperatures is an important aspect of understanding how the recent warming has evolved over the past several decades. Many systems, both natural and man-made, are more sensitive to the tails of the distribution. To illustrate the complexity of the problem Karl et al. (1991) show that the changes in mean maximum and minimum temperatures over the past several decades have not been symmetric in the USA, the PRC, and the former USSR. The rate increase of the mean daily minimum temperature in these areas was more than three times the rate of the mean daily maximum temperature. Similarly the rate of increase of the 1-day seasonal extreme high temperatures was negligible, but an increase was apparent for the 1-day seasonal extreme minimum temperature. This has effectively lead to a decrease in variability of the extreme temperature range. It is uncertain whether this change is related to an enhanced greenhouse effect, anthropic increases in aerosols, or perhaps natural climate variability. Whatever its cause, it is a fundamental characteristic of the observed change of temperature in much of the Northern Hemisphere. It must be better understood before we can hope to confidently project the impact of any anticipated change of temperature.

The ability to project the frequency of major "weather" events is often of critical importance to many systems. Even if we could project seasonal temperature changes with perfect accuracy over relatively small space-scales, in many instances we would require still higher time resolution in order to project the impact of the changes. For example, the frequency of killing freezes which have destroyed both citrus fruit as well as citrus trees has occurred both during winters with very cold temperatures as well as during more mild winters, especially those during the mild winters of the 1980s (Figure 1). Clearly, changes in the frequency of extreme weather events is very important.

UNDERSTANDING CHANGES OF PRECIPITATION

Precipitation is arguably the most important climate parameter related to life on Earth. Unfortunately, it is very difficult to accurately document important changes of this parameter. This is related to its high frequency variability, and measurement

problems. Moreover, it is exceptionally difficult to accurately project long-term regional-scale changes of this parameter. It requires detailed understanding of changes in large-scale and meso-scale thermodynamics as well as micro-scale cloud physics. Karl et al. (1991) demonstrate the problem in the central USA. They show that the IPCC (1990) projected changes of precipitation in this region (due to enhanced greenhouse gases) for summer and winter will not be detectable until well beyond the year 2030. Ironically, the magnitude of the change projected could have major impacts before we could be confident that we have detected a real change. Summer precipitation is projected to decrease by 5 to 10% and winter precipitation is projected to increase up to 15%. To make matters more complicated the observed change in the ratio of summer to winter precipitation during the Twentieth Century in the Central USA is not consistent with the projected changes, if greenhouse forcings are the only important factor.

Our ability to work with projected changes of seasonal mean precipitation that may be of the order of 5 to 10% is fraught with difficulties. First, virtually all in-situ operational measurements of precipitation, the data we use to measure climate variations, have significant measurement biases due to a number of factors, e.g. evaporation losses, aerodynamic losses around the precipitation gauge, wetting losses inside the gauge, etc. (Karl et al., 1992). These biases are exposure and weather dependent. Moreover, the biases change over time as instruments change as illustrated in Figure 2. Second, just as knowledge of a seasonal mean temperature is often insufficient to project its impact on a variety of systems, changes in the short-term temporal variability of precipitation cannot be ignored. Extreme precipitation events and their frequency determine the climatology of floods and droughts. At the present time, there is not a clear picture that emerges with respect to systematic changes of temporal precipitation variability. Projected changes appear to be model and regionally dependent (IPCC, 1992). Lastly, as the temperature warms, the form of precipitation can change. This has important implications with respect to the water balance. The source term of the water balance equation (frozen versus liquid) can significantly affect the timing and distribution of water availability, and the diurnal changes of temperature affect the evaporative losses from the soil, lakes, and reservoirs.

In order to obtain more realistic estimates of the projected changes of day-to-day precipitation variability due to increased concentrations of greenhouse gases a number of statistically-based procedures have been developed to interpret the large and local-scale state of the AOGCMs free atmosphere with respect to the precipitation received at the surface. These statistical approaches (Wigley et al., 1990; Karl et al., 1990; Von Storch et al. 1991) can improve our ability to project more realistic precipitation simulations, but they too, are limited by our ability to project the state of the atmosphere in the future as well as the bounds of the data sample used to develop the

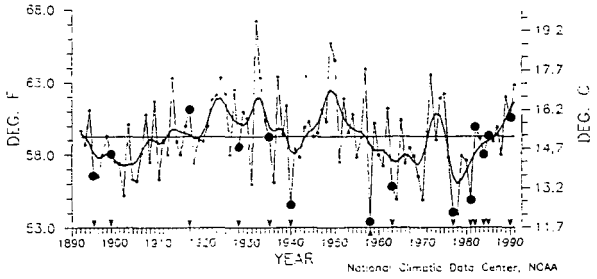

Figure 1 Mean winter temperature area-averaged over the state of Florida. Large bold dots indicate those years which had freezes so severe that extensive damage was inflicted upon both the citrus crop and the trees that bore the fruit.

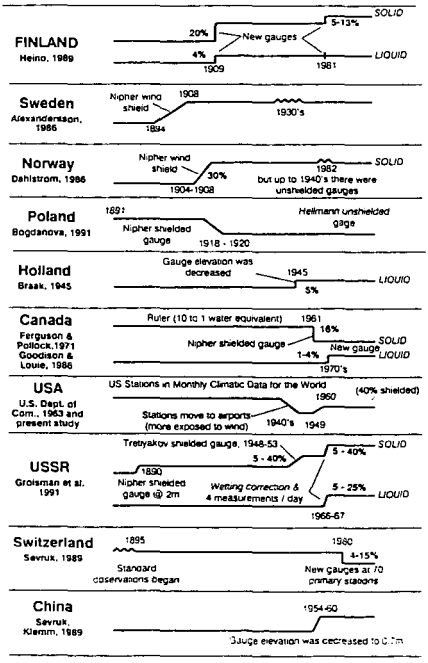

Figure 2 Changes of precipitation measurement which have led to biases in time series of precipitation data within national precipitation networks across the globe.

statistics. Because of these limitations efforts are now underway to mesh large-scale and meso-scale models to obtain a better understanding of the impact of large-scale changes at shorter time and smaller space-scales (Giorgi and Mearns, 1991).

CONCLUSIONS

Several steps need to be taken to reduce the uncertainties now associated with both understanding why and how climate has changes especially as related to the greenhouse effect.

1) Improve the reliability, continuity, and resolution of existing observations and data bases.

2) Expand the observational data base necessary to incorporate the physics necessary to include additional forcing functions, not now included in atmosphere/ocean GCMs. This includes those observations which may lead to a better understanding of anthropic and natural aerosol generation, and their subsequent interaction with water vapor, cloudiness, and the solar radiation budget.

3) Develop more sophisticated analysis techniques to assess the consistency or inconsistency of model projection with observed changes.

REFERENCES

Alexandersson, H. 1986: A homogeneity test applied to precipitation data. *J. Climatol.*, 6, 661-675.

Bogdanova, E.G., 1991: Personal Communication, Main Geophysical Observatory, St. Petersburg, USSR.

Braak, C. 1945: Invloed van den vind op regnwaarnemingen. Koningklijk Nederlandsch. Meteorol. Inst. No. 102. Medeelingen en verhandelingen, No. 48 (102), 7-74.

Bradley, R.S. and P.D. Jones (eds.), 1992: Climate Since A.D. 1500, Routledge Press, London and New York, 692 pp.

Baker, D.J. and Barnett, T.P., 1982: Possibilities of detecting CO_2-induced effects. In, Proceedings of the Workshop on First Detection of Carbon Dioxide Effects, DOE/CONF-8106214 (H. Moses and M.C. MacCracken, Coordinators), Office of Energy Research, U.S. Dept. of Energy, Washington, D.C., 301-342.

Barnett, T.P. and Schlesinger, M.E., 1987: Detecting changes in global climate induced by greenhouse gases. J. Geophys. Res, 92, 14,772-14,780.

Charlson, R.J., S.E. Schwartz, J.M. Hales, R.D. Cess, J.A. Coakley, Jr., J.E. Hansen, and D.J. Hofmann, 1992: Climate Forcing by Anthropogenic Aerosols. Science, 255, 423-430.

Dahlström, B. 1986: The improvement of point precipitation data on an operational basis. Nordic Hydrological Programme, NHP-Report No. 17, 86 pp.

Ferguson, M.L., and D.M. Pollock. 1971: Estimating snowpack accumulation for runoff prediction. Proc. of Canadian Hydrology Symposium No. 8 "Runoff from snow and ice," Quebec City, 1971, 7-27.

Folland, C.K., T.R. Karl and K. Ya. Vinnikov, 1990b: Observed climate variations and change. In: Climate Change, the IPCC Scientific Assessment, J.T. Houghton, G.J. Jenkins and J.J. Ephraums (Eds.) WMO/UNEP/IPCC, Cambridge University Press, pp 195-238.

Giorgi, F. and L.O. Mearns, 1991: Approaches to the simulation of regional climate change: A review. J. Geophys. Res., 29, 191-216.

Groisman, P.Y., V.V. Koknaeva, T.A. Belokrylova, and T.R. Karl. 1991: Overcoming biases of precipitation measurement: A history of the USSR experience. *Bull. Amer. Meteor. Soc.*, 72, 1725-1733.

Hansen, J.E. and A.A. Lacis, 1990: Sun and dust versus greenhouse gases; an assessment of their relative roles in global climate change. Nature, 346, 713-719.

Hansen, J., A. Lacis, R. Ruedy and M. Sato, 1992: Potential cliamte impact of Mount Pinatubo eruption. Geophys. Res. Lett., 19, 215-218.

Hansen, J., and S. Lebedeff, 1987: Global trends of measured surface air temperature. J. Geophys. Res., 92, 13345-13372.

Hansen, J., and S. Lebedeff, 1988: Global surface temperatures: update through 1987. Geophys. Res. Letters., 15, 323-326.

Hansen, J., Fung, I., Lacis, A., Rind, D., Lebedeff, S., Ruedy, R. and Russell, G., 1988: Global climate changes as forecast by Goddard Institute for Space Studies three-dimensional model. J. Geophys. Res., 93, 9341-9364.

Heino, R. 1989: Changes of precipitation in Finland. Proc. of conference on climate and water, Helsinki, Finland, 11-15 September, 1989. Ed., Vation Painatuskeskue, 111-120.

IPCC, 1990: Climate Change, The IPCC Scientific Assessment. J.T. Houghton, G.J. Jenkins and J.J. Ephraums (Eds.). Cambridge University Press, UK. 365 pp.

IPCC, 1992: Scientific Assessment of Climate Change, 1992 IPCC Supplement. Cambridge University Press, UK. 200 pp.

Jones, P.D., 1988: Hemispheric surface air temperature variations: recent trends and an update to 1987. J. Clim., 1, 654-660.

Jones, P.D., S.C.B. Raper, R.S. Bradley, H.F. Diaz, P.M. Kelly and T.M.L. Wigley, 1986a: Northern Hemisphere surface air temperature variatione, 1851-1984. J. Clim. Appl. Met., 25, 161-179.

Jones, P.D., S.C.B. Raper, R.S. Bradley, H.F. Diaz, P.M. Kelly and T.M.L. Wigley, 1988b: Southern Hemisphere surface air temperature variations, 1851-1984. J. Clim. Appl. Met., 25, 1213-1230.

Karl, T.R., R.R. Heim, Jr. and R.G. Quayle, 1991a: The greenhouse effeect in Central North America: If not now when? Science, 251, 1058-1061.

Karl, T.R., G. Kukla, V.N. Razuvayev, M.J. Changery, R.G. Quayle, R.R. Heim, Jr., D.R. Easterling and C.B. Fu, 1991b: Global warming: evidence for asymmetric diurnal temperature change. Geophys. Res. Lett., 18, 2253-2256.

Karl, T.R., R.G. Quayle and P. Ya. Groisman, 1992: Detecting climate variations and change: new challenges for observing and data management systems. J. Clim. (In Press).

Karl, T. R., W.-C. Wang, M.E. Schlesinger, R.W. Knight and D. Portman, 1990: A method of relating general circulation model simulated climate to the observed local climate. Part I: Seasonal statistics. J. Climate, 3, 1053-1079.

MacCracken, M.C. and Moses, H., 1982: The first detection of carbon dioxide effects: Workshop Summary, 8-10 June 1981, Harpers Ferry, West Virginia. Bull. Am. Met. Soc., 63, 1164-1178.

Madden, R.A. and Ramanathan, V., 1980: Detecting climate change due to increasing carbon dioxide. Science, 209, 763-768.

Manabe, S., M.J. Spelman and R.J. Stouffer, 1992: Transient responses of a coupled ocean-atmosphere model to gradual changes of atmospheric CO_2. Part II: Seasonal response. J. Clim., 5, 105-126.

Manabe, S., R.J. Stouffer, M.J. Spelman and K. Bryan, 1991: Transient responses of a coupled ocean-atmosphere model to gradual changes of atmospheric CO_2. Part I: Annual mean response. J. Climate, 4, 785-818.

Robock, A., R.P. Turco, M.A. Harwell, T.P. Ackerman, R. Andressen, H.-S. Chang and M.V.K., Sivakumar, 1991: Use of general circulation model output in the creation of climate change scenarios for impact analysis. (Unpublished manuscript).

Sevruk, B., and S. Klemm, 1989: Catalogue of national standard precipitation gauges. Instruments and Observing Methods, Report No. 39, 50pp., Geneva, Switzerland.

Vinnikov, K. Ya., P. Ya. Groisman and K.M. Lugina, 1990: Empirical data on contemporary global climate changee (temperature and precipitation). J. Clim., 3, 662-677.

Von Storch, H., E. Zorita and U. Cubasch, 1991: Downscaling of global climate estimates to regional scales: An application to Iberian rainfall in wintertime. Max Planck Inst. Meteor. Report No. 64, Hamburg.

Wigley, T.M.L., P.D. Jones, K.R. Briffa and G. Smith, 1990: Obtaining sub-grid-scale information from coarse-resolution general circulation model output. J. Geophys. Res., 95, 1943-1953.

THE USE OF CLIMATE MODELS IN FORECASTING FUTURE CLIMATE CHANGE

Anthony J. Broccoli
Geophysical Fluid Dynamics Laboratory/NOAA
Princeton University
P. O. Box 308
Princeton, NJ 08542

ABSTRACT

For more than 25 years, climate models have been used to investigate the impact of greehouse gases on the earth's climate. These models, which have become increasingly comprehensive, have provided much of the scientific evidence regarding the potential changes in climate due to anthropogenic increases in greehouse gases. Recently, the advent of more realistic models of the coupled atmosphere-ocean system have made it possible to simulate the response of climate to gradually increasing greehouse gases. Is it appropriate to regard the output from such models as forecasts of future climate change? The answer depends on a careful analysis of the mechanisms affecting climate and the ability to incorporate them faithfully in climate models.

DESIGN OF CLIMATE MODEL EXPERIMENTS

Climate models have been used to investigate the impact of greenhouse gases on the earth's climate for more than 25 years. The state of the art has progressed dramatically during this period, from relatively simple one-dimensional models of radiative-convective equilibrium to three-dimenional models of the coupled atmosphere-ocean system. The development of a hierarchy of climate models for the study of climate change due to anthropogenic increases in greenhouse gases has led to a variety of research studies. Most of these can be separated into three categories based on their experimental design. Using terminology taken from the recent Intergovernmental Panel on Climate Change (IPCC) Scientific Assessment (Houghton et al.[1]), these are equilibrium response studies, transient response studies, and time-dependent response studies. Experiments in the last category will be the primary subject of this paper.

Time-dependent response studies use models of the coupled atmosphere-ocean system to simulate a change in climate in response to gradually increasing greenhouse gas concentrations. Such gradually increasing concentrations are similar to what is occurring in the real climate system. A number of time-dependent response studies have been performed, primarily using general circulation models of the atmosphere coupled with dynamical ocean models. An important result from these studies has been the identification of important regional variations in the rate of warming due to increasing greenhouse gases. In addition, these studies have allowed estimates to be made of the rate of warming in response to an increase in greenhouse gas concentrations with a rate similar to that occurring presently. But can these estimates be regarded as forecasts of climate change? To answer this question, it is necessary to consider the mechanisms influencing climate and the ability to represent them faithfully in climate models.

FACTORS INFLUENCING CLIMATE

A variety of external factors can be important on the time scales relevant to anthropogenic climate change (i.e., years to decades). These include atmospheric greenhouse gas concentrations,

volcanic aerosols, variations in solar radiation, and anthropogenic sulfate aerosols. In addition, internal variability inherent to the climate system may produce variations in climate comparable in magnitude to some of the externally forced variations.

A number of greenhouse gases have been increasing in concentration since the pre-industrial era as a result of human activities. These gases, which include carbon dioxide, chloroflourocarbons, methane, and nitrous oxide, produce a tropospheric heating effect by increasing the infrared opacity of the atmosphere. The increases of all of these gases provide an enhancement of the heating associated with the natural greenhouse effect.

Large volcanic eruptions can inject sulfur dioxide gas into the stratosphere, forming sulfuric acid aerosols that can scatter incoming solar radiation, increase planetary albedo, and thus have a significant impact on the earth's radiation balance. The combination of a reduction of total solar radiation with the warming due to the thermal infrared effects of the aerosols results in a small net cooling effect at the earth's surface, which can persist for 1 or 2 years following an eruption.

Variations in solar radiation are capable of producing changes in changes in climate. Changes in the latitudinal and seasonal distribution of insolation associated with periodic variations in the earth's orbital parameters are believed to be responsible for the glacial-interglacial cycles of the Quaternary era. These orbital variations have time scales of 10^4 to 10^5 years. Much less is known about changes in insolation on shorter time scales (10 to 10^3 years), since precise monitoring of solar irradiance has existed for little more than a decade. However, some evidence has been offered for irradiance variations of up to 0.5 percent on these time scales.

Anthropogenic sulfur emissions may also have potential climatic effects through two mechansims. A direct effect is the scattering of incoming solar radiation by sulfate aerosols. However, this effect may not necessarily result in an increase of planetary albedo, depending on other factors such as the albedo of the underlying surface and the solar elevation angle. An indirect effect is the potential of aerosol particles to increase cloud albedo by acting as cloud condensation nuclei. Both of these effects are extremely difficult to assess quantitatively, although recent work suggests a net cooling effect at the surface.

In addition to variations in climate resulting from these external forcing factors, substantial variability appears to occur in the climate system even in the absence of external forcing, spanning a wide range of time scales. Much of this variability involves interactions between the atmospheric and oceanic components of the climate system. The well-known El Nino- Southern Oscillation phenomenon is an example, with climatic effects in widespread areas around the globe. More recently, models of the coupled ocean-atmosphere system have displayed variability of oceanic overturning (with accompanying atmospheric variations) on interdecadal time scales. On shorter time scales, climate model experiments have demonstrated that substantial variability can occur even without changes in the ocean. Interactions with the land surface and internal atmospheric dynamics are likely sources of this variability.

REPRESENTATION IN CLIMATE MODELS

The extent to which these external forcing factors can be incorporated in climate model calculations is crucial in determining whether model output can be used as forecasts of future climate change. Two conditions must be met for each to be successfully incorporated. First, we need to

know how to model the physical effect of that factor. Second, we need to know how that factor varies in time. For hindcasts (i. e., attempts to reproduce the variations in climate up to the present) only past variations in forcing need be known; for forecasts, both past and future variations are necessary. In this section, the state of our current ability to represent the external forcing factors in hindcasts and forecasts will be examined.

Greenhouse gases seem by far to be the external forcing factor most readily represented in a climate hindcast. The development of more accurate radiative transfer models has enabled reasonable estimates of the radiative effects of the various greenhouse gases as a function of their atmospheric concentration. Despite some uncertainties in the basic spectroscopic data for many gases (particularly the chloroflourocarbons) and differences among the radiative transfer models, the radiative effects of greenhouse gases is a relatively mature and well-understood component of the climate modeling problem. Evidence of past increases in concentration of the various greenhouse gases are readily available from two sources. In recent decades, direct measurements have been taken at locations relatively free of local contamination (e. g., CO_2 at Mauna Loa). Records from earlier times have been extracted from ice cores in Greenland and Antarctica. As snow is transformed into glacial ice, air becomes trapped as bubbles in the ice. These bubbles contain fossil air, which can be dated based on ice accumulation rates.

Representing the past history of the other forcing factors is much more problematic. In principle it should be relatively straightforward to model the effect of volcanic aerosols in the stratosphere, although in practice it can be difficult do so quantitatively. Measurements have only been available in recent years. Historical records provide clues to earlier eruptions, although it can be quite difficult to reconstruct the sulfur content of the erupted material and whether or not it reaches the stratosphere. This is important, since the sulfate aerosol particles have much longer lifetimes in the stratosphere than in the troposphere. Increased acidity in glacial ice cores has also been linked to sulfate aerosol-producing eruptions, but again there are difficulties in interpreting these proxy data. Thus reconstructions of past volcanic activity often differ from each other.

For changes in solar irradiance, the difficulty is in documenting past changes in this quantity based on the short period of precise observations. These have indicated that irradiance varies in conjunction with the 11-year cycle of solar magnetic activity (i. e., the sunspot cycle), with a total variation of approximately 0.1 percent. There has been speculation that variations in solar output may occur on longer timescales. Proxies of solar magnetic acitivity, such as sunspot numbers, carbon-14, and beryllium-10, indicate substantial variations on time scales of decades to centuries. Observations of solar radius also show variations on these time scales. There has been some suggestion that these changes may be correlated with solar irradiance, with variations of as large as 0.5 percent. Substantial work is underway to explore possible mechanisms for such variations, including physically-based modeling and astronomical studies of Sun-like stars. But at this time, little evidence exists to quantify them.

The radiative properties of tropospheric sulfate aerosols resulting from industrial activity contribute to substantial difficulty in representing them in climate model hindcasts. Large uncertainties exists in both their direct and indirect effects. Because of their relatively short lifetimes in the troposphere (days to weeks), the distribution of sulfate aerosols is not as uniform in space and time as those of the greenhouse gases, since their sources are confined to the continents, particularly the densely populated and industrialized areas. This adds another complication to including

their effects in climate model calculations, even though there are some estimates of the history of sulfur emissions which could be used in chemistry/transport models to estimate aerosol concentrations.

Many of the problems in representing the effects of these external forcing factors are exacerbated when forecasting future climate. Future changes in greenhouse gas concentrations depend on the emission rates of the gases and biogeochemical processes operating in the atmosphere-ocean system. Since future emission rates will be affected by economic conditions, technology, and public policy, substantial uncertainty exists as to their magnitude. To account for this, the IPCC used a variety of scenarios of future greenhouse gas concentrations, yielding a range of time-dependent climate change estimates. This method may be the only reasonable way to quantify the uncertainty inherent in estimates of future greenhouse gas concentrations. Projecting future concentrations of anthropogenic sulfate aerosols involves similar difficulties, including the added complication that their spatial patterns can be affected by changes in the geographical distribution of sulfur emissions.

Estimating future variations in solar radiation would probably require such a reconstruction of past variations along with evidence of a periodic nature that can be extrapolated forward in time. Until the causes of solar variability are better understood and the variations in solar output are better quantified, this remains a daunting problem. The obvious difficulty of forecasting future volcanic eruptions makes it impossible to include this effect in climate change projections more than a year or two in length. Fortunately, the climatic effects of an individual eruption are felt for no more than a few years, so only a period of frequent large eruptions would influence temperature on decadal time scales.

In making forecasts (or hindcasts) of climate change, the internal variability inherent in the climate system can be an additional complicating factor. While the coupled atmosphere-ocean climate models used for time-dependent response studies have shown an ability to simulate such variability in the frequency domain, there is no reason why the time variations in climate associated with this variability should by synchronous with those in the real climate system. While deterministic predictions of some of this variability may be possible given accurate specification of initial conditions in the atmosphere and ocean (as evidenced by reports of skillful forecasts of the El Nino phenomenon), further research is required to explore this possibility. For the time being, the manifestations of internal variability must of necessity be regarded as climatic "noise" that can obscure the climate variations associated with external forcing factors.

ARE CLIMATE MODEL SIMULATIONS FORECASTS?

In the time-dependent response studies that have been conducted to date, the impact of increasing greenhouse gases typically has been the only external forcing included. The time-dependence of this forcing (i. e., the time series of greenhouse gas concentations) has generally been idealized. In some experiments, the CO_2 concentration (taken as a surrogate for all greenhouse gases) has been increased at an annual rate approximately equivalent to the current rate of increase. In others, a range of future growth rates for atmospheric greenhouse gas concentrations have been used to yield a series of future climate change scenarios, in an effort to explicitly incorporate some of the uncertainty associated with future emission rates.

Representing only the greenhouse gas forcing (and doing so in an idealized manner) may have

a number of interesting consequences for the interpretation of these experiments. The idealized time-dependent greenhouse gas forcing differs from that actually observed. Thus quantitative comparisons of simulated and observed temperature changes may be of limited value. This is of particular concern given the possibility that changes in the other external forcing factors, along with internal variability, may also have influenced global temperature during this period. Since the increase in greenhouse gas forcing has been relatively small until the past few decades and the ocean should delay the response of the climate system, the effect of this forcing over the historical record may be comparable in magnitude to those associated with other factors. Thus there is no reason to expect quantitative agreement between the simulated and observed evolution of global temperature during this period.

For estimates of future climate change, these difficulties could become somewhat better resolved. For the range of emission scenarios considered by IPCC, the greenhouse gas forcing is expected to grow well beyond the plausible contributions of volcanic aerosols and solar variability during the next century. Thus the greenhouse gas effect would be expected to become dominant over that time, such that an estimate of its magnitude could be a good approximation of a climate change forecast. However, the effect of anthropogenic sulfate aerosols is a complicating factor. Because the sulfate forcing has been hypothesized to have the opposite sign and could also increase as a result of economic growth, some fraction of the greenhouse gas effect may be counteracted as a result.

Thus to increase the ability to make climate forecasts on time scales from decades to centuries, it seems important that the anthropogenic sulfate effect be better quantified. Much work also needs to be done on the effects of volcanic aerosols, solar radiation variations, and internal variability of the atmosphere-ocean system. Concurrently, progress in climate modeling is also necessary to narrow the range of uncertainty regarding climate feedback mechanisms that can amplify or reduce the direct effects of external forcing. Better observations of oceanic variations and processes may prove useful in understanding the role of the oceans. In the meantime, caution is required when interpreting the results from climate modeling experiments.

ACKNOWLEDGMENTS

The efforts of Working Group 1 of the Intergovernmental Panel on Climate Change[1] in compiling a comprehensive review of research reagrding this topic have been very helpful to me. I recommend their book as a starting point for those interested in this issue as it contains references for much of the information used in preparing this paper. I also thank S. Manabe and R. J. Stouffer for their comments.

REFERENCES

(1)Houghton, J. T.; Jenkins, G. J.; Ephraums, J. J.; eds. Climate Change: The IPCC Scientific Assessment, cambridge University Press, 1990, 365 pp.

PROFILE NOT AVAILABLE AT TIME OF PUBLICATION

THESE PAGES INTENTIONALLY LEFT BLANK

PREPRINT NOT AVAILABLE AT TIME OF PUBLICATION

THESE PAGES INTENTIONALLY LEFT BLANK

GLOBAL CLIMATE CHANGE:
THE UNCERTAINTIES AND THE CONTROVERSIES

Richard A. Kerr
Research News section, Science
1333 H St., N.W., Washington, DC 20005

Keywords: global change, greenhouse, uncertainties

ABSTRACT

Uncertainties abound with respect to global climate change. Records of past climate change are imperfect because measuring devices and practices have changed and because urban areas have encroached on observation sites. Past and future climate change may be affected to uncertain degrees by volcanic eruptions, solar variability, and ocean variability. Global warming itself can interact with numerous Earth systems to produce enhanced warming--positive feedbacks--and diminished warming--negative feedbacks. Potential feedbacks present some of the greatest uncertainties about global warming. Controversy arises from the two ways of treating these uncertainties: viewing them as a reason for further study, before taking action that may be unnecessary, or as a justification for action that may avert serious if not catastrophic consequences at low or modest cost.

Much of the United States was hot and dry in the summer of 1988. So when NASA climate expert James Hansen claimed that global warming was here, intensified public concern became inevitable. But in parts of the scientific community there was just as inevitable a response--skepticism. Some experts not only saw no evidence of greenhouse warming, they saw no clear prospect of a significant warming in the future.

And yet over the past 4 years, the tempest has abated, scientific support for a middle ground has solidified, and even the Bush Administration seems to be dropping its unqualified opposition to action on the greenhouse threat. In part, the administration is hearing from the scientific community that the consensus is as strong as ever--greenhouse warming does pose a serious threat for the planet's future. Indeed, a four-agency memo recently leaked to the press hews closely to the latest assessment of greenhouse science released recently by the Intergovernmental Panel on Climate Change (IPCC). Echoing the IPCC, the memo concedes that continued increases in greenhouse gases will likely lead to ''significant changes in the climate system.''

The administration memo cited ''a consensus view of a broad range of scientists, including most U.S. scientists,'' and quoted likely limits to greenhouse warming due to a doubling of carbon dioxide as a modest 1.5ÀC at the lower end and a hefty, if not catastrophic, 4.5Å at the upper end. That's the same range that National Academy of Sciences panels have been coming up with for the past 15 years. Not that there is unanimity about greenhouse warming. Academy reports come from highly competent but very small groups. The IPCC reports each involved dozens of chapter authors, hundreds of reviewers, and a half dozen rewrites, but dissenters are still scarce in these circles. In the media they number less than half a dozen, although they are usually paired with Hansen, an environmentalist, or a mainstream scientist, giving the appearance of a raging controversy between implacable opposites. The true proportions of

the debate are difficult to pin down, but there is no doubt that a consensus--in the sense of a majority opinion--exists in the scientific community.

Eventually, a quiet majority found fault with both extremes of the public greenhouse debate. For example, when Hansen, director of NASA's Goddard Institute for Space Studies in New York City, argued that the half-degree warming of the past century was driven by the steady increase of greenhouse gases, most greenhouse researchers eventually concluded that although the warming is consistent with an intensifying greenhouse, it is not clearly a result of it.

At the other extreme of the debate, questions were raised about temperature trends in general. If Earth is getting warmer, why is Minneapolis getting colder? Why isn't the United States getting warmer? Is the global warming of the past century even real? Most climatologists see no fundamental problems with the temperature trends seen so far. The lack of clear warming trends at every spot on Earth does not mean greenhouse warming is not at work, they say, because temperature varies too much to see a clear warming in every area at this early stage, even if the area is as large as the United States. And, contrary to a few critics, the globe as a whole has already warmed several tenths of a degree, even after accounting for warming due to urbanization. That a global warming is not obvious in the satellite temperature record does not surprise climatologists either. This record covers only the past decade, when temperatures were uniformly high after jumping upward in the 1970s. Climatologists are intrigued by the tendency of the warming, for the time being at least, to occur predominately during the nighttime, when presumably the least stress would be placed on living things.

The main problem with the temperature records is that greenhouse warming carries no distinctive signature that could have been clearly distinguished at this point from natural climatic variability. But if mainstream estimates of future greenhouse warming are anywhere near correct, most researchers feel, the warming should become obvious during the next decade or two as it overwhelms the coolness of the oceans and the protective effect of pollutant hazes that reflect some sunshine back to space.

Other uncertainties have been cited as justifications for complacency about the greenhouse. Could the sun possibly dim slightly during the next century and counteract any greenhouse warming? Maybe, maybe not. So many claims of a connection between the sun and climate have come and gone that most scientists believe no firm link of significant magnitude has been demonstrated. And those who do dabble in the field can't even agree whether the sun will dim or brighten in coming years. Won't plants just love the warmer, generally more moist greenhouse world rich in the atmospheric carbon dioxide that plants need for growth? Won't plants then store away the extra carbon dioxide we're putting in the atmosphere? Not necessarily. Greenhouse experiments at elevated concentrations of carbon dioxide have shown increased growth and carbon storage, but terrestrial ecologists are at a loss to predict how complex ecosystems will react. Natural plant communities might help out, but only until they get their fill of carbon, or rapid climate change might be so disruptive that the biosphere could become a net source of carbon dioxide rather than a sink. Most researchers view either salvation as dubious justification for skepticism.

Other uncertainties have attracted more serious attention within the climate community. In 1989, prominent meteorologist Richard Lindzen of MIT proposed that the computer climate models predicting a few degrees' warming for a doubling of carbon dioxide misrepresented the way that the atmosphere controls the abundance of water vapor--a greenhouse gas--in the upper troposphere. If a warming atmosphere tended to dry the upper troposphere, as Lindzen suggested, that could limit warming to a few tenths of a degree--that

is, nothing to worry about (Science, 1 December 1989, p. 1118). Lindzen argued that the greenhouse effect has an inherent limit--indeed, one that has nearly been reached, due to the water vapor and other natural greenhouse gases that already warm the atmosphere by 33ÀC. Such a renegade proposal coming from a prominent researcher made front page news and prompted considerable new study. But after several years of scrutiny, most climatologists would agree that Lindzen has not proven his case. Among the strongest evidence against Lindzen's self-limiting greenhouse are satellite and balloon observations showing that water vapor in the upper troposphere increases, not decreases, whenever and wherever the lower troposphere is warmer--in summer versus winter, in the warm western Pacific versus the cooler eastern Pacific.

Most scientists in the mainstream readily admit that greenhouse science is still pervaded by uncertainties. The single largest uncertainty in the climate models is the behavior of clouds as the world warms. In one model, created by researchers at the United Kingdom's Meteorological Office, the warming due to a doubling of carbon dioxide dropped from 5.2ÀC to 1.9ÀC when the computer was switched from one ''equally plausible'' way of rendering clouds to another. Getting clouds right will take 10 to 20 years because researchers must understand better how clouds work, not just increase the speed of their computers, and then get computer clouds to act like the real ones. In addition, the interconnected system of ocean-atmosphere-biosphere has a host of ways of changing its behavior in response to warming that might in turn affect global temperature. Ice and snow, for example, might recede, exposing darker ground or ocean that would absorb more sunlight and accelerate the warming. Other possible feedbacks involve everything from methane production in wetlands to increased decomposition of soil organic matter. Most feedbacks that researchers have been able to imagine tend to enhance any warming. And most are not included in present climate models.

Uncertainties abound, but climate researchers see some constraints on the uncertainties. First there is the basic physics of the greenhouse, which is already responsible for warming Earth 33 degrees C through water vspor and carbon dioxide. This physics must continue to operate as humankind's enhancement of the greenhouse since 1765 is doubled during the next 35 year, assuming no action is taken to avoid it. And then there is the performance of climate models. They are rudimentary, everyone agrees, but their behavior bears a considerable resemblance to reality. They produce reasonable seasonal changes. They do not wildly overreact to injections of volcanic debris or small changes in solar output. With all this in mind, the IPCC has twice now accepted the 1.5- to 4.5-degree warming for a doubling of carbon dioxide as sound, characterizing their confidence in these numbers as falling midway between "virtual certainty" and "low confidence."

Given the uncertainties, some researchers are arguing for a delay of perhaps 10 years in reining in greenhouse emissions while the science settles down. If the climate system turns out to be relatively insensitive to added greenhouse gases, they reason, no harm will be done, and if it is highly sensitive, the effort to avert rapid warming will be so great that a mere 10-year delay will not make it perceptibly more harsh. Another line of reasoning is that society can adapt to climate change reasonably well and with less expense than required to limit the emission of greenhouse gases.

But environmentalists and many scientists can't agree with even this modest wait-and-see approach. Even 10 years of increasingly faster computers won't narrow the uncertainties enough, they say. A decade will see only the beginning of crucial observations of the behavior of oceans and clouds. The 1990 IPCC report foresaw the cloud and ocean uncertainties narrowing only in the 10- to 20-year range, by which point the globe might be committed to major climate change. And the ability to adapt will vary greatly from society to society;

natural ecosystems could be even harder pressed to adapt to rapid climate change.

The other reason for not waiting is uncertainty itself, some say. The possibility that greenhouse-induced change could turn out to be much more dramatic than any model predicts is spooking a generation of Earth scientists who remember the nasty surprise sprung on stratospheric ozone. No one foresaw the Antarctic ozone hole or accelerated ozone losses at mid latitudes due to natural atmospheric particles. Greenhouse specialists, too, are wondering what they might have overlooked. One possibility is an abrupt change in ocean circulation, although some studies have now discounted that idea. Or perhaps unanticipated feedbacks from polar ice caps or green plants, other workers venture.

The philosophy that many scientists are now espousing amounts to buying some insurance--in the form of no-cost or low-cost reductions in greenhouse gas emissions. Even some greenhouse skeptics, if pressed, would concede the prudence of no-cost measures that can be supported by other justifications. Greater energy efficiency seems a reasonable goal in a country that consumes energy prolifigately while importing half of its oil. While such measures fall far short of complete coverage, advocates admit, such tie-in steps seem prudent against the possibility that the higher predictions of global warming turn out to be right or some nasty surprise is lurking in the greenhouse.

REFERENCES

J.T. Houghton et al., Eds., Climate Change 1992: The Supplementary Report to the IPCC Scientific Assessment (Cambridge University Press, 1992).

W.W. Kellogg, "Response to skeptics of global warming,'' Bull. Am. Met. Soc. 74, 499 (1991).

R.S. Lindzen, "Some coolness converning global warming," Bull. Am. Met. Soc. 71, 288 (1990).

Greenhouse Gas Emissions from Fossil Fuel Use and Technical Approaches to their Control

John A. Ruether, Dennis N. Smith, and Nagaraja S. Rao[1]
U.S. Department of Energy
Pittsburgh Energy Technology Center
Pittsburgh, PA 15236

1. Burns and Roe Services Corp.

Keywords: radiative forcing, greenhouse gas, fossil fuel

Introduction

Radiative trapping or forcing by so called greenhouse gases in the atmosphere causes the mean surface temperature of Earth to be 33 K higher than it would be in their absence. While the greenhouse effect is thus necessary for life as we know it, there is concern that additional unwanted warming may occur as a result of increasing concentrations of greenhouse gases. Analysis of air bubbles trapped in glacial ice shows that starting roughly with the onset of industrialization in the late 18th and early 19th centuries, the concentration of all greenhouse gases found in nature began to increase[1]. Through 1991 the concentration of CO_2, the gas causing the greatest amount of radiative forcing, had increased by over 25% from its preindustrial value. The other main greenhouse gases that occur in nature, CH_4 and N_2O, exhibit similar increases since the early 1800s. While the timing and extent of global warming that may result from increased concentrations of greenhouse gases is uncertain, it is prudent to understand the main sources of anthropogenic greenhouse gases and the conditions governing their release. All three of the principal greenhouse gases existing in nature are released in the course of fossil fuel use, and for all three, fossil fuel emissions are a significant component of total anthropogenic emissions[1]. In this paper the emissions of CO_2, CH_4, and N_2O in the contemporary United States due to use of the fossil fuels natural gas, oil, and coal are presented. Details of the calculations will be given in a subsequent publication[2]. The relative importance of each of these gases for radiative forcing is shown. Some technologies under development that can reduce emissions of these trace gases per unit of useful heat or work obtained are discussed.

The amount of radiant energy a mole of a particular greenhouse gas absorbs during its atmospheric lifetime depends on its lifetime and its absorption strength, integrated over all active wavelength bands. An index called the global warming potential, or GWP, has been developed to compare the lifetime effect of one mole (or one kg) of a particular greenhouse gas to that of a similar amount of CO_2. The GWP for trace gas i is defined[3]:

$$GWP_i = a_i \int_0^T c_i(t)\, dt \;/\; a \int_0^T c(t)\, dt \qquad (1)$$

Here a_i is an absorption coefficient, c_i is concentration in mass or molar units, and t is time. Unsubscripted values refer to CO_2. The average atmospheric

lifetimes of the trace gases are as follows: CO_2, 100-120 y; CH_4, 10-12 y; N_2O, 150-180 y. When eq. 1 is integrated over a time T of 100 y, the computed GWPs for CH_4 and N_2O are 7.6 and 290, respectively, expressed on a molar basis[3].

1. Emissions of CO_2

For complete combustion of any fuel, the specific carbon emission, or carbon emission factor, defined as g C as CO_2 per MJ heat released, is determined by its composition and heating value. It is preferable to use the lower heating value (LHV) for the calculation, since in most applications water produced in combustion leaves the process as a vapor. A correlation of heating value as a function of elemental composition of a fuel shows how the carbon emission factor depends on fuel composition[4]. Although developed specifically for coal, it describes oil and natural gas as well.

$$\Delta H_L = 341\ C + 1102\ H + 68.4\ S - 15.3\ A - 119\ (O + N) \quad (2)$$

Here, C,H,S, and (O+N) are the percentage of elements and A is ash or other inert by weight on a moisture free basis. The heating value is in J/g (LHV). It is seen that on a weight basis, hydrogen is the component with the largest energy content. Carbon is next largest, but it figures in the numerator as well as denominator of the expression for carbon emission factor. Oxygen and nitrogen have negative values because their presence in a fuel causes it to be partially oxidized. For coal, the combined effect of C, H, and O dependence causes the carbon emission factor to go through a minimum with the rank of hv bituminous.

Natural Gas

Consumption of natural gas in the U.S. in 1989 was 481 billion m^3 (20.3 EJ (HHV)). To convert this figure into CO_2 emissions requires information on composition of the gas at the wellhead and also at the burner tip. The difference between the two compositions is due to processing of the natural gas before transmission by pipeline. In processing, undesirable components including CO_2 are removed, the CO_2 being vented. The CO_2 produced due to flaring at the well must also be counted. Equations are developed for a carbon emission factor for natural gas that takes into account CO_2 emissions from venting and flaring. Application to domestically produced natural gas in 1989 yields an emission factor of 15.17 gC/MJ (LHV). Imported gas is analyzed similarly. Total CO_2 emissions in 1989 from consumption of natural gas is estimated to be 278.2 M tonne C.

Oil

In 1989, total crude oil processed in the U.S. was about 13.5 million barrels per day with the balance of liquid fuel consumption comprising natural gas liquids and imported refined products. A small fraction of petroleum (about 5 %) was exported. Total oil-based energy consumed in the U.S. was about 36 EJ. Emission factors for imported refined products and for crude oil (combined domestic production and imports) were computed and used to calculate carbon emissions by product class. The carbon emission factor for crude oil is 19.96 gC/MJ (LHV). The factor for products falls in the range 18.4-21.5 gC/MJ (LHV) depending on fuel composition. Total estimated CO_2 emissions from petroleum consumption in the U.S. during 1989 was 625.1 M tonne C.

Coal

The carbon content of coal per unit of heat content is found to vary with coal rank. Equation 2 has been used with composition data for U.S. coals to compute carbon emission factors by rank. The emission factor for lignite, the highest for all coal ranks, is 26.9 gC/MJ (LHV), about 8 % higher than for hvA bituminous, the lowest at 24.6 gC/MJ (LHV). The emission factors have been used with U.S. coal consumption by rank in 1989 to compute carbon emissions. In 1989 total U.S. coal production was 890 M tonnes, and coal consumption, expressed as energy, was 19.69 EJ (HHV). The largest carbon emission was from the bituminous grades, which represented 70% of total emissions, but supplied 74% of the total energy. Overall carbon emissions are calculated as 490.5 M tonnes C, which agrees well with the estimate of Marland[5], which was prepared without use of rank-specific carbon emission factors.

2. Emissions of CH_4

Methane emissions result from the production and distribution of oil and gas, and from the mining of coal. The losses from oil and gas operations are considered in three categories.

- Venting and flaring of methane occurring at the well head in the production of natural gas and oil.
- Production, gathering, and processing losses.
- Transmission and distribution losses.

The following discussion provides estimates of methane emissions from fossil fuel use in the U.S. during 1989.

Venting/Flaring Emissions in Oil/Gas Production

Venting and flaring of methane during production and processing of oil and gas is due to purposeful venting, routine maintenance, and system upsets and mishaps. There are insufficient data to apportion these emissions to oil or gas and to determine their composition. We estimate the fraction of methane in venting/flaring emissions to be 20%[6]. Based on total reported venting and flaring emissions for the U.S. in 1989, emissions of methane are estimated to be 0.41 Tg.

Production Losses

Leakage of methane occurs from field production and processing operations. These are primarily from fugitive emissions such as leaks from valves, pipes, compressors, and other equipment during normal operation of gas gathering, separation from condensate/oil, reinjection, and processing. The leakage rate varies between oil and gas wells and between offshore and onshore operations, due to significantly different processing equipment and conditions. Production losses of CH_4 are calculated to be 0.44 Tg.

Transmission/Distribution Losses

Natural gas is transported via high pressure pipeline throughout the U.S. with

local distribution networks consisting of low pressure delivery systems. Including low pressure distribution lines, the total length of pipe is estimated to be over 1.5 million miles. Several key components are subject to leakage: compressor shaft seals, valve stem packing, relief valve escapes, and flanged joints. Methane emissions from transmission/distribution losses is estimated as 1.77 Tg.

In addition to the three categories of CH_4 losses tabulated above, a relatively small amount is added for incomplete methane combustion. Allowing 0.5 g CH_4 per GJ adds an additional 0.009 Tg to 1989 emissions in the U.S. Total estimated CH_4 losses due to oil and gas operations thus sum to 2.63 Tg in 1989. By use of the GWP for CH_4 developed above, the importance of these losses for radiative forcing relative to the CO_2 emitted in the combustion of the oil and gas consumed in the U.S. in 1989 can be computed. The radiative forcing due to CH_4 emissions is 1.7% of that due to CO_2 from natural gas and oil combustion.

Methane Emissions as a Result of Coal Mining Activities

Correlations have been developed to relate CH_4 emissions to coal production by use of an overall emission factor. Such a factor, in m^3/tonne, expresses the ratio of total methane emissions to total coal production. Emission factors depend on in-place coal methane content. However, in addition to the gas contained in coal that is removed, methane may be released from adjacent gas-bearing strata and exposed but unmined coal during and after mining. Emissions from these sources are also included in computing an overall emission factor.

Overall emission factors have been developed by several workers in recent years and used to estimate CH_4 emissions from coal mining[6,7,8,9]. The emission factors fall in the range 6.02-11.77 m^3/tonne. Smith and Ruether calculate the emission factor as 7.74 m^3/tonne and estimate total CH_4 emissions in 1989 as 5.0 Tg[9]. The greatest fraction, 4.2 Tg, was due to deep mining operations. The importance of these emissions for radiative forcing relative to those of the CO_2 produced in coal combustion can be estimated as above. In 1989, U.S. production of deep mined coal was 357 million tonnes, and the radiative forcing of CH_4 emissions from deep mines was equivalent to about 9% of the forcing due to combustion of deep mined coal.

3. Emissions of N_2O

Production of N_2O in the course of fossil fuel use occurs via direct emissions and also via an indirect route from emissions of NO and NO_2, collectively called NOx. In the atmosphere, NOx are oxidized and return to the earth as acid precipitation. It is known that soil-bearing microbes reduce nitrates applied as fertilizer, resulting in N_2O emissions to the atmosphere. This mechanism presumably applies to nitrates originating as acid precipitation as well[13]. The extent of conversion of nitrate to N_2O by soil microbes is not well known, but Robertson estimated N_2O formation to be 1% of total fertilizer nitrogen, nitrate and ammonia[10]. If 1% of N as NOx is converted by microbes to N_2O, this is an important indirect route in fossil fuel combustion to N_2O.

About 30% of fossil fuels consumption in the U.S. is for the transportation sector with the remainder used in stationary sources ranging from residential heating to electric utility boilers. The N_2O emissions from the largest stationary sources, utility boilers, have been most studied. Early estimates of

N_2O emissions from stationary sources were erroneously high due to an artifact of the analysis procedure[11]. More recent results are given in Table 1 where both NOx and N_2O emissions are shown for a number of utility boilers firing all three fossil fuels[12]. It is seen that except for the circulating fluidized bed combustor, the greater contribution to N_2O emissions is due to the indirect route if the assumed 1% conversion of NOx to N_2O is correct. Because per molecule N_2O has two atoms of N while NOx has one, a 1% conversion of NOx to N_2O is equivalent to a direct N_2O emission of 0.5% of NOx. The right hand side of Table 1 shows the effect on NOx emissions of several technologies being developed for their control. The effect of these technologies on direct N_2O emissions is poorly understood at present.

The transportation sector produced 44% of total NOx emissions from fossil fuel use in 1989. It is thus an important producer of N_2O via the indirect route. It is also responsible for significant direct emissions of N_2O. These emissions vary with vehicle type and whether a catalytic converter is employed. (Catalytic converters increase N_2O emissions 10-fold[10].) On an energy basis, direct N_2O emissions from vehicles are substantially higher in general than those from high temperature stationary boilers. Due in large part to the unknown extent of indirect production of N_2O from NOx, estimates of N_2O production from fossil fuel use are highly uncertain. For instance, two recent estimates for global emissions were 0.3 Tg and 5.0 Tg[13,14].

4. Technologies to Reduce Greenhouse Gas Emissions

Carbon Dioxide

For a given fossil fuel, reduction of CO_2 emissions per unit of useful heat or work output requires increased energy conversion efficiency. Natural gas consumption is expected to rise in the U.S. in the 1990s primarily for increased power generation using gas turbines. The efficiency for power generation via simple cycle, e.g., gas turbine, for current typical units is 25-30% and for combined cycle units, 35-40%. With recent improvements, cycle efficiency has improved considerably to 35.5% for simple cycles and 52.5% for combined cycle. Further advances now on the horizon may increase combined cycle efficiencies to the range of 55-60%. Synthesis gas, the fuel for molten carbonate and solid oxide fuel cells, can be made by reforming natural gas. These fuel cells alone yield an efficiency in the range 45-50%, and when combined with a thermal bottoming cycle may give an overall efficiency of 60-65%.

There are similarly both short term and longer term efficiency improvements for coal-fired power cycles. In the current population of coal-fired power plants, 22% of the plants operate with an efficiency of less than 31%. Only about 10% have an efficiency of greater than 36%. Typical operating conditions for current pulverized coal-fired boilers are 2400 psig steam with 1000 °F superheat and reheat. Commercially proven technology is available with steam operating conditions in the range 3500-4500 psig with main and reheat temperatures in the range 1050-1100 °F, which yield efficiencies of about 40%. This is close to the efficiency expected for pressurized fluidized bed combustors, in an advanced state of development. In the medium term, new or revisited power cycles (Kalina cycle, employing water/ammonia working fluid; indirectly heated gas turbine combined cycle) are expected to yield efficiencies of 45-50%. Other high efficiency approaches are combined cycle gasification/fuel cell, and combined cycle gasification/gas turbines. Longer term, magnetohydrodynamics (MHD) shows

promise of an efficiency in the neighborhood of 60%.

Methane

The main contributor to CH_4 emissions from oil and gas operations is the transmission and distribution system, which accounts for two-thirds of the total. A more rigorous maintenance schedule and accelerated replacement of aging pipelines would help reduce these emissions. New transmission systems are estimated to leak only one-fourth as much as older systems, on average. One possible pipeline replacement program would result in about 0.6 Tg reduction in annual emissions after 10 years. There also appears to be scope for reduction of CH_4 currently vented. At a minimum, if this methane is flared (burned) before release, its effect on radiative forcing is reduced by a factor of about 7. Where venting or flaring is currently practiced on a regular schedule, it may be possible to install transportable electrical generating equipment employing gas turbine or internal combustion engines (see below). This would have the double benefit of converting CH_4 to CO_2 and generating usable power with no additional use of fossil fuel.

Much of the estimated 5.0 Tg CH_4 emitted from U.S. coal mines in 1989 has the potential for useful recovery. Components that are potentially useful are ventilation gas (2.8 Tg), typically 0.3-1.0% CH_4, gas produced by degasification systems (1.3 Tg), typically 25-95% CH_4, and emissions from abandoned deep mines (0.5 Tg), of variable composition. Ventilation gas is too dilute to support combustion by itself, but if used as the source of combustion air with another high concentration CH_4 source, it could contribute about 15% of the fuel to a gas turbine. Degasification gas can serve as the sole fuel source for power generation by internal combustion engines, as is presently being demonstrated[15]. Transportable generator modules are being developed that can be taken to remote mine sites to generate power used at the mine and potentially also for export to a power grid. If gas is purposely withdrawn from abandoned deep mines, it also could serve as the fuel for such a generator module.

Nitrous Oxide

As discussed above, both the transportation sector and stationary sources are significant sources of N_2O. Improvement of vehicle mileage would obviously reduce N_2O emissions from the transportation sector. Redesign of catalytic converters should be possible to reduce direct N_2O emissions. These emissions were not a consideration in the original design. Development of electric vehicles would also reduce N_2O emissions, since on an energy basis, stationary sources needed to generate the electricity to charge vehicle batteries, emit less N_2O and NOx than do vehicles.

For stationary sources, the Clean Air Act Amendments of 1990 will require a 2 million ton per year reduction in NOx emissions. A number of technologies for NOx control, some of them listed in Table 1, are being demonstrated at commercial scale through the U.S. DOE Clean Coal Technology program.

REFERENCES

(1) Bolin, B. in *The Greenhouse Effect, Climatic Change, and Ecosystems-SCOPE 29* (ed Bolin, B., Doos, B.R., & Jager, J.), Wiley, Chitester, 1986; pp 93-

156.

(2) Ruether, J.A.; Smith, D.N.; Rao, S.N. (in preparation).

(3) Shine, K.P.; Derwent, R.G.; Wuebbles, D.J., & Morcrette, J-J. in *Climate Change: The IPCC Scientific Assessment* (eds Houghton, J.T., Jenkins, G.J., & Ephraums, J.J.), Cambridge University Press, Cambridge, 1990, pp 41-68.

(4) Institute of Gas Technology *Preparation of Coal Conversion Systems Technical Data Book*; Quarterly Report for August-October 31, 1977, U.S. Department of Energy FE-2286-24, 1978.

(5) Marland, G. *Carbon Dioxide Emissions From Fossil Fuels: A Procedure For Estimation And Results For 1950-1981* Oak Ridge Associated Universities Report TR003, prepared for Department of Energy DOE/NBB-0036, Washington, DC, 1983.

(6) Barns, D.W.; Edmonds, J.A. *An Evaluation of the Relationship Between the Production and Use of Energy and Atmospheric Methane Emissions* Pacific Northwest Laboratory, prepared for the Department of Energy DOE/NBB-0088P, Washington, DC, 1990.

(7) Science Applications, Inc. *Overview of Unconventional Natural Gas Research and Development Activities* McLean, Virginia, NTIS, PB 80-227986, 1980.

(8) Boyer, C.M.; Kelafant, V.A.; Kuuskraa, V.A.; Manger, K.C.; Kruger, D. *Methane Emissions from Coal Mining: Issues and Opportunities for Reduction.* Prepared by ICF Resources Inc. under contract to U.S. EPA, Washington, DC, 1990.

(9) Smith, D.N.; Ruether, J.A. (in preparation).

(10) Robertson, K. *Ambio* **1991**, 20, 3, 151-154.

(11) Muzio, L.J.; Montgomery, T.A.; Samuelsen, G.S.; Kramlich, J.C.; Lyon, R.K.; Kokkinos, A. *Formation and Measurement of N_2O in Combustion Systems.* Comb. Institute Symposium. Orleans, France, 1990.

(12) Kokkinos, A.; Cichanowicz, J.E.; Hall, R.E.; Sodman, C.B. *J. Air Waste Manage. Assoc.* **1991**, 41, 9, 1252-1259.

(13) Levine, J.S. *The Global Atmospheric Budget of Nitrous Oxide*, in Proceedings: 1991 Joint Symposium on Stationary Combustion NO_x Control, NTIS, Springfield, VA.

(14) Prinn, R.; Cunnold, D.; Rasmussen, R.; Simmonds, P.; Alyea, F.; Crawford, A.; Fraser, P.; Rosen, R. *J. Geophysical Res.* **1990**, 95, D11, 18:365-18:385.

(15) Soot, P. *Coal Mine Natural Gas Power Generation*, Phase I Final Report, U.S. DOE Contract DE-AC02-89ER-80796.A00, 1990.

TABLE 1
NO_x AND N_2O EMISSIONS FROM UTILITY AND INDUSTRIAL COMBUSTION

Combustor Type	MWe	Fuel	Uncontrolled Emissions, (PPM)				Control Technology[1]	Controlled Emissions, (PPM)			
			NO_x	N_2O				NO_x	N_2O		
				Direct	Indirect	Total			Direct*	Indirect	Total
1. Tangential	160	Coal	490	1	2.5	3	OFA	223	@	1.1	
	165	Coal	400	1	2.0	3	LNCF	292	@	1.5	
2. Tangential	500	Coal	950	1	4.8	6	AOFA	730	@	3.7	
				2	4.0	6	LNB	380	@	1.9	
3. Wall Fired	800	Coal	800	1	3.7	5	GRB	360	@	1.8	
				2	0.6	3	LNB	80	@	0.4	
4. Wall Fired	800	Coal	730	2	1.3	2	GRB	80	@	0.4	
	110	Coal	120	2	0.4	84	-	-	-		
5. Cyclone	N/A	Gas	258	1			-	-	-		
6. Wall Fired	185	Oil	84		2.2	16				0.6	34
7. Wall Fired	N/A	Coal	81	14			SNCR	120	33	0.3	11
8. CFBC	N/A	Coke	430		1.0	2	SCR	60	10.6	0.6	24
9. Fluid Bed Catalytic Cracker		Coal	200*	1	1.5	3	SNCR	117	23		
10. Tangential	75	Coal	300*	1	1.5	3					
11. Tangential	N/A	Oil	291	1							
12. Wall Fired	110	Oil	increase due to post combustion NO_x control.								

* Includes direct emissions zone NO_x control
* Employed combustion air)
@ Not measured
1. OFA (over-fired reburning)
GRB (gas reburning)
SCR (selective catalytic reduction of NO_x)
LNCF (low-NO_x combustor)
SNCR (selective non-catalytic reduction of NO_x)
AOFA (advanced over-fire air)
CFBC (circulating fluidized bed combustor)
LNB (low-NO_x burner)

THE CAPTURE AND SEQUESTRATION OF POWER PLANT CO_2

Howard J. Herzog, Elisabeth M. Drake, Jefferson W. Tester
Energy Laboratory
Massachusetts Institute of Technology
77 Massachusetts Avenue, Room E40-489
Cambridge, MA 02139-4307

Keywords: Greenhouse Effect, Carbon Dioxide, Fossil-Fueled Power Plants

INTRODUCTION

Electrical utilities in the U.S. produce about 7% of the world's CO_2 emissions from energy use. Worldwide, about one-third of all CO_2 emissions from fossil-fuel energy sources comes from electric power plants. Since power plants have the highest density of CO_2 emissions in terms of mass per area per time, they provide an appropriate focus as a control target.

Assuming that the build-up of CO_2 in the atmosphere will have some adverse climatological and geohydrological affects, we can mitigate these effects by either counteracting the CO_2 emitted by the power plants or directly reducing the CO_2 emissions themselves (see Figure 1). In terms of counteracting power plant CO_2 emissions, natural fixation of biomass is the most serious contender. Some geoengineering options, such as fertilizing the ocean to increase CO_2 uptake from the atmosphere or dusting the upper atmosphere to reduce incident solar radiation, have also been suggested (National Academy of Sciences, *et al.*, 1991). In terms of direct reduction of power plant CO_2 emissions, improved efficiency is the most practical approach for the short-term, while switching to alternative energy sources (e.g., solar, wind, geothermal) or nuclear energy will probably be required for the long-term. However, power plants have traditionally dealt with adverse airborne emissions, such as NO_x and SO_2, through flue gas clean-up. In this paper, we will review the options for CO_2 reduction by flue gas clean-up followed by the use or disposal of the captured CO_2.

CO_2 CAPTURE

The idea of capturing CO_2 from the flue gas of power plants did not start with concern about the greenhouse effect. Rather, it gained attention as a possible economic source of CO_2, especially for use in enhanced oil recovery (EOR) operations. A very simplified flow diagram of a power plant is shown in Figure 2. A typical composition of the flue gas from a coal-fired power plant is 75% (by volume) N_2, 15% CO_2, 6% water, and 4% residual components (O_2 , SO_2 , NO_x). To be useful, capture processes should concentrate the CO_2 to over 90% by volume. Potential processes include:

- Water absorption systems
- Chemical solvent systems
- Physical solvent systems
- Molecular sieves
- Cryogenic fractionation
- Membrane diffusion

All of these processes have significant energy requirements, which reduce the plant's conversion efficiency or net power output, increasing the amount of CO_2 produced per net kWh_e of electricity generated. Therefore, in evaluating the cost of these processes, the amount of CO_2 emissions avoided (CO_2 emissions with capture compared to a no capture baseline) is more important than the total amount of CO_2 captured. For example, for a coal-fired power plant using a monoethanolamine (MEA) scrubbing process, it costs $25 to capture a ton of CO_2, but due to the large energy losses resulting from the capture process itself, the cost per ton of CO_2 emissions avoided is $62 on an equivalent power output basis.

Several commercial CO_2 recovery plants using MEA scrubbing have been built and operated in the U.S., with the North American Chemical Plant in Trona, CA being in operation the longest (since 1978). The Trona plant is based on Kerr-McGee technology, which is now licensed by ABB Lummus Crest (Barchas and Davis, 1992). An alternative process has been developed by Dow and is licensed by Fluor-Daniel (Sander and Mariz, 1992). Studies have shown that capture of power plant CO_2 by the MEA process will more than double the cost of electricity for reducing CO_2 emissions by 85% (Booras and Smelser, 1991; Herzog, *et al.*, 1991). Other capture techniques, such as membrane separation, cryogenic fractionation, or molecular sieves are even more expensive (see Table 1).

Because flue gas capture of CO_2 primarily requires separating N_2 and CO_2, the idea of separating the N_2 prior to combustion in the power plant has been investigated by Wolsky, *et al.* (1991). This is shown schematically in Figure 3. An air separation plant removes most of the nitrogen prior to combustion, while flue gas is recycled to moderate the temperature in the furnace. Water is easily removed by condensation either before or after the recycle, yielding a flue gas that contains over 95% by volume CO_2. Analysis shows that this process is somewhat more economical than the MEA process (Herzog, *et al.*, 1991).

The use of physical solvents, such as Selexol, in pressure-swing absorption processes are not competitive with the MEA process for atmospheric combustion because the cost of compressing the flue gas is prohibitive. However, for integrated gasification combined cycle (IGCC) plants that operate at elevated pressures, the use of a pressure swing absorption process is very efficient. CO_2 capture and disposal from an IGCC plant would only increase electricity costs in a range estimated from 30% (Hendriks, *et al.*, 1991) to 70% (Booras and Smelser, 1991).

CO_2 UTILIZATION AND DISPOSAL

Once the CO_2 is captured, concern shifts to disposal or sequestering. In the U.S., over 1.8 billion tons of CO_2 is produced each year from power plants. One option is to use the CO_2. However, the amount of CO_2 used annually in the U.S. is only 1-2% of the total amount produced by power plants, and much of the current supply of CO_2 comes from very inexpensive sources - natural formations or chemical by-products (e.g., from an ammonia process). Therefore, for utilization to be a significant sink of CO_2, new uses need to be identified. Also, many of the uses proposed for CO_2 only delay its eventual release to the atmosphere for a very short time.

One proposal that would satisfy the key criteria of reducing atmospheric emissions of CO_2 and of being able to process large quantities of CO_2 is to transform the CO_2 to a fuel, such as methanol. By producing a fuel, our need for "virgin" fuels would be reduced, thereby reducing our total CO_2 emissions. However, carbon in the form of carbon dioxide is in a low energy state and would require significant amounts of energy to be transformed to a high energy fuel. Two types of processes have been proposed to supply this energy, "light" processes utilizing photosynthetic pathways and "dark" processes utilizing chemical reformation (Aresta, *et al.*, 1992). The source of energy proposed in the *dark* processes is frequently hydrogen (H_2). However, if large amounts of inexpensive H_2 are available, it would be more efficient to burn them directly in a power plant and displace fossil fuel use rather than to try to reprocess the CO_2. The *light* processes use solar energy as a power source. For example, large microalgae ponds would be located near a power plant and the captured CO_2 would be distributed through the ponds. The microalgae would be routinely harvested, processed, and used as a fuel. While this scheme has many barriers (large land requirements, limited geographical applicability etc.), it is still the most promising large-scale utilization option currently available.

For CO_2 disposal, there are four primary candidates: oil reservoirs, gas reservoirs, aquifers, and the deep ocean. CO_2 is currently injected in oil reservoirs for EOR and, therefore, may also be considered utilization of CO_2. However, current EOR practices also inject water, which is not consistent with maximizing CO_2 sequestering. Also, the capacity of oil reservoirs is limited and they are not ubiquitously located. Depleted gas reservoirs have a somewhat larger capacity, but using CO_2 to enhance gas recovery is not a practical technique. Frequently, depleted gas wells have been cemented closed as required by law, so using them for CO_2 disposal requires reopening old wells or drilling new wells. The final land base disposal option is in aquifers, which are widely available. However, there is a great lack of geotechnical data on the behavior of pressurized CO_2 in such reservoirs. Some simulations suggest that flow processes would be dominated by viscous fingering and gravity segregation, resulting in a sweep efficiency of only 1-5% (van der Meer, 1992). Also, the integrity of aquifers as a long-term CO_2 storage system may be risky. Since CO_2, unlike natural gas, is heavier than air, a large release displaces oxygen and may cause death by suffocation. A relevant example occurred in 1986 in Cameroon, where naturally trapped CO_2 was released in large quantities from Lake Nyasa resulting in 1,200 deaths.

The deep ocean has the advantage of being an almost limitless repository for CO_2. However, the residence time of CO_2 sequestered in the deep ocean is finite, depending on the depth of injection; estimates range from 50 years at 500 m to 1000 years at 3000 m (Liro, *et al.*, 1992). Of course, the deeper the injection, the more the cost. While environmental concerns have been raised about ocean disposal of CO_2, impacts will probably be very localized. Transport and injection of CO_2 into the ocean, while expensive, is technologically feasible today. If CO_2 is injected below 500 m, the possibility of hydrate formation exists. Research into the kinetics of hydrate formation and how to use hydrates to increase sequester time and/or reduce costs is needed.

STATUS OF CURRENT RESEARCH

Research on global climate change can be divided into science, engineering, and policy. While the U.S. is the leader in global change science research, spending about

$1 billion per year, Japan in the leader in engineering research directed at mitigation. In FY91, the Japanese government's research budget just for CO_2 capture and fixation technology was about $22 million. In addition, research is also being funded by Japanese industry and utilities. The Japanese research on CO_2 capture is spread over most of the topics discussed in this paper, with a special emphasis on deep ocean disposal (Shindo, *et al.*, 1992).

In addition to Japan, both Norway and The Netherlands have very aggressive research programs. The Netherlands have focused on capture from IGCC plants, with storage in depleted gas wells. Their research agenda also includes studying membrane separation, the use of fuel cells, and storage in aquifers. The Norwegians' research projects include looking for improved chemicals for CO_2-removal from exhaust gas, new and improved gas turbines, EOR research, studying CO_2-hydrates, and funding system studies. Much of this research is being carried out through Statoil, the national oil company. Statoil is currently considering a project to inject a million tonnes/year of CO_2 into an offshore aquifer (Kaarstad, 1992).

An international effort (including the U.S.) under the auspices of the International Energy Agency (IEA) is underway, with British Coal as the operating agent. The goal of the IEA effort is to evaluate "technology options for the control of greenhouse gas emissions from fossil fuel utilisation." They will identify and conduct research into the most promising capture and disposal options (Jack, *et al.*, 1992). The U.S. Department of Energy's Office of Coal Technology budgeted $150,000 this fiscal year, focused mainly on biological utilization of CO_2. Next year's estimated budget is $900,000 for projects yet to be specified. In Canada, a project is underway in Alberta on using CO_2 for EOR and maximizing the storage potential of oil reservoirs (Bailey, 1992). In Germany, an IGCC demonstration plant with CO_2 capture using Purisol (a physical sorbent) is under construction for start-up in 1995 (Schütz, *et al.*, 1992). The above list is not complete, but gives a flavor of the activity currently on-going for CO_2 capture and disposal research.

CONCLUSIONS

While the capture of CO_2 from power plant flue gas may be energy intensive and expensive, it is technically feasible. Several flue gas CO_2 capture plants are currently in operation, producing CO_2 for industrial uses. While further research on CO_2 capture processes may reduce costs or lower energy requirements, the major research challenge is to find methods of sequestering or utilizing the captured CO_2 that are technically feasible, economically viable, and environmentally sustainable.

FURTHER DOCUMENTATION

For a more detailed analysis of the issues outlined in this paper, we refer the reader to the proceedings of the *First International Conference on Carbon Dioxide Removal.* The proceedings are scheduled for publication in the June issue of *Energy Conversion and Management* (Pergamon Press). Also, our report to the U.S. Department of Energy on *A Research Needs Assessment for the Capture, Utilization, and Disposal of Carbon Dioxide form Fossil Fuel-Fired Power Plants* should be available in the fall of 1992.

REFERENCES

Aresta, M., E. Quaranta and I. Tommasi, "Prospects for the Utilization of Carbon Dioxide," *Energy Conversion and Management* (1992).

Bailey, R.T. and I.C. Webster, "Progress in a Study of CO_2 Capture and Use for EOR," presented to the 41st Canadian Chemical Engineering Conference, Vancouver, B.C. (1991).

Barchas, R. and R. Davis, "The Kerr-McGee/ABB Lummus Crest Technology for the Recovery of CO_2 from Stack Gases, " *Energy Conversion and Management* (1992).

Booras, G.S. and S.C. Smelser, "An Engineering and Economic Evaluation of CO_2 Removal from Fossil-Fuel-Fired Power Plants," *Energy*, **16**(11/12), 1295-1305 (1991).

Fulkerson, W., R.R. Judkins, and M.K. Sanghvi, "Energy from Fossil Fuels," *Scientific American*, **263**(3), 128-135 (1990).

Hendriks, C.A., K. Blok and W.C. Turkenburg, "Technology and Cost of Recovering and Storing Carbon Dioxide from an Integrated-Gasifier, Combined-Cycle Plant," *Energy*, **16**(11/12), 1277-1293 (1991).

Herzog, H., D. Golomb, and S. Zemba, "Feasibility, Modeling and Economics of Sequestering Power Plant CO_2 Emissions in the Deep Ocean," *Environmental Progress*, **10**(1), 64-74 (1991).

Jack, A.R., H. Audus and P.W.F. Riemer, "The IEA Greenhouse Gas R&D Programme," *Energy Conversion and Management* (1992).

Kaarstad, O., "Emission-free Fossile Energy from Norway," *Energy Conversion and Management* (1992).

Liro, C.R., E.E. Adams and H.J. Herzog, "Modeling the Release of CO_2 in the Deep Ocean," *Energy Conversion and Management* (1992).

National Academy of Sciences, National Academy of Engineering, and Institute of Medicine, *Policy Implications of Greenhouse Warming - Report of the Mitigation Panel*, National Academy Press, Washington, D.C. (1991).

Sander, M.T. and C.L. Mariz, "The Fluor Daniel Econamine FG Process: Past Experience and Present Day Focus," *Energy Conversion and Management* (1992).

Schütz, M., M. Daun, P-M Weinspach, M. Krumbeck and K.R.G. Hein, "Study on the CO_2-Recovery from an ICGCC Plant," *Energy Conversion and Management* (1992).

Shindo, Y., T. Hakuta and H. Miyama, "The Present Status of Carbon Dioxide Removal in Japan," *Energy Conversion and Management*, (1992).

van der Meer, L.G.H., "Investigations Regarding the Storage of Carbon Dioxide in Aquifers in the Netherlands," *Energy Conversion and Management* (1992).

Wolsky, A.M., E.S. Daniels and B.J. Jody, "Recovering CO_2 from Large- and Medium-Size Stationary Combustors," *J. Air Waste Manage. Assoc.*, **41**(4), 449-454 (1991).

Table 1

Comparison of CO_2 Capture Technologies

Process	Energy Penalty (%)	Nominal CO_2 Recovery (%)	Net Reduction of CO_2 Emissions (% of Base Case)	Relative Cost of Electricity
Base Case -- No CO_2 Removal	0	0	0	1.0
IGCC[a]	13	88	86.2	1.3
IGCC[b]	20	90	87.5	1.7
Air Separation FG Recycling[c]	25	100	100	1.9
Amine Scrubbing with Congenerated Steam[b]	35	90	84.6	2.6
Molecular Sieves[d]	80	90	50	5.1
Cryogenic Fractionation[c]	75	90	60	---
Membrane Separation[c]	63	80	46	---

Sources:

[a]Hendriks, *et al.* (1991)

[b]Booras and Smelser (1991)

[c]Herzog, *et al.* (1991)

[d]Fulkerson, *et al.* (1990)

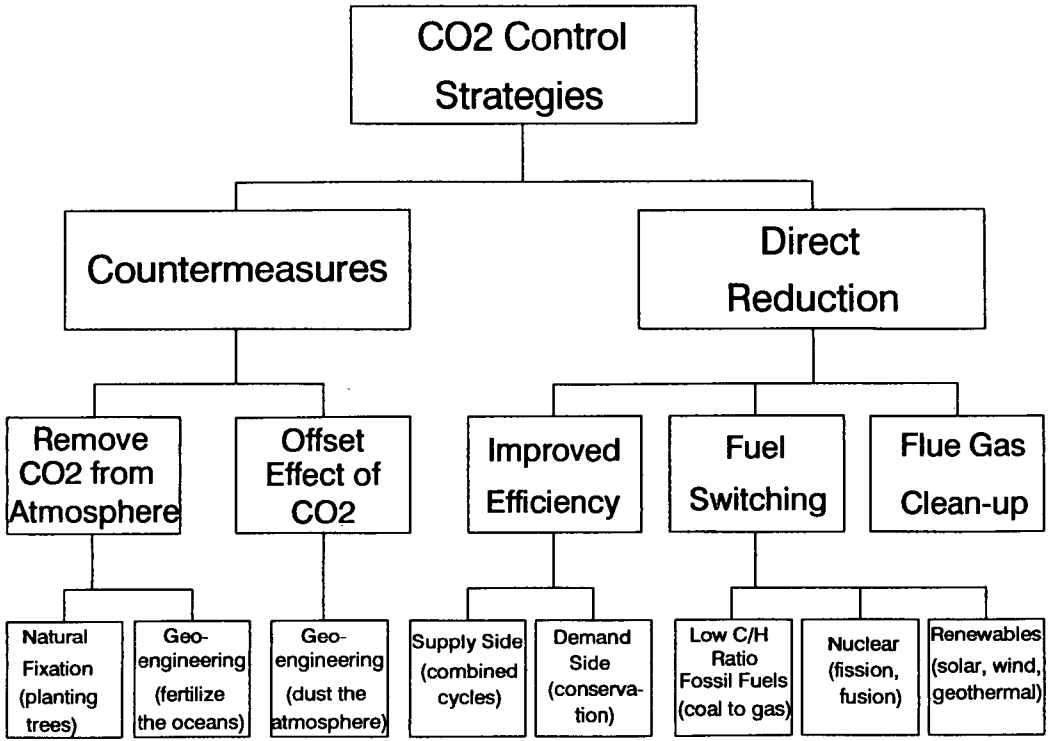

Figure 1: CO_2 Control Strategy Options.

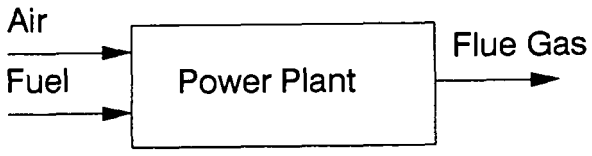

Figure 2: Power Plant Schematic.

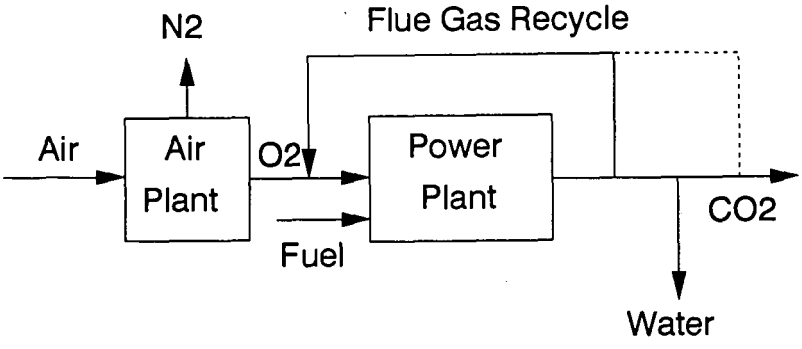

Figure 3: Air Separation/Flue Gas Recycle Power Plant Schematic.

AN ECONOMIC FRAMEWORK FOR THE CONSIDERATION OF CLIMATE CHANGE POLICY

Joel Darmstadter
Energy and Natural Resources Division
Resources for the Future
1616 P Street, N.W.
Washington, DC 20036

Keywords: Climate change policy, costs, benefits

BACKGROUND

While lacking unanimity, an emerging scientific consensus suggests that unconstrained trends in the growth of greenhouse gas emissions might, before the end of the next century, raise global mean temperature by 2-5^{0} Celsius, raise sea levels by 30-100 cm, and significantly alter weather patterns. Through damage to coastal infrastructure and settlements, impaired agricultural productivity, and a variety of impacts on both unmanaged ecosystems and manmade assets, these consequences of greenhouse gas emissions could seriously threaten social well-being. The offending gases principally include carbon dioxide (CO_2)--whose elevated presence in the atmosphere is attributed primarily to fossil-fuel combustion and secondarily to deforestation--nitrous oxide (N_2O), methane (CH_4), and chlorofluorocarbons (CFCs). Notwithstanding CFCs' assault on the stratospheric ozone layer, their pending phaseout under the Montreal Protocol and succeeding restrictions and recent scientific judgments questioning the severity of their contribution to greenhouse warming puts the spotlight on the other gases, principally CO_2, estimated to account for about half of the greenhouse warming that may now be materializing.

Given the public prominence accorded to the greenhouse question at UNCED in June 1992 and other forums, it seems almost superfluous to note the many interrelated ways--scientific, political, economic--in which this issue confronts us with an environmental challenge of truly formidable dimensions:

- On the ***scientific*** front, notwithstanding broad agreement as to the likelihood of increases in global mean temperature, there are widely acknowledged uncertainties, notably the regional nature of climatic change and the feedbacks (positive or negative) set in motion by greenhouse warming.

- Such uncertainties and the fact that there are at least some doubters about the general expectation of global warming undermine, or can be used to undermine, the basis for response strategies. In part, this feeds the ***political*** circumspection regarding greenhouse mitigation initiatives, which policy makers are loath to embrace, fearing unacceptably high costs to constituents and reluctant to address problems likely to manifest themselves over time scales that seem light years in the future.

- Questions of cost and time horizons underscore as well the important ***economic*** aspect of managing the greenhouse problem. Simply put, and in the disembodied language of benefit-cost analysis, efforts to lessen the severity or prospect of climatic change entails

spending money--mostly in the near term--on mitigating activities responsible for a heightened greenhouse effect or deploying measures to adapt to such degree of warming as may be inevitable or deemed tolerable. Such mitigation or adaptation investments should be weighed against the benefits thereby obtained; the value of those benefits is reckoned in terms of the avoidance of damage due to global warming.

The economic perspective on the greenhouse dilemma is, of course, largely an abstract formulation. Yet, even within such a limited conceptual framework, some important points can be usefully highlighted. The balance of these remarks will focus on greenhouse warming in its economic orientation.

RECKONING COSTS

An unexceptional statement that can be made right at the start is that, to the extent that emission reduction efforts are costless or even profitable (the so-called "win-win" or "no regrets" strategy), the benefit-cost conundrum dissolves: we can only be better off economically and environmentally if greenhouse gases and other pollutant emissions can be curtailed at minimum expense. (Proponents of the efficacy of a warmer climate--probably a very small minority--and those perceiving as great a likelihood of global cooling as warming would question that observation.) This self-evident statement of principle takes on practical significance when we take cognizance of a number of studies that attempt to show the feasibility of actually realizing such potential savings. As an example, a widely-publicized National Academy of Sciences (1991) report, assessing greenhouse gas mitigation possibilities in the United States, identified significant opportunities for emission reduction at negative, zero, low, or moderate cost. Depending on how aggressive an effort was mounted to exploit these available opportunities, between around 12-25 percent of this country's greenhouse gas emissions could be eliminated at negative or zero cost. Under the most favorable circumstances--100 percent implementation and marginal costs not exceeding $2.50 per ton of carbon equivalent reduction--emissions might be reducible by as much as 60 percent below levels otherwise prevailing. (That $2.50 translates into, say, 13¢ per gallon of gasoline.) It is important to note that the National Academy's graphic representation of these possibilities, many of which involve enhanced energy efficiency in transportation and housing, depicts a "timeless"--but otherwise unspecified--long-run adjustment path, presumably sufficient to allow capital turnover, behavioral change, and policy changes needed to realize the projections. All that might easily require 2-3 decades to accomplish.

To a greater or lesser extent, opportunities for emission reductions exist throughout the world--perhaps somewhat less in a place like Japan, with its energy-efficient industrial operations; but no doubt more in countries emerging from communist dictation, with their lack of economic incentives and rampant inefficiency, as well as in numerous developing countries. But to point to elimination of prevailing economic waste and energy inefficiency as priority routes to greenhouse gas mitigation does not remove the prospect that, sooner or later, attempts to limit emissions to some maximum level may mean rising marginal costs--whether due to a shift to costlier low- or non-carbon fuels or other economic losses attributable to greenhouse gas constraints. Of course, induced technological advances might blunt, and in the extreme case, offset these cost increases.

RECKONING BENEFITS

To the extent that some considerable cost increases would follow in the wake of greenhouse gas mitigation policies, the problem shifts to one of valuing of the benefits--that is, what damages are avoided?--so obtained. Only limited analysis has focused on that question. The principal effort along this line has been that by Yale economist, William Nordhaus (1991). Nordhaus, concentrating principally on the United States, but then broadening his discussion (to the extent data allow) to the world as a whole, spotlights those economic sectors particularly vulnerable to the degree of global warming associated with a doubling of CO_2-equivalent atmospheric concentrations: agriculture, forestry, energy, and several other sectors assumed to be more moderately affected. Considering the weight of each of these activities in the overall economy and subjecting them to net damage impacts leads, in the author's own words, "to a surprising conclusion:"

> ...Our best guess is that CO_2-induced climate change will produce a combination of gains and losses with no strong presumption of substantial net economic damages. However, these changes are likely to take place over a period of a half century or more and may get lost in the background noise of social, economic, and political change. This conclusion should not be interpreted as a brief *in favor of* climate change. Rather, it suggests that those who paint a bleak picture of desert Earth devoid of fruitful economic activity may be exaggerating the injuries and neglecting the benefits of climate change.

In Nordhaus' assessment, those surprisingly mild damage estimates content with greenhouse gas control costs that, as he suggests, grow rapidly and become extreme for substantial reductions. Thus, while 10 percent of worldwide CO_2 emissions can be reduced at the modest cost of $10 per ton, a 50 percent reduction entails a cost of $150 per ton and a drain on world GNP of about $180 billion--or around one percent of prevailing price and output levels. The moral of the story: "count before you leap," which, as it happens, was the title assigned to a short summary article Nordhaus wrote on the climate-change question in The Economist a couple of years ago (Nordhaus 1990).

Notwithstanding Nordhaus' welcome effort to frame the greenhouse dilemma in benefit-cost terms, it must be emphasized that the scope of such an analysis lends itself to greater or narrower latitude, with potentially marked effect on the numerical outcome. For example, economists' kit of tools are much more congenial to the valuation of resources denominated in market prices than to those things which, while highly prized, are not easily amenable to dollar estimation that would allow them to be combined with market assets. Unmanaged forests, wetlands, and other ecosystems, biodiversity, endangered species--all of which may be perturbed by climatic change--fall into this "difficult to measure" category. Whether, and to what extent, their inclusion would alter Nordhaus' more restrictive benefit-cost calculus is open to question. It should be noted that efforts and techniques to allow for consideration of these non-market assets need not be unavailing, although progress along these lines presupposes close collaboration between physical and social scientists. (A workshop conducted at Resources for the Future in March 1992 focused precisely on this issue.)

What may be another limitation in Nordhaus' perspective--though, again, one not easily handled--is that of the assumed time horizon. By restricting the analysis to the doubled CO_2-

equivalent atmospheric concentrations likely to materialize around the middle of the 21st century, one ignores the prospects for and consequences of steadily rising concentrations in the decades--indeed, centuries--beyond that milestone. Insofar as subsequent impacts may be nonlinear--coastal resources may be resilient to a one-meter sea-level rise but devastated by greater increases--the question of what time perspective to employ can become critical.

A recent study by William Cline (1992) begins to confront these problems. Cline extends his analysis 300 years into the future. By varying such parameters as discount rates, temperature increases, and damage functions, he develops multiple trajectories over this period, but settles on a "central" estimate based on 10^{o} Celsius warming and a damage estimate approximating 6 percent of world GNP. Incorporating those factors in a benefit-cost analysis, Cline derives an overall benefit-cost ratio of 1.3, stating that "if policy makers are risk averse...this study finds that aggressive action to restrain global warming is desirable from the standpoint of social benefit-cost analysis."

THE ROLE OF ADAPTATION

Although, in the somewhat stark schematics presented here, the choices pit emission reduction against damage avoided, there is bound to be a role for adaptation in steps taken to deal with climate change. Adaptation could, in principle, be a purposeful least-cost rational strategy: it's cheaper to build seawalls or inhibit coastal development than to limit emissions leading to sea-level rise. But more realistically, adaptation is likely to involve the ability to cushion climatic impacts across a range of affected activities--e.g., farmers' ability to shift to crop varieties more resilient to climatic stress, thereby substantially (though not totally) offsetting the reductions in crop yield they would otherwise face under climatic change. (See Rosenberg and Crosson 1991). Of course, such adaptation presupposes an evolutionary process whereby one is always forced to adjust to new circumstances, climatic or otherwise. But if climatic change were sudden, severe and triggering major discontinuities in economic and social affairs, this presumption of adaptive capabilities would be a very fragile one.

CONCLUDING REMARKS

The principal purpose here has been to sketch out a simple economic framework as one way of viewing the global warming problem. The idea has been to sharpen our thinking, certainly not to use such a framework as a unifying device to integrate the many strands--scientific, economic, political--that make up the problem. Indeed, the political impediment to addressing the issue forthrightly may be the thorniest one of all. That is understandable in situations where many resource needs compete for policy makers' attention. It is also understandable--but a lot more disheartening--where the policy process, operating within its own glaze of myopia and by its own set of rules, finds it impossible to focus far beyond the elective term of office, let alone over the time horizon that a problem such as greenhouse warming demands.

REFERENCES

(1) Cline, William R. 1992. Global Warming: The Economic Stakes (Washington, DC, Institute for International Economics).

(2) National Academy of Science. 1991. Policy Implications of Greenhouse Warming (Washington, DC, National Academy Press).

(3) Nordhaus, William D. 1991. "Economic Approaches to Greenhouse Warming," in Rudiger Dornbusch and James M. Poterba, eds., Global Warming: Economic Policy Responses (Cambridge, MA, MIT Press), pp. 33-66.

(4) Nordhaus, William D. 1990. "Count Before You Leap," The Economist, July 7, pp. 21-23.

(5) Rosenberg, Norman J. and Pierre R. Crosson. 1991. "Processes for Identifying Regional Influences of and Responses to Increasing Atmospheric CO_2 and Climate Change - The MINK Project," U.S. Department of Energy, Document DOE/RL/08180T-H5, August.

PREPRINT NOT AVAILABLE AT TIME OF PUBLICATION

THESE PAGES INTENTIONALLY LEFT BLANK

PREPRINT NOT AVAILABLE AT TIME OF PUBLICATION

THESE PAGES INTENTIONALLY LEFT BLANK

CHARACTERIZATION OF COAL SULFUR FUNCTIONAL FORMS BY PROGRAMMED-TEMPERATURE OXIDATION

R. B. LaCount, D. G. Kern, W. P. King, T. K. Trulli, D. K. Walker*

ViRoLac Industries, Waynesburg, PA 15370
and
Dept. of Chem., Waynesburg College, Wayneeburg, PA 15370.
* Dept. of Computer Science, Marshall University, Huntington, WV 25755

Keywords: coal analysis, sulfur, oxidation

ABSTRACT

This paper describes the current status for characterization of coal by using a multiple sample controlled-atmosphere programmed-temperature oxidation ($CAPTO_{TM}$) instrument. Dietinctive gas evolution patterns are observed among coals of different rank and between raw and treated coals. In addition to resolved SO_2 peake, assignable to the oxidation of pyrite and the decomposition of sulfate, two othsrs, assignable to organic structures in the coals, are observed. Coals from the Argonne Premium Coal Sample Program have been characterized by this technique.

INTRODUCTION

Interest continues to be strong in methods to reduce the levels of SO_x and NO_x in the atmosphere as a route to reduce acid deposition. This interest intensified development of advanced coal cleaning technologies which, in turn, generated a need for suitable analytical techniques to monitor progress of the work. A number of these analytical techniques, including CAPTO were reviewed in a previous report[1]. This work utilized a CAPTO instrument designed to characterize multiple coal samples in either an oxidative or pyrolysis mode. The instrument has been used in an oxidative mode to characterize the sulfur functional forms for the Argonne Premium Coal Samples.

EXPERIMENTAL

The CAPTO technique is used to characterize coals, treated coals, and other high molecular weight substances reduced to a particle top size of -60 mesh, or smaller. For oxidative characterization, the sample is thoroughly dispersed in a diluent (to reduce exotherms that occur during oxidation), inserted near the center of a quartz tube and positioned in a horizontal "primary" furnace. The sample is exposed simultaneously to a linear increase in temperature (normally 3°C/min) up to 1000°C and to a mass flow controlled oxygen stream of 100 mL/min. The gases flow through a catalytic "secondary" furnace held at 1050°C and through a heated transfer line for analysis using a Fourier Transform Infrared (FTIR) spectrometer equipped with multiple gas cells. The system shown in Figure 1 is designed to characterize four samples simultaneously. A single sample system has been previously described[1].

Using the multiple sample CAPTO instrument in oxidative mode, characterization of the sulfur functionality was completed for the eight coals available from the Argonne Premium Coal Sample Program.

DISCUSSION

The distinctive gas evolution patterns observed among coals of different rank and between raw and treated coals have been related to the structural entity producing each peak[1,2]. The SO_2 evolution peaks obtained from oxidation of coal pyrite and decomposition of sulfate are resolved and appear at temperatures distinct from those observed from combustion of the organic

structures in coal[1]. Two major SO_2 evolution maxima resulting from organic structures are observed. Each of these peaks has CO_2 and H_2O associated with it, implying that the organic matrix is oxidized in stages. Using model systems for comparison, these two major evolution maxima have been related to the probable structural types producing the evolutions[1]. The temperatures observed for the evolution maxima are sensitive to the experimental conditions[1,2].

Previous ^{13}C CP-MAS n.m.r. work[2] was completed on coal samples both before and after a CAPTO experiment that was terminated at 400°C. The n.m.r spectra prior to the experiment indicated the presence of both aromatic and non-aromatic structures (f_a = 0.69). After the sample was exposed to CAPTO conditions up to 400°C, the spectra revealed an essentially unchanged aromatic region; however, the non-aromatic region had been almost totally eliminated (f_a = 0.87). Thus, the lower temperature CO_2 and SO_2 evolutions resulting from organic structures were attributed to carbon and sulfur lost primarily from oxidation of non-aromatic coal etructures. The CO_2 and SO_2 evolutions from organic structures above 400°C were attributed primarily to carbon and sulfur lost during oxidation of the aromatic coal matrix. We still believe this to be a generally valid premise, and it is supported by the H/C ratio of 0.7 observed for the evolved gas at 400°C[2]. As also noted in the earlier work, stable aryl sulfides and sulfones oxidize above 400°C and should be included along with thiophenic structures in what we term "aromatic" sulfur.

The Argonne Premium Coal Sample Program coals were characterized using the multiple sample CAPTO instrument. One example, the absorbance/temperature CAPTO profiles for the Illinois No. 6 Argonne Premium Coal Sample is shown in Figure 2. The SO_2 evolution profile shows a peak at 274°C produced from oxidation of non-aromatic organic sulfur structures and a peak at 404 °C from the aromatic organic sulfur structures. The peaks at 439°C and 469°C are both derived from oxidation of pyrites and the small evolution at 580°C is produced from decomposition of iron sulfate. The CO_2 and H_2O evolution profiles are also monitored and shown in Figure 2. Each profile shows a major peak related to oxidation of non-aromatic organic structures and aromatic organic structures. The ratio of non-aromatic/aromatic carbon or hydrogen is readily available from these profiles in addition to a continuous plot of the H/C ratio.

The relative areas of non-aromatic organic, aromatic organic, pyritic, and sulfate sulfur from the CAPTO evolution profiles were related to the ASTM total sulfur values of the Argonne coals for a comparison of sulfur forms. The preliminary results are shown in Table 1. As noted in Table 1 the Wyodak-Anderson and Beulah-Zap coals produced an additional SO_2 peak in the temperature range where SO_2 evolution from decomposition of several inorganic sulfates[3] is observed.

CONCLUSIONS

Quantitative studies are in progress to evaluate the CAPTO technique as a one-step determination of the organic, inorganic, and total sulfur present in coals and treated coals. The multiple sample CAPTO instrument has been used to characterize the sulfur forms of the Argonne Premium Coal Samples and the preliminary results are reported.

ACKNOWLEDGEMENTS

This work has been supported in part by Department of Energy SBIR Phase II Grant No. DE-FG01-90ER81055 and in part by the Ben Franklin Technology Center of Western Pennsylvania through Pennsylvania's Ben Franklin Partnership Program. The authors wish to thank the Pittsburgh Energy Technology Center (PETC) and specifically Sidney Friedman, Robert Warzinski, and Bernard Blaustein for their interest and support in the early phases of the work. The authors also thank Waynesburg College for its cooperation and support.

We are grateful to Dr. Karl S. Vorres for providing the Argonne National Laboratory Premium Coal Samples. We also wish to acknowledge the efforts of K. D. Robertson and T. J. Schroyer toward development of the multiple eample CAPTO instrument.

REFERENCES

1. LaCount, R. B., Kern, D. G., King, W. P., LaCount, R. B. Jr., Miltz, D. J. Jr., Stewart, A. L., Trulli, T. K., Walker, D. K., Wicker, R. K., "Advances in Coal Characterization by Programmed-Temperature Oxidation", Prepr. Pap. - Am. Chem. Soc., Div. Fuel Chem. 1991, 33(3), 1217.

2. LaCount, R. B., Anderson, R. R., Friedman, S., Blaustein, B. D., "Sulfur in Coal by Programmed - Temperature Oxidation", Fuel, 66, 909 (1987).

3. LaCount, R. B., Gapen, D. K., Dell, David A., Simpson, F. W., Helms, Charles A., "Thermal Oxidative Degradation of Coal as a Route to Sulfur Functionality: An Initial Study", New Approaches in Coal Chemistry, eds., B. D. Blaustein, B. C. Bockrath, S. Friedman, A.C.S. Symposium Series, 169, 415 (1981).

Table 1

DETERMINATION OF SULFUR FORMS OF THE ARGONNE PREMIUM COALS RELATIVE TO ASTM TOTAL SULFUR (mf basis)

Argonne Premium Coal Sample	Wt% Total Sulfur	% Pyrite	% Non-Aromatic	% Aromatic	% Sulfate
Pocahontas #3, VA	0.66	0.09	0.13	0.44	nd.
Upper Freeport, PA	2.32	1.64	0.25	0.43	<0.01
Pittsburgh #8, PA	2.19	1.54	0.20	0.43	0.02
Lewis.-Stock., WV	0.71	0.26	0.08	0.37	nd.
Blind Canyon, UT	0.62	0.29	0.10	0.23	nd.
Illinois #6, IL	4.83	2.65	0.56	1.62	<0.01
Wyodak-Anders., WY*	0.63	0.19	0.11	0.15	0.02
Beulah-Zap, ND**	0.80	0.25	0.27	0.16	nd.

* 0.16% Sulfur evolved at 832°C.
** 0.12% Sulfur evolved at 756°C.

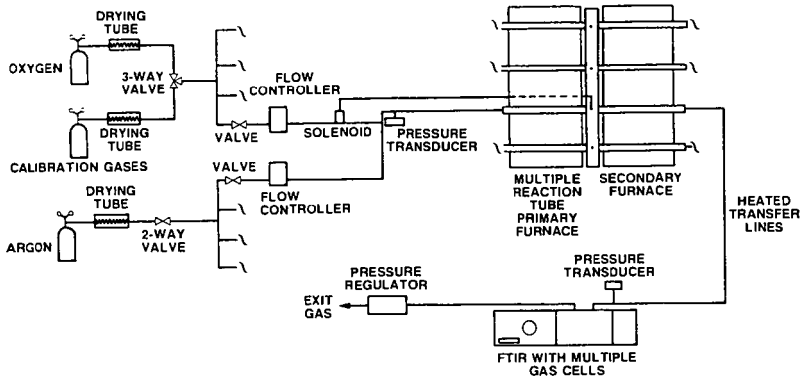

Figure 1. Flow system for the multiple sample controlled-atmosphere programmed-temperature oxidation (CAPTO) instrument.

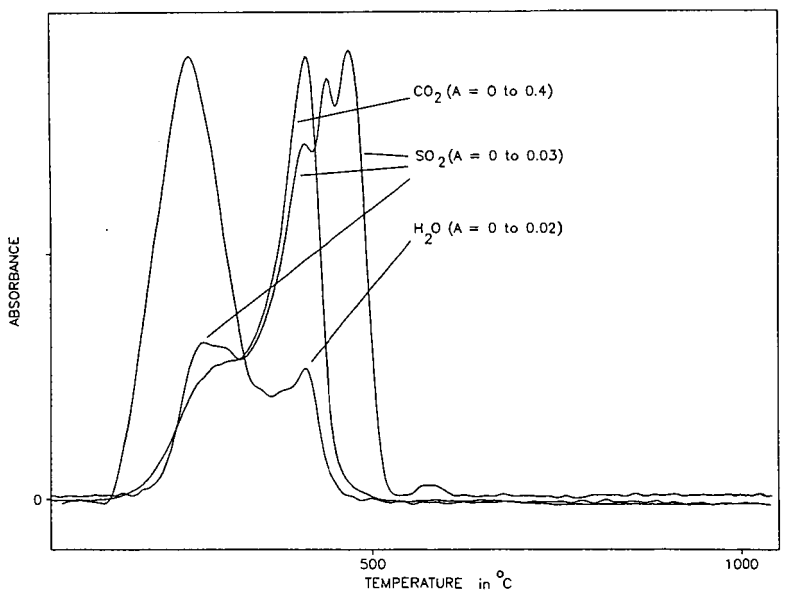

Figure 2. CAPTO evolution profiles from the Illinois No. 6 Argonne Premium Coal Sample.

DETECTION OF ORGANIC SULFUR BY ^{15}N AND ^{19}F NMR VIA FORMATION OF IMINOSULFURANES

James A. Franz, John C. Linehan and Claude N. Lamb

Pacific Northwest Laboratory
Battelle Memorial Institute
P. O. Box 999
Richland, Washington 99352

INTRODUCTION

Determination of the forms of organic sulfur in coal remains a topic of wide interest in coal science. Recent efforts to characterize organic sulfur include analysis by XANES (1-3), pyrolytic methods (4-7), mass spectrometric analysis of coal extracts (8), and preparation of ^{13}C-labelled sulfonium salts from organic sulfides (9). Direct observation of the ^{33}S nucleus by NMR is unsatisfactory, due to low natural abundance, poor receptivity, and unfavorable quadrupolar relaxation properties. ^{13}C NMR is of limited utility for the indirect analysis of sulfur, since ^{13}C chemical shifts for carbons with sulfur substituents are similar to those of carbons with carbon substituents. The aim of the present study is to develop NMR methods for characterization of organic sulfur functional groups which do not suffer from the ambiguities of pyrolytic and hydropyrolytic methods. Thus, we have examined the potential for spectroscopic discrimination of categories of organic substituents at sulfur by conversion of organic sulfides to iminosulfuranes, $R_2S{=}NR$, for analysis by ^{15}N NMR spectroscopy (10). In this paper, we present results of measurement of ^{15}N chemical shifts for various alkyl and aryl substituents at sulfur. We discuss a second approach under study, the attachment of ^{19}F labels to groups attached to sulfur, with *chemical* selectivity providing the basis for structural discrimination.

Iminosulfuranes have been prepared from the reaction of N-haloamides with dialkyl sulfides (eq 1) (11). The reaction is selective for dialkyl sulfides: diaryl sulfides and aryl alkyl sulfides are unreactive.

$$BrNHCOCH_3 + CH_3SCH_3 \text{ ----> } (CH_3)_2S{=}NCOCH_3 \quad (1)$$

Iminosulfuranes have been prepared by the reaction of sulfoxides with trifluoroacetic anhydride or oxalyl chloride (eqs 2-3) (12). The intermediate sulfonium salt formed in eq. 2 can be trapped at low temperature (-60°C) with an appropriate amide to form the iminosulfurane (eq 3). At temperatures above -30°C, the intermediate undergoes the Pummerer rearrangement (eq 4).

$$(CH_3)_2SO + (CF_3CO)_2O \text{ ----> } (CH_3)_2SOCOCF_3^+ \ {}^-O_2CCF_3 \quad (2)$$

$$(CH_3)_2SOCOCF_3^+ \ {}^-O_2CCF_3 + H_2NCOR \text{ ----> } (CH_3)_2S{=}NCOR \quad (3)$$

$$(CH_3)_2SOCOCF_3^+ \ ^-O_2CCF_3 \ \text{----}> \ CH_3SCH_2OCOCF_3 + HO_2CCF_3 \qquad (4)$$

Finally, diaryl sulfides can be converted to diaryldialkoxysulfuranes (R_f = $C(CF_3)_2Ph$) by reaction with bromine or chlorine and a suitable alkoxide in dry aprotic solvents (ether, tetrahydrofuran, CCl_4). The diaryldialkoxy sulfuranes, e.g., **1**, can be isolated or easily prepared *in situ* for reaction with a wide variety of amides and amines to form iminosulfuranes (eq 6) (13). The acidic alcohol R_fOH is conveniently removed by basic aqueous extraction. The main requirements for application of this reaction in a coal product environment are (1) the absence of water, which hydrolyzes sulfuranes to sulfoxides, and (2) phenolic OH groups and other active hydrogen-containing groups must be alkylated to prevent oxidation.

$$Ph_2S + Cl_2 + 2\,K^+ \ ^-OR_f \ \text{----}> \ Ph_2S(OR_f)_2 + 2\,KCl \qquad (5)$$

$$R_f = C(CF_3)_2Ph \qquad \mathbf{1}$$

$$Ph_2S(OR_f)_2 + H_2NR \ \text{----}> \ Ph_2S{=}NR + 2\,HOR_f \qquad (6)$$

In this paper, we examine the possibility of discriminating between diaryl sulfides and alkyl sulfides by converting diaryl sulfides to iminosulfuranes, while arylalkyl sulfides are selectively converted to the Pummerer rearrangement product under the same reaction conditions. Sulfonium salts formed from arylalkyl sulfides (eq 7) do not form iminosulfuranes when the R_fO^- anion is present (eq 8), but rather undergo efficient Pummerer rearrangement (eq. 9). In this paper, we extend recent work which

$$PhSCH_3 + Br_2 + 2\,KOR_f \ \text{----}> \ PhSCH_3(OR_f)^+ \ ^-OR_f \qquad (7)$$

$$PhSCH_3(OR_f)^+ \ ^-OR_f + H_2NR \ \text{----}> \ PhS(CH_3){=}NR \qquad (8)$$

$$PhSCH_3(OR_f)^+ \ ^-OR_f \ \text{---}> \ PhSCH2OR_f \qquad (9)$$

determined ^{15}N chemical shifts for simple diaryl and dialkyl iminosulfuranes to include the dibenzothiophene structure, and we demonstrate introduction of ^{19}F and ^{15}N labels in iminosulfuranes prepared from diphenyl sulfide and dibenzothiophene. We examine reaction of a mixture of sulfides leading to selective iminosulfurane formation from a diaryl sulfide and Pummerer rearrangement from an arylalkyl sulfide. These reactions provide a strategy for *chemical* discrimination between dibenzothiophene, simple diaryl sulfides, aryl alkyl sulfides, and dialkyl sulfides.

EXPERIMENTAL

Preparation of Dibenzothiophene-N-(2,2,2-trifluoroacetyl) Iminosulfurane. The following is a representative procedure for preparation of iminosulfuranes. 2,2,2-Trifluoro-acetamide (Aldrich) was dissolved in ether and decanted from an insoluble component.

The alkoxide $K^+ \ ^-OC(CF_3)_2Ph$ (KOR_f) was prepared by heating R_fOH (1 eq.) and aqueous KOH (0.95 eq) at 100 °C and 10^{-2} Torr in a round bottom flask equipped with a vacuum adapter, with two interruptions to grind the white alkoxide cake to powder, following published procedures (13,14). The apparatus, reagents and solvents were rigorously dried. However, the white alkoxide powder can be quickly (less than 3-4 minutes) transferred in the open air for weighing into reaction flasks without appreciable yield losses. Similarly, solvents and reagents were quickly transferred to the oven-dried reaction flask through the air, followed by nitrogen purge of the reaction medium. Thus, dibenzothiophene (1.5 g, 8.15 mmol), and KOR_f (4.6g, 16.3 mmol) were dissolved in ca. 60 mL of dry tetrahydrofuran (Aldrich, stored over type 3A molecular sieves) in a 3-neck 100 mL round bottom flask equipped with two serum caps and a vacuum adapter. Chlorine (0.35 mL at -78°C, 8.1 mmol), was condensed in a calibrated trap and swept into the solution in a nitrogen stream via syringe needle. (When bromine was substituted for chlorine, no iminosulfurane was formed from dibenzothiophene in reactions using ether, CCl_4, or THF solvents.) The reaction mixture was stirred for 5 min. A THF solution of 2,2,2-trifluoroacetamide (0.92 g, 8.1 mmol) was added, and the solution was warmed to room temperature. THF was removed by rotary evaporation, and methylene chloride, 80 mL, was added. After extraction with 10% aq. KOH twice to remove acidic R_fOH, and once with water, the CH_2Cl_2 solution was dried over anhydrous $MgSO_4$ and concentrated to give crystalline product, 2.2 g (90% yield). The iminosulfurane was sparingly soluble in diethyl ether. Recrystallization from ether gave fine needles, mp 215-217°C, 1.8 g. ^{13}C NMR (75 MHz, $CDCl_3$, ppm using $CDCl_3$ center line at 77 ppm): 168.9 (quartet, J_{CF}=35.8 Hz), 138.6, 135.6, 133.4, 130.4, 129.0, 122.7, 117.1 (quartet, J_{CF} = 288 Hz). ^{19}F NMR (282 MHz), singlet at -73.5 ppm from $CFCl_3$. ^1H NMR (300 MHz, $CDCl_3$, ppm from TMS), 8.15 ppm (2H, d, J=7.9 Hz), 7.92 (2H, d, J=7.7 Hz), 7.71 (2H, d of t, J=7.6, 0.9) 7.57 (2H, d of t, J=0.9, 7.9 Hz).

Preparation of Other Iminosulfuranes. ^{15}N-Acetamide (Cambridge Isotope Laboratories) was recrystallized from $CHCl_3$-ether for preparation of ^{15}N-acetyl iminosulfuranes. S,S-Diphenyl-N-(2,2,2-trifluoroacetyl) iminosulfurane (mp 88.5-89.5 °C), dibenzothiophene-^{15}N-acetyl iminosulfurane (mp 165-165.5° C), and S,S-diphenyl-^{15}N-acetyl iminosulfurane (mp 94-95°C) (10) were also prepared by the method described above. Spectroscopic details will be published in detail elsewhere. Excellent crude yields of ca. 90% were achieved in all cases, with final isolated yields of pure product of typically greater than 75%. CCl_4 and diethyl ether can be substituted for THF. Unlike dibenzothiophene, diphenyl sulfide can be converted to iminosulfuranes using either bromine or chlorine. In general, iminosulfuranes can be recrystallized from ether/pentane (13).

Pummerer Rearrangement of Thioanisole. An ether solution of thioanisole was exposed to a 10% excess of Br_2 or Cl_2 at -78°C, followed by two equivalents of KOR_f in ether. ^{13}C NMR analysis revealed clean, quantitative conversion to the Pummerer rearrangement product, $PhSCH_2OC(CF_3)_2Ph$, isolated as a clear liquid after a workup similar to that of the iminosulfuranes. ^{13}C NMR, 75 MHz, $CDCl_3$, ppm using $CDCl_3$ centerline at 77.0 ppm, 133.8, 131.9, 130.3, 129.1, 128.8, 128.3, 128.0, 127.2, 122.3(quartet, CF_3, J_{CF} = 290 Hz), 83.2 (heptet, J_{CF} = 28.5 Hz), 72.2. ^{19}F NMR (282 MHz), singlet at

-71.2 ppm from internal $CFCl_3$. The 70 eV mass spectrum gave a strong molecular ion at m/e 366 and fragments at 227, 207, 177, 123, 109, and 77.

Reaction of mixture of Diphenylsulfide and Thioanisole. An equimolar mixture of diphenylsulfide and thioanisole were treated with Cl_2, KOR_f, and excess H_2NCOCF_3 in dry THF at -78°C. After the standard workup, the reaction mixture was examined by ^{13}C and ^{19}F NMR. This revealed complete conversion of thioanisole to the Pummerer product, $PhSCH_2OR_f$, and 60% conversion of diphenylsulfide to the iminosulfurane.

Conversion of Diphenylsulfide to S,S-Diphenyl-^{15}N-acetyliminosulfurane in the Presence of Illinois No. 6 Methylated Asphaltenes. Argonne premium coal no. 301 was heated for 15 min at 435°C in tetralin (1 g coal/1.75 g tetralin) in a stainless steel tubing bomb. The products were extracted with THF. The THF solution was poured into excess hexane to precipitate asphaltenes and preasphaltenes. A sample of 0.8 g of the product in 30 mL THF was stirred overnight with 10 g $^{13}CH_3I$ and 1.9 g KOH in 2.5 mL water. THF was removed, and a $CHCl_3$ solution of the products was concentrated and thoroughly dried under vacuum at 100°C. ^{13}C NMR revealed 70% O-alkylation (50-70 ppm) and 30% C-alkylation (10-50 ppm). A mixture of 0.39 g methylated coal product, 1.8 g KOR_f, 0.49 g Ph_2S in 10 mL CCl_4 and 2 mL benzene were treated with 0.2 mL Br_2. The reaction mixture warmed noticeably. The ^{15}N-labelled acetamide, 0.2 g, was added, the mixture was shaken for 30 min, and worked up in the standard way. Examination of a $CDCl_3$ solution of the products by ^{13}C and ^{15}N NMR, revealed ca. 70% conversion of Ph_2S to $Ph_2S{=}^{15}NCOCH_3$.

RESULTS AND DISCUSSION

Spectroscopic Discrimination of Sulfur Functional Groups. ^{15}N Chemical Shifts for N-acetyliminosulfuranes. As shown in Table I, ^{15}N chemical shifts for S,S-dialkyl and S,S-diaryl N-acetyliminosulfuranes span a narrow range of only ca. 10 ppm, with no separation of aryl from alkyl substituents, although changes in the nitrogen subsituent lead to a chemical shift range of about 100 ppm on going from N-benzyl to N-aryl to the N-acetyl substituent. In this paper, we have added data for the dibenzothiophene structure to previously reported data (10). Overall, these data indicate that the substituent at sulfur exerts little effect on the ^{15}N chemical shift, and that no simple spectroscopic discrimination of sulfur substituents into aryl or alkyl substituents will be accomplished using ^{15}N NMR, at least for the N-acetyl substituent.

Chemical Discrimination of Sulfur Functional Groups. ^{19}F Chemical Shifts. Organic sulfides differ greatly in their reactivity to oxidizing reagents. Thus, a strategy for discrimination of sulfur functional groups using NMR spectroscopy uses chemical selectivity to attached spectroscopically distinct groups to different categories of organic sulfur. The ^{13}C and ^{19}F chemical shifts of the methyl and trifluoromethyl groups of N-acetyl and N-trifluoroacetyl iminosulfuranes are unaffected by changes in the sulfur substituents. As shown in Table I, the ^{19}F shifts of N-trifluoroacetyl groups attached to diphenyl sulfide or dibenzothiophene are nearly identical. Diaryl sulfides in a coal-derived mixture thus may be expected to yield iminosulfuranes which will appear closely

clustered at about -73.5 ppm in the ^{19}F spectrum compared to $CFCl_3$, and Pummerer rearrangement products will appear around -73.5 ppm with the present choice of fluorinated alkoxide. Dibenzothiophene structures can be discriminated from diphenyl sulfide structures by selection of Br_2 or Cl_2 as an oxidant. Aryl alkyl and dialkyl sulfides are converted to Pummerer products in the sulfurane-forming reaction. Finally, dialkyl sulfides are converted to iminosulfuranes using N-bromo amides, but arylalkyl and diaryl sulfides do not react, providing a means for selective detection of dialkyl sulfides. Each of these categories of selective reaction can be used to introduce a unique ^{19}F or ^{15}N label. Introduction of two distinct ^{19}F labels for diaryl and alkyl aryl sulfides is demonstrated by the reaction of a mixture of diphenyl sulfide and thioanisole giving S,S-diphenyl-N-(2,2,2-trifluoroacetyl) iminosulfurane (^{19}F resonance at -73.5 ppm from $CFCl_3$) and $PhSCH_2OC(CF_3)_2Ph$ (-71.2 ppm from $CFCl_3$), respectively. Although the sulfurane-forming reactions may appear rather exotic for application to coal, we have shown in model compound experiments that the reactions can be successfully carried out in the presence of methylated preasphaltenes and asphaltenes, and are simple bench-top procedures.

SUMMARY

We have synthesized new iminosulfuranes from a variety of diaryl-and dialkyl sulfides and dibenzothiophene. The pattern of ^{15}N chemical shifts indicates that functional groups attached to sulfur are not simply resolved into aryl and alkyl groups. Thus, resolution of sulfur functional groups using ^{15}N NMR via iminosulfurane does not appear practicable. However, iminosulfurane formation, together with the N-haloamide reaction and the Pummerer rearrangement, provides pathways for chemical discrimination of different sulfur substituents using unique ^{15}N- or, ^{19}F-labelled fragments for different categories of sulfur functional groups. In efforts currently underway, we are applying these reactions to methylated extracts and conversion products of the high-organic-sulfur containing Yugoslavian Rasa and Spanish Mequinenza lignites.

ACKNOWLEDGEMENT

This work was supported by the Office of Energy Research, U. S. Department of Energy, under Contract DE-ACO6-76RLO 1830. The authors thank Dr. Ana B. Garcia of the Instituto Nacional Del Carbon, Ovieda, Spain for providing us with a sample of the Mequinenza lignite, and Dr. Curt M. White of the Pittsburgh Energy Technology Center for providing a sample of the Rasa lignite.

REFERENCES

1. George, G. N., Gorbaty, M. L., J. Amer. Chem. Soc. 1989, 111, 3182.

2. George, G. N., Gorbaty, M. L., Kelemen, S. R., Sansone, M. Energy & Fuels, 1991, 5, 93-97.

3. Kelemen, S. R., George, G. N., Gorbaty, M. L., Fuel, 1990, 69, 939.

4. Calkins, W. H., Tores-Ordenez, R. J., Jung, B., Gorbaty, M. L., George, G. N., and Kelemen, Proc. 1991 International Conf. Coal Science, S. R. Butterworth-Heinemann Ltd., Linacre House, Jordan Hill, Oxford OX2 8DP, 1991, pp. 985-988, and references therein.

5. Calkins, W. H., Prepr. Fuel Div. Am. Chem. Soc., 1985, 30(4), 450-465.

6. Calkins, W. H., Energy & Fuels, 1987, 1, 59.

7. Torres-Ordonez, R. J., Calkins, W. H., and Klein, M. T., ACS Symposium Series 429, Ch. 17, June 1990.

8. White, C. M., Douglas, L. J., Anderson, R. R., Schmidt, C. E., and Gray, R. J. ACS Symposium Series 1990, 429, 261-286.

9. Green, T. K., Lloyd, W. G., Gan, L., Whitley, P., and Wu, K. Prepr Fuel Div. Am. Chem. Soc. 1992, 37(2), 664-669.

10. Franz, J. A., Lamb, C. N., and Linehan, J. C. Proc. 1991 International Conf. Coal Science, S. R. Butterworth-Heinemann Ltd., Linacre House, Jordan Hill, Oxford OX2 8DP, 1991, 977-980.

11. Kise, H., Whitfield, G. F., and Swern, D., J. Org. Chem. 1972, 37, 1121-1128.

12. Huang, S. L., and Swern, D. J. Org. Chem. 1978, 43, 4537-4538 and Sharma, A. K., Ku, T., Dawson, A. D. and Swern, D. J. Org. Chem. 1975, 40, 2758-2764.

13. Franz, J. A., and Martin, J. C. J. Am. Chem. Soc. 1975, 97, 583-591 and 6137-6144.

14. Martin, J. C.; Arhart, R. J.; Franz, J. A.; Kaplan, L. J.; and Perozzi, E. F. Organic Syntheses, 1977, 57, pp. 22-26, John Wiley & Sons, New York, New York.

Table I. ^{15}N and ^{19}F Chemical Shifts of Iminosulfuranes and a Pummerer Rearrangement Product

Iminosulfurane	^{15}N Chemical Shifts[a]	^{19}F Chemical Shifts[b]
$Ph_2S{=}NC(CH_3)_3$	-293.5	
$Ph_2S{=}NCH_2Ph$	-330.4	
$Ph_2S{=}NPh$	-284.0	
$(CH_2)_4S{=}NCOCH_3$	-217.8	
$Ph_2S{=}NCOCH_3$	-227.6	
$(PhCH_2)_2S{=}NCOCH_3$	-228.9	
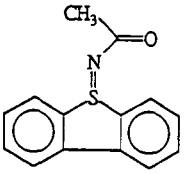	-219.0	
$Ph_2S{=}NCOCF_3$		-73.52
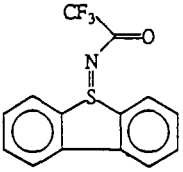		-73.45
$PhSCH_2OC(CF_3)_2Ph$		-71.2

[a]ppm from CH_3NO_2 [b]ppm from $CFCl_3$

Sulfur Speciation of Desulfurized Coals by XANES Spectroscopy

G.P. Huffman, S.A. Vaidya, N. Shah, and F.E. Huggins
CFFLS, 233 Mining & Minerals Res. Bldg., University of Kentucky,
Lexington, KY 40506-0107

Keywords: XANES, sulfur, XAFS, desulfurized

ABSTRACT

Least square analysis of the x-ray absorption near edge structure (XANES) region of sulfur K-edge x-ray absorption fine structure (XAFS) spectra can provide a quantitative analysis of both the organic and inorganic functional forms of sulfur in coal. In the current article, this method is applied to speciation of the sulfur forms in a number of desulfurized coals. The samples invesitgated include specimens treated with boiling perchlorethylene, samples subjected to selective chemical reactions, samples subjected to molten caustic leaching, and biologically desulfurized coals. In all cases, analysis of the XANES provides a reasonably quantitiative speciation of the changes in the sulfur forms resulting from the various treatments.

INTRODUCTION

In the past several years, it has been demonstrated that sulfur K-edge x-ray absorption fine structure (XAFS) spectroscopy can be used to speciate all of the major functional forms of sulfur. Two primary methods of analysis have been used: direct least squares analysis of the x-ray absorption near edge structure (XANES) [1-3] and a third derivative treatment of the XANES [4-6]. With the least squares analysis approach, it is possible to quantitatively determine the percentages of the total sulfur present in five principal organic functional forms and several inorganic forms with an accuracy of ±5-10%.

An obvious application of this capability is the investigation of the changes in sulfur forms produced by desulfurization treatments. Particularly of interest are treatments aimed at removing organic sulfur. In the current paper, we present the results of XANES analysis of coals subjected to a variety of chemical and biological desulfurization treatments.

EXPERIMENTAL PROCEDURE AND SAMPLE DESCRIPTION

The samples investigated were prepared in several laboratories. The desulfurization procedures have been described in detail elsewhere and will not be discussed here. Samples studied included coals treated by boiling perchlorethylene (PCE) prepared in the laboratories of Prof. Sunyu Lee[7] and Dr. Melissa Chou[8], specimens treated with single electron transfer and strongly basic reagents in the laboratory of Dr. Kuntal Chatterjee and Prof. Leon Stock [7-11], samples subjected to biological desulfurization by Dr. John Kilbane [12], and samples treated by molten caustic leaching [13] provided by Mr. Phil Goldberg of the Pittsburgh Energy Technology Center.

The sulfur K-edge XAFS spectroscopy was carried out at beamline X-19A at the

National Synchrotron Light Source (NSLS) at Brookhaven National Laboratory. To minimize x-ray absorption, the x-ray beam at X-19A is maintained in machine vacuum all the way from the synchrotron ring to the experimental hutch, and is thereafter is maintained in a helium atmosphere. All spectra were taken in the fluorescent mode using a Stearn-Heald ionization detector [14]. The x-ray energy was varied from approximately 100 eV below to about 400 eV above the sulfur K-shell absorption edge (2472 eV) using a Si (111) double crystal monochromator.

RESULTS AND DISCUSSION

Biologically Desulfurized Samples: Previously, we have used XANES to examine a number of biologically solubilized and desulfurized samples [2]. The primary conclusion of that earlier work was that biological agents did not discriminate greatly between different functional forms of sulfur, and little if any organic sulfur was removed by biological treatment. More recently, however, XANES has been used to examine several samples subjected to biotreatment using the microbe *Rhodococcus rhodochrous*, as discussed in detail elsewhere by Kilbane [12].

Typical fitted XANES spectra of a control sample and a biotreated sample of an Illinois #6 coal are shown in Figure 1. Prior to treatment, most of the pyrite was removed from the coal. The results are summarized in Table I and Figure 2. In both examples, it is seen that a substantial reduction in organic sulfur was accomplished. However, it is evident from Figure 2 that the relative amounts of the different functional forms of organic sulfur were essentially unchanged, within the standard error (±5%). It therefore appears that all of the organic sulfur functional forms were reduced approximately equally by the treatment [12].

Coals Subjected to Molten Caustic Leaching: A molten caustic leaching process for removal of both ash and sulfur from coal has been developed by TRW Corporation [13]. The fitted XANES obtained from a Kentucky #9 coal subjected to this process is shown in Figure 3. It is evident that the sulfur has undergone considerable oxidation. The results obtained by quantitative analyses of the XANES are summarized for three coals in Table 2: a Kentucky #9 coal and a Pittsburgh #8 coal subjected to the molten caustic leaching process, and the Pittsburgh #8 coal prior to leaching [1]. It is evident that the forms of sulfur are drastically changed and reduced by this rather severe process. In particular, no pyrite or organic sulfide remain, and thiophenic sulfur, which is the dominant organic sulfur form in the original coals is reduced to only about 0.1% in the treated coals. Elemental sulfur, sulfone, and sulfate are the dominant sulfur species remaining, indicating severe oxidation.

Perchlorethylene Treated Samples: We have examined a number of samples before and after treatment with PCE. For the samples investigated to date, it is concluded that the primary effect of the treatment is to remove elemental sulfur. Typical results for a number of samples are summarized in Table 3. It is seen that elemental sulfur is the primary sulfur form removed for all of the samples which exhibited a decrease in sulfur due to PCE treatment. It is also noted that all of these samples contain a significant amount of sulfate, indicative of substantial oxidation. In two cases, a fresh coal is compared to the sample before PCE treatment. It appears that an oxidative step is essential to produce the elemental sulfur that is removed by the PCE treatment. It is known that oxidation of pyrite will

produce both sulfate and elemental sulfur [15]. The current XANES data, however, have not included enough fresh coals before the oxidative step to conclude whether or not any significant amount of organic sulfur is being converted to elemental sulfur in this step. A more detailed paper is in preparation summarizing our results on PCE treated coals [16].

Coals Treated with Single Electron Transfer(SET) and Basic Reagents:

Chatterjee and Stock have discussed the removal of organic sulfur from coal by treatment with SET [9] and strongly basic reagents [10]. A suite of these desulfurized coals were previously examined by XANES spectroscopy by Chatterjee et al. using the third derivative method of XANES analysis developed by Gorbaty et al. [11]. We have examined the same suite of samples independently using the least squares analysis approach for deconvolution of the XANES. The results are summarized in Table 4.

The results for the raw Illinois no. 6 coal, obtained from the Argonne Premium Coal Sample Bank, are similar to those we have reported earlier [1], except for the presence of some sulfate. After treatment with lithium aluminum hydride (LAH), all of the pyrite and most of the sulfate have disappeared; additionally, the percentage of organic sulfide appears to have decreased relative to thiophenic sulfur. Following the SET treatment, the thiophenic sulfur percentage is significantly decreased, while the BASE treatment produces a substantial decrease in the sulfidic sulfur. This is exactly as proposed by Stock and Chatterjee [6,7] and as previously observed by the third derivative treatment of the XANES data of Gorbaty [11]. However, the results are obscured somewhat by the appearance of an unidentified sulfide which gives an s→p peak in the spectrum at -0.5 eV. Presumably, this is a potassium sulfide, in view of the nature of the chemical treatment. Since we have not conclusively identified this phase and have not determined a coefficient for conversion of its peak area percentage to sulfur percentage, we have simply assumed a conversion coefficient of 1.0 to derive the values in Table 4. This should not significantly affect the relative percentages of the other functional forms of sulfur, however.

For the samples treated with SET then BASE, and with BASE then SET, the thiophenic sulfur is markedly decreased in both cases, but there does not appear to be any decrease in the organic sulfide. In this regard, however, it should be noted that the accuracy of our method with an unknown inorganic sulfide present is not better than about ±10%.

The final two treatments indicated in Table 4 both produce significant sulfur oxidation and a decrease in thiophenic sulfur, by 50% for the last treatment. In the last treatment, it is seen that the process also produced a significant amount of elemental sulfur.

ACKNOWLEDGEMENT

This research was supported by the Office of Exploratory and Applied Research of the Electric Power Research Institute under EPRI Contract No. RP-8003-20. We are grateful to Prof. Sunyu Lee, Dr. Melissa Chou, Dr. John Kilbane, Mr. Phil Goldberg, Prof. Leon Stock and Dr. Kuntal Chatterjee for providing samples for this investigation.

REFERENCES

1. Huffman, G.P.; Mitra, S.; Huggins, F.E.; Shah, N.; Vaidya, S.; Lu, F. *Energy & Fuels* **1991**, *5*, 574.

2. Huggins, F.E.; Mitra, S.; Vaidya, S.; Taghiei, M.M.; Lu, F.; Shah, N., Huffman, G.P. *Processing and Utilization of High Sulfur Coal IV*, Dugan, P.R.; Quigley, D.A.; Attia, Y.A.; Eds.; Elsevier Sci. Pub., **1991**, *4*, 13.

3. Taghiei, M.M.; Huggins, F.E.; Shah, N.; Huffman, G.P. *Energy & Fuels*, **1992**, *6*, 293-300.

4. George, G.N.; Gorbaty, M.L. *J. Am. Chem. Soc.*, **1989**, *111*, 3182.

5. Gorbaty, M.L.; George, G.N.; Kelemen, S.R. *Fuel*, **1989**, *69*, 939.

6. Gorbaty, M.L.; George, G.N.; Kelemen, S.R. *Fuel*, **1989**, *69*, 945.

7. Lee, S.; Fullerton, K.L.; Kesawan, S.K. *Proceedings: Fourteenth Annual EPRI Conference on Fuel Science*, Ed., Lebowitz, H.E., 1990, EPRI GS-6827, pp. 7-1-7-24.

8. Chou, Melissa; Work in progress.

9. Chatterjee, K.; Wolny, R.; Stock, L.M. *Energy & Fuels*, **1990**, *4*, 402.

10. Chatterjee, K.; Stock, L.M. *Energy & Fuels*, **1991**, *5*, 704-707.

11. Chatterjee, K.; Stock, L.M.; Gorbaty, M.L.; George, G.N.; Kelemen, S.R. *Energy & Fuels*, **1991**, *5*, 771-773.

12. Kilbane, J.J.; *Proceedings: 1991 Second International Symposium on the Biological Processing of Coal*, Ed., S. Yunker; EPRI GS-7482, 1991, pp. 5-1-5-18.

13. Anastasi, J.L.; Barrish, E.M.; Coleman, W.B.; Hart, W.D.; Jonis, J.F.; Ledgerwood, L.; McClanathan, L.C.; Meyers, R.A.; Shih, C.C.; Turner, W.B. *Processing and Utilization of High Sulfur Coals III*; Eds., Markuszewski, R.; Wheelock, T.D.; Elsevier Sci. Pub., 1990, 371-377.

14. Lytle, F.W.; Greegor, R.B.; Sandstrom,D.R.; Marquies, E.C.; Wong, J.; Spiro, C.L.; Huffman, G.P.; Huggins, F.E. *Nucl. Instrum. Methods*, **1988**, *226*, 542.(26).

15. Duran, J.E.; Mahasay, S.R.; Stock, L.M. *Fuel*, **1986**, *65*, 1167-1168.

16. Huggins, F.E.; Vaidya, S.; Shah, N.; Lu, F.; Huffman, G.P.; paper in preparation.

Table 1: Sulfur Analytical Data - Biotreated Coals Samples from J. J. Kilbane (I.G.T.)

	Ill. #6 Coal Control	Ill. #6 Coal Biotreated	Ill. #6 Coal Control	Ill. #6 Coal Biotreated
Total S, Wt%	3.45	1.03	3.00	2.14
Organic S, Wt%	3.20	0.92	2.54	1.72
Pyritic S, Wt%	0.25	0.15	0.50	0.45

Table 2: Sulfur Forms in Gravimelt Coals from XANES Analysis

% of Total Sulfur in Different Forms

	Pittsburgh #8 2.19 wt% S	Gravimelt Pgh#8 0.43 wt% S	Gravimelt KY#9 0.70 wt% S
Pyrite	52	0	0
Elem. Sulfur	0	28	37
Org. sulfide	13	0	0
Thiophene	35	19	16
Sulfonate	0	16	14
Sulfate	0	37	33

Table 3. Weight percentages of sulfur contained in different functional forms for a number coals before and after PCE treatment, as determined from the XANES spectra. Precision estimated as ±0.2 wt.%

Sample	Pyrite	Elemental S	Sulfide	Thiophene	Sulfone	Sulfate
IBC-104 fresh	2.22*	0.0	0.72	1.18	0.0	0.11
IBC-104 2wk ox before	2.17*	0.0	0.61	1.07	0.0	0.12
IBC-104 2wk ox after	2.18*	0.0	0.61	1.12	0.0	0.07
IBC-104 5yr ox before	1.40*	0.17	0.53	0.86	0.13	1.01
IBC-104 5yr ox after	1.40*	0.0	0.56	0.88	0.07	0.41
Ohio #5/#6 before	0.79*	0.26	0.50	1.00	0.14	0.82
Ohio #5/#6 after	0.87*	0.0	0.54	1.04	0.04	0.29
Freeport, before	1.8*	0.65	0.25	0.85	0.0	0.2
Freeport, after	1.9*	0.0	0.25	0.7	0.0	0.25
Freeport, before	0.95*	0.87	0.05	0.25	0.05	0.82
Freeport, after	0.94	0.25	0.07	0.35	0.08	1.15
Indiana #5, before	0.85*	0.35	0.4	0.4	0.05	0.45
Indiana #5, 30 min PCE treatment	0.85*	0.2	0.3	0.4	0.05	0.45
Indiana #5, after	0.85*	0.0	0.25	0.4	0.05	0.35

*Pyritic sulfur values from Mössbauer spectroscopy.
*ASTM chemical analysis value

Table 4. Percentages of total sulfur contained in different functional forms (±5-10%).

Sample	Inorganic Sulfide	Elemental Sulfur	Organic Sulfide	Thiophenic Sulfur	Sulfoxide	Sulfone	Sulfate
Illinois No. 6 raw coal	48 - pyrite	0	18	26	0	0	9
Lithium aluminum hydride (LAH) treated coal	0	0	25	66	4	3	2
SET-treated coal	15 - unk.	0	25	36	5	15	4
BASE-treated coal	18 - unk.	0	13	49	7	8	5
SET, then BASE	21 - unk.	0	24	21	11	13	10
BASE, then SET	0	9	26	36	7	9	13
Pyrite free coal + nickelocene + LAH in THF (24 hr, 67°C)	6 - unk.	0	24	47	13	9	1
Pyrite-free coal + K + napthalene + BASE in heptane (24 h, 98°C), protonated	0	23	21	32	5	10	10

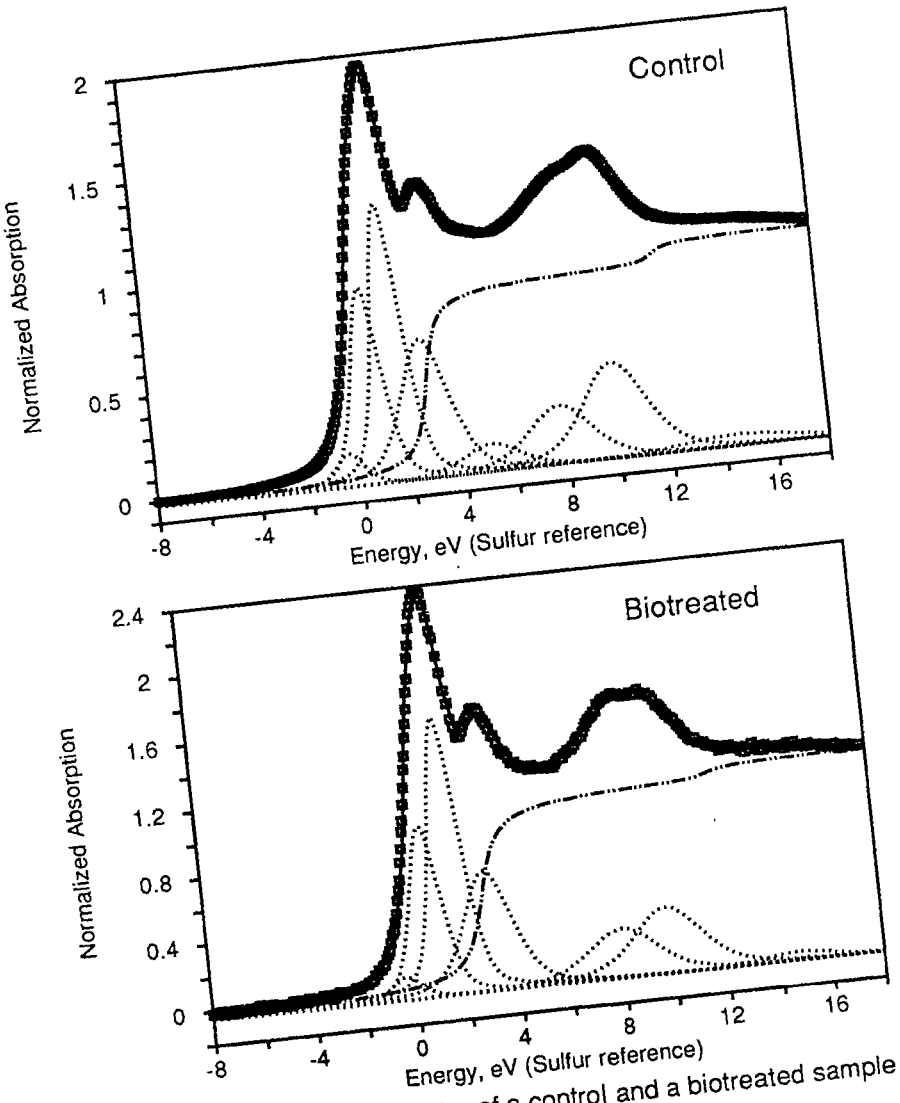

Fig 1: S K-edge XANES spectra of a control and a biotreated sample of Illinois #6 coal.

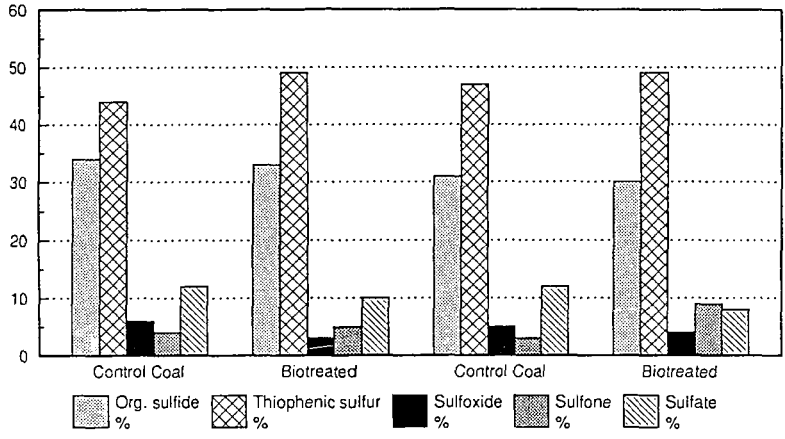

Fig. 2: Percentages of organic functional forms of sulfur in control and biotreated Illinois #6 samples as determined from the S K-edge XANES analyses.

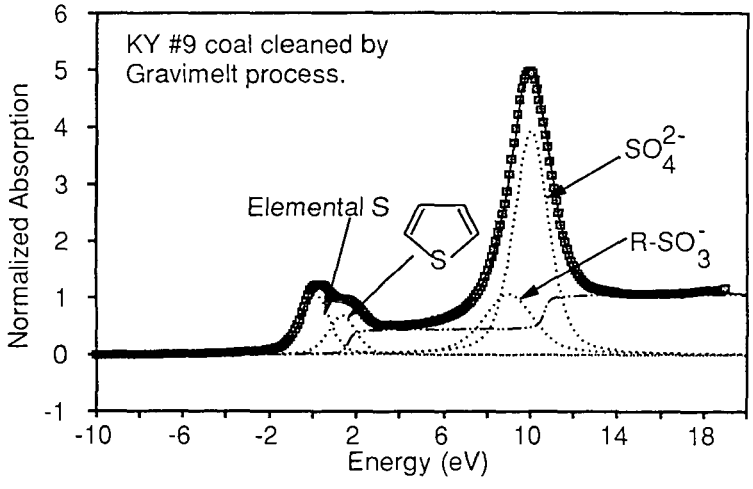

Fig. 3: Sulfur XANES spectrum of coal cleaned by molten caustic leaching.

Nitrogen Chemical Structure in Petroleum Asphaltenes and Coal by X-Ray Absorption Spectroscopy

Sudipa Mitra Kirtley,[@*] Oliver C. Mullins,[@] Jan van Elp,[*] & Stephen P. Cramer[*#]
[@] *Schlumberger-Doll Research, Ridgefield, CT 06877;*
[*] *Lawrence Berkeley Laboratory, Berkeley, CA 94720;*
[#] *University of California, Davis, Davis, CA 95616*

Keywords: nitrogen, XANES, fossil-fuel

ABSTRACT

Nitrogen chemical structure in fossil-fuel samples has been determined using x-ray absorption near-edge structure (XANES) spectroscopy. XANES data on three petroleum asphaltenes, a coal, and a number of nitrogen model compounds have been analyzed by comparing normalized areas under corresponding resonances in the spectra of the fossil-fuel samples and the model compounds. In the asphaltene and coal samples, we find that nitrogen occurs mostly in aromatic forms; very little or no evidence of saturated amines is found. The coal and asphaltenes show substantial quantities of pyrrole and pyridine fractions, and the pyrrole content is found to be greater than or equal to the pyridine content in all cases. XANES methodology is shown to be promising for the investigation of nitrogen structures in fossil-fuels, similar to its success in determining sulfur forms in similar samples over the past decade.

INTRODUCTION

Heteroatom chemistry of the heavy ends of petroleum and of coals has long been of interest for both processing and environmental concerns.[1,2] However, the study of the heteroatom chemistry in these fossil fuels is problematic. Nondestructive chromatographic methods are largely precluded due to the high molecular weights of these materials. Spectroscopic studies, particularly of nitrogen and sulfur, are difficult due to the low concentration of the heteroatoms and the elemental nonspecificity of many spectral methods. X-ray methods are element specific, and x-ray photoelectron spectroscopy (XPS) methods have been employed to study nitrogen in coals. However, XPS studies to date have suffered from the lack of resolution; peak separations from different chemical forms of nitrogen are comparable to or less than peak widths.[3,4] Additionally, XPS is particularly sensitive to surface effects. Here we report the study of nitrogen chemistry in three petroleum asphaltenes and in a coal using x-ray absorption near-edge structure (XANES). Nitrogen K-edge XANES spectra are found to have distinct and well resolved features which allow identification of the corresponding chemical forms of nitrogen. The fossil fuel spectra are satisfactorily interpreted in terms of two different kinds of aromatic model compounds, pyrrole and pyridine analogues. In both the asphaltene and coal samples, these aromatic nitrogen fractions

account for all of the nitrogen, and there are no indications of saturated amines. The coal and asphaltene samples differ in that the asphaltene has a greater fraction of pyrrolic nitrogen while the coal has comparable fractions of pyrrolic and pyridinic nitrogen fractions.

Over the past decade, XANES has emerged as perhaps the most powerful tool[5] for the analysis of sulfur in coals,[6-11] coal macerals,[10] and petroleum asphaltenes.[12,13] This is a moderately sensitive, nondestructive and element-specific method that relies on changes in positions and shapes of spectral features near the K-edge (or other edge), that depends on the chemical environment. In coals,[7,10] the organic and inorganic fractions of sulfur have been determined. In both coals[8-11] and asphaltenes,[12,13] the fractions of sulfidic and thiophenic forms of sulfur have been resolved. Different oxidized forms of sulfur have been readily identified in coals[8-10] and asphaltenes.[13] Although x-ray absorption methods have been very useful in the determination of the chemical forms of sulfur,[5-13] the application of XANES to the study of nitrogen in asphaltenes and coals is more difficult due to the low energy of the nitrogen K edge. Recent availability of high resolution soft x-ray beam lines[14] and of efficient fluorescence detectors[15] facilitates nitrogen XANES studies.

EXPERIMENTAL SETUP

Measurements were performed at the National Synchrotron Light Source at Brookhaven National Laboratories using the AT&T Bell Lab's 'Dragon' beam line (U4B).[14] Typical incident x-ray resolution in the experiments was 0.14 eV. The powdered samples were placed on silicon supports using nitrogen-free double-stick tape. The sample was then placed in the vacuum chamber fitted with a cryopump which maintained the pressure at ~10^{-9} torr. Energy calibration was performed using zinc octaethylporphyrin which has a resonance at 399.72 eV. Fluorescence detected x-ray absorption spectra were obtained using a seven element Ge detector,[15] with single channel analyzers set to select the shaped pulses corresponding to the nitrogen Kα emission.[15] The coal sample was obtained from Argonne National Labs (Pittsburgh #8), the asphaltenes were prepared from crude oils from California, USA (CAL), France (FRA), and Kuwait (UG8), by 40cc/g dilution with n-heptane, and the pure model compounds were obtained from the Aldrich Chemical Company.

RESULTS AND DISCUSSION

Figure 1 compares the fluorescence excitation spectra of the petroleum asphaltenes and Pittsburgh #8 coal.[16] (Figure 1 also shows the composite spectrum consisting of the weighted sum of the spectra of acridine and carbazole, see below). Three distinct spectral regions are apparent in all spectra, at 399.5 eV, 403 eV, 408 eV. To assign these features, we have resorted to the fluorescence detected x-ray absorption spectra of model compounds, as shown in figure 2. Acridine, a pyridine analogue, has a particularly strong resonance at ~399 eV which is assigned to a 1s$\rightarrow\pi^*$ transition.[17] Carbazole, a pyrrole analogue, has a strong resonance at ~403 eV which is also assigned to a 1s$\rightarrow\pi^*$ resonance.[17] 1,3,5-

tribenzylhexahydro-1,3,5-triazine, a saturated amine, exhibits only a broad σ resonance at ~408 eV, a slightly lower energy than the σ resonances of the aromatic compounds.[17] The π* resonances of the two different types of aromatic compounds are well resolved which is advantageous for interpreting the data.

There is a clear correspondence in the spectra between the peaks of the aromatic compounds with peaks of asphaltenes and coal in figure 1. Assuming the oscillator strengths of these transitions remain in constant ratio with post threshold continuum absorption at 420 eV, these spectra can be used to quantitatively determine the various nitrogen fractions. Small energy shifts between peaks in the spectra of models and fossil fuel samples are observed. Furthermore, peak widths in the spectra of the fossil fuel samples are somewhat larger than for the pure model compounds. Therefore, we did not simply fit the asphaltene and coal spectra with sums of model spectra. We fit all spectra with a sum of Lorentzian peaks and an arc-tangent step function. We used peak areas normalized by the step height to determine nitrogen fractions in the fossil fuels. For the asphaltene and coal spectra, the area of the lowest energy resonances at ~399.7 eV was assigned to the pyridine analogue, thereby determining the pyridine fraction. The resonances near 403.5 were assigned to both pyridine (already determined) and pyrrole. The contribution of pyridine to the area of the broad peak centered at ~403.5 eV was subtracted and the remaining peak area was assigned to the pyrrole analogue, thereby determining the pyrrole fraction. Likewise, the peak area of the 409 eV peak was assigned to both aromatics (already determined) and the saturated amine. The contribution of the aromatics to the very broad peak at ~409 eV was subtracted and any remaining, unaccounted for peak area was assigned to the saturated amine.

The fitting procedure resulted in the following peak positions (listed in eV). UG8 asphaltene: 399.3, 399.8, 402.55, 403.4, 406.77, 408.0, 410.8, 412.5, 415.5 and step 408.6; FRA asphaltene:399.6, 402.2, 403.2, 406.5, 407.8, 412.8, and step 408.6; CAL asphaltene: 399.8, 402.4, 403.5, 406.2, 407.4, 412.3, 416.9, and step 408.3; Pittsburgh #8 coal: 399.5, 400.05, 402.7, 404.05, 407.08, 408.2, 412.9, and step 408.6; acridine: 399.25, 399.6, 401.8, 403.3, 406.4, 407.9, 408.9, 412.9 and step 408.6; carbazole: 402.3, 403.2, 404.2, 406.1, 408.0, 410.4, 413.3, 418.4, and step 408.4; and tribenzylhexahydrotriazine: 402.3, 402.9, 405.3, 407.5, 410.0, 413.3, and step 408.5.

The normalized fractional forms of nitrogen are for CAL: 50% pyridine, 48% pyrrole, and saturated amine 2%, for FRA: 40% pyridine, and 60% pyrrole, for UG8: 37% pyridine, 63% pyrrole, and for coal: 47% pyridine, 53% pyrrole. The error estimate, based on the unnormalized nitrogen fraction, is considered to be about 10%. Figure 1 shows the similarity of the overall features of the spectra of the fossil fuels, although there are some differences in peak positions and widths. For the sake of comparison, a weighted spectral sum with 42% acridine and 58% carbazole (fractional values intermediate between coal and asphaltene results) is also shown. Examination of a greater selection of model compounds may reduce

discrepancies between spectra of fossil fuels and the spectral sum of model compounds. The coal and the three asphaltenes exhibit appreciable fractions of both pyrrolic and pyridinic nitrogen, with the pyrrolic nitrogen content being either greater than or equal to the pyridinic content in all four samples. Little evidence of saturated amine is found in any sample. XPS methods employing pyrrole and pyridine models have been used to study coal-derived materials,[3,4] and coals.[4] Coal asphaltenes[3] were found to contain 49-62% and coals[4] 65-85% pyrrolic nitrogen, the rest being assigned to pyridine analogues in both cases. Our determination of pyrrolic and pyridinic nitrogen fractions for our asphaltene samples is similar to the XPS results for coal asphaltenes, and the pyrrolic estimate for our coal is somewhat lower than the XPS coal results. Uncertainties exist in the XPS results as a result of resolution difficulties. For all asphaltenes and coals, the nitrogen is much more aromatic than the (organic) sulfur where large sulfidic fractions are found. Additionally, for asphaltenes, the fraction of aromatic nitrogen is much larger than the fraction of aromatic carbon (~40%), whereas in coal, such a comparison can not be easily made, since the aromatic carbon content varies significantly among different coals.[18]

CONCLUSIONS

Nitrogen XANES methods are powerful for determining different chemical forms of nitrogen in asphaltenes and coals. The high degree of specificity of this technique coupled with the well resolved resonances of various forms of nitrogen provide one of the best methods for differentiating nitrogen chemical forms in fossil fuels. Aromatic pyrrolic and pyridinic nitrogen are the most prevalent forms of nitrogen found in the asphaltenes and coal; pyrrolic nitrogen is generally more abundant than pyridinic nitrogen, although considerable variability is observed in the pyrrole and pyridine fractions of nitrogen in the asphaltene and coal samples. Little evidence of saturated amines is found in these fossil-fuel samples. Non-destructive and direct XANES methodology for nitrogen characterization in amorphous fossil-fuel samples is shown to be very successful, and holds promise for further work in this area.

Acknowledgments

Research carried out at the National Synchrotron Light Source at Brookhaven National Laboratory which is supported by U.S. Dept. of Energy, Division of Material Science and Division of Chemical Science. SPC acknowledges support by Lawrence Berkeley Lab, Exploratory Research Fund and by the National Institutes of Health, Grant GM-44380.

References

1) Coal Science II, H.H. Schobert, K.D. Bartle, and L.J. Lynch Eds., ACS symp. Series #461 Amer. Chem. Soc., Washington D.C., (1991)

2) Chemistry of Asphaltenes, J.W. Bunger, N.C. Li, Eds., Amer. Chem. Soc., Washington, D.C., (1981)

3) S. Wallace, K.D. Bartle, D.L. Perry, Fuel, 68, 1450, (1989)

4) P. Burchill, Intl. Conf. Coal Science, J.A. Moulijn et al eds., Elsevier Pub., Amsterdam, 5, (1987)

5) L.M. Stock, R. Wolny, B. Bal, Energy & Fuels, 3, 651, (1989)

6) Z. Hussain, E. Umbach, D.A. Shirley, J. Stohr, J. Feldhaus, Nucl. Instrum. Methods. Phys. Res. 195, 115, (1982)

7) C.E. Spiro, J. Wong, F. Lytle, R.B. Greegor, D. Maylotte, S. Lampson, Science 226, 48, (1984)

8) G.P. Huffman, F.E. Huggins, H.E. Francis, S. Mitra, and N. Shah, Coal Science and Tech.16: Proc. and Util. of High Sulfur Coals III, 21, (R. Markuszewski et al eds.), 21, (1990)

9) M.L. Gorbaty, G.N. George, S.R. Kelemen, Fuel, 69, 1065, (1990)

10) G.P. Huffman, S. Mitra, N. Shah, S. Vaidya, and F. Lu, Energy & Fuels, 5, 574, (1991)

11) G.N. George, M.L. Gorbaty, S.R. Kelemen, and M. Sansone, Energy & Fuels, 5, 93, (1991))

12) G.N. George, M.L. Gorbaty, J. Amer. Chem. Soc., 111, 3182, (1989)

13) G.S. Waldo, O.C. Mullins, J.E. Penner-Hahn, S.P. Cramer, Fuel, 71, 53, (1992)

14) C.T. Chen, Nucl. Instrum. Methods Phys. Res. A, 256, 595 (1987); C.T. Chen, F. Sette, Rev. Sci. Instrum. 60, 1616, (1989)

15) S.P. Cramer, O. Tench, M. Yocum, H. Craner, L. Rogers, V. Radeka, O.C. Mullins, and S. Rescia, X-Ray Absorption Fine Structure - Proc. 6th Intl. XAFS Conf., S.S. Hasnain, Ed., Ellis Horwood Chichester, 640, (1991)

16) Using x-ray absorption tables (J.J. Yeh, I. Lindau, Atomic Nuc. Data Tables, 32, 1, (1983)), maximum nonlinearities from concentration effects in the model compound spectra are calculated to be ~7% and were corrected

for in the data using Eqn. 23, in J. Goulon, C. Goulon-Ginet, R. Cortes, J.M. Dubois, J. Physique. 43, 539, (1982)

17) J.L. Dehmer, A.C. Parr, S.H. Southworth, Ch. 5 in Handbook on Sychrotron Radiation, Vol. 2, G.V. Marr Ed., North-Holland, Amsterdam, (1987)

18) R.M. Davidson, Coal Science, Vol. 1, I. G. Dryden Ed., Academic Press Inc., 83, (1982)

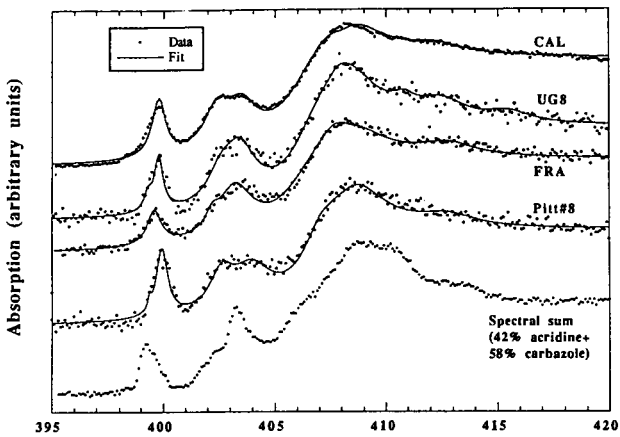

Figure 1. Nitrogen K-edge absorption spectra of three asphaltene samples: CAL, FRA, and UG8, and one coal sample: Pittsburgh #8. Dots are data and the solid lines are fits consisting of a sum of lorentzians and an arc-tan function. Also shown (at the bottom) is the weighted sum of the spectra of a pyridine analogue, acridine (42%), and a pyrrole analogue, carbazole (58%).

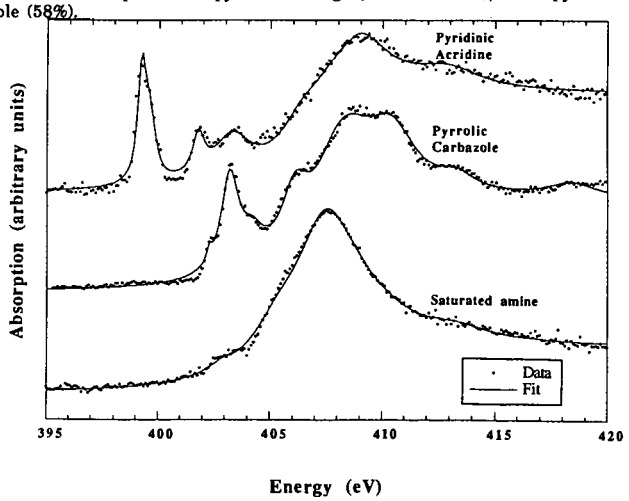

Figure 2. Nitrogen K-edge absorption spectra of three model compounds used to fit the fossil fuel spectra, acridine - a pyridine analogue, carbazole - a pyrrole analogue, and tribenzylhexahydrotriazine - a saturated amine. Dots are data and the solid lines are fits consisting of a sum of lorentzians and an arc-tan function.

APPLICATION OF XAFS SPECTROSCOPY TO THE SPECIATION OF CRITICAL TRACE ELEMENTS IN COAL UTILIZATION

Frank E. Huggins, Naresh Shah, Jianmin Zhao, Fulong Lu, and G. P. Huffman,
University of Kentucky, Lexington, KY 40506.

Keywords: XAFS spectroscopy, chromium, arsenic, trace elements, coal

ABSTRACT

The environmental impact of specific trace element species in coal utilization and waste disposal depends not only on the abundance, but also on the form(s) of occurrence of the element present in such materials. While there are a number of analytical methods for determining the abundance of trace elements in coal, there are very few methods available for determining the form of occurrence (speciation) of a trace element in coal at abundances as low as 10 ppm. In this report, the potential of XAFS spectroscopy for trace element speciation is demonstrated by means of measurements on two important trace elements, arsenic and chromium, in coal and ash.

INTRODUCTION:

In the United States in recent years, almost one billion tons of coal have been mined each year, of which 85-90% is used for electrical power generation [1]. Combustion of such huge tonnages of coal has the potential to release vast amounts of undesirable elements into the U.S. environment. For example, for an element such as arsenic that occurs in many U.S. coals only at the 10 - 50 ppm level [2,3], there is the potential for 10,000 - 50,000 tons of arsenic to be released to the environment from coal utilization annually. Some of the arsenic may be removed by coal washing, some will be trapped in the solid products (ash and slag) of coal combustion, some will be collected in fly ash, and some will escape to the environment in combustion gases and fugitive emissions. The collected wastes from coal washing and combustion are often dumped into ash settling ponds, where, due to aqueous leaching of the wastes, there is additional opportunity for arsenic to enter the environment through groundwater. Such a scenario will be followed by many of the eleven trace metal species identified as potentially hazardous to the environment by the 1990 Amendments to the Clean Air Act.

It is clear that the environmental impact and hazard assessment of a specific element in coal combustion is a highly complex issue. For instance, it is apparent that minimization of an element's contribution to degradation of air quality either by coal cleaning prior to combustion or by efficient capture of fly ash and effluent gases in scrubbers after combustion may exacerbate problems with groundwater quality because of the leaching and reactivity characteristics of higher amounts of the element in cleaning or combustion wastes. Moreover, little is known about the forms-of-occurrence of most trace elements in coal, ash and other wastes and how such factors might influence the behavior of the element during combustion and its segregation into various solid and gaseous forms during cleaning, combustion, and waste disposal.

In order to understand the behavior of a given element in coal combustion and waste disposal and perhaps remedy some of the potential problems associated with environmental contamination by hazardous trace elements, it is not enough just to determine the amount of an element in the coal and various waste fractions. It is essential to know also how the element

occurs in the coal and other fractions. The mode or form of occurrence of the element in the coal (i.e., whether the element forms a specific mineral, whether it is dispersed within a particular host mineral or in the coal macerals, with which fraction of the coal the element is associated, in which oxidation state the element occurs in the coal, etc.) controls to a great extent the potential hazard posed by the element to human health and the environment.

There are many different methods of quantitatively determining the amount of an element in coal; such methods include atomic absorption, X-ray fluorescence, instrumental neutron activation analysis, proton induced X-ray or gamma-ray emission, inductively coupled plasma techniques, etc. However, there are very few methods for determining the forms of occurrence of a trace element in materials as complex as coal, ash, slags, and solutions (e.g. leachates). A technique that has excellent demonstrated potential for investigating the forms of occurrence of trace elements in coal and other materials is X-ray absorption fine structure (XAFS) spectroscopy [4-6]. This technique has the ability to focus on a specific element in a material and to provide detailed information relevant to the local bonding and structure of the element in the material, from which the form of occurrence can usually be deduced. Furthermore, this technique is both direct and nondestructive. In this report, the application of XAFS spectroscopy to the speciation of trace element species is demonstrated by a preliminary survey investigation of chromium and arsenic in coal and ash. Both of these elements have been identified as potentially hazardous to the environment in the 1990 Amendments to the Clean Air Act.

EXPERIMENTAL:

Samples: For this survey study, coal samples were obtained from a variety of sources. Samples unusually high in arsenic (up to 2,000 ppm) were provided by Dr. Leslie Ruppert at the U.S. Geological Survey [7]; the Upper Freeport coal in the Argonne Premium Coal Sample Bank (APCSB), which has an arsenic content of 17 ppm [3], was also investigated as its abundance of arsenic is more typical of that in the majority of U.S. coals. This coal was also subjected to laboratory float/sink tests; a 1.6 float sample, a 1.6 sink - 2.85 float sample, and a 2.85 sink sample were prepared by centrifugation using perchloroethylene (C_2Cl_4, sp. gr. 1.6) and bromoform ($CHBr_3$, sp. gr. 2.85) as the heavy liquid separation media. A raw coal with a typical (≈20 ppm) chromium content and the corresponding clean coal after treatment by the spherical oil agglomeration process (SOAP) and the resulting ash samples were obtained from combustion studies performed at Physical Sciences, Inc., by Dr. J. Helble; coals with somewhat higher than average chromium contents (up to 140 ppm) were obtained from the Penn State Coal Bank.

XAFS Spectroscopy: XAFS spectroscopy was performed at beam-line X-19A at the National Synchrotron Light Source, Brookhaven National Laboratory. For chromium in coals and ash samples, the absorption of X-rays was measured over the spectral range from 5.9 keV to 6.2 keV; over the X-ray absorption near-edge structure (XANES) region (5.97 to 6.03 keV), absorption data were collected every 0.2 eV. For arsenic in coals and ash samples, the absorption of X-rays was measured over the spectral range from 11.75 keV to 12.0 keV; over the XANES region (11.85 to 11.90 keV), absorption data were collected every 0.25 eV. Absorption of the X-rays was measured by means of a thirteen-element germanium array detector [8] that detected the fluorescent X-rays only in a specified tunable energy window that corresponded to the energy of the chromium or arsenic fluorescent K_α X-rays. In addition, the appropriate 6μ vanadium or germanium filter was used to minimize background. Up to ten scans were recorded and summed for the weakest absorbers. The spectral summations, the pulse-height windowing, and the low-energy filtering all contributed to enhance the signal-to-noise ratio of the trace element spectra. For reference standards, conventional ion chambers were used to measure both the fluorescent and absorption XAFS spectra in a single scan. Depending on the amount of arsenic or chromium

in the standard, the standard was diluted in graphite to optimize the absorption spectrum. As is normally done, the chromium or arsenic XAFS spectra were divided into separate XANES and, where feasible, EXAFS regions and standard XAFS analysis methods were employed to analyze the spectral regions. The arsenic K-edge XANES spectra shown in this report are calibrated with respect to a zero energy point (11.867 keV) defined as the position of the white line in the spectrum of As_2O_3 that was run simultaneously with all arsenic spectra. The zero energy point (5.989 keV) for chromium was defined as the first inflection point in the XAFS spectrum of chromium metal foil.

RESULTS AND DISCUSSION:

Arsenic: Arsenic K-edge XANES spectra for three high arsenic coals from Alabama are shown in Figure 1. It is clear, by inspection, that the spectra are the combination of at least two distinct forms-of-arsenic as the white line features (the prominent peaks near 0 eV) consist of two components. All standards with a single oxidation state of arsenic investigated to date merely give a single component white line, the position of which shifts to higher energy with increasing formal oxidation state of the arsenic atom. Based on comparison of peak positions with standards, the lower-energy component is assigned to arsenic substituting for sulfur in the pyrite structure and the higher-energy component to arsenic in the arsenate anion (AsO_4^{3-}). Furthermore, the radial structure functions (RSFs) derived from the EXAFS region for the high-arsenic coals also show two peaks at the appropriate distances for As-O bonds in arsenate anions and for As-Fe(S) bonds in pyrite (Figure 2). The relative heights of the two peaks in the XANES spectra show the same order as the relative heights of the corresponding peaks in the RSFs.

Arsenic K-edge XANES spectra of three Upper Freeport APCSB coal fractions are shown in Figure 3. In comparison to Figure 1, the signal-to-noise ratio is significantly lower, but the spectra are still informative. In the two fresh samples, there is essentially only one white line component, which arises from arsenic associated with pyrite; only a trace amount (<5% of the arsenic) is present in arsenate form, as indicated by the very small peak on the higher energy side of the white line. The arsenic XAFS spectra of these samples were measured just a few days after opening the APCSB vials. Similar measurements made on whole coal and float/sink samples of the Upper Freeport coal from APCSB vials that had been opened six months previously and left exposed to the laboratory atmosphere showed much greater amounts of arsenate, as for example in the spectrum of the oxidized 2.85 sink sample in Fig. 3. An ash sample prepared from an unrelated Upper Freeport coal showed that all of the arsenic was present in the arsenate form (bottom spectrum, Fig. 3)

Chromium: It is a relatively easy matter to discriminate by means of XAFS spectroscopy among the two most common oxidation states of chromium, Cr^{3+} and CrO_4^{2-}, found in natural and environmental samples. Chromium XAFS spectra of two chromic oxide and two chromate samples are shown in Figure 4. The chromate oxidation state is characterized by the presence of a large pre-edge feature at about 0 eV that is highly distinctive of first series transition metal $3d^0$ species in tetrahedral coordination by oxygen anions. In addition, it should be noted that the maximum absorption in the chromate species occurs at about 40 - 50 eV, at which energy a minimum in the absorption occurs for the Cr^{3+} compounds. These observations appear to be quite general and to apply to all the chromium standards so far examined.

Figures 5 and 6 show chromium XAFS spectra obtained for coal and ash samples. In Figure 5 are shown spectra for the parent Illinois #6 coal and the SOAP cleaned coal. These spectra are virtually identical in appearance and clearly demonstrate that all (>95%) of the chromium is present in the Cr^{3+} oxidation state. In addition, the abundance of chromium in the two samples is essentially the same. These observations suggest that there is only one significant

chromium form of occurrence and that it is not strongly associated with the mineral matter, otherwise the chromium abundance would have dropped significantly upon cleaning and the XAFS spectrum would have shown significant variation. Chromium in the ash sample is also predominantly Cr^{3+}, although the spectral shape differs somewhat from that of the coal samples. The chromium XAFS spectra of the high chromium bituminous coals (Ohio #5 and Illinois #6) shown in Figure 6 are very similar to those shown in Figure 5. The spectrum of the anthracite sample, although similar to those of the bituminous coals, exhibits a somewhat sharper white line peak.

CONCLUSIONS:

This survey study demonstrates that XAFS spectroscopy is capable of obtaining significant information on the oxidation state and form of occurrence of trace elements that exist in coal at about the 10 ppm level. This information complements conventional analytical data on trace element abundances and provides additional information for evaluation of the potential environmental hazard of specific elements in coal combustion. For example, of the two oxidation states of chromium considered here, the CrO_4^{2-} oxidation state is both toxic and carcinogenic, whereas the Cr^{3+} oxidation state at such low concentration levels (<100 ppm) does not pose a significant health risk [9]. If the results of this study can be considered to be general, then the absence of the chromate state in both coal and ash would imply that the hazard posed by chromium in coal utilization is minimal. In contrast, the investigation of arsenic in coal and ash by XAFS reveals significant oxidation of the arsenic associated with pyrite to arsenate (AsO_4^{3-}) species that can be easily leached from coal wastes and which may pose a significant health hazard.

Acknowledgements:

We are grateful to Dr. L. F. Ruppert (U.S. Geological Survey) and Dr. J. Helble (Physical Sciences, Inc.) for their donation of analyzed samples for this study. This study was supported by the Office of Exploratory Research of the Electric Power Research Institute (Palo Alto, CA) under EPRI Contract No. RP-8003-20, and by the U.S. Department of Energy (Pittsburgh, PA) under DOE Contract No. DE-AC22-86pc90751. The XAFS spectra were obtained at the National Synchrotron Light Source at Brookhaven National Laboratory, which is supported by the U.S. Department of Energy.

References:

1. 1992 Keystone Coal Industry Manual, MacLean Hunter Publications, Chicago, IL (1992).
2. H.J. Gluskoter, R.R. Ruch, W.G. Miller, R.A. Cahill, G.B. Dreher, and J.K. Kuhn, Illinois State Geological Survey, Circular 499, 154 pp., (1977).
3. C.A. Palmer, Energy & Fuels, 4, 436-439, (1990).
4. J. Wong, C.L. Spiro, D.H. Maylotte, F.W. Lytle, and R.B. Greegor, in EXAFS and Near-Edge Structure III, (eds. K.O. Hodgson, B. Hedman, and J.E. Penner-Hahn), Springer Proc. Phys. 2, 362-367, (1984).
5. J.E. Silk, L.D. Hansen, D.J. Eatough, M.W. Hill, N.F. Mangelson, F.W. Lytle, and R.B. Greegor, Physica B (Proceedings, XAFS V), 158, 247-248, (1989).
6. F.E. Huggins, G.P. Huffman, and S.H. Bauer, J. Coal Qual., 8(3,4), 119, (1989).
7. L.F. Ruppert, J.A. Minkin, J.J. McGee, and C.B. Cecil, Energy & Fuels, 6, 120-125, (1992).
8. S.P. Cramer, O. Tench, N. Yocum, and G.N. George, Nucl. Instr. Meth. A266, 586-591, (1988).
9. N. Tietz (Ed.), "Clinical Guide to Laboratory Tests", (2nd. Edition), W. B. Saunders, Philadelphia, PA, (1990).

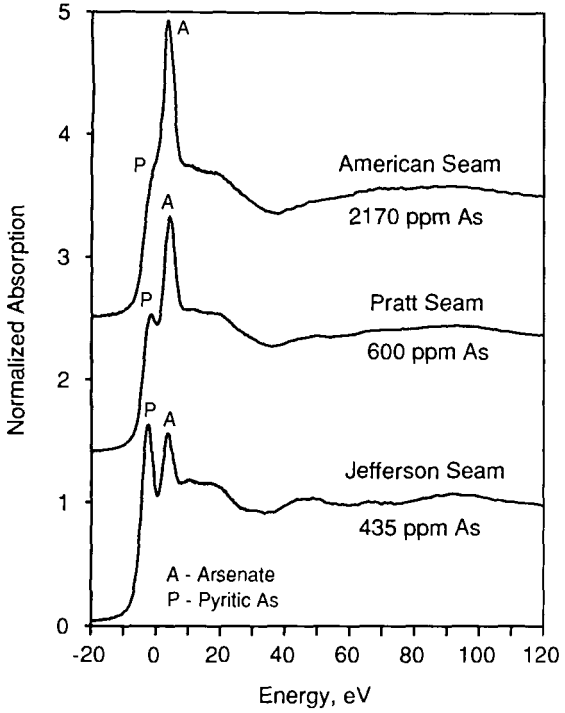

Figure 1: As K-edge XANES spectra of three high arsenic coal fractions from bituminous coal seams in Alabama.

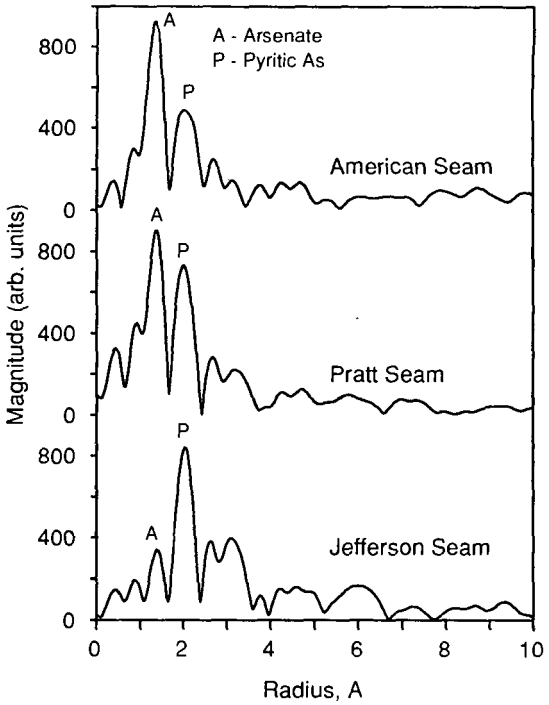

Figure 2: RSF's derived from EXAFS regions of As XAFS spectra for high arsenic coal fractions from Alabama.

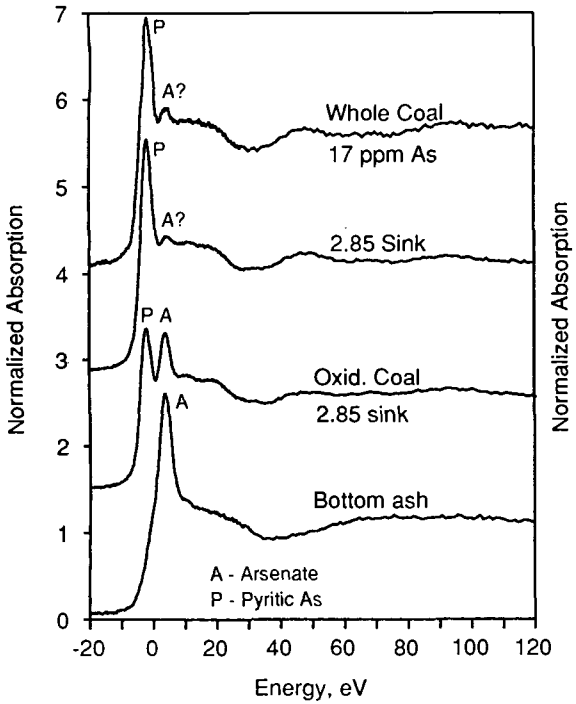

Figure 3: As K-edge XANES spectra of three Upper Freeport coal fractions and an ash sample.

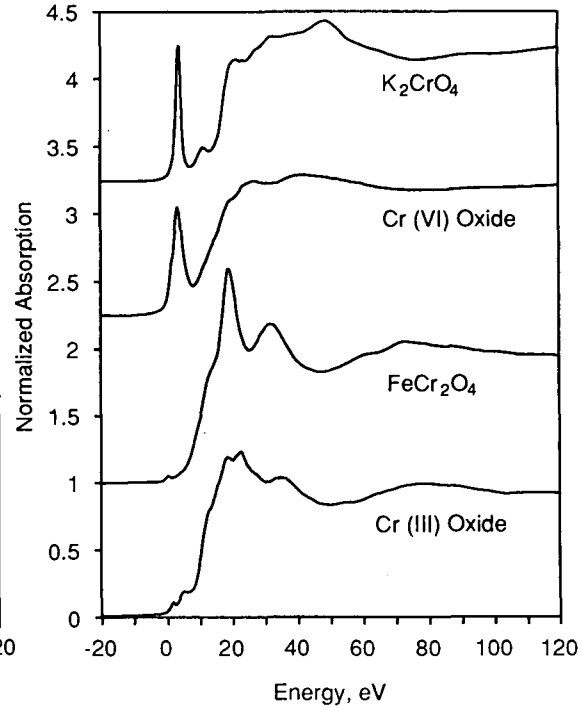

Figure 4: Cr K-edge XANES spectra of two chromic and two chromate oxide reference standards.

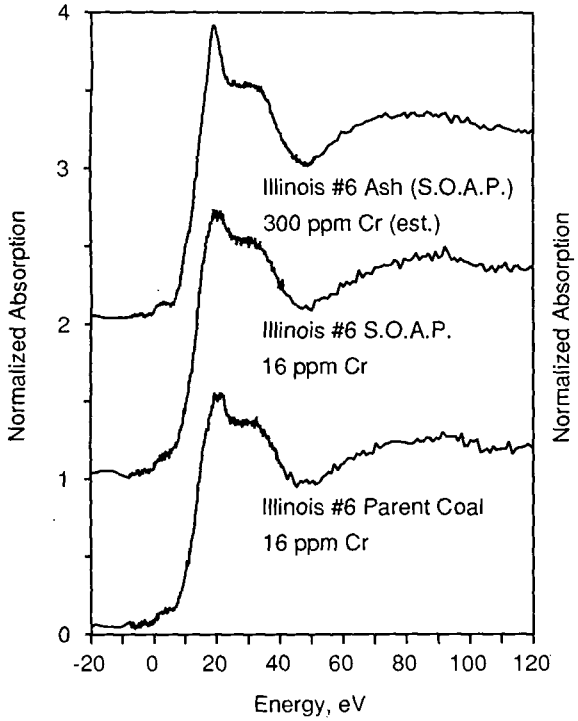

Figure 5: Cr XANES spectra of Illinois #6 parent coal, a cleaned coal, and a derived ash sample.

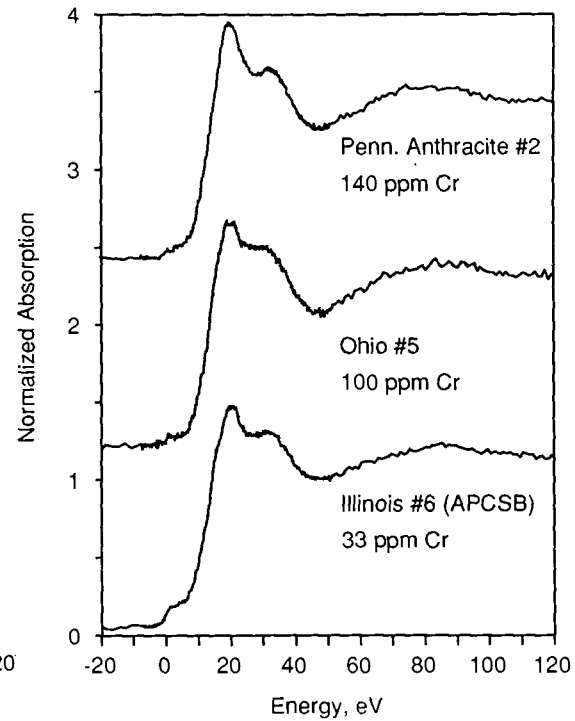

Figure 6: Cr XANES spectra of three high chromium coal samples.

MULTI-ELEMENTAL ANALYSIS OF ARGONNE PREMIUM COAL SAMPLES BY SIMULTANEOUS PROTON-INDUCED GAMMA-RAY/X-RAY EMISSION SPECTROMETRY

A. S. Wong and J. D. Robertson
Department of Chemistry and Center for Applied Energy Research
University of Kentucky, Lexington, KY 40506-0055

Keywords: Argonne Premium Coals; trace elements; PIXE/PIGE

INTRODUCTION

Although the Argonne Premium whole coal samples are widely used by the coal research community,[1] relatively little work has been done on determining the trace element composition of these materials. Of the more than 340 references in the Users Handbook for these reference materials,[2] only three papers report trace-element concentration data. Instrumental neutron activation analysis (INAA)[3], inductively coupled argon plasma-atomic emission spectrometry (ICAP-AES)[4] and X-ray fluorescence spectrometry (XRF)[5] have been applied to the Argonne Premium coal samples. The INAA measurements were performed on the whole coals while the XRF and ICAP-AES measurements utilized ashed samples.

We have used external beam proton-induced gamma-ray and X-ray emission (PIGE/PIXE) analysis to determine the concentration of 28 minor and trace elements in 8 Argonne Premium whole coal samples. Briefly, PIGE and PIXE are rapid, nondestructive multielemental analysis techniques that can be *instrumentally* applied to coal, fly ash, and coal derived materials. Because PIGE and PIXE can be applied to whole coal, they can, like INAA, be used to measure elements that might be volatilized during ashing. The other chief advantage of these two ion beam analysis techniques is that they are free of the chemical interference effects that arise in the elemental analysis of such complex matrices by more traditional methods such as ICAP-AES and GF-AAS. In principle, PIXE is capable of determining the concentration of all elements from sodium through uranium with relatively uniform sensitivity . In practice, up to 20 elements are commonly determined per irradiation at fractional mass sensitivities of 1.0 to 10.0 ppm. Unlike PIXE, the sensitivity of PIGE varies greatly from element to element. It does, however, provide concentration information for the light elements lithium, fluorine, sodium and aluminum in these samples.

EXPERIMENTAL PROCEDURE

Sample Preparation. The samples were oven dried for 24 hours at 105 °C and prepared by pelletizing *c.a.* 200 mg of the coal (-100 mesh) in a 13 mm stainless steel die at 90 Mpa. Single and multielemental graphite standards were used in the thick-target PIXE analysis. High purity graphite powder (-100 mesh) was spiked with single ($CaCl_2$ and KCl) and NIST multielement SRM spectrometric solutions (SRM 3172 and 3174) and dried at 105° for 24 hours. The spiked graphite was then mixed in a methacrylate vial on a mixer mill for 30 minutes and pressed into a 13-mm diameter pellet.

Thick-Target PIGE/PIXE Analyses. The measurements were performed at the University of Kentucky 7.5 MV Van de Graaff accelerator.[6] The γ-rays were detected with a

HpGe detector with a full-width-half-maximum (FWHM) resolution of 1.87 keV at 1274 keV which was placed 3.0 cm from the target at an angle of 90° relative to the beam direction. The X-rays were detected with a Si(Li) detector with a FWHM resolution of 165 eV at 5.90 keV that was placed 5.4 cm from the target at an angle of 45°. A 700 μm thick mylar filter and a 10 μm thick Cr critical absorber were placed in front of the Si(Li) detector to reduced the bremsstrahlung background and the intensity of Fe X-rays. A total of five irradiations were performed; the critical absorber was removed during two of the irradiations in order to determine the concentration of Cr. All irradiations were performed at 2.5 MeV (on target) with an external proton beam in helium using on-demand beam pulsing. The beam, normal to the target surface, was rastered over the sample at 1 Hz irradiating a spot of 5 mm by 7 mm. The proton beam current, on the extraction foil, ranged from 50 to 100 nA and the irradiation times ranged from 10 to 15 min. per sample. Rather than adjust the beam current to maintain a constant count rate, a pulser was used to correct for the dead time in the PIGE spectra. In this case, the dead time in the PIGE spectra was less than 3% for all coal samples. The accuracy of the measurements was determined by analyzing three NIST coal SRM's (1632a, 1632b, 1635).

RESULTS and DISCUSSION

PIGE Analysis. A typical PIGE spectrum of an Argonne Premium coal sample is shown in Figure 1. The nuclear reactions utilized in the PIGE measurements were $^{7}Li(p,p_1)^{7}Li$, Eγ = 478 keV; $^{19}F(p,p_2)^{19}F$, Eγ = 197 keV; $^{23}Na(p,p_1)^{23}Na$, Eγ = 439 keV; and $^{27}Al(p,p_2)^{27}Al$, Eγ = 1013 keV. The concentrations of Li, F, Na and Al were determined by comparison of the normalized γ-ray yields with those obtained from either the NIST 1632a or NIST 1635 coal SRM's. In the comparative method, the concentration of an element (C) is determined by:

$$C = C_{std} \cdot (Y \cdot S)/(Y_{std} \cdot S_{std})$$

where Y is the normalized γ-ray, S is the stopping power of the proton beam (at 2.5 MeV), and C_{std} is the concentration of the element in the standard. NIST 1632a was used as the reference standard for Li and Na in all samples. The Argonne samples with a F concentration of less than 100 ppm and an Al concentration of less than 1 wt. percent were compared to NIST 1635. The PIGE results given in Table I are the average values obtained from 7 irradiations of each Argonne sample. The errors are reported as the standard error of the mean.

The sensitivities for these four light elements in whole coal samples are: Li, 5 ppm; F, 5 ppm; Na, 10 ppm; and Al, 200 ppm. These limits of detection (LOD) are based upon a minimum observable peak area of $3\sqrt{bkg}$ where bkg is the background over 1 FWHM about the γ-ray peak's centroid. The relative standard deviation, based upon counting statistics, for a single measurement ranged from 2% to 20%.

The Na concentration values given in Table I agree well with the values determined both by INAA[3] and ICAP-AES[4] and the Al values are in good agreement with those obtained by ICAP-AES.[4] In the case of Li, the PIGE values for two of the Argonne coals (POC and UT) agree with the FAAS results of Doughten and Gillison.[4] For the remaining six samples, the PIGE results are consistently lower than the FAAS values. Similarly, the F values given in Table I for the ND, POC, and UT samples are in good agreement with the ISE results of Doughten and Gillison.[4] Our results for the remaining five samples are, again, considerably lower than the ISE values.

PIXE Analysis. A typical PIXE spectrum of an Argonne Premium coal sample is shown in Figure 2. A comparison of our thick-target PIXE results with the literature values for the NIST SRM's[7] are given in Table II. With the exception of Cr, Ge, and Th, the values obtained by PIXE in this study agree, within the error bars reported, with the literature values for the NIST SRM's.

The results of the PIXE analysis for 24 minor and trace elements in the Argonne premium coal samples are given in Table I. The errors are the standard error of the mean from the 7 irradiations. In the majority of cases, the PIXE results agree, within the error bars reported, with the values obtained by INAA[3] and ICAP-AES.[4]

CONCLUSION

The concentrations of 28 minor and trace elements in 8 Argonne premium coal samples have been determined by simultaneous PIXE/PIGE analysis. In general, the PIXE/PIGE results agree with the values obtained by INAA[3] and ICAP-AES.[4] However, additional analyses are needed to resolve the discrepancy between the Li and F concentration values reported in this work and by Doughten and Gillison.[4] From previous work on the determination of F in similar reference materials,[8] we would suggest that a series of pyrohydrolysis measurements could resolve the differences observed for fluorine.

ACKNOWLEDGEMENTS

This work was supported by the DOE Kentucky EPSCoR Doctoral Traineeship Program. We are indebted to H. Francis from the Kentucky Geological Survey for providing the Argonne coal samples used in this work.

REFERENCES

1. Vorres, K. S., *Energy and Fuels 4*, 420 (1990).
2. Vorres, K.S. Users Handbook for the Argonne Premium Coal Sample Program, Argonne National Laboratory, Argonne, IL, ANL/PCSP-89/1 and Newsletter.
3. Doughten, M. W. and Gillison, J. R., *Energy and Fuels 4*, 426 (1990).
4. Palmer, C. A., *Energy and Fuels 4*, 436 (1990).
5. Evans, J. R., Sellers, G. A. and Johnson, R. G., *Energy and Fuels 4*, 440, (1990).
6. Robertson, J.D., Bates, J.B., Dudney, N.J. and Zuhr, R.A., *Nucl. Instr. and Meth. B56/57*, 722 (1991).
7. Gladney, E.S., O'Malley, B.T., Roelandts, I. and Gills, T. E., Standard Rederence Materials Compliation of Elemental Concentration Data for NBS Clinical, Biological, Geological and Environmental Standard Reference Materials. NBS Spec. Publ., 260-111, (1987).
8. Wong, A.S., Lurding, E.A., Robertson, J.D. and Francis, H., to appear in the proceedings of The 2nd Int. Conf. on the Elemental Analysis of Coal and Its By Products, G. Vourvopoulos, ed. (1992).

Table Ia. Concentrations of elements (μg/g) in 8 Argonne premium coal samples by PIGE/PIXE.

Element	WV	ND	POC	UT	PITT	IL	UF	WY
Li	36 ± 2	**	5 ± 1	5 ± 1	26 ± 3	21 ± 4	26 ± 8	17± 2
Na	340 ± 30	5600 ± 500	760 ± 30	1300 ± 170	320 ± 30	1000 ± 55	355 ± 30	1110 ± 90
Al*	2.96 ± 0.12	0.44 ± 0.05	0.53 ± 0.01	0.39 ± 0.03	0.89 ± 0.06	1.14 ± 0.07	1.58 ± 0.09	0.80 ± 0.03
F	130 ± 30	35 ± 6	20 ± 4	56 ± 7	90 ± 40	86 ± 7	86 ± 12	56 ± 9
K	4700 ± 460	320 ± 80	225 ± 90	264 ± 40	1090 ± 30	2330 ± 50	2300 ± 250	230 ± 65
Ca*	0.05 ± 0.01	1.44 ±0.05	0.42 ± 0.01	0.43 ± 0.02	0.21 ± 0.02	0.88 ± 0.06	0.35 ± 0.01	1.13 ± 0.07
Ti	2860 ± 270	202 ± 6	360 ± 20	217 ± 4	550 ± 30	610 ± 20	620 ± 50	610 ± 50
Cr	37 ± 2	4 ± 1	8 ± 2	7 ± 1	18 ± 1	36 ± 4	23 ± 3	7 ± 1
Mn	12 ± 2	85 ± 9	12 ± 1	5 ± 1	20 ± 4	87 ± 7	27 ± 6	23 ± 5
Fe*	0.39 ± 0.06	0.05 ± 0.03	0.57 ± 0.02	0.28 ± 0.02	1.11 ± 0.01	2.01 ± 0.01	1.35 ± 0.1	0.38 ± 0.01
Co	9.4 ± 3.7	**	3.2 ± 1.4	1.3 ± 0.3	1.5 ± 0.7	**	**	1.0 ± 0.6
Ni	14 ± 3	3.3 ± 0.1	4.1 ± 0.7	5.1 ± 0.1	4.7 ± 0.8	15 ± 3	9.4 ± 1.2	3.5 ± 2.1
Cu	20 ± 4	4.2 ± 1.1	12 ± 1	5.4 ± 0.4	5.1 ± 1.6	7.7 ± 1.1	12 ± 1	15 ± 5
Zn	12 ± 1	5.7 ± 2.5	4.3 ± 1.3	6.8 ± 2.1	9.7 ± 2.1	130 ± 20	18 ± 3	23 ± 7

* Concentrations in weight percent.
** Below detection limit.

Table Ib. Concentrations of elements (μg/g) in 8 Argonne premium coal samples by PIGE/PIXE.

Element	WV	ND	POC	UT	PITT	IL	UF	WY
Ga	10 ± 1	**	2.1 ± 0.1	1.5 ± 0.2	3.8 ± 0.6	3.9 ± 0.6	4.3 ± 0.1	3.5 ± 0.5
Ge	1.3 ± 0.8	**	0.8 ± 0.7	**	1.1 ± 0.5	7.0 ± 0.4	4.0 ± 1.3	3.5 ± 0.8
As	6.9 ± 0.4	3.3 ± 0.1	6.9 ± 0.4	1.2 ± 0.8	4.5 ± 0.4	3.2 ± 1.4	11 ± 1	3.5 ± 0.4
Se	8.0 ± 0.9	2.2 ± 1.2	2.1 ± 0.5	1.9 ± 0.6	2.2 ± 1.0	3.1 ± 0.4	1.4 ± 0.5	1.2 ± 0.1
Br	13 ± 2	0.9 ± 0.4	40 ± 3	1.6 ± 0.4	12 ± 1.5	4.6 ± 0.5	50 ± 2	2.1 ± 1.1
Rb	34 ± 4	0.9 ± 0.2	6.1 ± 1.3	0.7 ± 0.2	6.7 ± 0.2	16 ± 2	17 ± 3	9.6 ± 1.2
Sr	65 ± 5	650 ± 50	100 ± 2	72 ± 4	68 ± 7	28 ± 1	53 ± 1	240 ± 50
Y	12 ± 1	2.4 ± 1.3	5.8 ± 0.7	2.1 ± 0.5	3.4 ± 0.5	3.7 ± 0.7	11 ± 1	4.3 ± 1.0
Zr	72 ± 9	16 ± 5	12 ± 2	24 ± 2	19 ± 3	16 ± 2	16 ± 1	20 ± 3
Mo	**	**	3.3 ± 1.8	**	**	5.7 ± 0.8	1.5 ± 0.2	2.1 ± 0.4
Ba	140 ± 40	480 ± 60	130 ± 50	32 ± 7	37 ± 6	**	88 ± 11	270 ± 31
Pb	3.6 ± 0.6	0.2 ± 0.1	1.3 ± 0.7	1.9 ± 0.6	3 ± 0.9	2.5 ± 0.8	1.5 ± 0.4	1.4 ± 0.5
Th	4.4 ± 1.0	**	**	0.9 ± 0.2	1.3 ± 0.9	**	2.4 ± 0.5	2.0 ± 0.9
U	1.7 ± 0.7	**	**	**	1.2 ± 0.4	1.7 ± 0.4	2.9 ± 0.8	1.4 ± 0.8

** below detection limit.

Table II. Concentrations of elements (μg/g) in NIST coal standards by PIGE/PIXE.

Element	NIST 1632b	NIST 1632a	NIST 1635
K	716 ± 14	4310 ± 310	101 ± 50
	[748 ± 28]	[4110 ± 60]	[96 ± 16]
Ca*	0.22 ± 0.01	0.25 ± 0.02	0.55 ± 0.06
	[0.20 ± 0.01]	[0.24 ± 0.02]	[0.54 ± 0.03]
Ti	436 ± 7	1707 ± 11	187 ± 11
	[454 ± 17]	[1750]	[202 ± 6]
Cr	11 ± 2	28 ± 3	4 ± 1
	[11]	[34.3 ± 1.5]	[2.5 ± 0.3]
Mn	8 ± 3	24 ± 5	23 ± 7
	[12.4 ± 1.0]	[28 ± 2]	[21.4 ± 1.5]
Fe*	0.74 ± 0.02	1.10 ± 0.03	0.23 ± 0.02
	[0.76 ± 0.05]	[1.11 ± 0.02]	[0.24 ± 0.05]
Cu	5.1 ± 0.8	14 ± 2	4.8 ± 2.3
	[6.3 ± 0.3]	[15.9 ± 1]	[3.6 ± 0.3]
Zn	14 ± 2	26 ± 1	6.0 ± 1.4
	[11.9 ± 0.8]	[28 ± 2]	[4.7 ± 0.5]
Ga	2.6 ± 0.2	8.8 ± 0.9	1.4 ± 0.5
	---	[8.49]	[1.05]
Ge	2.7 ± 0.2	3.3 ± 0.1	1.1 ± 0.6
	---	[2.5]	[0.5]
As	3.8 ± 1.1	9.3 ± 1.6	**
	[3.7 ± 0.1]	[9.3 ± 1.0]	[0.4 ± 0.2]
Se	1.7 ± 1.1	2.4 ± 0.5	0.8 ± 0.5
	[1.3 ± 0.1]	[2.6 ± 0.7]	[0.9 ± 0.3]
Br	18 ± 1	41 ± 1	1.4 ± 0.6
	[17]	[41 ± 2]	[1.4 ± 0.4]
Rb	**	32 ± 8	0.8 ± 0.1
	[5.1 ± 1.1]	[30 ± 2]	[0.9 ± 0.1]
Sr	98 ± 2	77 ± 3	139 ± 14
	[102]	[85 ± 6]	[121 ± 19]
Zr	13 ± 1	52 ± 5	17 ± 4
	---	[53 ± 5]	[16 ± 2]
Ba	60 ± 6	140 ± 50	45 ± 16
	[67.5 ± 2.1]	[120 ± 15]	[73 ± 5]
Th	**	3.7 ± 0.1	1.4 ± 0.7
	[1.3 ± 0.1]	[4.5 ± 0.1]	[0.6 ± 0.1]
U	**	1.2 ± 0.3	1.1 ± 0.5
	[0.4 ± 0.1]	[1.3 ± 0.1]	[0.2 ± 0.1]

[ ] NIST compilation value[7] *Concentrations in weight percent **Below detection limit.

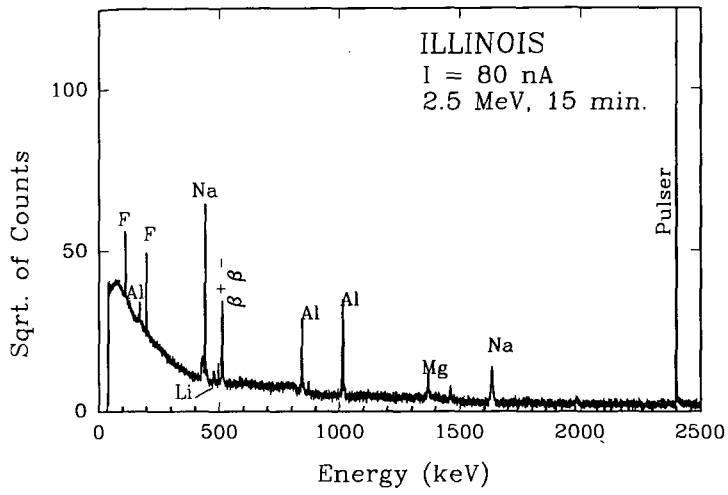

Figure 1. PIGE spectrum of an Argonne premium coal sample.

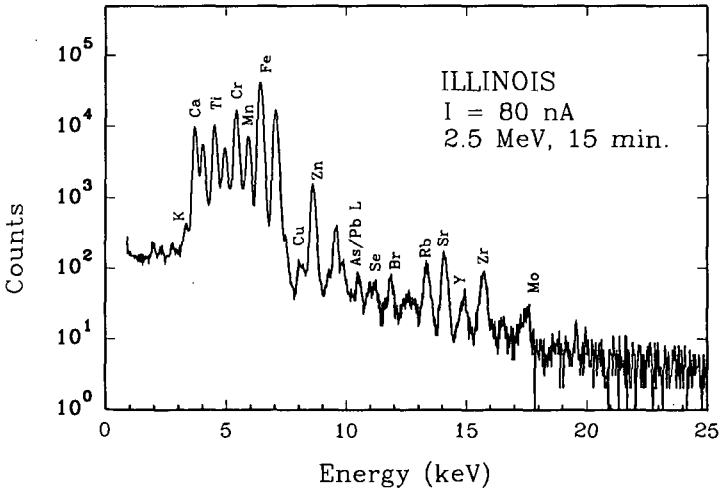

Figure 2. PIXE spectrum of an Argonne premium coal sample with 700 μm mylar and 10 μm Cr filters

STM CHARACTERIZATION OF COAL STRUCTURES, DERIVED EXTRACTS, MODEL COMPOUNDS, AND GASIFIED CARBONS:

Edwin J. Hippo, Neil Murdie, Jane F. Byrne, and Eric B. Sebok
Mechanical Engineering and Energy Processes
Southern Illinois University, Carbondale
Illinois 62901

KEYWORDS: Scanning Tunneling Microscopy

ABSTRACT

Techniques for characterizing coal and coal derived structures using scanning tunneling microscopy are being developed. These techniques allow surface structures of coal to be viewed with a fraction of an angstrom resolution. Images of inertinite structures have been obtained. A monolayer of THF extract from an Illinois #6 coal was deposited on HOPG and images obtained. One of the difficulties in interpreting the images is lack of knowledge about the tunneling efficiencies of various functional groups. Model compounds are being deposited onto well oriented surfaces and images at different bias and gain settings are being obtain to determine if spectral analysis can spot oxygen, sulfur, and nitrogen atoms in their various chemical forms thought to be present in coal. Analysis of pits formed from the gasification of HOPG have shown that oxygen complexes can be identified, pitting mechanisms can be followed and initial direction of gasification can be deduced. There is some evidence that oxygen complexes can form between carbon atoms of two different planes.

INTRODUCTION

The scanning tunneling microscope(STM) was invented in 1982 by Binning and Rohrer(1), who were awarded the Nobel Prize in physics for their work. The STM operates on the principle that a tunneling current can be established between an anatomically sharp tip and the surface electronic orbitals near the Fermi level of a sample(2). An image is obtained by scanning the tip across a samples surface with the use of a set of three piezo electric crystals(3). A voltage is applied to the crystal controlling the z-direction (the distance between the tip and the sample surface). The tip is then lowered until the tip crashes into the surface(non-conducting material) or a tunneling current is established(conducting material). Once the current is established, work functions can be measured over a certain spot or xyz images can be obtained. The images are obtained by one of two operating modes. In the constant current mode varying voltages are applied to the x and y crystals which drives the tip first across the surface in the x-direction and then increments the y-spacing and drives the tip in the reverse x-direction. A feedback loop measures current and adjusts the voltage on the z-direction crystal. This raises and lowers the tip. Since current is highly dependent on distance from the surface, the variation in z-distance allows a constant current to be maintained. A computer keeps

track of the z variations in a xy matrix which is transformed by using Fourier analysis into a three dimensional image. A second mode of operations employs a constant z-setting and as the tip moves variations in current are recorded. The current xy matrix is then converted to an image.

The actual image obtained is a charge density map of the eigen states localized above a surface(4). This means that the images should be viewed in terms of electronic interactions(5,6). Interpretation of the images is therefore dependent on complex theories. Although this should be kept in mind, the images can be viewed as simple atomic geometries (5,6). For well ordered systems including silicon, gold, platinum and highly ordered graphite(7,8,9, and 10) the atomic spacings and orbital shapes agree with X-ray, and TEM data, and HMO theory.

STM is dependent on the conductivity of the sample being image. However if a sample is non-conducting then atomic force microscopy (AFM) can be used (11-15). AFM is a closely related offshoot of STM. It drags a diamond tip across the sample surface and measures the repulsion of the tip from the samples surface. the tip is set on a cantilever and a laser beam is used to measure the deflection of the cantilever. This technique is not as highly developed as STM imaging but has been used to investigate structures of polymers and ceramics.

Depending on scan size of the STM image; resolution as low as 0.01 nanometers for lateral and 0.001 nm for vertical measurements can be obtained. Scan sized can be varied from 14x14 microns to 2x2 nanometers. The depth of resolution is much greater than for SEM and TEM. In addition little or no sample preparation is required and the instrument can be operated under ambient environments with little sample preparation. Thus, surfaces can be examined in far greater detail than previously and with much less degradation of the sample. These capabilities make STM an ideal candidate for application to in situ coal structure determinations and the study of coal reactions in various conversion technologies.

The purpose of this paper is to describe some preliminary work on applying STM to coal analysis and utilization technology. To the authors knowledge this is the first work to obtain actual images of coal and coal derived materials. The paper also discusses methods used to follow gasification of highly oriented pyrolytic graphite(HOPG).

EXPERIMENTAL

All STM nanographs were obtained using a nanoscope II scanning tunneling microscope manufactured by Digital Instruments of Santa Barbara Ca. Details of the operating procedures can be found in reference (16). The HOPG was obtained from Union Carbide. An Illinois #6, IBCSP 101, coal was used to obtain extract and Maceral concentrates. Maceral concentrates were obtain employing a density gradient centrifugation procedures described elsewhere(17,18). THF extraction was carried out in a soxhlet extractor for 48 hours. About 20 grams of coal are extracted with 150 mls of THF. The average yield is 16% solubles based on weight of dry solids recovered after extraction.

STM ANALYSIS OF COAL

The first attempt to image coal was made by polishing a block of coal, painting the back of the block with a conducting paint, and mounting the block on the STM base. Blocks where mounted with the tip perpendicular and parallel to the bedding plane. The instruments allows various gains and bias to be set along with scan rate and size. The tip crashed into the surface whenever engagement was attempted.

During engagement the tip is lowered manually to within 250 microns of the surface using a set of position bolts which are turned to raise or lower three ball bearings on which the STM scan head sets. The software package is then activated and automatically lowers the tip to the surface. As the tip approaches the surface it will begin to tunnel if the sample is conducting but the program will continue to lower the tip into the sample if a tunneling current is not established. Since the tip must be atomically sharp, lowering the tip to far will blunt the tip and good images will not be obtain with that tip. Since tips are expensive, this approach was abandoned after 20 attempts.

Next, particles of whole coal were scattered on the STM base. The coal was ground in an fluid energy mill prior to mounting. The smaller particles of coal were expected to be more conductive. A scan of the base was made to determine its structure before attempting to analyze the coal particles. During engagement the tip would either push particles aside and engage the base, or pin a particle and bend the tip.

Steel slides were then prepared, painted with conducting paint and coal dust was sprayed over the wet surface. This method produced a sample which could be imaged. Blank painted slides were also imaged. Although there are some differences between the blank slides and the images obtained with whole coal particles, it is difficult to describe these.(slides will be shown at the presentation). The percentage of successful engagements range between 50 and 70%. To obtain a clearer understanding of what was imaged, the process was repeated on sporinite, cutinite, vitrinite, inertinite, and mineral concentrates. The liptinites and mineral fractions could not be engaged. The Vitrinite concentrates had a 40% engagement rate and the inertinite had a 90% engagement rate. This follows the general order of conductivity of the macerals. Since most of the mineral in this coal was clay this fraction was also expected to be nonconductive.

Because of the problem with imaging the painted surfaces as well as coal particles, another approach was attempted. Coal macerals were physically pressed into a wafer with the aid of a hydraulic press. The back of the wafer was painted and the sample was mounted. Engagement was obtained for the inertinite wafer only. The images obtained with the inertinite wafer were identical to those obtained from the painted slide method. Not much can be said about the chemical structures imaged at this point. This is because there is little known about tunneling of organic structures. A good deal of model compound work will need to be carried out. It can be said that the imaged orbitals vary a great deal but the significance of these variations can not be estimated at this time. More can be said about the size and shape of the pore openings. When scanned on the nanometer range; pore diameter ranges between 5 to 20 angstroms. About half of the pores

have circular openings and half slit shape openings. Area of the slit shaped openings were greater than those of the circular openings.

SOLVENT DEPOSITION

Those carbon materials which are unsuitable for STM studies due to their poor conductivity, porosity, and surface heterogeneity may be imaged, in some cases, by depositing a dissolved portion (from solution) onto HOPG in very small amounts. The tetrahydrofuran (THF) soluble portion of Herrin,IL No.6 coal, as well as materials such as n-dotriacontane (n-C_{25}), which readily dissolve in heptane, were analyzed. These solvents (THF and heptane) do not alter the HOPG surface. Blank experiments were carried out by pipeting drops of solvent on newly cleaved HOPG surfaces. After the solvent evaporates the hexagonal basal plane image of the HOPG is observed. This is somewhat unexpected because even the purest solvent contain some residual material. A quick calculation shows that the concentration is high enough to more than cover the HOPG surface. However, their usage did not effect STM images. Upon evaporation solvent/solute mixtures left behind deposited material that could be imaged.

The THF extract was diluted from its original concentration of about 0.02 gram/ml by an approximate ratio of 10:1. A portion of this solution was further diluted to approximately 100,000:1 in increments of 10:1, until STM images showed only a thin layer deposited onto the HOPG. Deposition was carried out using a pipette to place a drop of the diluted solution onto the HOPG. The THF was allowed to evaporate, leaving behind a thin layer of coal extract. The specimen could then be placed directly onto the sample stage for STM imaging. This technique is suitable for molecules with large atomic weights which adsorb strongly to the graphite surface.

Although areas could be imaged where more than a single monolayer are present these images where chaotic and individual structures were not easily recognized. A monolayer of the deposited material (or scattered areas of monolayer) gave very clear images. Various aromatic compounds are evident, as well as side-chains branching off from these rings. The images are easily differentiated from the defined HOPG basal plane surface. HOPG is an ideal substrate for organic molecules which align with the basal plane and adsorb fairly strongly, depending on the size and planarity of the molecule.

The n-dotriacontane/heptane solution was created by dissolving n-dotricontane in heptane. This solution was deposited onto the HOPG with a micropipette. The sample was then placed directly onto the sample stage for STM imaging.

The n-C_{25} on the surface of the HOPG gave spacings of 0.30 nm, instead of 0.25 nm, between hexagon centers of the HOPG. An elliptical shape of many of the atoms was due to the hydrogen atoms attached to the carbon atoms, and the carbon atoms themselves are imaged as one. A somewhat repeating pattern on the surface was observed and believed to be due to the fact that the n-C_{25} molecules align themselves along the carbon atoms of the top basal plane layer. Other compounds such as steroids, acids, alcohols have

been imaged by others using a similar technique(19). Other model compounds such as dibenzothiophene,, thiols, carbazol and others scheduled for analysis in the near future.

GASIFICATION OF HOPG

In this portion of the program HOPG was exposed to air oxidation at 650°C in a TGA system until 5 and 30% burnoff was reached. After various exposure times the size, shape, and distribution of pits and the linear dimension of the graphite were determined. The STM was used to image the pits, determine the direction of oxygen attack and to determine the amount and type of oxygen complexes on the surfaces of the graphite. In the initial stage of pit formation at 5% burnoff, the pits seem to align in a parallel orientation. Also some pits extend 3-5 layers deep without enlarging. The familiar large hexagonal pits are formed by the 30% weight loss level. A zoom into the base of the pits formed at 30% weight loss showed that although the large scale hexagonal morphology is observed; attack on pristine planes is linear. Long parallel high points were observed at the end of narrow elongated pits. These high points or streaks were originally thought to be carbon atoms but cross-sectional analysis showed them to have bond lengths indicative of adsorbed oxygen molecules. The length of the streaks are multiples of 4.2 angstroms which indicate attack parallel to the 101 face. We are not sure if this is indicative of catalytic attack or if the highly oriented graphite contains a large amount of elongated crystalites. It is possible to measure bond length and depth of penetration using the cross sectional analysis routines which were provided with the STM. By measuring heights from the base of pits it is possible to obtain an idea of the composition of the atoms in the pit. For example, if the vertical distance is 3.35 angstroms then the pit is one layer deep assuming that the atoms at the pit base are carbon. Likewise an atom appearing 6.7 angstroms above the pit floor would be a carbon atom 2 layers above the floor of the pit. It is interesting to note that 3.53 and 3.22 angstroms are encountered in measurements more often than 3.35(the ideal basal plane spacing) These measurements are probably the results of edge carbon atoms waging up or down around the pit edge. This is reasonable. In fact, edge sites on a graphite model behave the same way. Also values between these measurements are not encountered very often. Thus, any multiple of Of 3.35 plus or minus the wag distance of 0.12 angstroms is likely to be carbon. Alternately measurements of 3.35 multiples plus or minus 0.75 and 1.5 are observed. these appear to be oxygen complexes. These values appear over and over again. The large pits have nearly vertical walls (slope > 75°) these walls are over 500 layers deep. Cross sectional analysis of smaller pits vary in angle depending on size. Some are steep like the larger pits but some have gentle slopes which seem to indicate that oxygen forms adsorbed species between layers. A similar effect was observed on edge cite studies(20,).

CONCLUSIONS

STM has been shown to be a powerful tool for exploring atomic structures of coal and graphite. Additional work is required to assign structures, but the techniques developed in this study demonstrate that it is possible to image coal and coal derived material.

ACKNOWLEDGEMENTS

This work has been sponsored by the Department of Mechanical Engineering and Energy Processes Southern Il. University. Dr. Robert Clarkson of Univ. of Il. and Dr. J. Crelling of SIU supplied pressed wafers.

REFERENCES

1. G. Binning and H. Rohrer, Scanning Tunneling Microscopy, Helv. Phys. Acta., 55, pp.726-735 (1982)

2. P. C. W. Davies, Quantum Mechanics, Routledge and Kegan Paul, London, U.K. (1984).

3. P.K. Hansma, J. Tersoff. "Scanning Tunneling Microscopy". Journal of Applied Physics. 61(2), pp. R1-R3, January 15, 1987.

4. C.J. Chen. "Theory of Scanning Tunneling Spectroscopy". Journal of Vacuum Science and Technology. Vol. A 6(2),

5. P. Batra, et al. "A Study of Graphite Surface with STM and Electronic Structure Calculations". Surface Science. Vol. 181, pp. 126-138, 1987.

6. S. Gauthier, et al. "A Study of Graphite and Intercalated Graphite by STM". Journal of Vacuum Science and Technology. A 6(2), pp. 360-362, Mar./Apr. 1988.

7. R.M. Tromp, et al. "Atomic and Electronic Contributions to Si(111)-(7X7) STM Images". Physical Review. B15, Vol. 34, No. 2, pp. 1388-1391, 1986.

8. P. N. First, J.A. Stroscio, R. A. Dragoset, D. T. Pierce, and R. J. Celotta, Physical Review Letters, 63,No. 13. pp. 1416-1419(19B9).

9. J. Schneir, H. H. Harary, J. A. Dagata, P. K. Hansma, and R. Sonnefeld, Scanning Microscopy,3, No. 3, pp. 719-724(11989)

10. Sebok, E.B., Hippo, E.J., Murdie, N., Byrne, J.F., and Rehak, J., "Scanning Tunneling Microscopy of Various Carbon Materials," Materials Technology Center 7th Annual Conference, 111-117, SIUC, April 10-11, 1991.

11. P.K. Hansma, et al. "Scanning Tunneling Microscopy and Atomic Force Microscopy: Application to Biology and Technology". Science. Vol. 242, pp. 209-216, Oct. 14, 1988.

12. I.P. Batra, S. Ciraci. "Theoretical STM and AFM Study of Graphite Including Tip-Surface Interaction". Journal of Vacuum Science and Technology. A 6(2), pp. 313-318, Mar./Apr. 1988.

13. R. Pool. "Children of the STM". Science. Vol. 247, pp. 634636, Feb. 9, 1990.

14. E. Meyer, J. Frommer. "Forcing Surface Issues". Physical World. pp. 46-49, Apr. 1991.

15. A.L. Wersenhorn, et al. "Molecular Resolution Images of Langmuit-Blodgett Films and DNA by Atomic Force Microscopy". Langmuir. Vol. 7, No. 1, pp. 8-12, 1991.

16. Digital Instruments, Nanoscope II Instruction Manual, Version 5, 6780 Cortona Dr., Santa Barbara, California, 93117.

17. Crelling, J.C., Hippo, E.J., Woerner, B.A., and West, D.P., "Combustion Characteristics of Selected Whole Coals and Macerals," Fuel (in press).

18. Hippo, E.J., Crelling, J.C., and Mukherjee, J., "Desulfurization of Single Coal Macerals," Fuel Processing Technology, 27, 287-305, 1991.

19. J. P. Rabe, and S. Buchholz, Science, 253 pp. 424-426, July 1991.

20. Sebok, E.B., Hippo, E.J., Byrne, J.F., Rehak, J., and Murdie, N., "Scanning Tunneling Microscopy of Various Carbon Materials," Proceedings of 20th Biennial Conference on Carbon, 418-419, Santa Barbara, CA, June 24-28, 1991.

AN APPARATUS FOR IN-SITU HIGH TEMPERATURE/HIGH PRESSURE ESR SPECTROSCOPY AND ITS APPLICATIONS IN COAL CONVERSION STUDIES

Manjula M. Ibrahim and Mohindar S. Seehra, Physics Department,
West Virginia University, Morgantown, WV 26506

Keywords: hydroliquefaction, coal, free radicals, ESR

Abstract

An apparatus for carrying out in-situ ESR (Electron Spin Resonance) spectroscopy studies from ambient to 500°C and for gaseous pressures up to 800 psi at x-band frequencies (~9 GHz) is described. ESR signals can be monitored as a function of time, temperature or pressure in the above stated ranges. Using this apparatus, results on the hydrogenation of a Blind Canyon coal carried out at 440°C in hydrogen pressures up to 600 psi, and with and without the shell 324 catalyst (presulfided $NiMo/Al_2O_3$), are described. A non-linear decrease of the free radical density with H_2 pressure is observed and the catalyst increases the free radical density. Significance of these results is discussed.

Introduction

The fundamental mechanisms of coal pyrolysis and direct hydroliquefaction are believed to involve free radicals and the interaction of the free radicals with available hydrogen.[1,2] Generally accepted view of pyrolysis is that thermally generated free radicals extract internal hydrogen from coal to form tar or combine with other coal molecules to form high molecular weight char. In hydroliquefaction, when hydrogen is available readily from a donor solvent and/or molecular H_2, free radicals extract this hydrogen to produce low molecular weight product.[1,2] In order to provide direct evidence for these views, direct and in-situ monitoring of the free radicals during pyrolysis and hydroliquefaction is necessary. In previous papers from this laboratory,[3-7] we have used the in-situ ESR (electron spin resonance) spectroscopy of free radicals in coals to investigate pyrolysis and the effect of zinc halide catalysis in coal conversions. These studies were however carried out either in vacuum-sealed samples or in flowing gases (N_2 and H_2). Since direct hydroliquefaction is usually carried out under high pressures (1000-3000 psi) of hydrogen, it is essential to carry out ESR measurements under the realistic conditions of high temperatures/high pressures. Here we describe a microwave cavity system in which in-situ ESR spectroscopy can be carried out at temperatures up to 500°C and gaseous pressures up to 800 psi (pressures are limited by the use of the pyrex tubes). The design of our apparatus differs significantly from that reported by Petrakis and Grandy[2] but somewhat similar to that described by Yokono et al.[8-10] The major improvement in our apparatus is that pressure can be varied in-situ at a given temperature. Using this apparatus, we have investigated the hydrogenation of a Blind Canyon coal as a function of H_2 pressure at 440°C, with and without a catalyst. This apparatus, along with the results of these experiments, are described in this paper.

High Temperature/High Pressure ESR Cavity System

The high temperature/high pressure ESR cavity system consists of three primary units: (i) A rectangular TE_{102} cavity in which the field modulation coils are located outside the cavity and a circular hole through the center of the cavity which allows the insertion of the quartz dewar and the sample; (ii) A heating unit external to the cavity (see Fig. 1) and purchased from Wilmad Glass Co. in which a flowing N_2 gas over a voltage-controlled chromel heater is used to deliver heat to the sample without heating the microwave cavity; and (iii) a high pressure unit (Fig. 2) to which a pyrex ESR tube is attached which can be inserted in the TE_{102} cavity. If the sample is to be exposed to a flowing gas (such as N_2 or H_2), then the high pressure unit is replaced by the flow-chamber unit shown in Fig. 3, a description of which was also given in our recent paper.[7] Thus in this apparatus, the cavity remains at ambient temperature and pressure and no cooling coils as for example used in the design by Yokono et al,[8-10] are used anywhere in the apparatus. The system is pressurized directly from a gas cylinder and so the pressure can be easily changed during the course of the experiment. The maximum pressure is limited by the strength of the ESR tube and in our experiments, the pyrex and quartz tube could not withstand pressures beyond 800 psi. To attain higher pressures, search for a better non-conducting material for the ESR tube is underway.

There are several special features of the high pressure unit which deserve special mention. As shown in Fig. 2, the ESR tube is screwed to a stainless steel (#316) tube which in turn is connected to a high pressure gage and a valve to let in or shut off the gas supply. A Swagelok quick-connector connects this attachment to a stainless-steel bellow-type tube leading to the gas cylinder. To secure the sample tube firmly with the attachment, a stainless steel nut is glued to the tube using a high pressure glue (Torr-seal by Varian) and a stainless-steel block holds the tube below the nut giving additional support. The large temperature gradient between the bottom of the tube where the sample is kept and the top of the tube where the high pressure attachment is connected eliminated the need for any cooling of the tube. The high-temperature quartz dewar which is inserted in the hole of the TE_{102} cavity, has an evacuated double-wall ensuring only minimal heat transfer from the sample to the cavity. The gage connected to the tube enables direct reading of the inside pressure during experiment. Since inserting a thermocouple inside the cavity distorts the microwave signal, the thermocouple is placed outside, just at the cavity entrance. The temperature is calibrated by an initial run with an additional thermocouple inside the sample, the experiment being carried out under realistic identical conditions. In the heater unit, the temperature is controlled by the voltage input to the heater, controlled by a variable transformer. For each data point, at least 10 minute interval is allowed to ensure temperature stability.

Experimental Procedures

All experiments reported here were carried out with the Blind Canyon coal, DECS-17, obtained from the coal bank of the Pennsylvania State University. In Table 1, we list the proximate analysis, the ultimate analysis and the maceral content of this coal as provided by the coal bank. A presulfided catalyst, Shell #324 ($NiMo/Al_2O_3$) was obtained from the Consolidated Coal Co. An x-ray diffractogram of this catalyst is shown in Fig. 4. Not all the Al_2O_3 oxides lines are observed. From the two prominent lines observed near $2\theta \simeq 46°$ and $2\theta \simeq 67°$ and

using the Scherrer eq. $L = (0.9)\lambda/\beta \cos\theta$ (where L is the particle dimension, β is the corrected linewidth and λ is the x-ray wavelength) and the procedures outlined in our recent paper,[11] we find L = 38 Å for the $2\theta \simeq 38°$ line and L = 42 Å for the $2\theta \simeq 67°$ line. These measurements show that for the 324 catalyst, the average particle size $\simeq$ 40 Å. In our experiments, the 324 catalyst was dry mixed with the coal, in the ratio of 2.1% by weight of the coal.

The free radical density N is calculated by double integration of the derivative ESR spectra using an on-line computer and comparing it with a standard.[4] Also the values of N are corrected for the Curie-law variation of the spins with temperature i.e. $N = N_T(T/RT)$, where N_T is the measured value at a temperature T in degrees Kelvin and RT is the room temperature in degrees Kelvin. If there is no change in the free radical concentration with temperature, then N will be independent of temperature and a plot of N vs T will be a horizontal line. To account for any changes in mass with temperature, thermogravimetric studies using the Mettler 3000 TG system were done. Typically 10 mg of the sample was heated in an alumina cell from 30°C to 600°C at a heating rate of 10°C/min., in flowing N_2 and H_2 gases.

Results and Discussion

In Figs. 5 and 6, results of the thermogravimetric studies of the change in weight of the coal and the coal with catalyst, as a function of temperature and in flowing N_2 and H_2 gas, are shown. Two results are evident: more volatiles are lost in H_2 flow and second, the catalyst significantly reduces the evolution of volatiles in the presence of N_2. These data were used to correct the free radical density N/mass for experiments carried out in N_2 and H_2 flow.

In Fig. 7, we have plotted N against temperature for the Blind Canyon coal under three conditions: (i) sample sealed under vacuum; (ii) experiments in flowing N_2; and (iii) experiments in flowing H_2. For these cases, the variations of N with temperature are similar except above about 400°C, where N is lower in H_2 flow. This difference persists (shown in insert) even after applying the mass correction for N_2 and H_2 flow experiments. The lowering of N in H_2 flow is presumably due to capping of the free radicals by H_2. Discussion of this variation of N with T, somewhat similar to the observation in other coals, is given in our earlier publications.[3,4]

The effect of 2.1% loading of the coal with the 324 catalyst on N is shown in Fig. 8 where the experiments were carried out in flowing H_2 gas and the data are corrected for the change in mass from Figs. 5 and 6. These studies clearly show an additional mechanism for the generation of the free radicals by the catalyst. No additional details about this mechanism are, however, available at this time.

Since most of the experiments in direct coal liquefaction are carried out above 400°C and in H_2 pressures, we studied the variation of N as a function of pressure but at a fixed temperature of 440°C. A novel feature of our apparatus is that pressures can be varied in-situ. Results of N vs pressure are shown in Fig. 9, for the cases of coal and coal with catalyst in both H_2 and Ar gases. We used Ar gas suspecting that N_2 may have some effect on N. However later experiments showed that just as in Ar gas, there is no variation of N with N_2 pressure either. In H_2 pressure, however, there are significant changes in N with pressure as the

results in Fig. 9 show. For the coal alone, N decreases nearly linearly with P with initial pressures, approaching saturation above 400 psi. For the catalyst loaded coal sample, N increases slightly with initial pressures of H_2 but above 150 psi, N decreases nearly linearly with H_2 pressure. From these experiments, it is quite evident that molecular H_2 caps at least some of the free radicals whereas in the presence of the 324 catalyst, an additional mechanism for the generation of free radicals is operative.

There are only two reports available in literature on the variation of N with pressure in coals. Earlier studies by Petrakis and Grandy[2] were done at two pressures viz. 1200 and 1600 psi of H_2 gas in the presence of tetralin. These studies showed no change in N with pressure, although the presence of tetralin which is an excellent hydrogen donor might have obscured the effect of H_2. On the other hand, it is possible, that as we observe in Fig. 9, the effect of H_2 is saturated above about 400 psi in the absence of a catalyst. Yokono et al[8-10] measured N at 6 and 13 MPa of H_2 and N_2 (1 MPa $\simeq$ 145 psi) and found that H_2 aids in capping some of the free radicals. The results presented here in Fig. 9 are unique in that for the first time, a systematic study of N with H_2 pressure in the absence of tetralin is now available.

The results presented above have demonstrated that molecular H_2 is involved in free radical quenching reactions, supporting the hypothesis forwarded by Vernon.[12] More recent studies on model compounds by McMillan et al[13] and by Shin et al[14] on the Argonne coals have shown that hydrogen can also take part in the hydrogenolysis of strong C_{ar}-C_{alk} bonds. Similar observations were made on hybrid studies in which known structures were either mixed with[15] or grafted to coal.[16] Although there is no direct proof of hydrogenolysis from our studies, the quenching of the thermally generated free radicals upon hydrogenation is quite evident. In addition, significant enhancement of the free radical density in the presence of 2.1% loading of the coals by the 324 catalyst provides strong evidence for catalytic cracking of coals. There is some evidence from the data in Fig. 9 that for initial H_2 pressure, this catalytic hydrogenolysis is more significant than the quenching mechanism for hydrogenation. Additional experiments in the presence of hydrogen donor solvents such as tetralin are now planned to further elucidate these mechanisms.

Acknowledgments

The authors thank C. Weber, T. Milam and C. Sicina for their assistance in fabricating the high temperature/high pressure apparatus, and S. D. Brandes of Consolidated Coal Co. for providing the Shell 324 catalyst used in these experiments. This research was sponsored by the U.S. Department of Energy under DOE Contract No. DE-FC22-90PC90029.

References

1. Neavel, R. C. Fuel 1976, 55, 237-242.

2. Petrakis, L. and Grandy, D. W. 'Free Radicals in Coals and Synthetic Fuels' 1983 (Elsevier Science Publication Co. N.Y.).

3. Seehra, M. S.; Ghosh, B.; and Mullins, S. E. Fuel 1986, 65, 1315-1316.

4. Seehra, M. S. and Ghosh, B. J. Anal. Appl. Pyrolysis 1988, 13, 209-220.

5. Seehra, M. S.; Ghosh, B.; Zondlo, J. W.; and Mintz, E. A. Fuel Process. Technol. 1988, 18, 279-286.

6. Ibrahim, M. M.; Seehra, M. S.; and Keogh, R. Fuel Process. Technol. 1990, 25, 215-226.

7. Ibrahim, M. M. and Seehra, M. S. Energy & Fuels 1991, 5, 74-78.

8. Yokono, T.; Iyama, S.; Sanada, Y., Shimokawa, S.; and Yamada, E. Fuel 1986, 65, 1701-1705.

9. Yokono, T.; Iyama, S.; Sanada, Y.; and Makino, K. Carbon 1984, 22, 624-626.

10. Yokono, T.; Iyama, S.; Makino, K.; and Sanada, Y. Fuel 1985, 64, 1014-1026.

11. Ibrahim, M. M. and Seehra, M. S. J. Mater. Res. 1992, 7, No. 7 (in press).

12. Vernon, L. W. Fuel 1980, 59, 102-106.

13. McMillen, D. F.; Malhotra, R.; Hum, G. P.; and Chang, S. J. Energy & Fuels 1987, 1, 193-198.

14. Shin, S.-C.; Baldwin, R. M.; and Miller, R. L. Energy & Fuels 1989, 3, 71-76.

15. McMillen, D. F.; Malhotra, R.; Chang, S. J.; Ogier, W. C.; Nigenda, S.E.; and Fleming, R. H. Fuel 1987, 66, 1611-1618.

Table 1: Relevant analysis of Blind canyon coal-DECS-17. Data obtained from Penn State Coal Bank.

proximate analyses (DAF %)		ultimate analysis (DAF %)		maceral content (DMMF vol%)	
volatile	50.04	C	81.61	inertinite	2.1
fixed C	44.93	H_2	6.21	exinite	11.2
		N_2	1.38	vitrinite	79.7
		total S	0.47	fusinite	6.0
		O_2 (diff)	10.33		

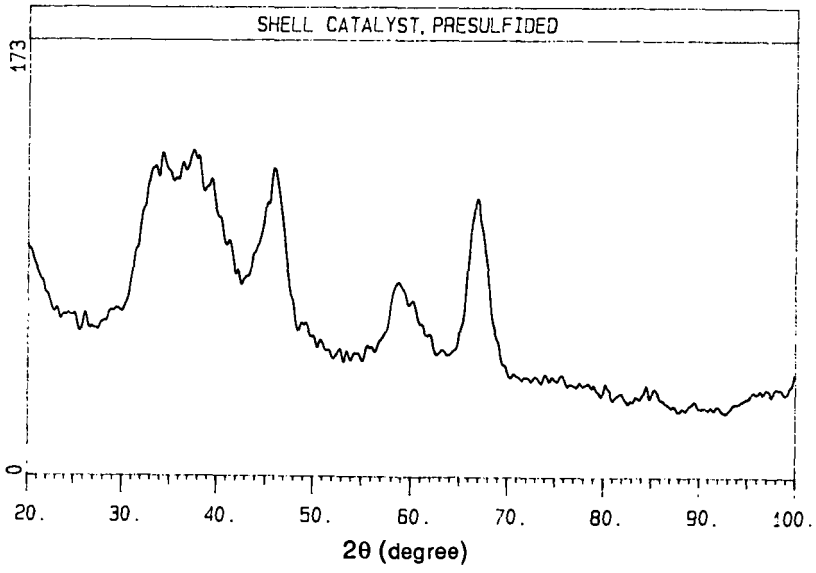

Figure 1: X-ray powder diffractogram of the catalyst, shell 324.

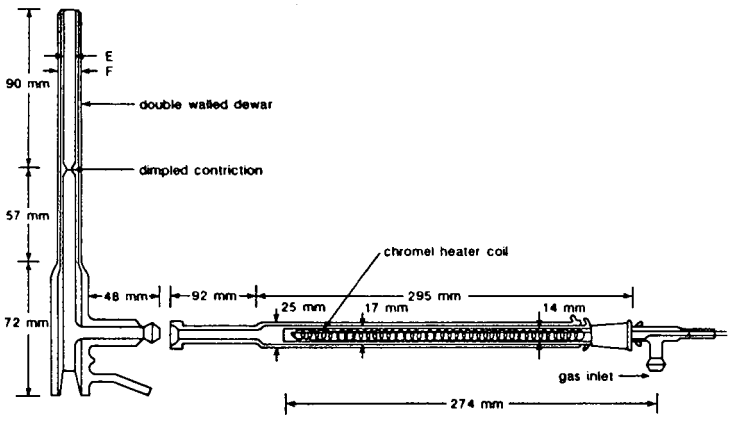

Figure 2: Block diagram of the high temperature dewar for ESR cavity

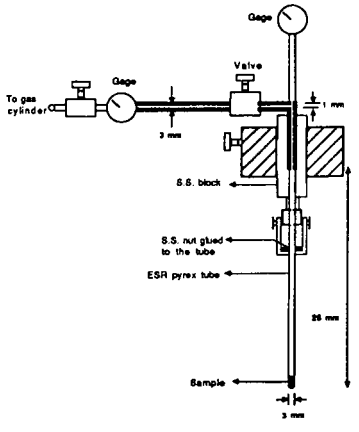

Figure 3 : Block Diagram of the high pressure set up fabricated for in-situ experiments up to 800 psi of any gas and up to 500 ℃

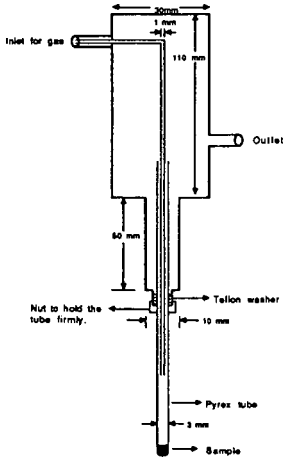

Figure 4 : Diagram of the flow chamber used for experiments under flowing gas.

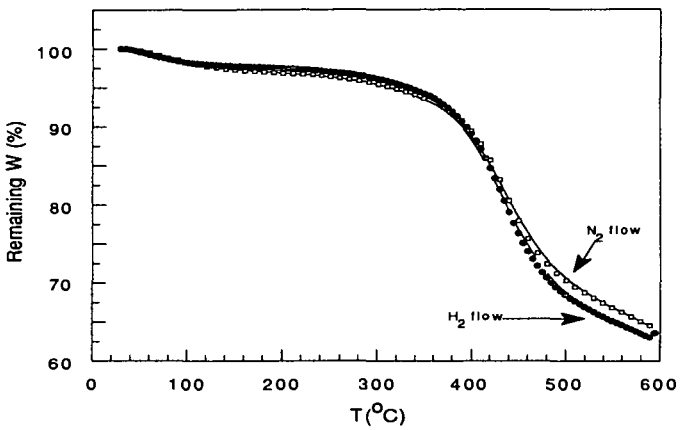

Figure 5: Remaining weight of blind canyon coal plotted against temperature, from TG experiments under nitrogen/hydrogen flow.

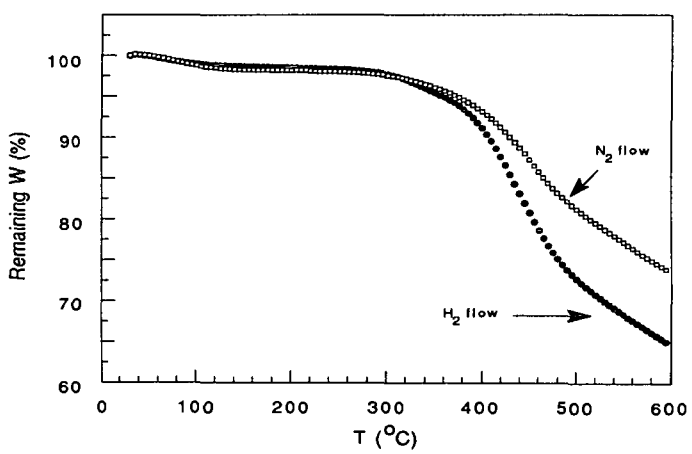

Figure 6: Variation of remaining weight with temperature for blind canyon coal mixed with 2.1% shell 324, under nitrogen/hydrogen flow.

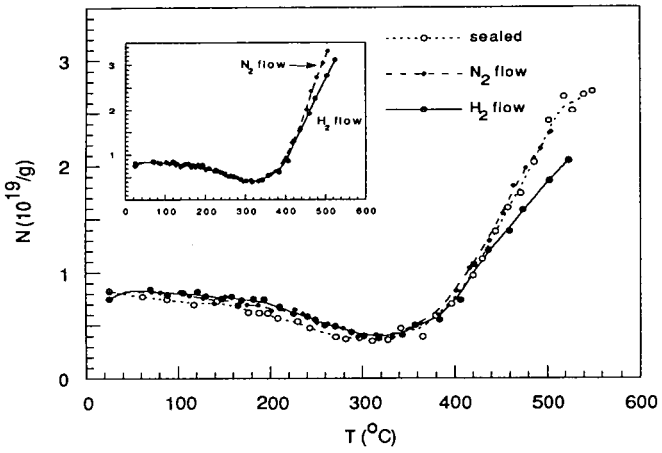

Figure 7: Variation of N with T for blind canyon coal. Plot after applying mass correction is shown in the insert.

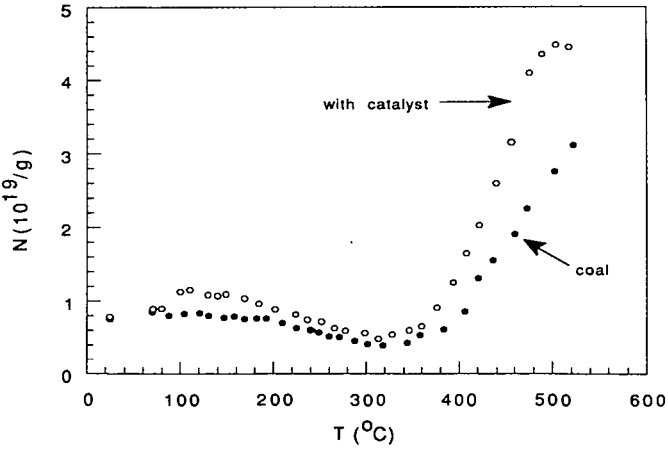

Figure 8: Variation of N with temperature for blind canyon with and without shell catalyst 324, in hydrogen flow. The values of N are corrected for the change in mass from TG data.

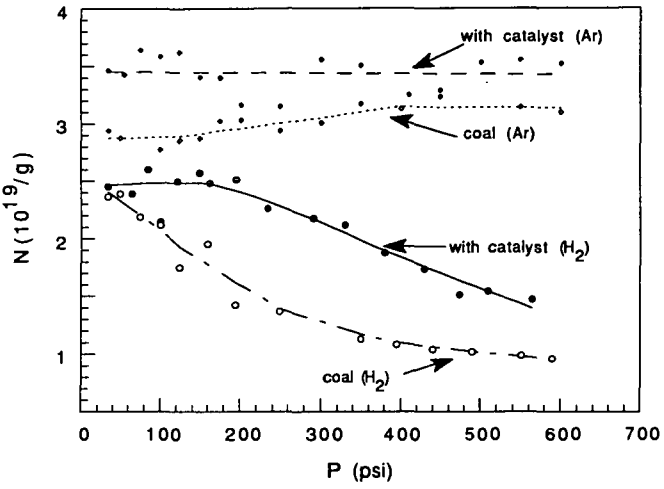

Figure 9: Variation of N with argon/hydrogen pressure for blind canyon coal with and without the shell catalyst 324.

VERY HIGH FREQUENCY EPR SPECTRA OF ORGANIC SULFUR COMPOUNDS

Wei Wang,[ψ] R. B. Clarkson,[ψ] F. P. Auteri,[ψ]
P. Kovacs,[ψ] M. V. Williamson,[#] and R. L. Belford[ψ]

[ψ]Illinois EPR Research Center; Departments of [*]Veterinary Clinical Medicine, and
[#]Chemistry, University of Illinois, 505 S. Mathews, Urbana, IL 61801

Key Words: Sulfur (organic), thiophenic radical cations, EPR (ESR)

ABSTRACT

Radical cations formed from several sulfur-containing heterocyclic aromatic compounds have been studied, both as subjects in their own right and as models for organic sulfur in coal. Since for most organic radicals, the g shift and g anisotropy are expected to be small, they have seldom been resolved at conventional X-band (9.5 Ghz) EPR. Our very high frequency (VHF) EPR spectrometer (W-band, 95 GHz) provides a tenfold increase in spectral resolution, which enables us to obtain, for the first time, the principal g matrices of thiophenic radical cations in amorphous or disordered state. The EPR experimental results are presented, along with observation of certain trends of g shift and g anisotropy among the homologous series.

INTRODUCTION

Identification of the chemical forms of sulfur-containing heterocyclic aromatic compounds in coal continues to be a challenging problem. Our previous studies[1] hypothesized that the very high frequency (VHF) EPR spectra of Illinois #6 coal could be approximated by superposition of two main classes of organic radicals. The first class was polycyclic aromatic hydrocarbon radicals and the second was the radicals from heterocyclic aromatic compounds containing sulfur, oxygen, or nitrogen. It was suggested that the spin-orbit coupling from sulfur could be responsible for the low field feature of the W-band spectra of the coal.

In order to fully explore this hypothesis, we are investigating a number of sulfur- and oxygen-containing organic radical ions by VHF EPR spectroscopy. The goal is to obtain their anisotropic g-factors and to assess the influence of heavy atoms such as sulfur and oxygen and extent of aromatic conjugation on EPR parameters, especially g anisotropy and EPR line-shape. Here we present some of our experimental results on cation radicals from thiophenic compounds.

The g-factor, one of the most important and fundamental EPR parameters, characterizes the position of a resonance signal: $g=h\nu/\beta B_0$ where B_0 is external magnetic field strength at the resonance (also called spectral center or resonance field center). A g-factor for a molecule containing an unpaired electron is generally viewed as characteristic of its electronic structure. But there are several reasons which can prevent the g-factor from being a straightforward and definitive structural indicator.

For most organic radicals, g-factors are very close to the free-electron value (g_0=2.00232). The g shift, $\Delta g = g - g_0$, is consequently small. A typical Δg for carbon centered radicals is ca. 20×10^{-5} and only several-fold greater for heterocyclic containing oxygen or sulfur. Experimentally resolving such small g shifts is difficult, especially in non-single-crystal solids (powders, frozen solutions, glasses) where the situation is more complicated.

Since for most cases, g-factors are intrinsically anisotropic, due to spin-orbit coupling, the resonance field positions vary with the orientation of the molecules in the external magnetic field. Therefore, g is represented as a matrix with three principal values. If molecules are tumbling rapidly, then the g matrix is motionally averaged to a single average (scalar) value $\langle g \rangle = (g_1+g_2+g_3)/3$, where $\langle g \rangle$ determines the averaged resonance line center. In a disordered solid, the resonance spectrum will be a superposition of the individual absorption spectra of the variously-oriented molecules. In the typical macroscopically isotropic specimen, the whole ensemble assumes with equal probability every possible orientation relative to the external magnetic field. The resulting composite is known as a powder spectrum. Principal g matrix values or components can still be resolved providing that extreme g values differ enough. But as stated earlier, for most organic radicals the g values are all quite close together. Thus, under the effect of other line broadening mechanisms, powder spectra of organic radicals often show a single, featureless (and boring) line with varied width and symmetry and very limited information content, as illustrated in Fig. 1(a).

One possible way to overcome this problem is to work at higher magnetic fields (requiring higher microwave frequency) to enhance the spectral resolution.[2] From the simple resonance condition one can see easily that the difference in resonance fields corresponding to slightly different g-factors is proportional to the product of the microwave frequency with the difference in g-factors. Therefore the spectral resolution will be enhanced by a factor of 10 in going from X-band (9.5 GHz) to W-band (95 GHz) providing the line does not broaden substantially with microwave frequency. Fig. 1(b) demonstrates this greatly enhanced g-resolution.

Thiophenic compounds have been thought to be abundant in Illinois coal[3]. Upon chemical oxidation on catalyst surface or UV irradiation in boric acid glass, such compounds yield immobilized and extremely long-lived cation radicals suitable for EPR studies. EPR spectra of the radical cations so prepared from thiophene and four more structurally related compounds were obtained at both X-band and W-band frequencies. The principal g matrix components obtained from analyses of these spectra and are reported here. We have found in the literature no previous reports of g matrices for these radicals.

EXPERIMENTAL SECTION

Thiophene (THI), benzothiophene (BTH), dibenzothiophene (DBT) and benzo[*b*]naphtho-[2,1-*d*]thiophene (BNT) were purchased from Aldrich; dinaphthylene thiophene (DNT), from ICN. The highest commercially available grades (typically 99+% pure) were obtained and used without further purification.

To generate free radical ions, we have tried several different methods. Two of them proved to be quite versatile and thus are used routinely. The first is chemical oxidation at a metal oxide

catalyst surface with O_2; the catalysts can be either alumina or alumina/silica like Houdry M46. The second is UV photolysis in boric acid glass. Both methods can produce sufficient populations of stable radical ions in a powder or glassy matrix, thus mimicking the disordered state of chemical species in coal.

In method I, γ-alumina from Akzo was loaded into an EPR tube attached to a three-way Y-shaped connector with a connector to vacuum line and a septum seal. After the alumina was calcined at ca. 650 °C for 12 hours, a small amount of gaseous oxygen was let in for about 4 hours. The benzene solution of the thiophenic compound was injected onto the alumina to form a suspension. Over some time (a few minutes to several days), the color developed which indicates formation of radical ions. The suspension was then freeze-thaw-pumped (three cycles) to deplete the oxygen. The EPR tube was then flame-sealed. A W-band sample prepared this way can be used in both X-band and W-band resonators.

In method II, a mixture of powdered boric acid and the desired thiophenic compound (1000:1 mole ratio) is heated to the melting point of boric acid (ca. 180 °C). The molten mass is allowed to cool to a glass, broken into small fragments or crashed into fine powder, and loaded into a quartz sample tube. The tube is placed in a Ray-O-Net irradiation unit and subjected to UV irradiation at 254 nm for 30 minutes. The sample tube is then removed and sealed for analysis. Samples of cation radicals still give the same strong EPR signal even one year after their preparations.

X-band spectra were obtained from a Varian E-line 12" EPR spectrometer outfitted with a tracking Varian NMR gaussmeter and a Fluke frequency counter. Different microwave levels were used to ensure no power saturation, and different magnetic field modulation amplitudes were used to find the best balance between S/N and resolution. W-band EPR was performed on a locally-built spectrometer described elsewhere (reference 1). All radicals have been prepared at least three times and each sample run at least four times.

The resolution of W-band spectra is usually so high that one can read the principal g matrix directly, which is impossible at much lower frequencies. Nevertheless, a computer-assisted analysis using an EPR powder spectrum simulation program[2] was still performed to confirm the direct measurements.

RESULTS AND DISCUSSION

The g-shifts at W-band and X-band and the measured principal g-matrix components of the heterocyclic sulfur cation radicals are summarized in Figs. 2 and 3.

The g shifts measured at X-band seems compare well with those measured at W-band. Actually, g shift measurement at W-band have more than three times better accuracy than at X-band, because not only is the W-band g shift calculated as an average of three separately measured individual matrix components, each better defined spectroscopically than the line center measured at X-band. It is rather difficult to define the resonance center for a usually broad and asymmetric line.

There is a general agreement between g shifts measured for the alumina surfaces and those for the corresponding boric acid glasses (Fig. 2). But this agreement should not be viewed as proving that these two different preparations yield precisely the same radical species; comparison of the full g-matrices would be much more revealing. Moreover, careful analysis of the g matrices might result in additional information on these radical ions.

It is also observed that g shift or g matrix components do not follow a monotonic trend among our series (Fig. 2). Rather, the g shift starts from THI, rises up, peaked at DBT, then falls down toward DNT. Also, the lowest field g matrix component g_1 and g_2 behave similarly while g_z stays constantly near the free-electron g value (Fig. 3). The latter is expected because all these radicals are planar π radicals, where delocalized p_z electrons have zero shift on g_z.

The fact that both g shift and two of the three principal g-matrix values vary substantially with the number of fused benzene rings is very encouraging. It demonstrates that W-band EPR spectroscopy of these organic sulfur radicals is very sensitive to their structures. Thus the EPR parameters of those model compounds, especially anisotropic g values, have the potential to help identify the sulfur-containing heterocyclic moieties in coal. Clearly, studies on more model compounds are needed in order to build a library of VHF EPR spectra. We are currently investigating a dozen more alkyl-thiophenes or benzothiophenes as well as an analogous furanic series.

Based on notions including 'frozen orbitals' and additive property of g shifts, Stone[4] proposed the g shift of aromatic hydrocarbon to be $\Delta g = b + \lambda C$ where λ is the coefficient in the simple Hückel Molecular Orbital (HMO) energy expression $E = \alpha + \lambda\beta$, where α and β are the Coulomb and resonance integral, respectively; b and c are empirical parameters. Fig. 4 shows the measured g shift plotted against λ from HMO's. It seems that four of the five points fall into a straight line in this particular sulfur heterocyclic series. We are a bit surprised by this observation in view of the crudity of this simple treatment. We cannot guarantee that this 'correlation' is not accidental; more experimental examples are required to establish a generalization at a high level of confidence.

Fig. 5, 6, and 7 show g matrix components (g_1, g_2 and g_3), g shift, and g_{xy} anisotropy vs. spin density calculated by McLachlan's method of perturbation on HMO[5]. Fig. 5 indicates that both g_1 and g_2 increase with the π spin density, with g_1 faster than g_2. Fig. 6 shows that the g shift also increases with the π spin density at the sulfur atom. From Fig. 7 one sees that the difference between g_1 and g_2 (so called xy anisotropy) increases with the π spin density at the sulfur atom. These probably suggest that one of the g matrix components g_1 is more sensitive to the change of π spin density distribution in the aromatic ring. One tentative conclusion from these comparisons of theory and experimental data is that one of the g matrix components, g_1, is more sensitive to the change of π spin density distribution in the aromatic ring than the others. We are currently using more elaborate MO calculations to examine how structural features other than the number of benzene rings should affect the anisotropic g values.[6]

SUMMARY

Radical cations prepared from thiophene and some of its aromatic homologues were studied by

a novel technique — VHF (W-band) EPR spectroscopy. The first unambiguous results on principal g matrices and g shifts for these species are presented. Since the EPR parameters determined from W-band spectra of these compounds prove very sensitive to their molecular structure, this technique is promising for the nondestructive analysis of the chemical forms of organic sulfur in coal, where nearly identical g-factors have been observed and correlated with organic sulfur content[1].

ACKNOWLEDGEMENT

Facilities of the Illinois EPR Research Center (IERC), partially supported by the National Institutes of Health, Division of Research Resources under BRTP Grant RR01811 were used in this work. The authors thank Prof. Mark J. Nilges, Illinois EPR Research Center, for many helpful discussions and for his key role in the design and improvement of the W-band spectrometer. This work was prepared with the support, in part by grants made possible by the Illinois Department of Energy and Natural resources through its Coal Development Board and Center for Research on Sulfur in Coal, and by the U. S. Department of Energy (Grant Number DE-FG22-91PC91334). However, any opinions, findings, conclusions, or recommendations expressed herein are those of the authors, and do not necessarily reflect the views of IDENR, CRSC, and the DOE.

REFERENCES

1. R. B. Clarkson, W. Wang, M. J. Nilges, and R. L. Belford, in *Processing and Utilization of High-Sulfur Coal*, R. Markuszewski and T. D. Wheelock, Eds., Elsevier: Amsterdam, 1990; pp. 67-79.

2. R. L. Belford, R. B. Clarkson, J. B. Cornelius, K. S. Rothenberger, M. J. Nilges, and M. D. Timken, in *Electron Magnetic Resonance of the Solid State*, J. A. Weil, Ed., Chemical Institute of Canada: Ottawa, 1987; p 21.

3. A. Attar, and F. Dupuis, *Am. Chem. Soc. Div. Fuel Chem.* Preprints, **24**, 166 (1979)

4. A. J. Stone, *Mol. Phys.* **6**, 509 (1963)

5. The calculation was based on HMO and McLachlan parameters taken from P. D. Sullivan, *J. Am. Chem. Soc.*, **90**, 3618 (1968)

6. W. Wang, Ph.D. Thesis, University of Illinois, Urbana, IL (1992).

Fig. 1. EPR spectra of dibenzothiophene (DBT) cation radical in boric acid glass. a) At X-band, b) At W-band.

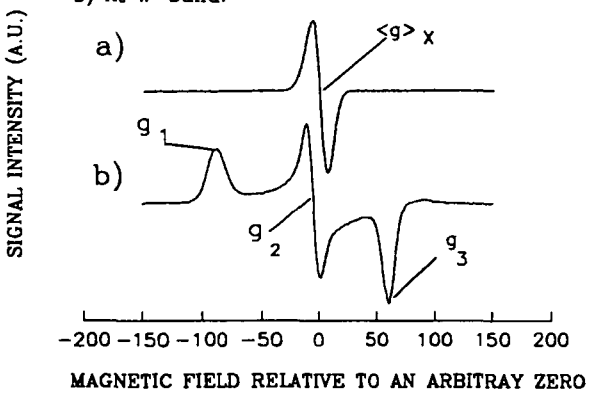

Fig. 2. g-shifts of thiophenic cation radicals on alumina (A) surface and in boric (B) acid glass.

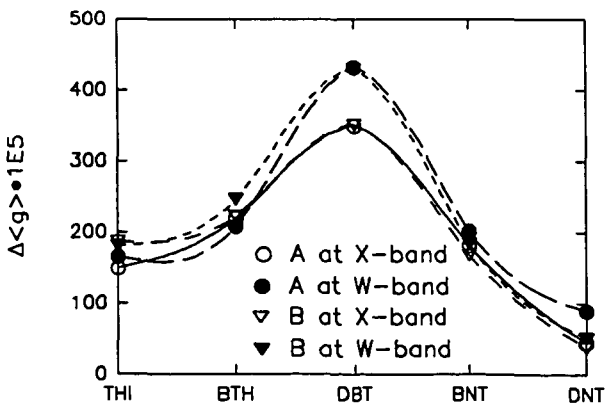

Fig. 3. Measured three principal g-matrix components, (A) on alumina (B) in boric acid glass

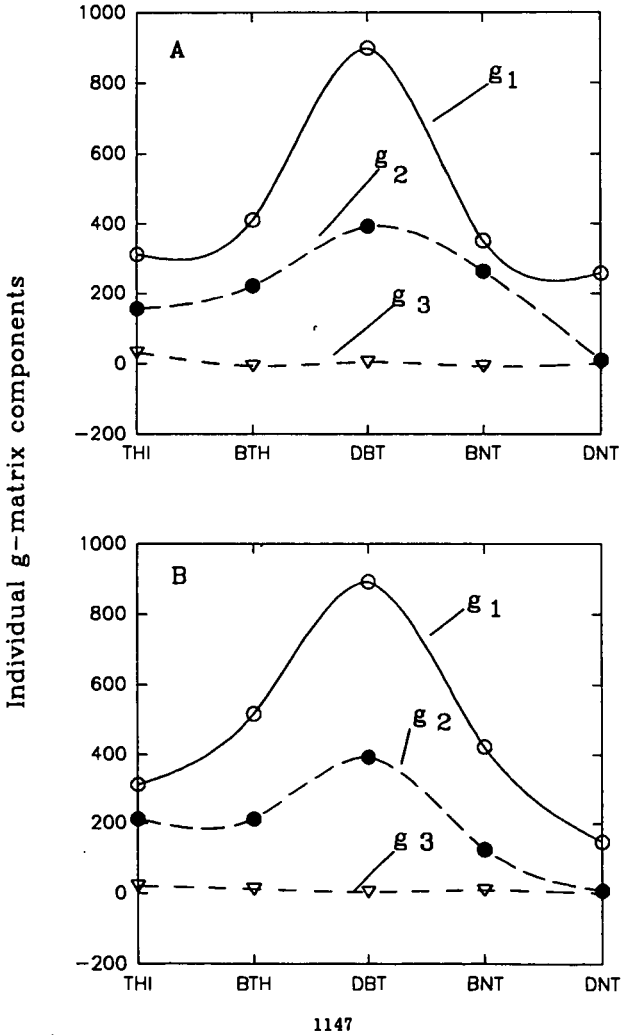

Fig. 4. Experimental g-shifts plotted against λ in HMO calculation.

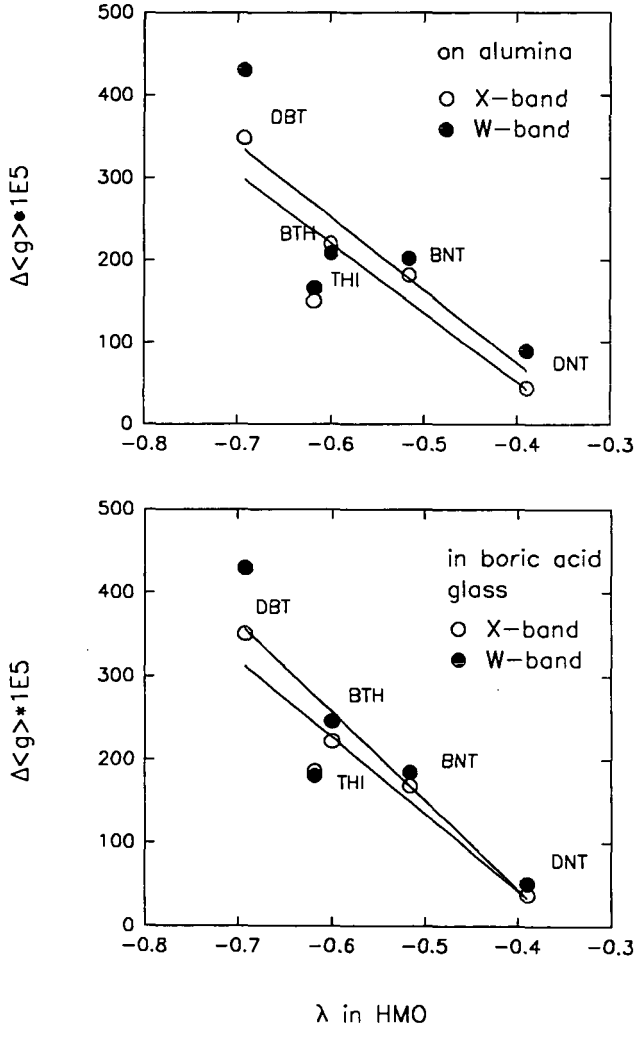

Fig. 5. A plot of principal g−matrix components against calculated π spin density on sulfur

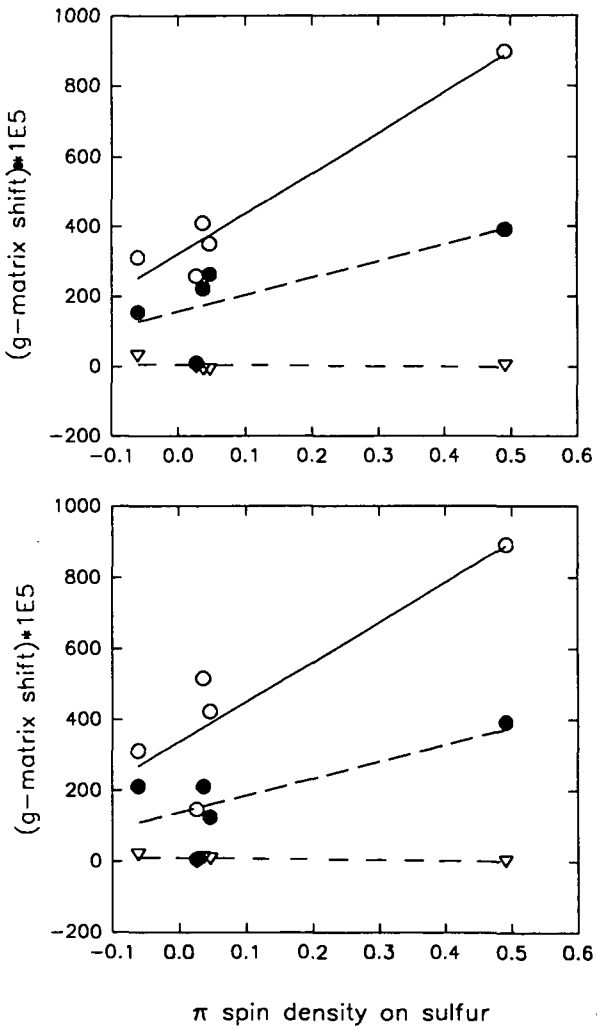

Fig. 6. A plot of g−shift at W−band vs. calculated π spin density on sulfur

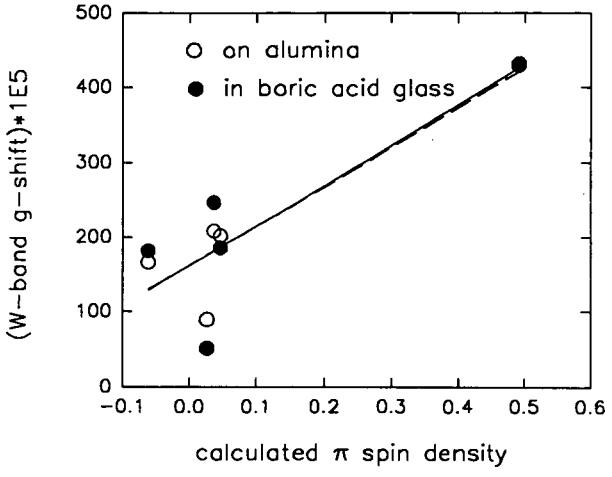

Fig. 7. g xy anisotropy vs. calculated π spin density on sulfur

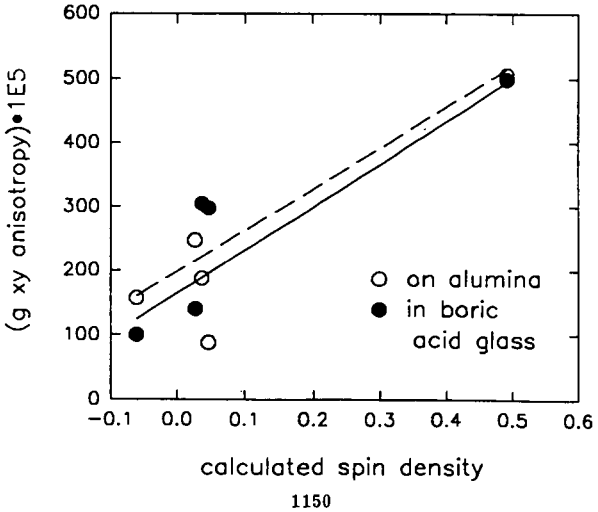

AN EPR SPIN PROBE METHOD FOR CHARACTERIZING CHANGES IN THE ACCESSIBLE REGIONS OF COAL UPON OXIDATION

Wojciech Sady, Lowell D. Kispert, and Dennis R. Spears

Box 870336, Chemistry Department
The University of Alabama, Tuscaloosa, AL 35487-0336

KEYWORD: porosity, oxidation, coal swelling, EPR, nitroxyl spin probe

ABSTRACT

Eight Argonne Premium Coal Samples (APCS) were weathered in air and the structural and chemical changes that occurred upon swelling with toluene and pyridine were examined by an EPR spin probe method developed in this laboratory. Under mild oxidation conditions and swelling with toluene large structural changes were observed for lignite (Beulah-Zap) which suggested the collapse of the coal structure. This did not occur for higher rank coal. Upon oxidation and swelling with toluene and pyridine an increase occurred in the amino substituted spin probe concentration for coals with the carbon percent above 80%. A maximum was found for the creation of 5 Å diameter pores upon swelling with pyridine at 85% C.

INTRODUCTION

The conversion of coal by an economically feasible catalytic method is an area of research for our future energy requirements. However, knowledge of the coal structure (1, 2) is necessary before optimum use of a catalyst can be made. For instance, in addition to the normal surface catalysis, the catalyst must be able to diffuse into the coal, enabling catalysis to occur from within. This requires knowledge of the pore molecular accessibility size and shape in the coal. Any conversion process, however, involves exposure of the pore structure to solvents of various polarity, temperature and pressure variation, and catalytic action. Complicating the process can be oxidation processes that occurred before the coal is processed.

Oxidation (3) is of the utmost importance in many respects. Autogenous heating in a coal stockpile causes oxidation and even combustion of coal. In either case, sever detrimental changes to coal properties occur. Oxidation affects thermal and swelling properties which are important in coke production. Oxidation also affects solvent swelling properties, important in catalytic conversion.

However, the oxidation process is difficult to study, quantitatively or qualitatively. The amount of oxygen has been determined by neutron activation analysis (4) and by XPS analysis of the coal surface (5,6). Relative changes in the properties of the coal have also been used to measure oxidation. These include FTIR signatures, (7) pH, (8) Gieseler fluidity, (9,10) pyrolysis response, (11, 12) and free swelling index (13). In spite of these advance techniques, it is difficult to quantify the low temperature oxidation, as the amount of solid oxidation products are small (14). XPS measurements in conjunction with GC analysis of the gas products and thermal gravimetric analysis (GA) of the fuels (15) can be useful in determining the oxidation process.

In addition, drying of the coal results in pore collapse which changes the mechanical properties (1, 2) so the coal becomes more friable. Reswelling the dried coal is believed (1, 2) to cause autogenous heating of the coal.

The micropore structure of coal has been characterized by both sorptive methods (16-18) and spectroscopic methods. The spectroscopic methods have included small-angle X-ray (SAXS)

(19) and neutron (SANS) (20-22) scattering where micropores can be observed in the presence of solvent molecules. Low field NMR spin lattice relaxation measurements (23, 24) of the water in the pores of the coal enabled a study of pore radius from <0.5 mm to 0.5 mm.

EPR spin probe studies in the absence of oxidation

Previous electron paramagnetic resonance (EPR) spin probe (25-30) studies of APCS samples have dealt with the effect of swelling temperature, micropore size and shape, solvent polarity, spin probe imbibition, and polarity of the spin probes. The results of these studies have correlated well with SANS (19), SAXS (20-22) and NMR (23, 24) studies of APCS coals upon coal swelling.

It was observed by the EPR spin probe method that APCS samples swelled at 298 K in toluene did not changed the micropore structure in any significant way (29). It was found (28, 29) that coals swelled in toluene contained small, spherically shaped pores and a broad distribution of cylindrical shaped pores of short length. Elevating the swelling temperature from 298 K to 333 K had no effect on nonpolar solvents (toluene), only a mild effect on slightly polar solvents (nitrobenzene) and a significant affect on very polar swelling solvents (pyridine).

Polar solvents caused elongation of the micropores (29). The greater the swelling temperature and the greater the swelling solvent polarity, the greater the degree of micropore elongation. Nitrobenzene at 298 K showed only small micropore elongation. However, small spherical pores did disappear entirely. At 333 K in nitrobenzene, significant pore elongation did occur, with the creation of a bimodal pore size distribution. Coals swelled in pyridine at 298 K exhibited significant pore elongation, and the creation of a bimodal pore size distribution. Elevation of the swelling temperature to 333 K caused much greater micropore elongation. This bimodality was confirmed through the use of alkylammonium spin probes, which behaved more like nonpolar spin probes than as cationic moieties.

The effect of solvent polarity was found to be related to the types of cross-linking in coal. Toluene did not disrupt either covalent or noncovalent linkages and so did not swell coal significantly under these conditions. Polar solvents like nitrobenzene and pyridine swelled coal by disrupting hydrogen bonds. A solvent which was more polar (i.e., had a greater hydrogen bond accepting ability) could disrupt more bonds and swell coal to greater degree. More polar solvents took longer to reach swelling equilibrium. Increasing the swelling temperature had the effect of hastening the approach to equilibrium and so caused greater pore swelling and elongation.

Micropore elongation was ascribed to swelling anisotropy in coal. It was determined that most of the micropore elongation took place parallel to the bedding plane. This led to the development of a "zipper" model for coal swelling (29).

Rank effects was shown to be an important factor in spin probe imbibition (29). Coals at 85% carbon (dmmf) and above typically showed similar spin probe retention curves. Spin probe concentration, where significant retention occurred, decreased with rank. The retention curves showed a minimum in the range 85-92% carbon (dmmf). For coals swelled in toluene, the minimum was directly related to a minimum in porosity in this range.

For coals swelled in polar solvents, the decrease in spin probe concentration was associated with rank, and the increase in covalent cross-links. The decrease in hydrogen bond cross-link density in APCS coals was in turn associated with the decrease in oxygen functionality concentration, especially hydroxyl content, with rank.

Spin probes with polar R groups showed selective retention over nonpolar spin probes of same size. Spin probe retention was dependent on the polarity of the R group, which proceeded in

the order -H << -OH < $-CO_2H$ < NH_2. Spin probe retention for moderately polar spin probes increased with swelling temperature for coals swelled in toluene. This increase was ascribed to hydrogen bond disruption by the spin probes. The most polar spin probe (R = $-NH_2$) showed no temperature effects up to 333 K, apparently because its R group was strong enough to cause significant hydrogen bond disruption.

Varying the swelling solvent polarity resulted in a competition of the solvent molecules with the polar spin probes for hydrogen bonding sites. Raising the swelling temperature resulted in increased solvent competition for hydrogen bonding sites. The effect of temperature was significantly greater as solvent polarity increased.

It was shown that "acidity" and "basicity" were incorrect terms in considering coal micropore wall chemistry. The terms "hydrogen bond donor" and "hydrogen bond acceptor" were used instead. Polar spin probes interacted with coal primarily as hydrogen bond acceptors. Acidic spin probes showed some indication of acting as hydrogen bond donors, but the primary mechanism of interaction was as an acceptor.

For coal swelled in polar solvents, the decrease in spin concentration was associated with the decrease in hydrogen bond-type cross-link concentration with rank, and the increase in covalent cross-links. The decrease in hydrogen bond cross-link density in APCS coals was in turn associated with the decrease in oxygen functionality concentration, especially hydroxyl content, with rank.

Recently, measurements of Argonne Premium Coal Samples (APCS) in our lab using the EPR spin probe technique that we developed suggests that the study of the oxidation processes and the change in structure upon drying can be followed by the EPR spin probe technique. This paper details the study of oxidizing coal for eight days and outlines additional experiments which lead to a further understanding of the oxidation process in the pore structures of coal.

EXPERIMENTAL

Ampoules containing all eight APCS coals were opened and their content was placed in a number of vials, 250 mg of coal in each vial. The vials with coals were weighted, and then placed on a shelf in room temperature and humidity about 60% protected from dust. The coals were stirred every day.

At the beginning samples from fresh coals were made, then samples were prepared from coals weathered for 8, 15, 36, 64 and 119 days. The vials with weathered coals were weighed, the values of the loss of weight after n days of weathering are given in Table 1.

Our standard procedure of imbibing spin probes into the pore structure of coals in the presence of swelling solvent was applied (28, 29). Coals were swelled in 60 °C for 18 hours in toluene or pyridine. Spin probes used were VI (3-carboxy-2,2,5,5-tetramethylpiperidine-1-oxyl), VII (TEMPAMINE, 4-amino-2,2,6,6-tetramethylpiperidine-1-oxyl), and VIII (TEMPO, 2,2,6,6-tetramethylpiperidine-1-oxyl). All spin probes are spherically shaped and are similar in size, the difference between then is the polarity of the R group [Figure 1]. Spin probes I-X were previously defined (26).

EPR spectra of the spin probe doped coal samples were recorded. The method of computing the nitroxide radical spin probe concentration was described previously (26,27). The results of the first 8 days of oxidation are presented in Figures 2-4.

RESULTS AND DISCUSSION

The concentration of spin probe VI (carboxyl substitutent, polar group interactions) as a function of toluene and pyridine as the swelling solvent for APCS coal in the absence of air is given in Figure 2a. A general increase in the number of hydrogen bonding sites is observed as the rank decreases. It is known that the lignites contain more hydroxyl functional groups than the higher rank coals, thus the observed increase in the concentration of trapped spin probe VI for both solvents. The lower concentration of VI in pyridine is due to competition of pyridine for the polar sites, which does not occur in the case of toluene. Upon weathering the coal for 8 days in air (Figure 2b), a large decrease in the concentration of VI is observed for lignite (74-76% C) swelled in toluene. This can be explained by the data of Yost and Creasy (31) that the loss of water from the coal structure (which we also observed) collapses the structure, making it more difficult to trap the small spin probe VI in the coal structure unless the energy barrier can be overcome. A weight loss of 20-25% occurred for 74% C but none for 92% C (Table 1). However, the use of pyridine disrupts the collapsed coal structure so no difference is observed for pyridine solvent in the concentration of spin probe VI over the entire coal rank, while the same is true above 76% C when toluene is the swelling solvent. This observation suggests that we can follow changes in the hydrogen bond energy distribution. Further oxidation for 15 days shows an increase in spin probe concentration at 85% C content when toluene solvent is used indicating an increase in the formation of oxygen groups. This suggests that we can follow oxidation kinetics as well as changes in pore shape and size.

The biggest effect upon weathering in an oxygen atmosphere occurs when solutions of spin probe VII (NH_2 substituent) is slurried with the APCS coals. In the absence of air (Figure 3a) the concentration of VII is similar to VI using toluene as the swelling solvent but is larger for VII than VI when pyridine is the swelling solvent. However upon exposing the coal for 8 days to air a dramatic increase occurs in the concentration of VII for both toluene and pyridine as the swelling solvent above 76% carbon (Figure 3b). Below 76% C, the collapse of the coal structure upon loss of water is observed when toluene is used preventing the trapping of VII. Use of pyridine as the swelling solvent opens up the collapsed structure, allowing the trapping of VII. Upon oxidation for 15 days, the concentration of spin probes VII in pyridine solvent continues to increase due to the interaction of the NH_2 group with the oxidized coal.

The concentration of a spin probe with no substitutent (VIII) and thus only size effects are studied, is depicted in Figure 4a. The concentration of VIII for both toluene and pyridine solvents is an order of magnitude or more lower for VIII than for VI and VII. Interestingly the concentration of VIII in toluene increases with decreasing rank while VIII in pyridine reaches a maximum at 86% C. These features can be rationalized by the opening of the coal structure by the pyridine – allowing all the spin probe concentrations to be washed out at low rank and the coal structure opened sufficiently in some places to trap VIII at 86% C. Upon weathering in air (Figure 4b), the concentration of VIII increases with the maximum still at 86% in a pyridine solvent while the loss of structure can be detected when swelled in a toluene solvent. Further oxidation for 3 weeks shows the maximum at 86% C – suggesting some interesting changes in the swelling characteristics as a function of oxidation. It is important to note that the concentration of VIII is very small but the polar VI and VII spin concentration is large. This observation indicates that even small degrees of oxidation can be detected.

CONCLUSION

The large decrease in the concentration of the spin probe after oxidation of lignite (74%) for eight days and swelled in toluene, appears to be due to the collapse of the coal structure upon oxidation as a result of water loss. However swelling with pyridine reopens the collapsed structure and no detectable difference is observed upon oxidation. For higher rank coal, a larger concentration of amino substituted spin probes was trapped upon swelling with toluene and pyridine after air oxdiation for 8 days. The decrease in amino substituted spin probe for fresh Beulah-Zap showed a measurable increase upon oxidation and swelling in pyridine. Swelling with pyridine opens up small pores for 81-86% which is not observed for swelling with toluene. Changes in coal structures due to oxidation can followed by the EPR spin probe method.

ACKNOWLEDGMENT

This work was supported by the U. S. Department of Energy, University Coal Research Program under grant no. DE-FG22-90PC90284.

REFERENCES

1. N. Berkowitz, "An Introduction to Coal Technology" Academic Press, New York, 1979.

2. E. L. Fuller, Jr., In "Coal Structure, "Ed. by M. L. Gorbaty and K. Ouchi, Adv. in Chem. Series, Washington, DC, 1981, Chapter 19.

3. L. Petrakis and J. P. Fraissard, "Magnetic Resonance, Introduction Advanced Topics and Applications to Fossil Energy"

4. W. D. Ehmann, D. W. Koppenaal, C. E. Hamrin, Jr., W. C. Jones, M. N. Prasad and W. Z. Tian, *Fuel*, **65**, 1563 (1986).

5. D. L. Perry and A. Gint, *Fuel*, **62**, 1029 (1983).

6. D. T. Clark and R. Wilson, *Fuel*, **62**, 1034 (1983).

7. P. M. Fredericks and N. T. Moxon, *Fuel*, **65**, 1531 (1986).

8. Y. Yun, B. Hoesterey, H. I. C. Meuzelaar and G. R. Hill, *ACS Fuel Div. Preprints*, **32**, 302 (1987).

9. G. P. Huffman, F. E. Huggins, G. E. Dunmyre, A. J. Pignocco and M. Lin, *Fuel*, **64**, 849 (1985).

10. A. Grint and D. L. Perry, *Proc. Int. Conf. Coal Sci.* 879 (1985).

11. B. S. Ignasiak, D. M. Clugston and D. S. Montgomery, *Fuel*, **51**, 76 (1972).

12. H. Iyuhara, R. Tanibata and S. Nishida, *Proc. Conf. Coal Sci.*, 491 (1985).

13. J. W. Larsen, D. Dee, T. Schmidt and A. Grint, *Fuel* **65**, 595 (1986).

14. J. S. Gethner, *Fuel*, **66**, 1091 (1987); J. J. Isaacs and R. Liotta, *J. Energy & Fuels*, **1**, 349 (1987).

15. S. R. Kilemen and H. Freund, *ACS Div. Fuel Prepr.* **33**, 706 (1988).

16. S. Fuji; H. Tsuboi*Fuel* **46**, 361 (1967).

17. O. P. Mahajan and P. L. Walker, Jr. In *Analytical Methods for Coal and Coal Products*, vol. 1.; C. Karr, Jr., Ed.; Academic; New York: 1978.

18. M. L. Gorbaty, *Fuel*, **57**, 796 (1978).

19. Z. Spitzer and L. Ulicky, *Fuel*, **55**, 212 (1976).

20. R. E. Winans and P. Thiyagarajan, *Energy & Fuels*, **2**, 356 (1988).

21. J. S. Gethner *J. Appl. Physics*, **59**, 1068 (1986).

22. J. S. Gethner *Prepr. Pap.-Am. Chem. Soc., Div. Fuel Chem.* ,**32**, 239 (1987).

23. C. L. Glaves, P. J. Davis, D. P. Gallegos and D. M. Smith, *Energy and Fuel* (1988).

24. C. H. Bartholomew, W. E. White, D. Thornock, W. F. Wells, W. C. Hecker, L. D. Smott, D. M. Smith and F. L. Williams, *ACS Div. Fuel Chem. Prepr.*, **33(3)**, 24 (1988).

25. S.-K.Wuu and L. D. Kispert, *Fuel* **64**, 1681 (1985); M. L. S. Cooray, Sc. Thesis, University of Alabama, 1988.

26. J. Goslar and L. D. Kispert,*Fuel* **69**, 564 (1990).

27. J. Goslar and L. D. Kispert,*Energy & Fuels* **3**, 589 (1989).

28. D. R. Spears; L. D. Kispert, and L. Piekara-Sady*Prepr. Pap.-Am. Chem. Soc., Div. Fuel Chem.* **36**, 29 (1991); D. R. Spears; L. D. Kispert, and L. Sady, *Fuel*, In Press, 1992; D. R. Spears; L. D. Kispert, and W. Sady,*Prepr. Pap.-Am. Chem. Soc., Div. Fuel Chem.* **36**, 1277 (1991).

29. D. R. Spears, Ph.D. Dissertation, The University of Alabama, 1991.

30. J. Goslar, L. S. Cooray and L. D. Kispert, *Fuel*, **68**, 1402 (1989).

31. R. S. Yost and D. E. Creasy, *Fuel*, **69**, 648 (1990).

Table 1. Weight loss (% ± 0.4%) of APCS coals after n days of weathering.

Coal	Carbon Content	days 8	15	36	64	114
Beulah-Zap	74.05%	21	25	23	23	25
Wyodak-Anderson	76.04%	19	20	20	21	21
Illinois #6	80.73%	4.5	5.5	5.5	5	5.3
Blind Canyon	81.32%	1.2	2	1.5	1.6	1.2
Pittsburgh #8	84.95%	0	0	0.2	0.4	1.2
Lewiston-Stockton	85.47%	0.8	1	1	1.4	1
Upper Freeport	88.08%	0.6	0.8	1	1	0.6
Pocahontas	91.81%	0	0	0	0	0

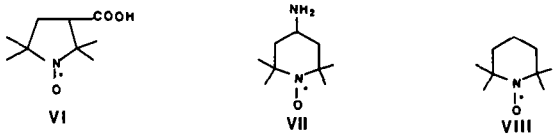

Figure 1. Spin probes VI, VII, and VIII.

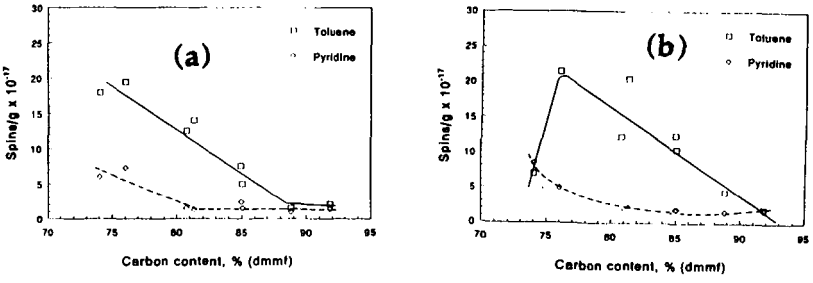

Figure 2. Concentration of spin probe VI versus percent carbon content (dmmf) in APCS coal swelled at 60 °C in toluene (□) and in pyridine (●), (a) as received and (b) after weathered for 8 days in air at room temperature.

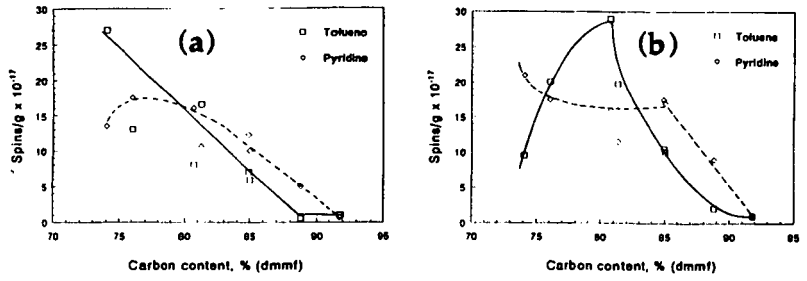

Figure 3. Spin probe VII versus percent carbon content (dmmf) in APCS coal swelled at 60 °C in toluene (□) and in pyridine (♦), (a) as received and (b) after weathered for 8 days in air at room temperature.

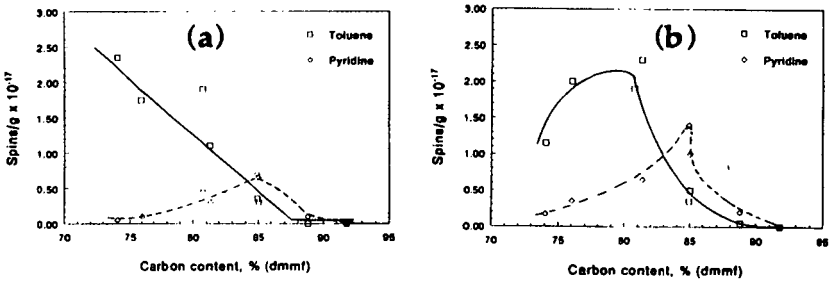

Figure 4. Spin probe VIII versus percent carbon content (dmmf) in APCS coal swelled at 60 °C in toluene (□) and in pyridine (♦), (a) as received and (b) after weathered for 8 days in air at room temperature.

ENDOR Characterization of Free Radicals in Coals at Temperatures Upto 200°C

Naresh Dalal and Jeffrey P. DeLooze, Chemistry Department
West Virginia University, Morgantown, WV 26506-6045

Summary

The lack of information about the chemical structure of coal-based radicals has been a major obstacle in the understanding of the structural-chemical reactivity relationship. Our past research has indicated that the electron nuclear double resonance (ENDOR) technique has the potential of providing the most accurate structural information on the coal-based radicals. Unfortunately, the sensitivity of the best available ENDOR instrumentation was too low for liquefaction studies. We have developed an ENDOR probe which yields an increase in the sensitivity of the technique that enables us to investigate the structural-chemical reactivity patterns of coal-based free radicals under mild conditions suitable for liquefaction. We have used this technique to examine chemically characterized Illinois #6 coal at temperatures up to 200°C. Analysis of the resulting ENDOR signals identified at least three different types of protons. Analyses were also performed on the temperature dependence of the ENDOR signal intensity. Efforts are currently being made to enhance the measurement methodology's sensitivity above 200°C.

Introduction

It is well established that free radicals must play a dominant role in coal liquefaction [1]. Thus, a detailed understanding of the reaction mechanism(s) of the free radicals in coal is thought to be essential for the further improvement in the efficiency of coal liquefaction. However, a lack of knowledge concerning the chemical structure(s) of these same coal-based radicals has been a major hinderance in the development of the possible reaction mechanism(s) and, hence, an impediment to the improvement of liquefaction technology. The difficulty in this aspect has been that the structure(s) of the radicals is (are) complex and, hence, standard methods of radical structure determination, such as ESR, are not adequate. Following earlier leads [2-4], it was felt that the high resolution possible with the electron nuclear double resonance (ENDOR) technique would enable us to provide the much needed structural information on the radicals.

Commercially available ENDOR instrumentation does not provide the sensitivity for the required measurements at temperatures of interest to coal liquefaction scientists. Thus, our first task was the development of a new probe that would enable us to make measurements at 200°C and higher. We have developed such a probe, as described elsewhere [5] and the results obtained with it in the studies of Illinois #6 coal are summarized below. Illinois #6 was chosen because it has been accepted by many researchers as a model coal for liquefaction studies. Thus, it is possible to obtain large amounts of uniformly processed coal along with a detailed analysis of the chemical constituents of each sample.

Experimental Results

The ENDOR measurements were made with a Bruker ER-200-D ENDOR spectrometer, using an ENDOR probe designed in our laboratory, as described in our earlier report [4]. The ENDOR spectral lineshape was found to be quite sensitive to the instrumental parameters as well as sample preparation. A most important factor was the removal of oxygen from the sample via evacuation; the lower

the overall pressure in the sample tube, the stronger became the ENDOR signals, especially those corresponding to the larger couplings. In order to find the experimental parameters which would lead to the optimum signal-to-noise ratio, we carried out systematic ENDOR measurements on the Illinois #6 coal, by varying the microwave power, radio frequency (rf) power, and sample temperature.

Figure 1 is a typical plot of the ENDOR spectrum of protons in an Arkwright, West Virginia, coal as reported earlier [4] with the original, non-optimized probe under the previously stated operating parameters. The spectrum shows quite high baseline noise and a poor signal-to-noise ratio.

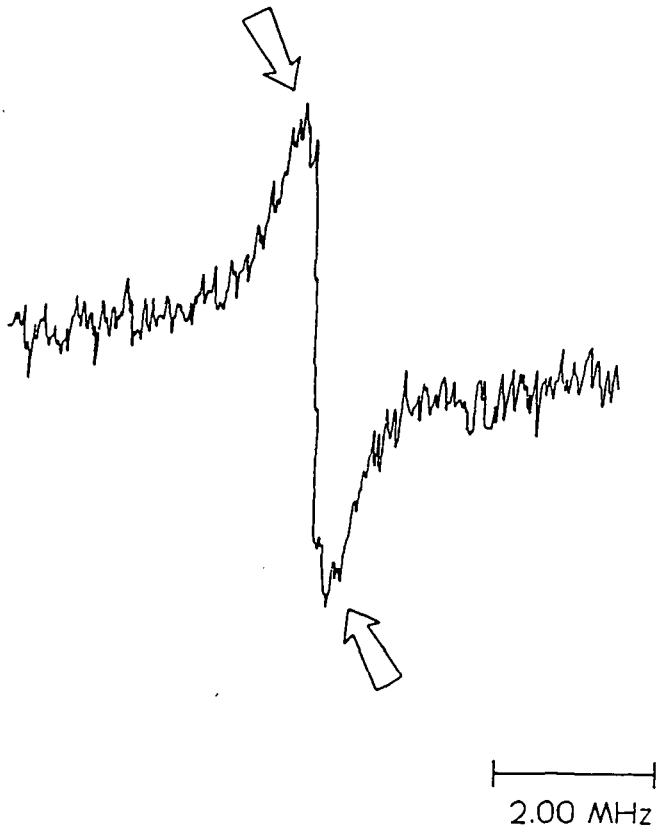

Figure 1: ENDOR spectrum of Arkwight, West virginia coal sample
Arrows indicate the sidebands separated by approximately 750 kHz

Figure 2 shows a typical ENDOR spectrum of the Illinois #6 coal, obtained with the new probe; the greatly reduced noise level and, hence, the much higher signal-to-noise ratio is readily apparent. The improvement in the signal-to-noise ratio was found to be at least a factor of 200. This improvement in signal-to-noise also made it possible to obtain still higher spectral resolution via second harmonic detection, as demonstrated by the lower plot in figure 2.

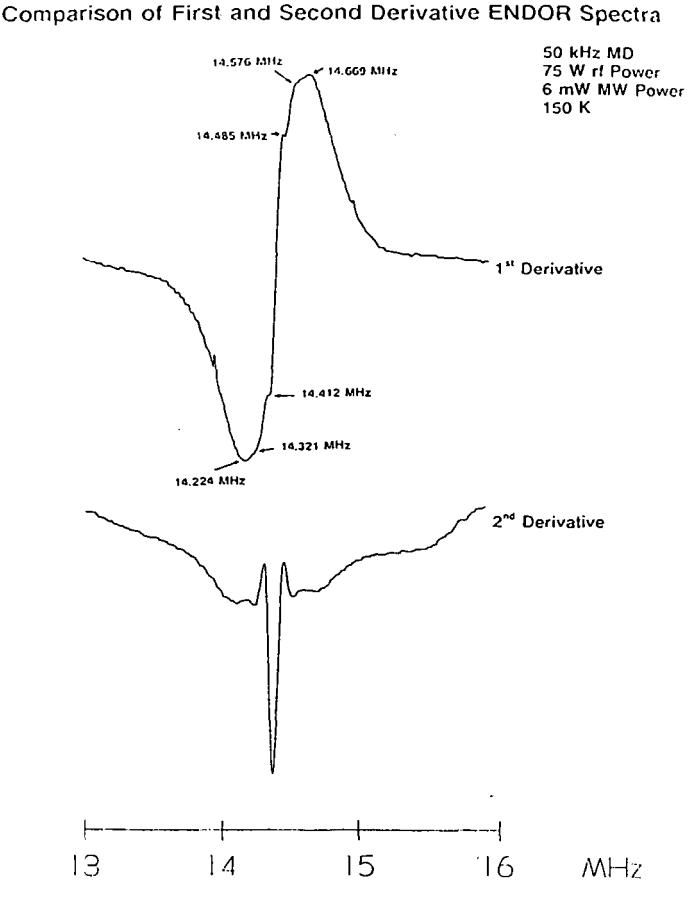

Figure 2: ENDOR spectra of Illinois #6 coal (a) first derivative and (b) second derivative. The higher resolution of the second-derivative presentation (as compared to the first-derivative presentation) can be noted from a comparison of (a) and (b).

Figure 3 is an expanded scale view of the optimized spectra in Figure 2. Note that the apparent discrepancies in the measured ENDOR frequencies is due to the re-tuning of the cavity for optimum response.

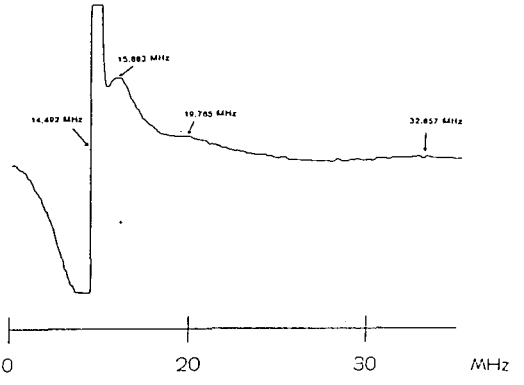

Figure 3: A wide-scan, optimized ENDOR spectrum of Illinois #6 coal at 150K.

Figure 4 shows typical ENDOR spectra of Illinois #6 as a function of temperature. It can be clearly seen that the new probe allows not only for a significant improvement in the room temperature signal, but also provides spectra at previously unheard of temperatures higher than that ever achieved before.

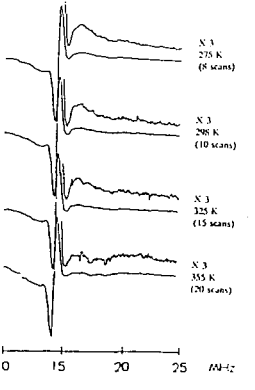

Figure 4: Temperature dependence of the ENDOR spectra of Illinois #6 coal.

Figure 5 shows a plot of the intensity of the ENDOR response as a function of temperature. It is clearly seen that the ENDOR intensity drops as a near-quadratic power function above room temperature to the point that the signals become undetectable above ≈ 425 K (≈ 150°C).

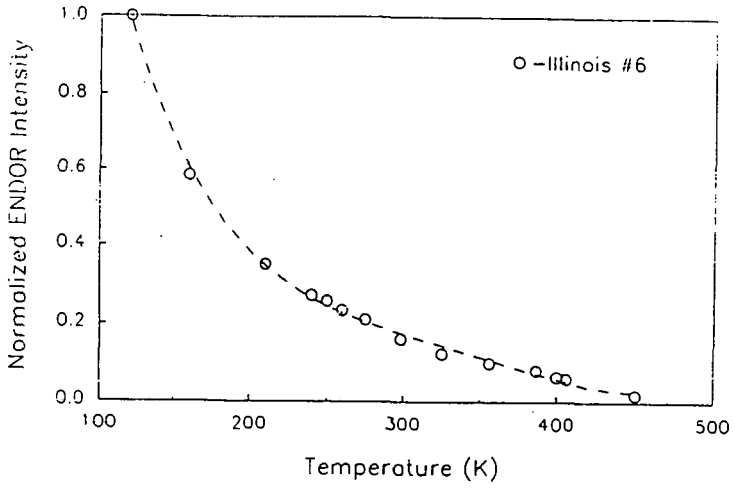

Figure 5: ENDOR signal intensity (optimized) versus temperature for Illinois #6 coal. Signal intensity normalized to $I_{ENDOR\ 120} = 1$.

Analysis Procedure

The measured ENDOR frequencies, υ_E, were analyzed in terms of the corresponding hyperfine coupling, $\underline{A}_H$, via the following effective spin Hamiltonian [6, 7]:

$$\mathcal{H} = \langle S \rangle \, \underline{A}_H \cdot \hat{I} - g_n \beta_n \hat{H} \cdot \hat{I}, \qquad (1)$$

where <S> is the effective electron spin; $\hat{I}$, the electron spin; $\hat{H}$, the applied magnetic field; and $g_n\beta_n$, the magnetic moment of the nucleus under consideration, in this case, protons. The general solution of equation (1) will give the energy levels as a function of the applied magnetic field $\hat{H}$ and the properties of the hyperfine coupling tensor, $\underline{A}_H$. The ENDOR transitions are then given by the differences in the energy levels, with the selection rules $\Delta m_s = 0$, $\Delta m_I = 1$, where m_s and m_I are the electronic and nuclear spin quantum numbers. In the high-field approximation, i.e., when $\hat{H} > \underline{A}_H$ (in Gauss), and along the principal directions, the ENDOR transition frequencies, υ_E, are related to $\underline{A}_H$ and $\hat{H}$ via:

$$\upsilon_E = \underline{A}_* / 2 + g_n \beta_n H \qquad (2)$$

For the spectrum shown in figure 3, $g_n \beta_n H$ was equal to 14.492 MHz, and thus equation (2) provides a direct method of calculating hyperfine couplings from the measured ENDOR frequencies. The hyperfine couplings calculated via equation (2) are listed below in Table 1.

Table 1: Proton ENDOR transition frequencies, υ_E, and hyperfine couplings, $\underline{A}_H$, for the free radicals in Illinois #6 coal.

Proton #	υ_E / MHz	$\underline{A}_G$ /MHz	Assignment
1	14.448 (two)	0.0	coal matrix
2	15.448	2.87	meta- para-
3	19.765	10.63	ortho-, para-

It is clear that the ENDOR measurements show that there are essentially three types of protons in the structure of the free radicals in Illinois #6 coal. The majority of the protons, labeled #1 in the table (ref. figure 3), exhibit no measurable isotropic hyperfine coupling with the unpaired electron. These protons are assigned to the coal matrix, although some of these might belong to the radical itself but located at positions of negligible spin density. The second set of protons, labeled #2, exhibits a coupling of about 3 MHz. The third set of protons (labled #3) exhibits the largest hyperfine coupling ($\approx$ 10.6 MHz).

The above results indicate that the free radicals imbedded in the matrix of the Illinois #6 coal are essentially highly delocalized aromatic structures: protons of type #3 being located at the positions of high spin density, i.e. ortho-to the free electron center. Protons of type #2 might be located at either the meta - or para - positions.

Theoretical Model

While exact details of the model explaining the rapid decrease in the ENDOR intensity upon heating the illinois #6 coal have not yet been worked out, it is well established [6] that the ENDOR response is determined by an effective electron-nuclear spin-lattice relaxation time (T_{1e}). In general, one then sees that the temperature dependence of the ENDOR signals simply reflects the decrease in T_{1e}. For simple model compounds, T_{1e} is a sensitive function of the molecular motion of the radical, given by the autocorrelation function, $J(\omega_L)$, as:

$$(T_1)^{-1} \approx B_i\, J(\omega_L), \text{ where} \quad (3)$$

$$J(\omega_L) = 2 / \tau\,(1 + \omega_L^2\, \tau^2) \quad (4)$$

$$\tau = \tau_0 \exp\,(E / k_B T) \quad (5)$$

Where τ is the correlation time for the relevant molecular motion, τ_0 the pre-exponential factor, and E the activation energy. From these relationships, it is seen that T_{1e} will decrease rapidly with increase in temperature when $\omega_L^2\tau^2 < 1$ (i.e., fast motion limit).

We are now carrying out a detailed analysis of temperature dependence of the ENDOR intensity as shown in figure 4 as assuming different values for τ_0 and E. A satisfactory set of these parameters fitting the data in Figure 4 will provide us with further insight into the chemical structure and, more importantly, the relevant molecular motions in the radical entities in the Illinois #6 coal, and likely also in other coals.

References Cited:

[1] See for example, H.L. Retcofshy, *Coal Science* 1, 43 (1982).
[2] I. Miyagawa and C. Alexander, *Nature* 278, (1979).
[3] S. Schlick, P.A. Narayana, and L. Kevan, *J. Am. Chem. Soc.* 100, 3322 (1978).
[4] H.L. Retcofsky, M.R. Hough, M.M. Maguire, and R.B. Clarkson, *Appl. spectros.* 36, 187 (1982).
[5] N.S. Dalal and J.P. DeLooze, paper presented at the Fifth Annual Technical Meeting of the consortium for fossil Fuel Liquefaction Science, Lexington, Kentucky, August 14, 1991.
[6] *Electron Spin Double Resonance*, L. Kevan and L.D. Kispert, Wiley Interscience, New York, 1976.
[7] N.S. Dalal, *Advances in Magnetic Resonance* 10, 119-218 (1982).

SELECTIVE FLUORINATION OF COALS: STRUCTURE AT REACTIVE SITES BY HIGH RESOLUTION TRIPLE RESONANCE SOLID STATE NMR

Edward W. Hagaman and Suk-Kyu Lee
Chemistry Division, Oak Ridge National Laboratory
Oak Ridge Tennessee 37831-6201

Keywords: fluorinated coal, ^{1}H-^{19}F-^{13}C triple resonance solid state NMR

INTRODUCTION

As part of our program to define the chemical reactivity of coals, we are systematically investigating methods to introduce fluorine into specific sites in the organic matrix of these materials. The methodology is guided by analysis methods appropriate for solid derivatives. The spectroscopic technique that we use most heavily is solid state NMR.[1] In addition to the triple resonance experiments of reference (1), we have recently achieved the capability to observe ^{19}F directly. The utilization of the large ^{19}F chemical shift dispersion and cross correlation with the ^{13}C chemical shift will provide a powerful approach for analysis in these complex materials. We use Fourier transform infrared spectroscopy (FTIR) as a rapid method to assess fluorine incorporation into the coal matrix.

RESULTS AND DISCUSSION

Treatment of North Dakota lignite (Argonne Premiun Coal No.8) with Sulfur Tetrafluoride. The chemistry of sulfur tetrafluoride with organic carbonyl compounds is well known.[2,3] Under mild reaction conditions it converts carboxylic acid functionality into acyl fluoride moieties. The reaction proceeds with aliphatic and aromatic acids although the latter require acid catalysis in some cases. The following experimental reports our initial trials using SF_4 to convert carboxylic acid functional groups in coal into acyl fluoride residues. Dry lignite (110°C vacuum oven, 24 h), 0.5 g, is placed in a monel pressure vessel and evacuated. Sulfur tetrafluoride, 15 g, is transferred to this vessel, cooled in a dry ice/acetone bath. The reaction is accomplished by warming the vessel to the desired temperature and allowing the mixture to stand for the prescribed time. Excess SF_4 and gaseous byproducts of the reaction are destroyed in aqueous KOH traps. The coal is then washed with water until the filtrate is neutral and then dried at 110°C.

The reactivity of the coal with SF_4 is dependent on pretreatment. Lignite, as received, produces a material that shows minor reaction after contact with SF_4 for 72 h at 110°C. Reaction progress is judged by the relative intensity of the acid fluoride absorption in the infrared spectrum (IR) at 1830 cm^{-1} and by the ^{1}H-^{19}F-^{13}C double cross polarization (DCP)/MAS ^{13}C NMR spectrum. Washing the coal with 1N HCl or with citric acid[4] and then with water until the filtrate is neutral to pH paper, followed by overnight drying, yields a much more reactive coal. The source of the difference in reactivity is suggested in the FTIR spectra of the APC #8 lignite and of the HCl washed material, shown in Figure 1a and b, respectively. The change in the carbonyl absorption indicates the

REFERENCES

1. F. Bergius, "Chemical Reactions Under High Pressure", Nobel Lecture, May 21, 1932.
2. A. N. Stranges, *Fuel Proc. Tech.*, **16**, 205 (1987).
3. W. R. K. Wu and H. H. Storch, "Hydrogenation of Coal and Tar", Bulletin 633, Bureau of Mines, U.S. Department of the Interior, Washington, DC, 1968.
4. E. E. Dovath, *Fuel Proc. Tech.*, **1**, 3 (1977).
5. A. Eamsiri, W. R. Jackson, K. C. Pratt, V. Chreston and M. Marshall, *Fuel*, **71**, 449 (1992).
6. J. M. Lee, C. E. Cantrell, S. V. Gollakota, O. L. Davies, M. M. Corser and P. Vimalchand, *ACS Div. Fuel Chem. Preprints*, **36**, 1915 (1991).

Table 1

Crystalline Phases in Fe-S System

Formula	Crystal Structure	Lattice Parameters Å		
Fe_7S_8	HCP	a = 6.867	c = 17.062	
FeS	HCP	a = 5.967	c = 11.735	
Fe_3S_4	HCP	a = 3.47	c = 34.5	
$Fe_{1-x}S$	HCP	a = 6.88	c = 22.90	
FeS_2	Cubic	a = 5.417		
FeS	Cubic	a = 5.423		
Fe_7S_8	Monoclinic	a = 11.902	b = 6.859	c = 22.787
β-$Fe_{1-x}S$	HCP	a = 6.894	c = 40.15	
Fe_9S_8	Tetragonal	a = 3.679	c = 5.047	
FeS_2	Orthorhombic	a = 4.436	b = 5.414	c = 3.381
Fe_3S_4	Cubic	a = 9.876		
FeS	Tetragonal	a = 3.676	c = 5.032	

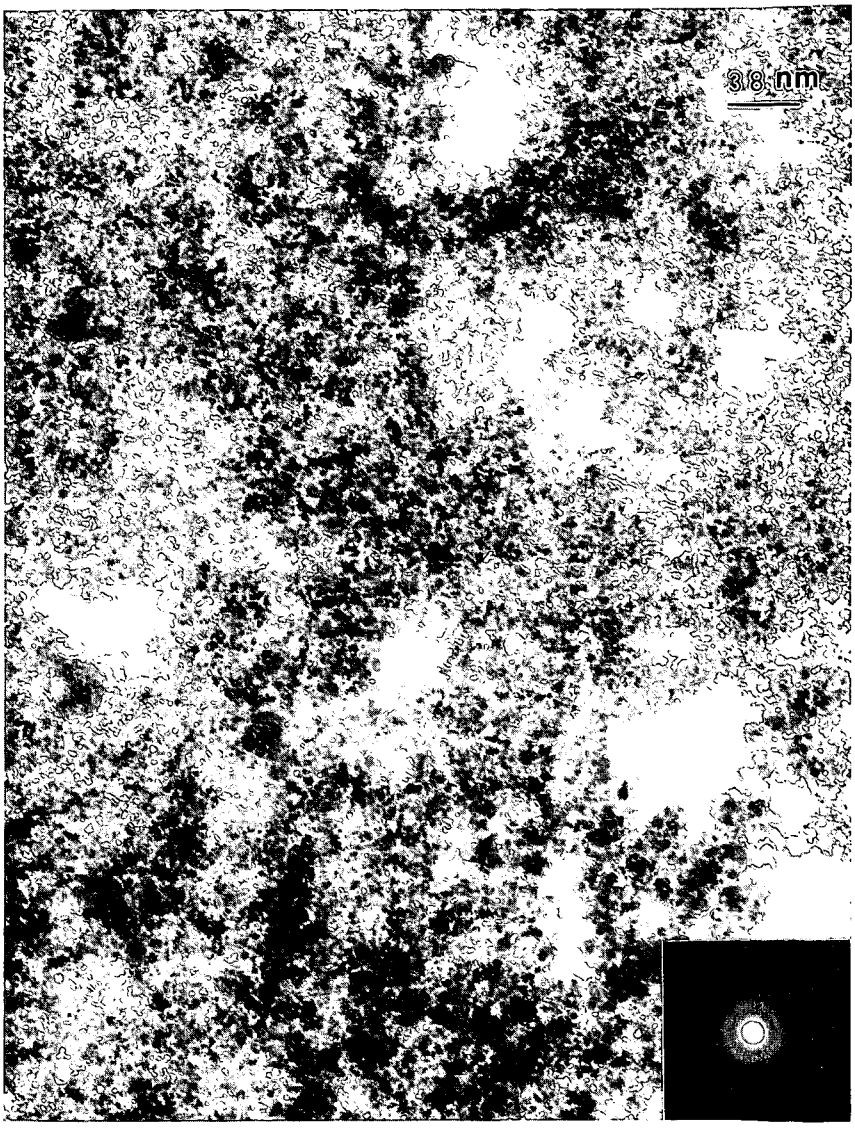

Figure 1. Transmission electron micrograph from the as-received Fe_2O_3 catalyst (inset). Microdiffraction pattern showing diffuse rings.

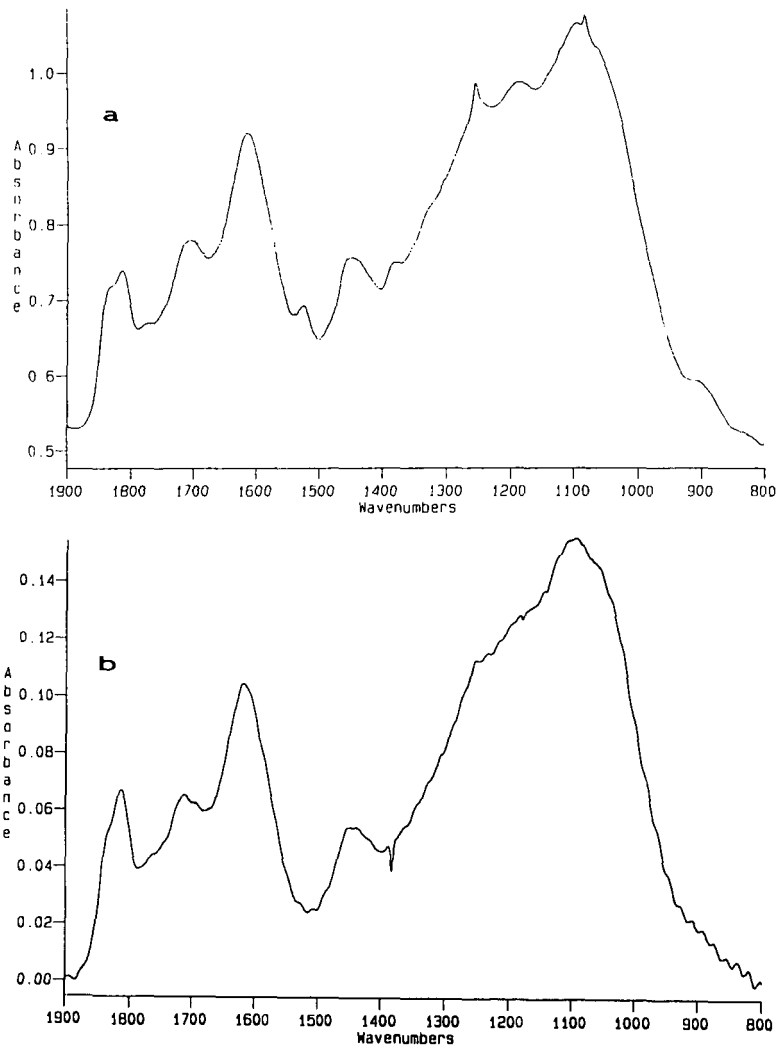

Figure 2. Infrared spectra (KBr pellet) of the products obtained from fluorination of North Dakota lignite with SF_4 (a) at 110° C for 15 h, (b) at 170° C for 18 h.

AUTOMATED ANALYTICAL SCANNING ELECTRON MICROSCOPY AND IMAGE ANALYSIS METHODS FOR CHARACTERIZING THE INORGANIC PHASES IN COAL AND COAL COMBUSTION PRODUCTS

K.C. Galbreath, D.W. Brekke, and B.C. Folkedahl
Energy and Environmental Research Center, University of North Dakota,
Box 8213, University Station, Grand Forks, North Dakota 58202

Keywords: scanning electron microscopy, digital image analysis, coal and coal ash

ABSTRACT

Particle-by-particle scanning electron microscopy (PBPSEM) and scanning electron microscopy point count (SEMPC) are being developed and applied for characterizing the inorganic phases in coal and coal combustion products. PBPSEM sizes, identifies, and quantifies coal mineral constituents and the degree of mineral-coal association. SEMPC determines the chemical composition and abundance of inorganic phases in coal ashes and deposits. Both methods are automated to minimize operator bias and to facilitate the acquisition of a statistically significant number of analyses to fully characterize heterogeneous samples.

INTRODUCTION

This paper describes two analysis methods: particle-by-particle scanning electron microscopy (PBPSEM) and scanning electron microscopy point count (SEMPC), being developed and applied at the Energy and Environmental Research Center (EERC) for characterizing the inorganic phases in coal, coal ashes, and deposits. Both methods employ an automated analytical scanning electron microscope (SEM) integrated with a digital image analysis system. This instrumentation is very useful for characterizing complex heterogeneous materials because it provides the capability to efficiently analyze a statistically significant number of individual microparticles for both compositional and morphological information.

In recent years, considerable attention has been focused on developing and applying image processing and analysis techniques for quantifying the association of mineral grains with the organic coal matrix (1-3). Most image processing and analysis systems provide algorithms for acquiring the required morphological data for such an analysis. These algorithms are based on the creation of binary images from an original gray-scale image. The binary transformation process requires operator intervention to select thresholds for segmenting the coal and mineral phases from the gray-scale image. Unfortunately, this process can be very time-consuming and involves subjective judgement by the operator to create binary images that accurately represent the original image. At the EERC, we have formulated an automatic threshold selection algorithm and incorporated it into an image analysis application program. The program completely automates image acquisition and processing, thus enhancing the objectivity of analysis results. The PBPSEM method integrates this automated image analysis capability with electron-probe microanalysis to measure various morphological and compositional parameters for individual mineral grains in coal. These data are compiled and classified according to

compositional criteria into various mineral/chemical categories using a modified version of the Particle Characterization (PARTCHAR) program (4). The program provides a complete statistical summary for all the mineral/chemical phases in a sample, including the proportion of each phase directly associated with coal.

The SEMPC method for chemically characterizing and classifying the crystalline and amorphous phases in coal ashes and deposits has been improved greatly since its initial development (5). The method involves performing quantitative electron-probe microanalysis on a statistically significant number of randomly selected points on a sample. The compositional analyses are compiled and then classified according to stoichiometric criteria into standard phase categories using a best-fit algorithm (6). Applications of the method are presented elsewhere (7, 8). Recent improvements discussed in this paper include an automation routine for randomly selecting discrete image areas and analysis points on the sample, the capability to store digital images with documented analysis locations, and a more efficient and comprehensive phase classification program.

DESCRIPTION OF THE PBPSEM METHOD

Sample Preparation and Instrumentation. Coals to be analyzed by PBPSEM are pulverized to a standard combustion grind (i.e., approximately 80% of the particles -200 mesh), mounted in carnauba wax (9), cross-sectioned, and polished using standard petrographic procedures. Samples are then sputter-coated with carbon to minimize electron-beam charging artifacts. A JEOL JSM-35 analytical SEM equipped with a NORAN Instruments (formally Tracor Northern, TN) Micro-Z ultrathin window x-ray detector, TN-5500 x-ray analyzer, TN-5600 stage automation system, TN-8500 image analyzer, and GW Electronics annular solid-state backscattered electron (BSE) detector is utilized for performing PBPSEM analyses.

Digital Image Acquisition, Processing, and Analysis. The automated analytical SEM, operating in the BSE imaging mode, is programmed to analyze preselected areas on the sample. The electron microbeam is rastered across the analysis areas to acquire a digital image at a spatial resolution of 512 pixels in both the line-scan (x-) and frame-scan (y-) directions. Frame averaging is employed to enhance image quality.

A modified version of NORAN Instruments Locked and Liberated image analysis program is used to locate particles and measure various morphological, phase correlation, and compositional parameters. Coal and mineral particles are delineated based on the atomic number contrast inherent in BSE imaging. An automatic threshold selection algorithm has been formulated to segment the coal and mineral phases from the gray-scale BSE image into separate binary images. The selection algorithm utilizes the image's gray-level histogram. Gray-level histograms of prepared coal samples are generally bimodal consisting of two peaks corresponding to the average brightness (i.e., mean atomic number) of mounting medium and coal, a valley that separates the peaks and represents the less heavily populated intermediate gray levels of coal particle edges, and an essentially featureless region corresponding to a large range in mineral gray level intensity as a result of compositional variation. In some coal samples, the mounting medium and coal peaks are poorly resolved, and the selection algorithm has difficulty in

locating the histogram valley separating the two peaks (Figure 1a). A median filter is applied to the image to create a more strongly bimodal histogram (Figure 1b). The filtered histogram facilitates the selection of thresholds by the method described in this section. The median filter was chosen because it suppresses digital image noise without significantly affecting particle edges or other image features (10). The automatic threshold selection algorithm searches for the mounting medium and coal peaks and then selects a threshold at the minimum intensity value in the histogram valley (Figure 1b). This method of threshold selection is referred to as the mode method or standard histogram method (11, 12). The threshold segments coal from the mounting medium. Another threshold is selected to segment the coal from minerals. The placement of this threshold involves a peak-modeling procedure to account for any asymmetry of the coal peak caused by the overlapping of coal and mineral gray levels. The procedure models the coal peak assuming a Gaussian distribution of gray levels and then establishes a threshold at the base of the modeled peak (Figure 1b). Thresholds are determined for each area of the sample analyzed. Automatic thresholding eliminates operator bias in the results and compensates for instrument drift.

After transforming the gray-scale image into coal and mineral phase binaries, the following morphological parameters are determined for each phase of a given particle using standard image analysis routines: minimum, maximum, and average cross-sectional diameter; area; and external perimeter. Two correlation parameters are also determined for each mineral phase: an indication of whether the mineral grain is included, attached, or excluded relative to the coal matrix; and the amount of mineral perimeter in contact with the coal or mounting medium. In addition to this morphological and phase correlation data, compositional information is obtained by acquiring an energy-dispersive x-ray (EDX) spectrum from each mineral grain's center. Spectral regions-of-interest (ROI) are defined to measure the characteristic x-ray emission intensities of twelve common, mineral-forming, major and minor elements (Na, Mg, Al, Si, P, S, Cl, K, Ca, Ti, Fe, and Ba). Relative intensities are calculated by dividing the net counts for each element by the total ROI counts for all elements. Morphological, phase correlation, and compositional data for approximately 3000 particles are collected at three magnifications to provide the spatial resolution necessary to analyze particles ranging widely in size. These data are transferred on-line to a personal computer where they are tabulated and stored to disk for subsequent reduction, report generation, and archival. The acquired BSE images with the locations of EDX analysis are stored to tape.

Data Reduction and Reporting. A modified version of the PARTCHAR data reduction program (4) classifies the mineral compositional analyses based on elemental relative intensities, relative-intensity ratios, and stoichiometric criteria into one of 33 mineral/chemical and mineral association categories. Analyses that do not conform to any of the specified criteria are termed unclassified. The program allocates the classified particles according to average diameter into six intervals so that the size distribution of mineral/chemical phases can be determined. A report is generated that summarizes the results in a series of tables containing information on the number, area, and proportions of mineral/chemical phases in their respective size intervals and according to their association with the coal matrix (i.e., included, attached, or excluded). Mineral weight percentages are calculated assuming that particle area is proportional to particle volume (13) and mineral densities are constants.

DESCRIPTION OF THE SEMPC METHOD

Sample Preparation and Instrumentation. Coal combustion products to be analyzed by SEMPC are mounted in epoxy resin, cross-sectioned, and polished; or dispersed ultrasonically and mounted on filter paper. Samples are sputter-coated with carbon prior to analysis. The SEMPC analysis is performed with a NORAN Instruments Automated Digital Electron Microscope (ADEM). The ADEM is a fully integrated analytical SEM and image analysis system equipped with a Z Max 30 diamond window EDX detector and LaB_6 gun. The ADEM has the capability to perform SEMPC analyses on multiple samples with unattended operation.

Digital Image Acquisition and Electron-Probe Microanalysis. The stage/electron-beam automation system is programmed to randomly select discrete locations on a representative area of the sample for digital imaging and quantitative electron-probe microanalysis. Specifically, the analyst specifies a rectangular analysis area on the sample. The number of analysis frames available in this area is calculated based on the magnification employed. An analysis frame is randomly selected, and a digital image is acquired. Brightness, contrast, and focusing adjustments are performed automatically by the instrument for each frame analyzed. A location grid is established on the image, and the electron beam is sent to an address on the grid to acquire an EDX spectrum for eight seconds. The x-ray count rate is monitored during the 8-second acquisition to exclude points that emit insufficient x-ray counts for complete chemical characterization. The count rate must exceed a predefined threshold value, typically 1000 counts/second, for the analysis to be accepted. If the count rate is less than the threshold value, the beam is moved to another location. However, if the point is acceptable, the acquisition continues for an additional 17 seconds. The spectrum is then transferred to another memory location for processing, while the next point is selected and analyzed. Elemental peaks are deconvoluted, and their net intensities are extracted from the spectrum using the filter-fit method (14). The x-ray intensity data are corrected for matrix effects, and concentrations are calculated using the ZAF correction procedure. Mineral standards are used to calibrate the procedure. A maximum of 18 elements may be included in the analysis. Quantitative analyses for typically 250 points per sample are collected and transferred on-line to a personal computer for reduction and archival purposes. The acquired digital images with documented analysis locations can be archived for additional analysis.

Data Reduction and Reporting. An off-line program classifies each compositional analysis according to stoichiometric criteria into one of 56 standard phase categories using a best-fit algorithm (6). The program has the option to incorporate a maximum of 10 additional user-defined phase categories in the classification scheme. Analyses that do not conform to any of the specified criteria are termed unclassified. The program calculates the abundance of each phase in frequency percent and a normalized cumulative bulk composition for the sample on a weight percent oxide basis.

SEMPC analysis results, when combined with crystalline phase identifications obtained by x-ray powder diffraction (XRD), can be used to infer a composition for the vitreous (i.e., liquid) phase of a deposit. This inferred liquid phase composition can be used as input for a subroutine of the program to calculate base-acid ratio and viscosity (15).

Liquid phase chemistry and viscosity is important for understanding deposit strength and development (7).

Quality Control. Bulk analysis techniques are utilized to validate SEMPC analysis results. The SEMPC calculated bulk composition is compared to the bulk composition determined directly by EDX fluorescence analysis to assess whether the SEMPC analysis is strictly representative of the sample. In addition, XRD crystalline phase identifications are referred to for confirmation of SEMPC phase identifications. Comparisons of SEMPC analysis results to mineralogical and chemical data obtained by bulk analysis techniques are presented elsewhere (5).

DISCUSSION

Development of the PBPSEM method is in its infancy, and several refinements are required before it can be used routinely for characterizing coal mineralogy. The automatic threshold selection algorithm requires a bimodal gray-level histogram for segmenting the coal particles from the mounting medium. This requirement is violated when the area imaged on a sample consists of only coal or mounting medium. Currently, the analysis is performed at low magnifications, generally less than 500, to prevent such an occurrence. This practice, however, results in rather poor spatial resolution, thereby limiting the method to analyzing relatively large particles, generally greater than about three microns in average cross-sectional diameter. Other methods for automatic threshold selection are being investigated to negate this particle-size restriction. Another limitation of the method is the inability to distinguish and quantify mineral-mineral associations for agglomerated particles. This information is extremely important when considering inorganic transformations that occur during combustion. Additional development of the data reduction program is needed to present quantitative mineral-coal association results in formats appropriate for various applications, such as in the field of physical coal cleaning or ash modeling. Work also needs to be done to optimize and validate the method.

In contrast to the PBPSEM method, the SEMPC method is in a mature stage of development. Efforts are primarily focused on developing automated image analysis methods for utilizing the stored digital images to relate the morphology in the vicinity of an analysis point to chemical composition. Porosity and the recognition and quantification of neck-growth development between particles are measurements being investigated for assessing deposit strength.

CONCLUSION

The PBPSEM and SEMPC analysis methods have been developed to provide detailed morphological and compositional information on the inorganic phases in coal and coal combustion products. Developmental efforts are in progress to optimize the methods and assess their performance characteristics (i.e., limitations, repeatability, and reproducibility). Work will also continue to extract and quantify the wealth of information provided by these methods for various applications.

ACKNOWLEDGEMENT

This work was supported by the U.S. Department of Energy under Cooperative Agreement No. DE-FC21-86MC10637. The authors are grateful to the Contracting Officer's Representative, Mr. Philip M. Goldberg, for permission to publish.

REFERENCES

1. Huffman, G.P.; Shah, N.; Huggins, F.E.; Casuccio, G.S.; Mershon, W.J. "Development of Computer-Controlled Scanning Electron Microscopy (CCSEM) Techniques for Determining Mineral-Maceral Association," *ACS Fuel Chem. Division Preprints* **1991**, *36* (3), 1155-1163.

2. Straszheim, W.E.; Markuszewski, R. "Automated Image Analysis of Minerals and Their Association with Organic Components in Bituminous Coals," *Energy & Fuels* **1990**, *4* (6), 748-754.

3. Straszheim, W.E.; Markuszewski, R. "Automated Image Analysis of the Association of Ash-Forming Mineral Matter with Coal Particles," *ACS Fuel Chem. Division Preprints* **1991**, *36* (1), 216-222.

4. Zygarlicke, C.J.; Steadman, E.N. "Advanced SEM Techniques to Characterize Coal Minerals," *Scanning Microscopy* **1990**, *4* (3), 579-590.

5. Kalmanovitch, D.P.; Montgomery, G.C.; Steadman, E.N. "Computer-Controlled Scanning Electron Microscope Characterization of Coal Ash Deposits," *ASME Paper* 87-JPGC-FACT-4, 1987.

6. Folkedahl, B.C.; Brekke, D.W.; Steadman, E.N. "Advanced SEM Techniques for Determining Mineralogy of Coal Combustion Products," *Scanning Microscopy*, in press.

7. Steadman, E.N.; Benson, S.A.; Zygarlicke, C.J.; Brekke, D.W. "Characterization of Liquid Phase Components in Coal Ashes and Deposits," *In proceedings of the Seventh Annual International Pittsburgh Coal Conference*; 1990, pp 43-51.

8. Jones, M.L.; Kalmanovitch, D.P.; Steadman, E.N.; Zygarlicke, C.J.; Benson, S.A. Application of SEM Techniques to the Characterization of Coal and Coal Ash Products," *Advances in Coal Spectroscopy*; Meuzelaar, M.L.C., Ed.; Plenum Publishing Corp.: New York, 1992, Chapt. 1, pp. 1-27.

9. Straszheim, W.E.; Younkin, K.A.; Greer, R.T.; Markuszewski, R. "Mounting Materials for SEM-Based Automated Image Analysis of Coals," *Scanning Microscopy*, **1988**, *2* (3), 1257-1264.

10. Twogood, R.E.; Sommer, F.G. "Digital Image Processing," *IEEE Transactions on Nuclear Science* **1982**, *NS-29* (3), 1076-1086.

11. Weszka, J.S. "A Survey of Threshold Selection Techniques," *Computer Graphics and Image Processing* **1978**, *7*, 259-265.

12. Kohler, R. "A Segmentation System Based on Thresholding," *Computer Graphics and Image Processing* **1981**, *15*, 319-338.

13. DeHoff, R.T.; Rhines, F.N. *Quantitative Microscopy*; Materials Science and Engineering Series, McGraw Hill Book Company, 1968.

14. McCarthy, J.J.; Schamber, F.H. "Least-Squares Fit with Digital Filter: A Status Report," *National Bureau of Standards Special Publication 604*, 1981, pp. 273-296.

15. Kalmanovitch, D.P.; Frank, M. "An Effective Model of Viscosity for Ash Deposition Phenomena," Conference on Mineral Matter and Ash Deposition from Coal, The Engineering Foundation, Santa Barbara, CA, Feb. 21-26, 1988.

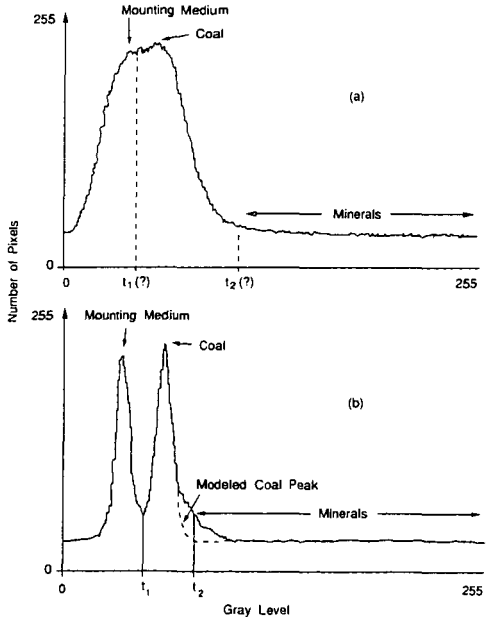

Figure 1. Grey-level histograms, (a) original histogram, the selection of thresholds segmenting mounting medium from coal (t_1) and coal from minerals (t_2) is arbitrary; (b) median filtered histogram (5 x 5 filter), mounting medium and coal peaks are resolved, thus facilitating automatic threshold selection by the method described in the text.

COAL SURFACE THERMODYNAMICS BY INVERSE GAS CHROMATOGRAPHY*

A. S. Glass and J. W. Larsen
Department of Chemistry
Lehigh University
Bethlehem, PA 18015

(Keywords: coal surfaces, surface thermodyamics, inverse gas chromatography)

Introduction

Determination of coal surface interactions is important for the development of improved coal liquefaction and beneficiation methods. Knowledge of interactions at coal interfaces will aid the development of such technologically important coal reactions.

Although coals possess pores, they probably do not possess interconnected internal surfaces[1,2]. Coals have the properties of absorbents, including an external surface and the ability to absorb molecules in the bulk. A technique that determines coal surface interactions must be sensitive to interactions at the external coal surface.

Many techniques are available for studying interactions at surfaces, but most are not suitable for measuring interaction thermodynamics of complex coal surfaces. Static adsorption and calorimetric techniques measure coal-solute interactions, but they are plagued by diffusion of the solute into the coal[3-5]. In contrast, inverse gas chromatography (IGC) is a dynamic sorption technique. Only those interactions that occur during the time of travel of the solute contribute to the signal in IGC. Therefore, IGC is sensitive to coal-solute interactions that occur in the rapid uptake regime rather than those that occur during the slow approach to equilibrium that characterizes static sorption measurements of coals.

Theory

IGC is most straightforward in the regime of linear chromatography. In this regime, also called the "Henry's Law" or "infinite dilution" regime, the retention volume is most characteristic of the interaction between the solute and the stationary phase. For a single type of retention mechanism, i.e., surface adsorption, the Henry's Law constant, K_s, expresses the equilibrium thermodynamic interaction between the adsorbate and the stationary phase. K_s is the retention volume per accessible surface area of the stationary phase and per unit pressure of adsorbate in the gas phase[6]:

$$K_s = \frac{V_N}{SRT} = \frac{V_s}{RT} \qquad (1)$$

where V_N is the net retention volume, S is the surface area of the stationary phase that is accessible to the solute, R is the gas constant, T is the column temperature, and V_s is the specific

retention volume.

The dependence of retention volume on surface area has been used to determine S for stationary phases. If V_s is determined for a given probe molecule on a stationary phase of known S, then S can be calculated for a column of unknown S from[6]:

$$S=\frac{V_N}{V_g} \tag{2}$$

For polymers below T_g where adsorption occurs on the external geometrical surface, it has been shown that S is equivalent to the external geometrical surface, S_{geom}[7]. For spherical particles of radius r and particle density ρ, S_{geom} is given by[8]

$$S_{geom}=\frac{3}{\rho r} \tag{3}$$

Since K_s is the equilibrium constant for surface adsorption, then

$$K_g=K_{s,o}e^{\frac{q_{st}}{RT}} \tag{4}$$

where q_{st} is the isosteric heat of adsorption. Substituting equation 1 and converting to natural logarithms gives

$$\ln(V_N/T)=\frac{q_{st}}{RT}+\ln K_{s,o}+\ln SR \tag{5}$$

The slope of a plot of $\ln(V_N/T)$ vs. 1/T gives q_{st}. The adsorption entropy, $\Delta S°$, may be determined from[9,10]

$$\Delta S^{\circ}=\frac{-q_{st}}{T}+31.61+R\ln V_g \tag{6}$$

Experimental

Experiments were conducted by injecting gas samples at pressures of 0.01 to 10.0 Torr from a glass manifold via an 8-port Valco GC valve with 0.015 and 0.100 ml sample loops. Pressures were measured with a 1 Torr Baratron gauge (MKS Instruments, Inc.) or a mercury manometer attached to the sample reservoir.

Gases were 99% purity or better. Liquids obtained from Aldrich in "sure-seal" bottles were subjected to at least three freeze-pump-thaw cycles before being introduced as gases at pressures below their vapor pressures.

Argon premium Illinois No. 6 coal was sieved to give the desired fraction (80/100, 60/70, or 40/60 mesh) and about 4g was packed into a 1/8 inch O.D., 2.1mm I.D. ss column about 1.5m in length. The particle density was 1.3 g/ml[11]. The coal was degassed overnight at 150°C before each day's experiments. The

GC was a Hewlett-Packard 5890A equipped with both TCD and FID detectors. 0.03 inch I.D. ss tubing was used between the GC valve and the column inlet to minimize dead volume.

Data were collected over the range 30 to 150°C, with injector and detector temperatures at 180°C. The temperature of the chromatograph oven was accurate to ±0.1°C and was constant to within 0.2°C over different parts of the oven. Flow rates ranged from 5 to 35 ml/min. They were determined using a bubble meter and were corrected for the effect of water vapor. The pressure drop was determined using a pressure transducer (Omega Engineering, Inc.) on the column inlet and a barometer for measuring atmospheric pressure. Typical pressure drops were about 1 atm. Retention volumes were corrected using the pressure drop correction term, j[12].

Column dead volumes were determined from geometrical considerations for the different mesh fraction particle sizes and checked using columns of the same length and diameter packed with the same mesh fraction of nonporous glass beads. Retention times for various solutes on the glass bead columns were characteristic of the dead volume.

Data were collected using Lab Calc software (Galactic Industries Corp.) at rates of one point per second. Retention times were determined as first moments of the peaks using Simpson's rule. Adsorption entropies were calculated using de Boer's approach[9], assuming a standard gaseous state with a pressure of $1.01*10^6$ dyne/cm^2 and a standard adsorbed state with a pressure of 0.338 dyne/cm.

Results and Discussion

I. Technique

With injection sizes greater than about 10^{-4} μmole of adsorbate, peak tailing increased greatly. With injection sizes below this saturation limit, peak shapes and retention times were independent of injection size. This behavior resembles that seen with column overload[13]. Assuming close packing of adsorbates on the coal surface, the injection sizes corresponding to the onset of column saturation gave specific surface areas of about 0.02 m^2/g, similar to the geometrical surface area of coal in the column. This indicates that the accessible surface of coal in the column was equal to the external surface of the coal. All thermodynamic data were obtained using injection sizes below the saturation limit.

Table I shows accessible and geometrical surface areas calculated using equations 2 and 3 for columns containing different particle sizes of coal using three different adsorbates. From the table it is seen that the agreement between S and S_{geom} for methane and n-butane is good. The agreement for neopentane is worse and this will be discussed in the next section. These results show that the accessible surface is equal to the external surface of the coal, and provide further support for the idea that coal behaves as an absorbent in IGC.

The surface areas in Table I, when corrected for the amount

of coal in the column, give specific surface areas on the order of 0.05 m^2/g. Assuming coal particle sizes of 25μm, typical of those used in static sorption experiments, gives an external geometrical specific surface area of 0.10 m^2/g. This value is smaller than specific surface areas determined by static sorption by at least 1 to 2 orders of magnitude[1,4]. This provides evidence that static sorption determines a "coal surface area" which contains a contribution from absorption. In contrast, IGC measures a coal surface area that is due to surface adsorption only.

II. Thermodynamics

Figure 1 is a plot of q_{st} vs. polarizability, α, for linear alkanes, neopentane, and cyclopropane on Illinois No. 6 coal determined by IGC. In plot 1A, it is seen that the strength of interaction with the coal surface increases linearly with the polarizability of the adsorbate. The increase in q_{st} from methane to ethane is 3.2 kcal/mol, while that between ethane and propane is 2.8 kcal/mol. Between propane and n-hexane, the increase in q_{st} per CH_2 group of the adsorbate levels off to a constant value of about 2.1 kcal/mol. On carbon surfaces, the increase in q_{st} per CH_2 group of the adsorbate varies between about 1.0 and 3.0 kcal/mol, depending on the history of the carbon[10,14]. Our values for Illinois No. 6 coal are higher than for graphitized carbon black surfaces and fall within the range for non-graphitized and oxidized surfaces.

While the adsorption enthalpies for the linear alkanes scale with polarizability, neopentane does not fall on the line. The effect of increased branching of the adsorbate on retention is well known for graphitized carbon surfaces[15]. This effect is probably responsible for the relatively low adsorption enthalpy of neopentane on Illinois No. 6 coal. In this context, it is interesting to reconsider the data in Table I. The data for neopentane show larger errors than those for methane and n-butane. This is probably due to the smaller coal surface area accessed by neopentane.

Plot 1B corresponds to adsorption heats on Illinois No. 6 coal extracted with tetrahydrofuran. The linear hydrocarbons show the linear relation between q_{st} and α, while neopentane falls slightly below the line. The decrease in the values of q_{st} for Plot 1B compared to 1A are greatest at high values of α, corresponding to the larger hydrocarbons. This indicates a decrease in carbon atom density as a result of extraction. For polyethylene glycol vs. carbon black, a decrease in the slope of a plot of q_{st} vs. carbon number was ascribed to a decrease in the energy of nonspecific interaction due to a decrease in the density of carbon atoms at the surface[16].

Figure 2 is a plot of q_{st} vs. $\Delta S°$ for linear hydrocarbons and neopentane on both the extracted and original Illinois No. 6 coal. The linear relationship is an example of the well-known isokinetic effect[17]. The fact that the isokinetic effect holds supports the existence of a common surface adsorption interaction of these molecules with the coal.

Conclusion

Thermodynamic data for adsorption at the external surface of Illinois No. 6 coal have been determined by IGC. The behavior of Illinois No. 6 coal in these experiments fits with the view that coals are crosslinked macromolecular networks capable of taking up molecules into their bulk[18,19]. This supports the position that coals do not contain interconnected pore networks[1,2].

The surface thermodynamic data are reasonable as they fall within the limits of those for non-graphitized carbon surfaces. The determination of surface thermodynamics for various coals and modified coals by IGC will enable the creation of a coal surface interaction database. This will aid the development of improved coal reaction strategies.

References

1. Larsen, J. W.; Wernett, P. C. Energy Fuels **1988**, 2, 719.
2. Larsen, J. W.; Wernett, P. C. Prepr. Pap.-Am. Chem. Soc., Div. Fuel Chem. **1992**, 37, 849.
3. Hsieh, S. T.; Duda, J. L. Fuel **1987**, 66, 170
4. Marsh, H. Fuel **1965**, 44, 253.
5. Fowkes, F. M.; Jones, K. L.; Li., G.; Lloyd, T. B. Energy Fuels **1989**, 3, 97.
6. Kiselev, A. V.; Yashin, I. Gas-Adsorption Chromatography; Plenum: New York, 1969; p. 121.
7. Braun, J.-M.; Guillet, J. E. Macromolecules **1975**, 8, 882.
8. Lowell, S. Introduction to Powder Surface Area; Wiley & Sons: New York, 1979; p. 5.
9. de Boer, J. H. The Dynamical Character of Adsorption; Oxford University: London, 1953; Chapter 6.
10. Crescenti, G.; Mangani, F.; Mastrogiacomo, A. R.; Palma, P.; J. Chromatogr. **1987**, 392, 83.
11. Van Krevelen, D. W. Coal; Elsevier: New York, 1961; p. 128.
12. Littlewood, A. B. Gas Chromatography, 2nd ed.; Academic: New York, 1970; p. 30.
13. Ruthven, D. M. Principles of Adsorption and Adsorption Processes; Wiley & Sons: New York, 1984; p. 226-227.
14. Elkington, P. A.; Curthoys, G. J. Phys. Chem. **1969**, 73, 2321.
15. Littlewood, A. B. Gas Chromatography; Academic: New York, 1970; p. 102ff.
16. Kiselev, A. V.; Yashin, I. Gas-Adsorption Chromatography; Plenum: New York, 1969; pp. 56-58.
17. Isaacs, N. S. Physical Organic Chemistry; Wiley & Sons: New York, 1987; pp. 102-103.
18. Van Krevelen, D. W. Coal; Elsevier: New York, 1961; pp. 127ff.
19. Larsen, J. W. In New Trends in Coal Science, NATO ASI Ser. vol 244; Yürüm, Y., Ed.; Kluwer Academic: Netherlands, 1988; p. 73.

*A full paper on this topic has been submitted to The Journal of Physical Chemistry.

Table I. Geometrical and Accessible Surface Areas for Columns Containing 4 grams of Illinois No. 6 Coal of Different Particle Sizes.

Column	1	2	3
Mesh Fraction	80/100	60/70	40/60
r (μm)†	82.5	115.5	169.0
S_{geom} (m^2)*	0.110	0.080	0.055
S^a (m^2)‡	--	0.091	0.061
S^b (m^2)‡	--	0.150	0.038
S^c (m^2)‡	--	0.078	0.051
Diff S^a-S_{geom}, %	--	13.8	10.9
Diff S^b-S_{geom}, %	--	87.5	-32.7
Diff S^c-S_{geom}, %	--	-1.25	-7.27

†particle radius for the average particle size of the given mesh fraction.

*Calculated from equation 3 assuming spherical particles.

‡Determined using equation 2 by setting the accessible surface area of column 1 to its geometrical surface area.

[a]CH_4 from data at 90°C; [b]neo-C_5H_{12} from data at 115°C; [c]$\underline{n}$-C_4H_{10} from data at 120°C.

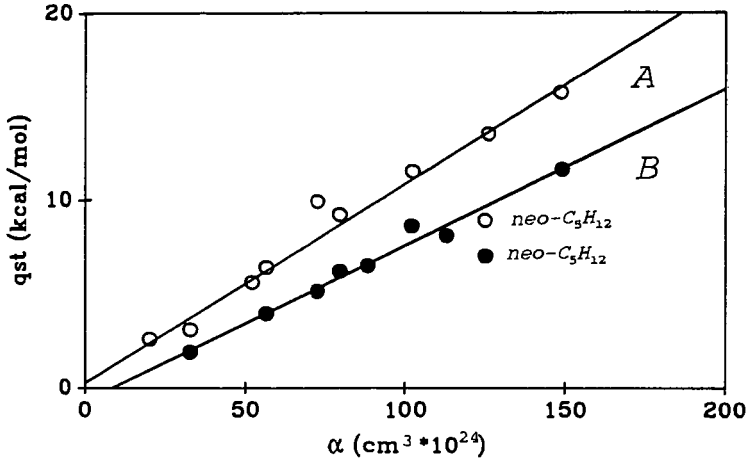

Figure 1. Heats of adsorption vs. polarizability for hydrocarbons on Illinois No. 6 coal. A, Original coal, o. B, Coal extracted with tetrahydrofuran, •.

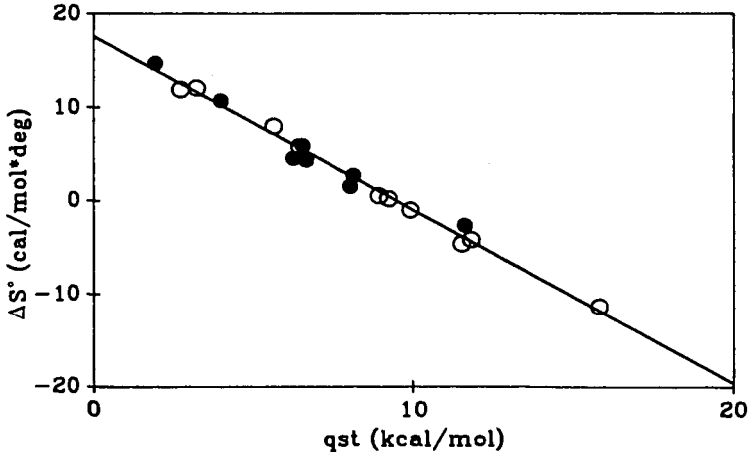

Figure 2. Heats of adsorption vs. entropies of adsorption for hydrocarbons on original and THF-extracted Illinois No. 6 coal. o, Original Coal; •, THF-extracted Coal.

Oxidation-Induced Structural Changes in Argonne Coals Studied by Differential Scanning Calorimetry and Solvent Swelling

Yongseung Yun and Eric M. Suuberg
Division of Engineering, Brown University
Providence, RI 02912

Key Words: Oxidation, Differential Scanning Calorimetry, Solvent swelling, Argonne coals

INTRODUCTION

It is widely known that oxidation/weathering has a profound effect on many important coal properties such as coking characteristics, slurry pH, flotability, tar yield, extractability, etc., as well as on coal utilization processes such as combustion, pyrolysis, gasification and liquefaction [1-5]. In addition, there have been many reports as to the high sensitivity of coal structure to aerial oxidation, especially in steam-pretreated coal. For example, Graff and Brandes [6] reported the decrease of liquid yield from 61% to 25% after exposing steam-treated Illinois No. 6 coal to air at room temperature for just two minutes. Because of these reports that have established the extreme vulnerability of coal structure to air, even at room temperature, major accommodations, to prevent air contact, have ensued in many studies on coal. The basic question here is how air causes change in coal structure, even at room temperature in such a short time (minutes). At higher temperatures, e.g., at temperatures which can cause the thermal degradation of coal structure, the sensitivity of the response of oxidized coal to heat or solvents has been well established, and can be easily understood, since even small amounts of oxidized functional groups might act as initiators of chain processes that can magnify the total response.

This paper is concerned with the effect of aerial oxidation on the solvent swelling ratio of several pretreated coal samples (i.e., water-treated, heat-treated). Our former studies [7,8] have clearly illustrated that heating under an inert environment renders coal structure relaxed in such a way that solvent and/or catalysts for liquefaction can be efficiently employed or incorporated into coal structure. The question that we pose here is whether the effects of oxidation make themselves known at low temperatures, in terms of changes in macromolecular structure, that might mitigate some pretreatment effects.

EXPERIMENTAL

Aliquots of three coal samples, obtained from the Argonne National Laboratory - Premium Coal Sample Program, were analyzed by differential scanning calorimetry (DSC) and solvent swelling techniques. These samples included Upper Freeport (-100 mesh), Pittsburgh No. 8 (-100 mesh), and Illinois No. 6 (-20 mesh) coals. Detailed petrographic, chemical, and physical analysis data on these coals can be found elsewhere [9]. Detailed experimental procedures for DSC and solvent swelling can be also found elsewhere [8,10]. One point should be carefully noted with respect to the latter measurements, the supernatant swelling solvent was replaced every day. This is important, because the coal is effectively solvent extracted by this procedure. Aerial oxidation was performed in two ways. One method involved oxidizing the coal sample in a tube furnace at 115°C or 120°C for one day under room air. Another method involved oxidizing the sample inside the DSC at 120°C for 15 hr with dry air flow of 100 ml/min over the aluminum pan containing the coal sample.

RESULTS AND DISCUSSION

First, we examined the effect of aerial oxidation on solvent swellability by comparing as-received and oxidized coals (this can give us some hint as to changes of structure). For this purpose, Upper Freeport medium volatile bituminous coal was oxidized at 120°C in the tube furnace for one day, under room air, and the resulting oxidized coal as well as as-received coal were heat-

treated inside the DSC under the continuous flow of nitrogen up to the specified temperature, followed by quench-cooling and pyridine swelling. The results are illustrated in Figure 1 in which pyridine swellability is shown as a function of heat-treatment temperature. In Figure 1, it is noteworthy that the aerial oxidation rendered the final pyridine swelling values higher than the corresponding values in as-received coal. Probably the newly formed oxygenated functional groups on the surface of coal provided additional capacity to hold pyridine molecules because of increased polarity of the coal surface. Thus, it is safe to say that aerial oxidation seems to have a significant impact on pyridine swellability, at least, in Upper Freeport coal.

The oxidation results in a considerable increase in swellability prior to thermal relaxation of the coal's structure (below 250°C). One would have to surmise that the thermodynamically favorable mixing of the new oxygen functional groups and pyridine overwhelms some of the thermally labile non-covalent interactions (though many are preserved). The vary slow nature of the swelling in this low temperature regime favors this explanation over one based upon the oxidation itself destroying some of the interactions.

Once the thermally labile interactions are destroyed by heating the coal to over 300°C, the time dependence of swelling apparently shifts (higher swelling is seen in shorter times). This is because the coal becomes quite extractable after thermal relaxation as compared to before, and the decrease in swellability with time is an artifact due to extraction of some of the coal. Temperatures above 350°C have not been explored in the case of the oxidized coal because the extraction already starts to become quite significant in the sample obtained at 350°C.

The main concern of this paper is with what kind of sensitivity an already relaxed coal structure (normally achieved here by heat treatment) might have upon exposure to air. Two coals, i.e., Upper Freeport and Pittsburgh No. 8 coals, were heat-treated and followed by aerial oxidation in this case inside the DSC at 120°C for 15 hr with air flowrate of 100 ml/min. Note that in this case heat treatment precedes oxidation, the opposite of the situation in the experiments of Figure 1. The temperature of heat treatment was selected based upon the difference DSC results reported in our earlier studies [7,8,10]. The differences in sensitivity to aerial oxidation were measured by pyridine swellability and the results are shown in Figure 2.

Figure 2 reveals several interesting results. While heat-treated-plus-oxidized Upper Freeport coal exhibits higher pyridine swellability compared to heat-treated-only coal (which agrees with the data of Figure 1), the opposite case was observed in Pittsburgh No. 8 coal. It appears that in the case of the Upper Freeport coal initial values of swelling ratio are more or less identical regardless of oxidation. However, appreciable differences in pyridine swelling ratios start to appear with further swelling time. The decrease of the pyridine swelling ratio with time is believed to be caused by extraction as noted earlier. In this case, note that the increase in swellability with oxidation of the Upper Freeport coal is modest at short swelling times. This makes sense, in that the structure is fully relaxed already by heat treatment, and the addition of oxygen functional groups does not provide pyridine an extra "handle" for relaxing the structure, as it does in non-heated coals. The actual short-time swelling ratio is quite similar to what it was for heat treated, non-oxidized coal itself (around 2.22 at 350°C from Figure 1, compared to 2.25 for non-oxidized coal in Figure 2 and 2.29 for oxidized coal in Figure 2).

Since the decrease in apparent swellability with time is attributed to extraction of the coal, it appears that the unoxidized coal is more extractable. While measurements need to be performed to establish quantitatively the relative extents of extraction, at present, we believe that this is the most likely explanation for the observed behavior. Because both the oxidized and non-oxidized Upper Freeport samples swell equally readily to their comparable maximum values, the later differences in extractability appear to indicate that oxidative crosslinking occurred in the oxidized sample. Thus we see evidence of a deleterious effect of 120°C aerial oxidation on the macromolecular structure of this coal, as regards any attempt to break down that structure or solubilize it.

In the case of the Pittsburgh No. 8 sample, oxidation is seen to be immediately deleterious. The Pittsburgh coal has a significant concentration of polar functional groups already, so it does not benefit from added oxygen providing more strong interaction sites for swelling. Evidence of oxidative crosslinking is visible in the first data points for swelling in pyridine. From that point on, the two curves for oxidized and non-oxidized Pittsburgh No. 8 samples, track each other closely, meaning that comparable amounts of extractable are lost from both samples. The effect

is not as large as in the Upper Freeport coal. This means that the incremental effect of aerial oxidation is not nearly as significant in the Pittsburgh No. 8 coal as in the Upper Freeport coal.

Figure 3 shows the effect of aerial oxidation on the DSC signatures of Upper Freeport coal. First, the coal was heat-treated inside DSC up to 350°C and the water evaporation process around 110°C as well as structural relaxation process around 310-350°C are both clearly visible (see thick-solid line (1) in Figure 3). Then the heat-treated coal sample was exposed to an air flow of 100 ml/min inside DSC for 12 hr at 120°C, followed by another two consecutive DSC scans up to 350°C (the first and second scans shown as a solid line (2) and a dotted line (3), respectively, in Figure 3). A clear exotherm, extending from 150-230°C with maximum at around 195°C, can be seen in (2). There was an earlier report [11] of observed an exotherm around 195°C in Upper Freeport coal following long exposure to air. The difference DSC (shown as solid line (4) in Figure 3) illustrates concisely the effect of aerial oxidation on coal structure, which results in an exotherm centered at around 195°C.

It has already been established in connection with the data of Figure 2 that oxidation at 120°C probably causes chemical reactions in the structure. The existence of this exothermic peak centered at 195°C suggests that a different set of processes is involved in that exotherm. Consequently, the search for oxidation effects by DSC can be misleading, if it implies that the peak at 195°C represents the beginning of oxygen functional group chemistry.

Figure 4 shows the effect of aerial oxidation on heat-treated Pittsburgh No. 8 coal. The coal's structure was relaxed by heat treatment, as is evident in the upper panel of Figure 4 from the fast swelling time for the heat-treated coal compared to as-received coal. Both the tetrahydrofuran (THF) and pyridine swelling ratios are higher for heat treated coal than for as-received coals. No appreciable differences can be noted between THF swelling responses from 5 hr and 15 hr oxidized samples, indicating that, after 5 hr of oxidation, further exposure to air does not cause any significant changes in the structure of Pittsburgh No. 8 coal.

We find it curious that in contrast to the results in pyridine, the swellability in THF is not strongly influenced by whether the sample is oxidized or not. Consistent with THF being a poorer solvent for this coal (note the lower swelling ratio compared to pyridine), the THF shows much less evidence of extraction. The visual appearance of the THF solvent also suggests a much lesser amount of extract compared to pyridine. So it appears that with a "weaker" solvent, oxidation effects are not as notable. This could be because the swellability of the coal structure is not linear in numbers of crosslinks; THF is unable to dissociate some non-covalent crosslinks that pyridine can, and existence of a few more covalent crosslinks makes little difference in swelling.

Pyridine swellability after heat-treatment exhibits quite different characteristics. The swelling time required to reach the maximum swelling ratio in pyridine is comparable to that for THF swelling after heat treatment. Before heat treatment, the pyridine is taken up much more quickly by the coal. This is again understood in terms of the pyridine's ability to dissociate some non-covalent crosslinks that THF cannot. A possibility is that there are strong acid-base interactions that pyridine, a strong base, can participate in, whereas THF cannot. Following oxidation, the same pattern of extraction is displayed in the data of Figure 4 as was shown in Figure 2, and the differences compared with THF, are large.

The mass gain upon oxidation was determined for the sample shown in the lower panel of Figure 4. The oxygen uptake (assuming no loss of any material during oxidation) was 1.83 wt%. This corresponds to an addition of 1.1×10^{-3} mol O/g coal, or using a density of 1.3 g/cc for this coal, the oxygen uptake was 1.4×10^{-3} mol O/cc. To help put this figure in perspective, the uptake of pyridine by the coal is initially about 18.8×10^{-3} mol pyridine/cc. Thus there is not a major addition of potential pyridine-holding groups to the coal. The actual loss of pyridine capacity as a result of oxidation is about 0.9×10^{-3} mol pyridine/cc, based on the earliest swelling points. The comparability of the equivalents of oxygen uptake and the loss of pyridine capacity is intriguing, but we cannot ascribe any significance to the comparability of these values at this time.

The DSC results on oxidized Illinois No.6 and Pittsburgh No.8 coals are shown in Figure 5. The difference DSC spectra clearly illustrate the exotherm around 200°C caused by added

oxygen. It should be pointed out that the temperature range of the exothermic peaks is remarkably similar to that observed in the Upper Freeport medium volatile coal (see Figure 3). These observations might suggest that aerial oxidation is actually concerned with certain specific components irrespective of coal rank (and pretreatment conditions).

In order to confirm the reportedly high sensitivity of Illinois No. 6 coal to air exposure after steam treatment [6], four sets of Illinois No. 6 coal samples were prepared and compared in terms of solvent swellability. Treatment was performed in water in a sealed bomb under a self generated pressure of 1000 psig for about one hour and then the sample was cooled to room temperature, so that the resulting sample remained submerged in water. Thus it is fair to call the treatment process as "water-treatment" instead of steam treatment. From the steam pressure, the temperature is known to be 285°C. The water was removed by drying under vacuum at room temperature for about three days. The tube-furnace was employed for quick oxidation experiments. As-received and water-treated coal samples were oxidized under room air for one day at 115°C. Figure 6 is the result on four sets of samples, in which dotted lines denote oxidized samples.

When the four sets of samples were compared as to solvent swellability in pyridine, no significant difference in pyridine swellability was caused by oxidation during the course of one day at 115°C. If there were any changes due to oxidation, they involved rather slight increases in equilibrium pyridine swelling ratio. The water treatment appears to have no significant effect on the pyridine swelling ratio, either with or without oxidation. We have no explanation for the curiously slower initial pyridine swelling that the oxidized coals experience. The fact that this feature is, however, unaffected by water treatment again supports the notion that not very much is changed in the structure by the treatment. The temperature of the treatment was below the range normally thought to be needed to see significant benefit [6] and is at the very beginning of what we believe to be a pre-pyrolytic structural relaxation in this coal. Thus, the lack of effect was not surprising.

What was, then, surprising was the significant effect of water treatment on THF swellability. First, water treatment decreases THF swellability. The lack of a corresponding decrease in pyridine swellability strongly suggests that covalent crosslinking is not involved. Water pretreatment in this temperature range appears to be promoting the formation of stronger, new non-covalent interactions. It is unclear from these data alone whether this involves formation of new intracoal bonding interactions, because the coal can rearrange structurally, or whether this involves addition of new oxygen functional groups, which contribute new interactions. Whatever the mechanism is, the oxidation promotes even more such non-covalent bonding interactions that THF is unable to dissociate.

The results of Figure 6 are replotted in a more concise form, with respect to each treatment, in Figure 7. After one day of swelling, pyridine swelling ratio reaches relatively similar values regardless of treatment, while THF swelling ratios indicate that oxidation was an important factor in reducing swelling.

The DSC results of Figure 8 show the effect of oxidation on the samples whose behavior was illustrated in Figures 6 and 7. As before with the Pittsburgh No. 8 and Upper Freeport coals, oxidation gives rise to an exothermic peak centered near 200°C. Unlike the situation in the earlier described coals, the peak does not have a well-defined upper temperature limit, in the case of Illinois No. 6 coal. This apparent peak "tailing" is independent of the fact that the coal experienced a temperature of 285°C during water treatment (thus the 200°C peak is caused by treatment), and is the same in both water treated and untreated coals. Thus the conclusion must be that the exotherm "tail" is a result of oxidation of this coal's structure in a manner different than observed in the Pittsburgh No. 8 coal or the Upper Freeport coal.

Careful examination of the peaks in Figure 8 strongly suggests that the "tail" does not in fact represent continuation of the exotherm to higher temperatures than those seen in Upper Freeport and Pittsburgh No. 8 coals. Instead, it actually appears that mass loss results in a "baseline shift" in the difference spectrum. Loss of mass, associated with the exotherm at near 200°C, would tend to decrease the apparent heat capacity of the sample after 200°C, during the first scan. When a second scan, which involves no mass loss, is subtracted from the first scan, the expected result would be a negative difference before the peak and a zero difference after the peak. The

former is seen, but the latter is not; the difference spectrum shows a positive baseline value after the peak, although it is heading towards zero. Some further processes apparently do occur above 250°C, but their magnitude is considerably less than a cursory look at Figure 8 might otherwise suggest. (The processes might include relaxations of the coal structure between 300 and 350°C, as we have discussed earlier; these relaxations may not have occurred during water treatment since the temperature was only 285°C). Further experiments to explore the effects of water and steam pretreatment are scheduled.

CONCLUSIONS

- Aerial oxidation in Upper Freeport coal rendered the pyridine swellability values higher than those in the corresponding as-received coal. This is due to addition of oxygen functionality, in all probability.
- Heat-treated Upper Freeport and Pittsburgh No.8 coals (in which coal structure was relaxed) show an appreciable impact of aerial oxidation. However, the nature of the effect was quite different. Aerial oxidation appears to cause less extraction from Upper Freeport medium volatile bituminous coal, due to crosslinking. Crosslinking is also promoted in Pittsburgh No. 8 coal, but relative extractability is unaffected.
- THF swellability of Pittsburgh No. 8 coal is not significantly affected by oxidation, whereas pyridine swellability is reduced. By contrast, the Illinois No.6 coal exhibits a significant decrease with oxidation of the THF swellability, while pyridine swellability remaining more or less the same.
- The comparison of DSC thermograms obtained from as-received and oxidized coal samples at 8°C/min demonstrate that an exothermic peak centered around 200°C was caused by the added oxygen and, interestingly, does not depend upon coal rank. These observations might suggest that the oxidation is actually concerned with certain specific components in coal structure, irrespective of coal rank as well as pretreatment conditions. However, this must be considered in light of the result below.
- According to DSC thermograms obtained from oxidized coal samples, the Illinois No.6 coal appears to be attacked in a different manner than the Upper Freeport and Pittsburgh No.8 coals. It appears to lose mass at the time of the exotherm.

ACKNOWLEDGEMENT The work reported here was financially supported by the Department of Energy Contract No. DE-AC22-91PC91027.

REFERENCES

1. Gray, R.J.; Rhoades, A.H.; King, D.T. *AIMMPE Trans.* **1976**, *260*, 334.
2. Cronauer, D.C.; Ruberto, R.G.; Jenkins, R.G.; Davis, A.; Painter, P.C.; Hoover, D.S.; Starsinic, M.E.; Schyler, D. *Fuel* **1983**, *62*, 1124.
3. Khan, M.R.; Jenkins, R.G. In *Chemistry of Coal Weathering*; Nelson, C.R. Ed.; Elsevier: Amsterdam, 1989; pp. 107-132.
4. Wu, M.M.; Robbins, G.A.; Winschel, R.A.; Burke, F.P. *Energy & Fuels* **1988**, *2*, 150.
5. Furimsky, E.; MacPhee, J.A.; Vancea, L.; Ciavaglia, L.A.; Nandi, B.N. *Fuel* **1983**, *62*, 395.
6. Graff, R.A.; Brandes, S.D. *Energy & Fuels* **1987**, *1*, 84.
7. Yun, Y.; Suuberg, E.M., accepted for publication in *Energy & Fuels*, 1992
8. Yun, Y.; Suuberg, E.M., submited to *Fuel*, 1992.
9. Vorres, K.S. *User's Handbook for the Argonne Premium Coal Sample Program*: Argonne, Illinois, 1989.
10. Yun, Y.; Otake, Y.; Suuberg, E.M. *Prepr. Pap.-Am. Chem. Soc., Div. Fuel Chem.* **1991**, *36(3)*, 1314.
11. MacDonald, R.A.; Callanan, J.E.; McDermot, K.M. *Energy & Fuels* **1987**, *1*, 535.

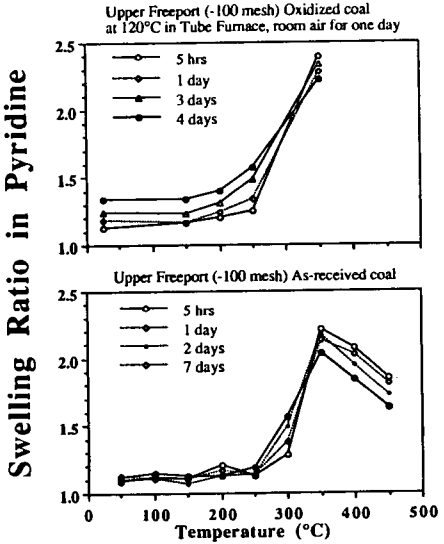

Figure 1. Comparison of pyridine swelling ratios with heat-treatment temperature between as-received and air-oxidized Upper Freeport medium volatile bituminous coal.

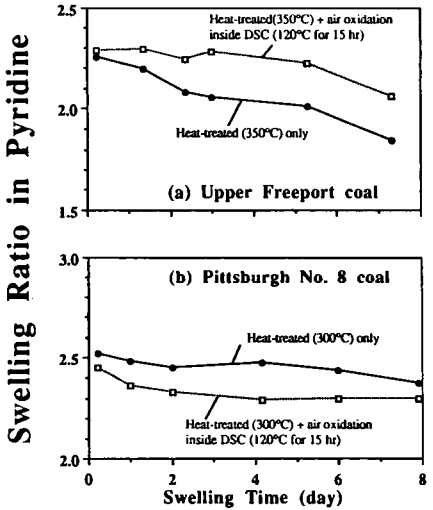

Figure 2. Effects of aerial oxidation on pyridine swelling characteristics in heat-treated and oxidized Upper Freeport, Pittsburgh No. 8 coals.

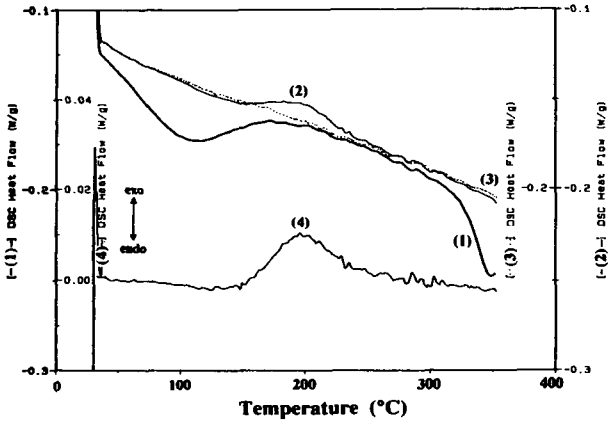

Figure 3. DSC and difference DSC thermograms obtained at 8°C/min from Upper Freeport medium volatile bituminous coal. The experiment was performed as follows: First, as-received coal was heat-treated up to 350°C, the result of which is denoted as (1) in the figure. Second, the purge gas inside the DSC was switched from nitrogen to air (100 ml/min) and the sample was kept isothermal at 120°C for 12 hr. Third, the resulting oxidized sample was scanned twice in the DSC, the results of which are (2) and (3). The difference DSC thermogram of the two consecutive DSC thermograms (2) and (3) is denoted as (4).

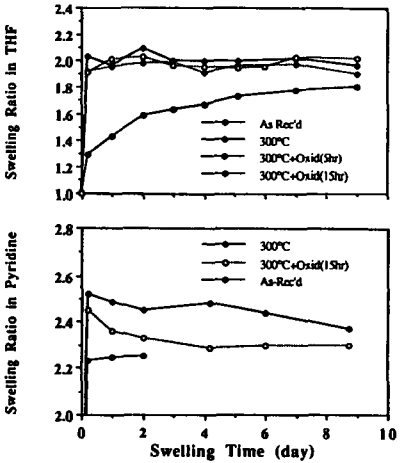

Figure 4. Effects of aerial oxidation on changes of THF and pyridine swelling ratios with swelling time in as-received and heat-treated Pittsburgh No. 8 coal. The notation of 300°C in the figure denotes that the sample was preheated inside the DSC up to 300°C at 8°C/min under a nitrogen environment. Oxidation was performed inside the DSC at 120°C with 100 ml/min air for 5 or 15 hr.

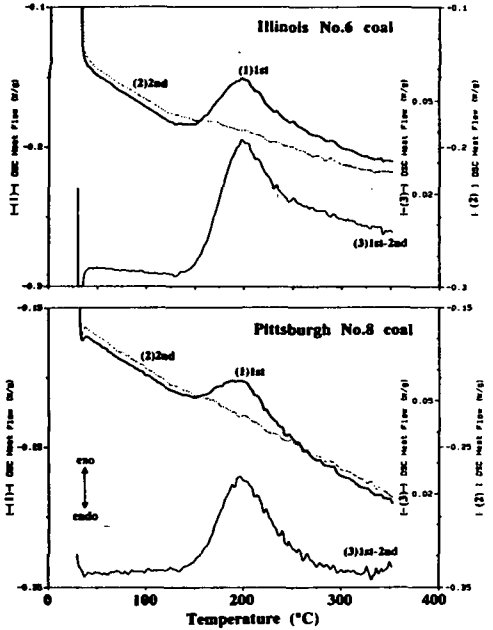

Figure 5. First and second DSC thermograms as well as the corresponding difference DSC thermograms for oxidized Illinois No.6 and Pittsburgh No.8 coals. Oxidation condition was 120°C for 15 hr while the sample was kept under air flow of 100 ml/min inside the DSC.

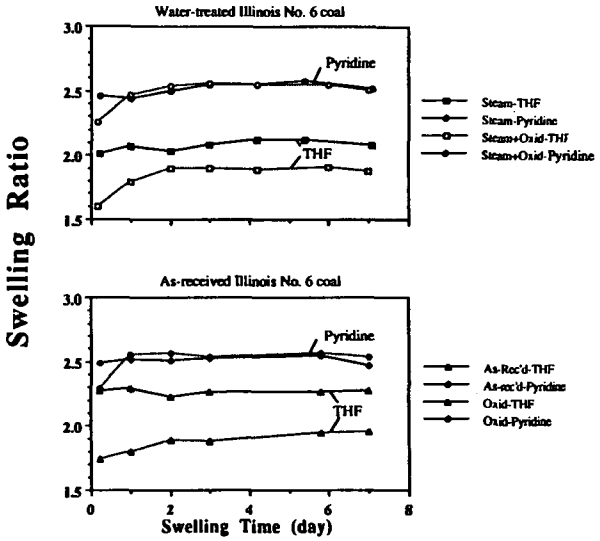

Figure 6. Effects of aerial oxidation and water-treatment on changes of solvent swelling ratios with swelling time in Illinois No.6 high volatile bituminous coal. Oxidation was performed in tube-furnace at 115°C for one day with room air.

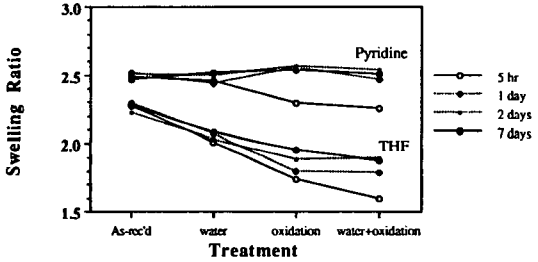

Figure 7. Comparison of solvent swelling ratios with respect to pretreatment conditions in Illinois No.6 high volatile bituminous coal. Water-treatment condition was at 1000 psig for about 1 hr and oxidation condition was at 115°C for 1 day with room air.

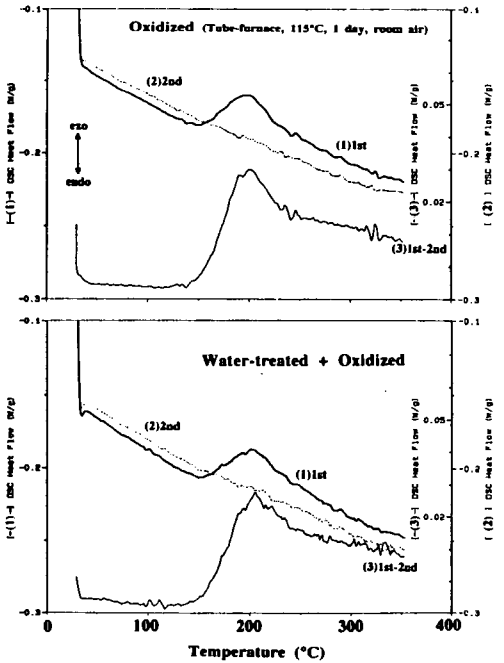

Figure 8. DSC (1st and 2nd) thermograms and the corresponding difference DSC thermogram obtained at 8°C/min from oxidized and water-treated-and-oxidized Illinois No.6 coal.

X-RAY DESCRIPTORS OF THE "NEAR" DIFFRACTION PEAK IN SOME ARGONNE PREMIUM COALS.

David L. Wertz
Department of Chemistry & Biochemistry
Center for Coal Product Research
University of Southern Mississippi
Hattiesburg, MS 39406 USA

Key words: [OOL] peaks, PAC layering.

INTRODUCTION

The Argonne Premium Coals are being thoroughly characterized by many research groups.

Four of the bituminous coals in the Argonne Premium Coal Program samples have been utilized to determine the ability of x-ray diffraction methodology to define several of the non-crystalline features of these coals.

Three of the subject coals, Pocahontas #3 (APC 501), Pittsburgh #8 (APC 401), and Upper Freeport (APC 101), reportedly have very low moisture contents, 0.5-1.5 %. The fourth coal, Lewiston-Stockton, has a higher moisture content, 4.6 %. Three of the subject coals reportedly contain ca. 75 % carbon, of which at least 75 % has been classified as aromatic. Both the carbon percentage and its aromatic fraction are reportedly much higher in Pocahontas #3.[1-4]

The subject coals differ in considerably in inorganic content, producing from 4.5% - 13.0% high temperature ash.[1] Furthermore, the coals differ considerably in volatile matter, ranging from 43.7 % for the Lewiston coal (high volatile bituminous) to 18.5% in Pocahontas #3 (low volatile bituminous). The coals also differ considerably in the reported volatile matter content.[1]

The extent to which diffraction may be used to measure the crystalline entities in coals has been established.[5] The effects of important other features on the diffractogram of a coal have not been so well established.[6] The purpose of this study is to determine which parameters that are important to coal scientists and/or environmental scientists may be measured by x-ray diffraction methods.

EXPERIMENTAL

COALS. The Argonne Premium Coals, well defined in numerous references, were provided as finely powdered samples sealed into an inert atmosphere. For these samples, the particle diameter < 0.15 mm.

A more detailed description of these subject coals is presented in Table One.

Division of carbon into aromatic and aliphatic fractions is based on the average of values reported by two different groups who analyzed these coals by MAS ^{13}C nmr methods.[2,3] Except for Pittsburgh #8, the aromatic (and aliphatic) fraction reported by each group differ by less than the experimental uncertainty of their results. The difference between the aromatic fraction reported by the two groups is ca. 0.10, which exceeds the

experimental uncertainty suggested by each of the nmr groups.

X-RAY EXPERIMENTS. A 0.5 gram sample of each finely powdered coal was mounted into our θ-2θ x-ray diffractometer which is equipped with a theta-compensating slit, a sample spinner, and a LiF crystal monochromator in the secondary x-ray beam. A diffractogram of each coal was obtained over the region from 2θ = 5.00° to 50.00° by measuring the secondary intensity for five seconds at angular increments of 0.02°. Diffractograms acquired over a much wider angular range but using a much shorter count time at each angle have already been presented.[5,6]

TABLE ONE. PARTIAL COMPOSITIONS OF THE HIGHEST RANK COALS IN THE ARGONNE PREMIUM COAL PROGRAM SAMPLES[1]

COAL DESCRIPTOR	COAL DESIGNATION			
	APC101	APC140	APC150	APC161
A. Rank	mvb	hvb	lvb	hvb
B. Volatile Matter	27.14%	37.20%	18.48%	43.72%
C. Moisture	1.13%	1.65%	0.65%	4.63%
D. High Temperature Ash	13.03%	9.10%	4.74%	4.49%
E. Carbon Content	73.34%	74.25%	86.15%	73.32%
E.1. Aromatic Fraction[2,3]	0.83	0.77	0.87	0.75
E.2. Aliphatic Fraction[2,3]	0.17	0.23	0.13	0.25

RESULTS

The abbreviated diffractograms of the four Argonne Premium Coals are presented in Figure One. Diffractograms of these four (and the other) Argonne Premium Coals obtained over a considerably wider angular range have been previously presented. The mass absorption coefficient (previously determined for these coals for Cu Ka x-rays[6]) was used to calculate the absorption corrected intensity. These diffractograms were partitioned into diffraction peaks (due to crystalline species in the coals) and a residual intensity which describes the amorphous scattering, as shown in Figure Two. Included in Figure Two is experimentally measured curve (2.A), the diffraction intensity due to the minerals (2.C), and the residual intensity (2.B). The latter is due to non-crystalline scattering, including the amorphous scattering due to the average poly-cyclic aromatic structural unit in each coal as well as other structural features.

The residual intensity curve, due to non-crystalline scattering, is shown for each of the four coals in Figure Three.

From the maxima and minima observed in each diffractogram, the molecular scattering associated with the average poly-cyclic aromatic hydrocarbon unit in each coal was calculated and then removed from the amorphous scattering intensity, as shown in Figure Four for APC 501. A well define peak results. Shown in Figure Five is the resulting "diffraction" peak, which (a) dominates the diffractogram, (b) is much broader than a typical diffraction peak, and (c) is asymmetrical.

In graphite, an ideal poly-cyclic aromatic compound (PAC), a corresponding diffraction peak, much more intense and much less broad, occurs at 3.35 Å and describes the stacking of its [00L] planes.

This unusually broad diffraction peak is due to imperfect diffraction from the [00L] planes present in each of the coals. As noted in Figure Five the shapes of the [00L] peak differ considerably, although each appears to be composed a symmetrical peak and a broad maximum. The symmetrical peak was simulated by the method of Kurita[8], i.e.

$$I(2\theta) = Q \cdot \exp(-a \cdot \Delta s^2) = Q \cdot \exp(-a' \cdot HW^2) \quad (1)$$

where Q is the maximum peak intensity and s is the half width at half maximum (HW) measured for the diffraction peak in reciprocal space. A summary of the symmetrical peak simulated for each coal is presented in Table Two.

TABLE TWO. SUMMARY OF SOME X-RAY DESCRIPTORS OF THE NEAR DIFFRACTION PEAK.

COAL	dmax	I*max (CPS)	HW (rad)	s ($Å^{-1}$)
APC 501	3.541 Å	1,880	0.0332	0.0210
APC 101	3.578 Å	1,471	0.0387	0.0244
APC 401	3.749 Å	1,328	0.0707	0.0447
APC 601	3.755 Å	1,271	0.0775	0.0490
*GRAPHITE	3.354 Å	75,466	0.0174	0.0027

PEAK MAXIMUM. The intensity of the broad [00L] peak, as measured by the peak height in the absorption corrected diffractograms, is related to the % aromatic character by:

$I^*_{max} = m \cdot (\%\ C_{ar}) + b$; where m and b are coefficients determined by linear least squares methods. For this analysis, R = 0.9989.

The [00L] maximum shifts, from 3.54 Å in APC 501 (the low volatile bituminous) to ca. 3.75 Å in the two high volatile bituminous coals -- APC 401 AND APC 601. This increase in the average inter-planar spacing parallels decreasing aromatic (and concomitant increasing aliphatic) content in the coals, suggesting that the aromatic PAC lamellae become further separated, on the average, as the rank of the coal decreases.

PEAK WIDTH. The width of a diffraction peak amy be affected by several factors. However, to a first approximation,
$\Delta 2\theta$ (in radians) = ef + $(0.9*\lambda/T*\cos\theta)$ + $(2\cdot(\Delta d/d)*\tan\theta)$; (2)
where ef is a characteristic function of the diffractometer, is the x-ray wavelength, T is the particle size of the diffracting material(s), $\Delta d/d$ is the deviation (strain) in the inter-planar spacing that cause diffraction peak characterized by the inter-planar spacing d.

(1) The Diffractometer Contribution. $\Delta d/d \rightarrow 0$ for graphite, as evidenced by the very intense and very narrow diffraction peak observed from the finely powdered graphite used as the reference in this study. As a consequence, the observed peak width (0.25° = 0.0174 rad) has been attributed to our diffractometer.

(2) Effect of Particle Size. The coal particles provided via the Argonne Premium Coal Sample Program and the graphite particles are 10^4-10^5 Å in diameter. Since λ= 1.5404 Å, $\lambda/T \rightarrow 10^{-4}$, which is considerably smaller than experimental uncertainty in these diffraction experiments. Consequently, for neither the coals nor the graphite is peak broadening due to particle size effects important.

(3) Effect of Inter-Planar Strain due to Distortions ($\Delta d/d$). For these coals, the peak broadening due to distortions in the distance between the PAH planes is given by:

$$\Delta 2\theta = 2\cdot\Delta d/d*\tan\theta. \quad (3)$$

(4) Approximate Solution to the Peak Broadening Effect for the Argonne Premium Coals. Since $\lambda/t \rightarrow 0$, the observed peak broadening, $\Delta 2\theta$, may be related only to $\Delta d/d$ by:

$$\Delta d/d = (HW - 0.0174)/\tan\theta \quad (4)$$

Shown in Table Three in the strain associated with the [00L] planes for these coals.

TABLE THREE. ESTIMATE OF THE STRAIN IN THE [00L] PEAK.

COAL	$\Delta d/d\cdot 100$
APC 101	9.6 %
APC 401	23.7 %
APC 501	7.1 %
APC 601	27.1 %

KEY REFERENCES

1. Vorres, K. S., Energy Fuels, 1990 (4) 420.

2. Solum, M. S., Pugmire, R. J., and Grant, D. M., Energy Fuels, 1989 (3) 187.

3. Shin, S. C., Baldwin, R. M., and Miller, R. L., Energy Fuels, 1989 (3) 193.

4. Weitzsacker, C. J. and Gardella, J. A., Anal. Chem., 1992 (64) 1068.

5. Wertz, D. L., Powder Diff., 1990 (5) 44.

6. Wertz, D. L., Energy Fuels, 1990 (4) 442.

7. Wertz, D. L., Powder Diff., 1988 (3) 153.

8. Kurita, M., Adv. X-Ray Anal., 1987 (31) 277.

9. Specht, E. D., Clausing, R. E., and Heatherly, L., J. Material Res., 1990 (5) 2351.

FIGURE ONE

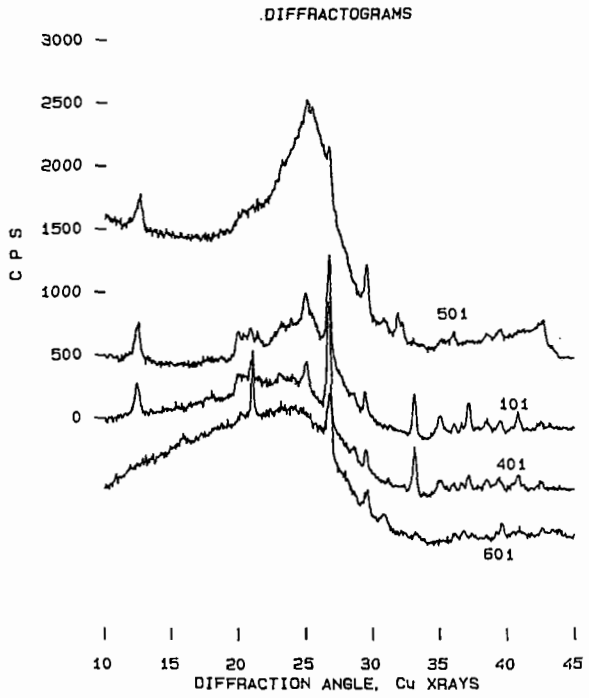

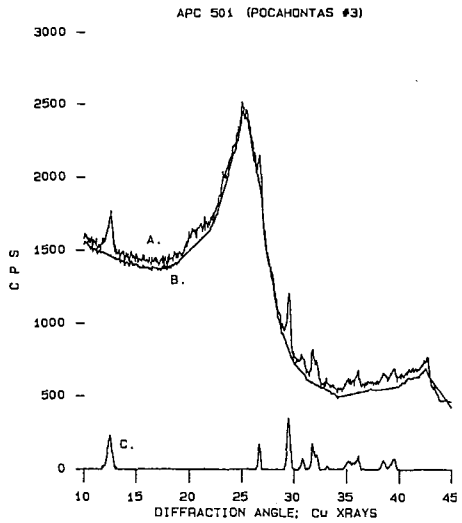

FIGURE TWO

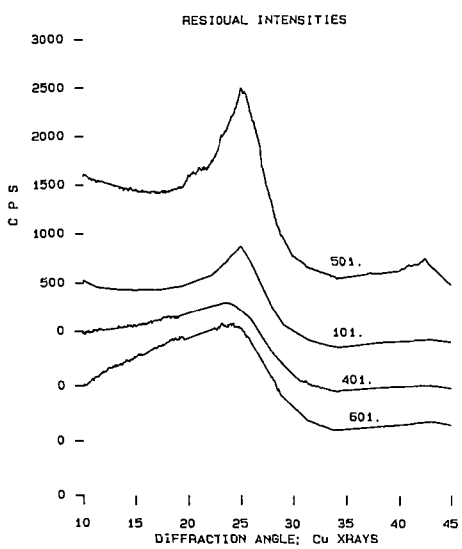

FIGURE THREE

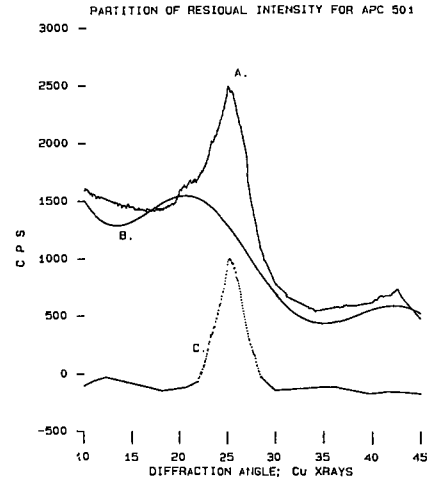

FIGURE FOUR

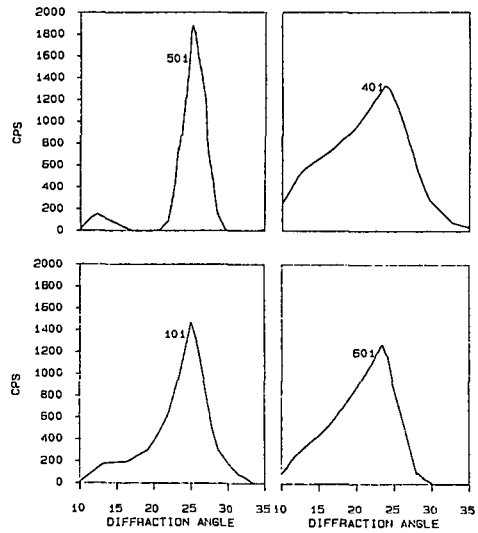

FIGURE FIVE

CO_2 Adsorption Techniques On High Surface Area Activated Carbons.

Mark L. Stewart and John M. Stencel.
Center for Applied Energy Research
University of Kentucky
Lexington, Kentucky
40511-8433

1. INTRODUCTION

For years the subject of CO_2 adsorption on activated carbons has been both challenged and supported. The question remains whether or not CO_2 is a valid adsorbate for characterizing pore structures of activated carbons. The predominance of nitrogen adsorption as a routine experimental technique for BET surface area approximations has more or less overshadowed the limitations of this technique in terms of activated diffusion phenomena[1]. As a result, it is thought that nitrogen adsorption at 77K generally underestimates the surface area of coals[1]. In some super-activated carbons, CO_2 is an attractive adsorbate for characterization due to its small molecular diameter and it's access to supermicropores. Although CO_2 adsorption models are not completely understood, for particular cases in which N_2 adsorption may be problematic or inconclusive, CO_2 adsorption may offer additional pore structure information.

The purpose of this communication is to address the concept of CO_2 adsorption phenomena experimentally and conceptually. Experimental data are compared for CO_2 adsorbed onto very high surface area activated carbons. From this information, optimal experimental conditions are theorized on the basis of ease and understanding. It is hoped that an adsorption procedure involving the benefits of N_2 and CO_2 together will provide insight into the pore structures of very high surface area activated carbons.

2. EXPERIMENTAL

Materials used:

Two activated carbons were used in the experiments; they were supplied by Amoco Research and Developement, and Norit N.V. Activated Carbon. They are classified as Amoco Super-A and Norit A-8982. The surface areas, as measured by nitrogen BET method[2], were 1500-1800 m^2/g for Norit A-8982 and 2500-2800 m^2/g for Amoco Super-A.

Experimental methods:

Adsorption analysis was performed on a Coulter Omnisorp 100CX Automated Gas Sorption System. Approximately 0.25 grams of sample was weighed prior to outgassing. All samples were outgassed at 250°C and sealed under vacuum prior to

analysis. Static volumetric mode was used for all CO_2 and N_2 adsorption measurements. N_2 was adsorbed at 77K in the relative pressure range (P/Po) of 0.001 to 0.98. CO_2 was adsorbed at three different temperatures and relative pressure ranges(P/Po) as follows:

195K: 0.0001 to 0.48
273K: 0.0001 to 0.027
298K: 0.0002 to 0.015

CO_2 saturation vapor pressures for each temperature were taken as follows:

195K: 1,410 torr[3]
273K: 26,068 torr
298K: 45,041 torr

Molecular diameters used for N_2 and CO_2 were 3.64 and 3.3 angstroms, respectively. All surface areas were calculated from the BET equation[2] and pore volumes were approximated using the Dubinin-Radushkevich equation[4].

3. RESULTS AND DISCUSSION

The CO_2 adsorption isotherms for the A-8982 and the Amoco Super-A carbons at 195K, 273K, and 298K are plotted in Figures 1 and 3, respectively. Upon initial examination for the Norit carbon, the CO_2 uptake at 195K in this low pressure region is markedly higher than in the other two temperature cases. At 273K and 298K, the isotherms are virtually identical with very little deviation in CO_2 uptake. The Amoco Super-A carbon exhibits similar characteristics in this region but with a noticable difference in the 273K and 298K temperature cases. These results suggest that, at 195K, complete micropore filling may occur giving higher potential for CO_2 adsorption. It is likely that incomplete micropore filling occurs at temperatures of 273-298K since the saturation vapor pressure of CO_2 is extremely sensitive to temperature changes and is very high. However, it seems reasonable to assume that, at 195K, a better estimate of internal pore uptake can be obtained.

The CO_2 DR plots for A-8982 and Amoco Super-A are indicated in Figures 2 and 4, respectively. In estimating pore volumes, a comparable range for each temperature was taken for extrapolation to the y-axis. The pore volumes are as follows:

Norit 195K = 1.22 cc/g	Amoco 195K = 2.00 cc/g
Norit 273K = 0.93 cc/g	Amoco 273K = 1.40 cc/g
Norit 298K = 1.09 cc/g	Amoco 298K = 1.64 cc/g

At an adsorption temperature of 195K the pore volumes are the highest which relates to the increased uptake observed in the adsorption isotherms in figures 1 and 3. Pore volume calculations from N_2 adsorption are slightly less than the 195K CO_2 case but higher than 273K and 298K CO_2 cases. Results obtained from BET surface

area calculations for the 195K CO_2 case yield higher surface areas than N_2 BET estimates.

4. CONCLUSIONS

CO_2 adsorption at 195K appears to be a valid technique for approximating pore volumes of high surface area activated carbons if complete micropore filling is assumed. Experimentally, due to instrumental limits, a larger relative pressure range can be analysed for 195K due to the temperature and vapor pressure sensitivities present at 273K and 298K. Because of this fact, CO_2 and N_2 surface areas can be compared. Since the relative pressure ranges for 273K and 298K are so low, (maximum p/po = 0.02-0.03), the micropore filling is incomplete, giving pore volumes that are underestimated. Although a strict comparison between CO_2 and N_2 needs to be investigated further, molecular size differences may still give some insight on the possible presence of any super microporosity.

5. REFERENCES

1. Om P. Mahajan, Carbon Vol. 29 No. 6. pp. 735-742. 1991.

2. Brunauer S., Emmett P.H., Teller E. J.A.M. CHEM. SOC., pg 6309. 1938.

3. H. Marsh, D. Crawford, T.M. O'Grady, and A. Wennerberg, Carbon Vol. 20 No 5, pp. 419-426, 1982.

4. Dubinin M.M., and Radushkavich L.V. Proc. acad. Sci. USSR Vol. 55 pg 331 1947.

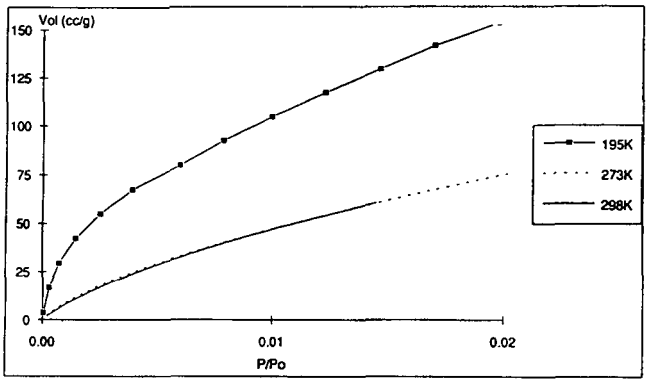

Fig. 1. CO_2 adsorption isotherms on Norit activated carbon at 195K, 273K, and 298K.

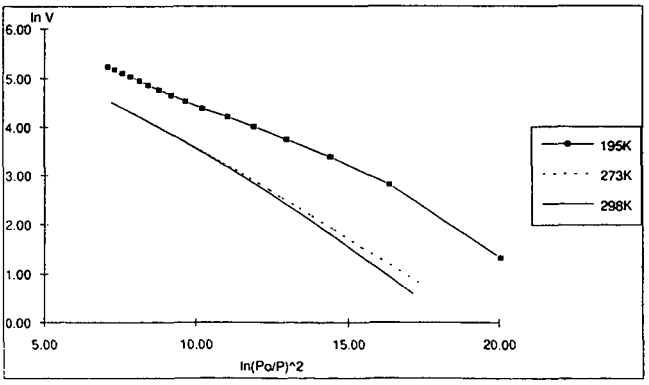

Fig. 2. CO_2 DR plots corresponding to isotherms in Fig. 1.

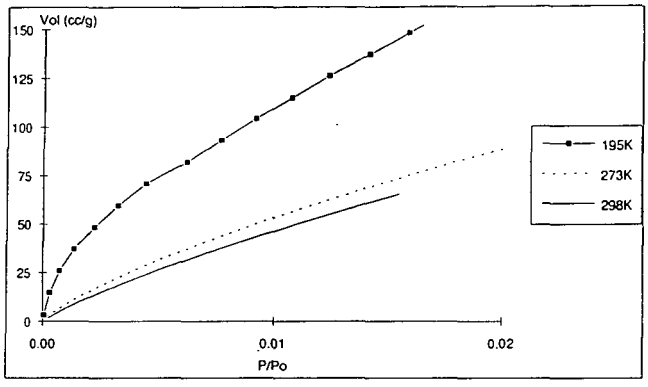

Fig. 3. CO_2 adsorption isotherms on Amoco Super-A activated carbon at 195K, 273K, and 298K.

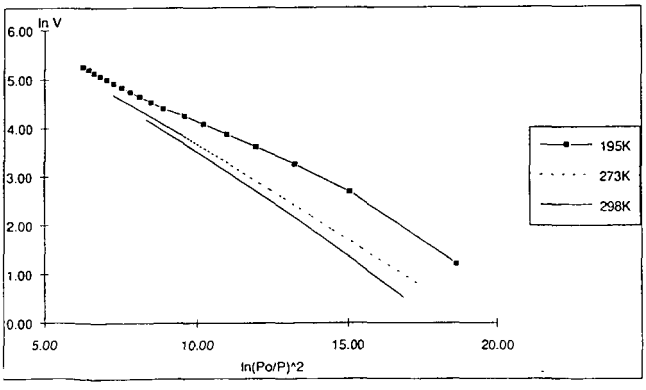

Fig. 4. CO_2 DR plots corresponding to isotherms in Fig. 3.

SYMPOSIUM ON ANALYTICAL TECHNIQUES FOR CHARACTERIZING
COAL AND COAL CONVERSION PRODUCTS
AMERICAN CHEMICAL SOCIETY
WASHINGTON, DC MEETING, AUGUST 23-28, 1992

TG-MS FOR CHARACTERIZATION OF ACTIVATED CARBONS FROM COAL

By

A.M. Rubel, M. Jagtoyen, J.M. Stencel, S. N. Ahmed, F. J. Derbyshire
University of Kentucky, Center for Applied Energy Research
3572 Iron Works Pike, Lexington, KY 40511-8433

Keywords: thermogravimetry, mass spectrometry, coal-based activated carbons

INTRODUCTION

The application of thermogravimetry coupled with a quadrapole mass spectrometer (TG-MS) to study coal-based materials was examined. First, TG-MS was used to analyze the gaseous decomposition products from activated coal-based carbons to obtain structural information related to their synthesis conditions. Secondly, adsorption/desorption profiles of physisorbed and chemisorbed gases were determined through temperature programmed desorption/evolved gas analysis (TPD/EGA).

There are a number of reviews on the use of TG-MS systems to study decomposition and kinetics of biological, organic, and inorganic compounds.[1,2,3] This method has several advantages over other instrumentation used for TPD/EGA. For example, methods that utilize gas chromatography (GC) to monitor gas release are limited to only a few gases and the time required for each analysis results in discontinuous gas evolution profiles[4,5]. Newer methods, which couple MS to the reactors used for TPD, provide a significant improvement; however many of these systems do not have continuous sample weight monitoring[6,7].

The TG-MS system used for this study provided the ability to accurately and continuously monitor weight changes simultaneously with evolved gas composition. The quadrapole MS system employed allows determination of multiple gas components in the range of 0-300 atomic mass units. Procedures for determining relative gas evolution rates and quantities have been developed. The system is equipped with multiple sweep and reaction gas purge, gas switching, and gas blending capabilities which make possible the study of adsorption and desorption of gases under a wide variety of conditions.

EXPERIMENTAL

Instrumentation

A Seiko TG/DTA 320 was coupled to a VG Micromass quadrapole MS. The TG was connected to a disk station which provided for programmable control of the furnace, continuous weight measurements, sweep gas valve switching, data analysis, and export of data to other computers. The TG has a temperature range of room temperature to

1300°C. The MS has a Nier type enclosed ion source, a triple mass filter, and two detectors (a Faraday cup and a secondary emissions multiplier). The MS was controlled by a dedicated personal computer which was also used to acquire and review scans before export to a spreadsheet for data manipulation.

The two instruments were coupled by a fused silica capillary transfer line leading from above the sample pan in the TG to an inert metrasil molecular leak which interfaced the capillary with the enclosed ion source of the MS. Connections at both ends of the capillary allowed sampling of very small fractions of the gases. The transfer line was heated to 170°C at which temperature the flow rate through the capillary was approximately 12 ml/min .

TG-MS procedures

The TG conditions used to study the relationship between the structure and synthesis parameters of carbons were: heating rate of 10°C/min to a 5 min hold at 900°C; sweep gas, 225 ml/min; constant sample volume weighing 10-25mg. The MS was scanned over a 0-100 amu range with measurement intervals of approximately 30 seconds.

The TG heating profile for TPD/EGA measurements was more complex and incorporated segments for outgassing, cooling, adsorption, desorption, and temperature-induced desorption (Table I). During outgassing and subsequent cooling of the sample to an adsorption temperature (segments a and b, Table I), an inert (He) gas sweep was usually used after which the gas to be adsorbed was introduced. After completion of an adsorption interval, He was again used to purge the system during segments d and e. Multiple and consecutive adsorption/desorption cycles were performed by recycling the temperature programmer to segment b.

The relative amounts of effluent gases monitored by the MS was determined using the He peak intensity, at a constant flow rate, to determine a sensitivity factor for each analysis. The area under the gas evolution curve for each gas was determined, normalized for the sample weight, and multiplied by the sensitivity factor obtained by arbitrarily assigning a value of one to the He intensity of one of the runs to be compared. This run was referred to as the standard run. The sensitivity factor was then calculated by dividing the He intensity of the standard run by the intensity of He in all subsequent runs. The intensities of all other gases of interest were multiplied by the sensitivity factor for relative comparisons.

Materials

Activated carbons produced by chemical and thermal procedures were studied during the first part of this work. They were produced from Illinois Basin bituminous coals supplied by the Illinois Basin Coal Sample Program and were prepared according to procedures detailed elsewhere[8,9,10]. Two types of chemical activation were examined, H_3PO_4 and KOH. Temperature treatments were 170 and 500°C for acid treated carbons and 75, 400 and 800°C for base treated carbons. All carbons were leached to a pH of 7 and dried before TG-MS analysis.

During the TPD/EGA study, a commercially (Carbotech) produced coal-based

carbon was used. This carbon was produced by thermal activation and had a N_2 BET surface area of 450 m^2/g. The adsorption gas mixture was 2% NO, 10% O_2, 15% CO_2 with He the balance.

RESULTS AND DISCUSSION

Structural determinations

TG-MS experimental data enables the correlation of weight loss to individual gas evolution. The temperature of evolution has been related to different functional groups on the surface of the carbon matrix[11]. For example, the data in Figure 2 were from a carbon sample thermally treated at 500°C. Maxima in the evolution profiles for CH_4 and H_2 were at 620 and 820°C . Dealklyation is a likely source of the CH_4 release[12]. H_2 and CH_4 evolution began at about the same temperature but H_2 continued to be evolved after CH_4 release had stopped. This suggests that H_2 from more than one source contributes to its evolution profile. Possible sources are the decomposition of aliphatics at lower temperatures and aromatics at higher temperatures[12]. Very little CO_2 (mass 44) was evolved which suggests that the CO_x (mass 28) evolution profile represents primarily CO release. Presently work is being done to correlate these TG-MS CO and CO_2 evolution determinations to carbonyl and aromatic C-O measurements by FTIR.

No significant amounts of other gases were detected by MS. Gas identification was based on a comparison of several ions. For instance, the identification of CH_4 was based on a comparison of mass 16 with mass 32 (O_2). Mass 32 did not deviate significantly from barely detectable levels. In this example, weight loss cannot be assigned to a specific gas since evolution profiles overlap. However, weight loss corresponded well with the onset of gas evolution.

Important to this study was a comparison of the relative amount of gas evolved from carbons produced under different synthesis conditions. A number of factors (condition of the capillary transfer tube, the ion source, and the efficiency of the vacuum system) affect the sensitivity of the MS. Therefore, comparison of spectra required the development of a method to correct for the sensitivity of the MS. Helium was used as an internal standard to calculate a sensitivity correction factor for each spectra. Since the flow rate and concentration of He was held constant for each experiment and the amount of gases evolved from the sample was negligible in comparison to the concentration of He, each spectra was corrected to the same He intensity arbitrarily chosen from the spectra to be compared. Further, comparison of gases on a unit basis required normalization of the relative amount of gas evolved for the differing initial sample weights.

Using the above approach, carbons produced under a number of thermal, acid and base treatments were examined. H_2 and CH_4 evolution profiles were compared for three carbons treated as follows: low followed by high temperature treatment (170°C and 500°C); low followed by high temperature treatment with H_3PO_4 ; and high temperature treatment with acid (Figure 3 and 4). These three samples, though activated at the same maximum temperature, had quite different H_2 evolution profiles. The acid treatment appeared to remove more low temperature H_2 since evolution began at 460°C for the thermal only sample and at nearly 600°C for acid treated samples. Additionally, the

temperature of maximum H_2 evolution was shifted slightly higher for acid treated carbons. CH_4 evolution was observed only for the carbon sample that had a thermal treatment without acid. If the CH_4 results from the pyrolytic cleavage of aliphatic carbon side chain in the parent coal structure, then acid treatment promoted these dealklyation reactions. The calculated relative amounts of H_2 released indicated that acid treatment promotes dehydrogenation (Figure 3 and 5) during synthesis. The relative amounts of evolved H_2 were consistent with H/C atomic ratios calculated from elemental analysis of the carbons.

TG-MS data of four activated carbons produced under different thermal and base (KOH) treatments were also compared (Figure 6). The relative amount of evolved H_2 and CH_4 decreased with increased severity of treatment . The base activated carbon evolved substantially more CO and CO_2 than the thermal only treated sample. This is consistent with FTIR analyses of these samples which showed carbonyl group development in base treated samples which was not present in the parent coal[9].

TPD/EGA determinations

The NO adsorption/desorption profiles (Figure 7) of a commercial coal-based activated carbon will be used as an example of a TPD/EGA determination performed by TG-MS. Adsorbing samples must be heated to a temperature as high as the maximum desorption temperature to remove any adsorbed gases. After this pre-conditioning step and sample cooling to 70°C, NO plus CO_2, O_2, and He were passed over the sample until its weight approached saturation. The NO was turned off and a He sweep gas was passed over the sample at the adsorption temperature for a period of time. This interval allowed purging of the NO from the system and removal of any physically bound NO from the carbon. The sample was then heated at 10°C/min to a maximum desorption temperature of 400°C. In Figure 7, some weight loss occurs during the low temperature desorption period but the MS spectrum showed an intense peak at mass 30 which correlated well with the weight loss during heating. The temperature at which maximum evolution occurred was 132°C. This temperature indicates NO is not strongly bound to the carbon matrix. The only gas evolved during desorption was NO which allows the direct correlation of weight loss with NO desorption. Any number of adsorption/ desorption cycles can be consecutively run. The sample in Figure 6 was repeated three times.

SUMMARY AND CONCLUSIONS

TG-MS has been successfully applied to the study of coal-based activated carbons providing information which relates synthesis parameters to the structure of the carbons. Procedures were developed to compare the relative quantities of evolved gases. The instrumentation was also used to do TPD/EGA analyses of activated carbons. Their adsorption and desorption properties are important in evaluating the practical applications.

REFERENCES

1. Dollimore, D., G.A. Gamlen, and T.J. Taylor. *Thermochimica Acta 75* (1984)59.
2. Wendlandt, W.W. *Thermal Methods of Analysis,* 3rd edn., Wiley, New York, 1986,482.

3. Eppler, H. and H. Selhofer. *Thermochimica Acta 20* (1977)45.
4 Carrizosa, I. and G. Munuera. *J. Catal., 49* (1977)174.
5 Cvetanovic, R.J. and Y. Amenomiya. *Adv. Catal., 17* (1967)103.
6 Bernal, S., R. Garcia, and J.M. Rodriguez-Izquierdo. *Thermochimica Acta 70* (1983)249.
7 Causton, P. and B. McEnaney. *Fuel 64* (1985)1447.
8. Derbyshire, F.J., J. Stencel, B. McEnaney, M. Thwaites, and M. Jagtoyen. Final Technical Report to CRSC, "An Investigation of the Conversion of Illinois Coals to Activated Carbons," for the period Sept. 1, 1990 through Sept. 3, 1991.
9. Derbyshire, F.J., M. Jagtoyen, R. Rathbone, and J. Stencel. Quarterly Report to the CRSC, "Synthesis of Absorbent Carbons from Illinois Coals," for the period of Dec. 1, 1991 through February 29th, 1992.
10. Derbyshire, F.J., M. Jagtoyen, J. Stencel, and B. McEnaney. Quarterly Report to the CRSC, "Synthesis of Adsorbent Carbons from Illinois Coals," for the period of Sept. 1 through Nov. 30, 1991.
11. Wang, J. and B. McEnaney. *Abstracts 19th American Conference on Carbon*, Pennsylvania State Univ. (1989)590.
12. Wen, C.Y. and S. Dutta. In *Coal Conversion Technology*, C.Y. Wen and E.S. Lee, Eds., Addison-Wesley Publishing Co., Reading, MA(1979)57.

Table I. TG heating profile for ADP.

Step	Temp C	Rate C/min	Hold min
a	0-400	20	10
b	400-70	50	10
c	70 (1)	0	60
d	70 (2)	0	30
e	70-400	20	10

[1]Adsorption
[2]Low temperture desorption

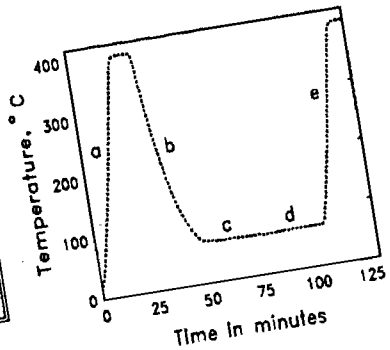

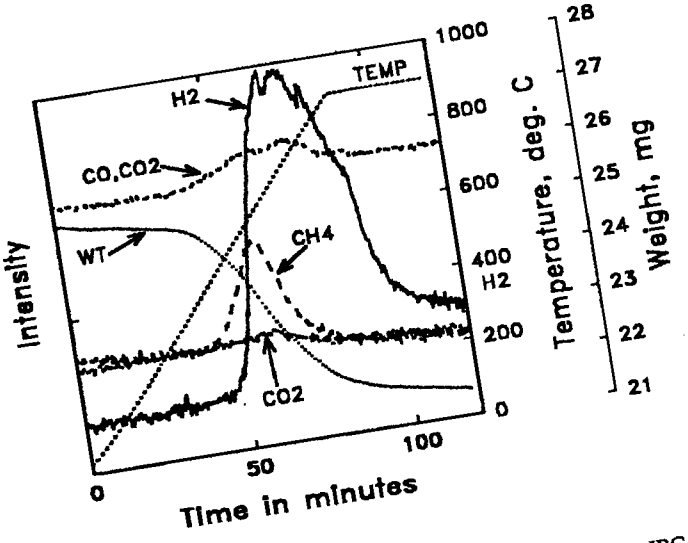

Figure 1. TG-MS analysis of thermally treated activated carbon from IBC sample.

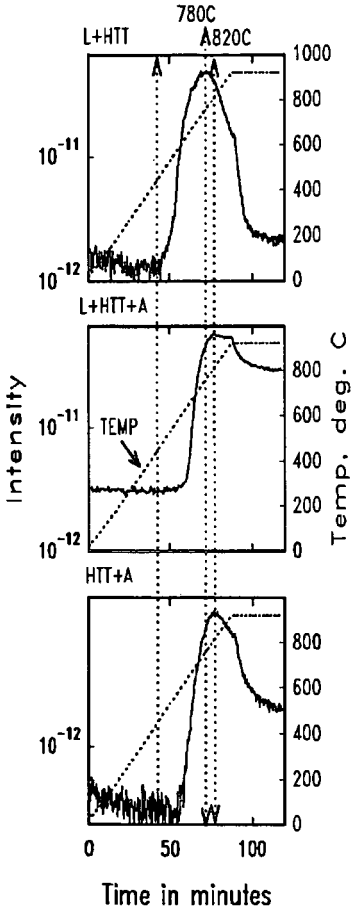

Figure 3. H_2 evolution curves from TG-MS analysis of acid and heat treated coal-based active carbons. A=H_3PO_4; L=low; HTT= high temperature treatment

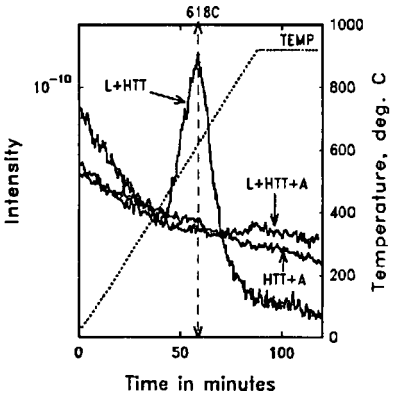

Figure 4. CH_4 evolutions curves from TG-MS analysis of acid and thermally activated coal-based carbons. A=H_3PO_4; L=low; HTT=high temperature treatment

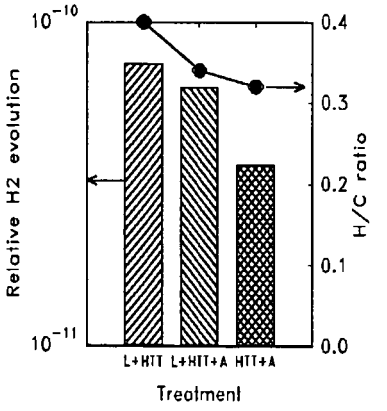

Figure 5. Relative amounts of H_2 evolved from acid and heat treated coal-based carbons. A=H_3PO_4; L=low; HTT=high temperature treatment

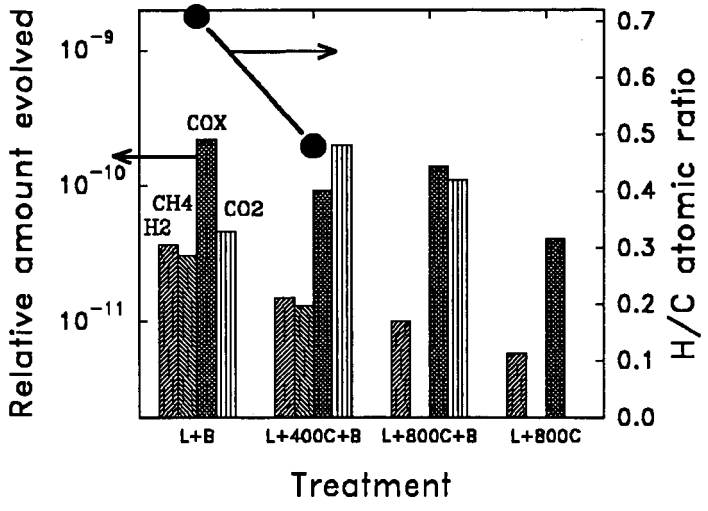

Figure 6. Relative amounts of H_2, CH_4, CO_x, CO_2 evolution from KOH activated carbons. B=KOH, L=low temperature treatment, 75°C

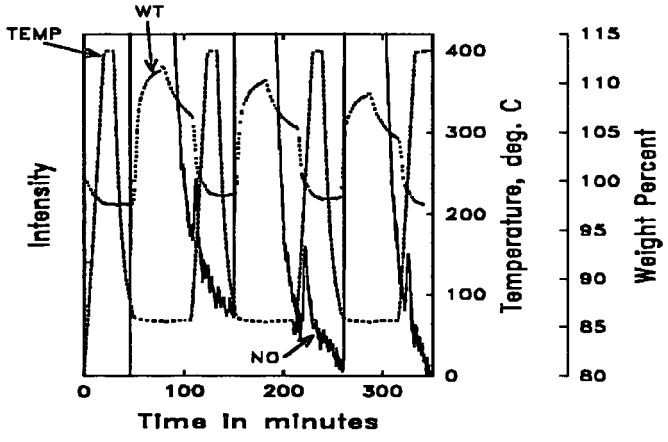

Figure 7. NO adsorption/desorption profile for coal-based activated carbon as determined by TG-MS.

FIELD IONIZATION MASS SPECTROMETRY FOR CHARACTERIZING COALS AND COAL-DERIVED LIQUIDS

Ripudaman Malhotra and Donald F. McMillen
Molecular Physics Laboratory
SRI International
Menlo Park, CA 94025-3493.

Keywords: FIMS, Coals, Coal Liquids, Heavy Oils

INTRODUCTION

The fossil fuel research program at SRI International has greatly benefited from the availability of on-site FIMS capability. In this paper we present a potpourri of FIMS applications from various aspects of coal research to demonstrate the technique's versatility. These applications include (a) differentiating coal types (b) analyzing coal tars, (c) determining the fate of a nitrogen-containing donor solvent in coal liquefaction, (d) identifying species responsible for catalyst deactivation, and (e) understanding why certain liquefaction resids are more difficult to upgrade. This list includes examples of characterization of individual species from peak intensities, which is possible in certain instances, and the use of overall FIMS profiles to identify trends in a series of samples.

EXPERIMENTAL

The technique of field ionization (FI) consists of passing the vapors of a material through a region of intense electric field to polarize and ultimately ionize the molecules. The ions are then mass analyzed using standard mass spectrometric techniques. For most organic compounds, this procedure causes minimal fragmentation and produces only the molecular ions. (1) Thus, complications arising from fragmentation during ionization are minimized. Another advantage of field ionization is that the relative field ionization efficiencies of various hydrocarbon types are within a factor of two of alkyl aromatics except for saturated acyclic hydrocarbons, which ionize about a third as efficiently. For many other ionization techniques, such as field desorption, low-voltage electron impact, secondary ion mass spectrometry (SIMS), or fast-atom bombardment (FAB), the relative ionization efficiencies can differ by more than one or two orders of magnitude. Thus, even without any corrections for sensitivity, the FI mass spectra represent the true molecular weight profile fairly accurately. This is particularly useful in complex unknowns where extensive calibration is not feasible. It should be noted that practical advantage can be taken of this similarity in ionization efficiency *only* if appropriate technique and care is used in preparing and operating the tantalum foil ion sources that are used at SRI.

SRI's FIMS instrument consists of a foil-type field ionizer interfaced with a 60-degree magnetic-sector mass analyzer and a PDP 11/23 computer for instrument control, data acquisition, and report production, as previously described.(2) The spectrometer has a resolving power (M/ΔM) of 1300, although it is capable of scanning up to 3000 Da. The sample is weighed into a melting point capillary and introduced into the spectrometer with a heatable direct insertion probe. It is heated at a fixed rate from ambient (or ~-67°C for samples with sufficiently high vapor pressure) to about 700°C. The spectra of the evolving volatiles are continuously recorded, and at the end of a run, they are added to produce a "sum" spectrum of the total volatiles. The capillary is weighed afterward to determine the percent volatilization.

The sum spectra consist of (a) intact molecular ions from individual chemical species originally present in the sample, (b) ions produced from any ion fragmentation that may occur, and (c) molecular ions of fragments that are generated thermally during the ramped heating. The ion fragments are most often totally negligible, as asserted above, but the thermal fragments can be substantial, depending on the volatility and reactivity of the sample. However, in both cases, the manner of presentation of the spectral intensities can generally indicate the extent to which (b) and (c) contribute. Since ion fragments will accumulate at the masses corresponding to the common stable positive ions, the typical absence of significant intensity at, for example, m/z 57 (where the

easily generated t-butyl ion fragment appears) indicates that the percent fragmentation at each of the other hundreds of masses that may have had attached t-butyl fragments must have been very small indeed. For cases where there is significant formation of volatiles through thermal decomposition in the heated source , this is usually revealed by the appearance of some smaller ions as the source is progresssively heated. Contributions from pyrolysis during heating are of course significant for heavy coal conversion fractions such as preasphaltenes and vacuum resids. These pyrolytically generated volatiles, when recognized, can sometimes provide valuable information.

RESULTS AND DISCUSSION

1. Differentiating Coals

We analyzed the eight coal samples from the Argonne Premium Coal Sample Program (APCSP) by programmed temperature pyrolysis directly in the inlet of the field ionization mass spectrometer.(3) The spectra of the evolved tars, but not of gases such as CO, CO_2, CH_4, and H_2O, were obtained. From these data we could identify several salient rank-dependent trends. Some of these trends are known from other studies, but FIMS provides an easy means for quantifying them and developing indices that could be used in modeling. In general, the spectra appear to be composed of two groups of peaks: (a) a cluster of peaks in the low molecular weight range corresponding to homologous series of phenols and dihydric phenols and (b) a broad, roughly Gaussian, distribution of peaks spanning the mass range of 150 to 1000 Da.

The low molecular weight cluster is particularly dominant in the Beulah Zap lignite and the Wyodak subbituminous coal, as shown in Figure 1. With increasing rank, the prominence of this cluster decreases relative to the broad Gaussian envelope, whose mean appears to shift to higher masses with increasing rank. Furthermore, the ratio of monohydric to dihydric phenols generally increases with rank. A detailed examination of the broad envelope revealed the buildup of polycyclic aromatic structures in the higher rank coals. Thus molecular species with five and more aromatic rings were discernible in the spectra of the Upper Freeport and Pocahontas coals. The observed periodicity revealed homologation via both benzolog formation ($\Delta m/z = 50$ as in naphthalene to phenanthrene and $\Delta m/z = 24$ as in phenanthrene to pyrene) and also in the formation of biaryl linkages (most noticeably in the formation of napthyl substituted aromatics with a $\Delta m/z = 126$).(3) The shift toward higher molecular weight and away from phenolic fragments with increasing coal rank is entirely consistent with the previously articulated view (4) that low-rank, high-oxygen coals are more crosslinked to begin with and/or become so during heating, such that the molecular weight between crosslinks is small and primarily small fragments are released. These observations parallel some of those recently reported by Schulten and coworkers.(5)

2. Characterizing Coal Liquids

Chemical analysis of coal- or petroleum-derived liquids as well is best accomplished by first fractionating the oil into different compound classes by HPLC and then subjecting these fractions to FIMS analysis. The most evident feature in these spectra is a 14-Da periodicity arising from the various alkyl-substitution homologous series. The HPLC-FIMS approach has been used by many investigators to follow the chemical changes that accompany processing.(6-10) In general, severe processing leads to dealkylation and formation of larger PAH structures. The net result is a simplification of the FI-mass spectra, which show an increasing dominance of a 50-Da periodicity instead of the more common 14-Da periodicity. An extreme of this behavior can be seen in high-temperature coal tars, which can consist almost exclusively of dealkylated aromatics, as shown in Figure 2.(7)

3. Fate of Amine Solvents during Coal Liquefaction

We examined liquefaction products obtained with and without 1,2,3,4-tetrahydroquinoline (THQ) as a solvent component to determine the fate of THQ.(8) At the time this study was undertaken, it was well recognized that (a) use of THQ dramatically increased coal conversion to soluble products, but these products were much less distillable than the normal toluene solubles, and (b) a

substantial portion of the THQ was not recovered from the solvent. The nitrogen content of the resid produced in batch autoclave liquefaction was significantly greater than without THQ. It was postulated that THQ was adducted into the resid by means of H-bonds that limited its recovery in the normal fashion, but that some physical or simple chemical separation would still make THQ available under recycle conditions.

FIMS of the resid showed a complete absence of a peak at 133 Da corresponding to THQ. Since even the strongest of hydrogen bonds would provide only a vanishingly small degree of association at the high vacuum field ionization condition, this observation provided incontrovertible evidence that THQ was not lost merely by H-bonding. FIMS also showed that after correcting for natural ^{13}C-content, the profile of the odd masses was significantly more intense for the resid obtained with THQ as a solvent component, as shown in Figure 3. The increase in the intensity of the entire odd-mass envelope indicated that THQ was incorporated by covalent linkages into a whole host of resid components, and is hence, for all practical purposes, irretrievably lost to the resid. FIMS and GC-MS analysis of the lighter fractions showed many specific coupling products, thereby providing insight into the types of reactions contributing to THQ loss.

4. Resid Reactivity

In a recent study (11,12) we analyzed fifteen recycle resids from five runs conducted at the Wilsonville facility to help address the question of what structural and process factors help make some resids much more convertible than others. At first glance, the spectra looked very similar with only a broad, featureless envelope. Closer examination, however, revealed that the mass spectra consistently showed the same set of a few prominent peaks in the low mass end, where the distillate-resid cut had sent lower boiling components (i.e., aliphatics) of similar molecular weights into the distillate fraction. Some of these prominant peaks are identified in Figure 4. Interestingly, these prominent masses left in the resid were identical to those previously identified by Sullivan et al. and associated (10) with increased difficulties in hydrotreating vacuum gas oils derived from petroleum resids. This coincidence is remarkable and we believe that a quantitative analysis could lead to an index of resid reactivity and help as well to understand the kinetic factors that control the ring-growth processes.

Apart from information contained in these few specific peaks, we can also derive useful information from overall FIMS profiles. Many of the liquefaction resid samples exhibited a bimodal molecular weight distribution. The relative amounts of the low and high molecular weight components differ significantly from sample to sample, and a simple mathematical deconvolution into Components A and B revealed a correlation between the variations in A and B on the one hand and coal type, process conditions, and process performance on the other. The deconvolution led to several conclusions reasonably in concert with what is already recognized in coal liquefaction. For example, this analysis clearly showed the occurrence of retrograde reactions after the second-stage reactor, while the oil was held at temperature and handled through the ROSE-SR unit.(13) This retrogression was evidenced by an increase in the amount of component B. It was satisfying to see this and other observations about reactivity reiterated, not on the basis of yields, but on the basis of differences in molecular weight distribution, when the streams are already constrained by process conditions and product fractionation to be as similar as possible.

5. Catalyst Fouling

In order to determine the types of compounds that strongly adsorb on supported liquefaction catalysts and likely deactivate them, we used FIMS to characterize the carbonaceous deposits on the spent catalysts from DOE's Wilsonville facility.(14) The spent catalyst extrudates (Ni/Mo on alumina) were washed with tetrahydrofuran (THF) to remove any weakly adsorbed oil, and only tenaciously held materials remained. The washed extrudates were analyzed by heating a single pellet in the direct insertion probe of the mass spectrometer, and the evolved volatiles were then field ionized to produce the molecular ions. The spectra appeared very much like that in Figure 2 above, except that they are dominated not by PAH, but by the corresponding azaaromatics and their alkylated derivatives. These basic compounds are expected to adsorb strongly to alumina and

may have indeed caused the deactivation. Peaks due to some purely hydrocarbon structures such as alkyl pyrenes and perylenes were also present, albeit at lower intensity than the azoaramatics.

CONCLUSIONS

Field ionization mass spectrometry, through definitely not a panacea, has been very useful in a wide range of fossil-fuel-related research. The vapor pressure requirements for desorption/ ionization under FIMS conditions definitely constitute a limitation relative to methods such as field desorption and fast atom bombardment. However, with FIMS the extent of fragmentation is often much lower than one typically observes in FAB spectra. Furthermore, the variation in substrate sensitivity is usually much less for FIMS, providing a reasonably accurate quantitative analysis without the necessity for calibration.

When field ionization is coupled with mass analysis at nominal mass resolution, it is of course often not strictly able to provide definitive molecular formula identification, let alone structural identification. However, observation of homologous series, together with any knowledge of the structural types present in the product mixture and the results of previous compound-class separation/FIMS analyses, often provide very good "provisional" identification of the structures at various masses. Furthermore, for very complex mixtures, the absence of discrimination between structural isomers can collapse hopelessly complex spectra to provide useful analyses. (For instance, considering that there are 15 different isomers among the dimethylpyrenes alone, it will generally be very useful, even in systems much simpler than coal liquefaction products, to have these isomers grouped together at m/z 230.) In the examples reviewed above, a complete separation of structural and geometric isomers, such as could be provided in principle by a chromatography-MS technique, would have presented severe problems in data-handling and chemical correlation and provided little, if any, net benefit. In summary, we find that field ionization mass spectrometry, coupled with judicious use of prior separation techniques, can provide useful information on the extremely complex mixtures that constitute coal liquefaction fractions.

Acknowledgment. Support for various aspects of this work from the U.S. Department of Energy, Electric Power Research Institute, Advanced Fuel Research, and several other commercial concerns is gratefully acknowledged.

REFERENCES

1. Beckey, H. D.; *Field Ionization Mass Spectrometry*, Pergammon Press, Elmsford , NY, 1971.
2. St.John, G. A.; Buttrill, S. E., Jr.; Anbar, M., in *Organic Chemistry in Coal*, J. Larsen, Ed.; ACS Symposium Series 71, Washington, D. C., 1978, p. 223.
3. Malhotra, R.; McMillen, D. F.; Huestis, D. L. *Am. Chem. Soc., Div. Fuel Chem. Preprints*, **1991**, *36*(3), 1252.
4. Solomon, P. R.; Serio, M. A.; Deshpande, G. V.; Kroo, E. *Energy Fuels* **1990**, *4*, 42.
5. Schulten, H-R.; Marzec, A.; Czajkowska, S. *Energy Fuels* **1992**, *6*, 103.
6. Boduszynski, M. M *Energy Fuels* **1988**, *5*, 597.
7. Rahimi, P. M.; Fouda, S. A.; Kelly, J. F.; Malhotra, R.; Malhotra, R. *Fuel* **1989**, *68*, 422.
8. Ueda, K.; Matsui, H.; Malhotra, R.; Nomura, M. *J. Japan Pet. Inst.* **1991**, *34*, 53.
9. McMillen, D. F.; Chang, S. -J.; Fleming, R. H.; Laine, R. M.; Malhotra, R.; Nigenda, E.; Ogier, W., "Effect of of Amine Solvents and Oxygen Functionalities on Coal Liquefaction," EPRI Research Project 2147-5 1985.
10. Sullivan, R. F.; Boduszynski, M. M.; Fetzer, J. C. *Energy Fuels* **1989**, *3*, 603.
11. Malhotra, R.; McMillen, D. F.; "Characterization of Coal Liquids," Final Report prepared for Consolidation Coal Co., under U.S. DOE Contract No. DE-AC22-89PC89883, 1991.
12. Malhotra, R.; McMillen, D. F.; Huestis, D. L. *Am. Chem. Soc., Div. Fuel Chem. Preprints*, **1992**, *37*(2), 908.
13. Brandes, S. D.; Winschel, F. P.; private communication, 1992.
14. Stohl, F. V., *Am. Chem. Soc., Div. Fuel Chem. Preprints*, **1988**, *33*(3), 210.

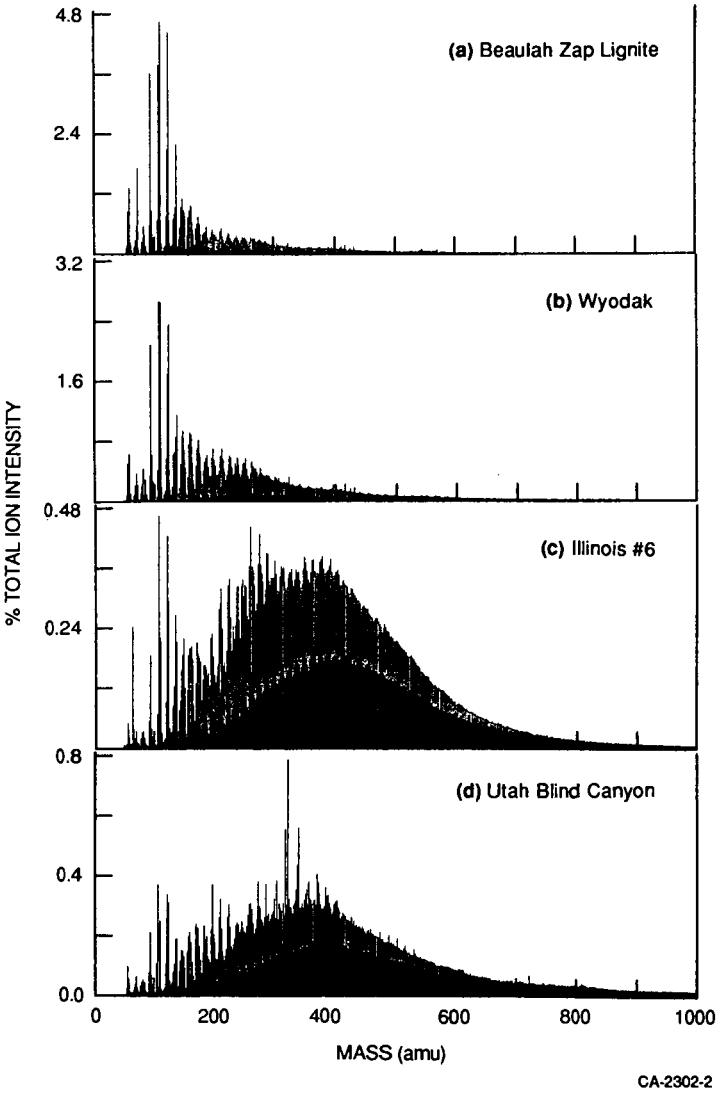

Figure 1. FI-Mass spectra of the four lower rank coals from the Argonne Premium Coal Sample Program.

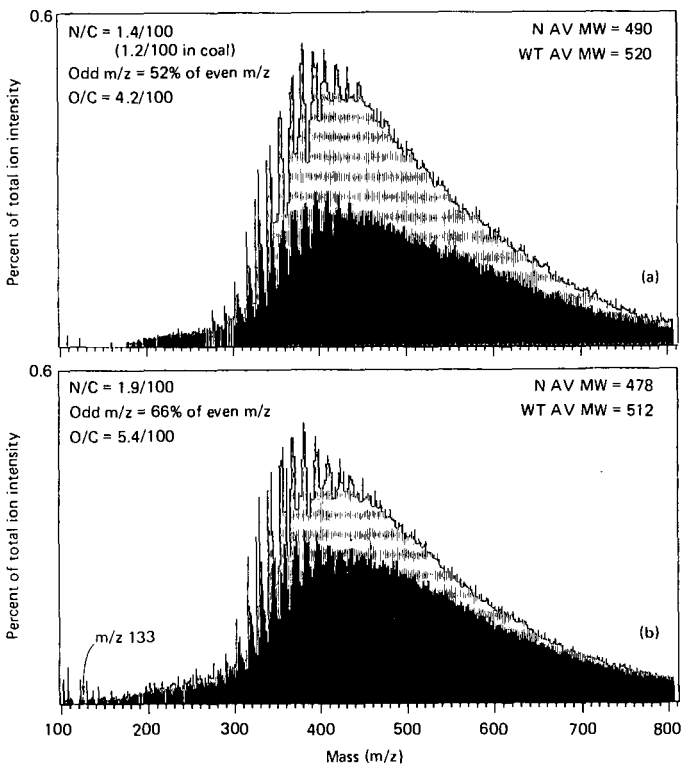

Figure 3. FI-Mass Spectrum Showing Increased Intensity of Odd Masses When THQ is Used in Liquefaction Solvent.

(a) 1090° F+ residue, without THQ in liquefaction solvent for Wyodak coal.
(b) 090°F+ residue obtained with 16% THQ in liquefaction solvent.
Spectra in this figure are corrected for ^{13}C contributions to odd masses on the basis of an average 86 wt% carbon.

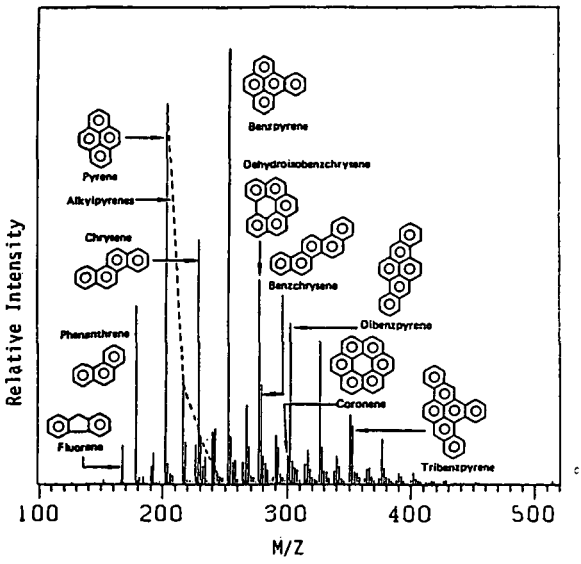

Figure 2. FI-Mass Spectrum of PCAH Fraction from Coal Tar

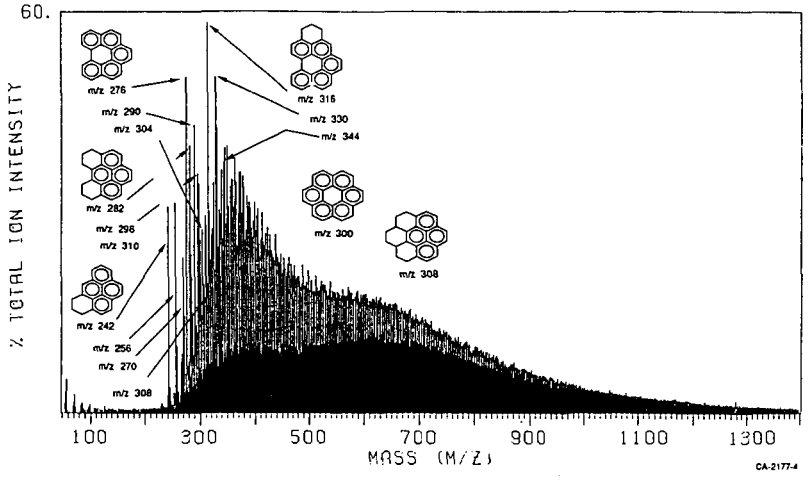

Figure 4. FI-Mass Spectrum of the 850°F+ Recycle Oil from Pittsburgh Coal (Wilsonville Run 259) Showing the Prominent PCAH Structures in the 200-350 Da Range.

APPLICATION OF ^{252}Cf-PLASMA DESORPTION MASS SPECTROMETRY TO ANALYSIS OF DIRECT COAL LIQUEFACTION HEAVY PRODUCTS.

Andrzej R. Lapucha and *John W. Larsen*

Lehigh University, Department of Chemistry,
Bethlehem, PA 18015

Keywords: Plasma Desorption Mass Spectrometry, Coal Liquefaction.

ABSTRACT

Californium Plasma Desorption Mass Spectrometry (PDMS) has been used to analyze heavy distillation residues obtained from direct coal liquefaction processes. The characteristics of the ^{252}Cf-PDMS technique for the analysis of these non-polar materials were determined, especially the ionization efficiency of molecules of different chemical type. The molecular weight distributions of several THF soluble 850°F+ materials ("resids") from the Wilsonville pilot plant were determined. These data were compared to the results obtained by Field Ionization Mass Spectrometry (FIMS) and Gel Permeation Chromatography (GPC). In general, number average molecular weights for all three techniques agreed well. Both GPC and PDMS give higher weight average molecular weights than FIMS and agree with each other for weight averages below 1500 amu.

INTRODUCTION

Field ionization and field desorption mass spectrometry have been applied to the analysis of coal liquefaction products.[1-3] ^{252}Cf-PDMS, a different kind of mass spectrometry,[4-6] has been incompletely explored for the analysis of coal products.[7,8]

The ^{252}Cf plasma desorption technique utilizes energetic fission fragments from the decay of ^{252}Cf to volatilize and ionize a solid sample. The ionization source is typically a 10-μCi californium sandwiched between two thin sheets of nickel foil. A sample is dissolved in an appropriate solvent and the solution is electrosprayed over a 1 cm^2 area on an aluminized poly(ethylene terephthalate) foil (Mylar disk). ^{252}Cf-PDMS is capable of producing mass spectra consisting primarily of molecular ions for a wide variety of compounds, including amino acids,[4] peptides,[9] nucleotides,[10] geoporphyrins,[11] polynuclear aromatic hydrocarbons,[12] polyethers[13] and other synthetic polymers.[14-16]

Gel Permeation Chromatography (GPC), also known as Size Exclusion Chromatography (SEC), has been used to determine the molecular weight distribution of coal extracts.[17-19] The limits of the method and lack of calibration standards for coal derived materials are well known.[20] Relative molecular weights values obtained using the same standards (often polystyrenes) and conditions can be satisfactorily compared.

EXPERIMENTAL

Mass spectra were obtained using a BIO-ION 20 commercial time-of-flight mass spectrometer (Bio-Ion Nordic, Upsala, Sweden) equipped with PDP-11 microcomputer data acquisition system (DAS). The instrument is

equipped with 10 μCi ^{252}Cf source and a short 15 cm flight tube. We used a positive 10kV acceleration voltage and the time resolution was set to 1ns/channel. Data collection was terminated at a preset count and 10^6 primary ion events were acquired. This took about 12 minutes. The samples of analyzed distillation resids were dissolved in THF (10 mg/mL) and 40 μl of each solution was electrosprayed onto nitrocellulose coated Mylar disks using the BIO-ION electrospray apparatus. Thin homogenous coverages were obtained. We also developed a software package (CFINT) that can be used on any IBM compatible PC to calculate the number average and weight average molecular weights using data imported from the Bio Ion 20 PDP-11 computer. In addition, this software package allows us to subtract the background spectrum which comes from the mylar film. The software supplied with the spectrometer also adds counts from surrounding channel to enhance the signal-to-noise ratio. This is undesirable for the determination of molecular weight distribution and has been removed from our data analysis.

The molecular weight distributions of five selected resids (#7, #13, #16, #19 and #22) provided by Consolidation Coal Company dissolved in pyridine were measured by a computer interfaced GPC with a mass sensitive detector. The components of the instrument were all commercially available. It consists of a Waters Liquid Chromatograph (Model ALL 201) equipped with high pressure pump, injector, and four μ-styragel columns (10^4 + 10^3 + 500 + 100 Å). The mass detector, built by Applied Chromatography Systems Ltd. (Model 750/14), works by nebulizing the liquid stream emerging from the column and then passing this uniform distribution of droplets down a heated tube in a flow of dry nitrogen, evaporating the solvent. The resulting solid passes a light scattering detector whose output is directly proportional to the mass of solid material passing in front of it. Between the mass detector and the columns is a digital thermal pulse flow meter. The outputs from the mass sensitive detector and the flow meter are directed to a Zenith Model 158 microcomputer, the former through a 12 bit resolution A to D converter (Data Translation Model DT 2805). The programs for data collection and manipulation were written in a high level language using the Asyst package (McMillan Software Co.). The instrument was carefully calibrated with polystyrene standards. HPLC grade pyridine was used as the eluting solvent with flow rate of ca. 1 mL/min. 50 μl of each sample with concentration of 10 mg/mL was loaded through the injector valve. For each run data were collected for the period of one hour.

RESULTS AND DISCUSSION

Five THF soluble samples of solid 850°F+ materials ("resids") obtained in the Wilsonville pilot plant during direct liquefaction of different coals were analyzed by ^{252}Cf - Plasma Desorption Mass Spectrometry. Molecular Weight Distribution curves were obtained and number average molecular weights (M_n) and weight average molecular weights (M_w) were calculated. These data are compared to the results obtained by Field Ionization Mass Spectrometry and Gel Permeation Chromatography.

Figure 1 shows the PDMS spectra of Mylar film (a), the software converted spectrum of resid #7 which includes the Mylar background (b), and of resid #7 with the Mylar background subtracted (c). As can be seen only traces of Mylar background remain in the range between 0-100 m/z.

Despite different coal feeds and processing conditions, all the samples show similarities. Table 1 summarize origin and physico/ chemical parameters of the analyzed recycle products. In Table 2. and Fig. 2 (a-c) PDMS results are compared with those obtained from FIMS and GPC. The PDMS M_n values are essentially identical to those from FIMS and GPC. PDMS M_w values are about twice the field ionization results. The FIMS spectra do not show any peaks with molecular weights higher than 1200 - 1300 m/z. Both PDMS and GPC detect molecules having molecular weight greater than 1300 amu. In fact, the PDMS intensity does not return to zero before 2000-2500 m/z. Based on these observations, much higher M_w values can be expected from PDMS and GPC. Probably the field ionization technique is not able to efficiently volatilize high boiling, high molecular weight species. GPC M_w values are higher than the corresponding PDMS results with an exception of resid #19. There are three possible explanations for this phenomenon. 1) The integral of GPC molecular weight distribution curve is very sensitive to small amounts of high molecular weight analytes which are not detected by PDMS. This leads to enormously high M_w values. 2) The recycle oils are fragmenting in PDMS. 3) PDMS is capable of producing maes spectra from a wide variety of natural products but less polar polymeric materials very often give low responses or no peaks at all. PDMS may not be detecting all of the sample.

As can be seen in Table 2, the molecular weights of Resid #19 are much lower then of the other samples. This sample has the highest percentage of condensed aromatics and is low in sulphur and beta and gamma protons (Table1). For this sample PDMS and GPC M_n and M_w values are in overall good agreement. Resids #7, #13 and #22 contain relatively low amounts of condensed aromatics, high numbers of cyclic and alkyl beta and gamma protons, and the highest percentage of oxygen. These resids show higher weight average molecular weights in GPC than in PDMS. The relatively low polarity and highly polymeric nature of these fractions are both unfavorable factors for PDMS. The instrument may not be providing a reliable analysis.

CONCLUSIONS

^{252}Cf-PDMS ie easy to operate, fast and less expensive than most other mass spectrometric techniques and is suitable for quantitative measurements of the molecular weight distributions of some coal conversion products.

Comparison of PDMS molecular weight distributions to the GPC and FIMS shows that, in general, number average molecular weights agree well. Both GPC and PDMS give higher weight average molecular weights than does FIMS.

ACKNOWLEDGMENTS

We thank Dr. Susan D. Brandes at the Consolidation Coal Company for providing samples for this study. This research was financed by the subcontract from Consolidation Coal Co. under DOE contract DE-AC22-89PC89883. We are most grateful to Dr. Patrick Wernett for writing the software used and to William Anderson for his instrumental advice and expertise.

REFERENCES

1. Aczel, T.; Laramee, J.; Hansen, G.J. in *Proceedings of the 30th Annual Conference on Mass Spectrometry and Allied Topics*, p.808 (1982)
2. Aczel, T.; Dennis, L.W.; Reynolds, S.D. in *Proceedings of the 35th Annual Conference on Mass Spectrometry and Allied Topics*, p.1066 (1987)
3. Larsen, B.S.; Fenselau, C.C.; Whitehurst, D.D.; Angelini, M.M. *Anal. Chem.* (1986), **58**, 1088
4. MacFarlane, R.D.; Torgeson, D.F. *Science* (1976), **191**, 920
5. MacFarlane, R.D. *Anal. Chem.* (1983), **55**, 1247 A
6. Cotter, R.J. *Anal. Chem.* (1988), **60**, 781 A
7. Lytle, J.M.; Tingey, G.L.; Macfarlane, R.D. *Anal. Chem.* (1982), **54**, 1881
8. Zingaro, R.A.; Macfarlane, R.D.; Garcia, J.M.; Vindiola, A.G.; Zoeller, J.H. in *Chemistry of Coal Liquefaction*, ACS Symposium Ser., Vol. 29, No 5, p. 22 (1984)
9. Alai, M.; Demirev, P.; Fenselau, C.; Cotter R.J. *Anal. Chem.* (1986), **58**, 1303
10. Scanlan, G.; Benson, L.; Tsarbopoulos, A.; Jardine, I. in *Proceedings of the 36th Annual Conference on Mass Spectrometry and Allied Topics*, Denver, CO. (1987), 80
11. Wood, K.V.; Bonham, C.C.; Chou, M.M. *Energy Fuels* (1990), **4**, 747
12. Zoeller, J.H.; Zingaro, R.A.; Macfarlane, R.D. *Int. J. Mass Spectrom. Ion Processes* (1987), **77**, 21
13. Chait, B.T.; Shpungin, J.; Field, F.H. *Int. J. Mass Spectrom. Ion Processes* (1984), **58**, 121
14. MacFarlane, R.D.; McNeal, C.J; Martin, C.R. *Anal. Chem.* (1986), **58**, 1091
15. Gehrig, C.C.; Wood, K.V. *The 38th ASMS Conference on Mass Spectrometry and Allied Topics* (1990), 255
16. Keough, T.; Lacey, M.P. *Anal. Chem.* (1991), **63**, 1482
17. Larsen, J.W.; Choudry, P. *J. Org. Chem.* (1979), **44**, 2856
18. Larsen, J.W.; Mohammadi, M.; Yiginsu, J.; Kovac, J. *Geochim. Cosmochim. Acta* (1984), **48**, 135
19. Larsen, J.W.; Wei, Y.C. *Energy Fuels* (1988), **2**, 344
20. Buchanan, D.H.; Warfel, L.C,; Biley, S.; Lucas, D. *Energy Fuels* (1988), **2**, 32

Table 1. Analysis of the Soluble Portion of the Distillation Resids

Weight %	Res.#7 Ill.#6	Res.#13 Tex.Lign.	Res.#16 Pitt.#8	Res.#19 Wyodak	Res.#22 Wyodak
C	88.75	89.39	90.54	90.90	89.46
H	8.15	7.12	6.74	6.32	6.69
N	0.66	1.23	0.91	1.11	1.13
S	0.14	0.09	0.39	0.03	0.05
O	2.30	2.17	1.42	1.64	2.67
Proton Dist.(%)					
Cond. Aromatics	16.7	22.4	26.1	32.2	22.5
Uncond. Aromatics	4.4	4.3	5.4	5.1	5.1
Cyclic Alpha	17.9	19.2	18.9	18.1	16.8
Alkyl Alpha	9.4	9.5	9.4	9.2	9.3
Cyclic Beta	18.6	15.9	14.8	13.6	14.4
Alkyl Beta	20.4	18.5	14.6	13.9	21.2
Gamma	12.5	10.3	10.8	7.8	10.8
Phenolic -OH Conc.	0.50	0.71	0.69	0.67	0.89

Table 2. Number Average and Weight Average Molecular Weights Obtained from Field Ionization Mass Spectrometry, Plasma Desorption Mass Spectrometry and Gel Permeation Chromatography.

Resid #	FIMS	PDMS	GPC	FIMS	PDMS	GPC
	M_n			M_w		
7	620	600	600	730	1370	1930
13	570	570	570	680	1340	2050
16	590	590	610	690	1340	1840
19	-	580	500	-	1300	1430
22	-	600	700	-	1460	2160

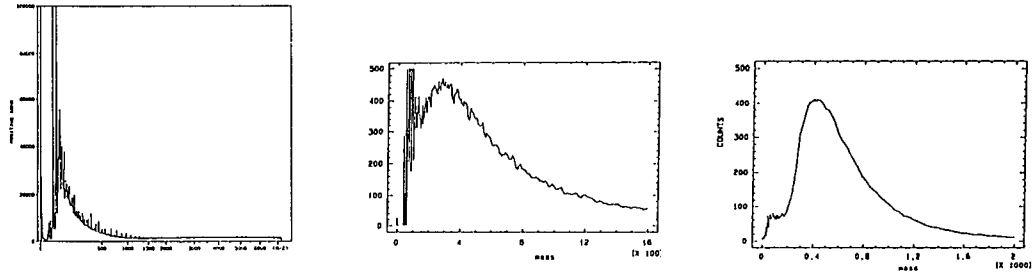

Figure 1. PDMS Spectra of Mylar Backround (a), Software Converted Spectrum of Resid #7 which Include Mylar Background (b) and Resid #7 with Mylar Background Subtracted (c).

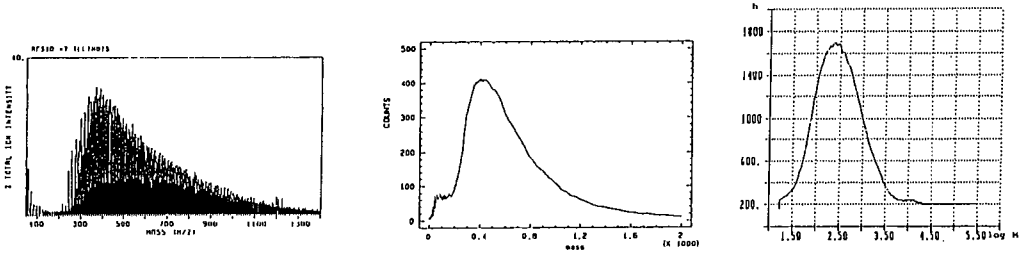

Figure 2. FIMS (a), PDMS (b) and GPC (c) Molecular Weight Distribution of Resid #7

TWO-DIMENSIONAL HPLC ANALYSIS OF FCC DECANT OILS

Y.Liu, S.Eser, P. G. Hatcher
Fuel Science Program, Department of Materials Science and Engineering
The Pennsylvania State University, University Park, PA 16802

Keywords: Decant oil, HPLC, mass spectrometry

INTRODUCTION

Fluid catalytic cracking decant oils (FCC-DO) are used as feedstocks for producing highly graphitizable petroleum cokes (needle cokes) in delayed cokers[1]. The chemical composition of decant oils depends on the nature of catalytic cracker feeds and the conditions used in the crackers. It is known that the quality of the needle coke product is, in turn, strongly dependent on the chemical constitution of the starting decant oil. Therefore, the need for a detailed analysis of FCC-DO is well recognized; elemental analysis, various solvent fractionation techniques, NMR, and gas chromatography and gas chromatography/mass spectrometry (GC/MS) have been used to analyze these materials[2,3]. One limitation of ordinary GC and GC/MS methods is that heavy ends and some polar compounds cannot be analyzed because of their low volatility.

High performance liquid chromatography (HPLC) and HPLC/MS can be used to separate and analyze high molecular weight and polar fractions of feedstocks[4,5]. However, traditional HPLC instruments with mono-UV wavelength detectors are not amenable to identify the molecular components of the fractions eluted from the LC columns. The development of on-line HPLC/MS has greatly facilitated the analysis of heavy hydrocarbons without, however, the capability of distinguishing between the isomers of polycyclic aromatic compounds[6]. A distinct advantage of a two dimensional HPLC technique, which provides UV spectra of separated fractions as a function of time, is its capability to identify the molecular components of the eluates, including the isomers of polycyclic aromatic compounds. In this paper, we present the results of a two dimensional HPLC and heated probe/MS analyses of some FCC-DO samples.

EXPERIMENTAL

HPLC analyses were carried out with a Waters 600 micro-flow syringe pump and a 4.6x150 mm column packed with C-18 stationary phase. A Waters Model 990 UV detector was used to collect UV spectra ranging from 200 nm to 400 nm. A mixture of distilled water and acetonitrile (EM Science, HPLC grade) was used as mobile phase. Decant oil samples and some model compounds were diluted in acetonitrile (4μg/μL), and 1 μL sample was injected. The scan time used was 50 ms and every four scans were averaged to obtain a UV spectrum. At a column temperature of 50 °C and mobile phase flow rate of 1 mL/minute, the separation of components took 40-50 minutes, collecting 2400-3000 UV spectra during each analysis. Two dimensional and contour graphs as well as single UV spectra obtained from each analysis were plotted and studied.

Selected FCC-DO were also analyzed by a heated probe/MS technique to assist in component identification. A KRATOS MFC 1500 instrument was used for these analyses with electron impact ionization potential of 70 eV. Samples were placed in a probe which was introduced into the MS source. The probe was heated from 50°C to 250°C at a heating rate of approximately 15°C/min and mass spectra were collected at every 2.5 °C temperature interval during heating.

RESULTS AND DISCUSSION

Before analyzing the FCC-DO samples, mixtures of six model compounds were analyzed by HPLC. Figure 1a and 1b show the two dimensional plots of the two ternary mixtures of naphthalene/anthracene /fluoranthene and phenanthrene/pyrene/chrysene, respectively. The

abscissa in the plots represents the retention time in the column, and the ordinate shows the UV wavelength. The UV absorption intensity is shown on the z axis. Samples of naphthalene, anthracene and fluoranthene were eluted at 4.90, 8.45 and 10.45 minutes, respectively, and well separated, as shown at the top of Figure 1. Similarly, phenanthrene, pyrene and chrysene, shown at the bottom of Figure 1, are also well separated with retention times of 7.75, 10.90 and 14.20 minutes, respectively. In addition to the different retention times, these six model compounds have distinctly different UV spectra which facilitate their positive identification in a mixture. For example, the isomers, phenanthrene and anthracene which give exactly the same mass spectra have quite different UV absorption characteristics; and pyrene and its homologues can be easily identified by the peaks located around the 340 nm region.

Figure 2 shows a classification of various PAH's according to the number of rings, cata- and peri-condensation, and linear versus angular configurations which are responsible for different UV absorption characteristics. For each aromatic compound shown in Figure 2, UV absorption wavelength increases as the number of aromatic rings increases. Also, one can distinguish between the aromatics of the same ring number with respect to differences in their molecular configurations, e.g., linear PAH's extend their absorption to the longer UV wavelengths than the angular PAH's.

A good separation of the components of the FCC-DO samples was obtained at a column temperature of 50°C and water/acetonitrile ratio of 2/3. Adding water to acetonitrile up to an optimum 40% in the mixture steadily improved the separation of the constituent compounds. All the FCC-DO samples were analyzed under the same conditions.

Figure 3 shows a two-dimensional plot of the HPLC results obtained for FCC-DO #1, indicating the series of identified compounds. One should note that the UV absorption intensities for the components in a mixture should not be taken as a quantitative measure of concentrations, since the observed intensity is not only a function of concentration,but also a function of molecular structure for each compound. Figure 4 shows the data for FCC-DO #1 as a contour graph. Contour lines in Figure 4 represent UV absorption intensities as a function of retention time and wavelength . The more lines cross a given region, the higher is the absorption intensity. One can see in Figure 4 that the highest intensity peaks are located at retention times of 11, 15 and 16 minutes. Peaks located around 21-22 minutes also appear as relatively strong but broad peaks. The use of a contour plot for plotting the data makes it easy to determine the right wavelength through which a representative HPLC chromatogram can be obtained. The trace shown at the bottom of Figure 4 is an HPLC chromatogram of the sample at a UV wavelength of 254 nm, showing a good separation of the constituent compounds. One should note that the identified compounds in Figure 4 are only the aromatic compounds present in FCC-DO #1, since aliphatic compounds do not absorb UV radiation in the wavelength range studied here. It is known that decant oils can contain high concentrations of paraffins and alicyclic compounds[2,3].

The UV spectra corresponding to the retention times of strong peaks seen in Figure 4 are plotted in Figure 5 to identify the individual compounds with respect to their retention time and the attendant UV spectra. The solid line in Figure 5a is assigned to phenanthrene. The spectrum shown with a dotted line in Figure 5a is assigned to pyrene structures. As different from the spectrum of pure pyrene, the dotted line trace has a shoulder at 260 nm which may be assigned to alkyl substituted pyrenes or phenanthrenes. The third spectrum shown in Figure 5a with a broken line can be attributed to chrysene and benzo(c)phenanthrene. Any contribution from naphthacene or benzo(a)anthracene can be ruled out, since there is no UV absorption beyond 340 nm in this spectrum. All of these four ring aromatics have the same molecular weight of 228.29 and similar fragmentation patterns which make their differentitation by mass spectroscopy very difficult.

Figure 5b shows the UV spectra obtained at retention times of 15.15, 16.10 and 21.80 minutes. The three spectra obtained at retention times of 15.15 minutes (solid line), 16.1 minutes (dotted line), and 21.8 minutes (broken line) have similar traces to the pyrene spectrum with a clear shift to longer wavelengths, and can be assigned to benzo- and alkyl- pyrenes. One should note again

that MS alone would not readily distinguish between the alkyl substituted homologues of pyrene, fluoranthene, 1,2-benzofluorene, and 3,4-benzofluorene. The molecular weight of pyrene and fluoranthene is 202.26, benzofluorenes is 216.28 and the alkylated homologues of these compounds have molecular weights of 216.28, 230.29, 244.31 and 258.33, etc., with similar fragmentation patterns.

To compare with the HPLC data, a heated probe/mass spectroscopy analysis was carried out on the same decant oil sample. The collection of mass spectra was started at 50 °C, obtaining one mass spectrum at every 2.5 °C interval up to 250 °C. As the probe temperature increased, the decant oil sample evaporated gradually starting with lower boiling point fractions and progressing to higher boiling materials with reasonable separation. Major compounds in FCC-DO #1 were identified by their mass spectra, pointing out the two most dominant compound series. One series has m/z=202+14n (n=0,1,2,3...) (pyrene+ alkylpyrenes), and the other has m/z=252+14n (n=0,1,2,3...) (benzopyrene + alkylbenzopyrenes). Typical mass spectra of these compound series collected at probe temperatures of 70 °C and 120 °C are shown in Figure 6a and 6b, respectively. Although the separation processes involved in HPLC and heated probe/MS are different, the general order of compounds released from LC column and the heated probe appears to be the same, controlled apparently by the molecular weight of the constituent molecules.

Comparing the HPLC and heated probe/MS data, one can see that the first major HPLC fraction eluting at 11 minutes is pyrene (MW=202.26), which corresponds to a probe temperature of 70 °C in the mass source. As the temperature of the probe increases, compounds with m/z=228+14n (n=0,1,2,3...) emerge starting with chrysene (MW=228.29) detected at HPLC elution time of 14.2 minutes, followed by the second major fraction with m/z=252+14n (n=0,1,2,3...) namely, benzopyrene at 15.2 minutes and alkylbenzopyrenes starting at 16.1 minutes of LC retention time. At a probe temperature of 165 °C, a compound series of m/z=290+14n (n=0,1,2,3...) appears with a corresponding LC retention time of 21.8 minute, assigned as dibenzopyrene and its alkyl homologues.

Figures 7 shows the contour plots of the HPLC data on two other decant oil samples, FCC-DO #2 and FCC- DO #3. By comparing the contour graphs of the three decant oil samples, one can clearly see that FCC-DO #2 and FCC- DO #3 contain more lower molecular weight aromatic compounds than FCC-DO #1. These lighter compounds consist of naphthalene, alkylnaphthalenes, phenanthrene and alkylphenanthrenes, which were eluted from the HPLC column in less than 10 minutes.

CONCLUSIONS

A two-dimensional HPLC technique is useful for separation and identification of aromatic compounds present in fluid catalytic cracking decant oils. This method combined with a heated probe/MS analysis provides a positive, and convenient identification of high-molecular-weight aromatic compounds. The analysis of three different FCC-DO's has shown significant variations in the composition of their aromatic fractions.

ACKNOWLEDGEMENTS

This study is part of a research project sponsored by the Carbon Graphite Group, Inc., Pittsburgh, PA. Helpful and stimulating discussions with Samuel Hoff, Peter Lefrank, and James Baldwin are gratefully acknowledged. We thank Barton Schober and Bernard Gordon of Polymer Science Program at Penn State for their help with the HPLC experiments. Jeffrey Blank and Robert Minard of the Department of Chemistry at Penn State provided the data from the heated probe/MS experiments.

REFERENCES

1. Stocks, C. A. and Guercio, V. J., *Erdöl Kohle Erdgas Petrochem.* **38**, 31, 1985.

2. Nesumi, Y., Oyama, T., Todo, Y., Azuma, A., Mochida, I. and Korai, Y ., *Ind. Eng. Chem. Res.* **29** (9), 1793, 1990.
3. Eser, S., Liu, Y., and Hatcher, P.G., Unpublished data.
4. Hsu, C. S., McLean , M. A., Qian, K., Aczel T., Blum S. C., Olmstead, W. N., Kaplan, L. H., Robbins, W. K., and Schulz, W. W., Energy & Fuel **5**, 395, 1991.
5. Vreuls, J. J., de Jong, G. J., and Th. Brinkman, U. A., Chromatographia **31**, 113, 1991.
6. Herod, A. A., Stokes, B. J., Major, H. J., and Fairbrother, A. E., Analyst **113**, 797, 1988.

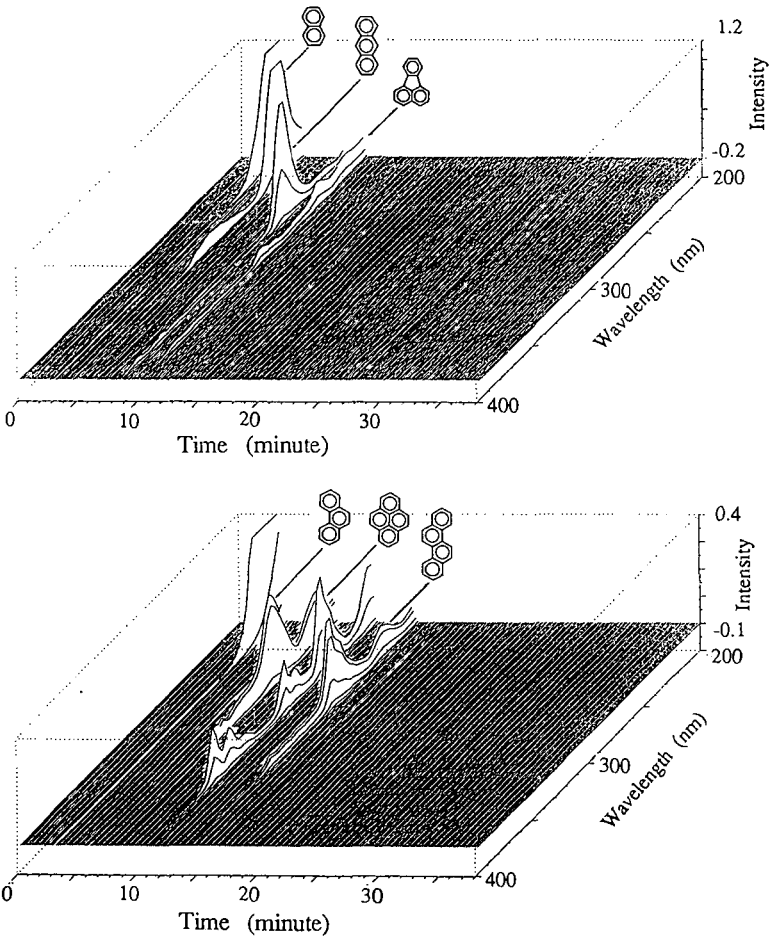

Figure 1. Two-dimensional HPLC plots for the two ternary mixtures naphthalene/anthracene/ fluoranthene (top, a) and phenanthrene/pyrene/chrysene (bottom,b).

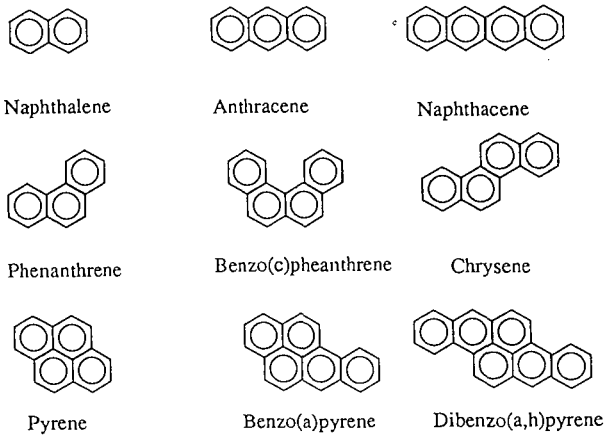

Figure 2. Different aromatic compounds found in FCC-DO.

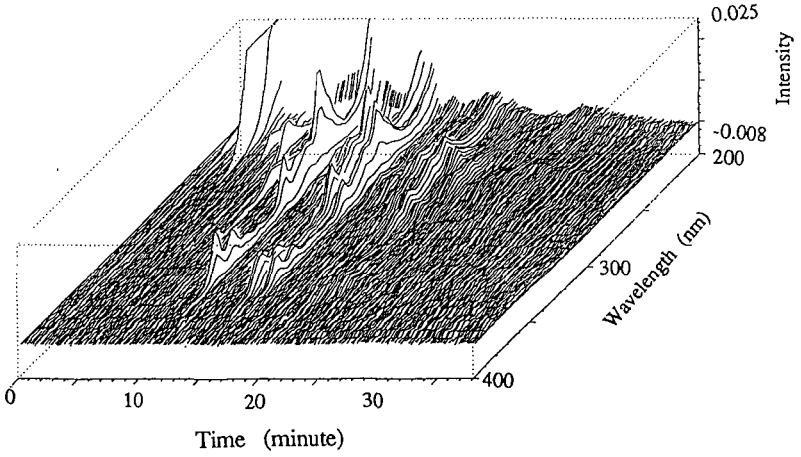

Figure 3. Two-dimensional HPLC plots for the sample FCC-DO #1.

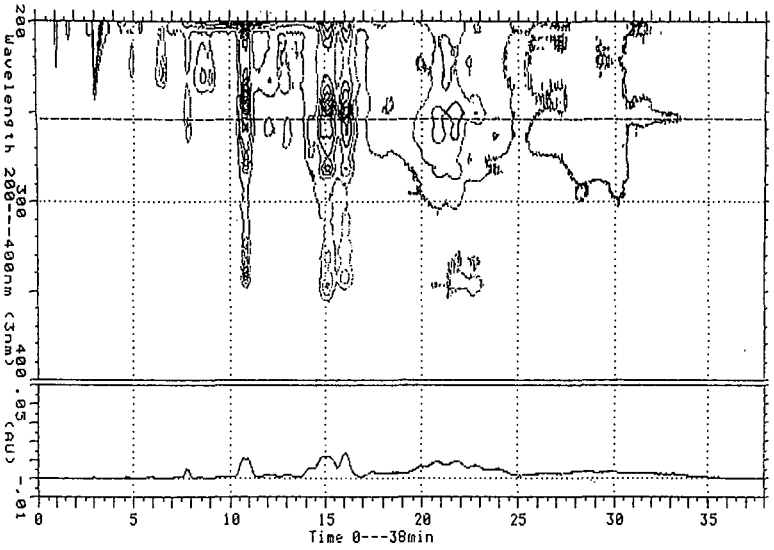

Figure 4. The HPLC contour plot for FCC-DO #1.

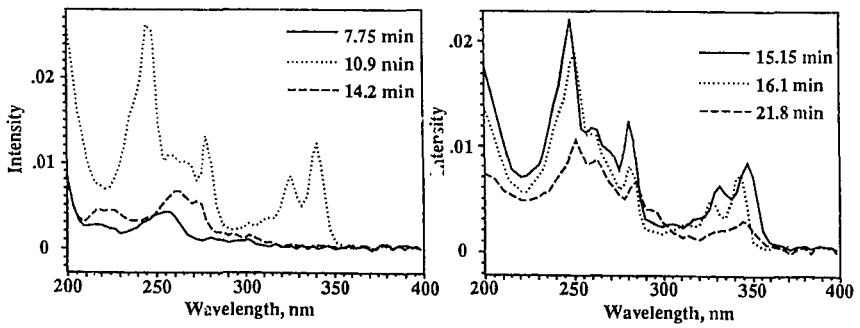

Figure 5. UV spectra of the compounds which elute at the indicated retention times.

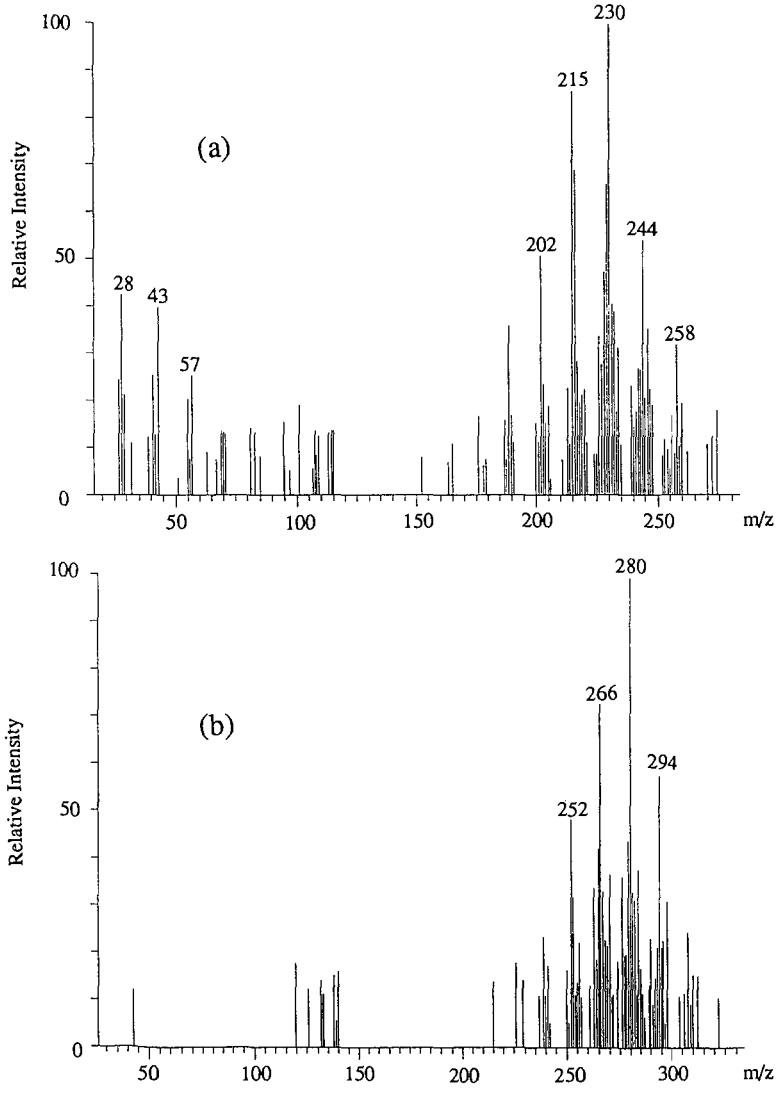

Figure 6. Mass spectra for sample FCC-DO #1 from the heated probe/MS experiment.

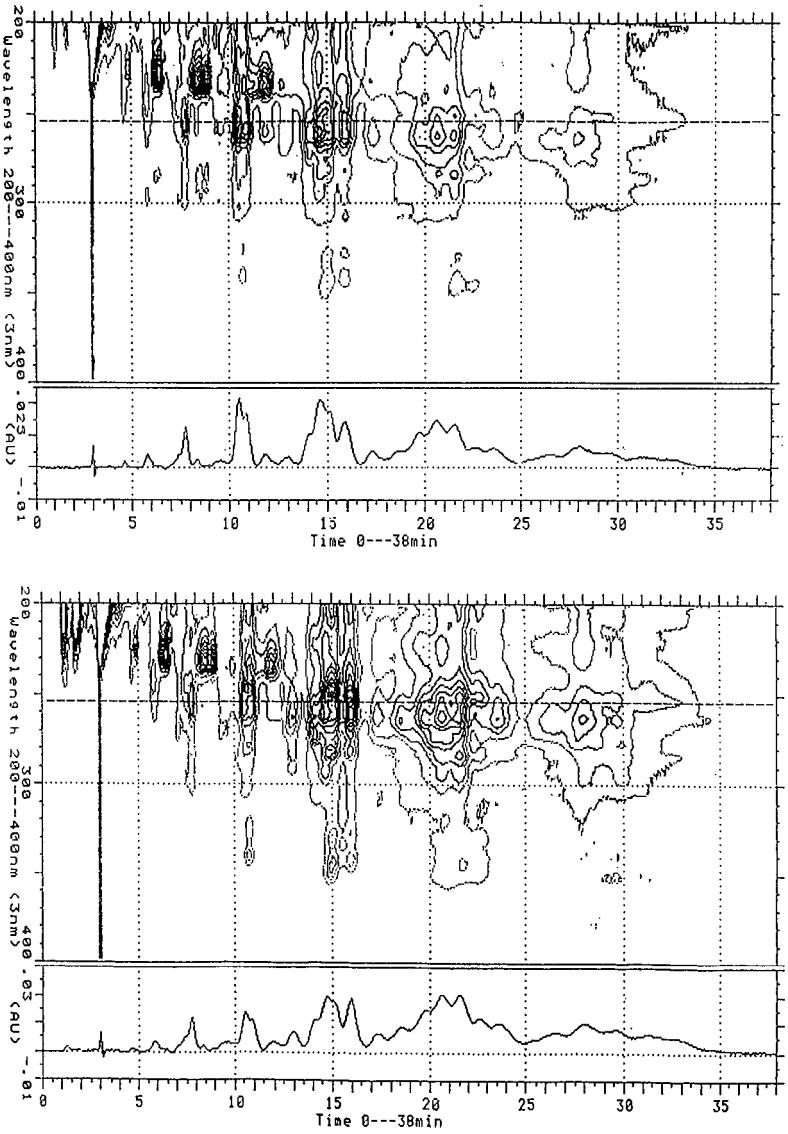

Figure 7. The HPLC contour plot for FCC-DO #2 (top) and FCC-DO #3 (bottom).

Characterization of Coal Structure and Low-Temperature Liquefaction Reactions by Pyrolysis-GC-MS in Combination with Solid-State NMR and FTIR.

Ajay K. Saini, Chunshan Song, Harold H. Schobert and Patrick G. Hatcher

Fuel Science Program, Department of Material Science and Engineering, 209 Academic Projects Building, The Pennsylvania State University, University Park, PA 16802, USA

Keywords: Solid-state ^{13}C NMR, Pyrolysis-GC-MS, Low-Temperature Liquefaction

INTRODUCTION

Coal conversion into liquids is an extremely complex process and involves both chemical and physical transformations. The dissolution of coal requires homolytic cleavage of bonds to yield free radicals and their immediate stabilization with a hydrogen, otherwise they may recombine or crosslink to form more refractory material. The rate of thermal fragmentation is mainly determined by coal reactivity and reaction conditions. Low-rank coals such as Wyodak subbituminous coal are more reactive than had been thought before. The thermally initiated reactions of coal can take place very rapidly (1,2) and especially for low-rank coals, can occur at lower temperatures (3,4). The previous work in our laboratory has demonstrated that more bonds in low-rank are thermally broken at lower temerature as compared to bituminous coals, and a concept of bond energy distribution has been developed from temperature-programmed pyrolysis (3,4).

It has been also demonstrated that the combination of low-temperature catalytic reaction followed by the high-temperature catalytic reaction using dispersed molybdenum catalyst significantly enhanced coal conversion (5-12). The work presented here is a part of an on-going project on the effects of low-temperature catalytic pretreatment on coal structure and reactivity in liquefaction. Recently, we have demonstrated that the combined use of solid-state NMR and pyrolysis-GC-MS has the potential to reveal the major and minor structural changes in the macromolecular network of coal induced by liquefaction (13, 14). The specific objectives of the present work are to identify the basic changes in coal structure induced by catalytic and thermal pretreatments by using modern analytical techniques.

EXPERIMENTAL

The coal used was a Wyodak subbituminous coal provided by the Penn State Sample Bank (DECS-8). The characteristics of this coal are as follows: 32.4% volatile matter, 29.3 % fixed carbon, 9.9% ash and 28.4% moisture, on a as-received basis; 75.8% C, 5.2% H, 1.0% N, 0.5% S and 17.5% O, on a dmmf basis. The coal was dried in a vacuum oven at 100°C for 2 h before use.

The liquefaction of coal was carried out at 300 and 350°C with and without catalyst (ammonium tetrathiomolybdate,1% wt. of molybdenum of the dmmf coal) and solvents. The solvents used were tetralin, a known H-donor, and 1-methylnaphthalene (1-MN), a non-donor. Liquefaction was carried out in 25 ml microautoclaves using 4 g of coal and 4g of solvent, under 1000 psi H_2 pressure. The reaction time was 30 minutes plus 3 minutes for the heat-up time for autoclave to attain the reaction temperature. After the reaction, the liquid and solid products were separated by sequential extraction with hexane, toluene and THF. After the extraction the THF-insoluble residues were washed first with acetone and then with pentane in order to remove all the THF, followed by drying at 110°C for 6 h under vacuum.

The residues were analyzed by Py-GC-MS, and solid state CPMAS ^{13}C NMR and FTIR techniques as discribed elsewhere (14). The FTIR analysis of the samples was performed on a Digilab FTS 60 FTIR spectrometer. The samples were analyzed as KBr pellets. A accurately weighed amount (approximately 3 mg) of the vacuum dried samples were grinded with pre-weighed amount of KBr (approximately 300 mg). The pellets were pressed under a pressure of 10 tones. The pellets were dried at 100°C under vacuum for 24 h before recording their infrared spectra.

RESULTS AND DISCUSSION

Products Distribution

The liquefaction at 300°C (with H_2, solvent and no catalyst) shows a very small conversion (11-15%). This conversion is not very significant as compared to the total THF-soluble materials (8%) extracted from the raw coal. The presence of solvents (tetralin or 1-methylnaphthalene) seems to have no appreciable effect on the

conversions. The presence of catalyst also did not cause any appreciable increase in the conversion at 300°C, because at low temperature ATTM is less likely to decompose into catalytically active phase.

The results from the liquefaction at 350°C, given in Table 1, show an appreciable effect of catalyst and solvent on the total conversion and quality of the products. In the non-catalytic liquefaction the variation in the total conversion with the solvent is quite significant, with a maximum conversion in presence of tetralin. The total conversions in a solvent-free run and the run with 1-MN are not much different from that at 300°C but with tetralin as a solvent the difference is significant. The presence of catalyst (ATTM) in the liquefaction at 350 °C shows a drastic increase in the total conversion with or without solvent. The larger increase in conversion is in the solvent free liquefaction, though the total conversion is maximum in the presence of tetralin.

Characterization of DECS-8 Wyodak subbituminous coal

The CPMAS ^{13}C NMR spectrum of THF-extracted DECS-8 raw coal, shown in Figure 1, did not show any noticeable difference as compared to that of the unextracted raw coal in terms of aromaticity and functionality. The loss of 8% of organic materials of coal did not produce any apparent changes in its chemical structure. This may not be true for some coals; the THF-extracted sample may display a substantially different spectrum. The NMR spectrum shows two major very broad bands between 0-60 ppm and 90-165 ppm. The first band (0-60 ppm) is due to aliphatic carbons and may also include aliphatic ether carbons. The second region (90-165) is identified as an aromatic region. This band consists of three types of aromatic carbons: an intense peak around 130 ppm (aromatic C), first shoulder at 142 ppm (catechol-like C) and another at 152 ppm (phenolic or aromatic ether C). The other weak and broad bands at 181 and 212 ppm are attributed to carboxylic and ketonic carbons, respectively. The FTIR spectrum of the THF-extracted raw coal was also recorded and compared with that of the unextracted raw coal and there was no significant difference between the two samples.

Figure 2 shows the total ion chromatogram (TIC) from Py-GC-MS of the THF-extracted raw coal up to the retention time 30 minutes, which is a part of the total pyrogram. All the major structural units produced by the flash pyrolysis of the coal other than the alkanes and alkenes are listed in Table 2.The low-rank coals are known to have higher oxygen functionalities: therefore, phenol, alkylphenols, catechol and alkylcatechol are the most intense peaks in the pyrogram of the raw coal. The other minor oxygen-containing compounds identified are indanol, alkylindanol and hydroxyindene. Among the most abundant hydrocarbons other than alkanes and alkenes are toluene, xylenes and C_3-benzenes. Indene, alkyl indene, dihydroindene, alkyldihydroindene and alkyl naphthalenes are also identified in minor amounts. There are several intense peaks between 0-2 min (RT) of the pyrogram (Figure 2). These peaks are C_5-C_8 alkanes plus alkenes which coelute. There is another quite intense peak around 25 minutes (RT); it is a branched alkene with m/z 266. There are many more peaks over the whole pyrogram, and selective ion monitoring at m/z 71 indicates that they are long chain alkanes and alkenes. Overall, Py-GC-MS of the THF-extracted raw coal indicates that Wyodak subbituminous coal contains significant amount of oxygen containing structures including phenol, alkylphenols, catechol and other benzenediols as well as indanols. These observations are consistent with our earlier findings (13,14).

Characterization of the residues from the liquefactions.

CPMAS ^{13}C NMR

Figure 1 compares the CPMAS ^{13}C NMR spectra for the THF-extracted raw coal and the coal after liquefaction at 300 and 350°C without any solvent or catalyst. The residue from the reaction at 300°C displays a spectrum very much similar to that of the residue from the raw coal. Integration of the spectrum gives only a slight increase in the aromaticity. The residues produced after the liquefaction at 300°C in presence of solvents with and without catalyst were also analyzed by NMR, and there was no significant difference observed, except a slight increase in the relative intensity of the aromatic region. This increase was relatively less in the case when catalyst was used in the liquefaction reaction.

The residues from runs at 350°C show different spectra as compared to the raw coal. The catecholic (142 ppm) and carboxylic (181 ppm) bands almost disappeared after the run at 350°C and there is a slight decrease in the intensity of the phenolic (152 ppm) band (Figure 1). The residue, obtained from the liquefaction at 350 °C in presence of a solvent (tetralin or 1-MN) were also characterized by NMR. As compared to that of the solvent-free run, the residue from the run with tetralin shows slightly more of catechol-like carbons, but less intense then that of the THF-extracted raw coal. Also a decrease in the aliphatic band is observed. With 1-MN as a solvent the decrease in the aliphatic band is very prominent but the aromatic region shows similar functionality to that of the residue from solvent-free run.

We have seen that the presence of catalyst improves the total conversion at 350°C. However, CPMAS NMR spectra of the samples from catalytic runs appear to be similar to those from thermal runs.

FTIR

The analysis of the residues produced from liquefaction at 300°C showed no marked changes in the FTIR spectrum as compared to that of the THF-extracted raw coal, except a slight decrease in the aliphatic band in the 2950 cm^{-1} region. Using a solvent during the liquefaction also did not cause any appreciable difference in the FTIR spectra of the residues. The residue produced after the liquefaction in presence of catalyst showed a slight decrease in the ether region (1110-1300 cm^{-1}).

Figure 3 shows the FTIR spectra of the residues from liquefaction at 350°C (solvent-free) with and without catalyst, along with that of the residue from the raw coal. There are substantial changes apparent in the structure of coal after liquefaction at 350°C. There is a significant decrease in the carbonyl band at 1700 cm^{-1} and hydroxyl region at 3400 cm^{-1} (presumably carbonyl loss). In presence of catalyst , which improves the total conversion at 350°C, the effect on the ether region is very significant. It appears that catalyst has enhanced the cleavage of the ether bonds in the coal network.

PYROLYSIS-GC-MS

Figure 2 shows the selected retention time region of the Py-GC-MS chromatogram of the THF-extracted raw coal and the residues from the liquefaction at 300 and 350°C (solvent- and catalyst-free). The major peaks which are identified are listed in Table 2. Compared to the pyrogram of the THF-extracted raw coal, all the major species such as phenol, alkylphenols, alkylbenzenes, as well as alkanes and alkenes, are formed from the pyrolysis of the residues from the liquefied coal, but there are apparent differences. A substantial decrease in the intensity of the catechol and alkylcatechol peaks in the pyrogram of the residue from the run at 300°C, and the disappearance of these peaks from the pyrogram of the residue from 350°C run, are the most significant. This change in the residue from the 300°C run is not apparent from NMR, but after liquefaction at 350°C the shoulder at 142 ppm in the CPMAS ^{13}C NMR spectrum disappears completely. From this it is clear that reaction at 300°C did cause some structural changes in the coal network.

The residues from the liquefaction experiments at 300 and 350°C in presence of solvents and with and without catalyst were also characterized by Py-GC-MS. The pyrogram of the residues from liquefaction at 300 and 350 °C in presence of tetralin as solvent (with and without catalyst) are shown in Figure 4. The peaks identified are given in Table 2. The peaks marked with an alphabet in the pyrograms are the new peaks observed after liquefaction in presence of a solvent. An intense methylnaphthalene peak observed here was also seen in the case of a solvent-free run, but with a very low intensity. These new peaks appear to have come from the adduction of solvent because they were not observed in the Py-GC-MS profiles of the residues from the solvent-free runs. When methylnaphthalene was used as solvent, the tetralin and dihydronaphthalene peaks were not observed and the 1-methylnaphthalene peak was very intense, showing that it is due to the solvent . The naphthalene peak was relatively weak in presence of 1-methylnaphthalene, as compared to that in the presence of tetralin . Since the residue was extracted with THF for 24 h and dried, the solvent remaining in the residue must be either chemically bound or physically entraped in the solvent-inaccessible micropores, or both, as also noted in an earlier work (14). In the residue from the liquefaction in the presence of catalyst and solvent, the adduction of solvent was decreased, as shown by the decreased intensity of the solvent peak in the pyrogram. The reason for the decreased adduction of solvent molecules could be due in part to the formation of reduced number of free radicals from the solvent molecules in presence of catalyst. This is also supported by the decreased amount of hydrogen transfer from tetralin and increased amount of hydrogen gas consumption during liquefaction in presence of catalyst compared to that of the catalyst-free experiment.

Table 3 shows the relative ratios of the oxygen-containing units to the alkylbenzenes before and after liquefaction. For oxygen-containing species the areas of the phenol, alkylphenols and catechol peaks were added and for alkylbenzenes, toluene, xylenes and C_3-benzenes were used. As compared to that for raw coal, the ratio decreased for the sample from solvent-free run at 300°C, and the sample from the run at 350 °C with 1-MN or without solvent. There ratios show that the presence of solvent does make a difference in the loss of specific type of species from the coal network and it is independent of the catalyst. In solvent-free reaction and with non-donor solvent (1-MN), more oxygen containing species are lost during liquefaction. In presence of tetralin during the liquefaction, this ratio did not decrease much from that of the raw coal and is highest as compared to the others.

The results of this work, though preliminary, have shown that there are significant changes in the coal structure as a consequence of the low-temperature catalytic pretreatments. Further work on the identification of specific changes in the coal structure is now in progress.

ACKNOWLEDGEMENT

This project was supported by the U. S. Department of Energy, Pittsburgh Energy Technology Center under contract DE-AC22-91PC91042. We wish to thank Dr. M. Baird of DOE/PETC for his kind support.

REFERENCES

1. Whitehurst, D. D., "Coal Liquefaction Fundamentals", Am. Chem. Soc. Sym. Ser. 1980, 139, 132.
2. Whitehurst, D. D., Mitchell, T. O. and Farcasiu, M., "Coal Liquefaction", Academic Press, New York, 1980.
3. Song, C. and Schobert, H. H., "Temperature-Programmed Liquefaction of Low-Rank Coals in H-donor and Non-donor Solvents", Am. Chem. Soc. Div. Fuel Chem. Prepr., 1992, 37(2), 976.
4. Song, C., Nomura, M., Ono, T., Am. Chem. Soc. Div. Fuel Chem. Prepr., 1991, 36 (2), 586-596.
5. Davis, A., Derbyshire, F. J., Finseth, D. H., Lin, R., Stansberry, P. G. and Terrer, M-T., Fuel, 1986, 65, 500.
6. Davis, A., Derbyshire, F. J., Mitchell, G. D. and Schobert, H. H., "Enhanced Coal Liquefaction by Low-Severity Catalytic Reactions", U. S. Department of Energy, Final Report DOE-PC-90910-F1, July, 1989, 175p.
7. Derbyshire, F. J., Davis, A., Lin, R., Stansberry, P. and Terrer M-T., Fuel Proc. Technol., 1986, 12, 127.
8. Derbyshire, F. J., Davis, A., Epstein, M. and Stansberry, P., Fuel, 1986, 65, 1233.
9. Derbyshire, F. J., Energy and Fuels, 1989, 3, 273.
10. Stansberry, P. G., Lin, R., Terrer, M-T., Lee, C. W., Davis, and Derbyshire, F., Energy and Fuels, 1987, 1, 89.
11. Burgess, C. and Schobert, H. H., ACS Fuel Chem. Prepr., 1990, 35, 31.
12. Burgess, C., Artok, L., Schobert, H. H., ACS Fuel Chem. Prepr., 1991, 36 (2), 462.
13. Song, C., Schobert, H. H., Hatcher, P. G., Energy & Fuel, 1992, 6, in press.
14. Song, C., Schobert, H. H., Hatcher, P. G., Am. Chem. Soc. Div. Fuel Chem. Prepr., 1992, 37(2), 638.

TABLE 1. Products distribution (dmmf wt %) for the liquefaction at 350°C with and without catalyst.

Solvent	Gas	Oils	Asphaltenes	Preasphaltenes	Total Conversion
Thermal					
none	3.3	2.1	2.6	4.5	12.5
Tetralin	4.2	4.1	7.6	10.0	25.9
1-MN	4.0	1.1	5.8	7.4	18.3
Catalytic					
none	3.0	10.0	5.4	11.4	29.8
Tetralin	3.0	10.2	12.9	10.6	36.4
1-MN	2.6	6.1	10.1	12.3	31.1

TABLE 2. Major identified peaks in pyrograms.

No.	MW	Identified Compounds
1	92	Toluene
2	106	p-Xylene
3	106	o-Xylene
4	120	C_3-benzene
5	120	C_3-benzene
6	120	C_3-benzene
7	94	Phenol
8	118	Indane
9	116	Indene
10	108	o-Cresol
11	108	m-+p-Cresol
12	132	Methylindane
13	130	Methylindene
A*	132	Tetralin
14	122	Ethylphenol
B*	130	Dihydronaphthalene
15	122	Ethylphenol
16	122	Dimethylphenol
C*	128	Naphthalene
17	146	Dimethylindene
18	122	Dimethylphenol
19	136	C_3-Phenol
20	110	Catechol
21	136	C_3-Phenol
22	144	Dimethylindene
23	136	C_3-Phenol
24	124	Methylcatechol
25	124	Methylcatechol
D*	142	2-Methylnaphthalene
E*	142	1-Methylnaphthalene
26	110	1,3-Benzenediol
27	134	Indanol
28	134	Indanol
39	132	Hydroxyindene
30	138	C_2-Catechol
31	156	C_2-Naphthalene
32	170	C_3-Naphthalene

* The compounds identified in Py-GC-MS profiles (Figure 4) of the residues from the liquefactions in presence of tetralin.

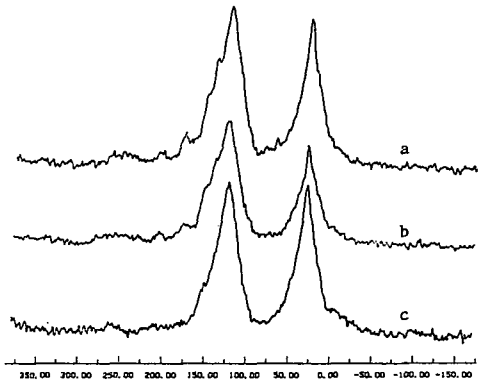

FIGURE 1 CPMAS ^{13}C NMR spectra of (a) THF-exuacted raw coal and the residues from the solvent free thermal liquefactions at (b) 300°C, and (c) 350°C.

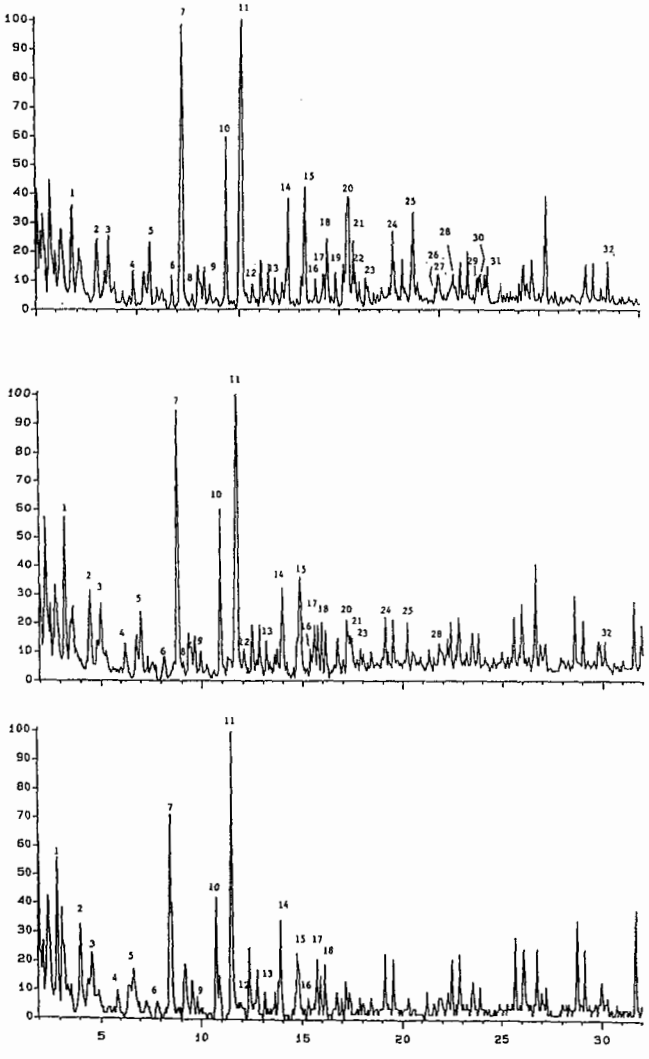

FIGURE 2. Py-GC-MS profiles of (a) THF-extracted raw coal and the residues from the thermal liquefactions at (b) 300°C, and (c) 350 °C.

TABLE 3. Ratios of the amount of the oxygen-containing units to the alkylbenzene units.

Temperature (°C)	Solvent	Ratio Phenolic/Alkylbenzenes	
		Thermal	Catalytic
Raw Coal		3.6	
300	none	2.4	2.5
300	Tetralin	3.5	3.1
300	1-MN	3.6	3.2
350	none	2.3	2.4
350	Tetralin	3.2	3.1
350	1-MN	1.9	2.3

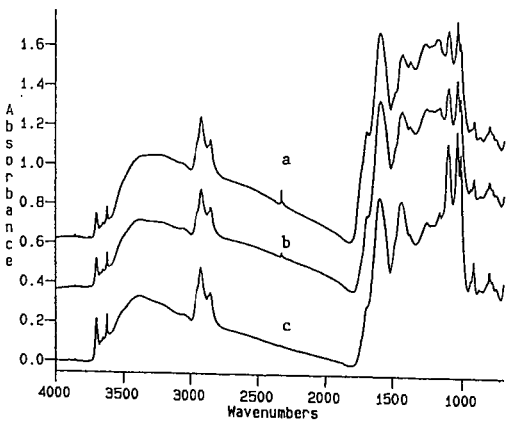

FIGURE 3. FTIR spectra of (a) THF-extracted raw coal and the residues from the solvent-free, (b) thermal, and (c) catalytic liquefactions at 350°C

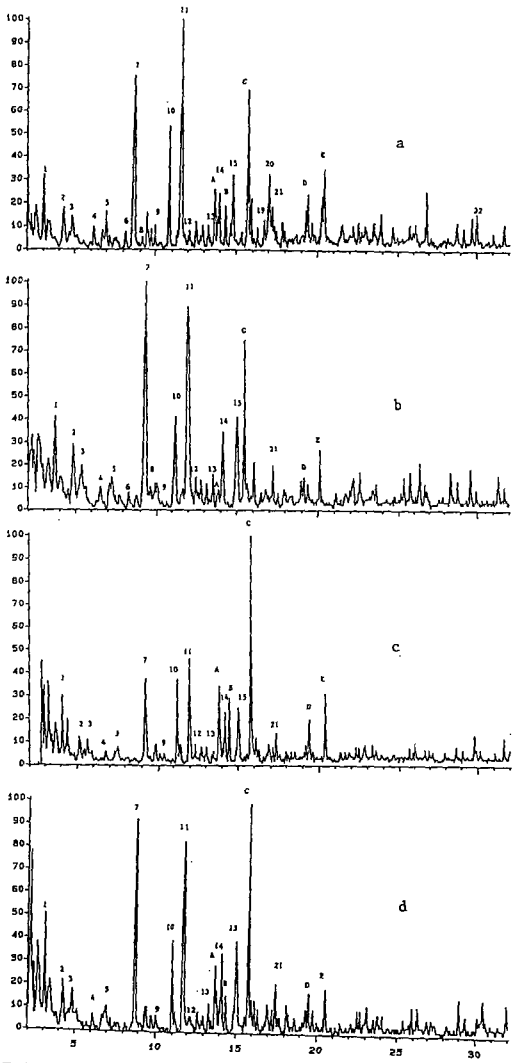

FIGURE 4. Py-GC-MS profiles of the residues from the liquefactions in presence of tetralin, (a) thermal, (b) catalytic at 300°C, and (c) thermal, (d) catalytic at 350°C.

THE CHEMICAL NATURE OF COAL LIQUID RESIDS AND THE IMPLICATIONS FOR PROCESS DEVELOPMENT

S. D. Brandes, R. A. Winschel, F. P. Burke
CONSOL Inc.
Research & Development
4000 Brownsville Road
Library, PA 15129

Key words: coal liquids, resids

INTRODUCTION

The informational needs for the advancement of direct coal liquefaction process development include the knowledge to choose the appropriate analytical tools. CONSOL Inc. is working with a number of research groups to evaluate various methods for analyzing direct coal liquefaction process-derived samples.[1] Each individual method was applied to process-derived samples and the advantages (and some drawbacks) for each have come to light.[2-8] The large database accumulated in the study may be useful in choosing analytical methods for process development and design of facilities. This paper will explore the usefulness of these data for that purpose by examining a few specific examples.

Close-coupled integrated two-stage direct coal liquefaction, on a pilot plant scale, is a continuous, multi-step operation. The process steps include mixing feed coal with recycled coal liquid to form a slurry; thermal and/or catalytic liquefaction of the coal in the slurry; stripping of the light, high-value products; and recycling of the heavy residues to near extinction. The coal concentration in the feed slurry is typically 30 wt %. The slurry oil consists mostly of relatively high molecular weight material (resids) and some light distillable materials. Each process stream, with the exception of the distillation column overheads, also is comprised of 50% or more of non-distillable (850°F$^+$) resid. Because of the preponderance of the resid in the system, and its influence on the overall properties of the process streams, the program described above was directed to the study of these materials.

RESULTS AND DISCUSSION

The results of the analyses of six 850°F$^+$ distillation resid samples, obtained from two process runs (Run 257[9] and Run 259[10]) conducted at the Wilsonville Advanced Two-Stage Direct Coal Liquefaction facility, will be used to demonstrate the potential usefulness of these data for process development. Each of the samples are composites of many daily samples obtained over the length of the liquefaction test. These tests lasted for a number of months and included numerous changes in operating conditions. The feed to Wilsonville Run 257 was Illinois No. 6 coal from Burning Star No. 2 Mine and the feed to Run 259 was Pittsburgh seam coal from Ireland Mine. The resid from Run 259 was notably more difficult to convert to distillate products, based on Wilsonville operating results. Both runs were carried out with catalyst in both reactors. Both runs operated, for the most part, with the first of the two reactors at a higher temperature than the second reactor. Samples were obtained from three locations in the plant (Figure 1): between the two reactors (Interstage), after the second reactor but before the deasher (2nd Stage Product), and at the vessel used to accumulate different process flows to form the slurry solvent that is recycled back through the system (Recycle). Samples obtained from these different locations during a single run are expected to represent different degrees of coal conversion in the direct liquefaction process. The samples analyzed were the 850°F$^+$ distillation resids of these three process streams, and, in some cases, the tetrahydrofuran-soluble portion of the resids.

The analyses performed by CONSOL on the samples include elemental analyses, proton NMR (and classification of the proton signal into defined groups), and determination of phenolic -OH by Fourier transform infrared spectroscopy (FTIR). Pyrolysis and subsequent detection and analysis of the pyrolysate by thermogravimetric (TG)-FTIR, fluorescence microscopy, reflectance microscopy, field ionization mass spectrometry (FIMS), and various separation techniques, including liquid chromatography were performed by Advanced Fuel Research,[7] University of Kentucky,[4] The Pennsylvania State University,[3] SRI International,[5] and Virginia Polytechnic and State University,[2] respectively.

Table 1 presents the elemental analyses of the six composite resid samples and the parent coals. It is readily apparent that the hydrogen content is increased and the heteroatom content is decreased in the resid as the coal slurry proceeds through the liquefaction process. Also given in Table 1 are the phenolic -OH contents of the tetrahydrofuran (THF)-soluble portion of each resid. Figure 2 shows that the phenolic -OH contents, determined by FTIR, correlate relatively well with the yield of the most polar liquid chromatography fraction of the THF-soluble portion of resids.[2] The data presented in Figure 2 were obtained from a number of resids obtained from different liquefaction runs made at different facilities, including Runs 257 and 259 made at Wilsonville.

The TG-FTIR results, presented in Table 2, show a reduction in gas make in the pyrolysis of the resids with a corresponding increase in tar yield as the coal is converted in the liquefaction system. The remaining ~2 to ~10% of the resid, not accounted for in these analyses, is converted to additional gases (NH_3, COS) and light hydrocarbons, such as C_2H_4 and benzene. It is notable that the resids produced in the Illinois No. 6 coal run generate a much larger proportion of these volatile materials and more tar than the resids produced from the Pittsburgh seam coal resid. The char yields from the distillation resids correlate with the phenolic -OH content of the THF-soluble portion of the resid, which, as discussed above, correlates to the very polar material found in the resid.

The proton NMR data for the THF-soluble portions of the resids (Table 3) are divided into five spectral regions corresponding to five proton types. These types are condensed aromatics, uncondensed aromatics, alpha protons, beta protons, and gamma protons. The condensed aromatic component of the Run 257 resids decreases from interstage to second-stage product samples and is relatively unchanged in the recycle stream by partial deashing. The increase in aromaticity from recycle to interstage samples comes about from the addition of fresh feed coal to the slurry which is then liquefied in the first reactor. The conversion of the 850°F$^+$ resid in each stage of the liquefaction process is not the same; it was approximately two times greater in the first stage than in the second stage for Run 257, and about 1.5 times greater in the first stage than the second stage in Run 259. Nonetheless, it is concluded that for Run 257, the aromatic coal structure is broken down in the first stage of the liquefaction system with little additional change of aromaticity in the second reactor. The liquefaction process conditions in Run 259 were more severe than in Run 257 (higher temperature, lower space velocity) and the rejection of resid in the deasher was lower. This accounts for the total aromaticity being higher in the Run 259 samples. However, within Run 259, an interesting trend is seen. The percent of condensed aromatic protons decreases and that of the uncondensed aromatic materials increases sequentially from the interstage to second stage product to recycle resid. This indicates that the process stream (which is mostly resid) is being converted to less-condensed aromatic moieties, but the unconverted resid is not being saturated. This is supported by a number of other analyses. For example, total volatile material of the resids (100% char) determined from the TG-FTIR experiment is essentially the same as the percentage of uncondensed aromatic protons for each sample from Run 257. However, for the Run 259 samples, there is

a large increase observed for total volatiles and uncondensed aromatic protons in the recycle sample.

Microscopy proved to be a useful technique in the examination of the resids, which are solid at room temperature. It was possible to distinguish different petrographic components in the samples that are related to the extent that the coal slurry had reacted. Point counts and mean random reflectance measurement were made of three components: the high-reflecting vitroplast, the partially reacted vitrinite, and the low-reflecting vitroplast. Values for the interstage and recycle materials in this example data set are given in Table 4. The concentration of low-reflecting vitroplast is higher for the interstage samples than the recycle samples in both Runs 257 and 259. However, for the recycle samples, its concentration is considerably lower in Run 259 than in Run 257. This indicates that across the second stage reactor and deasher, the Pittsburgh coal resid is less upgraded than the Illinois coal-derived materials, and may, in fact, be undergoing retrogressive reactions. This supports the NMR results described above.

Fluorescence microscopy[4,11] provides a great deal of qualitative information and some quantifiable values including the wavelength of maximum fluorescence (L_{max}) and the fluorescence intensity at L_{max}. It is possible to relate the intensity and the wavelength at L_{max} to the relative degree of aromaticity, and thus to the relative reactivity of the material; the lower the intensity and the longer the wavelength, the higher the aromatic concentration and therefore the lower the reactivity. Resids from Run 257 were found to contain two distinct populations; values of L_{max} and intensity are given in Table 5 for both. Comparison of samples from Run 257 (either population) and Run 259 (Table 5) shows the intensity of the Run 259 interstage sample is relatively low and the L_{max} is high (approaching 700nm). This suggests that the interstage resid from Run 259 is comprised of a more-condensed aromatic structure than the Illinois No. 6 interstage resid and it is thus inferred to be less reactive. The recycle resid samples follow the same trend; the Run 259 sample is also more aromatic and is inferred to be less reactive. Another quantifiable value is the quotient of the fluorescence intensities measured at 700nm (red) and 525nm (green). These red:green quotients (Q) can be used to assess the variability of the fluorescence properties within a heterogeneous sample. A shift to longer wavelengths (red) indicates a more extended pi-bond conjugation or a larger proportion of condensed aromatics. The red:green quotients usually are reported as histograms. Figure 3 shows the histograms for the Runs 257 and 259 interstage and recycle resid samples. The Run 259 samples exhibit much higher proportion of the material at higher Q values than the Run 257 samples. This is consistent with the ^{1}H-NMR data where ~20% of all protons are aromatic in the Run 257 recycle sample and ~32% are aromatic in the Run 259 recycle sample. Across the second-stage reactor (and including the part of the process stream that has been deashed), there is a considerable shift of the fluorescence of the material to the green (or shorter wavelength, lower aromaticity) in Run 257, but not in Run 259. This may help explain the greater propensity of the Run 259 resids to form char in the TG-FTIR experiments.

FIMS data and their interpretation for these samples have been presented elsewhere.[12] Because of a distinct bimodality, the FIMS profiles of the distillation resids were deconvoluted into two overlapping components, A and B. Component A represents a molecular weight (m/e) range centered at approximately 350 Da, component B is centered around 600 Da. The relative weight fractions of A and B were used to compare the resid samples. Table 6 presents the weight percent of component A for each of the six samples obtained from both the even- and odd-mass FIMS profiles. In agreement with the data discussed above, the concentration of component A in the Run 257 resid almost doubles as the coal slurry passes through the first-stage reactor indicating that the molecular weight of the resid was

reduced in the first-stage reactor. As discussed above, conversion of the resid in the first-stage reactor was approximately twice that of the second-stage reactor for Run 257, and correspondingly the concentration of component A in the second-stage product sample increases from the interstage sample, but is only about 1.5 times that of the interstage sample. In comparison, Run 259 interstage and second-stage samples are less enriched with lower molecular weight material. The concentration of low molecular weight material decreases across both the first-stage and second-stage reactors. It increases in the recycle sample only after part of the second-stage product stream passes through the deasher where high molecular weight materials are rejected along with the ash.

SUMMARY AND CONCLUSION

To briefly summarize the information presented above; relative to the Illinois No. 6 resids, the Pittsburgh seam resids are less hydrogenated, higher molecular weight, less fluorescent and they produce fewer volatiles upon pyrolysis. In addition, the Pittsburgh seam resids are more phenolic, more aromatic and contain more nitrogen. These characteristics are consistent with the lower observed reactivity of the Pittsburgh seam resids, which must have arisen from a combination of the coal and operating conditions. The NMR, FIMS and TG-FTIR data indicate that in Run 257, the upgrading of Illinois No. 6 coal to lower molecular weight, more volatile, less aromatic materials was primarily achieved in the first stage of the two-stage system. Additionally, reflectance microscopy data show that the resid derived from the Illinois No. 6 coal in the first-stage reactor is more upgraded in passing through the second-stage reactor and deasher than the Pittsburgh seam coal first-stage resid. Phenolic -OH determinations made on the THF-soluble portion of the distillation resids correlate with the amount of very polar fraction isolated from the resids by liquid chromatography and also with the char yield from the TG experiments. Fluorescence microscopic examination of the resids leads to inferences of resid reactivity. These inferences are supported by the other data. It is apparent that no single method fully describes process derived materials; however, the trends observed by any one method are generally mimicked in the response of the other methods. The implication for process development is that the choice of methodology for analytical use, among these methods tested, can be determined by the requirements of the process developer based on such factors as cost, time, or frequency of measurement.

ACKNOWLEDGEMENT

This work was funded by the U.S. Department of Energy under contract No. DE-AC22-89PC89883.

REFERENCES

1. Brandes, S. D.; Winschel, R. A.; Burke, F. P. "The Application of Advanced Analytical Techniques to Direct Coal Liquefaction," Am. Chem. Soc., Div. Fuel Chem. Preprints, 1991, 36(3), 1172.
2. Taylor, L. T.; Hellgeth, J. W.; Sequeira, A. "Coal Liquefaction Process Streams Characterization and Evaluation; Analysis of Coal Liquefaction Process Streams by Chromatographic and Spectroscopic Techniques, Topical Report," DOE/PC 89883-41, January 1992.
3. Mitchell, G.; Davis, A. "Coal Liquefaction Process Streams Characterization and Evaluation; Gold Tube Carbonization and Reflectance Microscopy, Topical Report," DOE/PC 89883-37, December 1991.
4. Rathbone, R. F.; Hower, J. C.; Derbyshire, F. J. "Coal Liquefaction Process Streams Characterization and Evaluation; Novel Analytical Techniques for Coal Liquefaction: Fluorescence Microscopy, Topical Report," DOE/PC 89883-30, October 1991.

5. Malhotra, R.; McMillen, D. F. "Coal Liquefaction Process Streams Characterization and Evaluation; Characterization of Coal Liquids by Field Ionization Mass Spectrometry and Iodotrimethylsilane Derivatization, Topical Report," DOE/PC 89883-39, January 1992.
6. Miknis, F. P. "Coal Liquefaction Process Streams Characterization and Evaluation; Solid-State NMR Characterization of Coal Liquefaction Products, Topical Report," DOE/PC 89883-36, November 1991.
7. Serio, M. A.; Hsisheng, T.; Bassilakis, R.; Solomon, P. R. "Coal Liquefaction Process Streams Characterization and Evaluation; FT-IR Methods for Characterization of Coal Liquefaction Products, Topical Report," DOE/PC 89883-45, April 1992.
8. Green, J. B.; Pearson, C. D.; Young, L. L.; Green, J. A. "Coal Liquefaction Process Streams Characterization and Evaluation; Application of Liquid Chromatographic Separation Methods to THF-Soluble Portions of Integrated Two-Stage Coal Liquefaction Resids, Topical Report," DOE/PC89883-47, May 1992.
9. Winschel, R. A.; Robbins, G. A.; Burke, F. P. "Coal Liquefaction Process Solvent Characterization and Evaluation, Technical Progress Report July 1 through Sept. 30, 1988," DOE/PC 70018-68, July 1989.
10. Winschel, R. A.; Robbins, G. A.; Burke, F. P. "Coal Liquefaction Process Solvent Characterization and Evaluation, Technical Progress Report April 1 through June 30, 1990," DOE/PC 89883-22, July 1991.
11. Rathbone, R. F.; Hower, J. C.; Derbyshire, F. J. "Application of Fluorescence Microscopy to Coal-Derived Resid Characterization," Am. Chem. Soc., Div. Fuel Chem. Preprints, 1991, 36(3), 1164.
12. Malhotra, R.; McMillen, D. F., Huestis, D. L. "Characterization of Coal Liquefaction Resids by Field Ionization Mass Spectrometry: Correlation Spectral Features with Processing Parameters," Am. Chem. Soc., Div. Fuel Chem. Preprints, 1992, 37 (2), 908.

TABLE 1
ELEMENTAL ANALYSES AND PHENOLIC -OH CONTENTS OF 850°F$^+$ DISTILLATION RESIDS AND PARENT COALS[9,10]

	Run 257				Run 259			
	Feed Coal	Inter-stage Resid	2nd Stage Resid	Recycle Resid	Feed Coal	Inter-stage Resid	2nd Stage Resid	Recycle Resid
wt % of 850°F$^+$ Resid in Process Stream	-	81.9	77.5	79.8	-	72.3	67.9	73.1
Ash wt % as det.	11.76	12.52	13.49	9.28	4.68	8.74	10.21	8.51
C wt % MAF	79.52	88.05	87.99	88.64	81.24	90.12	90.24	91.01
H wt % MAF	5.51	7.70	7.87	8.08	5.97	6.19	6.39	6.50
N wt % MAF	1.53	0.86	0.77	0.78	1.37	1.15	1.05	1.04
S wt % MAF	3.68	1.34	1.20	0.79	3.28	1.50	1.49	1.25
O wt % (by diff) MAF	9.58	2.05	2.16	1.71	8.07	1.04	0.83	0.20
Phenolic -OH, meq/g[(a)]	-	0.68	0.57	0.50	-	0.92	0.70	0.69

(a) determined on the THF-soluble portion of the resid

TABLE 2
TG-FTIR ANALYSES OF 850°F$^+$ DISTILLATION RESIDS[7]

TG Yield (wt % daf)	Run 257			Run 259		
	Interstage	2nd Stage	Recycle	Interstage	2nd Stage	Recycle
Tar	70.48	69.90	73.49	65.00	65.56	67.07
Gas[a]	4.85	4.32	3.71	5.59	3.89	3.61
Char	17.50	15.88	14.15	27.80	28.39	22.88
Unaccounted	7.17	9.90	8.65	1.61	2.16	6.44

(a) Gas = $CH_4+CO+CO_2+SO_2$

TABLE 3
PROTON NMR ANALYSES OF THF-SOLUBLE PORTION OF 850°F$^+$ RESIDS[9,10]

Proton Type (wt %)	Run 257			Run 259		
	Interstage	2nd Stage	Recycle	Interstage	2nd Stage	Recycle
Condensed Aromatic	18.1	16.9	16.8	30.7	27.8	26.1
Uncondensed Aromatic	3.7	3.4	3.1	2.6	3.8	5.4
Alpha	28.8	28.6	28.0	31.1	30.8	28.3
Beta	39.1	40.5	41.4	27.2	28.9	30.4
Gamma	10.4	10.7	10.6	8.4	8.7	10.8

TABLE 4
NORMALIZED CONCENTRATION OF PETROGRAPHIC COMPONENTS[a]
OF 850°F$^+$ DISTILLATION RESIDS[3]

Component, %	Run 257		Run 259	
	Interstage	Recycle	Interstage	Recycle
Low-Reflecting Vitroplast	78.0	73.5	79.0	63.5
Partially Reacted Vitrinite[b]	0.5	0.0	0.5	0.5
High-Reflecting Vitroplast	21.5	26.5	20.0	36.0

(a) 200 reflectance measurements made on each sample
(b) unreacted coal

TABLE 5
WAVELENGTH AND INTENSITY OF MAXIMUM FLUORESCENCE
OF 850°F$^+$ DISTILLATION RESIDS[4]

	Run 257		Run 259	
	Interstage	Recycle	Interstage	Recycle
Fluorescence Spectrum Maximum, L_{max}, nm	646[a]/604[b]	633[a]/585[b]	696	696
Intensity at L_{max}, counts	6714/12666	9284/32108	6658	8497

(a) Population 1
(b) Population 2

TABLE 6
wt % COMPONENT A OF 850°F$^+$ RESIDS
FROM EVEN- AND ODD-MASS FIMS PROFILES[5]

Weight %	Run 257			Run 259		
	Interstage	2nd Stage	Recycle	Interstage	2nd Stage	Recycle
A Even	22.4	32.0	13.1	13.7	9.2	18.5
A Odd	7.9	12.9	4.3	4.0	2.2	6.3

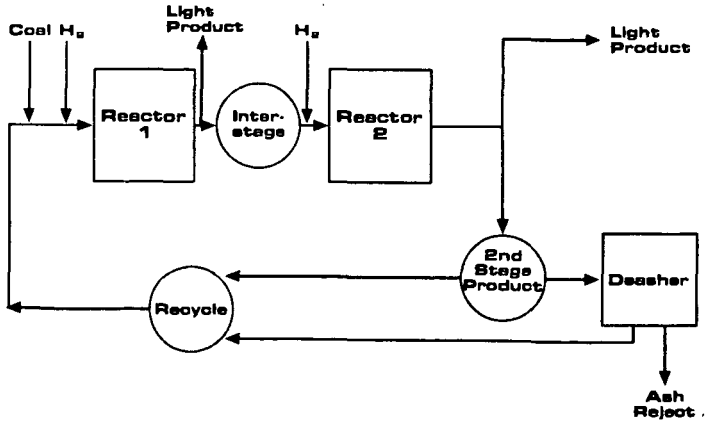

Figure 1. Simplified Flow Scheme Generic Integrated Two-Stage Direct Coal Liquefaction Unit.

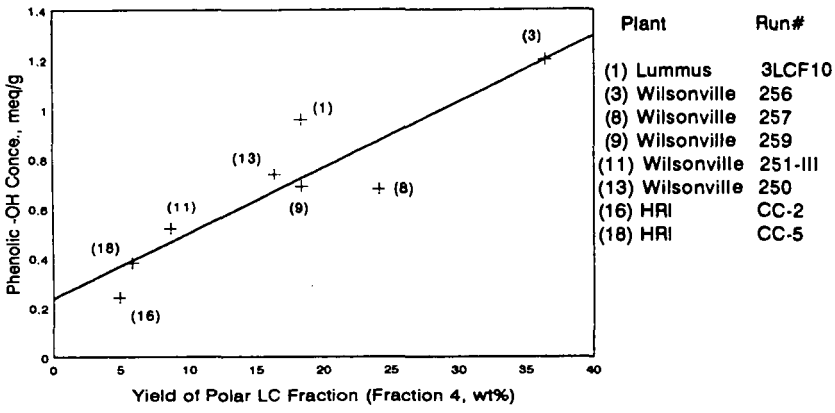

Figure 2. Phenolic -OH Concentration vs Yield of Liquid Chromatography Polar Fraction (F4).[2]

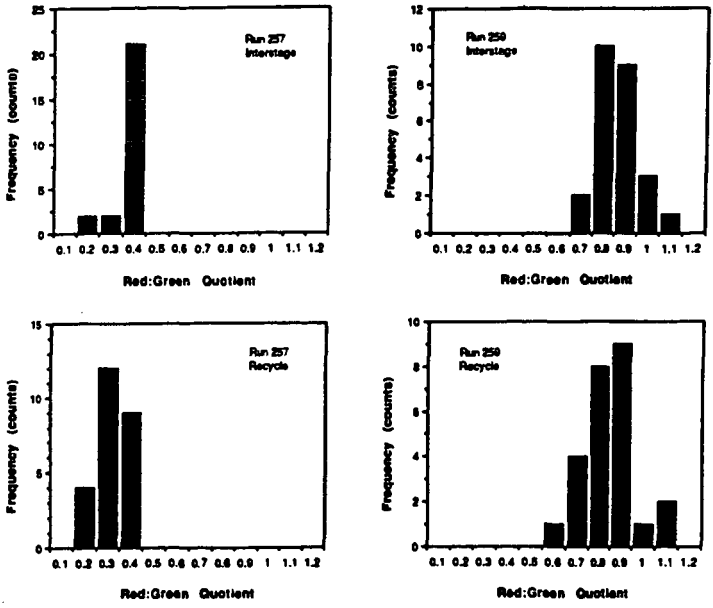

Figure 3. Red: Green Quotient Histograms for Run 257 and Run 259.[4]

Characterization of Petroleum Pitch Precursor Carbon Fibers Using Fourier Transform Infrared Photoacoustic Spectroscopy

Charles Q. Yang
Department of textiles, Merchandising and Interiors
The University of Georgia
Athens, GA 30605

John R. Simms
Department of Chemistry
Marshall University
Huntington, WV 25701

key words: *petroleum pitch, carbon fiber, infrared spectroscopy*

Introduction

The production of carbon fiber from petroleum pitch proceeds in several stages: the formation of a precursor carbon fiber; stabilization of the precursor carbon fiber; and carbonization of the stabilized precursor carbon fiber (1-2). The stabilization process is the most important stage, at which thermal oxidation takes place in the precursor carbon fiber. Only a properly stabilized precursor carbon fiber can assure satisfactory performance of the final carbon fiber product.

The main interest of this research is to study the nature of the chemical changes in a pitch based precursor carbon fiber during the stabilization and carbonization processes using Fourier transform infrared photoacoustic spectroscopy (FT-IR/PAS). Gas chromatography has been widely used to investigate the volatile oxidation products of petroleum pitch and pitch based precursor carbon fibers(3-7). The applications of infrared spectroscopy, however, was focused on the oxidation of coal(8-12). The infrared spectroscopy studies of carbon fibers were carried out using transmission techniques(13,14). To obtain a transmission infrared spectrum, a carbon fiber must be either ground into a powder to make a potassium bromide (KBr) pellet or dissolved in an organic solvent to be deposited onto a window. One problem for both methods is the destruction of sample integrity. Another problem associated with the KBr pellet method is the high light scattering of carbon powders and the consequent opaqueness of the KBr pellet, which results in poor signal-to-noise ratio. It is also very difficult to find a organic solvent, in which a carbon fiber will totally dissolve.

Photoacoustic detection was used in this research to collect infrared spectra of carbon fiber samples. When a photoacoustic cell is used as a detector in a FT-IR spectrometer, the absorbed infrared radiation is first converted to photoacoustic signals, which are detected by a microphone and Fourier transformed to yield a single beam spectrum. With photoacoustic detection, it is not the transmitted or reflected IR radiation, but the photoacoustic signals converted from the absorbed radiation which are detected by a detector. Samples are not altered during the analysis. Opaque sample can be examined without experiencing difficulties with the detection of transmitted radiation. FT-IR/PAS can also be used as a near surface analysis technique(15-17).

Experimental

Instrumentation. A Nicolet 20DXB FT-IR spectrometer with a MTEC Model 100 photoacoustic cell was used to collect the infrared spectra. Resolution for all the spectra was 8 cm^{-1}. A 6-mm sample cup was used for PAS data collection. Carbon black was used as a reference material, and helium was used to purge the photoacoustic cell prior to data collection. The mirror velocity used was 0.139 cm/s for PAS and 0.556 cm/s for transmission experiments. No smoothing function or base-line correction was used.

Materials. (1) *Raw materials*—Both the enriched petroleum pitch and the green fiber produced by a melt blown process were provide by Ashland Carbon Fiber Division, Ashland Oil Company, Ashland, Kentucky. The pitch has a softening point of 260°C. The diameter of the precursor carbon fiber is 14 microns.

(2) *The stabilized precursor carbon fibers*—The precursor carbon fiber stabilized by a programmed thermal oxidation process was provided by Ashland Carbon Fiber Division. The stabilization process began at 157°C and ended at 341°C for a total heating period of 80 min. Air was used as the oxidizing

medium. The precursor carbon fiber was removed from the heating apparatus at 10-min intervals.

(3) *The carbonized carbon fibers*—The precursor carbon fibers at different stages of the carbonization process were also provided by Ashland Carbon Fiber Division. The carbonization process started at 300°C at a 15°C/min temperature ramp to the final temperature (500, 700, 900 and 1100°C, respectively). The carbonization was carried in a nitrogen atmosphere. Immediately after reaching the designated temperature, the samples were cooled to below 300°C under nitrogen before being removed. Samples were ground to a powder prior to analysis.

(4) *Solvent extraction*—A Soxhlet extractor was used to extract 1 g of a carbon fiber sample by 65 ml of a solvent for 4 hr. The solvents used included: methylene chloride, hexane, benzene and tetrahydrofuran. The extraction mixture was finally filtered to remove solid particles from the solution.

Results and discussion

The Raw Materials. The photoacoustic infrared spectra of the enriched petroleum pitch precursor and the green fiber made from the petroleum pitch are presented in Figures 1A and 1B, respectively. The bands at 2968 and 2921 cm^{-1} in Figure 1 are due to the asymmetric stretching of CH_3- and -CH_2-, respectively. Both the bands at 2968 and 2864 cm^{-1} increased their intensities relative to the band at 2921 cm^{-1} in the infrared spectrum of the tetrahydrofuran extract of the green fiber. Therefore, the band at 2864 cm^{-1} in Figure 1 can be assigned to the symmetric stretching mode of CH_3-. The symmetric stretching mode of -CH_2-, usually at 2850 cm^{-1} (18), is probably overlapped by the band at 2864 cm^{-1} in Figure 1.

The broad band at 3045 cm^{-1} in figure 1 is due to the unsaturated hydrocarbon stretching mode. In order to determine the nature of the unsaturated hydrocarbons contained in the raw materials, the green fiber was treated in a 5% solution of bromine in carbon tetrachloride for 5 min at room temperature, then analyzed by FT-IR/PAS. The intensity of the band at 3045 cm^{-1} was reduced in the spectrum of the bromine-treated green fiber. The reduction in the intensity of the band at 3045 cm^{-1} was due to the saturation of the aliphatic unsaturated hydrocarbons by bromine. Therefore, it can be concluded that the unsaturated hydrocarbons in the green fiber have both aliphatic and aromatic components.

The green fiber was extracted by benzene and hexane. It was found that both the aromatic hydrocarbon stretching band around 3045 cm^{-1} and the -CH_2- asymmetric stretching band at 2918 cm^{-1} were significantly enhanced in the spectrum of the benzene extract compared with the spectrum of the green fiber(Figure 1B). This probably indicates that the -CH_2- in the green fiber has a major contribution from the methylene bridges linking aromatic rings. It was also found that the CH_3- asymmetric stretching band at 2960 CM^{-1} was much stronger while the band at 3045 cm^{-1} was weaker in the infrared spectrum of the hexane extract than in the spectrum of the green fiber(Figure 1B). Probably this can be explained by the fact that the methyl groups in the green fiber has a major contribution of methyl substitutes on the aromatic rings which have few hydrogens.

Three strong and distinct bands at 880, 834 and 750 cm^{-1}, respectively, due to aromatic out-of-plane C-H bending can be clearly identified in the spectra of the pitch precursor and the green fiber (Figures 1A and 1B). The assignment of the three aromatic out-of-plane C-H bending modes are listed in Table I. The strong band at 1600 am^{-1} in Figure 1 is due to the aromatic ring stretching mode. The intensity of the aromatic ring stretching mode is enhanced by the presence of phenolic groups or methylene bridges linking the aromatic rings (19). It is very likely that some other aromatic C-H bending modes are superimposed by the three strong bands at 880, 834 and 750 cm^{-1} in Figure 1 as reporteded in the IR study of coal samples (18).

The two weak bands at 3550 and 3450 cm^{-1} shown in both the spectrum of the pitch precursor (Figure 1A) and the spectrum of the green fiber (Figure 1B) are probably associated with the stretching mode of free hydroxyl and hydrogen-bonded hydroxyl. A weak carbonyl band at 1697 cm^{-1} , which is not visible in the spectrum of the pitch precursor (figure 1A), is present in the spectrum of the green fiber (Figure 1B). The carbonyl was the oxidation product formed during

the melt blown process, by which the green fiber was produced. The functional groups present in the green fiber and the corresponding IR vibrational band frequencies are summarized in Table I.

Table I. The functional groups and the corresponding IR vibrational frequencies of green fiber.

Functional Groups	IR Vibrational Frequency (cm^{-1})	
$-CH_3$	ν_{-CH}	2968, 2866
	δ_{-CH}	1444, 1377
$-CH_2$	ν_{-CH}	2918, 2850*
	δ_{-CH}	1444*
Unsaturated Aliphatic Hydrocarbon	$\nu_{=C-H}$	3045
Aromatic Hydrocarbons	$\nu_{=C-H}$	3075-3035
1,2-bisubstituted Aromatic Hydrocarbons	$\gamma_{=C-H}$	750
Trisubstituted Aromatic Hydrocarbons	$\gamma_{=C-H}$	834
Aromatic Hydrocarbons with Isolated Hydrogens	$\gamma_{=C-H}$	880
Aromatic Ring	$\nu_{C=C}$	1600
C=O	ν	1697
-OH	ν	3450, 3550

* Overlapped bands.

The Stabilization of the Pitch Precursor carbon Fiber. The petroleum pitch based precursor carbon fiber at different stages of the stabilization process were analyzed by FT-IR/PAS (Figures 2 and 3). It can be seen in the infrared spectra of the partially stabilized carbon fiber (Figures 2A-2D) that the band at 3550 cm^{-1} associated with the stretching mode of the free hydroxyl and band at 1697 cm^{-1} associated with the carbonyl stretching mode increased their intensities during the first 40 min of the programmed thermal stabilization process. This indicates that free hydroxyl and carbonyl were formed as the oxidation products at the early stages of the stabilization process. No changes are visible in the bands due to the C-H stretching and bending modes in Figure 2.

When the carbon fiber was oxidized for 50 min, the amount of the free hydroxyl was increased to such a extent that the hydroxyls form hydrogen bonding to each other as demonstrated by a broad band at 3400 cm^{-1} with a increased intensity in Figure 3A. The intensity of the carbonyl band at 1697 cm^{-1} is increased significantly, while the C-H stretching bands in the 3045-2864 cm^{-1} region, the aliphatic C-H bending bands at 1444 and 1377 cm^{-1} ,and the aromatic out-of-plane bending bands in the 880-750 cm^{-1} region were reduced in Figure 3A. All the infrared spectroscopy data demonstrated that an accelerated oxidation occured during the 40-50 min time period. A broad band around 1250 cm^{-1} was formed in Figure 3A. This is mainly due to the C-O stretching mode, since large amount of -OH were formed during the same period. There is more reduction in the 880 cm^{-1} band intensity than the bands at 835 and 750 cm^{-1} so that the relative intensity of the 880 cm^{-1} band is lower than those of the other two bands in the Figure 3A. This reveals that the isolated hydrogens in the aromatic rings were easier to be oxidized than the other types of hydrogens in the aromatic structures in the carbon fiber.

When the stabilization time was increased to 70 min, the hydroxyl

stretching band at 3400 cm^{-1} and the carbonyl stretching band at 1697 cm^{-1} continue to increase their intensities and to broaden, while bands due to both the aliphatic and aromatic C-H continue to reduce their intensities(Figure 3b and 3C). The broad band around 1250 cm^{-1} also increases its intensity. The band at 1600 cm^{-1} due to the aromatic ring stretching mode appeares to have changed little in Figures 3B and 3C. Oxygen attacked both the aromatic and the aliphatic hydrocarbons while the aromatic ring remained intact during this stage of oxidization.

To determine the nature of the carbonyl-containing oxidation products formed during the stabilization process, the carbon fiber stabilized for 70 min was treated with an 0.1M NaOH solution at room temperature for 5 min. The spectrum of the carbon fiber thus treated showed a reduction in the intensity of the carbonyl band at 1697 cm^{-1} and the formation of a new band at 1380 cm^{-1}, which was due to the symmetric stretching of carboxylate carbonyl. The symmetric stretching band of the carboxylate was obviously overlapped by the strong band at 1600 cm^{-1}. Formation of carboxylate upon the treatment of the carbon fiber by a NaOH solution reveals that the carbonyl band at 1697 cm^{-1} in Figure 3C has a contribution of carboxyl. The carbonyl band at 1697 cm^{-1} was further reduced after the carbon fiber had been treated in a NaOH solution for 140 hr. Because a extended treatment of the carbon fiber in a NaOH solution allows saponification to take place, the further reduction of the intensity of the carbonyl band at 1697 cm^{-1} demonstrated that ester was also formed in carbon fiber during the stabilization process. The carbonyl band, which remained in the spectrum of the carbon fiber treated in the NaOH solutin for 140 hr, was probably due to aldehyde and ketone.

The photoacoustic spectrum of the fully stabilized carbon fiber is shown in Figure 3D. The broad, intense band at 3400 cm^{-1} is due to the hydrogen-bonded -OH groups of alcohol and phenol. The carbonyl band appears to broadened toward the high frequency region so the peak is around 1735-1697 cm^{-1} region. When the fully stabilized carbon fiber was extracted in methylene chloride, the infrared spectrum showed two distinct carbonyl bands at 1841 and 1771 cm^{-1}, respectively, and a band at 896 cm^{-1}. When the methylene extract was exposed to moisture, the intensities of the two carbonyl bands at 1841 and 1771 cm^{-1} as well as the band at 896 cm^{-1} were reduced substantially while a strong and broad band at 1715 cm^{-1} due to carboxyl carbonyl was formed. Therefore, it can be concluded that anhydride was formed as an oxidation product in the carbon fiber. The anhydride formed in the carbon fiber is probably cyclic aromatic anhydride, the dehydration product of a 1,2-dicarboxylic acid which is in turn the oxidation product of two CH_3- groups bonded to the adjacent carbons in an aromatic ring. The band at 896 cm^{-1} in the extract of the methylene chloride extract was due to the C-O stretching of five-member cyclic anhydride. The oxidation products in the stabilized carbon fiber is listed in Table II.

Table II. The oxidation products of the pitch precursor carbon fiber.

Oxidation Products	IR band Frequency (cm^{-1})
Carbonyls of ketone and aldehyde	1697
Carbonyls of carboxylic acid and ester*	1697-1735
Carbonyl of aromatic cyclic anhydride	1841, 1771
Isolated hydroxyl	~3550
H-bonded hydroxyl	~3450

* Overlapped bands.

The Carbonization Process. The photoacoustic infrared spectra of the pitch precursor carbon fibers at different stages of the carbonization process are presented in Figures 4B-4E. After the stabilized carbon fiber was heated from 300°C to 500°C, the amount of hydroxyl and carbonyl in the carbon fiber was decreased as demonstrated by the significant reduction in the intensities of the

two bands at 3400 cm^{-1} and 1697 cm^{-1} in Figure 4B. It is also found that most of the aliphatic hydrocarbons were eliminated during this period, because the aliphatic hydrocarbon bands in the 2968~2864 cm^{-1} region (the C-H stretching modes) and in the 1444-1377 cm^{-1} region (the C-H bending modes) decreased drastically in the infrared spectrum of the carbon fiber heated to 500°C (Figure 4B). The aromatic hydrocarbon bands at 3050 cm^{-1} (the C-H stretching modes) and in the 880-750 cm^{-1} region (the aromatic C-H out-of-plane bending), as well as the aromatic ring stretching band at 1600 cm^{-1} appears to be unchanged in Figure 4B compared with the spectrum of the stabilized carbon fiber (Figure 4A).
The infrared spectrum of the carbon fiber heated to 700°C (Figure 4C) reveals that all the hydroxyl and most of the carbonyl groups were eliminated in the carbon fiber. Only a very weak carbonyl band at 1697 cm^{-1} is seen in Figure 4C. The intensities of the aromatic hydrocarbon stretching band at 3050 cm^{-1} as well as the out-of-plane bending of the 1,2-bisubstituted aromatic C-H band at 750 cm^{-1} were drastically reduced in Figure 4C. The intensity of the aromatic ring stretching band at 1600 cm^{-1} was also reduced significantly in Figure 4C. The infrared spectroscopy data indicated that the aromatic rings were condensing and the hydrogens in the aromatic rings were being eliminated when the carbon fiber was heated from 500 °C to 700 °C.

When the carbonization temperature reached 900 °C, all the vibrational bands in the infrared spectrum (Figure 4C) were diminished . As a result, the infrared spectrum (Figure 4D) appears to be a flat line . All the functional groups in the carbon fiber were totally eliminated at this stage of carbonization. The infrared spectrum of the carbon fiber heated to 1100°C (Figure 4E) is identical to Figure 4D.

Conclusions

1. The unoxidized pitch carbon fiber contains aromatic hydrocarbons, saturated and unsaturated aliphatic hydrocarbons, as well as small amount of carbonyl and hydroxyl.

2. Hydroxyls of alcohol and phenol, carbonyls of ketone/aldehyde, carboxylic acid, ester and anhydride are formed during the stabilization process of the pitch precursor carbon fiber.

3. All the carbonyls, hydroxyls and hydrocarbons in the stablized carbon fiber were gradually eliminated during the carbonization process. The aromatic ring condensation started to take place when the temperature reached above 500°C. All the functional groups were eliminated at 900 °C.

References

1. Otani, S. Carbon 1965, 3, 31.
2. Sawran,W.R.;Turill,F.H.;Newman,J.W.;Hall,N.W. U.S. Paten 4,497,789, 1985.
3. Saneta,R.; Wlochowicz,A.; Wysocki,M. Angew. Makromol. Chem. **1986**,140, 161.
4. Poxon, D.W.; Wright, R.G. J. Chromatogr. **1972**, 61, 142.
5. Searl, D.T.; Cassialy, F.J.; King, W.H.; Brown, R.A. Anal. Chem. **1970**, 42, 945.
6. Geinko, R.A.; Lewis, I.C. Anal. Chem. **1975**, 47, 2151.
7. Glajch, J.; Lubkowitz, J.A.; Roger, L.B. J. Chromatogr. **1979**, 68, 355.
8. Albers, G.; Lenart, L.; Oelert, H. Fuel **1974**, 53, 47.
9. Painter, P.C.; Yamada, Y.; Jenkins, R.G.; Coleman, M.M.; Walker, P.L. Fuel **1978**, 58, 293.
10. Fuller, E.L.; Smyrl, M.R. Fuel **1985**, 64, 1143.
11. Ito, I.; Seki, H.; Lino, M. Fuel **1988**, 67, 573.
12. Zawadski, T. Carbon **1988**, 26, 619.
13. Sajak, K.; Wlochowicz, A.; Wysocki, M. Acta Polym. **1984**, 35, 580.
14. Usami, T.; Itoh, T.; Ohtani, H.; Tsuge, S. Macromolecules **1990**, 23, 2460.
15. Yang, C.Q. Anal. Chem. Acta. **1987**, 194, 303.
16. Yang, C.Q. Appl. Spectrosc. **1987**, 45, 102.
17. Yang, C.Q. Ind. Eng. Chem. Res. **1992**, 31, 617.
18. Painter, P.; Starsinic, M.; Coleman, M. in Fourier Transform Infrared Spectroscopy; Ferraro, J.R.; Basile, L.J. Eds.; Academic Press: Orlando, 1985; pp. 177-182.
19. Painter, R.; Snyder, M.; Starsinic, M.; Coleman, M.; Kuehn, D.; Davis, A. Appl. Spectrosc. **1981**, 35, 475.

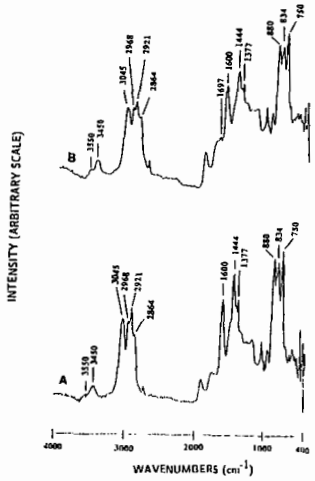

Figure 1 Photoacoustic infrared spectra of (A) the petroleum pitch; (B) the pitch precursor carbon fiber.

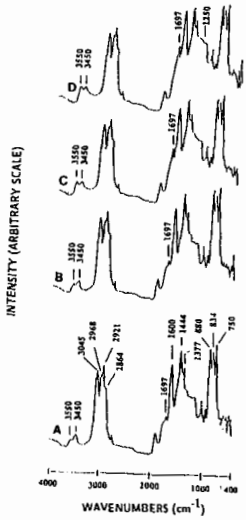

Figure 2 Photoacoustic infrared spectra of the pitch precursor carbon fiber stabilized for different times (min): (A) 10; (B) 20; (C) 30; (D) 40.

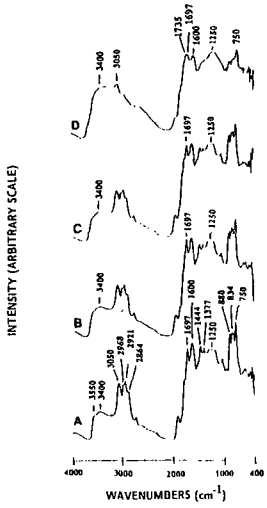

Figure 3 Photoacoustic infrared spectra of the pitch precursor carbon fiber stabilized for different times (min): (A) 50; (B) 60; (C) 70; (D) 80.

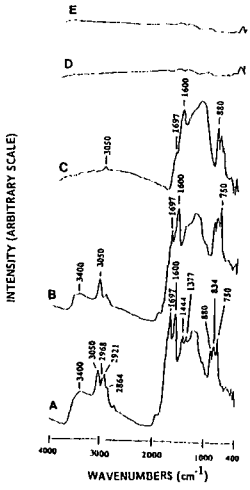

Figure 4 Photoacoustic infrared spectra of (A) the full stabilized carbon fiber. The photoacoustic infrared spectra of the carbon fiber heated to different temperatures during carbonization(°C): (B) 500; (C) 700; (D) 900; (E) 1100.

ON THE NATURE OF HYDROAROMATIC HYDROGEN IN MODEL COMPOUNDS AND IN COAL

Jianli Hu, James H. Whitcomb, John W. Tierney, and Irving Wender
Chemical and Petroleum Engineering Department,
University of Pittsburgh, Pittsburgh, PA 15261

Keywords: Catalytic Dehydrogenation, Hydroaromatic Hydrogen, Hydrogen Evolution/Transfer

ABSTRACT

The catalytic dehydrogenation of coal to yield molecular hydrogen using palladium on a support has been investigated by several workers. However, little has been reported on elucidation of the nature of the dehydrogenation reaction, the ease of removal of hydroaromatic hydrogen from different structural components or the effects of solvents of different boiling points, reduction potentials, hydrogen transfer ability, or the mechanism of hydrogen removal. The present study used model hydroaromatic compounds to gain information on the ease of catalytic removal of hydrogen either as H_2 or to a hydrogen acceptor. The course of the dehydrogenation of a number of model compounds was found to involve hydrogen transfer to intermediates, some of which have been identified. A mechanism for the palladium-catalyzed removal of hydrogen is proposed. The use of a hydrogen acceptor has permitted use of low-boiling solvents so as to minimize side reactions. Catalytic dehydrogenation, in addition to gaining information on hydrogen transfer to coal from hydroaromatic compounds, promises to be a valuable analytical technique to determine the amount and nature of hydroaromatic hydrogen in coal, recycle oils and heavy petroleum residues.

INTRODUCTION

The sources of hydrogen in direct coal liquefaction are molecular hydrogen and hydrogen in hydroaromatic structures in added solvents, recycle oils or in coal itself. It is important to have a measure of donatable hydrogen atoms available in hydroaromatic structures in coal and in oils derived from coal. Few efforts have been directed towards developing a direct method for determination of the nature and reactivity of hydroaromatic hydrogen that exists in coal. It is generally accepted that the main hydrogen sources in coal liquefaction are hydroaromatic structures containing two or more cyclic rings. Hydroaromatics may contain two available hydrogen atoms as in 9,10-dihydroanthracene (9,10-DHA), four as in a tetrahydroanthracene (THA), six as in a corresponding hexahydro compound (HHA) or eight as in an octahydroanthracene (OHA). Determination of the relative rates of hydrogen donation of hydroaromatics in recycle solvents is of particular important in achieving insights into the chemistry of coal liquefaction.

^{1}H-NMR and ^{13}C-NMR[1] techniques have been used for the evaluation of hydroaromatic hydrogen. This approach can be applied to distillate fractions, but the residual material gives diffuse spectra and analysis becomes uncertain.

Reggel and coworkers[2,3] studied the catalytic dehydrogenation of coal using a 5% $Pd/CaCO_3$ catalyst at the boiling point of a solvent. They found the compound *phenanthridine*(b.p. 350 °C), an excellent coal solvent, to be the most useful vehicle. It appeared that solvents with low reduction potentials were better than vehicles of higher reduction potentials in the removal of hydrogen from coal. With this technique, Reggel et al. concluded that high rank coals contain considerable hydroaromatic hydrogen with a maximum of about 40 atoms of hydrogen removed per 100 carbon atoms at coals of about 76% carbon(maf). Much of their work was aimed at studying coal structure and it was suggested that lignite and subbituminous coal contain substituted benzene rings with few hydroaromatic structures.

Heredy et al[4] felt that the use of high boiling solvents such as phenanthridine, which is also a polar solvent, might tend to adduction and condensation reactions leading to an incorrect measurement of hydroaromatic hydrogen.

The objectives of the present work are to study the catalytic dehydrogenation of model compounds and to relate the results to the catalytic dehydrogenation of coal, recycle solvents and liquefaction residues and to determine the fate of hydroaromatic hydrogen during these reactions. Kinetic analysis and the search for possible mechanistic pathways in catalytic dehydrogenation are also important aims of this research. In addition, these studies promise to shed light on the interchange and transfer of hydrogen involved between aromatic and hydroaromatic structures during coal liquefaction. It is hoped that an analytic method for determination and differentiation of hydroaromatic hydrogen will emerge from this research together with difficult to obtain information on the fate of hydrogen atoms attached to polynuclear systems during the liquefaction of coal.

We first investigated the effect of various high boiling solvents on the catalytic dehydrogenation of a number of model hydroaromatic compounds containing trinuclear polycyclic rings. Removal of hydrogen appears to be affected by both the boiling point of the vehicle and its reduction potential. We then found that solvents that boil as low as 245 °C could be used in the catalytic dehydrogenation of these model compounds if we added a good hydrogen acceptor such as stilbene. This unsaturated compound readily accepts hydrogen atoms to form bibenzyl under our typical catalytic dehydrogenation conditions.

EXPERIMENTAL

The dehydrogenation system is designed to provide for automatic data recording. Reactions were carried out in a three-necked flask at atmospheric pressure. The palladium catalyst was reduced with flowing hydrogen at 150°C for one hour prior to reaction. After the flask was cooled to room temperature under hydrogen, the model compound and vehicle were charged into the flask containing an Alnico stirring bar. The system was purged with He for 20 minutes and the flask then fitted with a mantle and heated. Evolved gases from the reaction were taken from the middle neck and collected over mercury in a burette. The mercury level used to maintain the pressure was controlled by a bulb mounted on a slide mechanism, by which the mercury level in both the bulb and burette were equalized. The level was recorded automatically, thus providing a continuous recording of the gas volume within the burette. The yield of hydrogen evolved was calculated from the difference of hydrogen evolved from the dehydrogenation of the model compound and a blank run. The hydrogen yield is expressed as the percentage of the theoretical available hydroaromatic hydrogen in the model compound. For example, the theoretical amount of hydroaromatic hydrogen in 9,10-DHA (2 atoms of hydrogen per molecule)

is 140.8 cc/gram, measured at 25 °C and 740 mm of Hg. In the presence of stilbene, a hydrogen acceptor, hydroaromatic hydrogen was mostly transferred to the hydrogen acceptor rather than evolved as hydrogen gas. The amount of hydrogen transferred was measured from the amount of bibenzyl formed.

Gas samples were removed from the sample port and analyzed by GC(Hewlett Packard 5880A). The residues were analyzed by GC and by GC-MS(The GC is a HP-5890 series II and the mass spectrometer is a HP-5970 series selective detector). Organic chemicals were obtained from Aldrich Chemical Inc.; catalysts were obtained from Strem Chemical Co. and from the Engelhard Corp.($Pd/CaCO_3$, Pd/C).

RESULTS AND DISCUSSION

Effect of Boiling Point and Reduction Potentials on Hydrogen Evolution

Thermodynamically, high temperature and low pressure favor dehydrogenation; coal liquefaction, therefore, requires high hydrogen pressure. Reggel et al. postulated that the reduction potential, the energy required to accept an electron of the solvent, is of importance in catalytic dehydrogenation. This is borne out by the data obtained from catalytic dehydrogenation of 9,10-DHA with several vehicles. Pyrene, with a high boiling point (393 °C) and a comparatively low reduction potential(-1.56V) gives 95.1 percent of the theoretical yield of molecular hydrogen. p-Terphenyl, b.p. 383°C, but with a high reduction potential gives only 82.1% of H_2. Phenanthridine and anthracene, with lower boiling points and low reduction potentials, give high H_2 yields. Comparison of the use of phenanthrene and anthracene, molecular isomers, as vehicles is quite dramatic. The lowest H_2 evolution occurs with phenanthrene which boils only 3°C below anthracene but has a significantly higher reduction potential. This effect, the relative importance of boiling point and reduction potential of solvents on catalytic dehydrogenation, bears further investigation.

Dehydrogenation of 9,10-DHA with Various Solvents in the Presence of Stilbene, a Hydrogen Acceptor

The suggestion that use of a high-boiling solvent, indeed a nitrogen-containing vehicle, could lead to side reactions, may well be valid. We found that we could use low-boiling solvents in the presence of a hydrogen acceptor and the following experiments used stilbene as the hydrogen acceptor. Interestingly, depending on the vehicle, some hydrogen was evolved as molecular H_2 while some hydrogen was transferred to stilbene to form bibenzyl. The results are summarized in Table 2.

Initial experiments were carried out with two high boiling solvents (p-terphenyl and pyrene)which tended to yield more H_2 as gas than that transferred to the acceptor. Examination of the results reveals that the ratio of hydrogen evolution and hydrogen transfer may also depend on both temperature and reduction potential.

Experiments were then carried out with quinaldine (b.p. 248°C, reduction potential -1.50V) and 2-methylnaphthalene (b.p. 243°C, reduction potential -1.98V). Similar results were obtained with both solvents. 2-Methylnaphthalene is a good electron transfer agent and this probably is responsible for its effectiveness. With these low-boiling vehicles, hydrogen transfer to stilbene is the main step in the catalytic dehydrogenation of 9,10-DHA.

Also shown in Table 2, the surface area of the Pd support had essentially no effect. The reduced Pd on carbon catalyst, with a surface area of 1000 m^2/g, gave the same or slightly higher amounts of hydrogen removal from 9,10-DHA as did reduced Pd on $CaCO_3$ (surface area

of $12m^2/g$).

An experiment with biphenyl (b.p. 255°C), a good electron transfer agent, resulted in 87% of the hydrogen in 9,10-DHA being transferred to stilbene with only 2.3% evolved as H_2 gas.

It is important that the palladium be in its lowest oxidation state; exposure of the catalyst to air affects the dehydrogenation deleteriously.

It is interesting to note that when 9,10-DHA is catalytically dehydrogenated in the presence of half the equivalent of stilbene, half the hydroaromatic hydrogen in 9,10-DHA is transferred to stilbene, half is evolved as gas (Table 2). It was observed that hydrogen evolution occurred after the stilbene was hydrogenated, indicating that hydrogen transfer to stilbene is preferred over H_2 gas evolution under these conditions.

Characterization of Hydrogen Transfer Mechanism of Hydroaromatics

Several hydroaromatic compounds were dehydrogenated in the presence of stilbene with quinaldine as the vehicle in an attempt to elucidate the mechanism of hydrogen transfer. Dehydrogenation of 9,10-DHA gives only anthracene and hydrogen; it is unlikely that intermediate polynuclears are involved.

The model compound 1,4,5,8,9,10-hexahydroanthracene (HHA) is neither an aromatic nor a hydroaromatic compound. It does not contain an aromatic ring but has four isolated double bonds. But catalytic dehydrogenation of this compound in quinaldine in the presence of stilbene yields the hydroaromatic compounds 9,10-DHA, 1,2,3,4-tetrahydroanthracene (THA) and 1,2,3,4,5,6,7,8-octahydroanthracene (OHA) as well as bibenzyl formed by addition of hydrogen to the stilbene. As shown in Figure 1, the concentration of HHA decreases rapidly as the reaction proceeds. The yield of THA increases to a maximum after 5 minutes and decreases thereafter; it is then maintained at very low concentrations. The initial formation rate of OHA is very slow and then increases to a maximum value as the concentration of THA decreases; its concentration then falls slowly to a constant value. As for 9,10-DHA, its concentration increases smoothly at first and reaches a maximum in 10 minutes, following the maximum observed for THA by 5 minutes. The hydrogen transfer rate to stilbene is higher than the rate of formation of anthracene, particularly in the initial stages. It is noteworthy that the concentration of anthracene increases significantly after 10 minutes, when the concentrations of the hydroaromatics begins to drop, suggesting that the precursor of THA is a key intermediate through which both OHA and DHA are produced.

When the hydroaromatic, OHA, was dehydrogenated in the presence of stilbene, its concentration slowly decreased with time. After 40 minutes, only 10% of hydrogen was transferred and 15% of THA was formed. No 9,10-DHA was formed and only trace amounts of anthracene were detected. This indicates that OHA is a relatively poor hydrogen donor compared with THA and DHA. This is in keeping with the recent findings of Bate and Harrison[6] who found, that for coal dissolution, the type of donor present may be more important than the total hydrogen donor content. The dehydrogenation of a mixture of DHA, HHA and OHA was carried out to compare hydrogen transfer rates of these model compounds (Figure 2).

On the Mechanism of Catalytic Dehydrogenation

Based on the above results, a mechanism of catalytic dehydrogenation and hydrogen transfer is proposed to explain the reaction pathways involved in dehydrogenation of these model compounds. The basic dehydrogenation pathway presented is based mostly on results of the dehydrogenation of 9,10-DHA both in the presence and in the absence of a hydrogen acceptor. S, BH_2, and B refer to vehicle, 9,10-DHA, and anthracene respectively.

$$S + Pd^{\circ} == S^{-}\text{--}Pd^{+} \quad (1)$$

$$S^{-} + BH_2 == SH + BH^{-} \quad (2)$$

$$SH + BH^{-} \longrightarrow S + B + H_2 + e^{-} \quad (3)$$

$$Pd^{+} + e^{-} \longrightarrow Pd^{\circ} \quad (4)$$

$$BH_2 \longrightarrow B + H_2 \quad (5)$$

It is assumed that the dehydrogenation step in the mechanism(eq.3) is rate controlling. A kinetic model expression based on this mechanism proposed describes the experimental curve of hydrogen evolved versus time very well. Further information is needed to improve this model and to apply it to the dehydrogenation of other substances containing hydroaromatic structures.

In the presence of a hydrogen acceptor, stilbene, a similar reaction pathway is involved, where the reduced solvent transfers hydrogen to adsorbed stilbene rather than further reacting with the BH^{-} intermediate to evolve hydrogen to gas phase.

CONCLUSIONS

For vehicles boiling above 340 °C, both boiling point and reduction potential of the solvent employed appear to influence the palladium-catalyzed dehydrogenation of model polynuclear hydroaromatic compounds to yield gaseous hydrogen. For certain solvents that boil about 100 °C lower(245 °C or so), the palladium-catalyzed dehydrogenation of the same compounds occurs readily in the presence of a good hydrogen acceptor such as stilbene. Depending on the model hydroaromatic compound and reaction conditions, hydroaromatic hydrogen may be evolved as molecular hydrogen or be transferred to the hydrogen acceptor. With lower boiling vehicles, adduction reactions are minimized with selective removal of hydroaromatic hydrogen.

A pathway for palladium-catalyzed dehydrogenation is proposed. The first step involves transfer of an electron from zerovalent palladium to the solvent. The solvent then remove a proton from the hydroaromatic compound. The slow step is the removal of hydrogen from reduced solvent.

The mechanism of removal of different hydroaromatic hydrogens may occur through various intermolecular transfers. There is a need to quantify not only total hydroaromatic content in coal and recycle solvents but also to determine the contributions from individual types of hydroaromatic compounds.

ACKNOWLEDGEMENT

The authors acknowledge the financial support from U.S. Department of Energy under Contract No. DE-PS22-89PC89998.

REFERENCES

[1].Burke, F.P. and Winschel, R.A., Annual Report to DOE, Contract No.DE-AC22-80-PC30027(1980)

[2].Reggel, L.; Wender, I.; Raymond, R. Fuel, 1968,47,373-390

[3].Reggel, L.; Wender, I.; Raymond, R., Science, Vol.137, 681-682(1962)

[4].Heredy,L.A.; McCoy, L.R.; Skowronski,R.P.; Ratto,J.J. Final Report on the Chemistry of the Extractive Phase of Coal Liquefaction, US-DOE Contract No. N45569(1985).

[5].Deshpande,A.P., M.S. Thesis, University of Pittsburgh,1991

[6].Harrison, G., Bate, K., Proceeding of International Coal Conference, September, 1991, England, 739-742

Table 1. Dehydrogenation of 9,10-DHA with Pd/C in the Presence of Various Solvent

Polynuclear Aromatics	B.P. °C	Reduction Potential,-V	Dehydrogenation, H_2 yield, cc	Blank, H_2, cc	Theoretical H_2 yield, %
Phenanthridine	348	1.58	28.9	1.1	98.3
Phenanthrene	337	1.90	24.7	2.0	80.5
Pyrene	393	1.56	29.8	3.0	95.1
p-Terphenyl	383	2.01	26.4	3.2	82.1
Anthracene	340	1.46	27.0	1.1	91.8

Table 2. Dehydrogenation of 9,10-DHA with Pd/C in the Presence of a Hydrogen Acceptor

Catalyst	Vehicle Reduction Potential and B.P.	Feed		H_2 Evolved, %	Bibenzyl %
		DHA, g	Stilbene, g		
Pd/C	p-Terphenyl 2.01, 383°C	0.2	0.2	79.7	20.3
Pd/C	Pyrene 1.56, 393°C	0.2	0.2	61.3	38.7
NONE	Phenanthridine 1.58, 348°C	0.2	0.2	11.1	16.5
NONE	o-Terphenyl 1.90, 337°C	0.2	0.2	1.0	9.1
Pd/C	Quinaldine 1.50, 248°C	0.2	0.2	2.7	92.5
$Pd/CaCO_3$	Quinaldine 1.50, 248°C	0.2	0.2	14.5	74.0
Pd/C	2-Methylnaphthalene 1.96, 243°C	0.2	0.2	5.5	93.4
$Pd/CaCO_3$	2-Methylnaphthalene 1.96, 243°C	0.2	0.2	8.8	90.4
$Pd/CaCO_3$	Biphenyl 2.18, 255°C	0.2	0.2	2.3	87.2
Pd/C	Quinaldine 1.50, 248°C	0.3	0.15	50	50

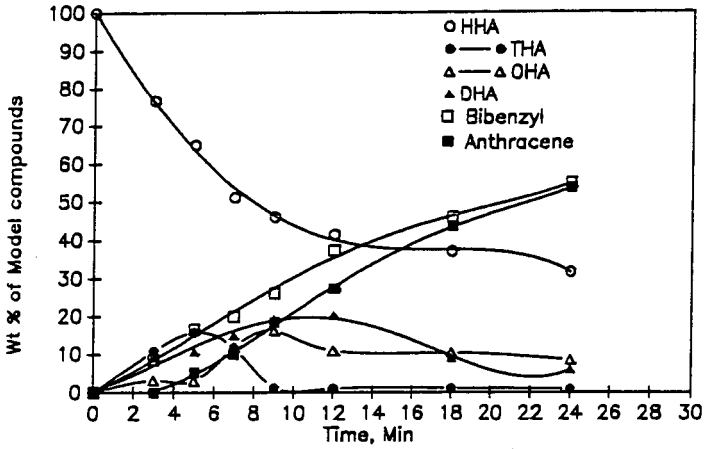

Figure 1. Dehydrogenation of HHA with $Pd/CaCO_3$, quinaldine as vehicle in presence of stilbene as a hydrogen acceptor.

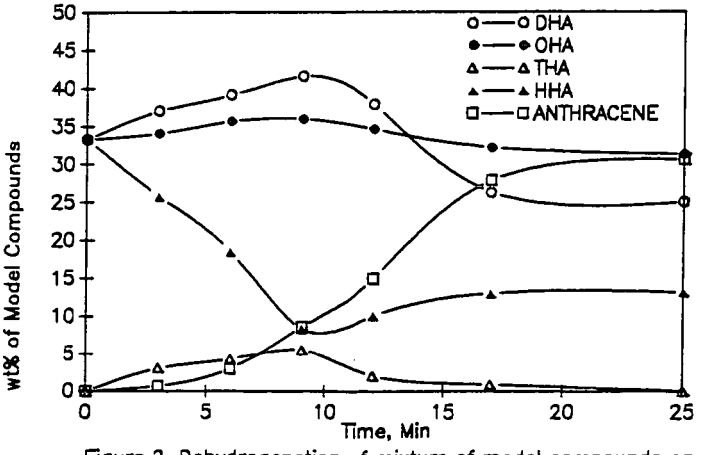

Figure 2. Dehydrogenation of mixture of model compounds on 0.5g reduced $Pd/CaCO_3$ with quinaldine as vehicle in presence of stilbene as a hydrogen acceptor.

CHARACTERIZATION OF IRON AND SULFIDED IRON OXIDE CATALYSTS BY ELECTRON MICRODIFFRACTION

Ram Srinivasan, Robert A. Keogh, and Burtron H. Davis
Center for Applied Energy Research
University of Kentucky
3572 Iron Works Pike
Lexington, KY 40511

Keywords: iron oxide, sulfidation, sulfation, microdiffraction, ferric naphthanate.

INTRODUCTION

The use of iron oxide as a catalyst for direct coal liquefaction was introduced soon after the initial discovery of the process (1-4). Iron oxide in the form of "red mud" has continued to be utilized (5). This was the catalyst of choice for the first stage reactor for many of the recent runs at the Wilsonville, Alabama Advanced Coal Liquefaction facility (6).

The availability of an ultrafine iron oxide catalyst (300 m^2/g) provided an opportunity to follow with time the sulfidation of iron under mild direct coal liquefaction conditions. The use of transmission electron microscopy permitted a determination of the crystal structure and the elemental composition of individual catalyst particles.

EXPERIMENTAL METHODS

The Fe_2O_3 as-received powder was sulfided using dimethyldisulfide (DMDS) at 385°C for different periods ranging from 15 to 60 minutes.

For X-ray diffraction analysis, a Philips X-ray diffractometer equipped with an XRG-3100 generator, was used. The radiation used was CuKα ($\lambda_{CuK\alpha}$ = 1.1548 Å). A graphite monochromator was placed on the diffracted beam path. The data was acquired from the VAX/VMS V5.3-1 system.

Electron microscopy work was done using a Hitachi H800 NA scanning transmission electron microscope (STEM) at an operating voltage of 200 kV. This STEM is equipped with a silicon-lithium diode detector (Link) and a multichannel analyzer (Tracor 500). The X-rays emitted by the specimen upon electron irradiation were collected in the range 0-20 KeV for 60 seconds.

RESULTS AND DISCUSSION

The Fe-S system is so complex that various phases could be obtained as a result of sulfidation process. Numerous crystalline phases that exist in this system are presented in Table 1.

The precursor used for sulfidation studies was Fe_2O_3 (Mach Inc.). The surface area of these powders was 300 m^2/g. The electron micrograph obtained from this as-received material is presented in Figure 1. An electron microdiffraction pattern obtained from a 5 nm region is shown in the inset in Figure 1, indicating that the material may be amorphous.

A particle size analysis indicates that the major fraction of the particles lies in the range 1-3 nm in diameter.

A typical X-ray diffraction pattern for the catalyst Fe_2O_3-sulfided for 15 minutes at 385°C is shown in Figure 2. The X-ray peak intensities and the Bragg positions of 2θ correspond clearly to Fe_7S_8 phase. This is a hcp system with a_o = 0.686 nm and c_o = 1.7062 nm. All the [hkl] indices corresponding to each profile are shown in this figure. The X-ray diffraction patterns obtained from other samples sulfided at longer times exhibited clearly the Fe_7S_8 (hcp) phase similar to that shown in Figure 2. However, the intensity was found to increase proportionately with the period of sulfidation time at 385°C. Thus, the crystal phase developed in all the catalysts is Fe_7S_8 according to the X-ray diffraction data (compare Table 1).

An electron micrograph obtained from the sample Fe_2O_3 sulfided at 385°C for 15 minutes is presented in Figure 3. Larger hexagonal crystals are formed after sulfidation at 385°C for 15 minutes. Several electron microdiffraction patterns were obtained from numerous individual crystals.

EDX analysis was also carried out along with the microdiffraction study. The particles appear to have grown into large hexagonal crystals, and yielded strong X-ray signals for $Fe_{K\alpha}$ and $S_{K\alpha}$ lines. Similar results were obtained for the Fe_2O_3 catalyst sulfided for 30 minutes. Likewise, large dense hexagonal crystals were observed for the one sulfided for 60 minutes. Similar size particles were obtained for either 15 minute and 60 minute sulfidation. Once the small oxide particles have undergone sulfidation for 15 minutes or more, they have grown to form hexagonal crystals which are larger than the precursor oxide particles, which show various iron sulfide phases. However, the majority of the diffraction patterns correspond to the Fe_7S_8 phase.

Ferric naphthanate was sulfided at 385°C for 15, 30 and 60 minutes respectively, under the same experimental conditions described above. A typical electron micrograph obtained from the 60 minute sulfided sample is shown in Figure 4(a) and a single hexagonal crystal is presented in Figure 4(b). The particle morphology for this catalyst is different from the other samples described above. The particles, although hexagonal in shape, consist of imperfections such as holes and dislocations. One such dislocation emanating from the boundary of the crystal can be seen in Figure 4(b). Several electron microdiffraction patterns revealed the structure to be FeS_2, FeS and Fe_7S_8.

The primary question plaguing the scientific community working in the area of direct coal liquefaction is the state of iron. Whether the iron oxide undergoes a phase transition directly to Fe_xS_y phases or it transforms to metallic iron first and then goes to form Fe_xS_y is the question to be addressed. While the major crystalline phase after sulfidation at 385°C for 15 minutes or more remains Fe_7S_8, evidence was presented to show the existence of minor amounts of other Fe_xS_y phases. No evidence was found for the existence of metallic iron in the sulfided iron catalysts nor in the sulfided ferric naphthanate catalysts. It therefore appears that 15 minutes of sulfidation produces large iron sulfide crystals.

ACKNOWLEDGMENT

This work was supported by the DOE contract #DE-AC22-90PC90049 and the Commonwealth of Kentucky.

REFERENCES

1. F. Bergius, "Chemical Reactions Under High Pressure", Nobel Lecture, May 21, 1932.
2. A. N. Stranges, *Fuel Proc. Tech.*, **16**, 205 (1987).
3. W. R. K. Wu and H. H. Storch, "Hydrogenation of Coal and Tar", Bulletin 633, Bureau of Mines, U.S. Department of the Interior, Washington, DC, 1968.
4. E. E. Dovath, *Fuel Proc. Tech.*, **1**, 3 (1977).
5. A. Eamsiri, W. R. Jackson, K. C. Pratt, V. Chreston and M. Marshall, *Fuel*, **71**, 449 (1992).
6. J. M. Lee, C. E. Cantrell, S. V. Gollakota, O. L. Davies, M. M. Corser and P. Vimalchand, *ACS Div. Fuel Chem. Preprints*, **36**, 1915 (1991).

Table 1

Crystalline Phases in Fe-S System

Formula	Crystal Structure	Lattice Parameters Å		
Fe_7S_8	HCP	a = 6.867	c = 17.062	
FeS	HCP	a = 5.967	c = 11.735	
Fe_3S_4	HCP	a = 3.47	c = 34.5	
$Fe_{1-x}S$	HCP	a = 6.88	c = 22.90	
FeS_2	Cubic	a = 5.417		
FeS	Cubic	a = 5.423		
Fe_7S_8	Monoclinic	a = 11.902	b = 6.859	c = 22.787
β-$Fe_{1-x}S$	HCP	a = 6.894	c = 40.15	
Fe_9S_8	Tetragonal	a = 3.679	c = 5.047	
FeS_2	Orthorhombic	a = 4.436	b = 5.414	c = 3.381
Fe_3S_4	Cubic	a = 9.876		
FeS	Tetragonal	a = 3.676	c = 5.032	

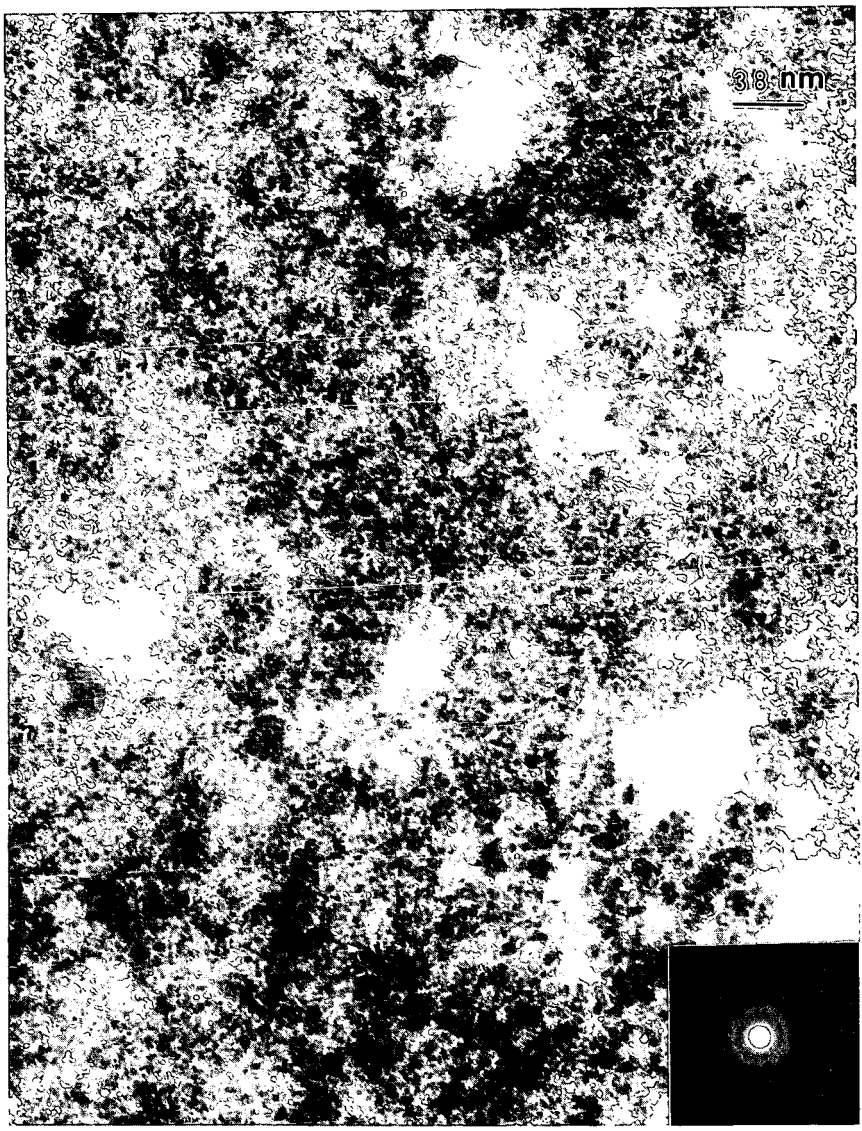

Figure 1. Transmission electron micrograph from the as-received Fe_2O_3 catalyst (inset). Microdiffraction pattern showing diffuse rings.

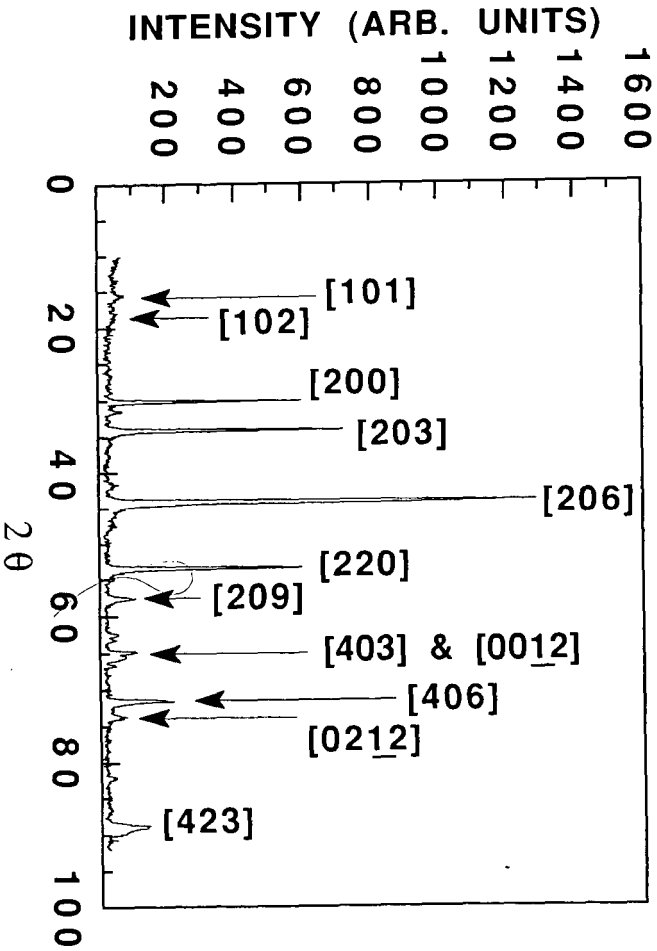

Figure 2. X-ray diffraction pattern from the Fe_2O_3 catalyst sulfided at 385°C for 15 minutes showing the Fe_7S_8 (hcp) phase.

Figure 3. Transmission electron micrograph from the as-received Fe_2O_3 catalyst after sulfiding at 385°C for 15 minutes showing large hexagonal crystals.

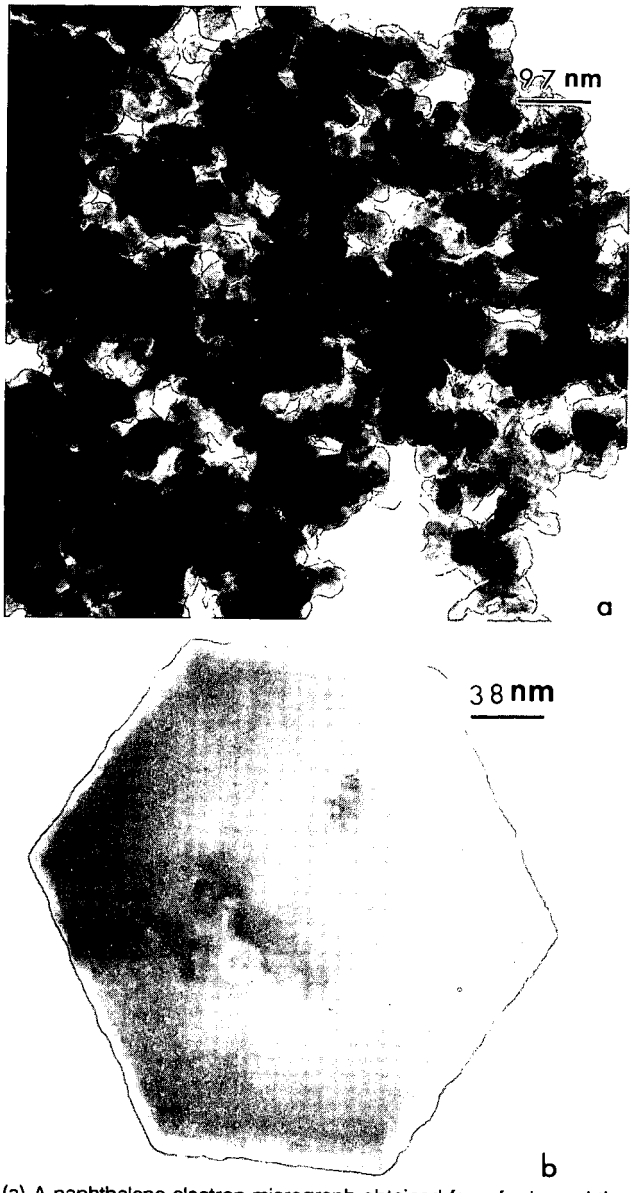

Figure 4. (a) A naphthalene electron micrograph obtained from ferric naphthanate after sulfidation at 385°C for 60 minutes. (b) A large single hexagonal crystal from the above sample.1

Development of a Performance Related Chemical Model of Petroleum Asphalt for SHRP

Raymond E. Robertson, Jan F. Branthaver, and J. Claine Petersen
Western Research Institute
P.O. Box 3395
Laramie, WY 82071

Keywords: Asphalt, Model, Aging

INTRODUCTION

In the three introductory papers for this symposium on petroleum asphalt used in roadway construction, the intent is to describe the current status of a comprehensive model of petroleum asphalt as developed during the Strategic Highway Research Program (SHRP). These papers are to lay out basic concepts which, in turn, are useful in describing the expected behavior of asphalt under various conditions in roadways. The primary purpose of this paper is to describe the current SHRP model in terms of the chemical composition of asphalt.

Any useful model must explain the observed behavioral characteristics as completely as possible for any given set of materials under any applicable set of conditions. In the case of petroleum asphalts, performance characteristics must include consideration of viscous and elastic properties at pavement service temperatures, nominally, -30 to +170 °F (-34 °C to +77 °C), over a wide range of shear conditions (high stress and rate under traffic to low rates associated with thermal stress) and must also describe the propensity to adhere to a wide variety of mineral aggregates under many conditions of temperature, stress, and moisture. Asphalts are chemically reactive with oxygen to the extent that their properties change upon oxidation, hence the model must also account for the effects of oxidation on their physical and performance properties.

The research that supports the model developed below has been conducted by numerous investigators and has been reported since the early part of this century. Much of the work during the Strategic Highway Research Program was refinement and validation to develop and report the current asphalt model. An extensive version of the research related to composition and physical properties of asphalt binders will appear within the next few months as the final report for SHRP Project A002A, "Binder Characterization and Evaluation." This report contains an extensive review and discussion of literature related to asphalt chemistry, physical behavior, and road performance as well as a review of the literature pertaining to petroleum. All of these areas were valuable in developing the current model, but too voluminous to cite here. Only selected publications of relevant SHRP studies are cited throughout the discussion of this paper.

RESULTS AND DISCUSSION

The function of petroleum asphalts in roadways is to serve as an adhesive to hold well compacted, graded aggregate together into what is commonly described as flexible asphalt concrete. Asphalt concretes should flex (rather than crack) under traffic load, yet be capable of viscous flow under stresses of day and night as well as summer and winter thermal cycling. Certain physical properties are unquestionably important for their behavior and their (perceived) performance in roadways. In order to understand and control physical properties, one must first understand what chemical structural units give rise to any given physical property, how the structure(s) change with various stresses, and finally what alterations in chemistry need to or can be made in order to adjust physical properties of asphalts to a desired performance.

The following discussion is devoted to a description of the chemistry of asphalts with reference to physical properties as necessary. The more detailed physical model of asphalts is presented in the following paper (1).

Current Model

The current SHRP version of a chemical description or model of petroleum asphalt can be stated rather simplistically as follows. Petroleum asphalts are roughly a half and half mixture of polar and nonpolar (neutral), relatively nonvolatile, organic compounds in which the polars are in such close proximity that a wide variety of interactions among polars occur. These interactions are presumed to be noncovalent bonds that range from a few to about 30 kilocalories per mole with a somewhat uniform distribution of bond energies. This is confirmed by rheological studies (1). Asphalts show rather uniform changes in viscoelastic properties with temperature suggesting again that a wide variety of low energy chemical bonds comprise some sort of microstructure.

The association appears to form a three dimensional network, or microstructure, that is intimately mixed with the neutral materials which behave somewhat as a plasticizer. Nuclear magnetic resonance (NMR) data have shown that intermolecular distances among polars are small, i.e. no major aggregations of polar species exist, but rather that polar species are relatively uniformly distributed within the neutral materials (2). A resulting whole asphalt is therefore somewhat elastic in nature but also has some viscous flow characteristics. The elastic nature is presumed to arise from the three dimensional network which behaves as if it is relatively high in molecular weight. However, under high shear and/or thermal stress, the molecular weight appears to decrease as viscous flow properties begin to appear. The viscous flow arises from the change in orientation of polars with respect to each other under thermal stress or stress of shear. The latter occurs without changes in any molecular structure; i.e., no chemical degradation occurs. Asphalts can also be described as metastable arrangements of polar molecules in a nonpolar medium, and the particular metastable state depends upon the thermal and shear history of each asphalt.

Elastic response, such as a rapid traffic loading, is the desirable characteristic in which the time of stress is too short for rearrangement of molecular orientation. Hence, an asphalt

responds elastically, flexing under traffic load, but returns to its original shape upon passage of the traffic. This property is important in avoiding a common failure mode known as rutting. Flow properties, or viscous flow commonly called "creep," are also desirable and occur under prolonged periods of stress in which asphalts experience day-night as well as summer-winter thermal cycling.

The evidence to support this model has been gathered from a variety of studies and experiments and is summarized as follows. Petroleum asphalts have been dissected into a series of compound types by ion exchange chromatography (IEC) (3, 4) and by size exclusion chromatography (SEC) (5). The component types are principally strong and weak acids, strong and weak bases, amphoterics (molecular species with acidic and basic sites), and neutral materials. Isolated neutrals may occur as waxlike (pseudocrystalline) materials or as oily materials which do not solidify. All fractions have aromatic and aliphatic carbon and hydrogen, but the carbon and hydrogen aromatic to aliphatic ratios vary among fractions and among asphalts (6). The polars, as defined by IEC, are generally a few percent bases, 10-20% acids, and 10-20% amphoterics. The specific percentage of each polar type varies with crude oil source.

Model compound studies using neutral (linear hydrocarbons) and their analogous mono and diamines, mono and dibasic carboxylic acids, and amphoterics (amino acids), show that addition of diacids and amphoterics had the most profound effect on physical properties. The viscosities of asphalts spiked with diacids and with amino acids rose sharply compared with all other model compounds. When naturally occurring amphoterics were isolated by IEC and then used to enrich tank asphalts, viscosities typically skyrocket with small levels of enrichment. Acids and bases have a similar but less pronounced effect. Neutrals reduce viscosities.

Further evidence for the existence of a microstructure was found using SEC experiments. The SHRP asphalts were separated into two major fractions (I and II) by SEC. The SEC experiments were conducted in toluene as a solvent, but as concentrated solutions which were chromatographed rapidly so as to disturb any microstructure as little as practically possible. Both fractions, as shown by carbon-13 NMR (6), contain sufficient condensed aromatic hydrocarbons to be highly fluorescent. Fraction I is nonfluorescent despite the significant amounts of condensed aromatic hydrocarbons. This quenching of fluorescence suggests strong association among the SEC I components. Further, the vapor phase osmometry (VPO) molecular weight of Fraction-I is always higher in toluene, a nondissociating solvent, than in pyridine, a strongly dissociating solvent. Fraction-II, on the other hand, is always highly fluorescent, suggesting a lack of association. The ratio of Fraction-I to Fraction-II is indicative of the ratio of the viscous and elastic moduli (7).

The probable existence of a microstructure was further demonstrated by cross blending SEC Fractions I and II. These experiments also demonstrated the sensitivity of each fraction to the other. Numerous examples were studied and one is cited here as a typical example. Asphalts AAD-1 and AAM-1 were separated into their SEC Fractions I and II, cross blends were prepared, and the viscosities of the resulting products measured. A portion of this experiment is as follows. Asphalt AAD-1 contains 23.4 wt % SEC-I and 76.6 wt % SEC-II.

When AAD-1 was reformulated from its own SEC-I and -II, the viscosity was 3,000 poises at 60°C. When a mixture of 23.4 wt % AAD-1 SEC-I and 76.6 wt % AAM-1 SEC-II was formulated, the 60°C viscosity was 234,000 poises. Asphalt AAM-1 is 30.6 wt % SEC-I and 69.4 wt % SEC-II with a viscosity of 5,400 poises. The crossblend of 30.6 wt % AAM-1 SEC-I and 69.4 wt % AAD-1 SEC-II had a 60°C viscosity of 380 poises. It is apparent immediately that Fraction I of AAM-1 is more dissociated by Fraction II of AAK-1 than by its own Fraction II. The opposite effect is observed for Fraction I of AAK-1 blended with Fraction II of AAM-1. In general the dispersive character of SEC Fraction II increases with decreasing average molecular weight. Molecular weight distributions of SEC Fractions II were determined by supercritical fluid chromatography (8).

Ion exchange chromatography is a time consuming and expensive process, so it was decided to investigate the use of nonaqueous potentiometric titration (NAPT) to determine the quantities and strengths of acids and bases in petroleum asphalts. The development of a method for measurement of bases was rather straightforward (9). However, upon attempting to titrate petroleum asphalts in chlorobenzene for quantities and strengths of organic acids, it was observed that there were no endpoints. In fact pyridine had to be used to dissociate the acids before endpoints could be found. This is further evidence for the persistence of a microstructure, even into dilute solution.

Still another series of experiments was carried out to imply the metastable nature of asphalts. In this study, which is noted as steric hardening experiments, asphalts were stored for extensive periods of time in a well protected atmosphere. In this particular case no atmospheric oxygen was available so no chemical reaction could take place. Yet, upon examining the viscoelastic properties, it was observed that the viscosities as well as the elastic moduli of the asphalts continued to rise as the asphalts were examined periodically over a time of several months.

Oxidative Aging

Prediction of aging of asphalts, that process in which asphalts increase in stiffness, has been of primary interest during the program. Aging is an unavoidable conditioning step, and not necessarily a cause of failure. In extreme cases, increases in stiffness to the point of embrittlement leads to cracking in roadways which in turn leads to deterioration to an unusable structure. Oxidation takes place naturally in asphalts as they are exposed to the atmosphere and this is a major contributor to aging. But other phenomena under the collective name of compatibility have a major effect upon how oxidation products affect the age hardening in asphalts (10). For clarity, the terms oxidation and aging are distinguished as follows. Oxidation is used to describe increases in oxygen-containing products while aging (age hardening) is used to describe increases in the viscoelastic properties. The prediction of aging for all asphalts then becomes oxidation plus some measure of the ability of asphalts to accommodate oxidation products. Said differently, the prediction of aging from analytical information becomes a constitutive relationship that includes, but cannot be limited to, the level of chemical oxidation. We have shown (11), as have others (e.g., 12, 13), that aging of some asphalts has a rather sharp temperature dependence at higher pavement service temperatures (60-85°C [140-185°F]). Aging at any temperature is related to asphalt source.

Age hardening in asphalts has been shown to correlate well with the concentration of ketones formed upon oxidation for asphalts from any given crude oil regardless of grade, but aging differs sharply among asphalts from different crudes. The amount of ketone formed in asphalt from one crude oil cannot be used to predict viscosity changes in asphalt from another crude oil based solely on ketone concentration (10).

A substantial series of experiments was conducted during the program to oxidatively age harden asphalts artificially. These experiments were based on those reported earlier by D.Y. Lee (14) and are collectively referred to here as those conducted in a pressurized aging vessel (PAV). The PAV experiments demonstrated clearly that both an increase in temperature and/or an increase in time resulted in an increasingly stiffer (aged) products. However, asphalts are not used in roadways as petroleum asphalts alone, but rather in contact with mineral aggregate. Hence a series of PAV experiments was conducted with asphalts in contact with a variety of different mineral aggregates together with control experiments. Asphalts recovered from mineral aggregate after PAV treatment generally had aged less than neat asphalt controls. The chemistry of aging does not appear to change over limited temperature ranges whether neat or on aggregate, only the rate appears to be substantially affected. This is predictable from the model. Polar sites on aggregates should promote structuring of polars in asphalt. As asphalts age the oxidizable sites are consumed hence the oxidation rate diminishes. An increasingly polar environment evolves as oxidation products are formed. Polar aggregate surfaces should induce greater amounts of structuring and hence quench, or slow, the observed rates of reaction compared to aging of asphalts in neat fonn. Aggregate induced structuring is consistent with the thermodynamic data reported in project A003B (15).

The effects of oxidation on aging can be explained further in terms of amphoterics (16). It is clearly understood that the oxidation of carbon and sulfur species, those that oxidize in asphalts, do not produce strong bases. More typically, highly oxidized products of carbon and sulfur are acidic. However, oxidation of asphalts at pavement service temperatures produces principally ketones and sulfoxides, both of which are weak bases. It follows then that new amphoteric materials will be formed by the introduction of new, weakly basic sites. This should promote development of the microstructure with the accompanying increase in viscosity and elasticity as was also demonstrated by spiking asphalts with amphoterics isolated by IEC. Nonaqueous potentiometric titration was an invaluable tool in determining the increase in weakly basic materials produced during oxidative aging of asphalts.

Oxidized asphalts exhibit yet another interesting behavior. Consider steric hardening again. Steric hardening of tank asphalts results in rather minor increases in viscoelastic properties with prolonged periods of storage. However, asphalts aged under PAV conditions show rather substantial increases in viscosity upon storage for prolonged periods of time. In one example, viscosity of an asphalt rose 11 million poise (1.1 million Pa·s) over a period of seven months while stored at 25 °C (77 °F). Again, this suggests the metastable nature of asphalts and further suggests that the particular state is sharply sensitive to oxidation products.

SUMMARY AND CONCLUSIONS

In summary, petroleum asphalts can be defined as concentrated mixtures of polar materials dispersed in neutral materials so that the polars form continuous, rather homogeneous, three-dimensional networks. Some molecular species in petroleum asphalts are sensitive to oxidation. This increases the polar content and hence the size and strength of the three dimensional microstructure. In turn, the viscosity and elasticity increase as aging proceeds.

ACKNOWLEDGMENTS

The work reported herein has been conducted as a part of Project A002A of the Strategic Highway Research Program (SHRP). SHRP is a unit of the National Research Council that was authorized by Section 128 of the Surface Transportation and Uniform Relocation Assistance Act of 1987. This project is titled "Binder Characterization and Evaluation" and is being conducted by the Western Research Institute, Laramie, Wyoming, in cooperation with the Pennsylvania Transportation Institute, Texas Transportation Institute, and SRI International. Dr. Raymond E. Robertson is the principal investigator. Dawn Geldien is the project administrator. The support and encouragement of Dr. Edward Harrigan, SHRP Asphalt Program Manager, and Dr. Jack Youtcheff, SHRP Technical Contract Manager, are gratefully acknowledged.

LITERATURE CITED

(1) Anderson, D.A., and Christensen, D.W., Presented at the Fall 1992 ACS Meeting, Div. Fuel Chem.

(2) Vander Hart, D.L., Manders, W.F. and Campbell, G.C., Preprints, Div. Petrol. Chem., ACS, 35 (3) 445 (1990).

(3) Branthaver, J.F., Catalfomo, M.W., and Petersen, J.C., Preprints, Div. Petrol. Chem., ACS, 35 (3) 376 (1990).

(4) Branthaver, J.F., Catalfomo, M.W., and Petersen, J.C., Fuel Science and Technol. Int., 10 (4-6) 855 (1992).

(5) Branthaver, J.F., Duvall, J.J., and Petersen, J.C., Preprints, Div. Petrol. Chem., ACS, 35 (3) 407 (1990).

(6) Jennings, P.W., Desando, M.A., Raub, M.F., Moats, R., Mendez, T.M., Stewart, F.F., Hoberg, J.O., Pribanic, J.A.S., and Smith, J.A., Fuel Science and Technol. Int., 10 (4-6) 887 (1992).

(7) Branthaver, J.F., Duvall, J.J., Petersen, J.C., Plancher, H., and Robertson, R.E., Fuel Science and Technol. Int., 10 (4-6) 1003 (1992).

(8) Barbour, F.A., and Branthaver, J.F., Preprints, Div. Petrol. Chem., ACS, 35 (3) 421 (1990).

(9) Robertson, R.E., Schabron, J.F., Gwin, A.A., and Branthaver, J.F., Preprints, Div. Petrol. Chem., ACS, 37 (3) 913 (1992).

(10) Petersen, J.C., Transport, Res. Rec., 999, 13 (1984).

(11) Harnsberger, P.M., Petersen, J.C., Ensley, E.K., and Branthaver, J.F., in press, Fuel Science and Technol. Int.

(12) Oliver, J.W.H., Fuel Science and Technol. Int., 10 (4-6) 501 (1992).
(13) Kemp, G.R. and Predoehl, N.H., Proc. Assoc. Asphalt Paving Technol. 50 492 (1981).
(14) Lee, D.Y., Final Report, Project 717S and 828S. Iowa Highway Research Board HR-124, Engineering Research Institute, Iowa State University (1972).
(15) Curtis, C.W., Final Report, Strategic Highway Research Program, Project A003B (1991).
(16) Branthaver, J.F., Kim, S.S., Catalfomo, M.W., and Goray, D.C., Presented at the Fall 1992 ACS Meeting, Div. Fuel Chem. (1992).

Chemical-Physical Property Relationships for Asphalt Cements and the Dispersed Polar Fluid Model

D.W. Christensen and D.A. Anderson
The Pennsylvania Transportation Institute
Research Office Building
University Park, PA 16802

Keywords: Rheology, chemistry, asphalt

Introduction

A comprehensive, quantitative model relating chemical compositional parameters to the physical properties of asphalt cement is needed in order to optimize the production and modifications of asphalt cements in terms of costs and potential pavement performance. The chemical-physical property relationships presented in this paper, although only semi-empirical in nature, represent a significant step towards the achievement of this goal.

This paper presents the results of research carried out under the auspices of the Strategic Highway Research Program (SHRP), on the chemical and physical properties of asphalt cement and the development of performance-related specifications for asphalt binders. The body of the paper discusses the materials and equipment used in the rheological characterization of the asphalts studied, and then presents a mathematical model for describing the linear viscoelastic behavior of asphalt binders. A series of empirical chemical-physical property relationships are then presented, relating various chemical compositional parameters to the viscoelastic model parameters. The significance of these empirical relationships are then discussed within the context of the dispersed polar fluid (DPF) model for asphalt microstructure, previously proposed by the authors as a more appropriate molecular structure for explaining the mechanical behavior of commonly used asphalt binders, as compared to the traditional micellar or colloidal model (1).

The Dispersed Polar Fluid Model

The DPF model is a conceptual model of the molecular structure of paving grade asphalt binders (1). It is an alternative to the traditional colloidal or micellar model. The most important difference between these two models is that the DPF model considers asphalt binders to be essentially single-phase systems, whereas colloidal models presume that there are two phases present, a continuous, low-polar phase, and a dispersed highly polar phase. In the traditional model, the dispersed phase is approximately represented by asphaltenes (2,3). According to the proposed DPF model, the mechanical properties of asphalt cement are dependent not upon the relative abundance of dispersed and continuous phases, but upon the magnitude and dispersion in both molecular weights and intermolecular forces (1). The DPF model applies only to paving asphalts currently in use. The authors do consider it is possible that certain asphalt binders, having very high concentration of polar molecules, may

be prone to phase separation, in which case a colloidal treatment of the microstructure would be entirely appropriate. It is however the authors' belief that the vast majority of asphalt binders now in use are best treated as single-phase systems.

Materials and Methods

The asphalt cements used in this research are those included in the Materials Reference Library (MRL) established for execution of various SHRP research projects. A total of 17 asphalts were included for study in the research presented in this paper.

Dynamic mechanical analysis was performed on these asphalts using a Rheometrics Mechanical Spectrometer, model RMS-803. In this type of characterization, the linear viscoelastic properties of asphalt cements are characterized by determination of the complex modulus (G*) and the phase angle (δ) as a function of frequency. In this research, the frequencies used ranged from 0.1 to 100 rad/s, at temperatures ranging from -35 to 60 °C. Time-temperature superposition was used to construct master curves of G* and δ, and to construct the associated plots of the shift factor (a(T)) as a function of temperature (4).

Use has been made in this research of various chemical data available in the SHRP database. These include Corbett fraction data and number average molecular weights determined by vapor pressure osmosis in toluene at 60 °C. These data are summarized in Table 1.

Results

The mechanical response of viscoelastic materials such as asphalt cement is generally both time (frequency) and temperature dependent. In order to mathematical describe the linear viscoelastic behavior of asphalt cement, it is necessary to separate these effects, and model them as independent phenomena.

The frequency dependence of the linear viscoelastic response of asphalt cement can be mathematically modeled using the following series of equations. For characterizing the complex modulus as a function of frequency:

$$G^* = G_g \left[1 + \left(\frac{\omega}{\omega_c} \right)^{\frac{\log 2}{k}} \right]^{\frac{R}{\log 2}} \qquad 1)$$

where:

G^* = complex dynamic modulus, in Pa, at frequency ω, rad/s
G_g = glassy modulus, typically 1 GPa

ω_c = the crossover frequency, rad/s
R = the rheological index

A similar equation can be used to predict the phase angle, which is not presented here in the interest of brevity. The temperature dependence at high temperatures can be modeled using the well known Williams-Landel-Ferry (WLF) equation:

$$\log a(T) = \frac{-19(T-T_d)}{(92+T-T_d)} \qquad 2)$$

where:

a(T) = shift factor at temperature T (T in °C)
T_d = the defining temperature, °C

At low temperatures, below T_d, an Arrhenius function is used to characterize the shift factors:

$$\log a(T) = \frac{H_a}{2.303R}\left[\frac{1}{T} - \frac{1}{T_d}\right] \qquad 3)$$

where:

H_a = flow activation energy, 250 kJ/mol for paving grade asphalts
R = ideal gas constant, 8.314 kJ/mol-°K

In applying equations 1 through 3, the frequency ω in equation 1 must be shifted relative to the selected reference temperature, which in this analysis has been chosen as T_d. This shifting simply involves multiplying the actual frequency at temperature T by the shift factor a(T). Additionally, the crossover frequency, ω_c, must be shifted to the reference temperature.

Another parameter of interest in evaluating the viscoelastic response of asphalt cements is the steady state viscosity, η_o. This represents the coefficient of newtonian viscosity, and is directly proportional to the resistance to flow under linear conditions.

Some explanation of the meaning of the various linear viscoelastic model parameters is in order at this point. The glassy modulus G_g represents the limiting complex modulus for a given asphalt cement, obtained at low temperatures and/or high frequencies. It is generally very close to 10^9 Pa for most asphalts; in the chemical-physical models presented below, G_g was assumed to be 10^9 Pa. The crossover frequency ω_c represents the frequency at which tan δ is equal to one. It is called the crossover frequency because at this point, the storage ($G' = G^* \cos \delta$) and loss moduli ($G'' = G^* \sin \delta$) are equal; at higher frequencies, the loss modulus will be lower than the storage modulus, and at lower frequencies, the storage modulus is the lower. Therefore, ω_c represents the point where G' and G" "crossover." The crossover frequency can be physically interpreted as representing the hardness of an asphalt;

higher values of ω_c are indicative of harder asphalt binders, with greater resistance to flow. The steady-state viscosity η_0, as mentioned above, simply represents the coefficient of viscosity under linear flow conditions. This parameter and the crossover frequency are closely related. The rheological index R is proportional to the broadness of the relaxation spectrum. As the relaxation processes of an asphalt become more disperse, the value of R will increase, and the transition from glassy to viscous behavior becomes more gradual. Typically, pitch type asphalts will have a low value of R (approaching 1), whereas highly oxidized asphalts will have higher values, approaching or exceeding 3. The rheological index is numerically equivalent to the log of the ratio of the glassy modulus to the complex modulus at the crossover frequency. The meaning of these various parameters are graphically indicated in Figure 1, which depicts a typical plot of G* versus ω for a paving grade asphalt binder. The values of these parameters for the asphalts used in this research are given in Table 2.

The defining temperature, T_d, is a parameter characteristic of the temperature dependency of a selected asphalt. The value of T_d ranges from about -20 to 0 °C for commonly used asphalts, and is thus in the same range as the glass transition. As the defining temperature increases, the change in the shift factor with respect to temperature becomes greater, indicating an increase in temperature dependency. This is shown in Figure 2, which shows a plot of the shift factors calculated from equations 1 and 2, using T_d values of -20 and 0 °C. The defining temperature can be thought of as analogous to, or closely related to, the glass transition temperature. The authors however consider the glass transition to be a somewhat nebulous and controversial concept; if it exists for asphalt cements, it is certainly quite broad and poorly defined. Therefore, we suggest the use of the term "defining temperature," meaning a characteristic temperature which defines the temperature dependence of an asphalt, and which, as will be pointed out in the discussion, represents an approximately equivalent rheological point for comparison of the flow properties of asphalt cements.

Taken together, equations 1 through 3 allow the calculation of the complex modulus over a wide range of temperatures and frequencies. From such information, rational evaluation of the potential performance of an asphalt can be made, based upon its predicted mechanical response. These equations are generally valid at low to intermediate temperatures. At high temperatures, as viscous flow is approached, modifications are needed, which in the interest of brevity, are not presented here.

Chemical-Physical Property Relationships

According to the DPF model, asphalt cement should be considered to be a single phase system, though exceedingly complex in composition and interactions among chemical species. The temperature dependence is primarily controlled by free volume effects; increasing temperature results in an increase in free volume among the constituent molecules, which increases molecular mobility and decreases resistance to flow (5). According to the proposed theory, the time dependence of asphalt cements is a function of the overall strength of molecular interactions, and the distribution in strengths of these interactions.

In developing chemical-physical property relationships, use was made of Corbett fraction data and number average molecular weights. Although these particular data should not be considered optimal for developing chemical-physical property relationships within the framework of the DPF model, they are adequate. Additionally, these are the only useful data available on all the SHRP asphalts at this time. Various linear regression models were proposed and evaluated, in which the rheological model parameters were predicted from one or two chemical parameters. Only those models which could be physically interpreted were considered. From this analysis, a series of empirical equations have been developed which can be used to predict the linear viscoelastic model parameters, and thus the stress-strain response, for a given asphalt cement. These equations are presented below.

For predicting the defining temperature, the following relationship was found (r^2 = 0.53, adjusted for degrees of freedom):

$$T_d = 16 - 0.57A - \frac{12{,}400}{M_n} \qquad 4)$$

where:

A = asphaltene content (n-heptane), weight percent
M_n = number average molecular weight, from VPO in toluene at 60 °C, Daltons

The following empirical equation was found to provide the best prediction of the crossover frequency ω_c at the defining temperature, T_d (R^2 = 0.47, adjusted for degrees of freedom):

$$\log \omega_c(T_d) = -0.79 - 0.055A \qquad 5)$$

The equation developed for estimating the rheological index R from the chemical data is as follows (r^2 = 0.81, adjusted for degrees of freedom):

$$R = -0.49 + 0.0018M_n + 1.90\frac{(A+S)}{(P+N)} \qquad 6)$$

where

S = saturate content, weight percent
P = polar aromatic content, weight percent
N = napthene aromatic content, weight percent

Measured and predicted values of R are compared graphically in Figure 3.

The final model presented here, for predicting the steady-state viscosity at the defining temperature $\eta_0(T_d)$, is given below (r^2 = 0.71, adjusted for degrees of freedom):

$$\log \eta_0(T_d) = 7.42 + 0.094\,A + 0.036\,P \qquad 7)$$

Predicted values of the steady-state viscosity are plotted against measured values in Figure 4.

In estimating the linear viscoelastic response of a selected asphalt using these equations, the various rheological model parameters are first estimated from the empirical chemical-physical property relationship. Then, equations 1 through 3 can be used to predict the dynamic mechanical response at any given temperature. To provide an indication of the overall accuracy of these models, Figure 5 is presented, in measured values of G* at 10 rad/s, for various temperatures, are plotted against predicted values. The agreement is within about a factor of two, which although not suitable for engineering design purposes, is certainly useful for a semi-quantitative evaluation of the effect of chemical compositional variables on the mechanical behavior of asphalts. A similar plot is shown as Figure 6, where measured and predicted shift factors are compared. The agreement between measured and predicted values is similar to that seen for G*. Predicted modulus values can be used to predict the potential performance of a given asphalt cement. For example, these equations can be used to estimate the limiting stiffness temperature, which represents the temperature at which at given stiffness is achieved at a selected loading time. This limiting stiffness temperature then represents the predicted cracking temperature for a pavement made with the given asphalt cement (4).

Discussion

The observed dependence of T_d on asphaltene content and molecular weight (equation 4), can be explained using the concept of free volume. The WLF equation can itself be derived from free volume considerations; from this sort of analysis, it can be shown that for a given form of the WLF equation, and assuming similar coefficients of thermal expansion above and below the glass transition, the reference temperature (T_d in this case) will approximately represent a point of equal free volume for a given family of materials (5). Therefore, for asphalt binders, factors which tend to increase free volume will decrease T_d, whereas factors which act to decrease free volume will increase T_d. For most viscoelastic systems, an increase in molecular weight will decrease free volume, which explains the observed dependence of T_d on the number average molecular weight. The observed decrease in T_d with increasing asphaltene content at first may seem contradictory. This however can be justified if it is assumed that increasing concentration of polar functions groups, rather than resulting in a net attraction among constituent molecules, results in a net repulsive force. This would tend to increase free volume, thus resulting in a higher defining temperature. The assumption of a net repulsive force among polar molecules is reasonable, since this is required for a stable dispersion (6). However, if the concentration of highly polar species is increased to the point of phase separation, a net attractive force would then exist. This should be expected to increase T_d, resulting in both a harder asphalt and an increase in temperature dependency. This may in fact explain the observed rapid failure of pavements constructed with asphalt cements having high asphaltene contents (6,7).

In developing the empirical relationships for the crossover frequency and the steady-state viscosity, both parameters were defined with T_d as the reference temperature. The discussion above concerning the effects of free volume should make the reason for this apparent to the reader. Since resistance to flow is so highly dependent on molecular mobility, and hence free volume, relating parameters such as ω_c and η_0 at random free volume states is pointless. By defining these parameters at T_d, which represents an approximately equivalent point of free volume, these effects are reduced or eliminated. The major factor effecting resistance to flow under such equal free volume states will then be intermolecular friction (5). From both equation 5 and equation 7, it is clear that resistance to flow for asphalt cements, at equal free volume, increases directly with increasing concentration of highly polar molecules. This is an obvious result of the increased intermolecular friction resulting from greater concentration of highly polar function groups within an asphalt.

The empirical model for estimating the rheological index R from molecular weight and Corbett data can be explained as follows. From consideration of various molecular models for viscoelastic materials, it can be deduced that the complex modulus at tan $\delta = 1$ should decrease with increasing molecular weight. Additionally, data on the molecular weight distribution of asphalt cements suggests that higher molecular weights are normally consistent with broader molecular weight distributions, which would also tend to decrease the modulus at the crossover point (8). As G^* at the crossover decreases, R will increase; thus, the observed increase in R with increasing molecular weight. The second term in equation 5 is a parameter suggested by the authors as being indicative of the dispersion in dipole strengths among an asphalt cements constituent molecules. This parameter, consisting of the sum of the asphaltenes and saturates, divided by the sum of the napthene and polar aromatic fractions, represents the ratio of the very strongly polar and non-polar fractions of the asphalt, divided by the fractions of intermediate polarity. As this parameter increases, the dispersion in the polar forces within an asphalt should increase. Increased dispersion in such intermolecular forces, according to the DPF model, should produce a broader relaxation spectrum, and hence a higher rheological index. This is in fact supported by the form of equation 5.

Although the above series of equations is empirical, each of these equations is based on clear assumptions about the nature of the molecular sources of viscoelastic behavior in asphalt binders. These assumptions stem from the primary hypotheses of the dispersed polar fluid model. In some cases, such as with the use of the Corbett fraction data in predicting viscosity and rheologic type, alternate explanations could be made using the standard colloidal model of asphalt. Therefore, the construction of the quantitative model for chemical-physical property relationships is unfortunately not irrefutable proof of the validity of the DPF model. However, the construction of the chemical-physical property model presented here was made possible only by discarding many of the aspects of the traditional colloidal theory of asphalt microstructure, and replacing them with concepts based upon a single-phased, though complex, model of molecular structure.

Conclusions

1. The temperature dependence of asphalt cements can be effectively explained using free volume concepts; increasing molecular weights decrease free volume, resulting in an increase in temperature dependency, whereas increasing polarity increases free volume, having the opposite effect.

2. Increasing amounts of highly polar material increase intermolecular friction in asphalt cements, increasing resistance to flow and overall hardness. This relationship can only be analyzed for a wide range of systems by comparison at a point of equal free volume, such as the defining temperature.

3. The rheologic type of an asphalt, or relaxation spectrum width, increases with increasing molecular weight and with increased dispersion in the strength of polar functional groups among constituent molecules.

4. The above relationships have been empirically quantified, and can be used in conjunction with a mathematical model to predict the linear viscoelastic response of a wide range of asphalts using chemical compositional parameters.

5. The results of this research lend significant support to the primary aspects of the dispersed polar fluid model of asphalt microstructure.

Literature Cited

(1) Christensen, D.W., and Anderson, D.A., International Symposium on the Chemistry of Bitumens, Rome, Italy (1991).

(2) Nellenstyn, F.J., J. Inst. Pet. Tech., 14, 134 (1928).

(3) Labout, J.W.A. In The Properties of Asphaltic Bitumen, p. 13 (1950), Elsevier, New York.

(4) Christensen, D.W., and Anderson, D.A., Proc. AAPT, 61, 437-475 (1992).

(5) J. D. Ferry, Viscoelastic Properties of Polymers, John Wiley & Sons, New York (1980).

(6) Zube, E, and Skog, E., Proc. AAPT, 38, 1-29 (1969).

(7) Halstead, W., Proc. AAPT, 54, 91-111 (1985).

(8) Barbour, F. A., and Branthaver, J. F., Chemistry and Characterization of Asphalts, ACS Preprints, 35(3), 421-430 (1990).

Table 1. Corbett Fraction Data and Molecular Weights.

Asphalt	Asphaltene Content Wt. %	Polar Aromatics Wt. %	Napthene Aromatics Wt. %	Saturates Wt. %	M_n Daltons
AAA-1	18.3	37.3	31.8	10.6	790
AAB-1	18.2	38.3	33.4	8.6	840
AAC-1	11.0	37.4	37.1	12.9	870
AAD-1	23.0	41.3	25.1	8.6	700
AAE-1	22.9	30.5	31.6	12.7	820
AAF-1	14.1	38.3	37.7	9.6	840
AAG-1	5.8	51.2	32.5	8.5	710
AAJ-1	10.6	41.5	35.9	10.9	1030
AAK-1	21.1	41.8	30.0	5.1	860
AAL-1	18.9	37.3	30.3	12.1	760
AAM-1	3.9	50.3	41.9	1.9	1300
AAN-1	15.7	33.9	40.1	10.3	890
AAO-1	16.4	32.9	41.8	8.6	930
AAP-1	12.6	36.9	36.4	13.2	1090
AAQ-1	16.2	25.9	44.8	12.5	810
AAR-1	18.4	30.5	41.1	10.0	880
AAS-1	18.3	34.1	39.7	5.9	960
AAT-1	17.3	42.5	32.3	7.7	880
AAU-1	17.7	40.5	33.6	7.9	880
AAV-1	9.2	39.5	38.9	10.9	890
AAW-1	17.9	35.7	37.1	9.3	890
AAX-1	11.9	41.3	39.6	7.9	970
AAY-1	22.4	31.4	35.4	9.4	860
AAZ-1	8.9	42.0	43.1	6.8	970

Table 2. Linear Viscoelastic Model Parameters.

Asphalt	T_d °C	Log ω_c at T_d rad/s	R	η_0 at T_d Pa-s
AAA-1	-19.3	-2.03	1.50	10.98
AAB-1	-11.6	-1.97	1.76	10.57
AAC-1	-5.5	-1.16	1.63	9.82
AAD-1	-17.1	-2.01	1.66	11.05
AAE-1	-10.4	-1.98	2.11	10.60
AAF-1	-7.0	-2.07	1.60	10.50
AAG-1	-3.9	-1.43	1.24	9.95
AAJ-1	-4.7	-1.67	1.90	10.00
AAK-1	-14.7	-2.33	1.60	11.31
AAL-1	-15.7	-1.28	1.61	10.37
AAM-1	1.0	-1.26	1.93	9.60
AAN-1	-5.4	-1.32	1.68	10.09
AAO-1	-10.1	-1.78	1.66	10.33
AAP-1	-5.1	-1.77	2.14	10.14
AAQ-1	-5.6	-1.46	1.66	9.94
AAR-1	-5.3	-1.54	1.89	10.08
AAS-1	-9.5	-1.93	1.79	10.49
AAT-1	-5.8	-1.96	1.72	10.50
AAU-1	-3.9	-1.34	1.72	9.94
AAV-1	-5.4	-0.93	1.53	9.60
AAW-1	0.0	-1.50	1.97	9.97
AAX-1	-0.9	-1.24	1.66	9.85
AAY-1	-8.5	-2.07	2.04	10.62
AAZ-1	-1.0	-1.09	1.44	9.52

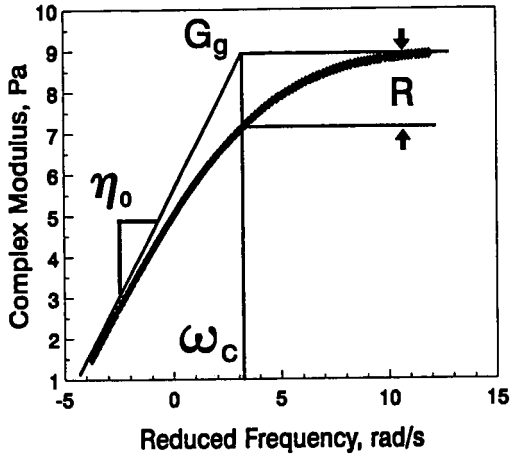

Figure 1. Typical master curve for asphalt binder, showing meaning of model parameters.

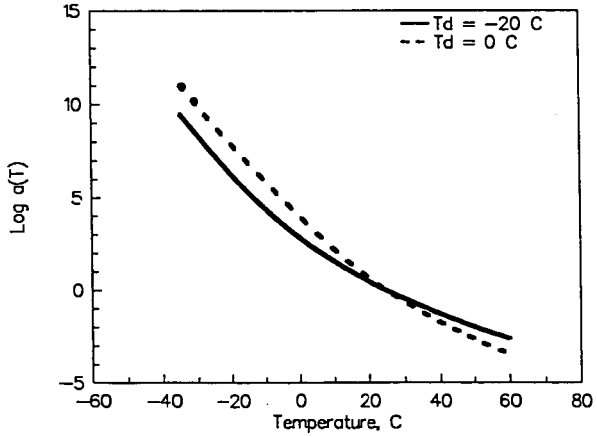

Figure 2. Shift factors as a function of temperature, for different T_d values.

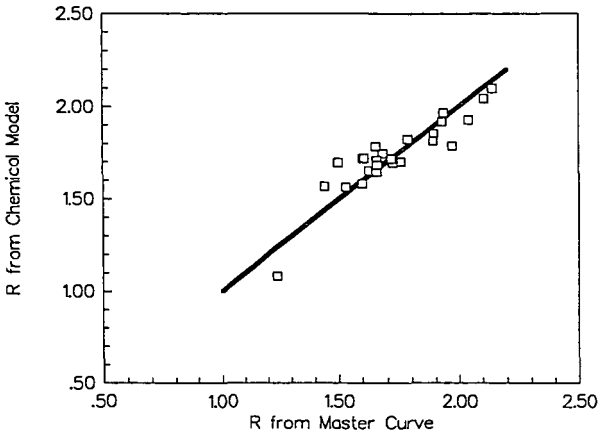

Figure 3. Values of the rheological index, R, as predicted from chemical-physical model and determined from analysis of dynamic shear data.

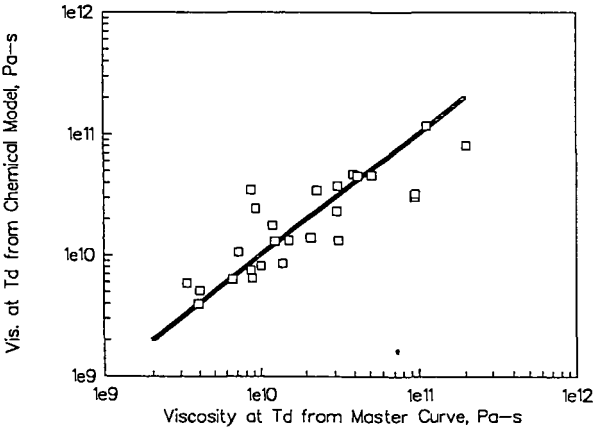

Figure 4. Values of η_0 at the defining temperature predicted from chemical-physical model, and as determined from analysis of dynamic shear data.

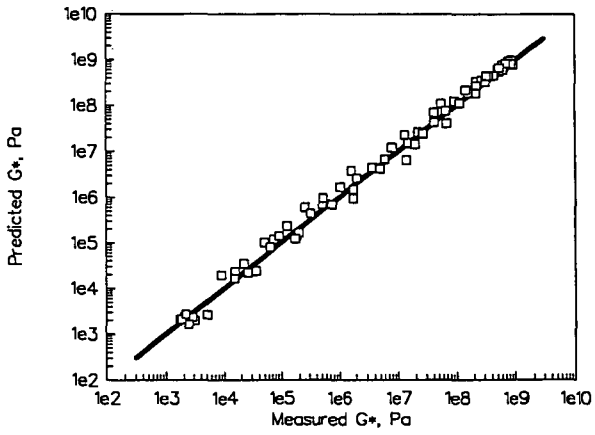

Figure 5. Comparison of predicted and measured values of the complex modulus, G*, at 10 rad/s and at various temperatures.

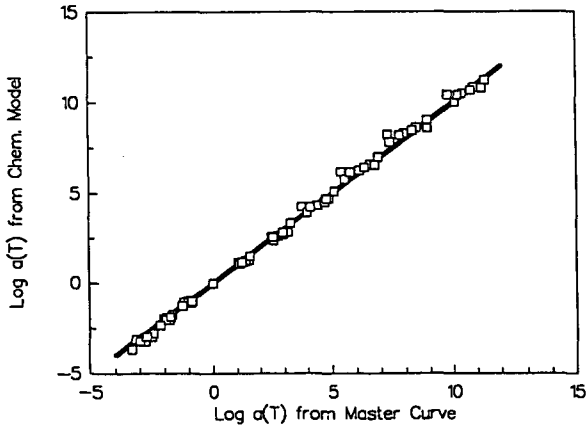

Figure 6. Predicted and measured values of log a(T).

INVESTIGATION OF ASPHALT-AGGREGATE INTERACTIONS IN ASPHALT PAVEMENTS

Christine W. Curtis
Chemical Engineering Department
Auburn University, AL 36849-5127

ABSTRACT

Asphalt-aggregate interactions in asphalt pavements directly influence the adhesion of asphalt to aggregate and determine the strength of the bond between them. These interactions also determine how well the bond is maintained in the presence of water. This investigation examined the physicochemical phenomena that occur at the asphalt-aggregate interface as well as the long-range effect of the interstitial asphalt on the asphalt-aggregate bond. The adsorption behavior of model asphalt components, asphalt fractions and asphalts on aggregates of various petrography was evaluated. The effect of water on the bond between asphalt and aggregate was described through desorption studies. The adsorption and desorption behaviors between asphalt and aggregate were more strongly influenced by the aggregate chemistry and properties than those of the asphalt. Although the influence of asphalt chemistry was smaller than that of the aggregate, asphalt chemistry did affect asphalt-aggregate interactions. A test was developed that evaluated the affinity of different asphalt-aggregate pairs and their suspectibility to water.

INTRODUCTION

Asphalt-aggregate interactions are important in the adhesion of asphalt cement to aggregate because the asphalt must adhere to the aggregate for the adhesive binding action of asphalt to occur. In a road pavement, aggregate composes 94 to 95% by weight of the mix while asphalt makes up the other 5 to 6%. Any additives that are added to improve the performance of the pavement are typically added to the asphalt. The aggregate is present in a multiplicity of sizes ranging from 3/4 inch fraction to fines that are in the -200 mesh range. The larger aggregate sizes are distinct entities in the asphalt pavement while the finer particles can be visualized as an extended portion of the asphalt itself. As asphalt contacts aggregate and forms the mix that is used for the various road courses, the asphalt molecules interact directly with the active sites on the aggregate surface. The surfaces of the aggregates vary considerably in their chemistry, surface area, pore-size distributions, and rugosity. Hence, the aggregate, which can be limestone, gravel, granite, greywacke, basalt, to name a few, can have markedly different active surface sites that are available for interaction with asphalt molecules. Asphalts, being the bottoms product from petroleum refining of crude oils, also vary considerably in their chemistry, because of the differences in their source crudes. Hence, the interaction between the asphalt and aggregate is dependent on the chemistries of both.

Many factors influence the strength and longevity of the bond between asphalt and aggregate. Environmental and traffic factors take their toll. Water, in the form of rainfall or humidity, can have a direct and insidious effect on the adhesive bond between asphalt and aggregate. Moisture damage to the asphalt-aggregate bond results in the deterioration of the

bond through adhesive failure at the interface or cohesive failure within the asphalt or aggregate. These failures cause the asphalt to separate or strip from the aggregate, leaving the aggregate loose without a binder to keep the aggregate particles and, hence, the pavement together.

The overall objective of this work was to investigate and understand fundamental aspects of asphalt-aggregate interactions including both chemical and physical processes. A number of different aspects of this problem was evaluated including chemistry of the interaction between asphalt and aggregate, the effect of the interstitial asphalt on the bond, the effect of the aggregate on aging, and the water sensitivity of the asphalt-aggregate pair. This work, performed under the Strategic Highway Research Program Contract A-003B, covered many different aspects of asphalt-aggregate interactions which are summarized in this paper. A number of researchers was involved in this study who will be referenced in the text.

ASPHALT-AGGREGATE INTERACTIONS

The initial model of asphalt-aggregate interactions that was postulated was the adherence of asphalt at the asphalt-aggregate interface, followed by the development of a structured interphase region, which lay between the interface and the bulk, unstructured asphalt. A new understanding and model of asphalt-aggregate interactions have emerged out of the research performed. During hot mix processing, asphalt components contact and adhere to the interfacial surface of the aggregate with the more polar constituents, those compounds containing heteroatoms of sulfur, nitrogen, or oxygen, being the most competitive for the active sties on the aggregate. Physiorption rather than chemisorption usually occurs with most of the interactions being electrostatic, dipole-dipole, or Van der Waals interactions. Asphalt once contacted with the aggregate surface remains relatively stationary; although under high temperature and stressful conditions the molecules have an opportunity to move, change orientation and diffuse (Hicks, 1991).

Effect of Chemistry on Adhesion

Asphalt is a complex material composed primarily of hydrocarbons but contains a variety of functional groups containing heteroatoms of C, N, H, and metals such as vanadium and nickel, which are present primarily in the asphaltene fraction. A study by Scott (1978) has shown that when asphalts were contacted with aggregates, oxygen-containing groups from asphaltenes were preferentially adsorbed on the aggregate surface. Fritschy and Papier (1978) observed a similar behavior from the polar asphaltenes. Likewise, Curtis et al. (1989a, b) have shown that asphaltenes adsorbed more on sandstone and limestone than did the parent asphalt.

Asphalt is a complex material with many different types of compounds and functional groups present. Adsorption studies were performed with both asphalt model compounds, that represented the type of functional groups present in asphalt, asphalt and asphalt fractions. Adsorption tests involving model compounds gave the following ranking averaged over a series of aggregates, including granites, limestones, gravels, and greywacke: sulfoxide > carboxylic acid > nitrogen base > phenol > ketone > pyrrole > 4-ring aromatic > 2-ring aromatic. The adsorption of polar asphalt model compounds on the different aggregates was much larger than the less polar or nonpolar compounds. Likewise, the larger molecular size

fraction of asphalt, that contains the most polar groups, adsorbed more on the aggregate surface than did the smaller molecular size fraction and, usually, even more than the asphalt itself.

Water attacks the bond between asphalt and aggregate. Evaluation of the effect of water on the adsorbed models showed that models with carboxylic acid and the basic sulfoxide functional groups desorbed readily while the phenolic and nitrogen-base models were more able to withstand the effects of water and remain on the surface of the aggregate. Components that had the most affinity for the aggregates also tended to have the most sensitivity to water.

Aggregate chemistry plays a key role in the adsorption of asphaltic components, the adhesion of the asphalt to the aggregate, and the retention of the asphaltic components in the presence of water. Each aggregate of a given bulk mineralogical type has a unique surface chemistry. These active sites promote adsorption of asphaltic components, particularly ones with polar functional groups. The covering of those active sites by nonpolar C_8 or C_{18} hydrocarbons completely masks their activity, while changing the chemistry of the sites by adding amine groups affects the adsorption behavior of both asphaltic models and asphalts themselves (Curtis et al., 1992). Dust coatings occurring naturally on aggregate surfaces can change the chemistry of adhesion and result in weak bonding between the dust and aggregate surface, leading to attrition of the bonding forces that help maintain the adhesion and, hence, the pavement.

Evaluation of asphalt-aggregate interactions in terms of the adsorption and desorption isotherm behavior of three different asphalts from solutions onto four different aggregates showed that aggregate chemistry is much more influential than asphalt chemistry for both adhesion and sensitivity to water. For a given asphalt, large differences were observed in the amount of asphalt adsorbed and retained after exposure to water when using both siliceous and calcareous aggregates (Brannan et al., 1991). Likewise, for a given aggregate, the differences observed in the adsorption of three different asphalts was much less than that for a single asphalt and several aggregates.

Net Adsorption Tests. A test that provides a method for determining the affinity of an asphalt-aggregate pair and its sensitivity to water was developed. This test is called the Net Adsorption Test. The test is composed of two steps: first, asphalt is adsorbed from toluene solution and the amount of asphalt adsorbed is measured; and second, a small amount of water (~280 mM) is introduced into the system, asphalt is desorbed from the aggregate surface, the amount of asphalt desorbed is measured and the net amount of asphalt remaining on the aggregate surface is measured. This value is termed the net adsorption and provides a means of directly comparing the affinity and water sensitivity of different asphalt-aggregate pairs (Curtis et al., 1992).

The net adsorption of an asphalt aggregate pair is dependent on both the asphalt composition and the aggregate chemistry and morphology. The amount of asphalt adsorbed for eleven aggregates, which were composed of limestones, granites, greywacke, gravels, and basalt, ranged over an order of magnitude for a given asphalt at a preselected asphalt solution concentration (Figure 1). Water sensitivity was also strongly dependent on the chemistry of the aggregate. For some aggregates, half or more of the initial asphalt adsorbed desorbed into a toluene solution that contained only a very small amount of water. For those aggregates that showed substantial water sensitivity, the asphalt chemistry seemed to have a larger influence than on those aggregates that were not sensitive to water.

Bonding Energy. The influence on the composition and chemistry of the aggregate on the amount of heat released or bonding energy was substantial (Ensley, 1990). The bonding energy of the asphalt-aggregate mixture is measured by immersing the aggregate in the asphalt and measuring the resulting exotherm. Eleven aggregates were evaluated with a series of different asphalts. The aggregates could be ranked according to their bonding energy because of the large differences observed among them. By contrast, the ranking of asphalts in conjunction with a given aggregate was not easily discernable.

Interphasal Asphalt. Early research involving determining the bonding energy associated with asphalt-aggregate resulted in an initial exotherm followed by a small release in energy over a fairly long time period (Ensley and Scholz, 1972). These results were interpreted as the development of an interphase region between the asphalt-aggregate interface and the bulk, unstructured asphalt. The interphase region was hypothesized to be a structured region where asphalt molecules were ordered according to their dipole-dipole interactions. However, the research performed recently (Ensley, 1992) did not show the same long-term, low energy release. Additionally, autoradiographic measurements of asphalt contacted to aggregate gave no evidence of the formation of a structured interphase region (Ross, 1990). Aging experiments, performed to evaluate the effect of aggregate on asphalt oxidation, examined the region between the asphalt-aggregate interface and 100 μm out from the aggregate surface. This region, which was sampled every 24 μm, showed no differentiation in the chemical composition that was detectable by infrared analysis.

Asphalt-Aggregate Model. The evidence obtained in this research indicated that the asphalt-aggregate mixtures can be modeled as a system in which large, small, and fine aggregate particles are either coated with asphalt or suspended within the asphalt. Asphalt adheres to the outer surface and penetrates into the pores, crevices, and interstitices of the aggregate. The active sites on the aggregate particle attract the most polar and bondable asphalt species upon initial contact. Competition exists among the various asphaltic constituents with the polar components being most competitive (Jeon and Curtis, 1992). Most asphalt molecules are directly contacted with an aggregate or with another asphalt molecule in contact with or close to an aggregate surface. The fines that compose 5 to 8% of the aggregate are interspersed with the aggregate forming a mastic, a medium in which it is difficult to distinguish macroscopically between asphalt and aggregate.

Aging. Aging studies showed that carboxylic acids, ketones, and sulfoxides increased with oxidative aging, at the interface and in the asphalt at distances of 25 μm to 100 μm from the aggregate surface (McKay, 1992). The number and type of oxidative aging products appear to be directly related to the compositional chemistry of the asphalt. The higher the indigenous sulfur content is in a particular asphalt, the higher the sulfoxide formation is under oxidative conditions.

The changes caused by oxidative aging can potentially affect the nature of the chemistry of the interface. The compounds typically produced are sulfoxides, carboxylic acids and ketones. Both sulfoxides and carboxylic acids have a high affinity for the aggregate surface. However, when the moisture sensitivity of these model compounds was evaluated, these two models with the high affinity for the aggregate showed the most sensitivity to water.

Hence, oxidative aging may produce substantial changes in the chemistry of the asphalt-aggregate interface, particularly with an asphalt-aggregate pair that is particularly susceptible to aging. The adhesion of the asphalt to the surface is dependent upon the types

of species at the interface and their ability to bond strongly to the surface. The resistivity of that bond to environmental factors, particularly the intrusion of water, is essential for maintaining long pavement life. Since several of the functional groups present after oxidative aging are susceptible to water, the resistivity of the asphalt-aggregate bond may be weakened by the presence of water.

Water Sensitivity

Stripping of asphalt from aggregate stems from the intrusion of water into the asphalt-aggregate system. The modes of failure depend upon the character of the system and include:

- Separation of the bond at the interface
- Cohesive failure within the asphalt
- Cohesive failure within the aggregate
- Phase separation of components when the presence of water increases the solubility of polar compounds through hydrogen bonding.

If the water-proofing layer of asphalt surrounding an aggregate particle is continuous, then water can penetrate the system by diffusing through the asphalt film removing along the way those asphaltic components that are solubilized. If cracks occur in the film, then water can intrude to the asphalt-aggregate interface, causing failure at or near the interface. The failure can be interfacial or cohesive either in the asphalt or in the aggregate. Reduction in water damage can be attained by modifying the aggregate surface through silylation or the addition of antistripping agents. However, complete covering of the particle by an asphalt film should decrease the quantity of water reaching the aggregate and reduce the deleterious effect of water on the aggregate. Building of roads with low air voids or good drainage may be most influential in reducing water damage, by limiting the exposure of the asphalt-aggregate bond to water.

Resilience of Asphalt-Aggregate Bonds. Adhesion between an asphalt-aggregate pair can be promoted or inhibited by processing and environmental factors. As part of this research, the effect of pH on the asphalt-aggregate bond was investigated. High pH found in a very basic medium was detrimental to most asphalt-aggregate bonds; however, treatment at somewhat lower but still basic pH did not affect the bond substantially (Tarrer, 1992). Curing at elevated temperatures after mixing promoted adhesion in some asphalt-aggregate pairs. A test involving the factors of increased pH and curing was incorporated into the modified Lottman (T-283) test and has been suggested as a means of differentiating among asphalt-aggregate combinations. Those particular asphalt-aggregate combinations that did not perform well under chemical preconditioning (high pH) or curing were treated with additives, either liquid antistripping agents or lime, to improve their performance. Retesting the treated mixture under the stringent pH conditions offers a means of determining the effectiveness of the treatment.

SUMMARY AND CONCLUSIONS

Asphalt-aggregate interactions are strongly influenced by the composition and surface chemistry of the aggregate. Aggregate properties are much more influential in determining adsorption and stripping behavior than are asphalt properties. The net adsorption test demonstrated the large differences in asphalt affinity and stripping propensity occur among aggregates of different minerialogy. Asphalt compounds with polar functional groups are

highly competitive for the active sites (i.e., those sites that contain metals or charged species) on the aggregate surface. Some polar compounds that adhere competitively to the aggregate surface are highly susceptible to water and are readily removed from the aggregate surface. Changes in pH, particularly very basic pH, can be detrimental to the bond between asphalt and aggregate. Curing of the asphalt-aggregate bond can improve bonding between a particular asphalt-aggregate pair although that interaction is highly specific. Specificity among the different asphalt-aggregate combinations was readily apparent in both the adsorption and desorption studies and the bonding energy measurements. The interactions between asphalt and aggregate are dominated by aggregate chemistry. Asphalt chemistry also has an influence, though much smaller than that of the aggregate, on asphalt-aggregate interactions.

Nomenclature for Figure 1.

RA = granite	RE = gravel	RG = gravel
RB = granite	RF = glacial gravel	RH = basalt
RC = limestone	RG = sandstone	RL = gravel
RD = limestone	RH = greywacke	

REFERENCES

Brannan, C.J., Curtis, C.W., Perry, L.M., Jeon, Y.W. Trans. Res. Rec., 1323, 1991, 10-21.

Curtis, C.W., Jeon, Y.W., and Clapp, D.J. Fuel Sci. Tech. Int., 7, (9), (1125), 1989a.

Curtis, C.W., Jeon, Y.W., Clapp, D.J., and Kiggundu, B.M. Trans. Res. Rec., 1228, (112), 1989b.

Curtis, C.W., Terrel, R.L., Perry, L.M., Al-Swailmi, S., and Brannan, C.J. Journal of AAPT, 60, 1991, 476.

Curtis. C.W., Gardiner, M.S., Brannan, C.J., and Jones, D.R. Trans. Res. Rec., *in* press, 1992.

Ensley, E.K. and H.A. Scholz, J. Inst. Petrol., 58, 1972, 95.

Ensley, E.K.. Final Report, SHRP Contract A-003B, 1992, 265.

Fritschy, G. and Papirer, E. Fuel, 57, 1978, 701.

Hicks, G. Personal Communication, 1991.

Jeon, Y.W. and Curtis, C.W. Fuel Sci. Tech. Int'l, 10, 1992, 697.

McKay, J. Final Report, SHRP Contract A-003B, 1992, 167.

Podoll, R.T., Becker, C.H., Irwin, K.C. "Surface Analysis by Laser Ionization of the Asphalt-Aggregate Bond," Phase I Progress Report, (SHRP AIIR 07), April 1990.

Podoll, R.T., Becker, C.H., Irwin, K.C. "Surface Analysis by Laser Ionization of the Asphalt-Aggregate Bond," Phase II Progress Report, (SHRP AIIR 07), 1991.

Ross, D.S. "Fundamentals of the Asphalt-Agregate Bond," Phase 2 Report (SHRP AIIR-11), 1991.

Ross, D.S. Presented by D. R. Jones at the SHRP A-003B Advisory Council Meeting, National Center for Asphalt Technology, Auburn University, May 1991.

Scott, J.A.N. Proc. AAPT, 47, 1978, 19.

Tarrer, A.R. Final Report, SHRP Contract A-003B, 1992, 151.

Figure 1. Net Adsorption of Asphalts on MRL Aggregates

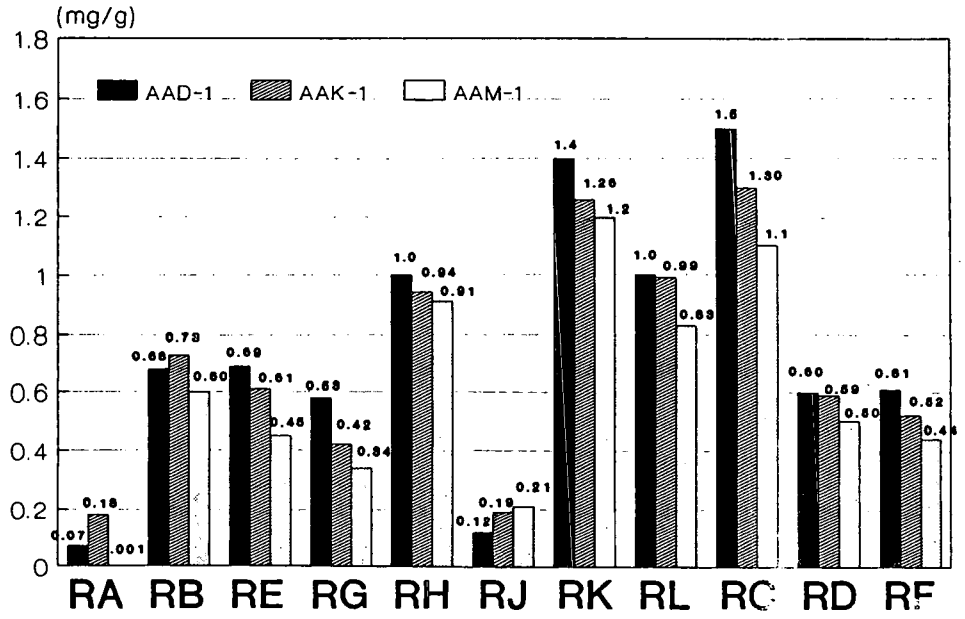

Isolation and Characterization of Amphoteric Components of SHRP Asphalts by Ion Exchange Chromatography

Jan F. Branthaver, S.S. Kim, M.W. Catalfomo, and D.C. Goray
Western Research Institute
P.O. Box 3395
Laramie, Wyoming 82071-3395

Keywords: Asphalt, Amphoterics, Ion Exchange Chromatography

ABSTRACT

An ion exchange chromatography separation procedure was devised for the purpose of isolating compounds of amphoteric nature from four asphalts studied in the Strategic Highway Research Program. Amphoteric materials constitute about 18-25% of the asphalts studied. Other defined chemical fractions (neutral, acidic, and basic fractions) also were collected. Of the four fractions, the amphoteric is the most polar and most aromatic in each of the asphalts. Number-average molecular weights of the amphoteric fractions are two-to-four times greater than those of the parent asphalts.

Several mixtures of the above ion exchange chromatography fractions with each other and with whole asphalts were prepared and their viscosities were measured. Based on these studies, amphoterics are the chemical component of asphalts most responsible for high viscosities. Polyfunctional compounds that are of purely acidic or basic character do not appear to be present in large amounts.

INTRODUCTION

One model of asphalt structure proposes that asphalts can be considered to be dispersions of polar, aromatic molecules in solvent moieties consisting of less polar, more aliphatic molecules (1). The relative amount of polars and the effectiveness by which they are solubilized will be major determinants of asphalt properties (2). If this model is correct, polyfunctional polar molecules should contribute disproportionately to the buildup of molecular associations, which presumably govern such asphalt bulk properties as viscosity. Polyfunctional molecules may be categorized as amphoteric, polyacidic, or polybasic. It should be possible to isolate these materials and study their properties if the model described above is correct.

The technique of ion exchange chromatography (IEC) has been used to separate tar sand bitumens, shale oils, crude oils and their components into defined chemical fractions (3-9). When used to separate the above mentioned substrates, IEC works as a form of affinity chromatography. Usually, neutral, acidic, and basic fractions of varying strengths are collected. An IEC separation method used for the separation of asphalts studied in the

Strategic Highway Research Program (SHRP) into neutral, acidic, and basic fractions (4, 5) was modified to separate asphalts into neutral, acid, base, and amphoteric fractions.

EXPERIMENTAL

The experimental details of the IEC separation of asphalts, including resin activation, have been published (4, 5). In the conventional IEC separation, solutions of asphalts in either a mixed solvent (benzene, tetrahydrofuran, ethanol) or cyclohexane are pumped through two columns, the first filled with activated anion resin, and the second filled with activated cation resin. For the separation of amphoterics, a solution of asphalt (16 g) in cyclohexane (64 mL) was pumped into a jacketed column filled with activated cation resin (Bio-Rad MP-50, 100-200 mesh). All molecules with one or more basic functional groups are adsorbed on the cation resin. Molecules containing only acidic or no functional groups are eluted, and these eluates are pumped through a jacketed column filled with activated anion resin (Bio-Rad MP-1, 100-200 mesh). Acidic materials are adsorbed on the anion resin, and neutral materials are eluted. Column temperatures of 37°C (98.6°F) are maintained by circulating warm water through the column jackets. Both columns are desorbed in the manner previously described (4, 5). The materials desorbed from the cation resin are divested of solvent and are redissolved in cyclohexane. This solution is pumped through another jacketed column filled with activated anion resin. Amphoteric materials are collected on the anion resin, and basic materials are eluted. The base fraction is recovered by solvent removal, and the amphoterics are recovered by desorption of the anion resin by formic acid-benzene, followed by solvent removal. A flow sheet for this process is illustrated in Figure 1.

To make mixtures of asphalts and IEC fractions or mixtures of IEC fractions, materials are added to a tared vial and methylene chloride is added to the mixture. The sample is allowed to stand overnight under argon. The mixture then is rotated on a rotary evaporator immersed in the waterbath at a temperature of 44°C (111.2°F). After most of the methylene chloride has evaporated off, the temperature is increased until boiling of the water is observed in the bath. Vacuum then is applied to the sample, approximately 208 mm Hg (8.19 in Hg). The vacuum is increased gradually to prevent any bubbling of the sample. A maximum vacuum of approximately 4.7 mm Hg (0.19 in Hg) is reached and the sample is allowed to rotate for 2 hours. The sample is then immersed into an oil bath of 125°C (257°F) for 2 hours at 2 torr (0.08 in Hg). The dried samples are submitted for rheological analysis.

Elemental analyses were performed by the Analytical Research Division of Western Research Institute, using standard methods. Number-average molecular weights ($\overline{M}_n$) were determined by vapor phase osmometry (VPO) in toluene or pyridine at 60°C (140°F) using ASTM Method D2503. Infrared functional group (IR-FGA) analyses were obtained on a Perkin-Elmer 983G infrared spectrophotometer using a method developed by Petersen (10). Rheological data were obtained on a Rheometrics mechanical spectrometer. Samples were annealed prior to measurement at 150°C (302°F) for one hour under an inert gas atmosphere. Measurements were performed within two hours after the samples had cooled to room temperature.

Liquid-state ^{1}H and ^{13}C NMR measurements were made on a JEOL GSX-270 NMR spectrometer. The experimental conditions for recording a ^{1}H spectrum were 8 scans, a pulse width of 5.4 μs (45°), an acquisition time of 1.5 s, a pulse delay of 20 s, and 16 K time-domain data points. The conditions for recording a ^{13}C NMR spectrum were 320 scans, 9.3 μs pulse width (90°), 0.8 s acquisition time, a pulse delay of 10 s, 32 K time-domain data points, and gated decoupling with the decoupler on during data acquisition. Carbon-13 spectra were obtained on samples containing ~0.05 M chromium (III) acetylacetonate as a relaxation agent.

DISCUSSION

Yields of amphoteric, base, acid, and neutral fractions from IEC separation of four SHRP asphalts (coded AAD-1, AAG-1, AAK-1, and AAM-1) are listed in Table 1. For some runs, neutrals were not subsequently separated from acids, so the combination of the two materials is listed under the entry neutral plus acids. In some other runs, amphoterics were not subsequently separated from bases, so this combination of materials is listed under the entry amphoterics plus bases. In each case, the neutral fraction comprises over half of the mass of the asphalt. Yields of neutral materials are similar to those reported using another IEC separation method on the same asphalts (4, 5). Of the three polar fractions, the amphoteric is by far the largest for each of the asphalts. The amphoteric materials are black solids which swell when contacted with small amounts of solvent. Bases and acids are tacky semisolids. Neutrals are viscous liquids.

Number-average molecular weights ($\overline{M}_n$) of amphoterics and bases are listed in Table 2. The $\overline{M}_n$ values of the amphoteric fractions vary from 1,540 Daltons (AAG-1) to 3,690 Daltons (AAK-1) in toluene, and from 1,240 Daltons (AAG-1) to 2,730 Daltons (AAK-1) in pyridine. The lower $\overline{M}_n$ values in pyridine compared with toluene indicate that amphoteric materials tend to form associations. The $\overline{M}_n$ values of the base fractions range from 815-880 Daltons (AAG-1) to 1,740 Daltons (AAM-1), and are the same in toluene and pyridine, indicating that by themselves the total base fractions do not engage in strong associations. The $\overline{M}_n$ values of the parent asphalts are: AAD-1, 700 Daltons; AAG-1, 710 Daltons, AAK-1, 860 Daltons, and AAM-1, 1,300 Daltons (4, 5). These $\overline{M}_n$ values are the same when measured in pyridine or toluene for those asphalts completely soluble in both solvents. Asphalt AAM-1 is not completely soluble in pyridine.

Infrared (IR-FGA) analyses of amphoterics, bases, and the combination of neutrals and acids of four asphalts are reported in Table 3. The bifunctional 2-quinolone compounds are found in abundance only in the four amphoteric fractions. Other polar functional groups measured by the IR-FGA method are distributed among the various fractions, largely according to expectation. Carboxylic acids and phenols are found in measurable amounts in amphoteric and neutral plus acid fractions. Sulfoxides and ketones are concentrated in base fractions. Pyrroles are found in measurable amounts in all fractions.

Elemental analyses for carbon, hydrogen, and nitrogen of the four amphoteric fractions (Table 4) show that these materials are aromatic and contain large amounts of nitrogen. Some of the nitrogen atoms are part of basic functional groups (11). Standard deviations of the

elemental analyses of the amphoteric fractions generally are small. Nuclear magnetic resonance (NMR) measurements (Table 5) show that about 40-50% of carbon atoms in the amphoteric fractions are part of aromatic structures, whereas aromatic hydrogens comprise only 6-13% of the total hydrogen, suggesting the presence of condensed aromatic structures.

All the above observations demonstrate that the amphoteric fractions of the four asphalts consist of polar, aromatic molecules which are of relatively high $\overline{M}_n$ compared with the parent asphalts and other IEC fractions (4, 5). These molecules should have the greatest tendencies to associate of all the asphalt IEC fractions, and therefore should be the principal viscosity-enhancing components of asphalts.

In order to test this hypothesis directly, mixtures of each asphalt with each of the four IEC fractions (neutral, amphoteric, acid, and base) were prepared. The compositions of these mixtures were calculated based on the observation that a specific natural abundance of each IEC fraction characterizes each asphalt. For example, asphalt AAD-1 consists of about 54% neutrals, 25% amphoterics, 9% bases and 8% acids. Asphalt AAG-1 consists of 52% neutrals, 18% amphoterics, 12% bases, and 14% acids. It was decided initially to add amphoterics to asphalts such that the resulting mixtures would contain double the natural abundance levels of amphoterics. However, the resulting materials were observed to be coal-like, and viscosities were barely measurable at 60 °C (140 °F). Solvent removal from the prepared mixtures proved to be very tedious. The amphoteric fractions impart great surface activities to the mixtures, and under vacuum, meringues form which flow from distillation flasks into the rotary evaporators used in the solvent removal process.

Accordingly, mixtures for each of the four asphalts were formulated such that amphoterics comprise a 50% excess of their natural abundance for each of the asphalts. For example, a 10.0 g sample of AAD-1 contains ~ 2.5 g amphoterics, a 25% natural abundance. A 50% excess would be 37.5%. So to make 10.0 g of a mixture having 37.5% amphoterics, enough amphoteric material (1.67 g in this case) was added to AAD-1 (8.33 g in this case) to yield 10.0 g of a mixture containing 3.75 g amphoterics. For AAG-1, the natural abundance level for amphoterics is 18%, much less than for AAD-1. A mixture of AAG-1 containing a 50% excess of this natural abundance would contain 27% amphoterics. Similar considerations apply to AAK-1 and AAM-1. Natural abundances of amphoterics in these asphalts are similar to those in AAD-1 and AAG-1 respectively.

Mixtures also were formulated by adding neutral, acid, and base fractions to the asphalts. In every case, the same amount of each fraction was added as for the amphoteric fraction. For example, in the AAD-1 mixtures, 1.67 g amphoterics was added to 8.33 g AAD-1. In the mixtures of AAD-1 with its neutral fraction, 1.67 g neutrals were added to 8.33 g AAD-1. Similarly, 1.67 g bases were added to 8.33 g AAD-1, and 1.67 g acids were added to 8.33 g AAD-1. The neutral, acid, and base fractions were not added in amounts commensurate with their own natural abundances, but in amounts corresponding to the natural abundance of the amphoteric fraction. This is so that effects of each fraction on rheological properties can be compared on an equivalent mass basis for each asphalt.

Viscosities of all these mixtures at 60 °C (140 °F) (Table 6) show that, as a fraction, the amphoterics are the components of the asphalts governing high viscosities, as predicted. Bases cause moderate viscosity increases when added to asphalts and acids cause hardly any increases. These results indicate that there may be few polyfunctional acidic and basic compounds present. Addition of neutral materials causes large viscosity decreases when mixed with parent asphalts. These results do not mean that no viscosity-enhancing species exist in acid, base, or neutral materials, or no viscosity-reducing species exist in the amphoteric fractions. The results apply to the fractions as a whole.

To verify the effect of the absence of amphoterics on asphalt properties, mixtures of a different kind were prepared. In these mixtures, the relative amounts of neutrals and polars were the same as in the parent asphalts. However amphoterics have been replaced by bases. In the mixtures discussed earlier, in which IEC fractions are added to whole asphalts, the ratios of neutrals to polars are different from the relative abundance of neutrals and polars in neat asphalts. Acids, bases, and amphoterics are considered to be the polar fractions. In the new set of mixtures, bases replace amphoterics, so the mixtures have much more than their natural abundances of bases, but relative amounts of total polars and neutrals are the same as for each of the original four asphalts studied. In Table 7, viscosities at three temperatures and tan δ values at 25 °C (77 °F) of four such mixtures are compared with the same measurements on the parent asphalts. Viscosities of the mixtures are much lower than those of the parent asphalts at all three temperatures. The tan δ (ratio of viscous to elastic moduli) values of the mixtures are high, compared with tan δ values of parent asphalts, particularly the mixture made up of IEC fractions of AAG-1. The rheological data obtained for these mixtures demonstrate that the amphoteric materials as defined by IEC are largely responsible for viscosity-enhancing phenomena in asphalts.

CONCLUSIONS

Separation of four different asphalts into neutral, acid, base, and amphoteric components by IEC shows that neutral fractions comprise somewhat over half of the asphalts. Amphoterics are the largest of the three polar fractions. Amphoterics are much more aromatic than their parent asphalts, and also have higher $\overline{M}_n$ values. These $\overline{M}_n$ values, determined by VPO, are higher in toluene than in pyridine, which indicates that amphoterics tend to engage in associative interactions.

Mixtures of asphalts with each of the four IEC fractions were prepared and their viscosities measured. Only the mixtures containing amphoterics were much more viscous than the parent asphalts. Mixtures containing only IEC neutral, acid, and base fractions were much less viscous than parent asphalts and had small values of elastic moduli (based on tan δ values) compared with those of parent asphalts. Thus the presence of amphoterics, presumably forming associations of varying strengths, is required to form elastic networks in asphalts, and asphalt rheological properties should be a function of the nature and relative amounts of amphoterics present.

ACKNOWLEDGMENTS

The work reported herein has been conducted as a part of Project A002A of the Strategic Highway Research Program (SHRP). SHRP is a unit of the National Research Council that was authorized by Section 128 of the Surface Transportation and Uniform Relocation Assistance Act of 1987. This project is titled "Binder Characterization and Evaluation" and is being conducted by the Western Research Institute, Laramie, Wyoming, in cooperation with the Pennsylvania Transportation Institute, Texas Transportation Institute, and SRI International. Dr. Raymond E. Robertson is the principal investigator. Dawn Geldien is the project administrator. The support and encouragement of Dr. Edward Harrigan, SHRP Asphalt Program Manager, and Dr. Jack Youtcheff, SHRP Technical Contract Manager, are gratefully acknowledged.

NMR spectra were obtained by D.A. Netzel. IR-FGA analyses were performed by G. Miyake. $\overline{M}_n$ values were obtained by G. Gardner. Rheological measurements were obtained by F. Reid. The manuscript was prepared by J. Greaser.

LITERATURE CITED

(1) Pfeiffer, J.P. and Saal, R.N.J., J. Phys. Chem., 44, 139 (1940).
(2) Petersen, J.C., Transport. Res. Rec., 999, 13 (1984).
(3) Boduszynski, M.M., Chadha, B.R. and Pochopien, T.S., Fuel, 56, 432 (1977).
(4) Branthaver, J.F., Catalfomo, M.W., and Petersen, J.C., Preprints, Div. Petrol. Chem., Am. Chem. Soc., 35 (3), 376 (1990).
(5) Branthaver, J.F., Catalfomo, M.W., and Petersen, J.C., Fuel Sci. Technol. Intl., 10 (4-6), 855 (1992).
(6) Green, J.B., Hoff, R.J., Woodward, P.W., and Stevens, L.L., Fuel, 63, 1290 (1985).
(7) Kircher, C.C., Fuel Sci. Technol. Intl., 9 (3), 379 (1991).
(8) McKay, J.F., Cogswell, T.E., Weber, J.H. and Latham, D.R., Fuel, 54, 50 (1975).
(9) Selucky, M.L., Kim, S.S., Skinner, F., and Strausz, O.P., in "Chemistry of Asphaltenes," Bunger, J.W. and Li, N.C., Eds., Advances in Chem. Series 195, ACS, Washington, DC, Chapter 6 (1981).
(10) Petersen, J.C., Transport. Res. Rec., 1096, 1 (1986).
(11) Robertson, R.E., Schabron, J.F., Gwin, A.A., and Branthaver, J.F., Preprints, Div. Petrol. Chem., Am. Chem. Soc., 37, 913 (1992).

Table 1. Mass Fractions of Amphoteric, Base, Acid, and Neutral Fractions Isolated from Four Asphalts by IEC

Asphalt	Operator (Initials)	IEC Fraction (mass %)						Total Recovery (% of Charge)
		Amphoterics plus Bases	Amphoterics	Bases	Neutrals plus Acids	Acids	Neutrals	
AAD-1	MC		25.9	9.3	59.8			95.0
	SK		25.5	9.5	60.4			95.4
	MC		25.0	8.6	62.2			96.7
	SK		25.8	7.7		8.6	54.0	96.0
	DG		22.3	12.1	—	7.3	53.1	94.9
	Avg. + Std. Dev.		24.9±1.3	9.4±1.5	60.8±1.0	8.0	53.6	95.6±0.7
AAG-1	MC		18.6	13.3	66.4			98.3
	SK		18.4	10.7	68.8			98.0
	DG		18.8	12.9		13.4	51.9	96.9
	DG		18.2	13.1	—	15.3	52.8	99.5
	Avg. + Std. Dev.		18.5±0.2	12.5±1.0	67.6	14.4	52.4	98.2±0.9
AAK-1	MC		24.1	9.6	61.7			95.3
	SK		24.6	10.9	61.5			97.1
	SK		24.2	8.7		8.1	53.8	94.8
	DG		23.5	12.9	59.0			95.4
	DG	27.7	—	—	—	7.6	55.2	90.5
	Avg.± Std. Dev.		24.1±0.4	10.5±1.6	60.7±1.2	7.9	54.6	94.6±2.2
AAM-1	MC		18.9	15.6	63.9			98.5
	SK		18.1	12.9	66.1			97.1
	SK		18.9	13.4		10.0	54.0	96.3
	DG	34.5	—	—	—	8.5	56.5	99.4
	Avg. + Std. Dev.		18.6±0.4	14.0±1.2	65.0	9.3	55.3	97.8±1.2

Table 2. Molecular Weights of IEC Amphoteric and Base Fractions

Asphalt	Run No.	Fraction	Molecular Weight (Daltons)	
			Toluene	Pyridine
AAD-1	1	Amphoteric	2,960	2,260
		Base	1,100	1,100
	2	Amphoteric	2,930	2,180
		Base	1,060	1,200
AAG-1	1	Amphoteric	1,540	1,170
		Base	880; 880	-
	2	Amphoteric	1,620	1,240
		Base	815	835
AAK-1	1	Amphoteric	3,690	2,730
		Base	1,260; 1,240	1,340
	2	Amphoteric	3,540	2,160
		Base	1,300	1,350
AAM-1	1	Amphoteric	3,560	insol.
		Base	1,740	insol.
	2	Amphoteric	3,410	insol.
		Base	1,670	insol.

Table 3. **Infrared Functional Group Analysis for IEC Amphoteric, Base, and Neutral Plus Acid Fractions of Four Core Asphalts**

Asphalt	IEC Fraction	Functional Group Concentration, Moles/L					
		Sulfoxides	Ketones	Carboxylic Acids	2-Quinolones	Pyrrolic N-H	Phenolic O-H
AAD-1	Neutrals Plus Acids	0.05	<0.01	0.01	<0.01	0.2	<0.1
	Bases	0.15	0.17	<0.01	<0.01	0.2	<0.1
	Amphoterics	0.09	<0.01	0.02	0.07	0.4	0.1
AAG-1	Neutrals Plus Acids	0.05	<0.01	0.05	<0.01	0.3	0.1
	Bases	0.08	0.13	<0.01	<0.01	0.2	<0.1
	Amphoterics	0.08	<0.01	0.03	0.07	0.6	0.1
AAK-1	Neutrals Plus Acids	0.08	<0.01	0.02	<0.01	0.1	<0.1
	Bases	0.15	0.10	<0.01	<0.01	0.2	<0.1
	Amphoterics	0.10	<0.01	0.06	0.04	0.3	<0.1
AAM-1	Neutrals Plus Acids	<0.01	<0.01	<0.01	<0.01	0.2	<0.1
	Bases	0.08	0.10	<0.01	<0.01	0.2	<0.1
	Amphoterics	0.06	<0.01	0.02	0.02	0.3	<0.1

Table 4. Carbon, Hydrogen, and Nitrogen Contents of Amphoteric Fractions

Parent Asphalt	Run No.	Element (mass %) C	H	N	H/C ratio
AAD-1	1	80.3	8.6	1.9	1.28
	2	81.1	8.6	1.9	1.26
	Avg.	80.6	8.6	1.9	1.27
AAG-1	1	84.7	8.4	2.5	1.18
	2	84.8	8.6	2.5	1.21
	3	84.8	8.6	2.4	1.21
	Avg. + St. Dev.	84.8 ± 0.1	8.5 ± 0.1	2.5 ± 0.1	1.20 ± 0.01
AAK-1	1	81.5	8.3	1.7	1.21
	2	78.5	8.2	1.6	1.24
	3	81.2	8.2	1.9	1.20
	4	80.9	8.2	2.0	1.19
	5	80.6	8.1	2.0	1.20
	Avg. + Std. Dev.	80.5 ± 1.1	8.2 ± 0.1	1.8 ± 0.2	1.21 ± 0.02
AAM-1	1	88.0	8.5	1.2	1.15
	2	86.4	8.6	1.1	1.19
	Avg.	87.2	8.6	1.2	1.17

Table 5. NMR Analysis of IEC Amphoteric Fractions of Four Core Asphalts

Asphalt	Run No.	% Aromatic Carbon	% Aromatic Hydrogen
AAD-1	1	41.1	7.1
	2	45.0	8.1
AAG-1	1	49.3	11.8
		51.8	12.9
AAK-1	1	44.8	8.3
	2	43.6	6.2
AAM-1	1	47.1	9.4
	2	46.1	9.2

Table 6. Viscosities (Pa · s) of Mixtures of Four Core Asphalts with Their IEC Amphoteric, Base, Acid, or Neutral Fractions at 60 °C and 1.0 rad/s

Asphalt	Run Number	Viscosity of Asphalt	Viscosity of Asphalt + Amphoterics	Viscosity of Asphalt + Bases	Viscosity of Asphalt + Acids	Viscosity of Asphalt + Neutrals
AAD-1	1	131	2,462	327	174	37
	2	-	2,815	301	211	43
AAG-1	1	240	1,740	346	285	132
	2	-	1,139	402	437	129
AAK-1	1	413	6,836	656	517	110
	2	-	6,755	1,004	550	124
AAM-1	1	258	4,032	399	292	140
	2	-	3,901	470	342	135

Table 7. Viscosities (Pa·s) of Mixtures of Neutral Plus Acid and Base Fractions of Four Asphalts at Three Temperatures Compared with Viscosities of Parent Asphalts

Asphalt	Viscosity of Asphalt (1.0 rad/s)			Tan δ, Asphalt (25°C)	Viscosity of Mixture (1.0 rad/s)			Tan δ, Mixture (25°C)
	25°C	45°C	60°C		25°C	45°C	60°C	
AAD-1	40,570	1,083	130.8	2.60	1,264	54.3	10.1	17.09
AAG-1	354,000	3,202	239.9	8.91	41,260	559.3	57.6	97.85
AAK-1	81,050	4,203	412.7	2.47	7,272	220.9	35.4	14.01
AAM-1	161,550	2,769	258.0	2.31	18,450	318.7	51.4	12.48

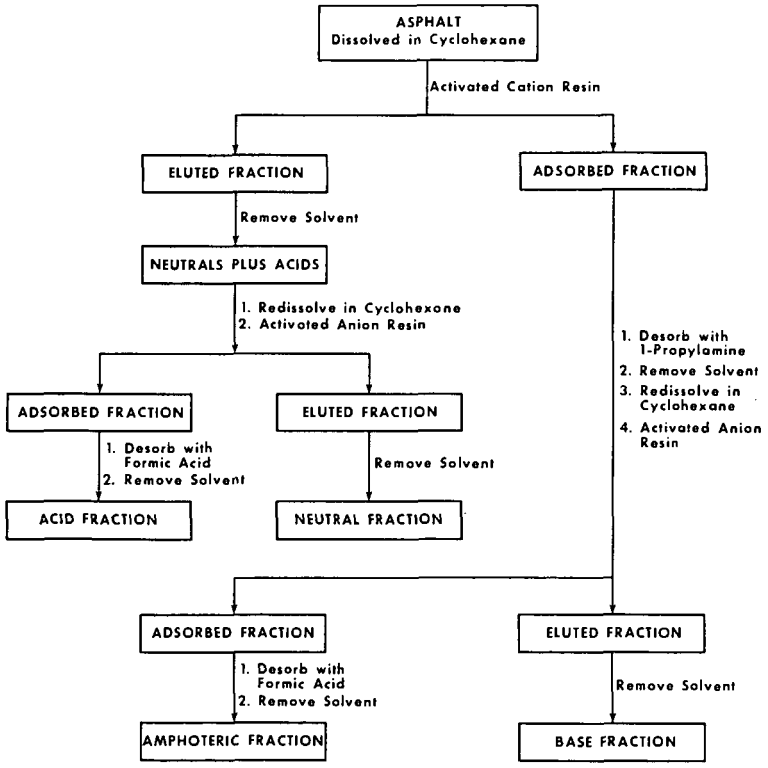

Figure 1. Flow Sheet for Isolation of Amphoterics by IEC

HP-GPC ANALYSIS OF ASPHALT FRACTIONS IN THE STUDY OF MOLECULAR SELF-ASSEMBLY IN ASPHALT

P. W. Jennings, J. A. S. Pribanic, J. A. Smith, T. M. Mendes
Department of Chemistry and Biochemistry
Gaines Hall, Montana State University
Bozeman, MT 59717-0340

Keywords: asphalt; intermolecular interactions; asphalt fractions

INTRODUCTION

The nature of intermolecular interactions in asphalt cement remains incompletely understood, although the body of evidence continues to grow. Several types of interactions are possible. In a number of papers, the theory has been propounded that micelles, formed by the stacking of flat aromatic molecules via pi-pi interactions, are important constituents of asphalt cements [1]. J. C. Petersen, on the other hand, has concentrated efforts on the study of functional groups containing oxygen, nitrogen and sulfur because some of these functional groups could interact through polar forces [2]. Less attention has been paid to possible van der Waals interactions except in cases in which long unsubstituted aliphatic chains (waxes) crystallize within the asphalt [3]. Nevertheless, all of these interactions could contribute to the formation of an intermolecular network, the characteristics of which may determine the behavior of the asphalt cement.

Because of the complexity of asphalt, such interactions are difficult to study. High Performance Gel Permeation Chromatography (HP-GPC) has been used to demonstrate the tendency of self-assembled units to form in whole asphalts and some fractions [4,5]. Molecules in many common asphalts show a distinct tendency to self-assemble; a few asphalts show little if any such character. The latter asphalts are likely to be thermally sensitive, that is, to be subject to early thermal cracking and/or permanent deformation [6]. In experiments in which the polarity of the eluting solvent was changed, it appeared that both polar and non-polar interactions are much more important in those asphalts which exhibit self-assembly than in those which do not [7].

In efforts to clarify the chemical nature of asphalt cements, two important fractionations of asphalt have been performed by Western Research Institute (WRI) under auspices of the Strategic Highway Research Program (SHRP). Preliminary work on the HP-GPC analysis of two fractions from Ion Exchange Chromatographic separations was described previously [5]. Further work on these and other fractions will be the subject of this paper.

EXPERIMENTAL PROCEDURES

Two fractions from preparative size exclusion chromatographic (SEC) separations of each of eight asphalts were supplied by WRI. This molecular size separation uses toluene as solvent. The separation is based on a transition from non-fluorescence to fluorescence of the eluting substances. The non-fluorescent fraction,

labelled SEC I, is thought to consist of associated entities whereas the fluorescent fraction (SEC II) is composed of individual molecules [8] or perhaps small associated units.

Using ion exchange chromatography (IEC), WRI obtained five fractions from each of the same eight asphalts. These are strong acid, strong base, weak acid, weak base and neutral materials [9].

Both SEC and IEC fractions were used as received and subjected to HP-GPC analyses as previously described [5]. Tetrahydrofuran (THF) was used as solvent.

RESULTS AND DISCUSSION

A Note about the Solvent

Tetrahydrofuran is a common solvent for HP-GPC analysis of asphalts and their fractions. At the low sample concentrations used (0.5% w/v), THF disrupts most intermolecular associations present in the neat asphalt. However, the strongest associative bonds, both polar and non-polar, apparently do survive in THF solution. Thus, we suggest that THF is the solvent of choice for indicating the *tendency* of molecules in an asphalt to form strong associations by any mechanism (polar and/or non-polar). This is particularly important because we theorize that the extent to which the molecules in an asphalt form an intermolecular network consisting of both polar and non-polar interactions contributes to the ultimate performance of the asphalt.

The SEC Fractions

The SEC I and II fractions from each of eight asphalts were analyzed by HP-GPC in THF. In Figure 1, the chromatograms which were detected by 340 nm absorption for SEC I and II fractions are superimposed on that of the parent asphalt for two asphalts, representing the range of results observed.

In all cases studied, SEC I is more aromatic[(1)] and has more large molecular size (LMS) material[(2)] than the corresponding whole asphalt, whereas SEC II is much less aromatic and shows no evidence in the LMS region for intermolecular association. However, there are significant differences among asphalts. For example, in THF, asphalt A shows strong evidence for intermolecular association in the whole asphalt and in SEC I, but asphalt G contains little, if any, self-assembled material in the whole asphalt and the least amount in SEC I of all asphalts tested (Figure 2). Furthermore, the percentages of LMS material in the whole asphalts bear a nearly linear relationship to the percentages of LMS in their respective SEC I fractions (r^2=0.89).

However, there are some interesting details within this data. First, there is much less evidence for the presence of self-assembled entities in the LMS regions of

[(1)]The aromatic content of samples can be compared by summing the areas in mAU under the chromatographic curves at 230, 254, 280, 340, 380, 410 and 440 nm. This is called the total conjugated volume, CV_t.

[(2)]Percentage of LMS is defined as the percentage of CV_t appearing in the large molecular size region of the chromatogram, before 17 minutes elution time in this system.

SEC I fractions from Group 1[3] asphalts than in SEC I fractions from other Groups. Furthermore, these fractions begin to elute as much as two minutes earlier than their parent asphalts. This indicates that the process of SEC separation in toluene may force some intermolecular polar associations that a) are not present in the original asphalt and b) are quite stable. That such a change is induced by the SEC process is further evidenced by the fact that SEC I fractions from Group 1 asphalts are not completely soluble in THF, whereas the parent asphalts are easily soluble.

Second, when one observes the strong response in the LMS region for SEC I fractions, it would be easy to assume that all the LMS material in the whole asphalt is accounted for by the SEC I fraction. However, when the amount of LMS material explained by SEC I and II[4] is compared with that found by analysis of the whole asphalt, differences among the asphalts are observed (Table I). For example, for asphalts A, B and D, less LMS material is calculated from the SEC I and II fractions than is observed in the whole asphalt. Since the SEC preparation using toluene should encourage polar interactions while disrupting pi-pi bonds, the HP-GPC data may indicate that pi-pi interactions are somewhat more important than polar interactions in these three asphalts.

For asphalts C, F and K, the difference between calculated and observed LMS percentages is small (within experimental error). This may mean either a) that neither interactive mechanism is important, or b) that both interactions contribute about equally in the whole asphalt. Earlier studies with changes in solvent polarity indicate that the latter is true for asphalt K. For asphalts C and F, in which little intermolecular interaction is noted, it may be that both polar and non-polar associations contribute about equally to the low LMS content.

Asphalts G and M present a different picture in that the total LMS percentage in SEC I and II is higher than in the whole asphalt. This difference is substantial in asphalt M, less so in asphalt G. We suggest that the SEC separation of G in toluene encourages polar interactions not present in the whole asphalt, as mentioned earlier. In the whole asphalt, in fact, neither polar nor non-polar interactions seem to be important.

Asphalt M (Group 4)[5], well known as an unusual material, does not change its reputation here. We suggest that, not only does the SEC separation encourage polar bonds not present in the whole asphalt, but also it disrupts non-polar interactions that are particularly strong in this asphalt. That is, toluene may actually invert the interactions prevalent in the neat asphalt. It should be noted that asphalt M is known as a highly compatible material from which little if any asphaltene can be precipitated by heptane. That is, heptane can not induce the separation of polar materials perhaps because they are so strongly solubilized by virtue of pi-pi interactions. This would be consistent with the HP-GPC results.

---

[3]Group 1 asphalts have narrow molecular size distribution, with little evidence for intermolecular association (i.e., little LMS shoulder area) in the HP-GPC chromatogram. These asphalts are often temperature sensitive and may crack early and/or rut in a pavement.

[4]Percent LMS whole asphalt, calc. = (% LMS SEC I)(wt % SEC I) + (% LMS SEC II)(wt % SEC II)/100.

[5]Asphalts in Group 4 possess narrower molecular size distributions than Group 2 asphalts, but the overall molecular size is quite large.

The IEC Fractions

Among the fractions from Ion Exchange Chromatography – strong acids, strong bases, weak acids, weak bases and neutrals – the strong acids exhibit most intermolecular association in THF. These fractions are highly aromatic (Table II) and, because of the isolation procedure, should contain molecules with strongly acidic functional groups as well as those with a strong acid and one or more additional functional groups. Thus, the extensive intermolecular association is not surprising. Nevertheless, there are significant differences among the chromatograms of strong acid fractions from different asphalts (Figure 3). The chromatogram of strong acids from asphalt G (representing Group 1 asphalts), although showing evidence for considerable intermolecular interaction, also indicates that most of the materials are unassociated. This contrasts with the situation for strong acids from asphalt A (Group 2)[6], which are seen to be predominantly in the LMS region and thus highly associated.

Strong base fractions are also quite aromatic (Table II). The molecules could also have more than one functional group (but not a strong acid since they have been removed). Their chromatograms indicate less self-assembly in the strong bases than in the corresponding strong acids and less self-assembly among Group 1 asphalts than others.

The weak acid and weak base fractions are quite aromatic but demonstrate little if any tendency toward self-assembly in THF, i.e., any intermolecular bonds are quite weak. Neutral fractions are the least aromatic of the IEC fractions and display no evidence for self-assembly in the LMS regions of their chromatograms.

It is expected that the process of IEC separation may destroy some intermolecular interactions because each contributor belongs in a separate category. Thus, the total LMS percentage for all the IEC fractions is expected to be significantly less than that obtained by HP-GPC analysis of the whole asphalt (Table III). For most asphalts, this is true. However, for asphalt G, there is no significant difference between these approaches, again suggesting that intermolecular interactions are not strong in this asphalt.

SUMMARY AND CONCLUSIONS

Separation of asphalts into fractions has provided somewhat simpler samples by which to study intermolecular interactions in the asphalts. Separation by size exclusion chromatography (SEC) using toluene has yielded SEC I, composed of large species associated by polar bonds, and SEC II, consisting of essentially nonassociated molecules (as evidenced by HP-GPC analysis). Analyses of these fractions by HP-GPC in THF emphasize the aromatic character of SEC I (but not of SEC II), agree that SEC I contains highly associating components, but distinguishes among asphalts as to the extent, strength and source (polar or non-polar) of the interactions.

Other fractions derived from ion exchange chromatography were also analyzed by HP-GPC. These analyses confirm that components in the strong acids fraction, which are highly aromatic and may include molecules with more than one functional

[6]Group 2 asphalts include most common materials. They have broader molecular size distributions and show strong evidence for intermolecular interactions.

group, are extensively associated. However, the strong acids do not account for all of the associated entities in the asphalt. Thus, even though the other polar fractions appear by HP-GPC not to be associating when separated, they must contribute significantly to the self-assembled materials observed in the whole asphalt. However, the strength, and therefore the contribution to behavior, of intermolecular associations, differ among asphalts.

ACKNOWLEDGEMENTS

The support of the Strategic Highway Research Program is gratefully acknowledged.

We thank researchers at Western Research Institute, Laramie, Wyoming, for providing samples.

REFERENCES

[1] Yen, T.F., "A Macrostructure of Petroleum Asphalt," PREPRINTS, Div. of Petrol. Chem., ACS, 35, (3)314 (1990).

[2] Petersen, J.C., "Chemical Composition of Asphalt as Related to Asphalt Durability. State of the Art," and references cited therein, in Transportation Research Record, TRB, National Research Council, Washington, D.C., 1984.

[3] Planche, J.-P., et al., "Relationships between Characterization of Asphalt Cements by Differential Scanning Calorimetry and their Physical Properties," PREPRINTS, Div. of Petrol Chem., ACS, 35, (3)330 (1990).

[4] Brulé, B., et al., "Characterization of a Road Asphalt by Chromatographic Techniques (GPC and HPLC)," J. Liquid Chromatography, 2, 437 (1979). Brulé, B., et al., "Contributions of Gel Permeation Chromatography (GPC) to the Characterization of Asphalts," in Liquid Chromatography of Polymers and Related Materials II. Cazes and Delamore, Eds., Dekker, 1980.

[5] Jennings, P.W., et al., "High Performance Gel Permeation Chromatography in the Characterization of Self-Assemblies in Asphalt," Fuel Sci. and Technol. Int., in press.

[6] Jennings, P.W., et al., unpublished results.

[7] Jennings, P.W., et al., "High Performance Gel Permeation Chromatography in the Characterization of Self-Assemblies in Asphalt. 2.," Proceedings, International Symposium on Chemistry of Bitumens, June, 1991, Rome, Italy.

[8] Branthaver, J.F., et al., "Separation of SHRP Asphalts by Preparative Size Exclusion Chromatography," PREPRINTS, Div. of Petrol. Chem., ACS, 35, (3)407 (1990).

[9] Branthaver, J.F., et al., "Separation of SHRP Asphalts by Ion Exchange Chromatography," PREPRINTS, Div. of Petrol. Chem., ACS, 35 (3)376 (1990).

Table I. Differences between % LMS observed in the whole asphalt and that calculated from amounts in SEC I and II.

Asphalt	a % LMS observed[1]	b % LMS calculated[2]	difference a − b
A	19.2	16.5	2.7
B	14.2	11.7	2.5
C	8.2	7.3	0.9
D	24.0	20.0	4.0
F	8.3	8.3	0.0
G	3.2	4.7	−1.5
K	19.5	18.6	0.9
M	20.1	24.2	−4.1

[1] Experimental error ±0.5
[2] See footnote 4

Table II. Relative aromaticity of fractions from Ion Exchange Chromatography from HP-GPC Analysis.

Asphalt	Whole	CV_t (x 10^5) SA[1]	SB[2]	WA[3]	WB[4]	N[5]
A	22.6	34.9	30.1	33.0	27.5	14.7
B	26.9	43.5	36.7	35.2	33.4	15.8
C	23.9	40.9	30.5	35.6	29.7	14.2
D	20.6	30.7	25.6	28.3	19.7	11.8
F	27.6	40.2	35.1	35.6	34.4	16.9
G	24.8	35.0	29.7	31.8	26.8	16.6
K	24.6	33.7	28.7	28.3	30.5	14.9
M	23.5	38.3	28.9	31.6	28.3	13.8

CV_t - total conjugated volume, see Footnote 1
[1] Strong acid [3] Weak acid [5] Neutral
[2] Srong base [4] Weak base

Table III. Differences between % LMS observed in the whole asphalt and that calculated from amounts in the IEC fraction.

Asphalt	a % LMS observed[1]	b % LMS calculated[2]	difference a − b
A	19.2	13.4	5.8
B	14.2	9.9	4.3
C	8.2	1.3	6.9
D	24.0	16.8	7.2
F	8.3	6.0	2.3
G	3.2	3.8	−0.6
K	19.5	13.2	6.3
M	20.1	16.3	3.8

(1) ±0.5

(2) from % LMS in all IEC fraction

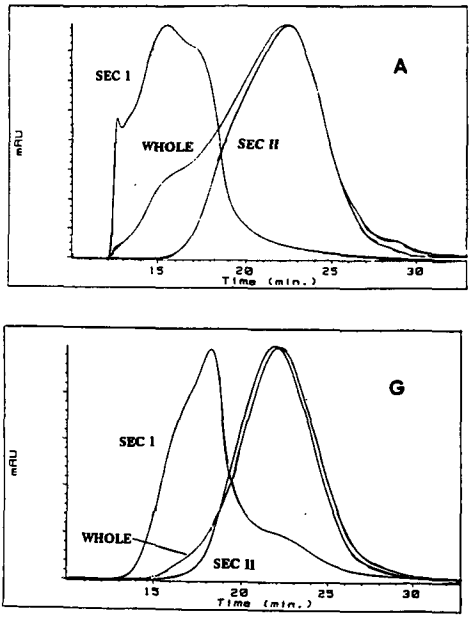

Figure 1. Chromatograms of SEC I, SEC II and whole asphalt for asphalts A and G. Chromatograms are normalized to same peak height for visual emphasis.

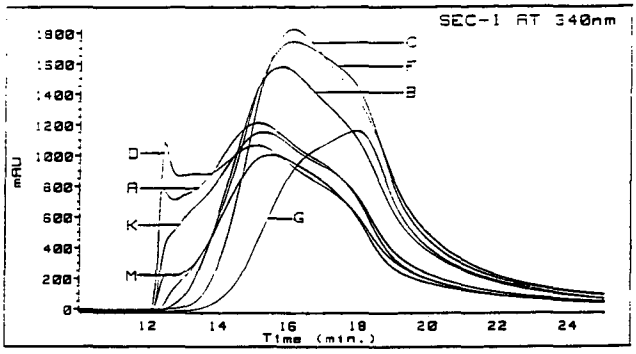

Figure 2. Chromatograms (340 nm) for SEC I fractions of eight asphalts.

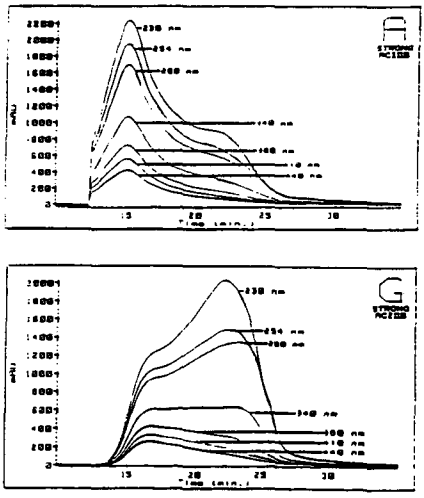

Figure 3. Chromatograms at seven wavelengths for strong acid fractions of asphalts A and G.

NUCLEAR MAGNETIC RESONANCE SPECTROSCOPY FOR THE CHARACTERIZATION OF ASPHALT

P. W. Jennings, F. F. Stewart, J. A. Smith,
M. A. Desando, T. M. Mendes and J. A. S. Pribanic
Department of Chemistry and Biochemistry
Montana State University
Bozeman, MT 59717

INTRODUCTION

Nuclear Magnetic Resonance (NMR) spectroscopy is a powerful tool used in a broad array of disciplines to describe the character of atoms, molecules and assemblies of molecules. This information may be gathered from samples solubilized in solvents or in the solid state. While carbon (^{13}C) and proton (^{1}H) characterizations are typically used, there is a variety of NMR active nuclei which include oxygen, phosphorus, nitrogen, silicon and many metals. With regard to applications, this tool has been used to characterize simple organic and inorganic compounds, proteins, carbohydrates, enzymes, coal and polymeric materials. Thus, it has broad use in a variety of disciplines. With regard to asphalt, NMR spectroscopy has been applied but not to the extent that it has in the areas previously mentioned.[1-6]

Before describing some of the results from our laboratory, it is appropriate to briefly describe the character of asphalt and some of the goals for which answers are sought. Asphalt is a hydrocarbon mixture containing minor elements, in bonded form, of O, N, S, V, Fe and Ni. None of these minor elements is present in more than a few percent. The hydrocarbon portion is approximately 25% aromatic and 75% aliphatic with average molecular weights in the range of 700-1000 amu. Thus, average structures for asphalt contain 4 or 5 aromatic rings joined in a planar polynuclear fashion and a couple of aliphatic chains (5-10 carbons in length). In every 2-3 molecules there is a heteroatom (O, N, S) as either an aromatic or aliphatic moiety. A variety of functional groups is present and includes carboxylic acids (COOH), phenols (ArOH), ketones (C=O), ethers (–O–), esters (–COOC–), amines (pyroles and pyridines) and sulfur derivatives (≈ 60-70% thiophenic and 30-40% sulfides).

The goals to be achieved in the characterization of asphalt include answers to the following questions.

1. What are the functional groups and how many of each are present?
2. How are the aromatic rings arranged and how many substituents are present?
3. How long are the aliphatic chains, how many are there and how many branches are present?
4. How are the heteronuclear aromatic nuclei arranged?
5. What is the sulfide content?

Finally, the big questions are derived from the interactions of these components in a macrosystem.

6. How do these components assemble for form the substance called asphalt?
7. How do these assemblies differ among the asphalts?
8. How do these features relate to performance?
9. How do these features change with modifiers. treatments and additives?

With this introduction. perhaps the results described below will be in context and more readily understood.

RESULTS AND DISCUSSION

Functional Group Analysis

In this portion of the work, carboxylic acid and phenol content of a variety of asphalts were measured. Two reactions were run to prepare derivatives which provided a NMR active probe for the analysis. They are:

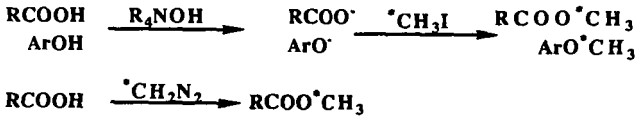

The first reaction involves a phase transfer type base followed by methylation with enriched ^{13}C.[7,8] For the carboxylic acid analysis a sharp resonance should result and does in a few cases. However, there often is a broader resonance band on the downfield side of the carboxylate which interferes with the correct analysis. Therefore, the diazomethane reaction was used to analyze carboxylic acids. In this case a sharp resonance was obtained. The phenolic content was analyzed using the phase transfer methodology. Due to the variation in aromatic residue these resonances are broad. Numerical results of these analyses are tabulated in Table I for selected asphalts and asphalt fractions.

The conclusions drawn here are that there is some variation among asphalts but there is not very much carboxylic acid or phenolic content since the numbers displayed are x 10^{-5} moles/gm. POV stands for pressure oxygen vessel and refers to an aging process used in the SHRP studies. Given the error associated with these analyses, it is concluded that POV aging does not reflect any increase in the carboxylic acid content of an asphalt.

Size exclusion chromatography on a preparative scale by WRI[9] provided these fractions. SEC-1 represents the larger molecular sized materials while SEC-2 fractions have smaller molecular sized units. The former are thought to have molecular assemblies of components while SEC-2 has fewer assemblies and are necessarily smaller. This separation was conducted using toluene which destroys pi-pi aromatic assemblies and facilitates polar interactions. Thus, it is interesting to note that there is little disparity for carboxylic acids between these two fractions, save asphalts F, G and K in which SEC-2 shows enhanced values. These authors are not

willing to speculate at this time on the application of these results to performance testing.

Hydrocarbon Characteristics

Both proton and carbon spectroscopy were used to characterize aromatic and aliphatic content. The numerical results for carbon are displayed in Table II. The conclusions here are that there is very little variation among the whole asphalt samples. Among the fractions it is noted that the aromaticity is less for SEC-2 vs SEC-1 and that the neutral fraction derived from ion exchange chromatography (IEC) has the least aromaticity among that group.

Two-Dimensional NMR Spectroscopy

From the one-dimensional data results cited above, we turned to the use of two-dimensional NMR spectroscopy in an effort to provide additional data on the aromatic and aliphatic resonances. Figures 1 and 2 are for the whole asphalt and represent the typical ^{13}C spectrum for comparison with a DEPT 135 spectrum. respectively. Using these data, one can better determine which resonances are due to CH_3, CH_2, CH and C. The DEPT 135 data nulls quaternary carbons which is particularly noticeable in the region of 130-150 ppm. Figure 3 reinforces this feature as it is run under conditions which facilitate quaternary carbons and suppress all others. The peak at 97 ppm is an impurity and the one at 78 ppm is $CHCl_3$. Those in the aliphatic region represent incomplete suppression of CH_2 resonances. The broad aromatic CH resonances occur from 115 to 129 ppm, with a rather sharp demarcation on the downfield side, Figure 3a. At this juncture, the quaternary carbons arise in earnest and range from 120 to 145 ppm, Figure 3b. In looking at the entire spectrum, Figure 1, one can readily see the break between these two moieties at 130 ppm. Given the relative amounts of these two moieties, one must conclude that a number of polynuclear aromatic sheets must be present.

Due to the long-standing conception that benzylic carbons bearing protons are sites for oxidation, it was desired to find a way to analyze for these units. After trying some direct methods such as HETCOR without success, we turned to looking for long-range coupling between the benzylic protons and the aromatic ipso carbons. Success was readily achieved with model compounds and asphalt was subsequently attempted. The results are shown in Figures 4, 5 and 6. In Figure 4, the correlation of interest occurs at intersection 2.3 ppm on the proton axis and 120 to 140 ppm on the carbon axis. These are protons on benzylic carbons attached to two different types of aromatic moieties. The first at 120-130 ppm is likely a substituent on a typical carbon based aromatic ring. The correlation at 130-145 ppm is likely to be of a heterocyclic ring system. From model compounds, it is believed that these are benzylic methyl groups. Figure 5 shows a similar correlation but now the CH_2 units are also present. This is achieved by altering the spectrometer parameters. Finally in Figure 6, the graph shows a projection of these peaks when the parameters have been adjusted so as to project benzylic CH (2.7 ppm), CH_2 (2.5 ppm) and CH_3 (2.3 ppm) on the proton axis. Efforts to investigate the effects of oxidation are underway.

CONCLUSION

A few techniques within the scope of solution NMR spectroscopy have been applied to the complicated mixture called asphalt. Through these uses, one can gain considerable insight into the details of asphalt compounds. These, in turn, should provide future scientists with data for correlations with performance and physical testing.

REFERENCES

(1) Hagen, A.P.; M.P. Johnson, and B.B. Randolph. ^{13}C NMR studies on roadway asphalts, *Fuel Science and Technology Int'L* (1989) **7**, 1289.

(2) Hasan, M.U., A. Burkhari and M.F. Ali. Structural characterization of Saudi Arabian medium crude oil by NMR spectroscopy, *Fuel* (1985) **64**, 839.

(3) Netzel, D.A. and F.P. Miknis. NMR study of U.S. Eastern and Western shale oils produced by pyrolysis and hydropyrolysis, *Fuel* (1982) **61**, 1101.

(4) Netzel, D.A. Quantitation of carbon types using DEPT/QUAT NMR pulse sequences; application to fossil-fuel-derived oils, *Anal. Chem.* (1987) **59**, 1775.

(5) Snape, C.E. Analysis of Fossil Fuels. In L.D. Field and S. Sternhell (eds.), *Analytical NMR*, (1989) John Wiley and Sons, Ltd., 66-115.

(6) Jennings, P.W., et al. High performance gel permeation chromatography in the characterization of self-assemblies in Asphalt. 1., *Fuel Science and Technology, Int.* (1992) **10**, 887.

(7) Rose, K.D. and M.A. Francisco. Characterization of acidic heteroatoms in heavy petroleum fractions by phase - transfer methylation and NMR spectroscopy, *Energy and Fuels* (1987) **1**, 233.

(8) Rose, K.D. and M.A. Francisco. A two-step chemistry for highlighting heteroatom species in petroleum material using ^{13}C NMR spectroscopy. *J. Am. Chem. Soc.* (1988) **110**, 637.

(9) WRI – Western Research Institute in Laramie, Wyoming provided SEC and IEC samples. We are deeply grateful for their generosity.

Table I. Carobxylic Acid and Phenol Content Asphalts and Asphalt Fractions.

Asphalt	[COOH] x 10^{-5} moles/g	[ϕOH]* x 10^{-5} moles/g	[ϕOH]** x 10^{-5} moles/g
AAA-1*	1.1	3.5	2.5
POV(1)	1.9		
SEC-1(2)	1.6	13.0	6.8
SEC-2	1.9		
AAB-1	0.5	4.2	3.1
POV	0.3		
SEC-1	0.5	10.0	5.5
SEC-2	small		
AAC-1	0.5	1.8	1.7
POV	0.4		
SEC-1	0.9	9.3	4.5
SEC-2	0.6		
AAD-1	1.1	2.2	2.2
POV	1.7		
SEC-1	3.2	14.0	7.8
SEC-2	3.2		
AAF-1	0.1	6.3	3.2
POV	0.1		
SEC-1	0.1	17.0	7.6
SEC-2	0.4		
AAG-1	4.5	4.2	5.5
POV	3.5		
SEC-1	0.3	11.0	7.0
SEC-2	1.7		
AAK-1	1.6	2.5	1.5
POV	1.5		
SEC-1	0.75	7.4	2.0
SEC-2	5.1		
AAM-1	1.0	3.5	2.4
POV	0.6		
SEC-1	0.8	3.2	3.2
SEC-2	0.9		

*Asphalts from SHRP-Whole Asphalt
**Hindered phenols
***Unhindered phenols
(1)Aged by pressure of oxygen
(2)Sized Exclusion Chromatography with toluene solvent from WRI

Table II. % Aromaticity from ^{13}C Analyses of Asphalt and Fractions.

Asphalt	Whole	SEC I	SEC II	Strong* Acids	Strong* Bases	Neutrals*
AAA-1	27.9	36.7	26.2	38.1	32.2	19.8
AAB-1	31.2	47.1	27.6	46.7	38.3	16.8
AAC-1	27.8	40.1	25.4	44.7	34.6	18.3
AAD-1	23.4	30.9	24.0	32.2	34.1	19.7
AAF-1	32.8	45.6	29.9	37.4	39.9	24.5
AAG-1	29.0	30.3	28.3	37.0	29.0	16.6
AAK-1	26.2	37.9	26.9	33.5	34.8	18.4
AAM-1	25.6	23.0	27.1	35.1	32.3	14.7

*Fractions from an ion exchange chromatograph (IEC) separated at Western Research Institute, Laramie, Wyoming[9]

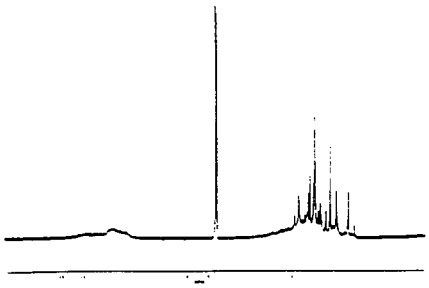

Figure 1. Carbon Spectrum of a Typical Asphalt in $CDCl_3$.

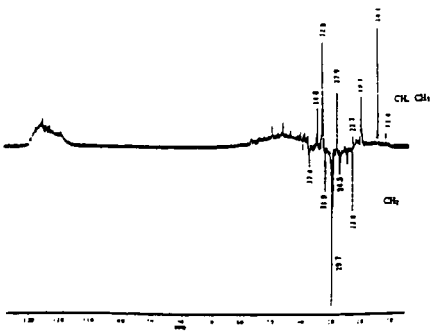

Figure 2. DEPT 135 Spectrum Showing CH and CH_3 Up and CH_2 Down.

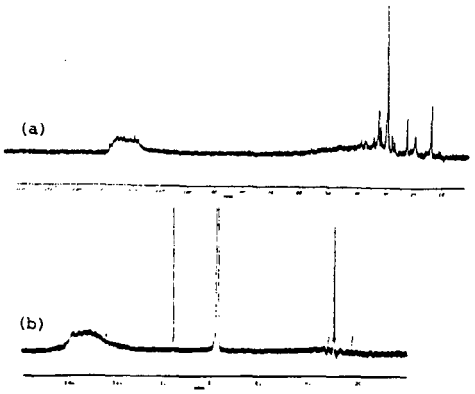

Figure 3. Selected DEPT Spectra of Asphalt: (a) DEPT 45 Where Quaternary Carbons Are Suppressed, (b) QUAT Spectrum Where Quaternary Carbons Are Emphasized and Other Resonances Are Suppressed.

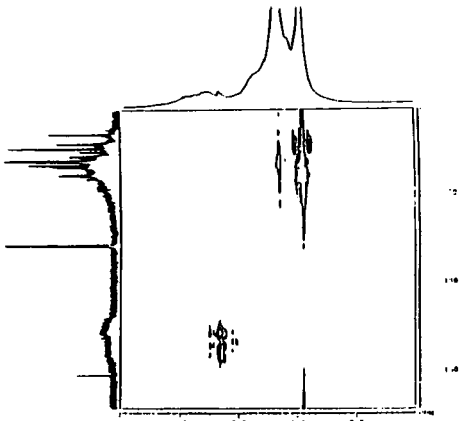

Figure 4. 2-Dimensional Correlation Between Benzylic Methyl Protons (Horizontal Axis) and Quaternary Aromatic Carbons (Vertical Axis).

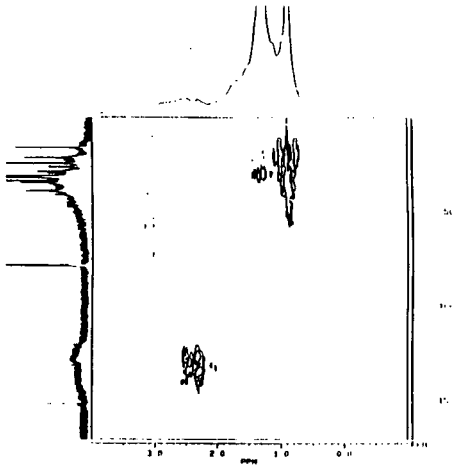

Figure 5. 2-Dimensional Correlation Showing Benzylic Methyl and Methylene Groups.

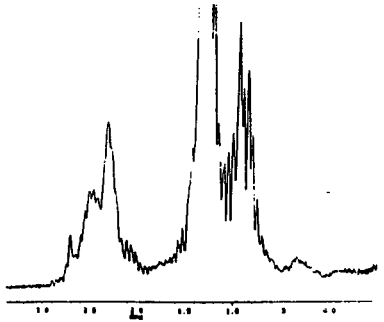

Figure 6. A Projection on the Proton Axis of a 2-Dimensional Correlation Between Benzylic Protons (CH, CH_2, CH_3) and Aromatic Carbons.

CHARACTERIZATION OF MICROSTRUCTURE OF ASPHALT, AND CORRELATION WITH THEIR PERFORMANCE

William H. Daly and Zhaoyao Qiu(Chiu), Macromolecular Studies Group, Department of
Chemistry, Louisiana State University, Baton Rouge, LA 70803-1804

Keywords: asphalt, rheology, nuclear magnetic resonance.

Introduction

Asphalt is a very complex mixture; even within a given grade the composition may vary significantly depending upon both the source of the crude and the refining process. Although tremendous efforts have been devoted to characterize asphalt, microstructure of asphalt remains to be defined. In particular a routine technique which quantifies the components controlling the long term behavior of an asphalt cement is required. In our laboratory, eight asphalt samples with grades ranging from 10 to 30 from four different sources were examined. The molecular structure of the asphalts was characterized quantitatively using NMR and FTIR techniques. Differential scanning calorimetry (DSC) was employed to estimate the crystallinity, and rheological properties of the asphalts were studied by dynamic mechanical analysis (DMA). Our goal is to achieve an understanding the relaxation mechanisms of asphalt under load at the molecular level.

Characterization of Asphalt Samples

NMR and FTIR Characterization of Asphalt The application of NMR to analysis of asphalt samples is well established [1-3]. Samples were dissolved in deuterated chloroform at a concentration of 10% (w/v), spectra were measured using a Bruker 200 MHz FTNMR. A relaxation agent, $Cr(acac)_3$, 12 mg/ml, was added to the ^{13}C nmr samples. Using an interpulse time of six seconds and more than 8000 scans, reliable quantitative spectra can be obtained [4]. Table 1 summarizes the observations on our eight samples from the nmr measurements.

It is known that methine structures, especially those attached directly to aromatic ring [5], are mainly responsible for oxidation of asphalt, a major cause of pavement failure. We identified the specific aliphatic carbon types in terms of methyl (8), methylene (19) and methine (6) structures with DEPT technique of 13C nmr (table 2). Comparison of DEPT nmr spectra with broadband nmr spectrum at aromatic band region (100-160 ppm) reveals that no aromatic carbons coupled to hydrogen appears at chemical shifts greater than 131 ppm. The large number of distinctive resonances emphasizes the complexity of the asphalts and suggests that correlating nmr analyses to asphalt chemical and physical properties will be very difficult.

Asphalt samples, 5% (w/v) chloroform solution in 1 mm cell were examined by quantitative FTIR using a Perkin Elmer 1700 FTIR. The overlapped peaks in 1550 - 1800 cm^{-1} were resolved by curve fitting program (figure 1) based on the work of J. C. Petersen and his colleagues [6]. The results (Table 1) show significant differences in composition between asphalt samples of the same grade. Thus comparison of asphalt properties based simply on the grade is rather imprecise.

Crystallinity of Asphalt Linear paraffins present in asphalt readily crystallize. The relative crystallinity of a given asphalt can be measured by DSC [7,8] We used DSC to estimate the relative volume of the crystalline phase in each of the asphalt samples. A Seiko DSC 220C calibrated for temperature and enthalpy with indium was employed for the measurement. The DSC was conducted on ≅ 10 mg samples sealed in an aluminum sample pan using an empty aluminum sample pan with cap as a reference. Initially each sample was cooled at 3 C/min to -45 C and then heated at 3 C/min. The heats of fusion (ΔH_f) observed are is listed in Table 3. The percent crystallinity was estimated from this data by assuming that completely crystallized hydrocarbons in an asphalt matrix exhibit an average enthalpy of 200 J/g (8).

Glass Transition Processes in Asphalt

The glass transition temperature is a very important property to most organic materials not only because it limits practical applications but also because it can provide valuable information about microstructure of a material. We believe that DMA is the best technique to determine Tg both in terms of accuracy and correlation with service conditions of asphalt on the road.

Molded asphalt bars, 20 x 9.495 x 1.64 mm (l x w x t) were mounted in a Seiko DMS 110; each sample was run in bending mode at cooling rate of 1 C/min at single frequency. Operation at single frequency over each temperature range yields more reproducible data that attempting to obtain multifrequency data in a single run. Since multiple runs are required establishing the relationship between frequency and temperature is very time consuming. The Tg was identified as the temperature corresponding to the maxima of loss modular E" at each frequency. If the Tg is plotted against corresponding frequency based on an Arrhenius equation, an activation energy for the relaxation process can be computed. Table 4 summarizes Tgs and the calculated activation energies, E_a, for our asphalt samples.

Scrutiny of table 4 reveals that asphalts with the same grade can exhibit very different Tg's, e. g., compare ACC and ACD. An asphalts with a higher grade may have the same or even lower Tg than that of an asphalt with lower grade. Another interesting thing to note is that the values of active energy for the transition process of the asphalt samples are close enough to be considered constant; an average active energy of 9.4 kcal/mol with a standard deviation of ±0.4 kcal/mol is observed. B. Brule et. al. [8] measured Tg of four asphalt samples with DMA at eight different frequencies from 0.015 to 7.3 Hz, a lower range of frequencies than we employed. We calculated the values for E_a from Brule's data: the results for the four samples are 9.6, 9.3, 9.3 and 8.4 kcal/mol, respectively, which are consistent with our results. The activation energy in this context is an energy barrier separating two set conformations which are in equilibrium. The height of the barrier determines the temperature dependency of wriggling rate. Thus, the constant activation energies imply that the molecular structures responsible for relaxation in each sample are the same. Previous authors [8, 9, 10] have examined fractionated asphalt samples and have shown that only saturates and aromatic fractions contribute to the glass transition. We determined the activation energy of low density polyethylene (LDPE) Tg to be 9.9 kcal/mol, which is very close to that of asphalt. Hence, we postulate that

only those segments primarily composed of aliphatic units are wriggling in the glass transition process.

Imposition of a larger strain (1 %) on the asphalt samples at 50 Hz in DMA experiments will induce cracking at a specific temperature during the cooling. The temperature, called cracking temperature (Tc), can be used to estimate the low temperature cracking resistance of asphalt. The cracking temperature (Tc) is listed in Table 4. Note that all asphalt samples cracked at temperature above their Tg at 50 Hz, which implies Tg measured at this frequency can be considered the limit of brittle temperature of asphalt. In five of the eight cases the asphalt sample cracked at temperature within 4° of its Tg, however sample ACC cracked 11.5° above its Tg. The reason behind this deviation is not clear, but we believe it is related to the morphology of the asphalt. Comparing the data on relative crystallinity of the asphalt samples with Tc (table 3), one observes the sample having exhibiting the highest Tc is the most crystalline. There is a general inverse correlation between the extent of crystallinity and the cracking temperature.

Viscous Flow Process of Asphalt

Flow curves of each asphalt samples were measured with a Bohlin CS rheometer using a cone and plate mode from 5° to 150°C. Initial Newtonian viscosities at different temperatures were determined. At temperatures well above the glass transition temperature, the viscosity is primarily governed by the energy required for a molecule to jump from one site to an adjacent site. The dependence of viscosity on temperature follows the Arrhenius equation [11]. Figure 2 is an example of the Arrhenius plot of the viscosity versus temperature for asphalt. One observes that the curve is basically comprised of two linear regions with a single inflection point. The different slopes imply that the energy barrier of the flow process changed at certain temperature, called the onset temperature T_O, where a significant change in interaction between molecules occurred. The T_O's determined for each asphalt samples are listed in table 5. The molecular nature of the activation energy change has not experimentally confirmed at this point, but we speculate that dissociation of aromatic π-complexes must contribute to the change in molecular interaction. In addition, polar aromatics may interact to form of a three dimensional network that extends throughout asphalt.

Acknowledgment

Support for this work was provided by Louisiana Transportation Research Center.

References

1 L. Petrakis, D. T. Allen, G. R. Gavalas and B. C. Gates, *Anal. Chem.*, **55**, 1557, (1983)
2 I. Gawel, *Fuel,* **66(5)**, 618, (1987)
3 A. P. Hagen, M. P. Johnain and B. B. Tandolph, *Fuel Sci. & Tech. Int'l.,* **7(9)**, 1289, (1989)
4 D. J. Cookson and B. Smith, *J. Magnetic Resonance,* **57**, 355, (1984).
5 T. Mill and D. Tse, *Prepr Am Chem. Soc., Div. Pet. Chem.*, **35(3)**, 483, (1990).
6. J. C. Petersen, *Transportation Research Record*, **1096**, 1, (1986)
7 F. Noel and L. W. Corbett, *J. Inst. Petrol.*, **56(551)**, 261 (1970)
8 B Brule, J. P. Planche. G. King, P. Claudy and J. M. Letoffe, *Prepre. Am. Chem. Soc., Div. Pet. Chem.* **35(3)** 330 (1990).
9 Y. Wada and H. Hirose, *J. Appl. Phys. Jpn.,* **30**, 40, (1961).
10 H. K. Huynh, T. D. Khong, S. L. Malhotra and L. P. Blanchand, *Anal. Chem.*, **50(7)**, 978, (1978).
11 G. V. Vinogradov and A. Y. Malkin, *Rheology of Polymers,* p105, Mir Publishers, 1980.

Table 1 NMR and FTIR Characterization of Asphalt Composition

Sample	ACA	ACB	ACC	ACD	ACE	ACF	ACG	ACH
Source	Calumet	Calumet	Exxon	Exxon	South-land	South-land	Texaco	Texaco
Grade	AC-10	AC-20	AC-10	AC-20	AC-10	AC-20	AC-20	AC-30
Arom H%	5.5	6.1	6.9	6.0	6.3	6.8	7.1	5.7
Arom C%	28.2	30.4	37.3	34.1	33.4	33.7	34.0	24.5
Linear Aliph%	41.8	41.6	22.5	21.8	19.5	21.2	22.3	23.2
Phenolics*	0.0086	0.0058	0.0069	0.003	0.012	0.0093	0.0036	0.004
Pyrrolics*	0.0142	0.0112	0,0225	0.0135	0.0137	0.014	0.0145	0.0137
Carboxyl Acid*	0.109	0.0828	0.0318	0.021	0.0220	0.0311	0.0242	0.0324
Ketone*	0.133	0.13	0.0275	0.0195	0.0796	0.043	0.027	0.0362
Quinolone*	0.0412	0.0298	0.0269	0.027	0.023	0.0238	0.0175	0.0109
Sulfoxide*	0.0022	0.001	0.0014	0.0036	0.0043	0.004	0.0008	0.0015

* in mmol/g asphalt.

Table 2 Types of Aliphatic Carbons in Asphalt

Structure Type	Chemical Shifts, ppm
CH_3	10.8, 11.4, 14.1, 14.4, 19.2, 19.7, 20.3, 23.0
CH_2	20.1, 21.6, 22.7, 24.5, 25.2, 26.7, 27.1, 27.4, 28.6, 29.4, 29.7, 30.1, 31.9, 33.7, 34.8, 37.1, 37.4, 39.1, 39.4
CH	28.0, 32.8, 34.4, 38.8, 40.2, 46.0

Table 3 Heat of Fusion (ΔH_f) of the Asphalt Samples

Sample	ACA	ACB	ACC	ACD	ACE	ACF	ACG	ACH
ΔH, (J/g)	7.7	7.8	8.5	9.2	5.8	8.6	11.3	9.6
% cryst.*	3.85	3.9	4.25	4.6	2.9	4.3	5.65	4.8
Tc, °C	-12	-9	-3	-5	-20	-10	0	-3

* Average entropy for 100 % crystalline = 200 J/g (8)

Table 4 Glass Transition Temperature (Tg) from E", Active Energy (E_a) of the Transition and Cracking Temperature (Tc) of Asphalts

Asphalt	1 Hz	10 Hz	50 Hz	E_a (kcal/mol)	Tc
ACA	-23.0°C	-17.8°C	-13.3°C	9.8	-12°C
ACB	-24.9°C	-17.6°C	-14.5°C	8.8	-9°C
ACC	-19.6°C	-17.6°C	-14.5°C	10.0	-3°C
ACD	-14.9°C	-9.9°C	-4.1°C	9.4	-5°C
ACE	-32.2°C	-26.6°C	-22.5°C	9.0	-20°C
ACF	-23.2°C	-18.8°C	-13.8°C	9.5	-10°C
ACG	-16.5°C	-10.5°C	-6.1°C	9.7	0°C
ACH	-16.0°C	-9.6°C	-5.1°C	9.2	-3°C

Table 5 Onset Temperature (To) of the Arrhenius Plot of Viscosity ver. Temperature

Sample	ACA	ACB	ACC	ACD	ACE	ACF	ACG	ACH
T_o C	74	72	63	74	86	75	70	71

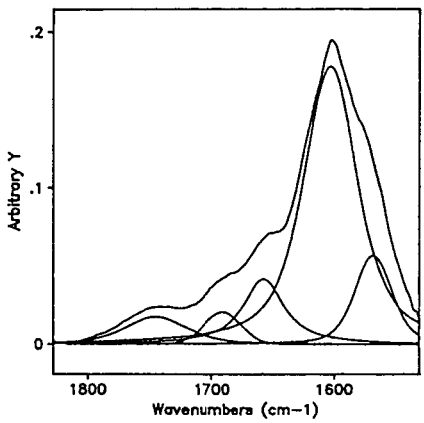

Figure 1 Deconvertution of Overlaped Peaks in a FTIR Spectrum.

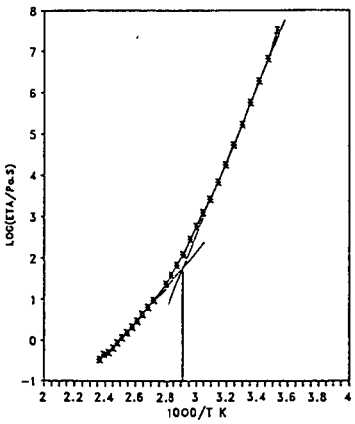

Figure 2 An Arrhenius Plot of Initial Newtonian Viscosity versus Temperature.

ASPHALTENE PRECIPITATION AND INCIPIENT FLOCCULATION IN MIXED SOLVENTS.

Simon I. Andersen,
Danish Natural Science Research Council,
H.C. Andersens Boulevard 40,
DK-1553 Copenhagen, Denmark.
and
James G. Speight,
Western Research Institute,
Laramie, WY 82071-3395

Keywords: Asphaltene, flocculation, interactions

INTRODUCTION.

The presence of asphaltenes is known to have a significant effect on both processability of crude oils and the properties of asphalts (1). Indeed, the presence of asphaltenes is particularly felt when circumstances permit their separation (precipitation) from the oil medium in such a manner that the phenomenon of phase separation causes either coke formation during processing or failure of an asphalt pavement by loss of physical structure of the asphalt-aggregate system (2).

Briefly, asphaltenes are defined as the fraction of petroleum that is insoluble in an excess of a low-boiling liquid hydrocarbon, such as n-heptane, but soluble in aromatic solvents (e.g. toluene or benzene) at ambient temperatures.

Thus, there is the need to understand the stability of crude oils and this can be achieved by an investigation of asphaltene precipitation/flocculation, by titration, using solvent/non-solvent mixtures. This may give an indication of both asphaltene and maltene properties (3,4,5).

At the point of incipient precipitation, i.e. the point at which separation of asphaltenes from a crude oil becomes apparent, the precipitated material is, presumably, a conglomeration of species based on molecular size and polarity of the type that constitute the asphaltenes (6,7). This phenomenon has, however, not been addressed in any detail and is certainly worthy of investigation in order to increase the understanding of crude oil (asphaltene/maltene) relationships.

Thus, in order to investigate the mechanism of asphaltene precipitation, the change in precipitated material with changes in the non-solvent/solvent composition have been examined. Material isolated at the point of incipient precipitation was recovered and characterized by high performance liquid chromatography-size exclusion chromatography (HPLC-SEC) and diffuse reflectance spectra (DRIFT-FTIR). The possibility of determining the solubility parameter (δ) of the asphaltenes from titration and precipitation experiments was investigated.

The change in solvent composition from aromatic to aliphatic may mimic the change in oil composition during refinery, where the oil phase becomes more aliphatic with increasing conversion (8,9).

EXPERIMENTAL

Asphaltenes were precipitated by addition of 30 mL precipitant per gm oil at 20°C. Mixtures of n-heptane and toluene containing up to 40% (vol/vol) of toluene were used as the precipitant.

A modification of the asphaltene separation method (IP 143) was used as described elsewhere (10). Thus, after a 16 hr. contact time, precipitated asphaltenes were further purified by treatment with 3 x 10 mL of the appropriate solvent mixture, sonication, centrifugation (4000 rpm), and decantation.

The flocculation threshold in solvent/non-solvent mixtures was determined by measuring the light absorbance at 740 nm of the titrated solution. From a burette n-heptane was added to a stirred asphaltene or oil solution in a beaker. Asphaltene concentrations in initial solution was kept at 4 g/L. The flocculation point or threshold (FT) is the solvent composition (i.e. the volume fraction of solvent in non-solvent) where the absorbance increases rapidly. The absorbance was measured 20 min. after each addition of non-solvent, allowing equilibrium conditions to be reached; shorter time periods gave inconsistent readings.

Two commercial asphaltene solvents (methylnaphthalene oil and Basen 140/160) supplied by Preussag Erdoel und Erdgas GmbH, Hannover, Germany were also examined.

The crude oil investigated was a Kuwait oil topped at 100°C and supplied by Kuwait Petroleum Denmark A/S.

Infrared spectra were recorded using a BIO-RAD (Digilab Division) model FTS-45 Fourier Transform infrared (FTIR) spectrometer with an attachment for diffuse reflectance spectra (DRIFT) (11).

Synchronous fluorescence spectra were obtained as described elsewhere (10); asphaltenes were dissolved in mixtures of n-heptane and toluene (10-100% toluene) at a specified concentration (5 mg/L). No precipitation or particle formation was observed by Rayleigh scattering at 460 nm.

Size exclusion chromatography (HPLC-SEC) analysis was performed using a Hewlett-Packard 1090 HPLC with a diode array detector (DAD) with 8 wavelengths, and a Waters R401 refractive index (RI) detector. Freshly distilled toluene was used as eluant at a flow rate of 2 mL/min at 30 C. The column was a Phenomenex 5 μm, 10^4 A, 30 cm 7.9 mm i.d. The DAD wavelengths were 305, 340, 380, 410, 420, 460, 500, and 575 nm. The injected sample concentrations were 10 g/L toluene.

RESULTS AND DISCUSSION.

In the flocculation titration experiments a difference was found for solutions of pure asphaltenes and of the original oil. The latter showed a lower flocculation threshold (0.31±0.02) in terms of toluene in n-heptane than the asphaltene solutions (0.41±0.03). This was also noted for asphaltenes precipitated under a variety of conditions. This indicates that more non-solvent is required to precipitate the asphaltenes in the presence of maltenes.

The effect of various asphaltene solvents on the flocculation threshold, using n-heptane as the non-solvent, was also examined. A comparison of the various flocculation thresholds with the effective Hildebrand solubility parameter (δ_{eff}) of the relevant solvent mixture (Table I) suggests that, although solvent-solute interactions vary, δ_{eff} is similar (16.7 $MPa^{1/2}$ ± 0.3) for all solvent systems except for 2,4-dimethylpyridine.

Immiscibility is known to occur at solubility differences between solvent and solute of ca. 3.5 to 4 $MPa^{1/2}$. Hence the solubility parameter of the precipitated material can be estimated to fall within the range 20.2-20.7 $MPa^{1/2}$ which is in accordance with previous work (12,13).

Using the data further, it is predictable that there will be no precipitation of material above a flocculation threshold of 0.33 (δ_{eff} = 16.2 $MPa^{1/2}$) for the total oil (Figure 1).

As expected the amount of precipitated material decreased with increasing content of toluene in heptane. Purification of the raw precipitate from the 40% toluene/heptane precipitant, led to the recovery of a toluene insoluble solid (0.26 %) which was partially soluble in methylene chloride.

It is possible that this material could be finely-suspended mineral matter which acts as nuclei for the part of the asphaltene, presumably the most polar, and which forms part of the initial precipitate with highly polar species (14). Without any such effect, these species would remain in "solution" and be precipitated in the usual manner. Investigations using FTIR spectroscopy and HPLC-SEC revealed that, at least part of, the material was low molecular weight and reacted through hydrogen bonding. In the presence of the remaining asphaltene material, the sample was soluble suggesting some rearrangement of the molecular interactions during the removal of lower molecular weight (polar) asphaltene species, which could indicate a co-solvency effect through association.

The material precipitated from n-heptane to toluene insolubles may have a δ-distribution between 19 and above 22 $MPa^{1/2}$ which is in disagreement with the data from the titration experiments which give an upper limit of 20.7 $MPa^{1/2}$, and hence were not able to predict the presence of toluene insoluble material. One titration experiment using 2,4-dimethylpyridine showed a flocculation threshold of 0.42 (18.3 $MPa^{1/2}$) indicating an upper limit of 22.3 $MPa^{1/2}$.

A reasonable explanation of this phenomenon is that asphaltenes associate less in pyridine (15). Hence, the interactions leading to dispersion of the least soluble part are not present, and the compounds behave as single molecular entities. The latter is possible as the asphaltene concentration of this sample is below the critical micelle concentration (4.32 g/L) at the beginning of the titration (16). Hence, if solubility parameters are determined from titration experiments, the data are relative to the conditions such as solvent system and equilibrium time.

Data from the FTIR spectra imply that the chemical nature of the precipitate changes gradually at first but become more obvious as the incipient precipitation conditions are approached. Thus, the relative content of long chain paraffinics (720 cm^{-1}) increases as do the content of carboxylic acid functions (1730-1700 cm^{-1}). The latter increases rapidly above a concentration of 25% toluene. This indicates that the the least soluble part, i.e. "hard core asphaltenes", which precipitates first are highly polar and contain long alkyl chains.

According to the group contribution approach for solubility parameter (δ) calculation, an increase in molecular weight does not strictly imply an increase in the magnitude of δ since long chain paraffin systems have low δ values (17). Hence, the precipitation may be governed by molecular weight differences between the solvent and the solute.

HPLC-SEC investigations showed that higher concentrations of toluene in the precipitant lead to shorter peak retention time, and changes take place on the low molecular weight side of the eluted profile. The largest change in profiles was seen when going from pure heptane to a mixture containing 10% toluene. The n-heptane asphaltenes had a close to bimodal profile where as for 10% (or higher amounts) of toluene, the profile is a single tailing peak indicating

that the incremental material, soluble in toluene/heptane but insoluble in heptane, is composed of lower molecular weight species. This suggests that asphaltenes may be composed of different molecular weight types as suggested from fractionation studies (18,19,20,21,22).

The relative change in chemical types was then investigated by a study of the ratios of total areas under the chromatograms obtained at different diode array detector (DAD) wavelengths (Figure 2). The amount of larger chromophores increases relatively as the toluene content in the precipitant rises. DAD and refractive index (RI) signals are different but the overall conclusion the same.

Hydrogen bonding is involved, to some extent, in asphaltene association and dispersion (23). Indeed, an examination of the FTIR spectra, particularly in the range 3100-3700 cm^{-1}, showed that the main change in the nature of the precipitates from that obtained with pure heptane to that obtained with a 40% solution of toluene in heptane, is the occurrence of less hydrogen-bonded structures.

In the spectrum of the precipitate from the "40% toluene" mixture, distinct, relatively large, bands for free hydroxyl and carboxylic hydroxyl are found. In the presence of the co-precipitated resin-type material these bands are extremely weak, indicating that dispersion of any toluene insoluble material may take place through association with the co-precipitate. A similar concept has been proposed for resin-asphaltene interaction (24). Co-precipitated material was in all samples of lower molecular weight.

In order to investigate the interactions occurring in solution synchronous fluorescence spectra were recorded in mixtures of n-C7 and toluene with toluene volume fractions (ϕ) from 0.1 to 1. Hence the entire range from total dissolution to flocculation conditions passing the previously reported (25) critical micelle concentration limit at $\phi = 0.68$. The asphaltene used was a n-octane insoluble, precipitated at 43°C.

No large changes occurred in the spectra with increasing toluene content, although the polarity of the solvent increases, which based on simple compounds should lead to peak shifts to longer wavelengths. The relative intensity of three peaks at 360, 395, and 460 nm was examined representing increasing molecular complexity (10). These results indicates a general blue shift of the intensities. If asphaltene molecules were associating a red-shift would be expected. That no interactions occurs may be caused by the very low concentration of 5 mg/L toluene. According to the solvent shell theory, asphaltenes will be dispersed as long as sufficient dispersion agent is present to form the so called solvate layer around the asphaltenes (26). This may also imply a concentration effect that can affect the titration and precipitation experiments.

CONCLUSIONS.

Discrepancies between methods (equilibrium precipitation and flocculation titration) employed to determine the incipient precipitation of asphaltenes have been found and may be related to slow kinetics of precipitation (27).

Solubility parameters of asphaltenes can be measured by the titration method but relative to the experimental parameters such as time, solvent and solute (asphaltene or oil) concentration. The recovery of a toluene insoluble fraction from a toluene soluble fraction shows the complexity of the asphaltene aggregation during precipitation. Evidence of rearrangements of molecular interactions is suggested.

ACKNOWLEDGEMENTS.

SIA thanks the Danish Natural Science Research Council and Thomas B. Thriges Fond (Denmark) for financial support and Western Research Institute (Laramie, Wyoming) for use of facilities.

REFERENCES.

1. Speight, J.G. The Chemistry and Technology of Petroleum. Second Edition. Marcel Dekker Inc., New York. 1991.
2. Speight, J.G. 1992. Proceedings. 4th International Conference on Stability and Handling of Liquid Fuels. U.S. Department of Energy, Washington, D.C. 1992, 169.
3. Heithaus, J.J. J. Inst. Pet. 1962, 48: 45.
4. Bichard, J.A. Proceedings. Annual Meeting. Canadian Society for Chemical Engineering. Edmonton, Alberta. 1969.
5. Fuhr, B.J., Cathrea, C., Coates, L., Kalra and Majeed, A.I. Fuel. 1991, 70: 1293.
6. Long, R. B. Preprints. Div. Petrol. Chem. Am. Chem. Soc. 1979, 24(4): 891.
7. Long, R.B. In The Chemistry of Asphaltenes. J.W. Bunger and N. Li (editors). Advances in Chemistry Series No. 195. American Chemical Society, Washington, D.C. 1981, 17.
8. Takatsuka, T., Wada, Y., Nakata S., and Komatsu, S. Proceedings 4th UNITAR/UNDP Conference on Heavy Crude and Tar Sands, AOSTRA, Alberta. 1988, Vol 5:515.
9. Lambert, D.C., and Holder, K.A. Proceedings 4th UNITAR/UNDP Conference on Heavy Crude and Tar Sands. AOSTRA, Alberta. 1988, Vol 2:449.
10. Andersen, S.I. and Birdi, K.S. Fuel Sci. Tech. Intl. 1990, 8: 593.
11. McKay, J.F., and Wolf, J.M. Fuel Sci. Tech. Intl. 1992, 10: 935.
12. Hirschberg, A., deJong, L.N.J., Schnipper, B.A., and Meijer, J.G. Soc. Pet. Eng. J. 1984, 283.
13. Burke, N.E., Hobbs, R.D., and Kashou, S.F. J. Pet. Tech. 1991,1440
14. Mitchell, D.L., and Speight, J.G. 1973. United States Patent No. 3779902. December 18.
15. Moschopedis, S.E., Fryer, J.F., and Speight, J.G. Fuel. 1976, 55: 227.
16. Andersen, S.I. and Birdi, K.S. Proceedings. International Symposium on the Chemistry of Bitumens. Western Research Institute, Laramie, Wyoming. 1991, 236.
17. Barton, A.F.M. Handbook of Solubility Parameters and Other Cohesion Parameters, CRC Press. 1983.
18. Bestougeff, M., and Darmois, R. Comptes rend. 1947, 224: 1365.
19. Bestougeff, M., and Darmois, R. Comptes rend. 1948, 227: 129.
20. Speight, J.G. Fuel. 1971, 50: 102.
21. Speight, J.G. Proceedings. NSF Workshop on Coal. Knoxville, Tennessee. 1975, 125.
22. Bestougeff, M. A., and Mouton, Y. Bull. Liason Lab. Pont. Chaus. Special Volume. 1977, 79.

23. Moschopedis, S.E., and Speight, J.G. Fuel. 1976, 55: 187.
24. Koots, J.A., and Speight, J.G. 1975. Fuel. 54: 179.
25. Andersen, S.I. and Birdi, K.S. J. Coll. Interface Sci. 1991, 142:497.
26. Morozova, L.A., Syunyaeva, R.Z. and Kaporovskii, L.M. Chem. Tech. Oil and Gas, USSR. 1982, 280.
27. Speight, J.G., Long, R.B., and Trowbridge, T.D. Fuel. 1984, 63: 616.

Table I: Flocculation thresholds Kuwait petroleum asphaltenes in volume fraction of solvent in n-heptane.

Solvent	Asphaltenes (%) Flocculation threshold C5**	C6***	δ*	δ_{eff}*
Toluene	0.34	0.38	18.2	16.3
Quinoline	0.24	-	22.0	16.9
Methylnaphthalene oil	0.29	-	20.3	16.8
Basen 140/160	-	0.36	19.8	16.9
2,4-dimethylpyridine	0.43	0.42	22.2	18.3

* $MPa^{1/2}$.
** C5: pentane asphaltenes, yield: 21%
*** C6: hexane asphaltenes, yield: 18%
$\delta_{eff} = \Sigma \phi_i \delta_i$

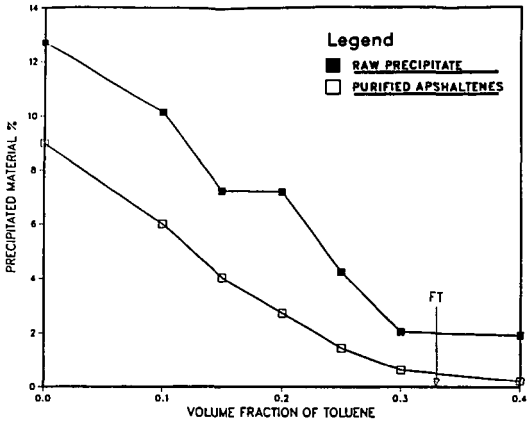

Figure 1. Amount of precipitated asphaltenes (raw and purified) versus volume fraction of toluene in n-heptane precipitant.

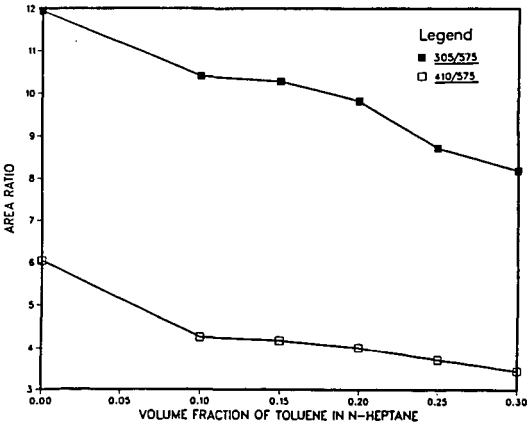

Figure 2. HPLC-SEC Peak area ratios of various detector wavelengths versus volume fraction of toluene in n-heptane precipitant. 305/575 nm and 410/575 nm.

Separation of a Quinolone-Enriched Fraction From SHRP Asphalts

Stephen C. Preece[1], J.F. Branthaver[2], and Sang-Soo Kim[2]

[1]Arizona Department of Public Safety
P.O. Box 6638
Phoenix, AZ 85005-6638

[2]Western Research Institute
Box 3395 University Station
Laramie, WY 82071-3395

Keywords: Asphalt, Modified Silica, Quinolone

ABSTRACT

A method originally designed to separate a carboxylic acid concentrate from asphalts has been modified so that quinolone concentrates also can be extracted from asphalts. The quinolone concentrates are high in molecular weight and contain large amounts of oxygen, nitrogen, and sulfur. Infrared spectra of the quinolone concentrates are similar to those obtained from petroleum distillates by a multistep separation scheme. Some of the sulfur atoms associated with the quinolones are readily oxidizable.

INTRODUCTION

The rheological properties of asphalts are believed to be influenced by associative interactions of polar, polyfunctional molecules in a non-polar hydrocarbon matrix (1). The identities of some of the functional groups involved in associative interactions in asphalts are carboxylic acids, phenols, pyridines, and quinolones. Other heteroatom-containing functional groups are probably involved. Compounds containing one or more of these groups have been identified in petroleum.

Asphalts contain non-volatile constituents of petroleum, which are also the largest and most polar components. The isolation of individual compounds, and even compound types, from asphalts for special study is a formidable task. This is because of the existence of large numbers of multifunctional compounds and extended methylene homologues in these residua.

As mentioned above, quinolones are one of a number of polar, associating species in asphalts, and thus may be major viscosity-controlling components of asphalts. Therefore the isolation and study of these compounds would be of interest. Quinolones were identified in petroleum by Copelin (2), who concentrated them from a gas oil fraction using a separation scheme involving hydrochloric acid treatment, ion exchange separation, and alumina chromatography. The quinolone fraction was characterized by a prominent peak at 1655 cm^{-1}

in the infrared spectrum. Based on a comparison with infrared spectra of model compounds, Copelin deduced that the quinolones were 2-quinolones and not 4-quinolones. Snyder et al. (3) detected the same materials in gas oil fractions of other crude oils. Petersen et al. (4) observed the 1655 cm^{-1} peak in the infrared spectrum of asphalts, and assigned the peak to 2-quinolones. These workers observed that asphalts contain molecules that are too large to be typical pyridones. They showed that the 1655 cm^{-1} peak was unaffected by treatments with hydrochloric acid or sodium hydroxide solutions, but disappeared when asphalts were treated with hexamethyldisilazane, which reacts with the enol form of the quinolones. Lithium aluminum hydride treatment of asphalts also resulted in loss of the 1655 cm^{-1} peak in the infrared spectrum of treated asphalts. In this reaction, carbonyl groups are reduced.

The work of Petersen et al. (4) identifies 2-quinolones as probable constituents of asphalts. The complex separation schemes of Copelin (2) and Snyder et al. (3) are not easily applied to asphalts, due to irreversible adsorption of asphalt components on alumina and difficulties in extracting asphalts with acids. However, separation of highly polar carboxylic acids from asphalts using base-treated silica gels have been reported by Ramljak et al. (5). In this report, a modification of the Ramljak et al. (5) separation scheme was developed as a rapid method for the concentration of 2-quinolones from asphalts.

EXPERIMENTAL

Asphalts used in this study were obtained from the Materials Reference Library of the Strategic Highway Research Program (SHRP).

The modified silica gel was prepared according to the procedure of Ramljak et al. (5). A typical preparation consists of slurrying 400 g silicic acid (BIO-SIL A, 100-200 mesh, Bio-Rad Labs) in 4.0 L dichloromethane and then adding in portions a solution of 40 g potassium hydroxide (J.T. Baker) in 800 mL 2-propanol (J.T. Baker). After stirring the mixture for 30 minutes, it was poured onto a Buchner funnel having a sintered glass disc (C porosity) and washed with another 500 mL 2-propanol. Then the filter cake was washed with dichloromethane to remove alcohol.

The isolation of carboxylic acid concentrates was performed according to the procedure of Ramljak et al. (5), except that chromatographic columns were employed in place of extractors. In order to successfully concentrate quinolones, carboxylic acids must be removed from asphalts first. A flow sheet for the separation of asphalts into carboxylic acid concentrate, quinoline concentrates, and quinolone-free material is illustrated in Figure 1.

After the adsorption of the carboxylic acid concentrate on the modified silica gel, chloroform was removed from the eluted fraction on a rotary evaporator. The flask containing the chloroform solution was immersed in a hot water bath, and a vacuum of about 2 Torr was applied to remove the last of the chloroform. Approximately 20 g of this eluted fraction, which comprises 95% or more of the parent asphalt, was dissolved in 80 mL dichloromethane (Omni Solv, HPLC Grade). This solvent was poured onto the top of a column 2.5 cm i.d. x 100 cm filled about three-fourths full with modified silica gel. A small layer of sand was placed in the bottom of the column before adding the modified silica gel. In filling the

column, dichloromethane was poured into the column and then the gel slurry was added while the column stopcock was opened. Gel was added to fill the column with a well-packed bed to the 75 cm level. Flow rates for the separation were set by opening the column stopcock fully. About 4.0 L dichloromethane were required to complete the separation. Eluates were divested of solvent as described above, and designated the quinolone-free fraction. The modified silica gel and adsorbate were transferred to a Buchner funnel (M porosity) and a mixture of 20% formic acid (Aldrich Chemical Co.) and 80% dichloromethane was poured onto it to desorb the quinolone concentrate. These eluates were dried on a rotary evaporator as described above and then redissolved in dichloromethane and again filtered to remove potassium silicate associated with the quinolone concentrate. It may be necessary to use benzene as solvent for the quinolone concentrate in order to remove residual formic acid on the rotary evaporator.

Infrared Spectra of films of the quinolone concentrates were obtained on a Perkin-Elmer 983 Spectrophotometer. Molecular weights were detennined by vapor phase osmometry using ASTM method D 2503 using toluene (60 °C; 140 °F) as solvent.

Elemental analyses were performed by the Analytical Research Division of Western Research Institute using standard methods.

RESULTS AND DISCUSSION

The Strategic Highway Research Program (SHRP) has designated eight asphalts for special study. Four of these asphalts, AAA-1, AAD-1, AAG-1, and AAK-1 were separated on modified silica gel to collect carboxylic acid concentrates and quinolone concentrates. The asphalts contain about 0.01 to 0.02 M/L of quinolones (Table 1), based on the infrared functional group analysis of Petersen (6). Recoveries of material range from 96-98% in each step, so that the two concentrates are small in amount compared with the whole asphalts. The replication of the separation for AAK-1, using two different operators was not good, but this does not affect the utility of the method in concentrating quinolones.

Elemental analyses and number-average molecular weights of the parent asphalts and the quinolone concentrates (Table 2) show that in each case, the quinolone concentrates are more aromatic and contain more nitrogen, oxygen, and sulfur than the parent asphalts. Large sulfur contents in quinolone concentrates in distillates were observed by Copelin (2), who claimed that substantial amounts of thioquinolines were present in the materials he studied. Number-average molecular weight ($\bar{M}_n$) values of the asphalt quinolone concentrates determined by vapor phase osmometry (VPO) in toluene at 60 °C (140 °F) are much higher than those reported by Copelin (2), which were about 300 Daltons. These materials were derived from 340-450 °C (644-842 °F) distillates. Evidently quinolones occur in crude oils over a large molecular weight range. The $\bar{M}_n$ value of the quinoline concentrate of AAK-1 also was determined by VPO in pyridine at 60 °C (140 °F). This value is about half that of the $\bar{M}_n$ value determined in toluene, which demonstrates that quinolones have strong tendencies to associate. In contrast, $\bar{M}_n$ values for whole asphalts are similar in pyridine and toluene.

Infrared spectra of quinolone concentrates of asphalts are shown in Figures 2-5. Copelin (2) identified the peak at about 1650 cm^{-1} as the carbonyl peak of the quinolone amide

function. This peak is prominent in Figures 2-5. The quinolone concentrate of AAG-1 (Figure 4) is contaminated by some carboxylic acids, as shown by the presence of a peak at about 1705 cm^{-1}. No peak corresponding to thioquinolones is observed in any of the asphalt quinolone concentrates. Instead, large sulfoxide peaks (~ 1020 cm^{-1}) are observed. The quinolones contain (or possibly are associated with) readily oxidizable sulfur functionalities.

In another study, the quinolone concentrate of AAD-1 was further separated into fractions using a column of modified silica gel (7). Retention times of most of the components of the concentrates were similar to those of model compounds having 2-pyridone or 2-quinolone structural units.

It is possible to collect both carboxylic acids and quinolones by eliminating the initial step and directly separating the original asphalt on activated silica with dichloromethane. Yield of the combination of quinolones and acids for AAA-1 is 4.8 wt %.

CONCLUSIONS

Quinolones can be concentrated from four asphalts by a modification of a method originally developed to concentrate carboxylic acids from asphalts. The quinolone concentrates are characterized by a prominent peak in their infrared spectra at about 1650 cm^{-1}. Nitrogen, oxygen, and sulfur concentrations in these materials also are high. The sulfur functionality associated with the quinolone concentrates is readily oxidizable. The number-average molecular weights of the quinolone concentrates are approximately twice those of the parent asphalts.

The method used to concentrate quinolones from asphalts is rapid and simple and it presumably can be extended to other petroleum-derived fractions. It is estimated that quinolones are concentrated about ten- to twenty-fold by this method based on concentrations of these compounds in parent asphalts. The concentrates can be further purified by other separation methods (7).

DISCLAIMER

The contents of this report reflect the views of the authors, who are solely responsible for the facts and accuracy of the data presented. The contents do not necessarily reflect the official view or policies of the Strategic Highway Research Program (SHRP) or SHRP's sponsors. The results reported here are not necessarily in agreement with the results of other SHRP research activities. They are reported to stimulate review and discussion within the research community. This report does not constitute a standard, specification, or regulation. Mention of specific brands of materials does not imply endorsement by SHRP or Western Research Institute.

ACKNOWLEDGMENTS

The work reported herein has been conducted as a part of Project A002A of the Strategic Highway Research Program (SHRP). SHRP is a unit of the National Research Council that was authorized by Section 128 of the Surface Transportation and Uniform Relocation Assistance Act of 1987. This project is titled "Binder Characterization and Evaluation" and is being conducted by the Western Research Institute, Laramie, Wyoming, in cooperation with the Pennsylvania Transportation Institute, Texas Transportation Institute, and SRI International. Dr. Raymond E. Robertson is the principal investigator. Dawn Geldien is the project administrator. The support and encouragement of Dr. Edward Harrigan, SHRP Asphalt Program Manager, and Dr. Jack Youtcheff, SHRP Technical Contract Manager, are gratefully acknowledged. Analytical work was performed by G.W. Gardner. The manuscript was prepared by J. Greaser.

LITERATURE CITED

(1) Petersen, J.C. 1984. Transport. Res. Rec., 999, 13-30.
(2) Copelin, E.C. 1964. Anal. Chem., 36, 2274-2277.
(3) Snyder, L.E., B.E. Buell, and H.E. Howard. 1968. Anal. Chem., 40, 1303-1317.
(4) Petersen, J.C., R.V. Barbour, S.M. Dorrence, F.A. Barbour, and R.V. Helm. 1971. Anal. Chem., 43, 1491-1496.
(5) Ramljak, Z., A. Solc, P. Arpino, J.M. Schmitter, and G. Guichon. 1977. Anal. Chem., 49, 1222-1225.
(6) Petersen, J.C. 1986. Transport. Res. Rec., 1096, 1-11.
(7) Preece, S.C. 1992. Master of Science Dissertation, University of Wyoming, Laramie, Wyoming.

TABLE 1

Yields of Quinolone Concentrates from Four Asphalts

Asphalt	Yield of Quinolone Concentrate, wt % of Asphalt
AAA-1	2.6
AAD-1	6.7
AAG-1	2.7
AAK-1	5.0; 6.8

TABLE 2

Elemental Analyses and Number-Average Molecular Weights of Four Asphalts and Their Quinolone Concentrates

Substrate	Element, wt %					H/C	$\bar{M}_n$ (Daltons)	
	C	H	N	O	S		toluene	pyridine
Asphalt AAA-1	84.2	10.5	0.48	0.6	5.5	1.48	790	810
AAA-1 Quinolone Concentrate	-	-	0.90	2.8	8.4	-	1,400	-
Asphalt AAD-1	81.4	10.8	0.77	0.9	6.9	1.58	700	710
AAD-1 Quinolone Concentrate	78.5	9.3	1.50	2.9	8.6	1.41	1,500	-
Asphalt AAG-1	85.6	10.5	1.10	1.1	1.3	1.46	710	700
AAG-1 Quinolone Concentrate	-	-	1.57	3.6	1.9	-	1,360	-
Asphalt AAK-1	80.7	10.2	0.71	0.8	6.5	1.51	860	820
AAK-1 Quinolone Concentrate, run 1	79.6	8.5	1.20	2.7	7.2	1.27	1,800	-
AAK-1 Quinolone Concentrate, run 2[1]	76.6/76.3	9.0/9.0	1.1/1.2	3.9/3.9	8.3/8.4	1.40	2,172	1,113

[1] Replicate elemental analyses were performed for this sample

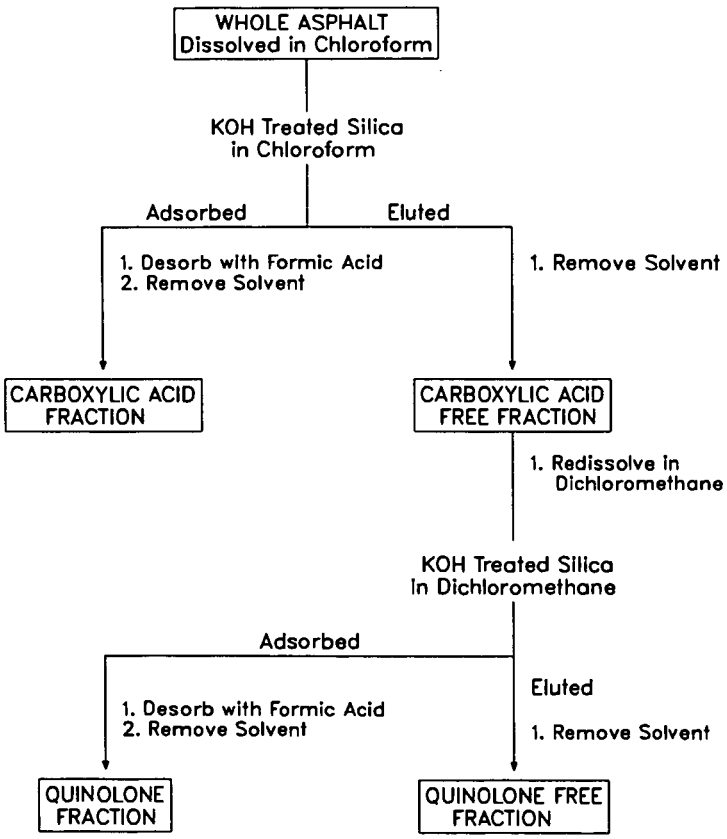

Figure 1. Flow Scheme for the Isolation of Quinolones

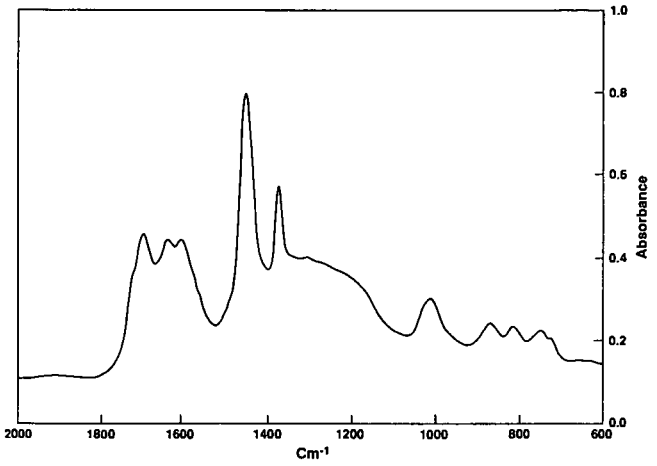

Figure 4. Quinolone Concentrate from AAG-1

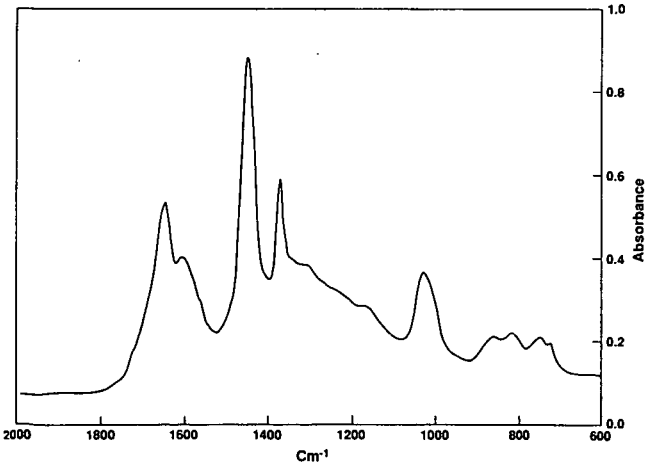

Figure 5. Quinolone Concentrate from AAK-1

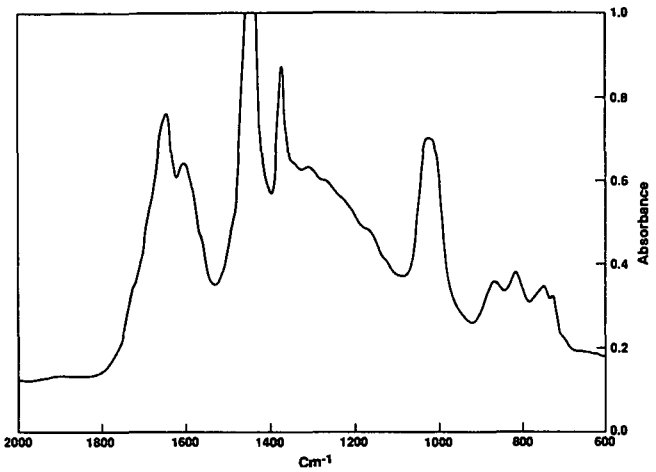

Figure 2. Quinolone Concentrate from AAA-1

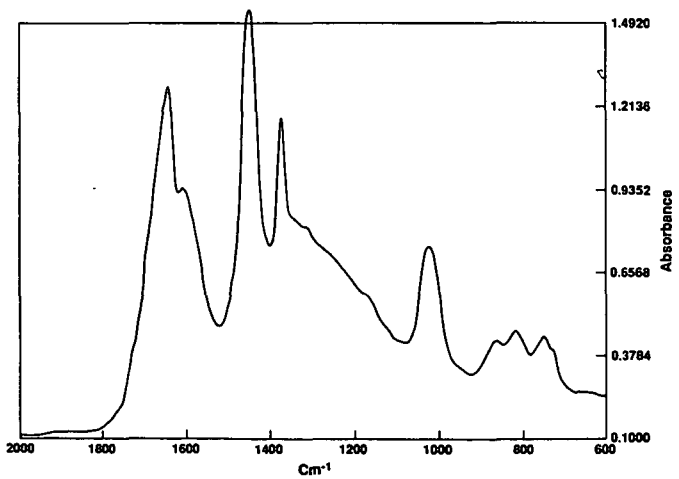

Figure 3. Quinolone Concentrate from AAD-1

DEVELOPMENT OF A REPRODUCIBLE IATROSCAN METHOD TO CHEMICALLY CHARACTERIZE ASPHALT

C. C. Wan, T. H. Waters, R. D. Wolever
Owens-Corning Fiberglas Corp., Technical Center
2790 Columbus Road, Rte #16
Granville, OH 43023-1200

Keywords: asphalt; Iatroscan, TLC, asphalt fractions

ABSTRACT

A rapid, reproducible method has been developed which quantitatively separates an asphalt into four generic fractions. This paper describes the impact of variables such as spotting technique, humidity, sample size, etc. on the quantitative reproducibility of the TLC-FID technique. With minor modifications, this method is being evaluated by the Asphalt Roofing Manufacturers Association (ARMA) as their standard Iatroscan method.

INTRODUCTION

The ability to predict the performance of a finished product that has been prepared from an asphalt and to understand the effects of various processing steps and modifications of asphalts requires a knowledge of the chemical composition of the asphalt. Since asphalts are complex mixtures of thousands of different compounds, separation of this material into each individual moiety would overwhelm currently available chromatographic data systems not to mention the analyst as well as the asphalt chemist. A better approach would be to separate the asphalt into groups or classes of compounds similar to the Corbett method.

Recently, a new technique which couples thin layer chromatography with a flame ionization detector has been introduced by Iatron Laboratories, Inc. The unit is called an Iatroscan. This unit takes advantage of the high separation power, simple and rapid operating procedures, and small sample size of the thin layer technique and couples that to the excellent quantitation of a flame ionization detector. With the Iatroscan all sample components are accessible to the detector.

Model compounds were used to develop a separation scheme that fractionates an asphalt into four reasonably distinct chemical classes. Although the precision for the same time period, one to three days, was generally excellent; within a matter of months it was apparent that the repeatability of week-to-week and month-to-month data was very poor. For example, a Cross roofers flux was analyzed on two different dates. As the results that are given in Table 1 indicate, the precision for both dates is excellent; however, the repeatability was unsatisfactory. By contrast, analysis of a synthetic standard which contained four distinctly different compounds with respect to polarity showed no day-to-day repeatability problems. See Table 2. This data clearly points to the fact that the chromatography was not adequate to affect the same separation day after day.

Thus, studies were conducted to examine the impact of various chromatographic parameters on repeatability. The most obvious parameters to study are: humidity, sample size and spotting technique.

EXPERIMENTAL

Apparatus:

All data was generated on a Iatroscan model Mark IV. The instrument was set up according to the manufacturer's specifications. The hydrogen gas flow rate was set to 160 mL/min and the air flow rate was set to 2.0 L/min. Flow rates were read from the bottom of the balls located inside the Iatroscan gauges. The chromarods were blank scanned twice prior to spotting. All scans were made at 30 seconds per scan. The unit was interfaced to a Hewlett Packard 1000 Data System.

Procedure:

The manufacturer's procedures were followed to start up the Iatroscan. The chromarods were blank scanned twice at 30 seconds/rod to remove contaminants.

Samples were prepared by dissolving 150 mg/20 ml of carbon disulfide.

A sequential solvent development technique was used to separate the asphalt into four fractions.

1. N-heptane 8.5 cm
2. Toluene 4.5 cm
3. Tetrahydrofuran 2.0 cm

A constant humidity chamber was used to deactivate the chromarods to a constant state prior to each development step. Also, the rods were suspended over the solvent vapors for fixed time periods prior to development. After each development step, the rods were dried in an oven at 60°C for one minute.

Only the areas of the four main peaks are used in the calculation. Report the normalized area percent of each peak. Peak 1 should be reported as saturates. Peak 2 should be reported as naphthene aromatics. Peak 3 should be reported as polar aromatics. Peak 4 should be reported as asphaltenes.

DISCUSSION

Development of Separation Scheme

The Iatron Company supplies both alumina and silica chromarods. Model compounds were used to evaluate the ability of these adsorbents to resolve compounds representing saturates, aromatics, polars and asphaltenes. Nujol, an infrared spectroscopy mulling oil, was used to simulate the saturates and 1-phenyltridecane was used as the model for the aromatic fraction. The 1-phenyltridecane was at best partially resolved from the Nujol on the alumina adsorbent. A much better separation was obtained using the silica adsorbent with all other parameters being held constant. See Figures 1 and 2.

Similarly, model compounds were used to verify that the solvent development scheme separates the asphalt into saturates, aromatics, polars and asphaltenes. Neat solvents of increasing polarity were selected as opposed to solvent blends that contain low concentrations of the strong solvent. This eliminates the hassles of accurately generating and maintaining this solvent blend. The solvents selected are N-heptane, toluene and tetrahydrofuran (THF). With this system, all saturated hydrocarbons are eluted in the first peak. Fused ring

aromatics, alkyl substituted aromatics plus thiophenes are eluted with toluene in peak number 2. Nitrogen and oxygen heterocyclic aromatic compounds plus compounds which have polar functional groups such as hydroxyl, amines (primary and secondary), carboxylic acids, ketones, etc., are eluted with THF as peak number 3. The peak at the origin is most likely metal complexes and salts. Table 3 gives the peak location of various compounds.

Impact of Relative Humidity on Quantitation

Different concentrations of calcium chloride in water were used to prepare 30%, 65% and 100% relative humidity (R.H.) chambers. The same asphalt was analyzed at these three relative humidities. The results are given in Table 4. Dramatic changes in the concentrations of the naphthene aromatics (NA) and polar aromatics (PA) were observed. At 30% R.H., the NA are 39.3% compared to 55.5% NA at 100% R.H. The PA are 28.5% at 30% R.H. and 18.6% at 100% R.H. Clearly, higher relative humidities deactivate the chromarods, thereby allowing more of the polar aromatics to be moved with the toluene solvent front. Thus, it is imperative that the laboratory be maintained at a constant relative humidity or the methodology include constant humidity chambers.

Impact of Sample Size on Quantitation

To study the impact of sample size on quantitation, different concentrations of the same asphalt were prepared in carbon disulfide. The initial study covered the range of 20 to 100 micrograms of asphalt on the chromarods. At these loadings, baseline resolution between the polar aromatics and asphaltenes was not achieved. In addition, peaks were distorted and, in some cases, the peaks spit into doublets. Also, rescan of these rods produced as high as 15% residue. Clearly for quantitative purposes this is not acceptable.

The next set of data spanned the range of 5 to 15 micrograms in 2.5 microgram increments. The data is given in Table 5. From this data, it appears that the optimum sample size is in the 7.5 to 12.5 microgram range. Rescan of these rods gave less than one percent residue.

Impact of Spotting Technique

Two spotting techniques were studied. The first technique involved the application of the sample on the chromarod as a discrete spot using a microliter syringe. This approach has two drawbacks. First, it would be difficult to ensure that the sample spot for all ten rods in a rack will remain constant with respect to the flame profile of the detector. Second, a spot does not give the sample full access to the total surface of the chromarod. The second spotting technique was to apply the sample as a narrow band around the circumference of the chromarod. Chromatograms for the spot and ring technique are illustrated in Figures 3 and 4, respectively. The loss of resolution between the asphaltene and polar aromatic peaks plus the band distortion of the asphaltene peak in the chromatogram of the sample applied as a spot indicates that breakthrough of the asphaltenes into the polar aromatics has occurred. Thus, optimum chromatography was obtained by applying the sample as a band rather than a discrete spot.

CONCLUSIONS

The Iatroscan method separates asphalts into four reasonably distinct groups of compounds: saturates, aromatics/thiophenes, polars and asphaltenes.

The repeatability of this technique has been improved by controlling the

following variables: relative humidity, sample size and spotting technique.

Table 1

Repeatability of the Iatroscan Analytical Results
for a Given Asphalt Sample

	Dec 1988		March 1989	
	$\bar{X}$	SD	$\bar{X}$	SD
SA	3.0	0.3	3.0	0.3
NA	29.0	0.6	44.0	1.0
PA	56.0	1.0	41.0	1.1
AS	12.0	0.9	12.0	0.8

Table II

Repeatability of the Iatroscan Analytical Results
for Synthetic Standards

		April 1989	May 1989	June 1989
Nujol	$\bar{X}$	20.6	20.8	20.8
	S.D.	0.9	0.8	0.7
Polystyrene	$\bar{X}$	29.2	28.0	28.7
	S.D.	0.7	0.6	0.7
Vegetable Oil	$\bar{X}$	21.4	24.0	20.9
	S.D.	0.4	0.5	0.5
Rhodamine	$\bar{X}$	28.7	27.2	29.6
	S.D.	0.4	0.6	1.1

Table III

Iatroscan Analysis of Model Compounds

Compound	Peak Location			
	Saturate	Aromatic	Polar	Asphaltene
Nujol	x			
1-phenyltridecane		x		
7,8-benzoquinoline			x	
3-pentadecylphenol			x	
Thianthrene		x		
6-methylquinoline			x	
Phthalazine			x	
4,4-dihydroxydiphenylmethane				x
Naphophthalein			x	
4-hydroxybenzyl alcohol			x	
p-nitrobenzoic acid			x	
4,4-dimethyldianaline			x	
4-(P-nitrophenylazo) resorcinol			x	
Rhodamine B				x
Vegetable Oil			x	
Low molecular weight polystyrene		x		
Anthracene		x		

Table IV

Effect of Humidity
on Iatroscan Results

	Relative Humidity		
	30%	65%	100%
Saturates	16.5	13.5	15.5
Aromatics	39.3	46.5	55.5
Polar Aromatics	28.5	25.0	18.6
Asphaltenes	14.8	13.0	10.5

Table V

Effect of Sample Size on Quantitation

Component	Sample Size 5 μG	7.5 μG	10 μG	12.5 μG	15 μG
SA	16.8	18.2	17.8	19.8	20.1
NA	23.2	26.3	27.6	27.6	27.4
PA	34.5	34.6	34.3	32.7	36.5
AS	25.5	20.9	20.3	19.9	16.0

Figure 1

Iatroscan Separation of Model
Compounds on Alumina Adsorbent

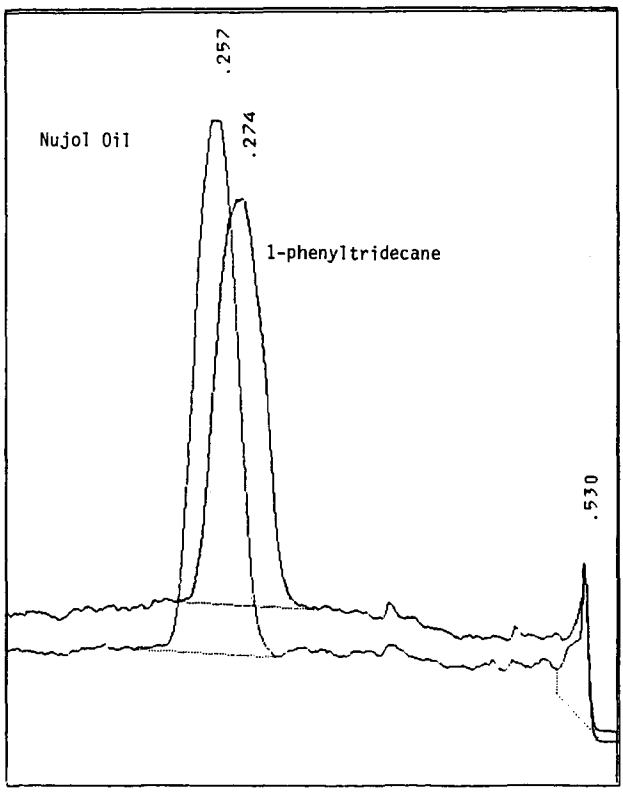

Figure 2

Iatroscan Separation of Model
Compounds on Silica Adsorbent

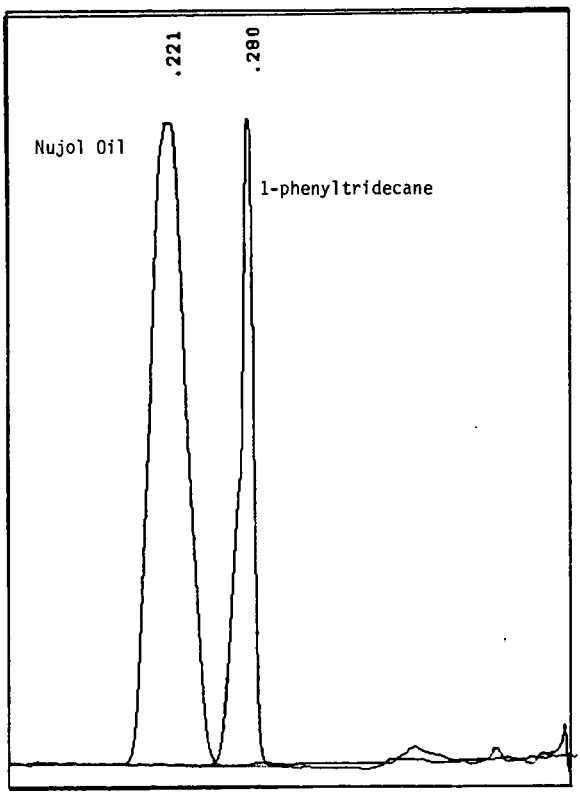

Figure 3

Sample Applied as spot

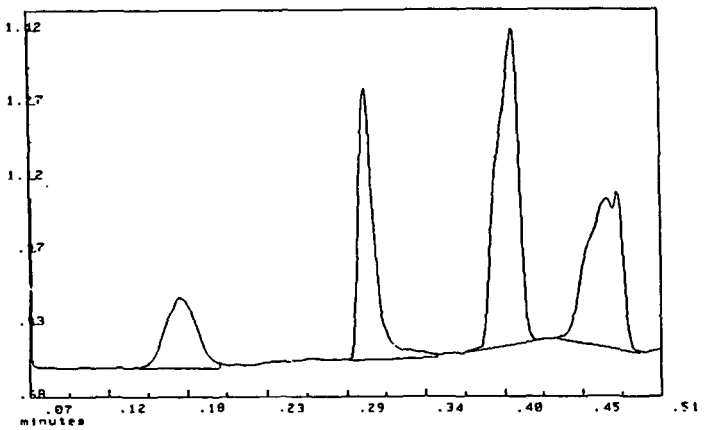

Figure 4

Sample Applied as Band

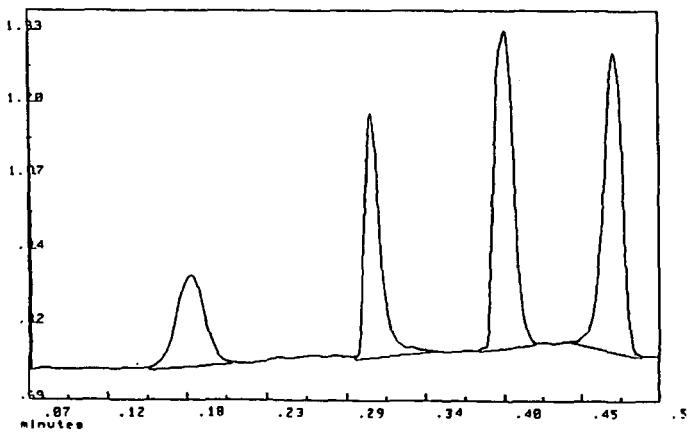

CHARACTERIZATION OF ASPHALTS AND ASPHALT/AGGREGATE MIXTURES USING FLUORESCENCE MICROPHOTOMETRY

Gareth D. Mitchell and Alan Davis
Energy and Fuels Research Center
The Pennsylvania State University
University Park, PA 16802

Keywords: Fluorescence microphotometry, fluorometric analysis, asphalt fluorescence

INTRODUCTION

Current techniques used in the paving industry for measuring pavement deterioration first require that the asphalt binder be recovered by solvent extraction [1]. This practice may disrupt the molecular structuring that has developed during asphalt aging and which may be responsible for some of the detrimental changes in pavement properties [2]. Fluorescence microphotometry is being developed as a non-destructive quantitative technique for the characterization of asphalt binder quality and deterioration, for both the raw asphalts as well as from cements and pavement cores.

EXPERIMENTAL

Analysis of fluorescence intensity at 600 nm and the measurement of spectral distribution between 510 - 750 nm were performed using a Leitz MPV-II microscope photometer system [3,4]. For both methods light energy from either a high-pressure xenon or mercury-arc lamp was passed through a heat filter (suppressing red and infrared wavelengths) and then through a series of interference filters which defined the appropriate excitation and measuring wavelengths. Analyses were performed using filter combinations utilizing 390-490 nm (blue light) excitation, 510 nm dichromatic beam splitter and 515 nm long-pass barrier filter. The excitation light was reflected by a 510 nm reflection short-pass dichromatic beam splitter and condensed onto the sample through a 50X NPL FLUOTAR air objective. All measurements were made using a dry nitrogen atmosphere to eliminate photooxidation and the total magnification of the optical system was 625 times. The light energy passed back through the dichromatic beam splitter, and a 515 nm long-pass barrier filter blocked any residual reflected excitation light. From this point, the measuring system became significantly different depending upon the desired measurement, i.e., intensity at a single wavelength or spectral distribution.

For measurement of intensity, the fluorescence emission passed through a measurement filter centered around 600 nm (570-630 nm). The optical signal(s) were transformed into electronic signals by an EMI 9558 photomultiplier and amplified. Once the photoelectric system was calibrated to a glass standard of stable fluorescence intensity (uranyl glass), a statistically adequate number of intensity readings were accumulated [4]. For the measurement of relative intensity by wavelength (spectra), fluorescence emissions were passed through a motor-driven Kratos GM200 double-grating monochromator with 20 nm bandwidth, and then to a RCA C31034A water-cooled photomultiplier for measurement. In this system wavelength and intensity were calibrated over the range of visible light and the spectra were corrected with respect to color temperature [5].

Various samples were obtained including twelve raw asphalts from the Materials Reference Library (MRL, [6]) as well as samples of thin-film oven residues (TFOT) and pressure vessel (TFO-PV-Air) aged asphalts from Western Research Institute. Each of these samples were prepared into plug-mount subsamples suitable for microscopy as discussed elsewhere [4]. About 30 plug mounts were made for each raw asphalt. Following a cool-down period (1h), one preparation was analyzed and the remaining subsamples were sealed in foil multilaminate bags in an argon atmosphere and refrigerated at -5° C. For comparison, some asphalt samples were exposed to room conditions (but protected from light) for various periods of time.

Four aggregates were also obtained from the MRL, including RC (high absorption limestone), RD (low absorption limestone), RB (granite) and RJ (gravel). Each aggregate was split and stage-crushed to pass a 200 mesh (<74 μm) screen. Along with these aggregates, particulate (< 1mm) teflon was used as an inert-surface additive to determine the effects of dilution. In addition, four fresh asphalts were obtained (AAA-1, AAG-1-2, AAM-1 and ABD) from the MRL for preparation of asphalt/aggregate mixtures or mastics.

Mastics were prepared by forming a 50/50% volumetric mixture of each asphalt and aggregate following the same methodology. About 50 g of each aggregate were dried in an oven at 150°C for 10h. A fresh asphalt was thoroughly heated and homogenized, each aggregate (or teflon) in turn was removed from the oven and, while still hot, an appropriate amount of asphalt was weighed into the aggregate. Mixtures were stirred until all particles were wetted with asphalt (~5 min). Subsamples of the mixture were then placed into several preheated 2.5 cm diameter steel molds fitted with steel end caps and pressed under 4000 psi using a hydraulic press. While still in their molds, some of the samples were placed in foil multilaminate bags under argon and refrigerated. Other samples were pushed from their molds and the sides and one end covered with masking tape and labelled. The exposed end was lightly ground on 600 grit abrasive paper to reveal interfaces between asphalt binder and aggregate. Samples were allowed to warm to room temperature in a desiccator before analysis.

Fluorometric and spectral analyses were performed on all mastics of a given asphalt on the day following preparation. Fluorescence intensity was determined using the standard set-up. A total of 50 readings was necessary to obtain repeatable mean fluorescence intensity values from the asphalt binder when aggregate materials were present. Spectral analyses were also performed on the asphalt binder portion of the mastics by determining the mean spectra of readings taken from five different areas.

RESULTS AND DISCUSSION

Measurement of mean fluorescence intensity has been shown to provide unique and characteristic values for individual raw (fresh) asphalts [4]. When measurements were made using xenon irradiation in a nitrogen atmosphere the mean intensity of 10 readings were found to be repeatable to within ±0.1%. A preliminary evaluation of fluorescence intensity of twelve asphalts with their initial physical and chemical properties revealed a weak correlation with viscosity (at 60°C). Figure 1 shows that fluorescence intensity decreases as viscosity increases. This relationship was independently supported by comparison of the intensity and viscosity values observed for the AAA-1, AAA-2 and AAE asphalts (Figure 1). These asphalts were derived from

the same petroleum source but were manufactured differently. The AAE asphalt was air-blown, which is a technique used to stiffen as asphalt, and is accompanied by a rather large increase in viscosity as well as volatile loss and oxidation. As seen in Figure 1, the fluorescence intensity of the AAE asphalt has been significantly reduced compared with the AAA-1 and AAA-2 samples.

The results of spectral analysis showed that 70% of the raw asphalts had their wavelength of peak fluorescence intensity fall between 664 and 672 nm, with two asphalts (AAD-1 and AAE) having slightly lower peaks at about 640 nm and another asphalt (AAK-1) having a significantly lower peak at 544 nm. Generally, all of the spectra show a very rapid rise in fluorescence intensity in the range of ~510-530 nm followed by a gentle increase to their respective peak values. Most of the asphalts show a slight decline in intensity for the next 70-100 nm following the peak value and then a sharp decline to zero between 730-760 nm. However, four of the asphalts (AAE, AAG-1-1, AAH-1 and AAK-1) show a sharper decline in intensity following peak fluorescence. Note that the peak wavelength of the AAE asphalt was lower (640 nm) and the spectral distribution narrower compared with the AAA-1 (665 nm) and AAA-2 (670 nm) asphalts.

A comparative study where two asphalts (AAA-1 and AAB-1) were maintained refrigerated in argon (RA-stored) or exposed (Exposed) to room conditions for different durations demonstrates the influence of molecular structuring. Figure 2 shows that fluorescence intensity decreased with increasing exposure to room conditions, whereas very little change was observed when stored under argon in a refrigerator. These tests were performed on samples from which the top millimeter of asphalt was removed before measurement, thereby removing the effects of skin development and surface oxidation [7] and revealing changes that have occurred in the bulk asphalt. Clearly, we believe that fluorescence intensity decreases with increased molecular structuring. Presumably, as asphalt molecules develop an interconnected structure through the development of hydrogen bonding, dipole interactions and Van der Waals forces, the viscosity of the material would increase as well.

The TFOT and TFO-PV-Air tests were used to measure the aging deterioration of asphalts through progressively more severe oxidation. Depending upon the asphalt employed, these tests can result in changes in asphalt viscosity of one to three orders of magnitude. Table 1 gives fluorescence intensity and wavelength of peak fluorescence as they compare to concentration of carbonyl and sulfoxides (as determined by Western Research Institute) oxidation products for four different asphalts. These functional groups represent potential fluorophoric sites, however, as found with air-blown asphalts (AAE), a progressive decrease in fluorescence intensity with increasing severity of aging/oxidation was observed. Upon severe aging (TFO-PV-Air), three of the four asphalts showed a decrease (blue shift) in the wavelength of peak fluorescence and a narrowing of the spectral distribution. As can be seen in Table 1 peak wavelength and concentrations of carbonyl and sulfoxides were more variable (i.e., some increasing, others decreasing) for the TFOT samples.

From the foregoing it appears that both molecular structuring and aging/oxidation decrease the intensity of fluorescence emissions and increase asphalt viscosity. However, this may not be a direct cause-and-effect relationship, but be due to the fact that the chemical changes occurring as a

result of asphalt oxidation or structuring influence both measurements. Figure 2 compares the fluorometric intensity information obtained from molecular structuring and TFOT tests of two asphalts. The figure shows that the fluorescence intensity of the AAB-1 asphalt has decreased to the range of the TFOT test within 80 days, whereas the loss due to molecular structuring of the AAA-1 asphalt has not been as extensive over about the same duration. Fluorometric differences in the setting and aging properties of different asphalts may prove to be extremely valuable for determining the hardening potential and service life of asphalt binders in contact with aggregate materials.

To determine the influences that aggregate materials might have on the fluorometric properties of asphalt binders, a series of mastic samples were prepared. Intensity and peak wavelength values for each are given in Table 2. Generally, these data show that addition of aggregate to a diversity of asphalt binders results in a rapid (within 17 h) and significant decrease in fluorescence intensity. In comparison, a much smaller decrease was observed when teflon was used as the aggregate, suggesting that neutralization of fluorophoric emissions in asphalt binders may be limited in the presence of materials of larger particle size or of relatively inactive surfaces like teflon. The average decrease in intensity was different for each asphalt, but does not differ significantly between aggregate materials. With some variation the wavelengths of peak fluorescence for the AAA-1 and AAM-1 asphalts were not changed significantly by the presence of the aggregates. However, peak wavelength decreased (blue shift) for the ADB and AAG-1-2 asphalts in the presence of aggregate. It must be mentioned that these two asphalts were from the sample petroleum source except that AAG-1-2 has added lime. However, the addition of aggregate to any one of the set of four asphalts results in a narrowing of the spectral distribution in a manner similar to that observed from the aging/oxidation experiments.

Fluorometric intensity analyses were repeated for two of the mastic sets (AAA-1 and AAM-1) and the results are shown in Table 2. Different procedures were used to obtain new samples for testing and these results were compared with results for mastics that were exposed to room conditions. The AAA-1 set of mastics were used to study the influence of storage in argon under refrigeration (RA-Stored) and the results show an average increase of 0.36% intensity for the mastic samples (excluding teflon) following storage. Thus, it appears that somewhat less than 3% of the 35% decrease in fluorescence intensity observed with the addition of inorganic aggregates to the AAA-1 asphalt may result from storage effects and/or measuring variation. A slightly different response was observed from reheating the AAM-1 asphalt. First, there was a relatively large decrease in the fluorescence intensity of the raw asphalt which may be a result of oxidation and/or volatile loss from the asphalt. Secondly, for the asphalt/aggregate mixtures there was mostly a decrease in fluorescence intensity averaging about 0.22% intensity. Therefore, about 2% of the ~43% decrease in intensity resulting from the addition of aggregates to the AAM-1 asphalt may be attributed to analytical errors.

When both sets of mastics were exposed to room conditions a significant decrease in fluorescence intensity was observed. On average the mastics made from AAA-1 (Exposed 64 days) lost slightly more intensity than those made with the AAM-1 (Exposed 101 days) asphalt, i.e., 1.74% vs 1.58%. The differences observed in measured intensity among the different mastics are not much

greater than the variation found during the repeat analyses which means that the type of aggregate used in our mastic preparation has much less influence on changes in fluorescence properties compared with the type of asphalt used.

CONCLUSIONS

Fluorescence microphotometry techniques employ optical microscopy to facilitate the differentiation of asphalt binder from aggregate materials thereby eliminating the need to solvent extract the binder for evaluation. In the current research, techniques for the uniform measurement of fluorescence intensity and spectra were developed and applied to the characterization of raw asphalts. Relationships were found between fluorescence intensity values and viscosity as measured in original and laboratory-aged asphalts. As viscosity increases, intensity decreases, a relationship thought to be due to the dependence of both these properties upon oxidation and/or molecular structuring. Fluorescence intensity also decreases significantly upon the mixing of aggregate materials with asphalt, the magnitude of the change being influenced more by the asphalt binder used rather than the aggregate type. Just as observed for raw asphalts, the fluorescence intensity of asphalt binders in contact with different aggregate materials continues to decrease with curing/aging time. Results of this investigation demonstrate that fluorometric measurement of asphalt intensity has potential for use in monitoring asphalt oxidation during manufacturing and plant mixing, pavement curing and as a technique to monitor the deterioration of asphalt pavements that are in service.

ACKNOWLEDGEMENTS

The authors are pleased to acknowledge the support of the Strategic Highway Research Program, under contract No. SHRP-AIIR-04.

REFERENCES

1. Welborn, J.Y., National Cooperative Highway Research Program, Synthesis, 59, Washington, D.C., 34 pp. 1979.
2. Petersen, J.C., Proc. 63rd Annual Meeting of the Transportation Research Board, Washington, D.C., 42 pp., 1984.
3. Mitchell, G.D. and Davis A., The Fluorescence Characterization of Asphalts, Am. Chem. Soc. Preprint, 35 (3) 469 1990.
4. Mitchell, G.D. and Davis A., The Fluorescence Characterization of Asphalts, Fuel Sci. Tech. Internat., 10 (4-6) 909 1992.
5. Lin, R. and A. Davis, The Chemistry of Coal Maceral Fluorescence: With Special Reference to the Huminite/Vitrinite Group, Spec. Research Report SR-122, Energy and Fuels Research Center, 278 pp. 1988.
6. Materials Reference Library, Section 5, Rev. 11-1-88, University of Texas at Austin, 1988.
7. Mill, T. and D. Tse, Oxidation and Photooxidation of Asphalts, Am. Chem. Soc. Preprint, 35 (3) 483 1990.

Table 1. Peak Fluorescence and Intensity Changes with Aging

Asphalt Code	*Fresh Asphalt*				*TFOT Aged 163°C/5 hr*				*TFO–PV–Air Aged 60°C/400 hr 300 psig*			
	Intensity at 600 nm	Primary Peak, nm	Carbonyl, abs†	Sulfoxides, m/L†	Intensity at 600 nm	Primary Peak, nm	Carbonyl, abs†	Sulfoxides, m/L	Intensity at 600 nm	Primary Peak, nm	Carbonyl, abs†	Sulfoxides, m/L†
AAD–1	10.06	640	0.04	0.05	4.85	646	0.02	0.06	3.14	622	0.09	0.37
AAG–1–1	28.72	686	0.03	Trace	11.20	640	0.04	0.09	5.22	663	0.25	0.22
AAK–1	2.20	544	0.03	Trace	1.77	549	--	--	1.10	552	0.08	0.32
AAM–1	9.55	668	0.02	Trace	4.72	666	0.04	0.06	2.70	640	0.16	0.12

† Western Research Institute

Table 2. Intensity and Peak Fluorescence Values of Raw Asphalt and Mastics

Asphalt Code	% Intensity Values at 600 nm and Primary (Minor) Peaks in nm											
	Raw		RB–Granite		RC–Limestone		RD–Limestone		RJ–Gravel		Teflon	
	% Intensity	Peak (nm)	% Intensity	Peak (nm)	% Intensity	Peak (nm)	% Intensity	Peak (nm)	% Intensity	Peak (nm)	% Intensity	Peak (nm)
AAA–1	11.72	664 (720)	7.44	665	7.85	677	7.65	670	7.72	665	11.13	664 (719)
RA–Stored	11.53		7.86		7.86		8.02		8.38		10.94	
Exposed	7.56		5.50		5.73		6.39		6.10		7.75	
ABD	20.90	600 (681)	14.15	556 (682)	13.50	552 (683)	12.65	553 (685)	12.86	555 (686)	17.79	598 (682)
AAG–1–2	28.7	686 (631)	16.18	559 (681)	16.83	555 (681)	16.61	558 (684)	15.00	556 (682)	Not Prepared	
AAM–1	9.55	668 (720)	5.23	607	5.62	676	5.66	665	5.40	668	7.44	668 (716)
Reheat	8.84		5.08		5.63		4.94		5.39		7.07	
Exposed	5.66		3.77		3.99		3.84		3.99		5.19	

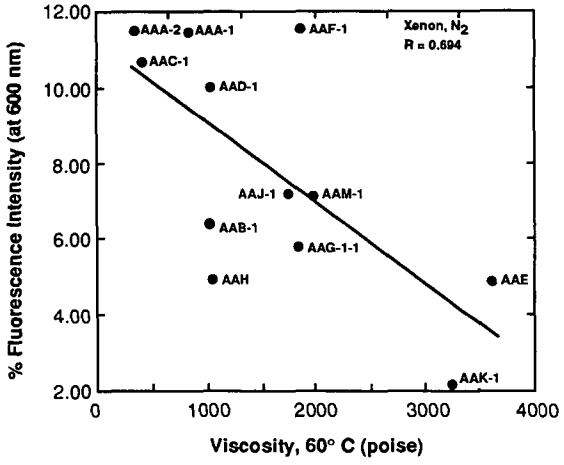

Figure 1. Relationship between Fluorescence Intensity and Initial Viscosity of SHRP Asphalts Measured in Nitrogen Using Xenon Illumination

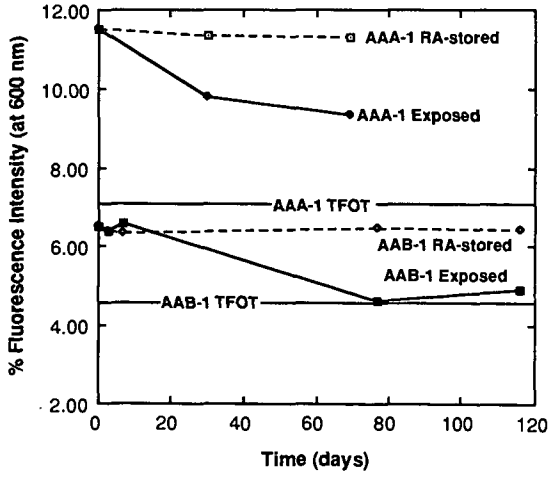

Figure 2. Comparison of Molecular Structuring and TFOT Aging on Fluorescence Intensity of the AAA-1 and AAB-1 SHRP Asphalts

OXIDATION PATHWAYS FOR ASPHALT

Theodore Mill, Doris S. Tse, Bock Loo, C.C. David Yao and Elizabetta Canavesi*
Chemistry Laboratory
SRI International
Menlo Park, CA 94025
*Euron
Milan, Italy

Keywords: Asphalt, Oxidation, Pathways

INTRODUCTION

Oxidation of asphalt is a major cause of pavement failure owing to hardening of the asphalt binder with accompanying changes in viscosity, separation of components, embrittlement and loss of cohesion and adhesion of the asphalt in the mix. Slow oxidation of asphalt continues during the service life of the roadbed at a rate that appears to be partly determined by the void volume of the roadbed, as well as the properties of the asphalt (1-3).

We have focused on understanding the chemical pathways for slow oxidation of asphalt in order to predict how rapidly an asphalt will oxidize, based on its composition, and to find better ways to inhibit the process under service conditions.

OXIDATION PROCESSES IN ASPHALT

Three different mechanisms proposed for asphalt oxidation include free radical oxidation, photooxidation and molecular oxidation. The first two processes may involve participation of free radicals while the last does not. The distinction is important in indicating whether phenolic inhibitors will be effective in slowing oxidation. Free radical processes are inhibited by antioxidants, whereas molecular oxidation requires removal of oxygen or the oxygen-reactive component. In very viscous bulk asphalt, added antioxidants may have limited value.

Oxidative aging is characterized by oxygen uptake, formation of sulfoxide and carbonyl bands in the IR spectrum and marked increases in dynamic viscosity and other rheological properties (4). No chemical changes are observed on heating asphalt at 60-130°C in the absence of oxygen, although small amounts of volatiles may be lost at elevated temperature, causing viscosity increases. Above 150°C non-oxidative reactions may begin to cause chemical changes, even without oxygen.

Nmr-derived average structures for SHRP core asphalts (4), two of which are shown in Figure 1, illustrate the point that oxidative aging in asphalts is not a single chemical process, but a composite of several independent and concurrent oxidation reactions at several sites in the asphalt structure. These reactions affect families of similar structural units. Therefore, to understand the process at the molecular level, we must rely for guidance on the behavior of model compounds and model probes. Moreover, the interactions of oxidation products with polar groups in asphalt lead to large changes in physical properties and can strongly affect service life.

Studies of the thermal oxidation of asphalt over the past thirty years have almost uniformly concluded that asphalts are not protected from oxidation by addition of most autooxidation inhibitors such as hindered phenols or zinc dithiocarbamates (5, 6) and that free radicals play no role in the oxidation process. This conclusion is based on a concept of free radical oxidation as it applies to reactive hydrocarbons where oxidation proceeds by way of long

chains. In asphalt, native phenol inhibitors already are present and asphalt oxidation may still involve free radicals, but not a chain oxidation.

SULFUR CHARACTERIZATION AND OXIDATION

Sulfur oxidation to sulfoxide is easily measured in asphalt by a single band in the IR near 1000 cm^{-1}. Many investigators have used sulfoxide formation as a measure of asphalt aging, but without clear evidence for the role of sulfoxides in the aging process or the relation of this oxidation to other oxidative changes in the asphalt such as carbonyl formation.

SHRP core asphalts have total sulfur contents ranging from 1 to 8 percent. Thermal oxidation at 50°-100°C converts a fraction of the total sulfur to sulfoxide (>SO) corresponding to conversion of aliphatic sulfide (>S) to >SO. Figure 2 shows that the concentration of >SO formed in asphalts heated in the TFOT correlates well ($r^2 = 0.95$) with the original concentration of S, but accounts for only 20-30 mole percent of it. The >SO formed by chemical oxidation accounts for a higher proportion of S in high S asphalts.

Sulfur K-edge X-ray Absorption Fine Structure (XAFS) spectra were used to characterize sulfur in several different unoxidized and oxidized asphalts (S). Analysis of the XAFS data are summarized in Table (1). Unoxidized samples of asphalts show the presence of only two kinds of sulfur: aliphatic sulfide and thiophenic sulfur in the ratio of 22:78 to 40:60; among unoxidized asphalts, only AAG-1 and AAM-1 show the presence of any sulfoxide. Comparison of XAFS and ESCA spectra for AAA-1 shows good agreement on the ratios of sulfide and thiophenic sulfur.

Thermally oxidized AAA-1, AAG-1 and AAK-1 show formation of sulfoxide which is derived only from sulfide sulfur. About 32 and 14% of AAA and AAK sulfides respectively disappear on oxidization, part of which is accounted for by sulfoxide, however in AAG, 51% of sulfide oxidizes to give the expected amount of additional sulfoxide. No other oxidized sulfur species was observed.

In a sample of AAG oxidized with t-BuOOH no sulfide sulfur remains after oxidation, consistent with the low initial concentration of sulfide sulfur in AAG- of 0.13 M and with the finding that thermal oxidation of AAG-1 gives only 0.15 M sulfoxide. Asphalt AAA-1 has 10 percent sulfide left after chemical oxidation with the difference almost all accounted for by sulfoxide. AAM-1 is especially interesting in having the lowest proportion of sulfide of any sample examined by XAFS; thermal oxidation AAM also gives the smallest amount of sulfoxide by IR.

Model compounds dimethylsulfide, di- n-butyl sulfide and dibenzyl sulfide (DMS, NBS, DBS) were used to study thermal oxidation of aliphatic sulfide sulfur in asphalts. Neither DMS, NBS nor DBS oxidized alone with oxygen at 100°C. By implication, >SO formation in asphalts must occur indirectly. DMS and NBS were added to AAA or AAG to probe the pathway for sulfoxide formation from aliphatic sulfides under conditions where direct oxidation is not detectable. A mixture of DMS and AAA-1 heated for three days at 110°C in air in a sealed tube developed a strong IR band near 1000 cm^{-1} due to DMSO. Similar experiments with 0.05-0.1 M NBS in asphalt gave similar results when analyzed by IR and by GC for Bu_2SO. Preoxidized AAG also oxidized NBS. The results clearly demonstrates that a peroxy intermediate (probably non sulfur) species which forms with oxygen can be intercepted by DMS or NBS.

One candidate for this oxidation species is peroxide or a hydroperoxide formed from reactive pyrrolic NH bonds or benzyl CH bonds.

$$AromCH_x + O_2 \longrightarrow AromCH_{x-1}OOH$$

$$AromCH_{x-1}OOH + DMS\ (AplkSR) \longrightarrow AromCH_{x-1}OH + DMSO\ (AplkS(O)R)$$

However, purified cumene (isopropylbenzene, CuH) was heated in oxygen at 110°C for three days with DMS gave no DMSO. This experiment shows that whatever the reactive oxidation centers might be, they are much more reactive to oxygen than cumene CH bonds.

The effect of oxygen pressure on rates of oxidation of sulfide was examined in AAA-1 thin films by heating samples in air or oxygen at 100°C for 25 hours and comparing the FTIR band for sulfoxide between 1100 and 960 cm^{-1}. The oxygen reaction was clearly faster by a factor of at least two and perhaps more, depending on the extent of conversion of alkyl sulfides in AAA-1. Although these data are consistent with rate-limiting oxygen diffusion, we find no significant difference between oxidation rates in thin films and lumps.

We have also measured the stability of several asphalt sulfoxides by first oxidizing asphalts at 100°C for 20-30 hrs and then heating them under argon in sealed tubes for 5-10 hrs at 165°C followed by FTIR analyses. Argon heated samples showed about 10-58 percent less >SO than unheated ones, indicating a modest degree of stability for >SO under TFOT conditions. The fastest >SO loss rate corresponds to a half life of 6 hrs at 165°, consistent with half lives found by Walling and Bullyky (6) for pyrolysis of long chain aliphatic sulfoxides. Table 2 summarizes >SO decomposition data.

OXYGEN UPTAKE AND BALANCES IN OXIDIZED ASPHALT

Oxygen and Product Balances

We have conducted detailed oxygen uptake and product studies on the four inner core asphalts AAD-1, AAG-1, AAK-1 and AAM-1 to evaluate how well the observable products including >SO and >CO account for the absorbed oxygen. In each case we examined the oxidation of both the tank asphalt and the TFOT asphalt which had been heated in air for 5 hours at 165°C (WRI supplied these samples). We oxidized several samples of these asphalts as thin films at 100°C in air for times as long as 409 hrs. We measured oxygen uptake for each sample and quantitatively measured >SO and >CO formation by FTIR to find out how much absorbed oxygen is accounted for by these two classes of products.

Table 3 summarizes the average oxidation product and rate data. The most important qualitative conclusions are that oxygen balances are generally low (20-60%), that carbonyl forms in low yield in most asphalts, but not in AAM or AAMT where sulfide is very low, and that there are no significant differences between tank and TFOT samples, again except for AAM and AAMT. The ratio of >SO/>CO is close to 10 in oxidized K and KT samples, whereas this ratio is closer to 3 or 4 in D and DT. Both asphalts have relatively high total sulfur, but D(DT) has a higher proportion of sulfide sulfur than does K (46% vs 36%). The 409 hr AADT experiment was analyzed for CO and CO_2 formation as well as oxygen uptake, but none could be found under conditions where we estimate we could detect <3 μmoles. Thus the missing oxygen is still largely in the asphalt, perhaps as water.

Uncertainty in oxygen uptake and product measurements is ±20% in O_2, ± 10% in >SO formation and possibly as high as ± 100% in >CO. The high uncertainty in >CO stems mainly from our uncertainty as to which model ketone standard to use for calibration of the FTIR spectrum around 1700 cm^{-1}. We chose valerophenone as a standard assuming that any ketones would form at benzylic positions and these would be well modeled by valerophenone. However, oxidation of phenols also leads to ketone formation (as cyclohexadienones) which

probably have very different IR spectral cross sections from arylphenones such as butyrophenone. But, even doubling the carbonyl concentrations still leaves oxygen balances short of the 2:1 stoichiometry for each O_2 to form one >SO or >CO and one ROH or H_2O.

Oxidation and Product Rates

Table 3 also shows average rates of oxygen uptake, normalized for time and sample size in micromoles mg^{-1} hr^{-1}. The striking feature of these data is the similarity in rates for all of the asphalt samples, with few exceptions. The rates are close to 5 x 10^{-3} micromoles mg^{-1} hr^{-1} for oxygen uptake; hardly a two-fold difference in rates among all asphalts studied even though AADT and AAKT have 1.2 M and 0.76 M sulfide sulfur compared with AAGT and AAMT with only 0.14 M and 0.065 M sulfide. Again diffusion limited oxidation is one explanation.

DISCUSSION

Sulfur oxidation is widely investigated in asphalts because the IR fingerprint for sulfoxide is so easy to measure, but the details of the process and the kinetics have been confused by several conflicting ideas about the origins of the reaction. The data from this study using XAFS and ESCA spectroscopies clearly shows that only aliphatic sulfide sulfur is oxidized during thermal oxidation or mild chemical oxidation by t-BuOOH; thiophenic sulfur is not significantly affected during these oxidations. This conclusion, first reached by Ruiz et al (7) and by Petersen et al. (8) for a few kinds of asphalts has now been extended semi-quantitatively to the SHRP core asphalts and by implication to all other asphalts as well.

It now becomes clearer why >SO-time curves for oxidation of different asphalts are so different and why asphalts with similar total sulfur content, but with different aliphatic:aromatic distributions of sulfur give different >SO yields. In the case of low sulfur asphalts, such as AAG or AAM, aliphatic sulfide is rapidly exhausted and formation of >SO almost stops after 30 hrs at 100°C. High aliphatic sulfide sulfur asphalts such as AAA or AAD continue to form much higher proportions of >SO for longer times.

The induced oxidation of DMS and NBS in oxidizing asphalt points to formation of an peroxy intermediate from direct interaction of asphalt with oxygen. Induced oxidation of NBS is found in both AAA and AAG asphalts, indicating that the source of the peroxy intermediate is both independent of the sulfur and in excess of sulfide sulfur, at least in AAA. Oxygen effects on rates of formation of >SO also are in qualitative agreement with this hypothesis.

Rates and products in oxidation of core asphalts points to oxygen imbalances in terms of the >SO and >CO products; in some cases the deficits are large. Rates of oxidation show a striking similarity among the four core asphalts even though they differ by twenty-fold in sulfide content and almost as much in vanadium and other metal ion contents. Oxidation rates do not appear to be controlled by these components, but by other components such as phenols or dihydroaromatic groups, the identity of which are currently under investigation. Other features of the rate and product studies also fit well with the overall concept. Thus we see that AAM or AAMT oxidize rapidly to form >SO but the oxidation continues after >SO production stops due to exhaustion of the aliphatic sulfide to form much more carbonyl. In that sense sulfide sulfur acts as internal redox inhibitor to limit >CO formation from the peroxy intermediate.

Figure 3 shows a schematic representation of the oxidation process. In this scheme, the first step forms peroxy intermediate which then can oxidize either sulfur and form >SO and an alcohol, or in the absence of sulfide sulfur, the intermediate may form carbonyl by one of several paths. Alcohols are difficult to detect and might account for part of the missing oxygen.

ACKNOWLEDGMENT

This work was supported under a subcontract from Western Research Institute as prime contractor on project A002 to SHRP>

REFERENCES

1. Welborn, J. Y. 1984. Physical Properties as Related to Asphalt Durability: State of the Art. Trans. Res. Record 999: 31-37.

2. Hveem, F. N., Zube, E., and Skob, J. ASTM Spec. Tech. Pub. No. 277 (1959(.

3. Rostler, F. S. and White, R. M. ASTM Spec. Tech. Pub. No. 277 (1959).

4. Jennings, W. 1992. Nmr Structure Determinations of SHRP Core Asphalts. MS in preparation.

5. Martin, K. G. 1966. Influence of Stabilizers on Bitumen Durability. J. Appl. Chem. 16:198-201.

6. Martin, K. G. 1968. Laboratory Evaluation of Antioxidants for Bitumen. Fourth Conf. A.R. R. B. pp. 1-14.

7. Huggins, F. E., S. Vaidya, G. Huffman, T. Mill and J. Youtcheff. 1992. Analysis of Sulfur Forms in Asphalt Using Sulfur K-Edge XAFS Spectroscopy. Preprints Div. Fuel Chemistry 204th Meeting Amer. Chem. Soc., Washington, D.C., 23-29 August.

8. Walling, C. and J. Bullyky. 1964. Thermal Decomposition of Sulfoxides. J. Org. Chem. 29: 2699-2703.

9. Ruiz, J. M.; B. M. Carden; L. J. Laura; E.-J. Vincent. 1982. Determination of Sulfur in Asphalt by Selective Oxidation and Photoelectron Spectroscopy for Chemical Analysis. Anal. Chem. 54: 688-691.

10. Petersen, J. C., S. M. Dorrence, M. Nazir, H. Plancher, and F. A. Barbour. 1981. Oxidation of Sulfur Compounds in Petroleum Residues: Reactivity-Structural Relationships. Div. Petrol. Chem., 181st Meeting Amer. Chem. Soc., New York, N.Y.

11. Hendry, D. G.; T. Mill; L. Piszkiewicz; J. A. Howard; H. K. Eigenmann. 1974. A Critical Review of H-Atom Transfer in the Liquid Phase. Phys. Chem. Ref. Data. 3: 937-978.

Table 1. Analysis of Sulfur XAFS and ESCA Spectra of Asphalt Samples[a,b]

Sample	%Sulfide (M)	(%ΔS)[c]	%Thiophene	%>SO Sulfoxide	(%Δ>SO)[d]	% S(M)
AAA-1	40[34][e]	–	60(66)[e]	–	–	7.3(2.3)
AAA-1 oxid[f]	27[24][e]	13	67	6	-7	7.3
AAB-1	31	–	69	–	–	5.6(1.75)
AAC-1	25	–	75	–	–	2.7(0.84)
AAD-1	46(1.2)	–	54	–	–	8.6(2.7)
AAF-1	28	–	72	–	–	3.5(1.1)
AAG-1	33(0.14)	–	59	8	–	1.3(0.41)
AAG-1 oxid[f]	15	18	60	25	-1[h]	1.3
AAK-1	36(0.76)	–	64	–	–	6.6(2.1)
AAK-1 oxid[f]	31	5	62	7	+2	6.6
AAM-1	17(0.065)	–	78	5	–	1.2(0.38)
Asph-X(AAA-1 oxid)[g]	10	30	63	27	-3	7.3
Asph-Y(AAG-1 oxid)[g]	0	33	53	17	+23	1.3

[a]Data from G. P. Huffman et al. (7). [b]Samples from WRI except X and Y from SRI. [c]Change in sulfide. [d]Difference between ΔS and >SO. [e]ESCA spectra taken at SRI. [f]Oxidized by heating at 113°C for 120 h. [g]Oxidized with t-BuOOH in cyclohexane at 25°C.

Table 2. THERMAL CHANGES IN SULFOXIDE AND CARBONYL IN PREOXIDIZED ASPHALTS IN ARGON AT 165°

Asphalts (≥SO, M)	Time, hr	% Change >SO	% Change >CO
NBSO[a] (0.29 M)	5	-58	–
AAD	7	-38	–
AAGT (0.19 M)	5	-7	+44
AAGT (0.19 M)	10	-7	+60
AAK (0.37 M)	5	-48	+12
AAK (0.37 M)	10	-54	+7

[a]Dissolved in unoxidized AAD.

Table 3. OXYGEN UPTAKE AND BALANCES FOR ASPHALTS[a]

Sample	Timee (hr)	Wt Sample (mg)	Products, umoles				
			$\Delta\Delta O_2$	>SO	>CO	%OB[b]	10^3 Oxid Rete, µmole/mg hr
D	114	79	38	13	4.1	23	4.2
DT	409	100	105	37	7	22	2.5
G	30	113	14	13	–	–	4.2
GT	140	184	61	34	12	38	2.3
K	24	86	7	13	1.0	100	3.4
KT	140	392	79	141	32	108	1.5
M	120	261	205	80	114	47	6.5
MT	120	250	74	76	121	130	2.5

[a]Oxidized in air as thin films at 100°C.
[b]OB = oxygen balance = $[(>SO + >CO)/2\Delta O_2] \times 100$.

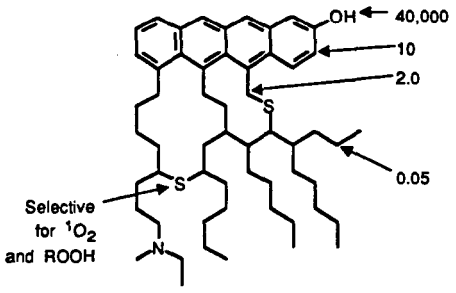

AAK-1 (6% S)

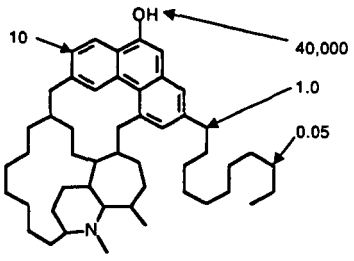

AAG-1 (1% S)

* From P.W. Jennings, Montana State University.

RM-6319-20A

Figure 1. Oxidizable structures in representative asphalt molecules with relative reactivities shown for RO_2• radicals (11).

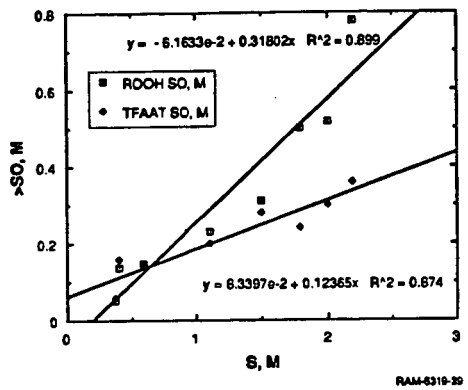

Figure 2. Correlation of >SO with S in core asphalts.

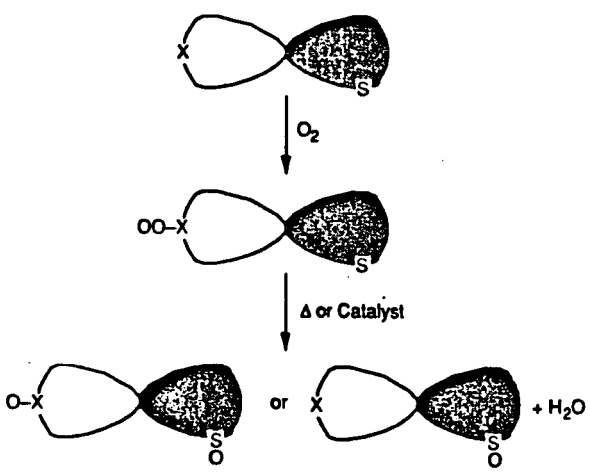

Figure 3. Possible pathways for >SO formation.

ANALYSIS OF SULFUR FORMS IN ASPHALTS USING SULFUR K-EDGE XAFS SPECTROSCOPY

Frank E. Huggins, Shreeniwas V. Vaidya, G. P. Huffman,
University of Kentucky, Lexington, KY 40506;
T. Mill,
SRI International, Menlo Park, CA 94205;
and J. Youtcheff,
Strategic Highway Research Program, Washington, DC 20006.

Keywords: Asphalt, Sulfur, X-ray Absorption Fine Structure Spectroscopy

ABSTRACT

The sulfur functional groups present in a number of asphalt samples, which varied in total sulfur content from 1.1 wt% to 6.9 wt%, have been investigated by means of sulfur K-edge XAFS spectroscopy. This method, which is based on a least-squares method of analysis of the sulfur XANES spectrum, is capable of quantitatively determining aliphatic sulfur forms, such as sulfides, aromatic sulfur forms, such as thiophenes, and oxidized sulfur forms, such as sulfoxides, sulfones, etc. In the unoxidized asphalt samples examined, oxidized sulfur forms are generally absent, and the principal sulfur form found is thiophenic. However, thiophenic sulfur forms vary from about 54% of the total sulfur to about 78% and there is a weak negative correlation in this trend with total sulfur content. Comparison of sulfur forms in asphalts before and after oxidation treatments shows that only the aliphatic sulfur component oxidizes to sulfoxide.

INTRODUCTION:

One of the many studies of asphalts being conducted under the Strategic Highway Research Program (SHRP) is an investigation of the mechanism of asphalt oxidation to determine those variables that influence oxidative aging. One of the predominant oxidation products found in asphalts is the sulfoxide functional group. Consequently, we are interested in understanding the role that different sulfur forms may play in the oxidation process. In this study, sulfur K-edge X-ray absorption fine structure (XAFS) spectroscopy has been used to characterize the different sulfur forms in asphalts and the changes in these sulfur species on oxidation.

EXPERIMENTAL:

Samples and Oxidation Treatments: All of the asphalt samples were obtained from the SHRP Material Reference Library. Thermal oxidation of the asphalts was conducted at the Western Research Institute. Asphalts were oxidized by the Thin-Film Oven Test followed by additional conditioning for 144 hours at 60°C under 300 psi air in a pressurized oxidation vessel. These two conditioning procedures mimic both short term ageing and the longer term ageing experienced by the pavement in the field.

Chemical oxidation was performed on samples of AAA-1 (Asphalt X) and AAG-1 (Asphalt Y) by dissolving about 1 g of asphalt in 25 ml of cyclohexane, and adding 5-7 equivalents of t-BuOOH based on the total sulfur concentration in the asphalt. This mixture was stirred for 4-8 hours at room temperature. The samples were then washed three times with 50

ml volumes of purified water, dried over sodium sulfate, and stripped free of the solvent. Since AAG-1 formed an emulsion during the water washing, sodium bisulfite was added to reduce and remove any residual hydroperoxide.

Sulfur K-edge XAFS Spectroscopy: XAFS spectroscopy at the sulfur K-edge was performed at beam-line X-19A at the National Synchrotron Light Source, Brookhaven National Laboratory. This beam-line is unfocussed and all components are in machine vacuum up to the experimental hutch to maximize the intensity of soft X-rays (2-5 keV) reaching the sample. The monochromator consists of a double channel-cut silicon (111) crystal assemblage that can be rotated by means of a precision stepping motor to select a specific range of energies for the spectral scan. Absorption of the X-rays was measured by means of an ion chamber that detects the fluorescent X-rays emitted over a large solid angle in response to the absorption process. For sulfur, absorption of X-rays was measured over the spectral range from 2.4 keV to 2.8 keV; over the X-ray absorption near-edge structure (XANES) region (ca. 2.45 to 2.50 keV), absorption data were collected every 0.08 eV. The ratio of the intensity of the fluorescent X-rays to that of the incident X-rays as a function of X-ray energy constituted the XAFS spectrum. The primary calibration standard employed was elemental sulfur diluted to 5 wt% in a boric acid pellet; the major peak maximum at 2.472 keV was defined as the zero energy point for the XANES spectra shown in this report.

The sulfur K-edge XANES spectra of the asphalt samples were obtained from the raw XAFS spectral data in the usual way (1,2). The sulfur XANES spectra were then analyzed by means of a least-squares fitting program and calibration procedure, which is described in detail elsewhere (1,2). Basically, this program fits the sulfur XANES spectra of fossil fuels and related samples as the sum of an arctangent function and a number of lorentzian/gaussian shaped peaks, which represent the "white lines" (1s - 3p electronic transitions) of specific sulfur functional forms. Although this program was primarily designed for analysis of sulfur forms in coals, the same procedure is actually easier and more precise for the analysis of sulfur in asphalts because the complications due to the presence of pyrite in coal (3,4) are avoided. The precision of the determinations is estimated to be ±5%.

RESULTS AND DISCUSSION:

As indicated in Figure 1 (top), most unoxidized asphalt samples can be fit with just two distinct components under the major feature in the XANES spectrum. These two components are interpreted as aliphatic sulfide and thiophene sulfur forms based on peak position systematics (1,5). The small peaks at higher energies represent secondary processes (resonant scattering phenomena) that occur in the same components. For oxidized asphalts (Figure 1, bottom), peaks for oxidized sulfur forms, principally sulfoxide, occur near where these secondary peaks are found. The calibration procedure allows for the different contributions in such cases and oxidized sulfur forms can also be estimated from the sulfur XANES spectrum (1,2).

Representative sulfur K-edge XANES spectra are shown in Figure 2 for some of the asphalt samples investigated in this study. The spectra of all asphalt samples were fit in similar fashion to those shown in Figure 1 and the derived data on percent sulfur in different functional forms are presented in Table 1. In addition, the third derivative spectra were also examined (not shown) and these data confirmed the presence of just two contributions, aliphatic sulfide and thiophene, to the main spectral peak.

Samples that were subjected to oxidation showed the presence of significant sulfoxide. For those samples that were available in both unoxidized and oxidized states, the difference spectrum obtained by subtracting the sulfur XANES spectrum for the oxidized asphalt from that

for the corresponding unoxidized sample was especially revealing (Figure 3). Such difference spectra invariably showed the presence of a positive peak at about 0.3 - 0.5 eV and a negative peak at about 3.0 - 3.5 eV. These peak positions correspond to those for aliphatic sulfide and sulfoxide sulfur forms, respectively. There was little or no difference between the oxidized and unoxidized spectra in the vicinity of 1.2 - 1.5 eV, where the peak for thiophene sulfur is found. It is clear then from this analysis, that the oxidation procedure converts aliphatic sulfur forms to sulfoxide, but does not significantly affect the thiophenic sulfur forms. It should be noted that whereas approximately 50% of the aliphatic sulfur in sample AAG-1 was converted to sulfoxide, significantly lesser amounts were oxidized in samples AAA-1 and AAK-1 because of their greater initial sulfide contents.

Comparison of the sulfur K-edge XAFS data with sulfur ESCA spectral analysis for AAA-1 showed reasonably good agreement for the sulfide to thiophene sulfur ratio [6].

XAFS analysis of the sulfur forms in thermally oxidized AAA-1, AAG-1, and AAK-1 indicate formation of varying proportions of sulfoxide derived only from sulfide sulfur. About 32 and 14% of AAA-1 and AAK-1 sulfides, respectively, disappear on thermal oxidation, part of which is accounted for by formation of sulfoxide. However in AAG-1, 51% of the sulfide oxidizes to give the expected amount of additional sulfoxide. No other oxidized sulfur species was observed in these samples. ESCA spectra of oxidized asphalt AAA-1 [6] showed that almost 40% of the sulfide sulfur disappeared in 48 hours at 110°C, in reasonable agreement with the XAFS result for AAA-1. Both spectral methods showed significant deficits between sulfoxide formed compared to sulfide oxidized in AAA-1.

The chemically oxidized sample, Asphalt Y (AAG-1), shows a high proportion of sulfate in the XAFS spectrum (Figure 4). This is probably attributable to the use of bisulfite to reduce residual t-BuOOH during clean up.

Information was available on the total sulfur contents of the asphalts and plots were prepared of the XANES derived data on sulfur forms against total sulfur for the unoxidized samples. As indicated in Figure 5 and also in Table 1, these data show that thiophenic sulfur in the asphalts averages approximately 66% of the total sulfur; however, there appears to be a weak negative correlation between % sulfur as thiophene and wt% total sulfur, such that the percentage of sulfur as thiophene varies from a high of 78% in low-sulfur asphalts to about 54% in high-sulfur asphalts. As thiophene is not affected by oxidation, these observations apply regardless of whether the asphalt is oxidized or not.

CONCLUSIONS:

A calibrated, least-squares method of analysis of sulfur K-edge XANES spectra has been used for the direct, non-destructive determination of sulfur species in asphalts. Although specific sulfur compounds are not identified, the technique is valuable for quantitatively determining the distribution of sulfur among various organic sulfur functionalities. In this study of eight asphalt samples, thiophene-like aromatic sulfur forms were found to constitute on average about two-thirds of the sulfur, with the remainder being aliphatic sulfide or oxidized sulfur forms. Samples oxidized by either a thermal or a chemical oxidation treatment showed that the aliphatic sulfur forms were partially oxidized to sulfoxide, and that the thiophenic sulfur forms were unaltered.

Acknowledgements:

The sulfur XAFS spectra were obtained at the National Synchrotron Light Source at Brookhaven National Laboratory, which is supported by the U.S. Department of Energy.

References:

1. G. P. Huffman, S. Mitra, F. E. Huggins, and N. Shah, Energy & Fuels, 5, 574-581, (1991).
2. F. E. Huggins, S. Mitra, S. Vaidya, M. M. Taghiei, F. Lu, N. Shah, and G. P. Huffman, in: Coal Science and Technology, Vol. 18: Processing and Utilization of High-Sulfur Coals IV (Fourth Internat. Conf., Idaho Falls, ID), (eds. P. R. Dugan, D. R. Quigley, and Y. A. Attia), 13-42, Elsevier, Amsterdam, (1991).
3. F. E. Huggins, G. P. Huffman, and N. Shah, Proceedings, 16th EPRI Annual Conference on Fuel Science, (Palo Alto, CA), Publication EPRI GS-xxxx, Electric Power Research Institute, Palo Alto, CA, (1992), in press.
4. F. E. Huggins, G. P. Huffman, and N. Shah, Proceedings, 2nd International Conference on Elemental Analysis of Coal, (ed. G. Vourvopoulos), to be published, (1992).
5. G. P. Huffman, F. E. Huggins, S. Mitra, N. Shah, R. J. Pugmire, B. Davis, F. W. Lytle, and R. B. Greegor, Energy & Fuels, 3, 200-205, (1989).
6. T. Mill, D. Tse, D. Yao, B. Loo, E. Canavesi, unpublished data, paper in preparation.

TABLE 1

Quantitative Analysis of Sulfur K-edge XANES Spectra
of Thirteen Asphalt Samples

Sample I.D.	Wt% Sulfur in Asphalt	% Sulfur in Sulfur Functional Groups*			
		Sulfide	Thiophene	Sulfoxide	Other
AAA-1	5.5	40	60	--	--
AAA-1 oxid.	5.3	27	67	6	--
AAB-1	4.7	31	69	--	--
AAC-1	1.9	25	75	--	--
AAD-1	6.9	46	54	--	--
AAF-1	3.5	28	72	--	--
AAG-1	1.3	33	59	8	--
AAG-1 oxid.	1.1	15	60	25	--
AAK-1	6.4	36	64	--	--
AAK-1 oxid.	5.9	31	62	7	--
AAM-1	1.2	17	78	5	--
Asph-X (AAA-1)†	---	10	63	27	--
Asph-Y (AAG-1)†	---	0	53	17	3 Sulfone 27 Sulfate

*Determinations of %Sulfur in Sulfur Functional Groups are accurate to ±5%.
†Chemically oxidized asphalts.

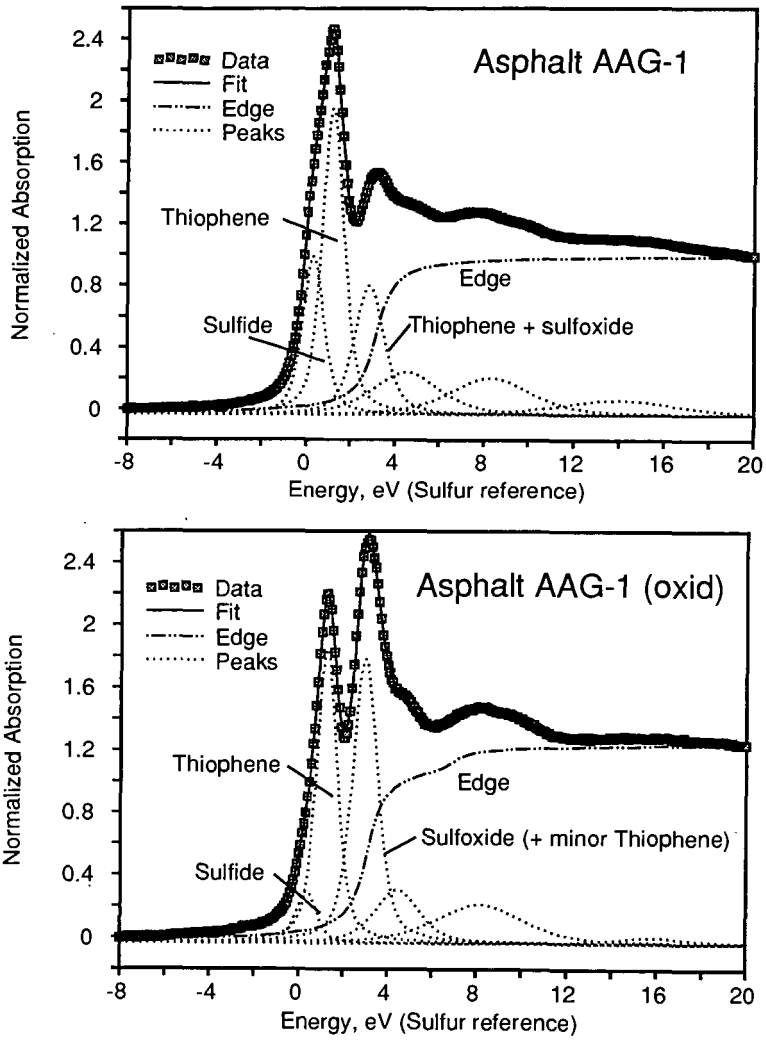

Figure 1: Least-squares fitted sulfur K-edge XANES spectra of asphalt sample AAG-1 before (top) and after (bottom) oxidation.

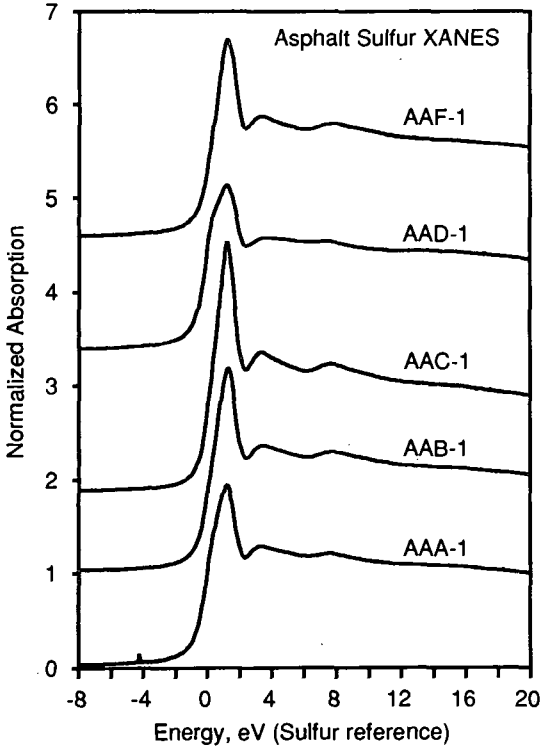

Figure 2: Sulfur XANES spectra of selected asphalt samples.

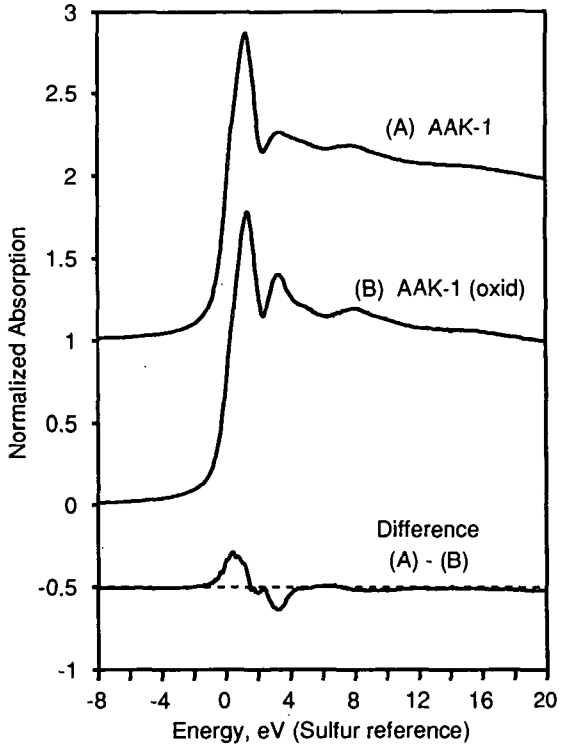

Figure 3: Sulfur XANES and difference spectrum for asphalt samples AAK-1 and AAK-1 (oxid).

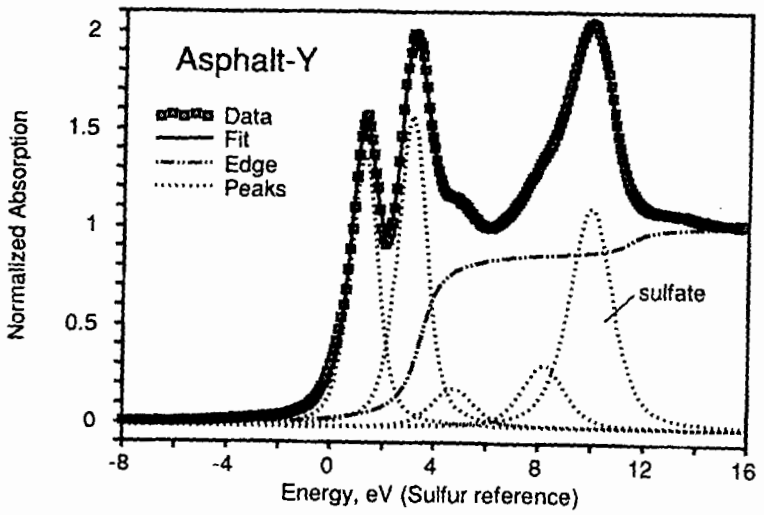

Figure 4: Sulfur K-edge XANES spectrum of chemically oxidized asphalt sample, AAG-1.

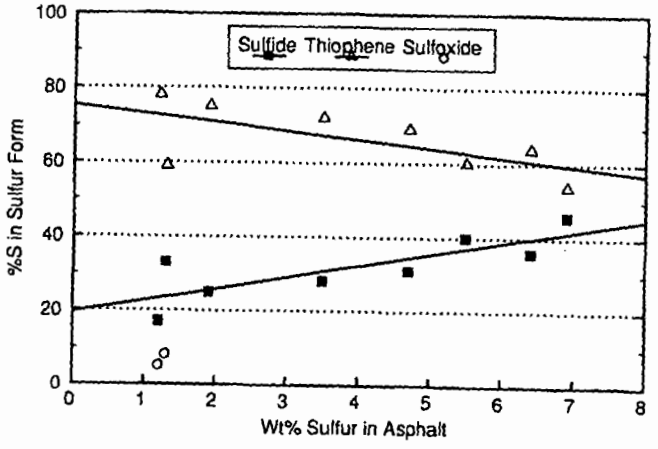

Figure 5: Plot of %S in specific sulfur form against wt% S in asphalt for the eight unoxidized asphalt samples.

EVOLUTION MECHANISMS OF L.C.O. GAS-OILS DURING STORAGE AND CHEMICAL MODELING OF ASPHALT AGING.

F. Tort and B. Waegell

Laboratoire de Stereochimie associe au CNRS URA 1409 LASCO. Faculte des Sciences St Jerome Case 532, Avenue Escadrille Normandie-Niemen
13 397 Marseille
(France)

and

L. Germanaud and C. Bemasconi

Centre de Recherche Elf-Solaize
Chemin du Canal B.P. 22
69 360 Saint-Symphorien d'Ozon
(France)

Keywords: gas-oils; instability; phenalene.

ABSTRACT

In order to control or arrest the instability of L.C.O gas-oils during storage using efficient stabilizing additives it is necessary to determine structures and reaction mechanisms involved in these degradation processes. The oxidation of phenalene into phenalenone, alkylindoles and thiophenols play a crucial role in color change and sediment formation. The condensation reaction between phenalenone and 2-methylindole in presence of stoichiometric amount of para-toluenesulfonic acid leads to a complex mixture of compounds. Seven sets of compounds have been isolated by chromatography and spectroscopically identified. A reaction mechanism is proposed and experimentally supported. It is suggested that the phenalane and its derivatives can be partly representative models of the structures involved in asphalt aging.

INTRODUCTION

The evolution of refining processes has lead to an increase in the production of catalytically-cracked distillates. Before, these products particularly the L.C.O.(Light Cycle Oil), were used as diluents of heavy fuels. The decrease of the consumption in heavy fuels and the increase in auto and diesel fuels have lead refiners to introduce limited amounts of L.C.O. in domestic fuels and gas-oils. However these products are often unstable. It is well-known that storage of unstable diesel fuels can result in the color change and formation of organic sediments that have deleterious effects on fuel systems and engine components. An extensive review of this problem of instability in liquid fuels is given by Batts (1). Stabilization of these products can be carried out by hydrotreatment, but this method is too expensive. On the other hand, classical antioxidants are ineffective. In spite of studies made, degradation reaction

mechanisms are still not well-known. In order to control or arrest the instability of L.C.O. gas-oils during storage using efficient stabilizing additives, it is necessary to determine structure and reaction mechanisms involved in these degradation processes. The presence of sulfur compounds, nitrogen heterocycles and condensed ring polycyclic oxidizable hydrocarbon compounds will bring about gas-oils instability which is also influenced by traces metal impurities such as copper. The decisive role of oxidizable sulfur compounds has been determined (2,3). Among the sulfur compounds, the thiophenols, because of their ability to oxidize into sulfonic acids, are the more deleterious (4,5). This observation can be easily rationalized by the fact that condensation reactions between nucleophilic derivatives such as nitrogen heterocycles (6), especially alkylindoles which are electron-rich (7) and electrophilic substrates essentially aromatic in nature, are acid catalyzed. The above mentioned electrophilic aromatic substrates are most likely to result from the presence of oxidizable hydrocarbons in gas-oils (8). Among the condensed ring polycyclic oxidizable hydrocarbons present in the L.C.O. gas-oils, the particular role of phenalene has first been emphasized by Pedley et al. (5). Furthermore phenalenyl radical has been identified in L.C.O. by E.S.R. (9), also phenalene seems to be an obvious choice for model studies of the behavior of oxidizable hydrocarbons in L.C.O. gas-oils.

EXPERIMENTAL

The condensation reaction between phenalenone 1 and 2-methylindole 2 in presence of para-toluenesulfonic acid 3 and spectroscopic NMR and IR data of the isolated compounds have previously been well describe (10,11), as have the two dimensional NMR experiments and hydrogenation reaction to determine the structures of the five tautomers of 2-methylindolylphenalene.

The two isomers 6 and 7 of bis(2-methylindolyl)phenalene have been synthesized as follows:
2-methylindolylphenalanone 10 (0.4mM, 120mg); 2-methylindole 2 (0.4mM, 58mg) (Aldrich Chemical Company) and para-toluenesulfonic acid 3 (0.4mM, 69mg) (Aldrich Chemical Company) were introduced in a round bottom flask and dissolved in 20ml of methanol. This solution was left under magnetic stirring in the dark under argon for 24 hours. The resulting colored green solution was washed with 20ml of an aqueous solution of sodium bicarbonate (saturated) and extracted with 3 * 20ml of ether. A dark precipitate obtained after evaporation on a steam bath was chromatographed on flash silica (Merck silica having particle size 0,040-0,063mm; 230-400 mesh ASTM), using a mixture of dichloromethane/pentane : 1/1 as eluent. We obtained 100mg of 6.
The second isomer 7 (40mg) was obtained using the same procedure in mixing 9 (0.1mM, 30mg); 2 (0.1mM, 13mg) and 3 (0.1mM, 17mg) in 15ml of methanol. The NMR and IR spectroscopy data of these two isomers have been described previously (10).

RESULTS AND DISCUSSION

Our work provide further informations on the origin of coloration and sediment formation in L.C.O. gas-oils. The pioneering work in this area is the one of Pedley et al. (5,12), who reacted 2-methylindole in methanol with either phenalanone or phenalenone in

presence of paratoluenesulfonic acid. In the first case 2-methylindolylphenalene was isolated, whereas in the second case bis(2-methylindolyl)phenalene was obtained.

In order to understand these degradation reactions which occur in L.C.O. gas-oils during storage, we have studied the condensation reaction between the phenalenone 1 and 2-methylindole 2 in presence of stoichiometric amount of para-toluenesulfonic acid 3 in methanol. We have shown that this reaction leads to a complex mixture of compounds. Seven sets of compounds have been isolated by chromatography and spectroscopically identified (Fig.1). The mechanism of this reaction has been studied and experimentally supported (10).

Phenalene 4, phenalanone 8 result from a disproportionation reaction of a key intermediate, similar to the one isolated by Murata (13) during the reduction of phenalenone with $NaBH_4$.

The 2-metylindolylphenalene 5 and bis(2-methylindolyl)phenalene 6 and 7 exist under the form of a complex mixture of tautomers.

The tautomerism between the five structures A,B,C,D,E of 2-methylindolylphenalene 5 has been studied in great details by Tort et al. (13) using two dimensional high field (500 MHz) NMR spectroscopy. The relative proportions of each tautomer could be determined using the integration of the ^1H signals of the methylene groups and of the indole methyl group (Fig.2). The bis(2-methylindolyl)phenalene is in fact a mixture of two isomers 6 and 7, each one existing under the form of tautomers. The ^1H NMR spectrum of this mixture is too complex to be analyzed. The isomer 6 and 7 could be obtained separately by reacting 1 equivalent of 2-methylindolylphenalanone 10 with 1 equivalent of 2-methylindole 2 and 1 equivalent of 2-methylindolylphenalanone 9 with 1 equivalent of 2-methylindole 2 in presence of para-toluenesulfonic acid in methanol. The tautomerism between the four structures F,G,H,I of 6 and the two structures J,K of 7 have been determined by NMR spectroscopy (Fig.3). These structures have also been confirmed by catalytic hydrogenation reactions on PtO_2 of each mixture of tautomers (Fig.2 and Fig.3).

As phenalene 4 oxidizes easily into phenalenone 1 (12,14), it can be assumed that the monoindolylphenalenones 11 to 13 and bis(indolyl)phenalenones 14,15 have respectively their origin in monoindolylphenalene 5 and bis(indolyl)phenalenes 6 and 7. However as the reaction has been carried out under argon, the latter oxidation process might have been occurred by disproportionation reaction. We have shown that phenalenone 1, in presence of 2-methylindole 2 and para-toluenesulfonic acid 3 lead to an unstable intermediate which disproportionates to form 5, 11, 12 and 13. Compounds 6, 7, 14 and 15 can be formed in the same way by reaction of 11, 12 or 13 with 2 in acid medium. Furthermore, 5, 6 and 7 are unstable and oxidize easily into the corresponding ketones in presence of air and light. These oxidation reactions seem to take place via the corresponding phenalenyl radicals which have been observed by U.V. spectroscopy of 5, 6 and 7 in chloroform solutions.

It is now clear that as soon as phenalenone is present in L.C.O. gas-oils, it will condense in presence of acid with nitrogen heterocycles such as 2-methylindole to form products which are colored, and insoluble in L.C.O. gas-oils, especially when they are in the

form of ammonium salts of the acid which has played the role of catalyst for the condensation reaction.

Questions which arise from this work are :
- what is the origin of phenalene or phenalane correlated structures?
- does phenalene proceed from phenalane by dehydrogenation?
- is it possible to arrest the phenalene oxidation, using classical anti-oxidants ?

The oxidation of phenalene into phenalenone , which occurs via the phenalenyl radical as we have seen, is likely to proceed by a classical chain reaction mechanism, where the first initiation step yielding the phenalenyl radical would result from the abstraction of one of the allylic-benzylic hydrogen by triplet oxygen which is not thermodynamically favored, but could be possible in this case with the highly delocalised phenalenyl radical formed. This oxidation reaction could also involve an ene reaction (15) of singlet oxygen on phenalene, especially as the phenalenone is known to be an efficient sensitizer (16) and could lead to the formation of an alkoxy peroxy radical, which as the phenalenyl, can play the role of propagating species. The role of a classical antioxidant such as 2,6-ditertiobutyl 4-methylphenol would be to quench these propagating species by being itself oxidized or dimerized. We have shown that 2,6-ditertiobutyl 4-methylphenol as well as α-tocopherol are inefficient in inhibiting the oxidation of phenalene into phenalenone. This means that phenalene oxidizes faster than these antioxidants.

The origin of phenalene or phenalane is a more difficult question. L.C.O. gas-oils have their origin in fluid catalytic cracking of vacuum distillates of petroleum crudes. During this process, aromatization might occur to generate structures similar to those also present in asphaltenes. It was therefore of interest to know whether it would be possible to interconvert phenalene, phenalenone, phenalane and phenalanone by oxido-reductive processes. We have demonstrated that phenalane might be oxidized under mild conditions using 20% $VO(acac)_2$, oxygen in refluxing methanol. The phenalane can also be dehydrogenated into phenalene with sulfur or DDQ. In addition, we have oxidized phenalenone by ozone into ketal lactone and 1,8-naphthalic anhydride . The latter compound is formed during the aging of asphalt (17).

Accordingly, it does not seem unreasonable to postulate that the phenalenic derivatives could be partly at the origin of the sensitivity of asphaltenes to oxygen leading to asphalt aging. Phenalene type structures can indeed be found in asphaltenes models which result from spectroscopic analysis (18), although the determination of asphaltene structural composition is presently a matter of controversy (19).

CONCLUSION

The condensation reaction between phenalenone and 2-methylindole in presence of para-toluenesulfonic acid leads to a complex mixture of products which is more complex than it was initially described by Pedley et al. (12). The compounds reported are representative of the structures responsible for the color and sediments observed in unstable L.C.O. gas-oils. The oxidation of phenalene into phenalenone via the phenalenyl radical plays a crucial role in the condensation reaction and in the color and sediment formation. This oxidation reaction is

not inhibited by classical antioxidants. Phenalane and phenalenic structures could be reasonably considered partly representative models of the structures at the origin of asphalt aging.

ACKNOWLEDGMENTS

We would like to thank the Elf Company for their generous financial support especially for a fellowship to Frederic Tort. The results presented here are part of his PhD thesis. We wish to thank also the University of Aix-Marseille III, the CNRS, the Region PACA and the French Ministry of Research for financial assistance.

LITERATURE CITED

(1) Batts, B.D. and Zuhdan Fathoni, A., Energy and Fuel, 5, 2 (1991).
(2) Daniel, S.R. and Henemann, F.C., Fuel, 62, 1265 (1983)
(3) Loeffler, M.C. and Li, N.C., Fuel, 64, 1047 (1985)
(4) Offenhauer, R.D., Brenau, J.A. and Miller, R.C., Ind. Eng. Chem., 49(8), 1265 (1957)
(5) Pedley, J.F. and Hiley, R.W., Fuel, 67, 469 (1988)
(6) Dorbon, M. and Bemasconi, C., Fuel, 68, 1067 (1989).
(7) Pedley, J.F., Hiley, R.W. and Hancock, R.A., Fuel, 66, 1646 (1987).
(8) Bhan, O.K., Tang, S.Y., Brinkman, D.W., Green, J.B. and Carley, B., Fuel, 67, 227 (1988).
(9) Senglet, N., Faure, D., Des Courieres, T., Bernasconi, C. and Guilard, R., Fuel, 69, 203 (1990).
(10) Tort, F., Waegell, B., Germanaud, L. and Bernasconi, C., Fuel Science and Technology International, (1991) accepted for publication.
(11) Tort, F., Waegell, B., Zahra, J.P., Bernasconi, C., Germanaud, L. Bessibes, C. and Bounoure, J., submitted for publication.
(12) Pedley, J.F., Hiley, R.W. and Hancock, R.A., Fuel, 68, 27 (1989).
(13) Sujikara, Y., Kawanaka, H. and Murata, I., Angew. Chem. Int. Ed. Engl.,28, 1268 (1989).
(14) Boekelheide, V. and Larabee, C.E., J. Amer. Chem. Soc., 72, 1245 (1950).
(15) Pagni, R.M., Burnett, M.N. and Hassaneen, H.M., Tetrahedron, 38, 843 (1982).
(16) Oliveros, E.P., Suardi-Murasecco, T., Aminian-Saghafi, Braun, A.M. and Hansen, H.J., Helv. Chim. Acta., 74,79 (1991).
(17) Petersen, J.C., Barbour, F.A. and Dorrence, S.M., Anal. Chem., 47, 107 (1975).
(18) Latif, H.A, Al-Ghannam, A.K. and Al-Rawi, J.L., Fuel, 69, 519 (1990).
(19) Speight, J.G. and Plancher, H., Proceedings Vol.II, International Symposium "Chemistry of bitumens", Rome (Italy), June 5-8 (1991).

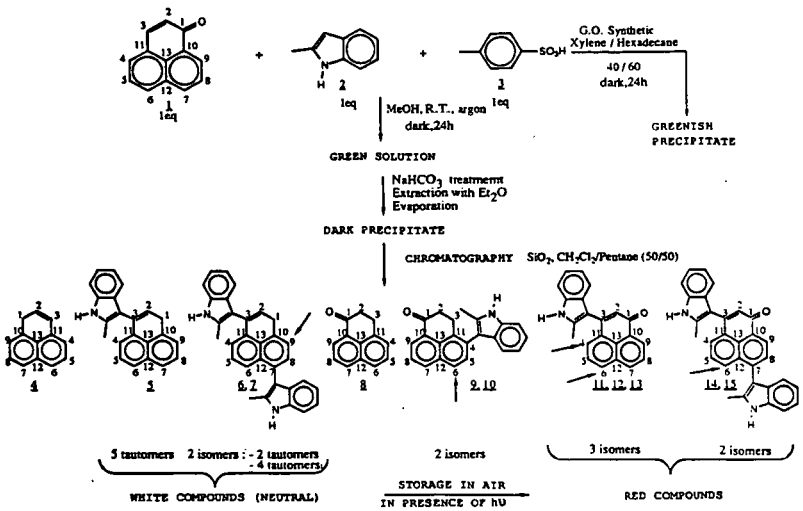

Figure 1: Compounds isolated after reaction of phenalenone 1 with 2-methylindol 2 in presence of stoichiometric amount of para-toluenesulfonic acid 3.

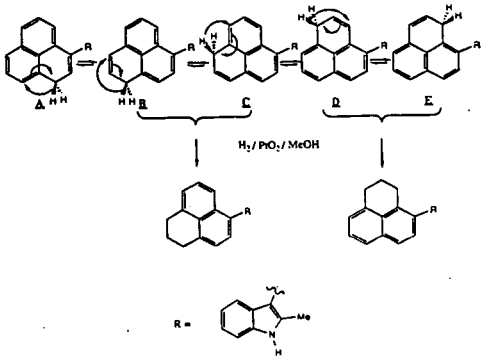

Figure 2: Tautomers of 2-methylindolylphenalene 5.

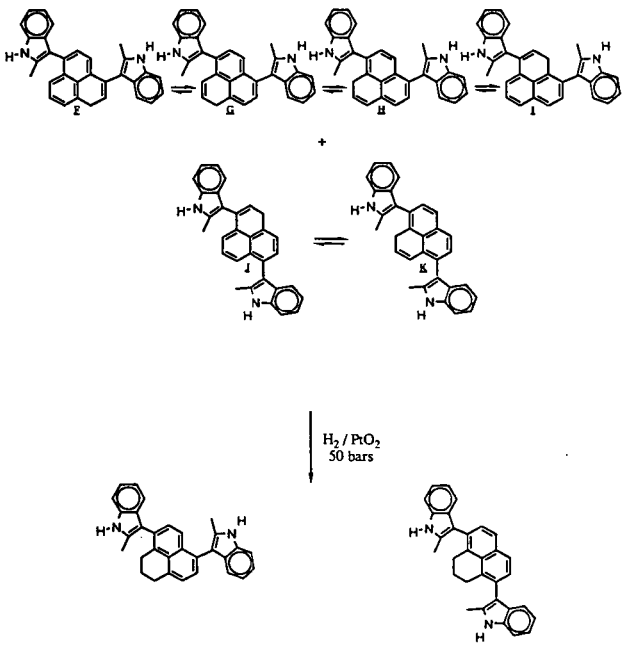

Figure 3: Tautomers of bis(2-methylindolyl)phenalene 6 and 7.

AGING OF COLD-MIX ASPHALT PAVEMENTS

J. Shiea*, S. Eser, Y. Liu, F. Firouzkouhi, R. Arumugam, P. G. Hatcher

Fuel Science Program, Department of Materials Science and Engineering
The Pennsylvania State University, University Park, PA 16802

Keywords: Emulsified asphalt, pavement, aging.

INTRODUCTION

One type of cold-mix asphalt is emulsified asphalt which is a mixture of unheated mineral aggregate with a dispersion of asphalt cement in water that contains a small amount of emulsifying agent. Emulsified asphalts offer the advantages of more favorable economics and less polluting operations which are more commonly used for medium and light-traffic than heavy traffic applications [1]. The focal point of our research on asphalt pavements is the emission of volatile organic compounds (VOC) from different cold-mix formulations[2]. It appears, however, that the emission (or retention) of volatiles is closely related to the aging of the cold-mix asphalt pavements. The objective of this study is to investigate the changes in the chemical composition of the emulsified asphalt pavements as a result of aging. We have analyzed the samples of pavements aged in-place on the roads from 9 months to 10 years by distillation, FTIR, GC, and GC/MS. Two different formulations of emulsified asphalts used in this study are a proprietary cold-mix (HGP) developed by Heilman Pavement Specialties, Inc, Freeport, PA and Pennsylvania State Department of Transportation standard cold-mix prepared with E-5 emulsion (FB-1).

EXPERIMENTAL

Along with the fresh asphalt samples, two, four, six, and ten year-old HGP pavements and , nine month and eight year-old FB-1 pavements were sampled from local roads exposed to similar climate and traffic load in Beaver and Armstrong counties in Pennsylvania. In laboratory, fresh samples of the two cold-mix asphalts were exposed to air under ambient conditions in a fumehood for fifty days.

Distillation tests were conducted on fresh and aged asphalt samples using a standard apparatus and procedure (AASHTO T 59-86, ASTM D-244-83 a) with some modifications[3]. A maximum temperature of 700°F was used in the distillation tests, collecting distillates also at lower temperatures (e.g., 350°F and 500°F). The distillates were analyzed in a Perkin-Elmer 8500 gas chromatograph with fused silica capillary column (30 m X 0.25 mm) coated with 50% methyl- and 50% phenylpolysiloxane (Rtx 50; Restek Co.) and in a Kratos MS-80 gas chromatograph / mass spectrometer.

FTIR analysis of the fresh and aged asphalt samples was carried out using a Digilab FTS-60 Infrared spectrometer. The samples were prepared as thin films on KBr windows from chloroform extracts obtained after soaking the asphalt samples in chloroform for 24 h . To obtain the FTIR spectra 64 scans were collected and averaged with a resolution of 2 cm^{-1}.

RESULTS AND DISCUSSION

The results from the GC and GC-MS analyses of the distillates from the fresh asphalts showed that the FB-1 distillates are dominated by normal and branched octane (C_8) and nonane (C_9) in

* Present Address: Department of Chemistry, National Sun Yat-Sen University
Kaohsiung, Taiwan, 80424

addition to higher alkanes with carbon numbers C_{10} through C_{17} and traces of alkylbenzenes and alkylcyclohexanes. The distillates obtained from HGP, on the other hand, consist principally of long chain normal and branched alkanes with nine to sixteen carbon atoms (C_9 to C_{16}). In addition, alkylbenzenes and alkylnaphthalenes (C_7 to C_{13}) as well as alkylcyclohexanes and alkyltetralins (C_9 to C_{15}) are present at low concentrations. As summarized in the chromatograms shown in Figure 1, the hydrocarbon additives in FB-1 are much more volatile than those in HGP, considering that the same asphalt cement was used in both HGP and FB-1.

The high volatility of the hydrocarbons in FB-1 was also demonstrated upon exposing the fresh samples of the two asphalts to ambient conditions in a fume hood for 50 days. After 50 days all the distillable hydrocarbons from FB-1 was lost, while HGP retained a major fraction (30% by volume) of the distillable hydrocarbons. The gas chromatogram of the distillate obtained from the exposed HGP is shown in the chromatogram c in Figure 1. It is interesting to note that both low and high ends of the hydrocarbons are absent in the distillate obtained from this sample. The distillation of the aged pavements heated to a maximum temperature of 700°F showed that distillate yield first decreased (from 3.5 mL in fresh sample to 1 mL in 4 year-old) and then increased (to 1.3 mL in 6 year-old sample and to 2.7 mL in 10 year-old sample) with the further increase in age. Figure 2 shows the gas chromatograms of the distillates obtained from the fresh mix and 2, 4, 6, and 10 year-old HGP pavement samples. No data were obtained for the FB-1 samples since the aged FB-1 pavements did not yield any distillate. Similar to the 50-day exposed asphalt,the aged HGP samples show different hydrocarbon distributions from that of fresh HGP. It can be seen that as the age of the samples increases, the distribution of dominant hydrocarbons shifts gradually from the higher mass region (C16 to C20 for fresh and 2 year old samples) to lower mass region (C14 to C18 for the samples older than two years). The distribution of the unresolved complex mixture (UCM), extending from retention time 20 min to 50 min., shows the same trend as that of the identified hydrocarbons in the samples- a decreasing maximum with increasing age. The total intensities of the peaks for selected isoprenoids (C14, C15, C16-isoprenoids, pristane, and phytane) and the corresponding normal alkanes (n-C14, n-C15, n-C16, n-C19, and n-C20) were calculated by integration. It was found that the relative ratio of the selected isoprenoids to the corresponding normal alkanes increased gradually with the increasing age.

These changes in the chemical composition of hydrocarbons in the asphalt pavements with the increasing age can result from various processes such as evaporation, microbial degradation, oxidation, and thermal/catalytic cracking and polymerization reactions. Possible effects of these processes are discussed below in relation to the experimental data obtained in this study.

According to a commonly used definition, volatile organic compounds (VOC) are defined as the chemicals which has 0.002 psi vapor pressure at 0°C. According to this definition, almost all the distillable hydrocarbons found in FB-1 (C8 to C9) can be classified as VOC. It is not surprising to find that these hydrocarbons evaporated after exposure to air for 50 days. The evaporation of light hydrocarbons from the samples also indicates that the hydrocarbons were bound loosely in the asphalt. This is probably the reason why none of the distilled hydrocarbons was observed in the 9 month and 8 year-old FB-1 pavements. The evaporation of the lower molecular weight hydrocarbons (C9 to C12) in HGP also explains the loss of lighter ends in the aged samples, as shown in Figures 1 and 2. The retention of higher molecular weight hydrocarbons (over C13), in HGP asphalts over extended periods of time (up to 10 years) is, however, noteworthy, and indicates that the hydrocarbons are more strongly bonded in HGP and are not readily released to the atmosphere. Evaporation alone does not, however, explain all the changes observed with aging.

It is well known that aerobic or anaerobic microbial degradation plays an important role in petroleum alteration processes and that anaerobic degradation is much slower than aerobic decay[4]. A suggested order of vulnerability of hydrocarbons to microbial degradation follows[5]:

n-alkanes > branched alkanes > low ring cyclic alkanes > aromatics > high ring cyclic alkanes.

A selective depletion of n-alkanes by microbial activity should result in decreasing the ratio of the concentration of n-alkanes to that of the isoprenoids. A gradual decrease in this ratio with age in the pavement samples suggests that anaerobic biodegradation may have contributed to the observed chemical changes. Microbial degradation does not, however, explain why the hydrocarbon distribution shifted from the higher mass (C16 to C20) to the lower mass region (C14 to C16) with the increasing age. Since the low molecular weight hydrocarbons is more readily consumed by the bacteria[4], a shift to a higher, not to a lower, mass region should be expected in the distribution of the hydrocarbons with the increasing age.

The results from the 50-day aging of the asphalt exposed to air combined with those obtained with the aged pavements strongly suggests that thermal/catalytic chemical reactions (oxidation, cracking, and polymerization) played a key role in producing the observed chemical changes. The shift in hydrocarbon distribution to lower mass regions in aged HGP pavements can be explained by cracking and/or polymerization of long paraffin chains. The dramatic change in the composition of distillable hydrocarbons obtained from the 50-day old sample, the complete removal of heavy ends in addition to light ends over a relatively short time period, can be explained by the polymerization of high molecular paraffins (in the presence of oxygen and light). For the aged pavement samples starting as compressed and sealed asphalts with limited access to oxygen and light, polymerization reactions should be expected to proceed much more slowly with thermal/catalytic cracking reactions becoming important over extended periods of time. It can be seen that the major change observed from the fresh to 4 year-old sample is the shift in the hydrocarbon distribution to lower masses, in addition to increasing ratio of isoprenoids to n-alkanes. This trend, combined with lower distillate yields obtained with 2 and 4 year-old samples, can be explained by polymerization of high molecular weight, but distillable alkanes to produce higher molecular weight nondistillable hydrocarbons. The increasing ratio of isoprenoids to n-alkanes can be attributed to higher reactivity of n-alkanes than that of isoprenoids in polymerization reactions and/or to bacterial degradation processes. The changes in going from 4-year to 10-year old sample are much less pronounced without a major shift in hydrocarbon distribution. The increasing distillate yield in going from the 4 year -old to 6 and 10 year-old pavements suggests that cracking reactions which produced distillable hydrocarbons were important in aging from 4 to 10 years period. The increasing concentrations of aromatic compounds with aging in this period also suggests that thermal/catalytic cracking reactions had taken place. Possible catalytic effects[6,7] of the aggregates used (limestone and blast furnace slag) and temperature increases within the pavement because of oxidation reactions are plausible conditions for thermal/catalytic cracking reactions which can occur over extended periods of time under the pavement conditions.

FTIR spectra obtained for the chloroform extracts of the fresh and aged samples FB-1 and HGP are shown in Figures 3. The spectra of the FB-1 fresh mix, 9 month- and 8 year- old pavement samples shown at the top of Figure 3 indicate that oxidation and cracking or aromatization reactions had taken place in the time period from 9 months to 8 years. The spectra of the fresh and 9-month old samples appear to be quite similar. The most notable change in the FTIR spectrum of the 8-year old sample is the appearance of a strong band in 1700 cm^{-1} region which is assigned to carbonyl groups, indicating the incorporation of oxygen into the asphalt pavement similar to the previous data obtained on different hot-mix asphalt samples[6,8,9]. Other distinct changes observed in the spectrum of the 8-year old are the stronger aromatic C-H stretch and out-of-plane bending bands at 3050 cm^{-1} and at 700-900 cm^{-1}, respectively, coupled with a decreased intensity of 2920 cm^{-1} peak relative to that of 2950 cm^{-1} peak. These changes can be attributed to cracking/aromatization reactions which would result in the shortening of paraffinic chains and removal of alkyl side chains from the aromatic rings. Instead of relatively strong absorption at 860 cm^{-1} seen in fresh and 9 month-old samples, assigned to isolated hydrogen, 8 year-old sample shows a more intense peak at 750 cm^{-1} which is assigned to four neighboring hydrogens on an aromatic ring. The shift from 860 cm^{-1} to 750 cm^{-1} indicates the formation of new aromatic rings and/or the removal of alkyl chains from the existing aromatic rings. The increasing intensity

of the aromatic carbon ring stretch band at 1600 cm^{-1} can be taken as a supporting evidence for the formation of new aromatic rings from alkanes.

FTIR spectra of the HGP series shown at the bottom of Figure 3 shows a more gradual change in composition than the FB-1 series, except for the broad bands observed at 3300-3600 and 1100 cm^{-1} region of the 10 year-old sample. These bands are tentatively assigned to water. Parallel to the behavior of the FB-1 samples, 9 month-old HGP sample has a very similar spectrum to that of the fresh asphalt. The 4 year-old sample shows the appearance of carbonyl band at 1700 cm^{-1} which becomes stronger in the 10 year-old sample. The relative intensity of this band however is much lower than that observed in the 8 year-old FB-1 pavement, indicating that the HGP pavement is more resistant to oxidation. Since no oxygenated compounds were observed in the distillates obtained from HGP samples, it can be inferred that only the high molecular weight constituents of the asphalt incorporate oxygen. As different from the trend observed for the FB-1 pavement, aromatic C-H stretch (3050 cm^{-1}) decreases with the decreasing out-of-plane bending at 860 cm^{-1} as a function of aging. In contrast to FB-1 8 year-old, there is no significant change in the intensity of the 750 cm^{-1} peak (four neighboring hydrogens on the aromatic rings) with the increasing age. These observations may be explained by the coupling of aromatic rings with other aromatic rings or aliphatic hydrocarbons during the aging of HGP as opposed to dealkylation or formation of new aromatic C-H functionalities in the aged FB-1 pavement. Another difference between the aging behavior of HGP and FB-1 is that in the period between 9 months and 10 years aliphatic functionalities in HGP do not show much change in structure.

The differences in the aging behavior of HGP and FB-1 pavements can be mostly attributed to the different abilities of these pavements in retaining the smaller molecular weight (distillable) hydrocarbons. The presence of these hydrocarbons at high concentrations in HGP pavements is believed to be responsible for their lower susceptibility to oxidation.

CONCLUSIONS

The aging behavior of the pavements from the two different emulsified asphalt mixes FB-1 and HGP are rather different in that FB-1 shows more extensive oxidation and thermal degradation whereas HGP is subjected to subsequent polymerization and cracking reactions during aging. These differences are believed to be due to the differences in the formulation of the two mixes, mainly to the ability of the HGP pavements to retain the distillable hydrocarbons.

ACKNOWLEDGEMENTS

This study has been partially funded by PA Commonwealth's Ben Franklin Partnership Program. All the asphalt samples and partial funding were provided by the Heilman Pavement Specialties, Inc. Helpful discussions with William Heilman and Glenn Heilman of Heilman Pavement Specialties, Inc. are gratefully acknowledged.

REFERENCES

1. "Asphalt Cold Mix Manual," Asphalt Institute Manual Series No: 14, Third Edition.
2. Eser, S., Shiea, J., Firouzkouhi, F., and Hatcher, P. G., 5th International Pavement Management /Maintenance Exposition and Conference, 4R Conference and Road Show, 1991 Compendium, p. 227, 1991.
3. "A Study of Volatile Organic Compounds in Cold Mix Asphalts," S. Eser and P. G. Hatcher, Year End Report to Ben Franklin Technology Center of Center and Northern Pennsylvania, Inc., September 1991.
4. Ward, D.M., Atlas, R.M.,Boehm, P., and Calder, J.A., AMBIO 9, 277, 1980.
5. Tissot, B. P. and Welte, D. H., "Petroleum Formation and Occurrence, a New Approach to Oil and Gas exploration," Spring-Verlag, Amsterdam, 1984.
6. McKay, J. F., Preprints, ACS Div.Petroleum. Chem , Vol. 35, 496, 1990.

7. Petersen, J. C., Barbour, F. A., and Dorrence, S. M., Proceedings of the Association of Asphalt Paving Technologies, Vol. 43, 162, 1974.
8. Jemison, H. B., Burr, B. L., Davison, R. R., Bullin, J. A., and Glover, C. J., ACS Div.Petroleum. Chem , Vol. 35, 490, 1990.
9. Dorrence, S. M., Barbour, F. A., Petersen, C. J., Anal. Chem. **46**, 2242, 1974.

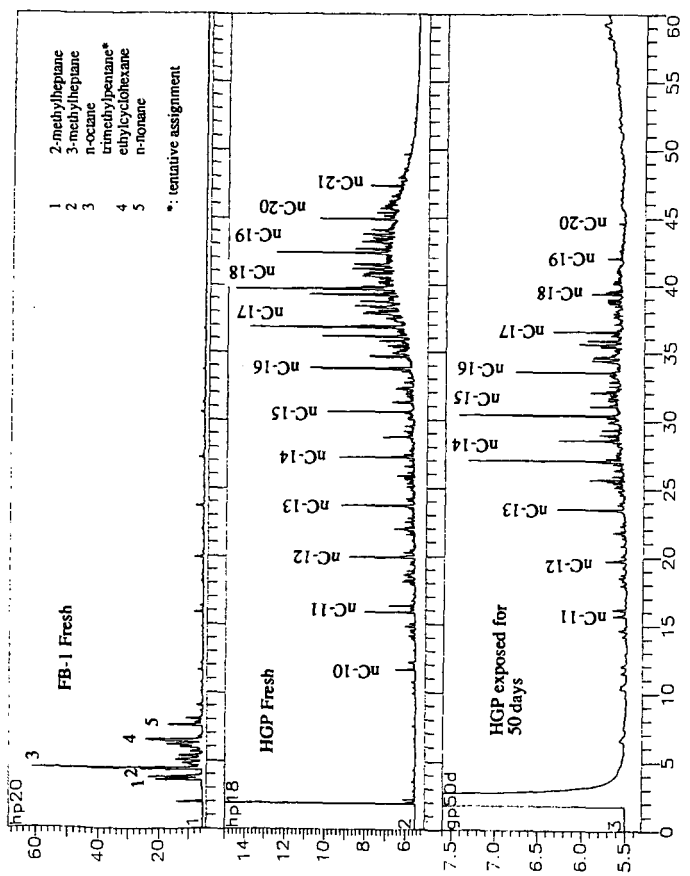

Figure 1. Gas chromatograms of the distillates obtained from FB-1 fresh (top), HGP fresh (middle) and HGP exposed to air and light for 50 days in a fumehood.

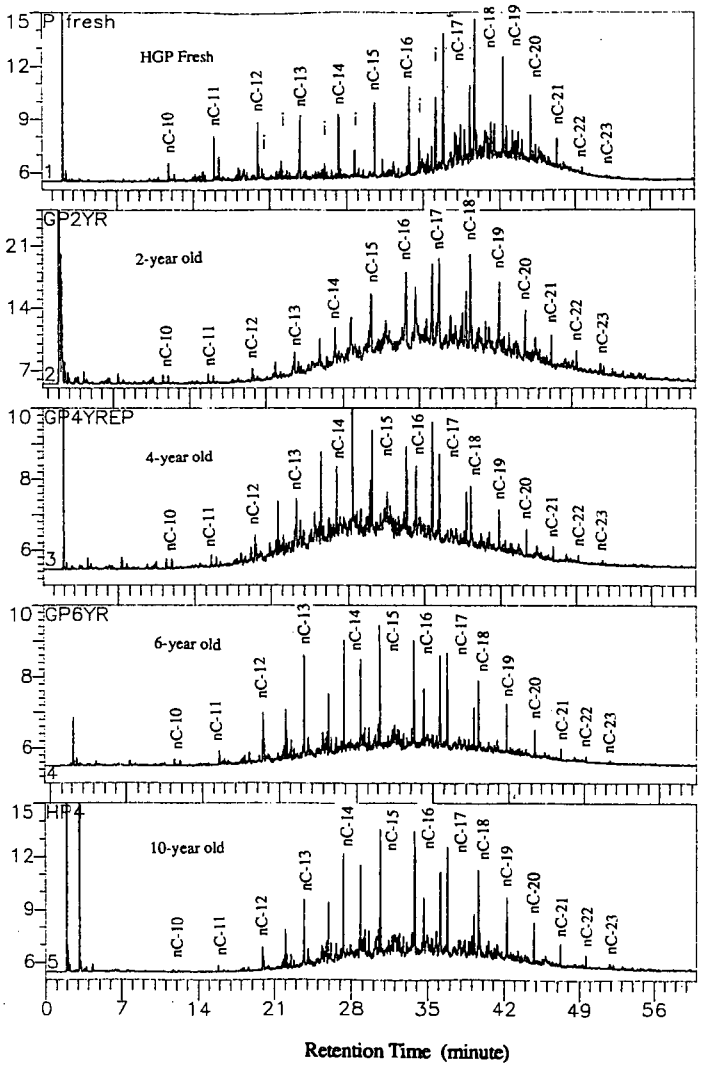

Figure 2. Gas Chromatograms of the distillates obtained from fresh HGP and 2, 4, 6, and 10 year-old pavement samples.

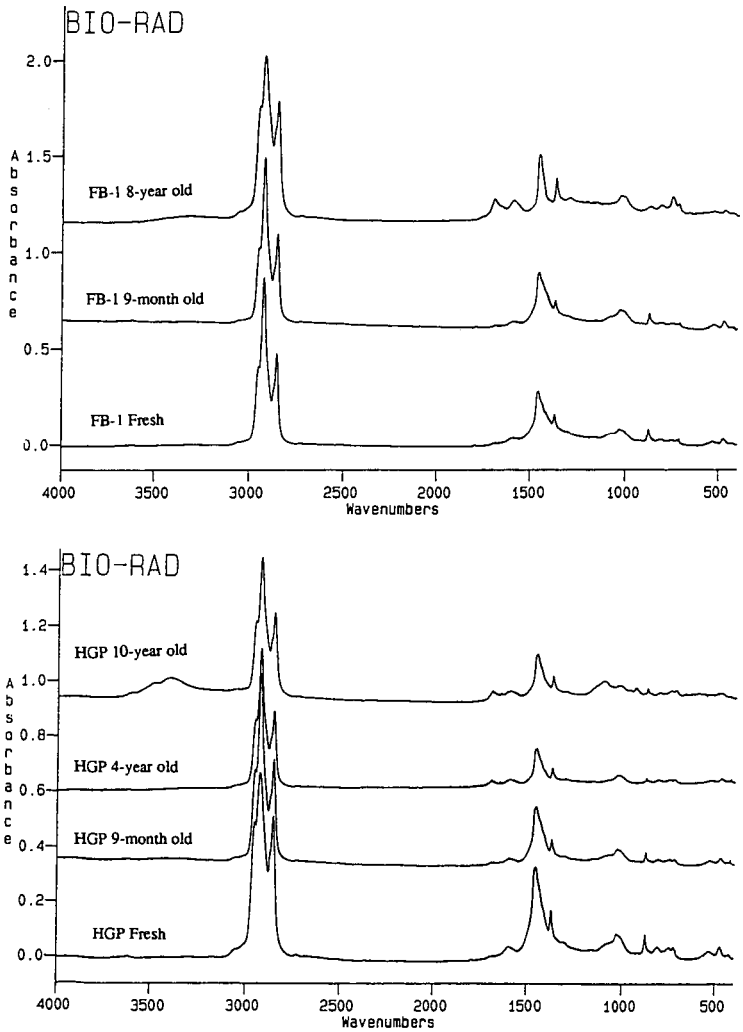

Figure 3. FTIR spectra of fresh and aged FB-1 and HGP pavements extracted with chloroform.

Physical Hardening of Paving Grade Asphalts as Related to Compositional Characteristics

H.U. Bahia and D.A. Anderson
The Pennsylvania Transportation Institute
Research Office Building
University Park, PA 16802

Keywords: Physical hardening, isothermal volume change, T_g, wax content, DSC.

Introduction

In a recent investigation of the rheological properties of paving grade asphalts a new hardening phenomenon was observed. The phenomenon, called "physical hardening" by the authors was observed to cause significant isothermal changes in the creep compliance and was shown to relate to the glass transition phenomenon of the asphalts (1). Physical hardening is similar to what is known as physical aging for many amorphous solids such as polymers and plastics. To explain physical hardening, creep compliance, glass transition, and isothermal volume measurements were made on a number of selected asphalts. The isothermal changes in creep compliance were related to volume measurements and a hypothesis was introduced to explain the hardening mechanism. Being a newly discovered phenomenon, there has been speculation regarding the mechanism responsible for the hardening. Crystallization of waxes and internal structuring of highly polar fractions have been offered as possible mechanisms. Data collected by the authors, however, indicates that the hardening is simply a collapse of free volume as the asphalt passes through the glass transition region. The different measurements obtained by the authors clearly proves that physical hardening of paving grade asphalts is no different than physical aging of other amorphous solids that are free of waxes or any crystallizable fractions.

The purpose of this paper is to give a brief review of the physical hardening behavior of selected asphalts and to present creep compliance and volume measurements that support the authors' hypothesis that physical hardening is the result of free volume collapse. Data collected by others for wax contents and melting points of waxes separated from the same asphalts are used to discuss relations between hardening and crystallized fractions. The work reported here is part of the Strategic Highway Research Program (SHRP) project A-002A, Bituminous Characterization and Evaluation.

Effect of Hardening on Creep Response

Using the bending beam rheometer (2) beam specimens of asphalt were tested for creep compliance in three point bending after storage for different times at several isothermal temperatures. Testing was done at four temperatures below -5 °C (23 °F) and for isothermal storage times ranging between 30 minutes and four months. The effect of isothermal storage

was consistently observed to decrease the creep compliance (increased stiffness). An example of the effect for one of the SHRP asphalts is shown in figure 1. The test results indicate that the creep compliance is affected by the isothermal storage temperature (T), isothermal storage time (t_i), and asphalt source (3). The lower the temperature, the higher the hardening level and rate. As a function of t_i, the hardening rate was observed to be very rapid at initial t_i, decreases rapidly with t_i, and not reach equilibrium within the time limits of experiment (four months).

Hardening and Resemblance to Temperature Effect

One of the basic characteristics of physical aging of many amorphous materials is that its effect on the viscoelastic properties is similar to the effect of temperature (4). For thermo-rheologically simple materials, the effect of temperature is reflected by a shift in the relaxation spectrum to longer times as the temperature is reduced without changing the shape of the master curve. The same behavior was observed for the asphalt cements that were tested. Figure 2 depicts creep compliance curves for asphalt AAM-1 measured after 30 minutes and 60 days of isothermal storage at -15°C. When plotted on logarithmic scale, the compliance versus loading time curves can be perfectly superimposed by a one dimensional shift along the loading time scale. The simplicity of the hardening effect was confirmed for many different asphalts at all testing temperatures at which physical hardening was observed (3). Therefore the effect of physical hardening on the creep compliance can be defined by a single parameter called the hardening shift factor, a_{t_i}, in which the shape of the relaxation spectra is unchanged by physical hardening.

Similar to other thermo-rheologically simple materials, asphalts are believed to change their properties with temperature mainly due to changes in free volume which decreases when the temperature is decreased (5,6). The decrease in free volume results in more closely packed molecular arrangement and reduced molecular mobility. During physical hardening, time dependent collapse of free volume is hypothesized to result in volumetric creep that continuously increases the degree of packing, thus producing hardening.

Isothermal Volume Measurements

To verify the free volume collapse hypothesis, isothermal volume measurements were obtained for eight asphalts at selected temperatures. A specially designed dilatometer equipped with precise capillary tubes was used to measure the volume changes for a period of 24 hours. The dilatometers were kept in a liquid bath controlled to within ± 0.1 °C and volume changes were measured to within 0.0002 ml. Figure 3 is an example of the measurements for three of the asphalts at the temperature of -15°C. Curves shown in the figure represent best fit curves for three independent replicates per asphalt. Using the isothermal-isobaric volume measurements, the reduction in volume relative to an initial volume (initial equals 30 minutes after quenching) were correlated to the hardening shift factors,, a_{t_i}, obtained from the creep compliance measurements. Isothermal ages of 2, 6, and 24 hours were used and the correlations were very high (R^2=92%) as shown in figure 4 for all asphalts. Each asphalt shows its own relation which, if the free volume hypothesis is true should have a slope that is equivalent to the thermal coefficient of contraction at sub-T_g temperatures (α_g). The slopes have an average slope of 0.45 log(s)/mm^3/g, which can be

converted to an α_g of 4.03 10^{-4}/°C using the average temperature shift function of 0.183 log(s)/°C calculated for these asphalts (3). The value of α_g is within the range of values reported by others (7) and measured in this study. The correlation found between the isothermal volume changes and the isothermal hardening shift factor confirms the analogy between temperature and isothermal storage time and gives strong evidence that favors the free volume collapse hypothesis.

T_g and the Physical Hardening

Physical aging of amorphous solids is known to be predominant below T_g (6,8). In fact, the results of isothermal volume measurements suggest that physical hardening is essentially a continuation of the glass transition phenomenon. When the asphalt is cooled from high temperature its volume shrinkage, which is mainly a reduction in free volume, reaches equilibrium almost immediately. When the glass transition region is approached, the transport mobility of molecules is reduced and, at some point, results in non-equilibrium volumes. At this point the asphalt is in a metastable state causing the material to continuously shrink isothermally. Asphalts, however, have a wide glass transition region that reflects the complexity of their composition and a multiplicity of transition temperatures.

To investigate the relation of the glass transition phenomenon to physical hardening, dilatometeric glass transition measurements were made for the asphalts using the same dilatometers used in the isothermal measurements but equipped with larger capillary tubes and a well-controlled ramping thermal bath. At the rate of 1 °C/min, the volume change in a 10 ml specimen was measured in a cooling and heating mode to an accuracy of 0.002 ml over a temperature range of -60 °C to 40 °C. The measurement clearly reflected a wide transition that for some asphalts extend to temperatures well above 0.0°C. Following the concept of free volume, the deviation of measured volume from the hypothetical thermodynamic equilibrium was used as an indicator of free volume that needs to be recovered (or collapsed) during isothermal storage (1). Figure 5 depicts the relation between isothermal hardening shift factors (a_{ti}) and the estimated deviation from thermodynamic equilibrium volume line. The correlation shown (R^2=85 %) reinforces the finding that free volume entrapped at the onset of the glass transition region is the cause of the meta-stable state that leads to the time dependent physical hardening.

Crystallizable Fraction (Wax) and Hardening

Being observed at low temperatures, and being completely reversible, has lead several researchers to propose to the authors that physical hardening is related to crystallization of waxes in the asphalts. Using a modified Shell method (SMS-1769) (9) the wax contents of SHRP asphalts were measured for SHRP by researchers of INTEVEP-Venezuela (10). The wax contents and the melting points are listed in table 1 for 16 of SHRP asphalts that have different chemical composition and different low temperature creep compliance properties. Figure 6 was prepared to show the correlation of the wax content and the hardening shift factor at -15°C. The shift factors were obtained for each asphalt by measuring the isothermal shift factor needed to superimpose creep response measured after 30 minutes at -15°C on the creep response after 24 hours at -15°C (see figure 2 for shift explanation).

There is a definitive relation between the wax content determined by the Shell method

and the physical hardening, $R^2 > 70$ %. What is surprising, however, is that the melting points of these asphalts are all above 30 °C while the hardening is observed only at temperatures below -5°C.

Hardening Potential and Endothermic Peaks in DSC Thermograms

Differential scanning calorimetry has been used by several asphalt researchers to determine glass and melting transition. In the early 1970's Noel and Corbett (11) compared wax determinations by several traditional methods and indicated that variations as high as 5 fold can be observed when these methods are used for the same asphalts. The authors stated that " the traditional concept of asphalt wax content is of questionable significance." The authors, however, presented DSC thermograms that show clear endothermic peaks at moderate temperatures. The peaks were typical of crystallite melting transitions and therefore led the authors to conclude that asphalts contain some kind of waxes that are not completely crystalline nor completely amorphous. They called the material crystallized fractions and offered a method for calculating them from DSC thermograms. Recently this concept was used by other researchers in the US and in Europe and relations between the crystallized fractions and physical properties were reported (12).

As part of another SHRP project, DSC measurements were conducted on eight of the asphalts used in this study (13). Very distinct endothermic peaks were observed for several of the asphalts in the temperature region of 0.0°C and 90° C, and the enthalpies of these peaks were reported to an accuracy of $\pm$ 10%. Asphalts showing the most hardening and the most isothermal volume change also showed the largest endothermic peaks, Figure 7. Although the temperatures at which these endothermic peaks occur do not correlate well with the melting points temperatures of the waxes extracted from the corresponding asphalt, the peaks are within the same temperature range as the melting points, 30°C to 90°C. In contrast, physical hardening is observed some 30 °C below the melting point temperatures and becomes more pronounced as the isothermal temperature is decreased (3). Further, the physical hardening is completely destroyed by heating the asphalt to 25°C, well below the melting point of the wax.

Discussion

The above results leave no doubt that there is some connection between physical hardening at low-temperatures and the amount of crystallizable or wax fractions in an asphalt. The isothermal volume measurements and the dilatometeric T_g measurements, on the other hand, also suggest that the hardening is caused by the time-dependent collapse of free volume below the glass transition temperature. Further, the creep compliance master curves (not shown here) do not reveal the presence of a crystallizable phase at low temperatures (14). The master curves and the relaxation spectra are smooth and without the shape that would suggest a second low-temperature phase. The only irregularity in the master curve is in the region of the melting point temperatures where a vertical shift in the data is required to produce smooth master curves (15).

Ignoring the temperatures at which these two phenomena--physical hardening and crystallization--occur, the answer could be that volume change is merely caused by the crystallization. The maximum volume change measured for an isothermal time of 23.5 hours

is 0.0025 ml/g for asphalt AAM-1. Considering the wax content of this asphalt, 4.21 percent, a 6 percent volume change in the wax would be sufficient to account for the 0.0025 ml/g volume change. Other studies indicate that a that wax changes volume by 4 to 10 percent upon crystallization. Therefore, it is plausible that crystallization of wax is the source of the low-temperature volume change. There are however a number of points that stands against this hypothesis:

First, the large difference between the melting points of the waxes and the temperature at which the isothermal volume change is being observed cannot be ignored. If dissolution of wax, and the endothermic peaks are observed at high temperatures, why is the hardening observed at much lower temperatures.

Second, physical hardening and isothermal volume change continue for very long times (hardening measured after 4 months for some asphalts). It is highly unlikely that crystallization continues for such long times and continues to effect the creep compliance in such significant way.

Third, the effect of physical hardening on the viscoelastic properties is analogous to the effect of temperature reduction of a thermo-rheological simple material. The rheological properties show no evidence of a second phase at the low temperatures but do seem to account for some orientation of the wax molecules in the region of the melting point temperatures.

Fourth, the rheological behavior of all SHRP asphalts is simple in that creep compliance master curves and the relaxation spectra show no sign of crystallization in the temperature region between -35°C and 60°C.

Conclusions

Circumstantial evidence suggests a link between the wax content and low-temperature physical hardening. A closer examination of the evidence suggests that this link is probably not a cause and effect link but that some third factor is the link between the wax content and physical hardening. Interestingly, both the wax content and the degree of physical hardening appear to increase with the molecular weight of the neutral fraction. Could it be that the molecular weight distribution affects both the percent of wax-like molecules present as well as affecting the low-temperature physical hardening? Most likely this is the case. Therefore, although there is a statistical correlation between measured wax content, DSC properties, and physical hardening it is unlikely that there is a cause and effect relationship between these variables. More research is needed to answer this question.

Acknowledgments

The authors gratefully acknowledge the financial support of the Strategic Highway Research Program (SHRP) under contract A-002A. The authors also acknowledge the cooperation of WRI, the main contractor for the project. The paper represents the views of the authors only, and is not necessarily reflective of the National Research Council, the views of SHRP, or SHRP's sponsors. The results are not necessarily in agreement with the results of other SHRP research activities. They are reported to simulate review and discussion within the research community.

Literature Cited

(1) Bahia, H.U., and Anderson, D.A.," Isothermal Low-Temperature Physical Hardening of Asphalt Binders," Presented at the International Symposium for Chemistry of Bitumens, 5-8 June Rome, Italy, 1991.

(2) Bahia, H.U., Anderson, D.A., and Christensen, D.W., Presented at the AAPT annual meeting, Charleston SC, Feb. 24-26, 1992.

(3) Bahia, H.U., *Low-Temperature Physical Hardening of Asphalt Cements*, Ph.D. dissertation, CE Dept., Penn State, University Park, PA, 1991.

(4) Struik, L.C.E., in W. Brostow and R.D. Corneliussen, *Failure of Plastics*, Ch. 11, p.209, Hanser Publishers, Munich-Vienna-New York, 1986.

(5) Williams, M.L., Landel, R.F., and Ferry, J.D., J. of ACS, 77, 3701 (1955).

(6) Ferry, J.D., *Viscoelastic Properties of Polymers*, 3rd ed., Wiley, New York, N.Y., 1980.

(7) Schmidt, R.J., and Santucci, L.E., Proc. AAPT, 35, 61 (1966).

(8) McKenna, G.B., "Glass Formation and Glassy Behavior," in C. Booth and C. Price (ed.), *Comprehensive Polymer Science*, Vol. 2, Pergamon, Oxford, 311 (1988).

(9) Krom, C.J., J. Inst. Petrol., 54, 239 (1968)

(10 SHRP A-001 Technical program director memorandum concerning wax studies conducted by INTEVEP, Feb. 4 1992, Center for Transportation Research, University of Texas at Austin.

(11 Noel, F. and Corbett, L.W., J. Inst. Petrol., 56,261 (1970)

(12 Brule, B., Planche, J.P., King, G., Claudy, P., and Letoffe, J.M., PREPRINTS, Div. of Fuel Chem.,ACS, 35, No.3, 330 (1990)

(13 Harrison, I., Wang, G., and Hsu, T.C., Final Report, SHRP contract No. SHRP-87-AIIR-05, National Research Council, SHRP, Washington, D.C. 20006.

(14 Anderson, D.A., Christensen, D.W., and Bahia, H.U., AAPT, 60, 437, 1991.

(15 Strategic Highway Research Program, A-002A, "Binder Characterization and Evaluation," Quarterly Report, Technical Section, Subtask 1.2.2.d, WRI, Laramie, WY, September (1990).

Table 1. Properties measured in this study and previuos studies of selected SHRP asphalts

Asphalt Source	Creep Compliance at -15 °C, 120s 1/GPa	Isothermal Shift, log (a_t)	Wax Content% after (10)	Melting Point, °C after (10)	Total Enthalpy j/g after (13)	Temp. of 2nd Endothermic Peak, °C after (13)
AAA-1	43.48	0.42	1.62	35.8	0.27	83.5
AAB-1	14.29	0.67	3.85	62.1	9.94	41.9
AAC-1	7.67	0.93	5.06	65.7	4.00	53.9
AAD-1	35.71	0.57	1.94	50.6	3.48	46.1
AAE	20.80	0.32	1.23	42.5		
AAF-1	4.98	0.83	4.19	59.6	7.93	44.8
AAG-1	2.05	0.24	1.13	33.0	2.42	82.9
AAH	13.5	0.65	4.41	52.8		
AAJ	7.69	0.76	4.91	43.2		
AAK-1	13.89	0.52	1.17	56.1	1.83	47.2
AAL	40.32	0.21	1.23	43.9		
AAM-1	5.71	0.94	4.21	32.9	7.69	42.7
AAP	13.69	0.70	4.77	51.3		
AAU	3.52	0.60	2.35	58.6		
ABC	21.20	0.50	2.90	56.6		
ABD	1.58	0.45	0.81	38.2		

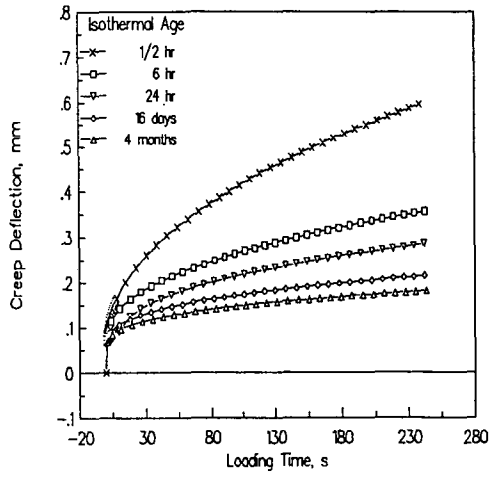

Figure 1. Reduction in creep deflection and rate due to physical hardening at -15°C for asphalt AAF-1.

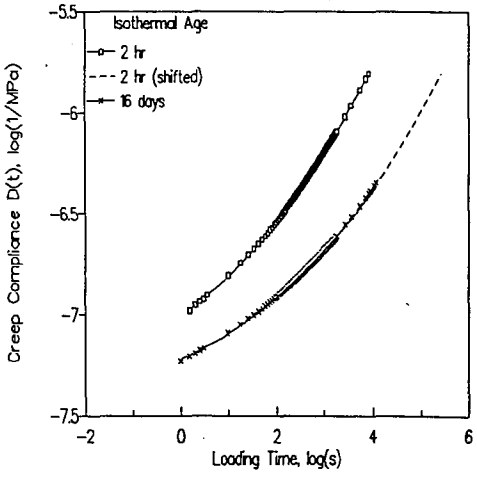

Figure 2. Superposition of creep curves of asphalt AAM-1 measured at isothermal ages of 1/2 hour and 16 days.

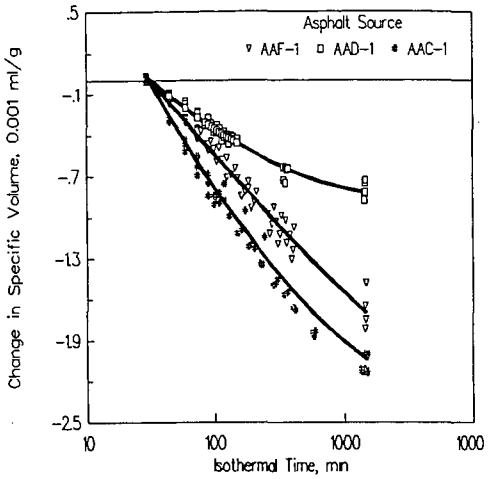

Figure 3. Isothermal Volume measurements for three asphalts at -15°C over a period of 24 hours.

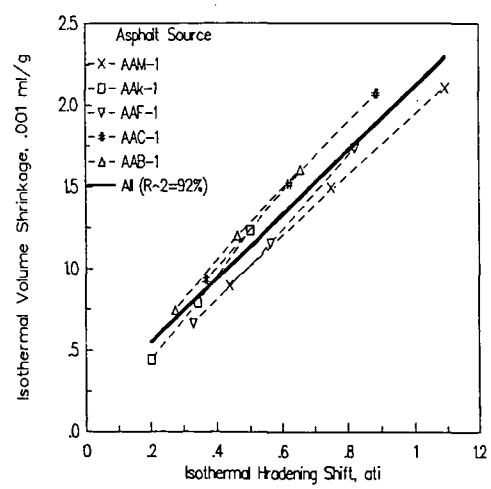

Figure 4. Correlation of volume change and hardening shift at equi-isothermal ages.

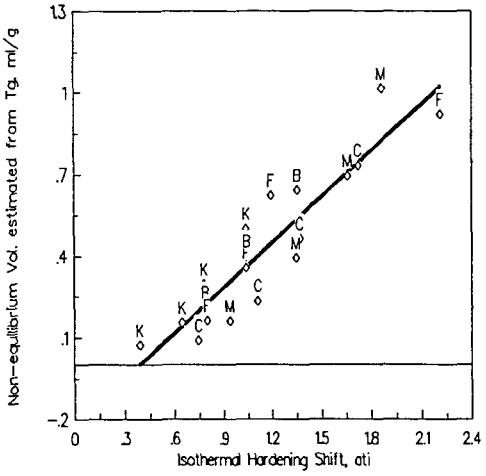

Figure 5. Correlation between hardening shift factors and the estimated deviation from equilibrium volume line.

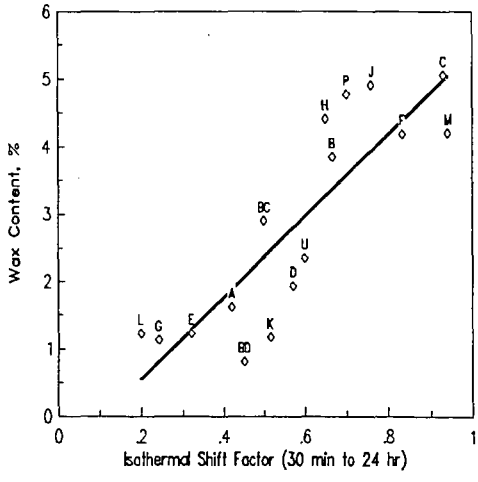

Figure 6. Correlation between hardening shift factor at -15°C and wax content for 16 SHRP asphalts.

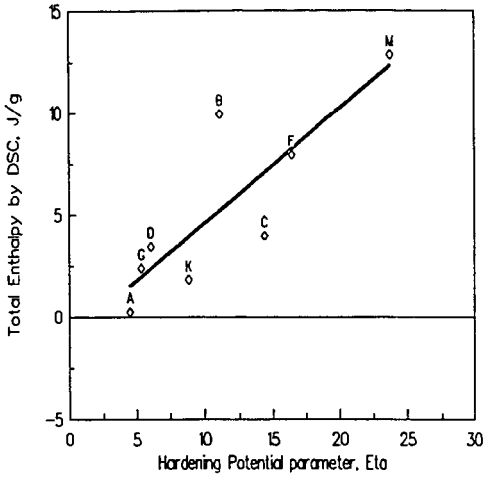

Figure 7. Correlation between total endothermic enthalpy and hardening potential for 8 core SHRP asphalts

A NEW INTERPRETATION OF TIME-DEPENDENT PHYSICAL HARDENING IN ASPHALT BASED ON DSC AND OPTICAL THERMOANALYSIS

P.Claudy, J.M.Letoffe, *F.Rondelez, **L.Germanaud, ***G. King and ***J.P. Planche.

Laboratoire de Thermochimie Minérale, CNRS URA 116,
20 Avenue Albert Einstein, 69621 Villeurbanne Cedex - France

*Université Paris VI, Laboratoire de Physico-Chimie des Surfaces et Interfaces, Institut Curie,
11, rue Pierre et Marie Curie, 75231 Paris Cedex 05 - France

**Centre de Recherche Elf,
BP22 60360 St Symphorien d'Ozon - France

***Elf Asphalt Laboratory,
400 North 10th Street, P.O. Box 1507, Terre Haute, Indiana - USA

Keywords: DSC, Asphalt Physical Hardening, Thermomicroscopy.

INTRODUCTION

As a part of their work for the Strategic Highway Research Program (SHRP), Anderson and Bahia recently reported an important phenomenon in asphalt cement they defined as "low temperature physical hardening" (1,2,3). This effect seems to be caused by a gradual density change that occurs over time when bitumens are held at low temperatures. The mechanical stiffness of the asphalt increases markedly in response to this decrease in volume. They were able to demonstrate that the changing stiffness can be explained by time-dependent shift factors not unlike those used to explain time-temperature superposition in conventional rheological measurements.
In other recent papers (4,5,6,7), Claudy and coworkers used Differential Scanning Calorimetry (DSC) and two thermomicroscopy methods (polarized light and phase contrast) to identify certain molecular associations within asphalt defined as "crystallized fractions". The associating species are more prevalent in the saturates fraction of the bitumen, and thus are thought to be highly aliphatic molecules. Even though Crystallized fractions are more evident at low temperatures, they begin to form at temperatures as high as 80°C, and then continue to precipitate as the asphalt cools.
This study was designed to characterize the temperature and time dependent structural changes that occur in the eight SHRP core asphalts. There are two important questions to be answered: "Are the newly observed phases truly crystalline?" and "Does the formation of multiple phases at low temperatures contribute to the low temperature isothermal

hardening of asphalt cement. It is not unreasonable to predict volume shrinkage should occur upon phase separation if the associating molecules occupy less volume than they did in a homogeneous liquid state. If this process occurs at the same temperatures and over the same time scales used in Anderson's experiments, then it should be possible to gain some insight regarding the physico-chemical changes which contribute to physical hardening. The first step is to relate the structuring observed by DSC and thermomicroscopy to the time-dependent changes in the rheological properties of the asphalt cement.

Then, the underlying chemical interactions which cause the observed structural changes will be characterized. Since previous DSC studies have demonstrated that the thermal effects are most evident in the saturates fraction, it seems most probable that weak Van der Waals forces are causing aggregation of the aliphatic chains, creating localized regions with a density and refractive index different from that of the bulk asphalt. These aliphatic species may be n-alkanes (waxes), or they may be long side chains on much larger molecules. As was discussed in some detail elsewhere (8), n-alkanes from C-10 to C-20 melt within the temperature range of -30 to 40 °C, which corresponds to pavement service temperatures. However, adding a double bond anywhere in the alkyl chain will typically reduce the melting temperature by 30 to 90°C. Placing the aliphatic chain in a sterically hindered environment, such as on an aromatic or aliphatic cyclic system, will also reduce its tendency to agglomerate with other molecules. To confirm that aliphatic species are indeed responsible for the enthalpy changes observed by DSC and the localized refractive index differences observed by microscopy, model asphalts have been formed by adding pure n-alkanes (n = 20 to 40) to selected asphalts.

Finally, we have attempted to describe how the physico-chemical changes occur. A mathematical analysis of the microscopic images was used to evaluate the polyphasic structure within the cooled asphalt and to identify the mechanism through which the phase changes occur.

EXPERIMENTAL

In order to relate the thermal properties to the observed rheological changes, the eight SHRP core asphalts were analyzed by DSC and two thermomicroscopy techniques as reported in previous papers and summarized below. SHRP asphalt AAO and a waxy Chinese crude residue (#12) that cannot meet current bitumen specifications were also evaluated.

The chemical composition of each asphalt was analyzed using IATROSCAN (a thin layer chromatography technique) to separate the nC7 maltenes into aromatic, polar, and saturates fractions (see Table 1a). The traditional physical properties of these asphalts were determined previously in ref. 7 (see also Table 1a).

The Chinese bitumen was evaluated for low temperature physical hardening by conditioning and testing samples at -15°C over a four day period. Anderson and Bahia's protocol was used to measure the creep response of conditioned samples in the Cannon Bending Beam Rheometer (BBR) (2,3).
DSC experiments were carried out using a Mettler TA 2000 B apparatus controlled by a computer. The experimental procedure for the calibration of temperature and enthalpy has been previously described (9). A DSC run typically sweeps a temperature range of -100 to +100°C at a heating rate of 5°C/min while the sample is maintained under an argon atmosphere. The amount of crystallized fraction (CF) was determined using a quantitative method previously described (4). Most of the detailed sample conditioning and test procedures used to obtain the DSC results presented herein have also been described elsewhere (7).
To study the effect of aliphatic compounds on thermal behavior, up to 7% pure n-alkanes (n = 20 to 40) were added to selected asphalts. The alkanes were supplied by Aldrich at 99+% purity. The resulting blends were stirred for 24 hours at 100°C to guarantee homogeneity. After storing the samples another 24 hours at room temperature, DSC sweeps were run following the conventional procedure. First the samples are cooled at a rate of 10°C/min to -100°C, and then thermal effects were monitored while heating the sample to 100°C at 5°C/min.
Optical microscopy can provide information regarding the internal structure of materials, including phenomena such as crystallization or phase separation. Binders were analyzed using equipment and experimental procedures previously described (6).
- Polarized light microscopy
This technique is most commonly employed to observe anisotropic behavior within substances which exhibit more than one refractive index, e.g. birefringent materials. Small crystallized regions within the sample may appear white or colored under polarized light. Amorphous materials such as polymers or glasses are isotropic and will not affect the light passing through them.
- Phase contrast microscopy (Zernike method)
This method is primarily applied to increase the contrast of unstained specimens when the refractive index within a region of interest is very close to that of the surrounding matrix. This device transforms differences in refractive indices into variable intensities of transmitted light.
By combining these two methods, one can observe both well-crystallized domains (polarized light) and amorphous fractions (phase contrast) contained in a glassy matrix.

THERMAL BEHAVIOR OF SHRP CORE ASPHALTS

The thermal behavior of each of the eight SHRP core asphalts was characterized using a previously described DSC procedure (7) (Figure 1). Several important features can be observed on each thermogram:
- In a narrow temperature range usually falling below 0°C, there is a clearly defined increase in heat capacity corresponding to the glass transition within the hydrocarbon matrix. The glass transition temperature (Tg) is assumed to be the midpoint of this temperature range. The corresponding change in heat capacity around Tg is designated DCp.
- In the temperature range above 0°C, there are two or three peaks which represent changes in enthalpy within the hydrocarbon matrix. These endothermal effects are attributed to a change of state related to the dissolution of fractions that had previously been precipitated upon cooling. The term CF (crystallized fraction) designates the relative amount of material which ultimately participates in this solid-to-liquid phase change over the entire test temperature range. It is calculated by integrating the enthalpy changes measured in a DSC sweep. It is now obvious that not all of these enthalpy changes are due to formation of purely crystalline materials. Thermal parameters for the tested asphalts are listed in Table 1a.

Four asphalts (AAG, AAO, AAM, #12) were selected specifically to provide samples with a broad range of dissociating materials. They were annealed at a temperature of -15°C for periods ranging from 1 to 8 days to determine the effect of storage time on the thermal events observable by DSC. Experimental curves for AAG and AAM are shown in Figure 2, and CF results for the four asphalts are listed in Table 2a. Since AAG has a very low CF, there are no drastic changes in either CF or Tg after annealing at -15°C. On the other hand, both AAO and AAM contained over 4% CF initially, and each exhibits very significant changes in thermal properties after conditioning. During the first 24 hours at -15°C, there is a 20-40% increase in CF accompanied by a 5-10°C increase in Tg. During the following seven days, the CF remains approximately constant, but the structure within the disassociating phases appears to change markedly. Over time, the low temperature thermal effect splits into two clearly defined peaks, with the peak near 0°C appearing to grow at least partially at the expense of the peak located near 30°C. The glass transition appears to shift until it almost becomes an extension passing below the baseline of this first endothermal peak. Given the experimental precision of ±5%, precipitation seems to be essentially complete within 24 hours. However, the continuing evolution in the DSC profile, particularly in the region near 0°C, proves that the orientation of molecules within the dissociated phases changes with time. Eight days or more may be required for the system to reach equilibrium at -15°C. It is hypothesized that shorter or highly substituted alkyl chains ultimately form a structure at thermodynamic equilibrium which

dissolves very easily at low temperatures. However, upon more rapid cooling, these molecules may temporarily precipitate with larger paraffins to form one single peak, rather than the two peaks observed upon extended storage. Further doping experiments with C24 in AAG should resolve some of these questions, but these data are not yet available.

In a previous study the SHRP core asphalts were preconditioned for 24 hours at storage temperatures varied in 5°C increments from -30°C to 25°C. Results of CF versus storage temperature are shown in table 2b (7). Very little CF was detected in AAG and AAA. Generally, for the other seven asphalts, there was a gradual increase in the amount of CF as the storage temperature decreased from +25°C down to -15°C. This is fairly consistent with the theory that CF results from the precipitation of aliphatic molecules. As the temperature decreases, additional precipitation would be expected as shorter alkyl chains phase separate. However, as the storage temperature continues to drop from -15 to -30°C, the CF begins to decrease, rather than increasing as expected. Molecular motion at these very low temperatures is probably so slow that 24 hours is not sufficient for complete precipitation to occur. It is also conceivable that the mixture can supercool in such a way that some of the available molecules will not separate from solution. Further study is needed here.

TIME-DEPENDENT CHANGES IN PHYSICAL PROPERTIES

As reported previously (7), penetrations of three bitumens with moderate to high amounts of CF were reduced by 15 to 40% after only one day of storage at 5°C, even though all conditioned samples were reheated to 25°C for two hours before testing. The greatest time-dependent hardening was observed in those asphalts with higher amounts of CF as determined by DSC (see Tables 1a and 1b). These results do suggest that most of the observed penetration change occurs within the first day of storage. This is apparently not consistent with DSC observations which show that structure may continue to form for days. This inconsistency can, however, be easily explained by recalling that the pen tins are reheated to 25°C before testing. DSC curves show that much of the structure (probably shorter or highly substituted aliphatic chains) which forms over time will dissolve between Tg and 25°C. Hence, consistency measurements must be made over appropriate time intervals at the storage temperature if physical hardening effects are to be correctly evaluated.

It is worth emphasizing the importance of physical hardening by comparing it to age hardening, the oxidation-induced irreversible structural changes that occur during the hot-mix operation or in the pavement. A hardening index can be defined by the ratio of the pen after 1 day storage at -15°C vs original pen. Table 1b compares this hardening index to traditional pen aging indices. Even when the samples are reheated to 25°C for testing, the

physical hardening index suggests changes in consistency almost on the same order as the aging indices observed after the RTFO test.
Unlike penetration or other physical consistency measurements made at lower temperatures, the ring and ball softening point remains relatively stable, regardless of the storage time and temperature prior to its determination (see Table 1b) (7). This result is consistent with DSC observations that enthalpy changes detectable above the softening point are fairly small. More importantly, this high temperature portion of the DSC curve is not significantly changed by storage conditions, probably because only very large aliphatic molecules that associate quickly remain agglomerated at high temperatures. This offers additional proof that the time-dependent hardening due to CF is thermoreversible.

Anderson's bending beam rheometer is an excellent tool for evaluating low temperature physical hardening, because it can provide accurate stiffness measurements at the prescribed conditioning temperature. It is also very easy to store and evaluate many samples at the test temperature without tying up the instrument or sample molds for long periods of time. But most importantly, it is possible to reduce all of the data to a single hardening shift factor, much like the shift factor derived for time-temperature superposition. The Anderson-Bahia protocol (2) was used to monitor the change in creep response of the highly paraffinic Chinese residue (#12) over 96 hours at -15°C. As shown on Figure 3, the creep compliance decreased significantly with time in storage. The hardening shift factor between 2 and 24 hours of isothermal aging is shown on Table 1b along with Anderson's data for the eight core asphalts. As expected, the shift factor for the waxy Chinese asphalt is somewhat higher.

RELATING PHYSICO-CHEMICAL CHANGES TO PHYSICAL HARDENING

Anderson reports that the hardening phenomenon, and its corresponding shift factor, is related to a measurable time-dependent volume decrease in the asphalt sample. This is probably a consequence of CF precipitation. The dominant mechanism which explains low temperature physical hardening is the formation of a new structure within the asphalt cement as phase separation occurs.
Before trying to develop any rigorous models relating chemical functionality to physical properties, it is worthwhile to review relevant data from two papers presented recently at the Rome Bitumen Chemistry Conference (2) (7). Since AAM shows the greatest physical hardening and highest CF content of the SHRP core asphalts, both Anderson and Claudy focused strongly on the evolution of this bitumen with time and temperature. First, one can visually compare the changes in the hardening shift factor of AAM as determined on the BBR (Figure 4) to the evolving endothermal effects observed by DSC after annealing at various temperatures for 24 hours

(Figure 5). As the annealing temperature decreases below -15°C, there is a gradual evolution to a third distinct endothermal effect centered around 0°C. This is consistent with the observation that lower molecular weight alkyl chains are able to precipitate upon annealing at lower temperatures. However it is also possible that a third type of structure forms at these very low temperatures which has a dissolution range lower than the other two thermal effects.

If one wants to establish a relationship between chemical and physical properties, the most obvious approach is to compare the hardening shift factor to the enthalpy changes observed by DSC. In Figure 6, CF is plotted against the hardening shift factor for the SHRP core asphalts. All samples were conditioned at -15°C for 24 hours. This simple approach resulted in a surprisingly good correlation coefficient of 0.79.

However, the hardening shift factor is not just affected by the amount of crystallizable material. When conditioning temperatures approach the glass transition range, the mobility of the molecules is greatly reduced, and the phase change occurs more slowly. Hence, some correction for molecular mobility should better explain the rate of hardening. One approach that provided a surprisingly good result for the eight core asphalts was to divide CF by the temperature difference between the conditioning\test temperature (Tc) and the glass transition temperature (Tg) as determined by DSC. When the hardening shift factor was plotted against the new parameter CF/(Tc-Tg) for samples conditioned for 24 hours at -15° C, the correlation improved to r2 = 0.96 (Figure 7). This suggests that asphalts harden faster when they contain more CF and when their Tg is lower (i.e. There is more molecular mobility at the conditioning temperature because the solvent phase is further from its glassy state). This represents a quite distinct difference from Anderson's interpretation, which relates the physical hardening to Tg. What is really important is the amount of crystallized fraction at the time of the measurement. Moreover, physical hardening occurs before Tg.

Even though the Chinese residue is an extreme case with a very high CF, it falls almost exactly on the line extrapolated from the SHRP asphalts. However, one must still be careful not to attach too much physical significance to the term CF/(Tc-Tg), because the denominator goes to zero and is therefore undefined at Tc=Tg. It would be preferable to relate molecular mobility to the rheology of the total bitumen or the neutral fraction at Tc. In addition, CF represents the entire crystallized fraction, not just the additional molecular reorientation that takes place over time at the conditioning temperature. It was unfortunately not possible to accurately quantify the change in CF with time, a property which would logically reflect rates of hardening better than the total CF.

Other time-dependent parameters identified by Anderson include the early hardening rate parameter and the limiting hardening parameter. Correlations between these two parameters vs CF/(Tc-Tg) were 0.93 and 0.74 resp..

Anderson also showed there is a very good correlation between physical hardening and a time dependent decrease in free volume. This, too, is consistent with DSC observations. As aliphatic molecules associate through weak Van der Waals forces, the long chains become immobile with respect to their immediate neighbors, and hence occupy less free volume. Therefore if the formation of CF is time dependent, there should be a corresponding decrease in volume as the process occurs.

ADDITION OF N-ALKANES

The excellent correlation between DSC and physical hardening immediately raises another question, "What chemical functionalities precipitate out of solution at low temperatures." A partial response was given by Claudy et al. (3) when they showed that only the saturate fractions from a SARA separation exhibit strong endothermal effects corresponding to a dissolution process. None of the other three fractions (aromatics, polar aromatics or asphaltenes) exhibit significant enthalpy changes above Tg, leading to the assumption that most of the agglomerating molecules come from the saturate fraction. Hence, the next logical step was to dope bitumens with various pure n-alkanes and then analyze the thermal behavior of each mixture.

First, six pure n-alkanes (C20, C24, C28, C32, C36, C40) were analyzed by DSC using the reference procedure cited above. The corresponding thermograms are compared on Figure 8. C20 and C40 each have one single peak, whereas the other four alkanes each show two different peaks, one related to a solid-solid transition and the other to melting.

In a second experiment, 3% of each alkane was added to asphalt AAG, which contains virtually no CF. The resulting thermal parameters are listed in Table 3, while Figure 9 shows the differential DSC thermograms of the doped AAG samples for each of the six alkanes. Several observations are notable:

- Both the pure n-alkanes and the doped asphalts exhibit increasingly higher melting and dissolution temperatures respectively as the molecular weight of the alkane increases.
- The dissolution temperature range of the alkane is much broader when it is dissolved in the bitumen.
- When dispersed in the asphalt, the n-alkane begins to dissolve at a temperature which is typically 20-30°C below its pure melting point. This suggests strong interactions between the paraffins and the asphalt matrix.
- Upon heating, the total enthalpy required to dissolve the alkane back into the asphalt is surprisingly close to the enthalpy of melting for the pure n-alkane,
- For C20, C32, C36, C40 only one endothermal peak is seen.

Observations of the data (Table 3) indicate that Tg is systematically lowered upon addition of paraffins, 18°C for C20, 9°C for C24, 4°C for C28.

In another doping experiment, 1 to 6% of C24 paraffin was added to asphalt AAG. DSC fingerprints are presented on Figure 10, and thermal parameters are included on Table 3. Two peaks are generally observed, but the relative area under each changes dramatically with concentration of paraffin. At the lowest concentration of 1.06%, the thermal effect above 35°C is very broad and no second peak is evident. Above 2% C24, the first peak between 0 and 35°C seems to reach a saturation point, and most of the enthalpy change resulting from continued addition of paraffin appears in the second peak above 35°C. This represents a dramatic difference in dissolution temperatures, implying there must be formation of two liquids within the solvent phase. Perhaps not coincidentally, virgin asphalts with significant amounts of CF also show two peaks with a minimum at 35°C. Hence one would like to postulate that paraffins cause asphalt to separate into two distinct liquid phases. This might explain the two different sized domains as observed by Phase Contrast (1-3 microns) and Polarized Light (10-15 microns) microscopy. Verney et al reported that there seems to be a natural transition in rheological properties around 35°C. This effect is so important that they propose two different rheological models to fit data above and below this temperature (10).

The same general trends were observed when 1 to 5% C24 was added to AAM, the SHRP core asphalt with the highest natural CF. Differential DSC curves, which subtract the pure bitumen curves from doped asphalt thermograms, clearly show two peaks splitting at 35°C (see Figure 11). However, since AAM already contains a large amount of CF, the second peak is much more strongly affected by the first percent of added paraffin. Apparently, there is already enough natural paraffin present in AAM to interact with one liquid phase. Therefore, most of the added C24 separates on cooling into a different type of structure, hypothesized to be a more crystalline waxlike solid which dissolves at higher temperatures.

When Claudy et al compared the thermal behavior of asphalt to that of other petroleum fractions (kerosene, diesel oil, crude oil) some curious anomalies were discovered (7). Even though all of these products exhibit aliphatic crystallization at low temperatures, only asphalt displays more than one endothermal peak in the dissolution range, and only asphalt exhibits time-dependent structural changes. The time-dependence might be explained by recognizing that the viscosity within the asphalt matrix at these temperatures is very high, so the mobility of molecules is greatly reduced. The two peaks observed may represent the following phenomenon:

- Below Tg, the precipitated paraffins are dispersed within the solid glassy matrix.
- Immediately above Tg, the liquid continuous phase (L) still contains organized paraffinic entities (P). As the solid paraffins begin to dissolve upon heating, the combined liquid (L+P) immediately begins to separate into two different liquid phases, (L'+P) and (L"). This process, which is responsible for the first peak, essentially continues until the solid paraffins are dissolved,

or until the portion of the solvent phase most compatible with the paraffins (L') is consumed.
- Assuming excess paraffin exists, then the remainder of (P) must dissolve in (L") to form (L"+P). Since this second liquid phase is much less compatible with alkanes, the paraffins cannot dissolve until the temperature becomes fairly high (>35°C). This explains the appearance of the second peak. Such behavior is well-known in other systems. For example, during polymerization, the polymer chain in formation begins to separate from the monomer phase and then dissolves in the solvent. Similar biphasic structure is also evident when some polymers are dissolved in asphalt. This hypothesis for two liquid phases is strongly supported by doping experiments in which a single pure n-alkane gives two clearly defined endothermal peaks .

Phase Contrast and Polarized Light Microscopy techniques were used to study asphalt AAG before and after doping with n-paraffins. Resulting photographs are presented in Figure 12:
- virgin AAG, which contains virtually no CF, appears to be perfectly homogeneous. There is no observable phase separation detectable by either of the two optical techniques.
- the addition of 7% C24 results in the formation of crystalline regions which are easily detected by polarized light. A definite biphasic structure is also apparent in the phase contrast photomicrograph.
- the addition of 15% n-paraffin emphasizes the phase separation and increases the crystallization phenomenon.
For comparison, photomicrographs of a vacuum distillation residue containing 14.6% natural CF are included on the same figure. The Polarized Light photos for AAG doped with 15% n-alkane and the asphalt with high CF show that the crystallized fractions are very similar in size and quantity. Phase Contrast photomicrographs also show very clear biphasic characteristics in both samples. Hence it is possible to approximately duplicate both the microscopic images and the DSC thermal effects of bitumens containing significant amounts of CF by doping asphalt AAG with n-alkanes, even though virgin AAG exhibits none of these properties.

Microscopy image statistical analysis

Microscopic images such as shown in Figure 12 were systematically analyzed by performing a two-dimensional Fourier transform. This mathematical method determines characteristic lengths of any heterogeneous regions located on the image. When phase separation within a bitumen was observed on the photomicrographs, the dissociating molecules initially formed domains of fairly uniform size, with a length of about 4 microns. Therefore, it appears that, although the final images seem to show isolated domains corresponding to crystalline fractions, the phase separation process may actually be more accurately described as a spinodal

decomposition phenomenon (11, 12). There is a periodic modulation of the concentration of paraffin within the asphalt matrix. More experiments are in progress to test this hypothesis which would, if confirmed, provide an important clue to understanding physical hardening at low temperature. The asphalt is no longer homogeneous in density. Instead, it appears to be a complex two phase structure, more akin to a gel, with enhanced visco-elastic properties.

CONCLUSION

There now seems to be no doubt that the molecular agglomerations observed by DSC and thermomicroscopy are at least partially responsible for the time-dependent shrinkage and resulting stiffening observed during low temperature isothermal aging. Ultimately, at any given temperature, the system will reach thermodynamic equilibrium, after which no additional hardening takes place. The amount of stiffening that does occur over time can be related to the number of molecules in the bitumen which coalesce to form microscopic crystalline or amorphous domains within the solvent phase. The rate at which hardening occurs is also affected by molecular mobility within the solvent phase. By correcting the total enthalpy change observed by DSC (CF) by an empirical mobility factor (Tc-Tg) relating the test temperature to Tg, it was possible to predict hardening shift factors with correlation coefficients of 0.96, which is quite remarkable for any chemical-physical relationships in bitumen.

Pure n-alkanes have been added to various asphalts and the resulting blends analyzed by DSC, Phase Contrast Microscopy, and Polarized Light Microscopy. It seems evident from these results that molecules containing long aliphatic chains are responsible for time-dependent structural changes. Using microscopy, one observes well-organized crystallized regions of 10-15 microns, as well as poorly-organized, amorphous domains 1-3 microns wide. Thus, asphalt microstructure is heterogeneous at low temperatures, with tiny paraffinic crystals and polar-associated molecular chains all dispersed within the solvent matrix.

One possible process for the phase separation of a single homogeneous liquid into two liquid phases upon cooling is called spinodal decomposition. It can be found in a wide variety of materials such as glasses, polymers or metals. Spinodal decomposition within asphalt was verified and quantified by applying statistical image analysis techniques to the photomicrographs.

Amphoterics, or highly polar molecules, have been shown to play a key role in performance-related asphalt rheology by increasing stiffness within the liquid matrix at high temperatures. Correspondingly, the understanding of aliphatic interactions may prove to be equally enlightening regarding the tendency for pavements to thermally crack in cold environments.

REFERENCES

1. Anderson, D.A. and Christensen, D.W., 65th Annual Meeting of AAPT, Seattle, Wash., March 4-6 (1991).
2. Bahia, H.U., Anderson, D.A., International Symposium on Chemistry of Bitumens, Rome, Italy, Proceedings, 1, 114-147, June 5-8 (1991).
3. Bahia, H.U., Anderson, D.A., and Christensen, D.W., 66th Annual Meeting of AAPT, Charleston, S.Carolina, February 24-26 (1992).
4. Brûlé, B., Planche J.P., King, G.N., Claudy, P. and Letoffe, J.M., A.C.S. Symposium on Chemistry and Characterization of Asphalts, Washington, D.C., August 26-31 (1990).
5. Brûlé, B., Planche J.P., King, G.N., Claudy, P. and Letoffe, J.M., Fuel Science and Technology International, 9(1), 71-91, (1991).
6. Claudy, P., Letoffe, J.M., King, G.N. and Planche J.P., Fuel Science and Technology International, 10(4-6), 735-765, (1992).
7. Claudy, P. and Letoffe, J.M., King, G.N. and Planche J.P., International Symposium on Chemistry of Bitumens, Rome, Italy, Proceedings, 2, 530-567, June 5-8 (1991).
8. King, G.N., International Symposium on Chemistry of Bitumens, Rome, Italy,Proceedings, 2, 742-769, June 5-8 (1991).
9. Bosselet, F., Thesis No 8, St Etienne, France (1984).
10. Verney, V., Michel, A., Planche, J.P., and Brûlé, B., 25eme Colloque du Groupe Français de Rhéologie, Session 4, Rhéologie des Bitumes et Bétons Bitumineux, Grenoble, France, November 28-30 (1990).
11. Binder, K., Material Science and Technology, 5, ed. by VCH Verlagsgesellschaft Weinheim, (1991).
12. Cahn, J.W., trans. Metallurgical Soc. of AIME, 242, 166-179, (1968).

Table 1a. Physical and Chemical Properties of Study Asphalts

Asphalt Cements	AAA	AAB	AAC	AAD	AAF	AAG	AAK	AAM	AAO	#12
Saturates, wt%	6	7.2	9.7	4.4	5.9	4.6	3.6	6.6	4.2	8.2
Aromatics, wt%	69.1	64	67.6	61.9	70.8	70.5	61.5	67.4	70.9	50.9
Polar Aromatics,wt%	13.4	15.1	10.6	18.7	14	21.6	22.9	23.3	12.5	28.5
nC7 Asphaltenes,wt%	11.5	13.7	12.1	15	9.3	3.3	12	2.7	12.4	11.7
Tg, °C	-29	-30.9	-26.5	-29.4	-26.1	-11.1	-24.8	-25.3	-31.5	-30.
DCp, J/g/K	0.267	0.225	0.235	0.297	0.189	0.337	0.25	0.222	0.164	0.15
CF,wt%	0.4	4.6	4.9	1.6	3.7	0.2	1.2	5.3	4.4	10.1
Penetration,25°C,dmm	155	90	102	137	54	55	65	63	105	119
Ring & Ball, °C	40.1	45.2	45	44	49.2	48	50.1	48.1	45.2	44.9
Viscosity, 60°C,P	640	920	670	880	1360	1450	2550	1690	960	326
Viscosity,135°C,cSt	263	240	195	292	306	217	500	453	317	194
Fraass Point, °C	-20	-16	-16	-18	-9	-5	-8	-17	-18	-17

Saturates, Aromatics, Polar Aromatics determined with IATROSCAN,

Tg (Glass Transition Temperature), DCp (Heat Capacity variation), and CF (crystallized fraction) measured with DSC Values from Claudy et al.1991.

Table 1b. Physical Properties of Study Asphalts after Aging

Asphalt Cements	AAA	AAB	AAC	AAD	AAF	AAG	AAK	AAM	AAO	#12
Ring & Ball*, °C	-	-	-	-	48.3	-	-	49.5	-	45.7
Penetration Ratio1,%	51.6	62.2	52.9	43.8	53.7	63.6	61.5	66.7	59.6	63
Penetration Ratio2,%	-	-	-	-	88.9	-	-	85.7	-	69.7
HSF, log(sec)	0.175	0.325	0.456	0.225	0.5	0.106	0.281	0.612	-	0.64

*Ring & Ball after 24 hour storage at -15°C. Values from Claudy et al.1991.

Ratio1: Ratio of 25°C Penetration ratio after and before RTFO

Ratio2: Ratio of 25°C Penetration after and before 3 day storage at -15°C

HSF: Hardening Shift Factor after 24 hour isothermal age at -15°C, measured with the Benbing Beam Rheometer. SHRP asphalt HSF are from Bahia et al.1991.

Table 2a. Isothermal Age* Influence on Crystallized Fraction and Tg (−15°C)

AC's		AAA	AAB	AAC	AAD	AAF	AAG	AAK	AAM	AAO	#12
CF, wt%	0	–	–	–	–	–	0.2	–	5.3	4.2	9.3
	1	–	–	–	–	–	0.2	–	7.4	5.5	13
	2	–	–	–	–	–	0.1	–	7.4	5	13.1
	4	–	–	–	–	–	0.1	–	7.5	5.2	13.2
	8	–	–	–	–	–	0.2	–	7.5	5.5	13
Tg, °C	0	–	–	–	–	–	−11.1	–	−28.6	−25.3	nm**
	1	–	–	–	–	–	−10	–	−24.2	−15.3	nm
	2	–	–	–	–	–	−8.9	–	−20.5	−15.1	nm
	4	–	–	–	–	–	−6.4	–	−23	−21.4	nm
	8	–	–	–	–	–	−6.4	–	−18	−17.6	nm

* Isothermal Age (days) - ** not measurable - Values from Claudy et al.1991.

Table 2b. Storage Temperature Influence on Crystallized Fraction (24 hrs)

AC's	AAA	AAB	AAC	AAD	AAF	AAG	AAK	AAM	AAO	#12
CF,wt% +25°C	0.4	4.6	4.9	1.6	3.7	0.2	1.2	5.3	4.2	9.3
+20°C	–	4.6	5	1.4	3.4	–	1.2	5.7	4.3	11.5
+15°C	–	3.8	4.5	1	2.9	–	1.4	5.1	3.1	11.2
+10°C	–	4.2	4.1	1.7	3.2	–	1.1	5.2	2.5	11.4
+5°C	–	4.3	4.5	1.3	3.9	–	1.4	4.8	3.5	10.4
0°C	–	4.6	5.8	1.9	4	–	1.5	6.2	3.9	12
-5°C	–	5.3	5.5	1.9	4	–	1.2	6.5	5	11.4
-10°C	–	5.4	6	1.8	4.3	–	1.7	7.3	4.7	12.7
-15°C	–	6	6	2.2	4.2	–	1.2	7.8	5	13
-20°C	–	5.8	6.3	2.2	4.1	–	1.1	7	5	12.6
-25°C	–	5.4	5.1	1.6	3.7	–	1.1	7.3	4.3	11.1
-30°C	–	5.6	5.2	1.7	3.6	–	1.3	6.3	4.2	11.9

Values from Claudy et al.1991.

Table 3. Influence of n-Alkane addition on AAG Thermal Behavior

% n-Alkane	Tg (°C)	DCp (J/g/K)	DHd (J/g)*	DHsl (J/g)**
0 (Neat AAG)	−11.4	0.337	–	–
3% C20H42	−29.2	0.134	217.5	226.7
3% C24H50	−20.4	0.266	222.5	230.2
3% C28H58	−15	0.255	252.5	245
3% C32H66	−13	0.295	239.8	254.6
3% C36H74	−10.8	0.3	245.8	256.6
3% C40H82	−12.5	0.304	220.4	215.6
1.66% C24H50	−15.4	0.244	118.5	230.2
2.04% C24H50	−21.3	0.158	233.3	230.2
3.11% C24H50	−21.3	0.174	236.5	230.2
5.35% C24H50	−18.5	0.22	238	230.2

*Dissolution and **Solid-Liquid Transition Enthalpy Variations, respectively.

Fig 1. DSC curves of SHRP Asphalts.

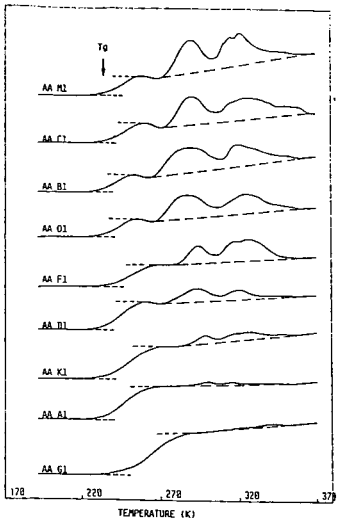

Fig 2. Effect of the Low Temperature Conditioning Time on DSC Curves for AAG and AAM.

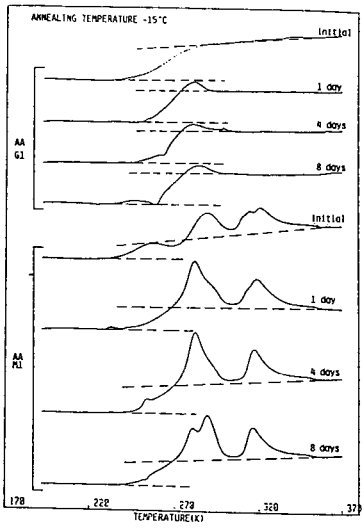

Fig 3. Change in Creep Compliance due to Physical Hardening Asphalt #12

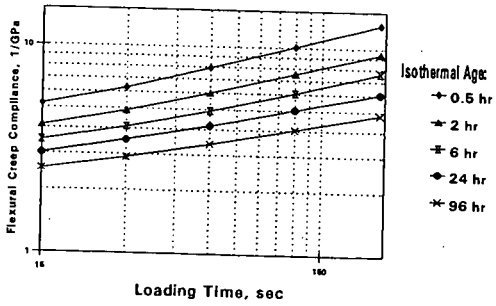

Conditioning Temperature, -15 C

Fig 4. Physical Hardening Trends of Asphalt AAM at Different Temperatures

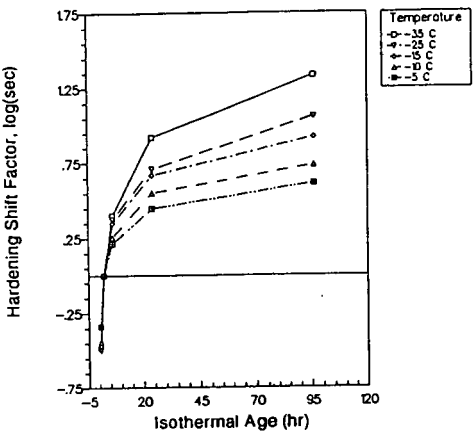

Reproduced from Anderson et al.1991, with Dr Anderson's permission

Fig 5. Effect of the Conditioning Temperature on DSC Curves for Asphalt AAM.

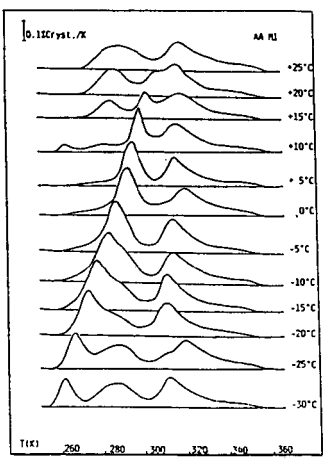

Fig 6. AC Hardening vs Crystallized Fraction

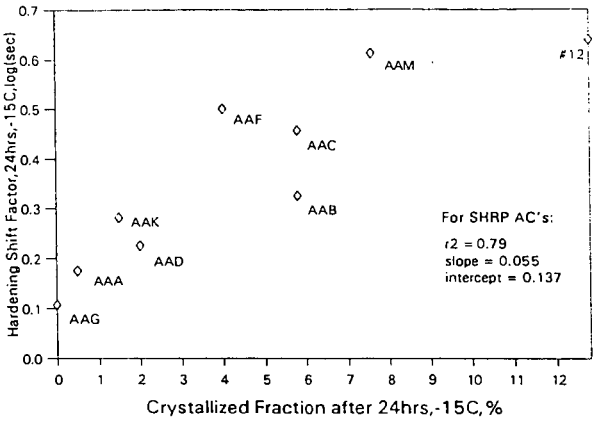

SHRP AC Hardening Shift Factor from Anderson et al. 1991

Fig 7. AC Hardening vs Crystallized Fraction and Tg

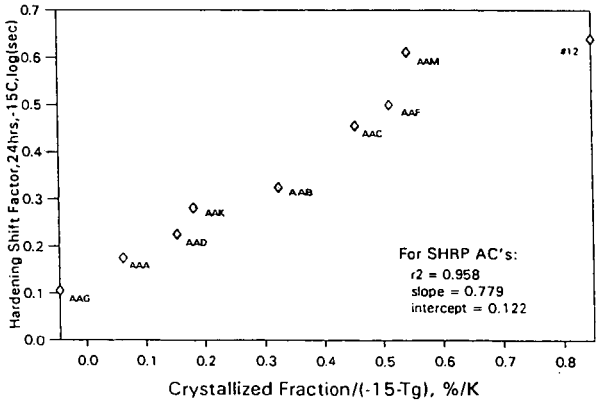

Crystallized Fraction & Glass Transition Temperature (Tg) by Differential Scanning Calorimetry (DSC)
Crystallized Fraction and Glass Transition Temp after 24 hr at -15C
Hardening Shift Factor from Anderson, et.al., 1991

Fig 8. DSC Curves of Pure n-Alkanes.

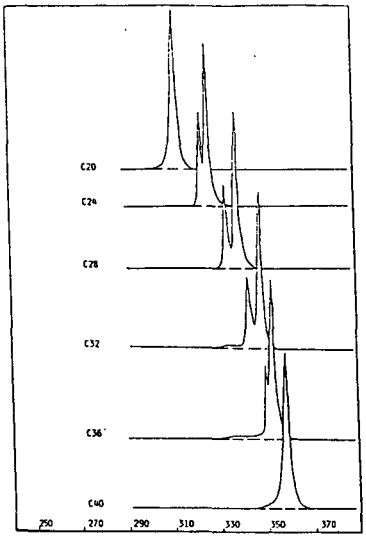

Fig 9. DSC Curves for AAG Doped with n-Alkanes.

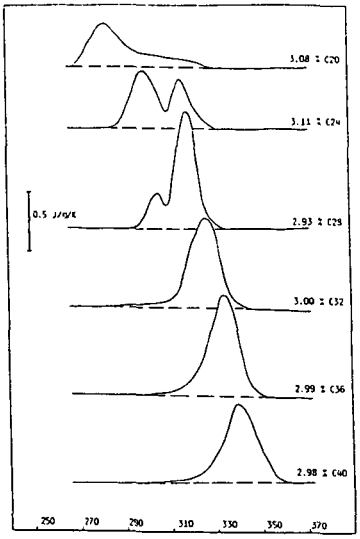

Fig 10. DSC Curves for AAG Doped with n-C24

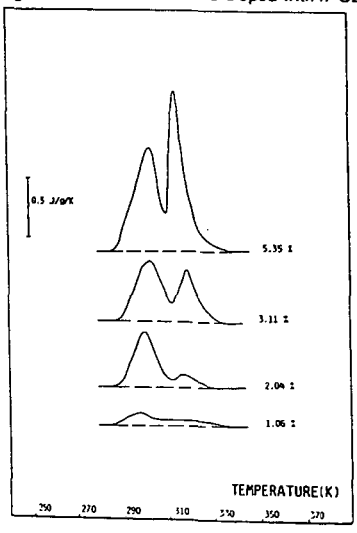

Fig 11. DSC Curves for AAM Doped with n-C24

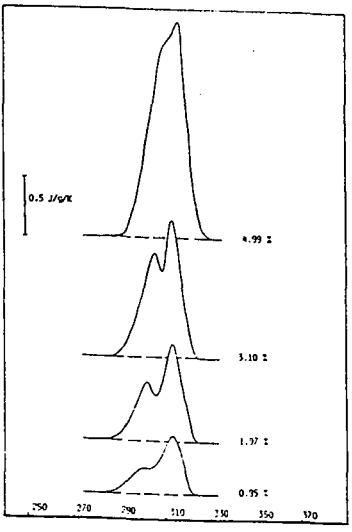

Fig 12. Influence of n-Alkane Addition on Thermomicroscopy Images for Asphalt AAG.

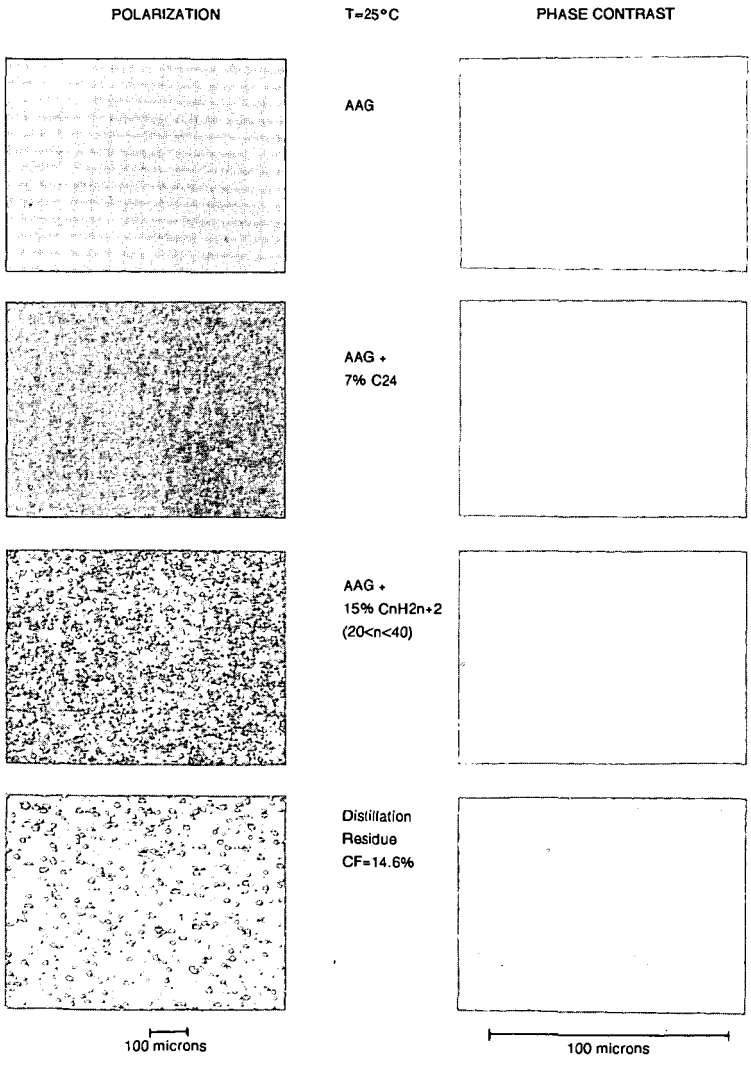

SYMPOSIUM ON CHEMISTRY OF ASPHALT AND ASPHALT-AGGREGATE MIXES
PRESENTED BEFORE THE DIVISION OF FUEL CHEMISTRY, INC.
AMERICAN CHEMISTRY SOCIETY
Washington, D.C. Meeting, August 23-28, 1992

Temperature Dependence of Complexation Processes in Asphalt and Relevance to Rheological Temperature Susceptibility

H. Sawatzky, B. Farnand, J. Houde Jr. and I. Clelland
Energy, Mines and Resources Canada, Energy Research Laboratories,
555 Booth St., Ottawa, Ontario, Canada K1A 0G1, (613) 996-7970

INTRODUCTION

It has been established that asphalts or petroleum distillation residues are not homogeneous, but micellar based systems (1). The composition of the micelles is controversial and is considered to involve aggregates of mainly asphaltenes or complexes of asphaltenes with other high molecular weight components. The approach described in this paper was developed using the latter concept with interchanges of components between the micelles and the continuous phase that are highly temperature dependent. Mechanisms are proposed that describe how the consistency of asphalt cements changes with varying temperatures. These mechanisms involve component interchanges between the micelles and the continuous phase in asphalt.

The viscosity of the complete asphalt system is caused by the major contributions from both the micellar and continuous phases. The continuous phase viscosity depends on that of each component, in particular those of high viscosity. If the micelles were spheres with no interaction then their contribution to the viscosity of the asphalt would be small. However, it is known (2) that there must be considerable bridging between the asphaltenic micelles resulting in various degrees of cross-linked networks. This can be explained by the fact that the micelles are considered to have polar groups on their surfaces which associate with polar groups on neighbouring micelles to form loose networks. These networks contribute markedly to the viscosity of asphalt cements.

The micelles are considered to be complexes with the most polar components,

namely the asphaltenes at their cores. Other less polar components are deposited on top of the more polar ones with the least polar components located at the extreme exterior surface of the micelle, as shown in Fig. 1. The continuous phase contains large amounts of the less polar components and they are major contributors of viscosity. The following colloidal model is proposed to explain resistance to changes in viscosities due to temperature changes and rheological temperature susceptibilities.

The less polar (and possibly higher molecular weight) high viscosity components can be interchanged between the micellar complexes and the continuous phase. On cooling, they are gradually withdrawn from the continuous phase due to complexation with the micelles in order of their degree of polarity. Therefore, as the cooling proceeds, the components undergoing complexation and also those that remain in the continuous phase become less and less polar. Thus, the surface of the micelles becomes less polar and this results in loosening of the bridging between micelles. Both the removal of the polar components and loosening of the micellar network result in the resistance to viscosity increases during cooling. These processes are shown in Fig. 2. On warming, viscosity decrease is resisted by the reverse processes.

This model can also be explained with the following equations:

$$[Pol]_{continuous} \overset{K_p}{\rightleftharpoons} [Pol]_{micellar} \qquad 1)$$

$$K_p = \frac{[Pol]_{micellar}}{[Pol]_{continuous}} \qquad 2)$$

$$K_p = f(T) \qquad 3)$$

where [Pol] represents the exchangeable components and K_p is the equilibrium constant. One way to demonstrate this model would be to show that the degree of complexation is highly temperature dependent, for example, at the extremes of the service temperatures experienced by asphalt pavement. The effect of temperature on precipitation from alkane solutions was chosen to prove that the degree of

complexation is temperature dependant. While precipitation with alkanes will not include all micelles/complexes, increased complexation should increase the amounts of precipitate. The procedure that was followed is similar to the standard method of determining pentane insolubles with two modifications: lower levels of dilution (solvent to sample ratio) were used; and the precipitates could not be washed because this would remove much of the complexed materials.

The effect of temperature on the determination of asphaltenes has been reported in the literature (3-6). Andersen and Budi (3) report a maximum precipitation in the region of 30°C. Mitchell and Speight(6) report that the amount of precipitated asphaltenes in Athabasca bitumen increases with temperatures up to 70°C, and this is related to the decrease of the Hildebrand solubility parameter with temperature. Among these referenced works, very little attention has been given to the material that precipitates with the asphaltenes. This material is removed and lost during the washing step required in the pentane insoluble determination method. Some of the materials that are removed by washing are the components that are complexed on the surface of the micelles.

The temperature susceptibility of asphalt cement is a function of the equilibrium distribution, K_p, of components between the micelles and the continuous phase, as shown in equation 1. Since temperature alters the equilibrium, it is the change in K_p with temperature that determines the temperature susceptibility, as shown in equation 3. The affinity of the distributing components for the micelles is dependent upon the chemical nature of the asphalt cement.

EXPERIMENTAL

Asphalt Samples

- Esso 85/100 asphalt cement containing 16.1% asphaltenes (heptane insolubles).
- PetroCanada 85/100 asphalt cement containing 17.9% asphaltenes (heptane

insolubles).

Determination of Temperature Susceptibility

The penetration index was used to measure temperature susceptibility. The equation used to calculate the penetration index is given as (7):

$$PI=(20-500A)/(50A+1) \quad 4)$$

where A is the slope obtained from the plot of logarithm (base 10) of the penetration in dmm with temperature in centigrade degrees.

Effect of Precipitation at Various Temperatures

The initial experiments consisted of thorough dispersion of the asphalt samples in pentane at room temperature. These mixtures were kept at the desired temperature overnight, then were filtered quickly through No.1 Whatman filter paper. The pentane was allowed to evaporate from both the precipitate on the filter paper and from the filtrate. The precipitate and liquids were then weighed. In another pilot experiment the mixtures were centrifuged at the desired temperatures and samples were taken of the supernatant liquids. The solvent was evaporated from the supernatant liquid and the amount precipitated was determined by the difference between the asphaltic material in the centrifuged liquid and the original mixture.

In later experiments, the mixtures were stirred at the desired temperatures for 6 h and allowed to remain at the desired temperature overnight. Samples were then taken with a syringe fitted with a 0.45 μm membrane filter to retain suspended solids. The amounts precipitated were determined by difference with the original mixtures.

DISCUSSION

Precipitation at Different Temperatures

The results from the initial temperature precipitation and filtration experiments are shown in Tables 1 and 2. These precipitates were not washed to retain the complexed components with the asphaltenes at the expense of retaining solvent and non-complexed asphalt components. The amounts of precipitate obtained at 25°C for the Esso 85/100 asphalt at different concentrations did not significantly differ significantly. However, at 0°C the amount of precipitate for the 20% concentration was almost twice that observed at 25°C. For the 5% concentration at 0°C, there is also a large increase in the amount of precipitates but considerably less than for the 20% mixture.

The filtrates from these experiments were analyzed by the ASTM D4124 method and are reported in Table 3. The filtrates obtained at the lower temperatures were enriched in saturates but depleted in polar aromatics compared with those obtained at the higher temperature. This is consistent with the model of micelle complexation described earlier since the saturates are expected to be the least complexed with the asphaltene micelles and the polar aromatics are expected to be among the most strongly complexed.

It is apparent that the reproducibility of the above experiments is poor, therefore thecentrifugation method was used, the results of which are shown in Table 4. There is evidence of changes due to temperature but the reproducibility of these experiments is also inadequate. It is considered that the reproducibility is limited by difficulties in the transfer of components from the continuous phase to the precipitate and thus the time required to attain equilibrium is long. Both the duration of the experiment and the absence of stirring or mixing may have prevented replication of results. Further, the size of the micelles may vary with temperature and sample, with considerably different rates of diffusion to and from the surface of the complexes (8).

The results of experiments where longer times and stirring were used are shown in Tables 5 and 6. For the Esso 85/100 asphalt cement, the amount of precipitate varied directly with dilution, as would be expected due to greater addition of alkanes per unit of asphalt cement, and indirectly with temperature. The reproducibility of this experiment was best at 30% concentration and worst at 10%. For the PetroCanada 85/100 asphalt, the amount of precipitate varied directly with dilution but the effect of temperature was greater at higher asphalt concentrations (lower dilutions).

These results, particularly those in Tables 5 and 6, demonstrate that the degree of complexation is highly temperature dependent. This supports the model's prediction of higher complexations at lower temperatures, and is the basis for predicting that changes in viscosity with temperature can be controlled by controlling the complexation of the micelles. Further study is necessary to demonstrate this effect, perhaps by adding both polar and non-polar oils and residues to asphalt cements to relate blending, to control the degree of complexation, and temperature susceptibility.

CONCLUSIONS

A model involving a colloidal system and temperature dependent complexation processes has been proposed to explain the mechanisms in asphalt that determine its rheological temperature susceptibilities. It has been shown experimentally that these temperature dependent complexation processes do occur.

REFERENCES

1. Storm, D.A., Barresi, R.J. and DeCamio, J.D., Colloidal Nature of Vacuum Residue, **FUEL**, 70, 779-782 (1991).

2. Altgelt, K.H. and Harle, O.L., The Effect of Asphaltenes on Asphalt Viscosity, **Ind. Eng. Chem., Prod. Res. Dev.**, 14(4), 240-246 (1975).

3. Andersen, S.I. and Budi, K.S., Influences of Temperature and Solvent on the Precipitation of Asphaltenes, **Fuel Science and Technology International**, 8(6), 593-615 (1990).

4. Rao, B.M.L. and Serano, J.E., Viscometric Study of Aggregation Interactions in Heavy Oil, **Fuel Science and Technology International**, 4(4), 483-500 (1986).

5. Andersen, S.I. and Budi, K.S., Aggregation of Asphalts as Determined by Calorimetry, **J. Colloid Interface Sci.**, 142(2), 497-502 (1990).

6. Mitchell, D. and Speight, J., The Solubility of Asphaltenes in Hydrocarbon Solvents, **Fuel**, 52, 149-152 (1973).

7. Pfeiffer, J.P. and van Doormaal, P.M., **J. Inst. Petrol. Technol.**, 22, 414- (1936).

8. Cussler, E.L., **Diffusion: Mass Transfer in Fluid Systems**, Cambridge Press, Cambridge, England, p.44 (1984).

Table 1 - Results of preliminary precipitation experiments, 25°C,
Esso 85/100 asphalt cement, pentane solvent

Concentration, Wt %	20	20	10	10	5	5
Sample	1	2	1	2	1	2
Precipitate, Wt %	32.8	30.7	37.0	35.7	33.2	33.5
Solubles, Wt %	68.3	70.7	64.3	65.7	66.4	67.1
Total, Wt %	101.1	101.4	101.3	101.4	99.6	100.6

Table 2 - Results of preliminary precipitation experiments, 0°C,
Esso 85/100 asphalt cement, pentane solvent

Concentration, Wt %	20	20	5	5
Sample	1	2	1	2
Precipitates, Wt %	59.0	63. 1	43.2	40.6
Solubles, Wt %	43.2	45.0	62.3	64.8
Total, Wt %	102.2	108.1	105.5	105.4

Table 3 - Effect of temperature on filtrate composition (ASTM D4124)

Concentration, Wt %	20	20	5	5
Temperature, °C	25	0	25	0
Saturates, Wt %	14.2	17.4	14.7	16.5
Naphthenic aromatics, Wt %	41.3	42.0	45.6	50.8
Polar aromatics, Wt %	45.5	40.8	37.9	35.2

Table 4 - Effect of temperature on precipitation, centrifugation experiments

Concentration, Wt %	5	20
Precipitation at +20°C, Wt %	38.3, 27.0, 23.8, 27.0	22.1, 35.1
Precipitation at -20°C, Wt %	40.6, 35.1, 32.8, 40.7, 38.9	49.7, 27.6, 55.5, 54.8

Table 5 - Precipitation from stirred mixture of Esso 85/100 asphalt cement in pentane

Concentration, Wt %	10	20	30	40
Precipitation at 20°C, Wt %	-	-	6.03	4.85
Precipitation at 0°C, Wt %	18.4, 17.0	13.55	8.40	5.13
Precipitation at -20°C, Wt %	16.4, 34.3	17.25	11.20, 10.77	8.67, 8.20
Precipitation at -35°C, Wt %	26.5, 36.8	23.7, 29.1	14.8, 14.7	8.18

Table 6 - Precipitation from stirred mixture of Petro-Canada 85/100 asphalt cement in pentane

Concentration, Wt %	30	30	40	40
Precipitation at 20°C, Wt %	8.63	8.50	3.65	2.72
Precipitation at 0°C, Wt %	10.03	9.13	4.92	4.65
Precipitation at -20°C, Wt %	11.17	11.23	7.18	7.10
Precipitation at -35°C, Wt %	15.0	14.5	11.1	10.7

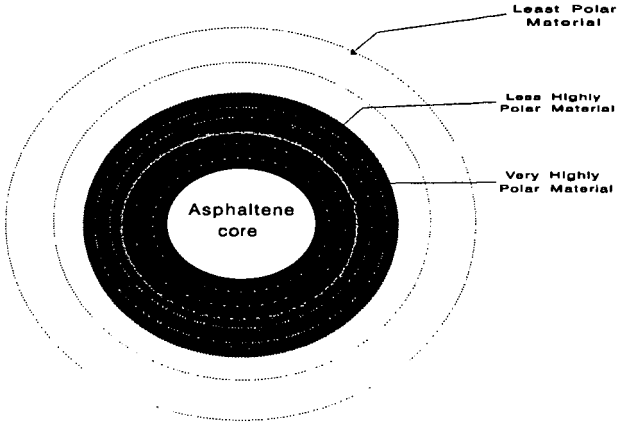

Fig. 1 - Diagram of micelle showing asphaltene core and decreasing polarity of surrounding material from core to surface.

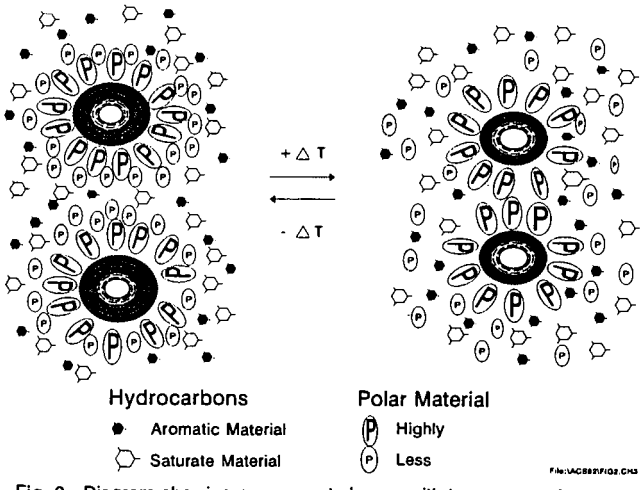

Fig. 2 - Diagram showing component change with temperature in a two phase asphalt system

SELF-ASSOCIATION, STRUCTURE, INTERACTION, AND DYNAMICS OF RATAWI ASPHALTENES IN SOLVENTS

E. Y. Sheu, D. A. Storm and M. M. De Tar
Texaco R & D Department, Beacon, N. Y. 12508

Keywords: asphaltene, micelles, small angle scattering, permittivity

INTRODUCTION

Asphaltene is a class of petroleum material commonly recognized as the heptane insoluble, but toluene soluble fraction of either the crude oil or the vacuum residue [1]. Asphaltene has long been suspected as the key component hindering refining yields, through micellization [2]. Although this scenario has been speculated, direct evidence was not available until recently [3,4]. Of particular importance is the direct evidence for asphaltene micellization, which correlates asphaltene properties with surfactants.

In this paper, we systematically report findings from our asphaltene study, in organic solvents. First, we measured the surface tension as a function of asphaltene concentration in pyridine to identify the critical micelle concentration. This experiment provided direct evidence of asphaltene self-association. Secondly, we characterized the rheological behavior of the asphaltene micellar solutions, from which hydrodynamic properties were quantified. Thirdly, the structure of the micelles were measured using small angle neutron scattering, along with the interactions between the micelles. Finally, we measured the dielectric relaxation of the asphaltene solutions in toluene, in order to investigate the forces that initiate micellization.

EXPERIMENTAL

Samples

Asphaltenes were derived from Ratawi (Neutral Zone) Vacuum Residue by solvent fractionation. One gram of vacuum residue (VR) was mixed with 40 cm^3 of heptane (HPLC grade), and stirred overnight. Heptane insolubles (C7I or asphaltenes) were extracted using Whatman number 5 filter paper and dried under a stream of nitrogen. Mass balances were performed to ensure complete solvent removal. The asphaltenes were redissolved in appropriate solvents, disscussed below, prior to measurements.

Surface Tension Measurements

Surface tension was measured as a function of asphaltene concentration in pyridine (from 0% to 1% by weight) with a Krüss K10ST Surface Tensiometer, using the Wilhelmy plate method. The details of this instrument and the technique used have been given elsewhere [5].

Zero-Shear Viscosity

Viscosity measurements were performed for asphaltene fractions in toluene as a function of concentration for volume fractions from 0.01 and 0.30, at room temperature, on a Brookfield Viscometer. The instrument's working range was from 0-1000 X 10^{-3} Pa-s and a 0.1% accuracy of full scale.

Small Angle Neutron Scattering

The small angle neutron scattering (SANS) measurements were conducted on the time-of-flight small angle diffractometer (SAD) at Argonne National Laboratory. The scattering vector covered a range from 0.007 to 0.34 $Å^{-1}$. In this experiment we measured asphaltenes in a series of deuterated toluene/pyridine mixtures for several asphaltene concentrations to study both the structure and polydispersity dependences on concentration and on solvent permittivity. All the measurements were performed at 22 ^{o}C.

Dielectric Relaxation Measurements

Dielectric relaxations were measured for asphaltene solutions, using an HP 4192A low frequency (5 Hz to 13 MHz) impedance analyzer. The cell used was an immersion type cell from Rosemont Analytical, consisting of four platinum black coated electrodes, with 1mm interplate spacing and a total area of 9 cm^2. The HP 4192A impedance analyzer measures the capacitance between the plates from which the dielectric storage ϵ' and the dielectric loss ϵ'' ($= \epsilon'/D$, D is the measured quality factor) can be computed according to $\epsilon' = C \cdot d/\epsilon_0 A$, where C is the capacitance, d is the electrode spacing, ϵ_0 is the calibration constant ($= 8.8854 \times 10^{-12}$ F/m), and A is the total electrode area.

RESULTS AND DISSCUSSION

Surface Tension

Fig. 1 shows the surface tension as a function of asphaltene concentration in pyridine. A breaking point was observed at ~ 0.025 wt%, signifying that there is an onset of self-association of asphaltenic molecules at this concentration. This phenomenon is similar to the micellization of surfactant molecules in aqueous solutions. In a previous report we had shown that the self-association of asphaltene molecules in organic solvents was reversible, and more or less followed the micellar thermodynamics [3].

Zero-Shear Viscosity

Fig. 2a shows a typical zero-shear relative viscosity plot for asphaltene in toluene, as a function of asphaltene volume fraction. As expected, the relative viscosity follows the Einstein's argument (linear) in the dilute regime, and gradually deviates from it as concentration increases. This is due to the combination effect of solvation, interparticle interaction, as well as the particle shape. Fig. 2b exhibits the analysis suggested by Pal and Rhodes [6]. In their argument, the zero-shear viscosity should exhibit linearity if the viscosity is plotted as $(1/\eta_r)^{0.4}$ versus Φ, where η_r is

the relative viscosity and Φ the volume fraction of asphaltene. The slope of the curve, k, is the solvation constant, representing the effect of solvation, provided the shape effect is negligible. The k value obtained from Fig. 2b was 2.79, different from unity which represents no solvation. Fig. 2c compares the viscosity behavior of asphaltene colloids with a hard sphere model, taking the solvation effect into account. The viscosity for the hard sphere model was developed based on the hopping probability of the particle in a percolated environment [7]. Based on this argument, Campbell and Forgacs derived a simple equation for a hard sphere system with a volume fraction higher than the percolation threshold, which is in the neighborhood of 0.16 for most colloidal systems [8]. As one can see from Fig. 2c, for volume fractions up to about 0.3, there is no appreciable difference. This explains why the shape effect can be neglected in Pal and Rhodes analysis (it still shows linearity, although Pal and Rhodes's argument is only applicable for hard sphere systems). The effect of interparticle interaction was analyzed using an equation derived by Grimson and Barker [10]. They derived the zero-shear viscosity for a $(1/r^n)$ potential. The equation reads

$$\eta = (1+2.5\Phi) + \eta_o(\Phi/\Phi_m)[1-(\Phi/\Phi_m)^{1/3}]^{-n}$$

where Φ_m is the maximum packing volume fraction (it was estimated to be about 0.64 for asphaltene in toluene [9]). With this equation we found that the interactions between asphaltene colloids can be well described by $1/r^2$ potential (see Fig. 2d).

As a summary from our zero-shear viscosity analysis, we found the asphaltene colloids in toluene to be solvated, but behaved rheologically like hard spheres for Φ up to ~ 0.3, and the interparticle interactions followed a $1/r^2$ potential. In the following, we shall discuss the detailed structure, the polydispersity, and the interparticle interactions obtained from a small angle neutron scattering study.

Small Angle Neutron Scattering

Small angle neutron scattering (SANS) measures the differential cross section per unit volume of the sample, based on the scattering of the nuclei contained in the sample. In our case, the scatterers are the solvent (toluene/pyridine) and the asphaltene. Since asphaltene molecules contain nuclei different from toluene/pyridine, the capability in scattering the defined incoming neutrons differs. This scattering contrast allows us to differentiate the suspended asphaltene colloids from the solvent material, in terms of their shapes and the interactions between them. The SANS measurement is usually represented in terms of the scattering intensity I(Q) as a function of the scattering vector Q (= $(4\pi/\lambda)\sin\theta$, λ is the neutron wavelength and θ the scattering angle). For colloidal system the I(Q) can often be expressed as [10]

$$I(Q) = N_p \cdot \langle P(Q) \rangle \cdot \langle S(Q) \rangle$$

where N_p is the number density of the asphaltene colloids, $\langle P(Q) \rangle$ is the average form factor, containing the shape information and the size polydispersity as well. $\langle S(Q) \rangle$ is the average structure factor describing the interactions between particles.

Fig. 3a shows I(Q), together with the theoretical curve, assuming the asphaltene to be spheres with a size distribution following the Schultz distribution function, and an $(1/r)\exp[-(\sigma r)]$ interparticle potential (σ is a constant characterizing the range of the interaction). Apparently, the agreement is reasonable. The SANS measurements were performed for a series of concentrations and solvents of various toluene to pyridine volume ratios, to study the effect of solvent permittivity (ϵ) . Fig. 3b and Fig. 3c show the effect of solvent permittivity on the particle radius (R), interaction range (i.e., σ) and on the particle polydispersity respectively. The particle radius was not sensitive to ϵ. However, σ decreased with increasing ϵ, which means that the interaction range becomes longer ranged upon increasing ϵ. This suggests that the asphaltene colloids are charged, and the interactions are mainly electrostatic. As ϵ increases, the charge dissociation is enhanced, and results in an increase in the charge screening length (or decrease in σ). As for polydispersity (Fig. 3c), the increasing polydispersity, with increasing ϵ, indicating that the solvent quality decreases as a function of ϵ [11].

Dielectric Relaxation

Fig. 4 gives the dielectric loss ϵ'' as a function of the frequency for a 20% asphaltene solution in toluene at 60 ^{o}C (circles), together with a fitting curve (solid line). This fitting curve was based on the Cole-Cole equation,

$$\epsilon''(\omega) = \epsilon_{\infty} + \Delta\epsilon/[1 + (i\omega\tau)^{1-\beta}]$$

where ω is the frequency in Hz, ϵ_{∞} is the dielectric constant at ∞ frequency, $\Delta\epsilon$ is the difference between ϵ_{∞} and the zero-frequency ϵ, τ is the mean dielectric relaxation time, and β is an exponent signifying the stretch of the relaxation, due to the interactions between particles. When $\beta = 0$, the system is a noninteracting ideal system (in this case, the relaxation is called a Dybye relaxation). The fitting quality is not perfect, mainly due to the high polydispersity of the particle size (and may be shape as well). For some cases at lower temperature, a shoulder was exhibited. This is likely due to the formation of a second mode, either resulting from percolation, or networking of the suspended particles. The β values obtained through the Cole-Cole fitting for all temperatures were very different from zero, meaning that there are significant interactions which may interfere the dielectric response. This clearly indicates that the interaction is dipole moment driven, and is electrostatic, confirming the result drawn from SANS measurements.

Conclusion

We have systematically studied the physical properties of asphaltene solutions, using various techniques. The properties we observed can be summarized as follows: (1) asphaltenes are similar to surface active agents, since there exists a threshold concentration (for a give organic solvent), above which the molecules self-associate into "micelles", (2) the aggregates are loosely packed (highly solvated), but with rheological behavior very similar to a hard sphere system until the volume fraction exceeds 0.3, (3) the interactions derived from the solution viscosity follows a $1/r^2$ potential, (4) the aggregates are charged and have significant size polydispersity, and (5) the interparticle interactions are electrostatic force driven.

References

[1] Speight, J.G. in "Chemistry of Asphaltenes," edited by Bunger, J.W. and Li, N.C., American Chemical Society, Washington, D.C., Sept. 10-11, (1979).
[2] Sheu, E.Y., Storm, D.A., and De Tar, M.M. J. Non-Cryst. Sol. **131-133**, (1991) 341-347.
[3] Sheu, E.Y., De Tar, M.M., Storm, D.A., and DeCanio, S.J. FUEL 71, (1992), 299-302.
[4] Andersen, S.I., and Birdi, K.S. J. Interface Sci. **142**, (1991) 497.
[5] Sheu, E.Y., De Tar, M.M., Storm, D.A. Macromolec. Rep. **A28** (Suppl.2), (1991) 159-175.
[6] Pal, R. and Rhodes, E.J. J. Rheol. **33** (1989) 1021.
[7] Campbell, G.A. and Forgacsm G. Phys. Rev. A **80**,(1990), 8.
[8] Bhattacharya, S, Stoke, J.P., Kim, M.W., and Huang, J.S. Phy. Rev. Lett. **55**, (1985) **1884**.
[9] Sheu, E.Y. De Tar, M.M., and Storm, D.A. FUEL **70**, (1991) 1151-1156.
[10] Sheu, E.Y. Phy. Rev. A. **45**, (1991) 2428-2438.
[11] Sheu, E.Y., and Chen, S.H. J.Phys. Chem. **92** (1988) 4466-4474.

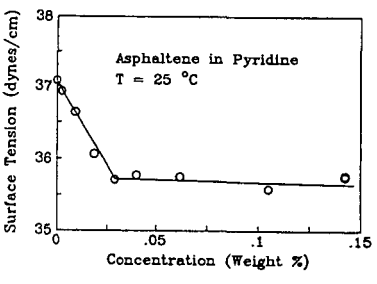

Fig. 1. Surface Tension of Asphaltene as a function of concentration.

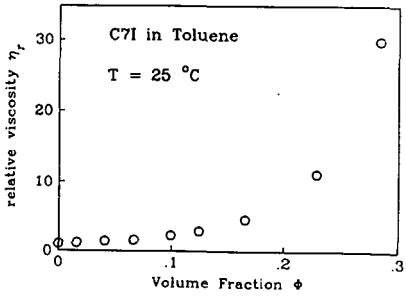

Fig. 2a. Relative viscosity for asphaltene/toluene solution.

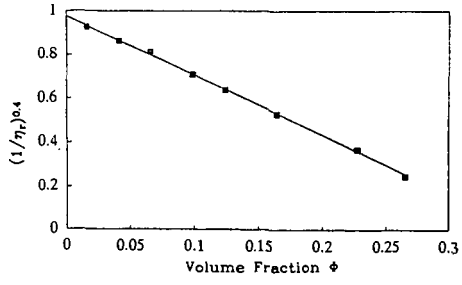

Fig. 2b. Pal and Rhodes Analysis.

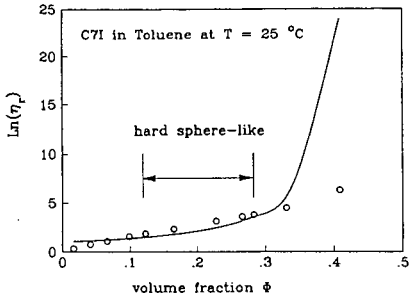

Fig. 2c. Comparison of asphaltene solution with hard sphere model.

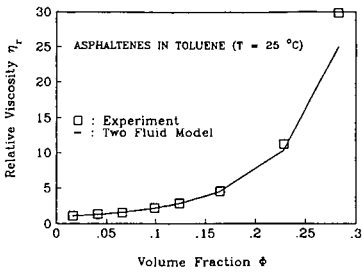

Fig. 2d. Interaction model for asphaltene solution.

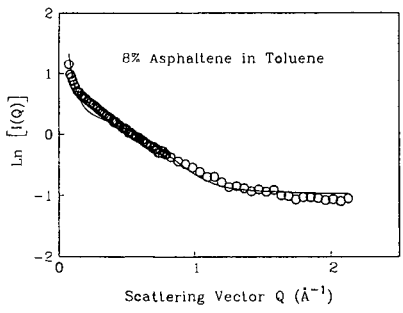

Fig. 3a. SANS dat and the analysis.

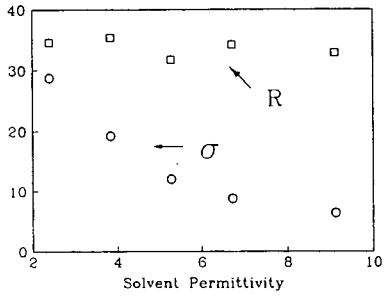

Fig. 3b. Radius and the interragne parameter, as a function of ϵ.

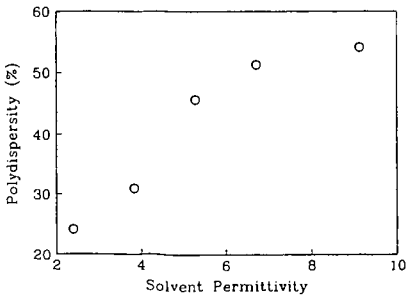

Fig. 3c. Polydispersity as a function of solvent permittivity.

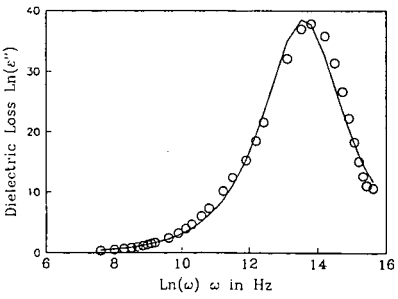

Fig. 4. Dielectric loss for asphaltene solution and the Cole-Cole analysis.

Improved Asphalt Specification Based on Physicochemical Properties

Sang-Soo Kim and Dah-Yinn Lee

Department of Civil and Construction Engineering
Iowa State University
Ames, Iowa 50011

Keywords: Asphalt, Physicochemical Properties, Specification

INTRODUCTION

Current specifications for asphalt cement contain limits on physical properties based on correlations established in the past with field performance of asphalt pavements. Recently, however, concerns have arisen that although current asphalts in use meet these specifications, they are not consistently providing the service life once achieved.

There are a number of logically possible explanations of this situation:

[1] A considerable concern is associated with the recent world crude oil supply and the economic climate after the 1973 oil embargo which may have affected the properties of asphalt of certain origin (1). Blending several crudes, as routinely practiced in refineries to produce asphalts meeting current specifications, may have upset certain delicate balances of compatibility among various asphaltic constituents, which may manifest itself in their long-term field performance but not in original physical properties specified in the specifications (2,3).

[2] The increased volume and loads of traffic on highways.

[3] Inadequate mixture design, poor gradation of aggregates, changing construction practices, and improper use of additives (1,4).

[4] Specifications based only on physical properties of asphalts do not guarantee adequate perfonnance.

While the performance of the asphalt pavements could be improved by judicious application of improved mix design techniques, more rational thickness design procedures, better construction methods and quality control measures, selection of asphalts based on performance-related properties, tests, and specifications is the key to durable asphalt pavements.

Asphalt samples were analyzed by high performance liquid chromatography (HPLC), thermomechanical analysis (TMA), differential scanning calorimetry (DSC), X-ray diffraction (XRD), and nuclear magnetic resonance (NMR). The results were correlated with properties known to affect field performance. On the basis of the correlations, performance-based trial specifications for the state of Iowa were developed.

EXPERIMENTAL

Materials

Three sets of asphalt samples were used in this study as follows:

1. A total of 12 virgin asphalts obtained from two local suppliers and their thin film oven test (TFOT) residues (ASTM D1754),
2. Two sets of asphalt samples recovered from two pavements of known performance (total 6 recovered asphalts from Sugar Creek and Wood River), and
3. Asphalt samples used in 10 hot mix field pavement projects in Iowa and their field and lab aged samples.

Aging of asphalts

Age hardening characteristics of the project asphalt samples were studied in the laboratory by use of three different aging procedures; TFOT, Iowa durability test (IDT), and mix aging. TFOT simulates age hardening due to the conventional batch mixing (5). The IDT or pressure-oxidation procedure consists of two aging stages: TFOT to simulate hardening during hot-plant mixing followed by pressure-oxidation under 20 atm of oxygen at 65 °C for oxidative hardening during field pavement service (6). In this study, two different durations of pressure-oxidation, 5 and 46 hour, were used. These are, based on the previous study, equivalent to 1 and 5 year field aging under Iowa climate, respectively (6).

The hardening of asphalt in a mix is believed to be affected by air void content, asphalt film thickness, characteristics of aggregate, and the durability of the asphalt. Marshall specimens were prepared by use of the same materials and job mix formula used at each project. To simulate asphalt aging in pavement of high and low void levels, mixes were compacted by 35 blows per side and 75 blows per side, respectively, and oven-aged at 60 °C for 12 days, equivalent to eight years of in-service asphalt aging in pavement (7). The asphalts were extracted and recovered.

Rheological properties

Penetrations at 5 °C and 25 °C (100g, 5sec), penetration at 4 °C (200g, 60sec), viscosities at 25, 60, and 135 °C, and ring-and-ball softening point tests were performed on the original asphalts, the lab aged asphalts, and asphalts recovered from plant mix and cores (0 and 1 year old). From these data, penetration ratio (PR), penetration index (PI), pen-vis number (PVN), viscosity temperature susceptibility (VTS), cracking temperature (CT), critical stiffness at -23 °C and 10,000 sec loading time (S23), stiffness at -29 °C and 20,000 loading time (S29), and critical stiffness temperature at 20,000 psi and 10,000 sec (TES) were calculated. Based on viscosity data at 25 °C, shear index (SI) and complex flow (CF) were also determined.

To correlate with low temperature field performance, the dependence of viscoelastic properties of selected five asphalt samples on their thermal history was studied at a low temperature. Newtonian viscosities and elastic shear moduli of these samples were determined using modified cone and plate viscometer at 5 °C after cooling from 25 °C and warming from a quenching temperature of -30 °C. Before cooling or warming, samples were allowed to be conditioned for 24 hours or 1 hour at the specified temperature (25 °C or -30 °C). Instrumentation, procedure, and the theory were described elsewhere (8).

High performance gel permeation chromatography (HP-GPC)

Waters' HP-GPC system was used during this study. It included three "Ultrastyragel" columns, one 1000Å followed by two 500Å units and a UV absorbance detector (Waters

model 481) set at 340nm. Asphalt samples of 0.02 to 0.05 grams were dissolved in HPLC grade tetrahydrofuran (THF) to be 0.5% (w/v) solution. Before injection, sample was centrifuged to remove foreign particles capable of plugging columns. The delay time between sample dissolution and injection was kept constant from sample to sample (approximately 30 minutes). Sample size was 100μl and THF was used as a solvent with 0.9 ml/min flow rate at 27°C.

Thermal analysis

Differential scanning calorimetry (DSC) analysis was performed on the first two sets of asphalts, scanning from -80°C to 80°C at a rate of 5°C/min. Precooling rate was 10°C/min. Thermomechanical analysis (TMA) was performed on the second and the third sets of asphalts. Samples were prepared having 3mm thickness. By using an expansion probe, samples were scanned from -70°C to 25°C at a rate of 5°C/min.

Nuclear magnetic resonance (NMR) and X-ray diffraction

Four samples from the first two asphalt sets were subjected to ^{13}C and ^{1}H NMR analysis, using a home-built solid state NMR spectrometer operating at 100MHz for ^{1}H and 25MHz for ^{13}C. This unit has extensively been used for studies of pyrolyzed pitches and coals. Solution ^{13}C NMR was also employed for two recovered asphalts, two original asphalts and their n-pentane asphaltenes (Bruker WM-200, 50MHz).

The first set of asphalts, 12 original asphalt and their TFOT residues were subjected to X-ray diffraction analysis by θ-2θ scanning, using monochromatized CuK_{α} beam with 1.54Å wavelength. The samples were molded in circular Plexiglas holders exactly flush with their brim.

RESULTS AND DISCUSSION

Rheological properties

The rheological properties of all asphalts studied were reported elsewhere (8,9,10). Among the rheological properties, temperature susceptibility may be the most important property determining pavement performance. Asphalt cements of high temperature susceptibility may contribute to rutting at high pavement temperatures and cracking at low pavement temperatures. The results of this study indicates that within each viscosity grade of asphalt cements available in Iowa meeting the current specifications, there were differences in temperature susceptibility between suppliers and between samples from the same supplier over time.

The viscoelastic properties of five asphalt samples measured at 5°C show the large differences among the responses of these sample to temperature conditioning and the lapse of time. Figures 1 and 2 show viscosities and elastic shear moduli of two recovered asphalts, Sugar Creek asphalt (SC) and Wood River asphalt (WR). Both were recovered from the surface courses after 80 months of field services. The viscoelastic properties of SC asphalt show large dependence on thermal history. Performance evaluation of these asphalts indicated that SC asphalt developed more cracks in much shorter time than WR asphalt (Mark and Huisman, 1985).

HP-GPC

Figure 3 shows typical HP-GPC chromatograms of original, TFOT residue, and asphalt pressure-oxidized for 46 hours (IDT). The amount of large size molecules is unidirectionally sensitive to aging, i.e., as the asphalt ages the amount of large molecules increases. Therefore, the HP-GPC technique can be used to monitor and predict aging.

To better characterize the molecular size distribution of the asphalts and to be used in statistical analysis, the HP-GPC profile were divided into three, four and eight slices following Montana State (11), Iowa State (8), and Purdue (12) procedures respectively. The elution cut-off times used in the three slice method were 22.5 and 30.5 minutes. The four slice method is a modification of the three slice method, in which the first fraction (earliest-eluted fraction) is further divided into two using a cut-off elution time of 18.125 minutes. The first and the second eluted fractions is denoted as LMS (large molecular size) and MMS1 (medium molecular size 1), respectively. In the 8-slice method, the cut-off times used were 19.875, 21.875, 23.875, 25.375, 26.875, 28.875, and 30.875 minutes and the eight slices were denoted as X1 ··· X8.

Results of regression analysis between the physical properties and HP-GPC parameter defined as above are listed in Table 1. The first two columns show one-parameter correlations using the first fractions in the 3-slice and 4-slice methods. LMS fraction which ranges from 1% to 11% has weak correlations with physical properties. LMS+MMS1 fraction ranges from 20% to 43% and shows significant correlations with all the rheological properties, some temperature susceptibility parameters and low temperature cracking properties. Molecular size distribution is best characterized by the 8-slice method thus correlating well with almost all physical properties. Among the 8 slices, the second slice (X2) and the seventh slice (X7) most predominantly control the rheological and low-temperature properties as indicated by results from stepwise regressions (the last column in Table 1 and Table 3).

Effects of aging on physical properties and on physicochemical properties are not the same. For example, the asphalt used in one of the ten projects had a large percent increase in LMS due to aging, but not reflected by changes in viscosity ratio. This implies that the chemical composition of the asphalt results in excess amount of oxidation products determined by molecular size but the increase of viscosity is also prevented by its chemical composition. The opposite was also observed. The asphalt used in another project showed high increase in viscosity after TFOT, but not reflected in LMS increase, suggesting the opposite chemical composition.

Thermal analysis

It has long been attempted to correlate some low temperature transitions in asphalts, which are believed to affect their low-temperature rheology, such as glass transition and phase transformations to their field performance. A typical DSC thermogram obtained in this study is shown in Figure 4. The low temperature inflection points on the thermograms interpreted as glass transition points (13,14), Tg, were determined. The rest of the thermograms consist of two shallow endothermic peaks. The two peak temperatures were determined. These regions were analyzed to determine the enthalpies of transformation. These endothermic transformations are referred to as melting of the crystallized asphaltic components (13) or dissolution of these components in the matrix (14). The DSC data shows no significant correlation with physical properties determined in this study. However, the enthalpies of transformation for asphalts from one supplier are significantly different from asphalts from the other supplier (the enthalpy values are on the average 24% higher).

The effect of aging on the DSC parameters appears to be in random directions. This might be due to overshadowing the gel to sol transition in thermal analysis by the large thennal effect of dissolution of the crystallized components as treated by Albert et al. (14).

Four parameters were determined from the TMA thermograms as shown in Figure 5:

1. The slope of the initial straight line (ML) which measures the low temperature thermal coefficient of expansion of the sample at the glassy state.
2. The slope of the nearly straight adjacent section of the plot at higher temperature (MH), which measures the coefficient of expansion after the glass transition.
3. The glass transition temperature (Tg) graphically determined as shown in the Figure 5.
4. The softening temperature (Tsp) at which the displacement of the TMA probe reaches a maximum.

The glass transition temperature, Tg, of the original asphalts ranges from -34 °C to -22.5 °C, increasing with viscosity from AC-5 to AC-20. In general, aging at high temperature (TFOT or hot mixing) reduced the TMA parameter values and the following low temperature aging (pressure-oxidation or field aging) increased the thermal responses. In other words, a different aging mechanism seemed to result in different trend of thermal responses.

Correlations between the TMA parameters and physical properties are listed in Table 2. Tg correlates well with low temperature properties, while Tsp and ML correlates well with both rheological and low-temperature properties. Among the temperature susceptibility parameters only penetration ratio (PR) and pen-vis number at 60 °C (PVN60) significantly correlate with Tsp and ML.

Nuclear magnetic resonance (NMR)

Based on the limited experiments, the following conclusions are drawn:

1. Oven treatment (TFOT) decreases the amount of aliphatic quaternary carbon in the original asphalt.
2. The quaternary carbon content of the Sugar Creek (SC) sample is strikingly less than those of all other samples subjected to NMR.

X-ray diffraction

As associative interaction between asphaltenes or polar molecules promote a structural order in the system, such an interaction is also expected to reflect on X-ray diffraction spectra of the sample.

According to Williford (15), the height of the shoulder of the spectral curve at low angles is a measure of the quality of the asphalt. This height above the background (at 2θ = 4.83 °) for the original asphalts and their TFOT residues were determined. No regular trend was found in these X-ray spectra regarding the viscosity grade, the sample source, and the effect of aging.

Correlation

In this section, the discussion will be confined to correlations among physical properties, TMA, and HP-GPC parameters of all samples related to the 10 field projects.

TMA parameters and HP-GPC parameters had less significant correlation with each other than their correlations with physical properties. For this reason, it was decided to treat these two sets of parameters as independent but complementary variables to correlate with the physical properties. Table 3 gives a summary of regression analyses performed as such on

physical properties against TMA and HP-GPC parameters combined. These regression analyses give considerably higher values of coefficients of determination (r^2) than the regression analyses using TMA or HP-GPC parameters alone. Figures 6 and 7 compare the measured viscosities at 25°C and 135°C with the predicted values from regression analyses.

PROPOSED TRIAL ASPHALT SPECIFICATIONS FOR IOWA

The selection of the proper grade of asphalt for a given paving project must be based on consideration of climate (temperature), traffic, thickness of the layer, and the prevailing construction conditions. The selection of asphalt within a grade must be based on temperature susceptibility and durability. The temperature susceptibility of asphalt influences the mixing, placing and compaction of paving mixture as well as the high and low temperature performance of the pavement. Durability of asphalt or asphalt's resistance to hardening and aging, during construction and in-service, affect the pavement life. Current specifications, while containing requirements for indirect control of temperature susceptibility and asphalt hardening during hot-plant mixing (short-term durability), have no control over long-term durability.

A trial specification based on Iowa pressure oxidation test is proposed. The Iowa pressure oxidation test is a realistic durability test for asphalt developed by consideration of the two stages of hardening processes of asphalt in their logical order and of their differences in mechanisms and effects. Furthermore, good correlations between field hardening and IDT exist (6). Results of this and more recent other studies confirm that chemical or compositional factors have a major impact on the performance of asphalt. While specification based solely on chemical composition would be costly and difficult to implement, a rational specification based on both short-term and long-term accelerated aging tests, containing time-honored physical tests and temperature susceptibility control, coupled with minimum chemical and low-temperature requirements is both desirable and feasible. HP-GPC and TMA parameters are determined to be included in the proposed specification.

Many researchers have proposed physical properties of asphalts and their critical limits for acceptable pavement performance. Some of these properties are penetration at 4°C and 25°C, Ring-and-Ball softening point, viscosity at 25°C, shear index, pen-vis number, and stiffness at a low temperature as summarized in Table 4.

Due to insufficient field performance data correlated with HP-GPC ant TMA parameters, critical values of HP-GPC an TMA parameters were indirectly estimated from correlation with the performance related properties as given in Table 4. Aging characteristics of asphalts are commonly expressed by a hyperbolic functions of time and changes of asphalt properties after 5 years of aging become very small. For this reason, the critical values discussed above are recommended as limiting values in specification for an asphalt pressure oxidized for 46 hours at 65°C and 20 atm oxygen.

Limiting values for penetration at 5°C were determined to meet the cracking temperature criteria to prevent a low-temperature asphalt transverse cracking. Long-term aging index, ratio of viscosity at 60°C after pressure oxidized for 46 hours to viscosity at 60°C after TFOT was introduced to assure long term durability. Based on observation of IDT data, a tentative critical long-term aging index was proposed.

The proposed specification, based on the pressure oxidation test and existing AASHTO M226, Table 2, is given in Table 5. Some of the limiting values can be refined as more field performance data become available.

CONCLUSIONS

Conclusions of a general natures are summarized as follows:

1. The strikingly different effect of thermal history on the viscoelastic properties at 5°C of the Sugar Creek core sample might have an important bearing on its poor field performance.
2. HP-GPC parameters are conclusively and unidirectionally sensitive to aging and can be used to predict behavior and performance of asphalts.
3. Both TMA and HP-GPC parameters correlates well with physical properties.
4. For some asphalts, aging characteristics during high temperature (short-term) and service temperature (long-term) were very different. Physical reponses to aging could be very different from physicochemical responses.
5. Improved asphalt specification should include evaluation methods for short-tenn and long-term aging characteristics in terms of both physical and physicochemical methods.

ACKNOWLEDGEMENTS

This research was sponsored by the Highway Division of the Iowa Department of Transportation (DOT) under Research Project HR-298. This study, under the same title, was also supported by and designated as Project 1942 of the Engineering Research Institute, Iowa State University.

The support of this research by the Highway Research Advisory Board and the Iowa DOT is gratefully acknowledged. The authors wish to extend sincere appreciation to the engineers of the Iowa DOT for their support, cooperation, and counsel. The authors would also like to thank Dr. Bernard C. Gerstein, Professor of Chemistry, Iowa State University for running the NMR work and Gerald Reinke, Koch Asphalt Co.; Alden Bailey, Jebro, Inc.; Brian Chollar, FHWA; and Joan Pribanic, Montana State University, for supplying the asphalt samples tested in the study. The following individuals contributed, in various capacities, to this investigation: B. V. Enustun, Jerry Amenson, Barbara Hanson, Shelley Mellcher, Paul Schmidt, Steve Troyer, Paul Martin and R. Suryanarayana.

LITERATURE CITED

(1) Hodgson, R.S., Transport. Res. Rec., 999, 10 (1984).
(2) Goodrich, J.L.,Transport. Res. Rec., 1096, 146 (1986).
(3) Petersen, J.C., Transport. Res. Rec., 999, 13 (1984).
(4) Anderson, D.A. and Dukatz, E.L., Report No. FHA/RD-84/095 (1985).
(5) Goodrich, J.L. and Dimpfl, L.H., Proc. Assoc. Asphalt Paving Tech., 55, 57 (1986).
(6) Lee, D.Y., Highway Res. Rec., 231, 34 (1968).
(7) Goode, J.F. and Lufsey, L.A., Proc. Assoc. Asphalt Paving Tech., 34, 430 (1965).
(8) Lee, D.Y. and Enustun, B.V., Task 1 Report, HR-298, Ames, Iowa (1988).

(9) Enustun, B.V., Kim, S.S., and Lee, D.Y., Progress Report No. 2, HR-298, Ames, Iowa (1989).
(10) Enustun, B.V., Kim, S.S., and Lee, D.Y., Final Report, HR-298, Ames, Iowa (1990).
(11) Jennings, P.W. et al., Research Report FHWA-MT-7930 (1980).
(12) Garrick, N.W. and Wood, L.E., Proc. Assoc. Asphalt Paving Tech., (1988).
(13) Noel, F. and Corbett, L.W., J. Inst. Petrol., 56, 261 (1970).
(14) Albert, M., Bosselet, F., Claudy, P., Letoffe, J.M., Lopez, E., Damin, B., and Neff, B., *Thermochimica* Acta, 84, 101 (1985).
(15) Williford, C.L., Texas Engr. Exp. Station Bull. 73, A & M College of Texas, College Station, TX (1943).
(16) The Asphalt Institute, Research Report No. 81-1, College Park, MD (1981).
(17) Finn, F.N. NCHRP Report 39 (1967).
(18) Kandhal, P.S., Sandvig, L.D., and Wenger,M.E., Proc. Assoc. Asphalt Paving Tech., 42, 99 (1973).
(19) McLeod, N.W., Proc. Assoc. Asphalt Paving Tech., 58, 410 (1989).
(20) Kandhal, P.S., Proc. Assoc. Asphalt Paving Tech., 47, 73 (1978).

Table 1. Regression Analyses between Physical Properties and HP-GPC Parameters (n=73)

Dependent Variables	LMS		LMS*MMS1		3-SLICE		4-SLICE		8-SLICE		Selected variables from stepwise reg
	P-value	R**2	P-value	R**2	P-value	R**2	P-value	R**2	P-value	R**2	
Rheological properties											
P5	0.0004	0.161	0.0001	0.245	0.0001	0.333	0.0001	0.356	0.0001	0.568	X2,X4,X5,X7,X8
P25	0.0001	0.248	0.0001	0.385	0.0001	0.432	0.0001	0.429	0.0001	0.549	X4,X6,X7,X8
P4	0.0001	0.191	0.0001	0.298	0.0001	0.378	0.0001	0.389	0.0001	0.560	X2,X7
VIS25	0.0012	0.139	0.0001	0.253	0.0001	0.302	0.0002	0.278	0.0001	0.462	X4,X6,X7,X8
CF	0.0500	0.053	0.0001	0.283	0.0001	0.339	0.0001	0.475	0.0001	0.546	X2
SI	0.0173	0.077	0.0001	0.311	0.0001	0.369	0.0001	0.457	0.0001	0.509	X2,X4
VISGO	0.0421	0.057	0.0001	0.185	0.0006	0.221	0.0006	0.249	0.0001	0.325	X2
VIS135	0.0036	0.113	0.0001	0.361	0.0001	0.416	0.0001	0.475	0.0001	0.588	X7,X8
SP	0.0001	0.208	0.0001	0.353	0.0001	0.391	0.0001	0.367	0.0001	0.505	X4,X6,X7,X8
Temperature susceptibility											
PR	0.0004	0.161	0.0001	0.258	0.0001	0.278	0.0001	0.307	0.0001	0.420	X5
PI	0.2533	0.018	0.1021	0.037	0.0523	0.105	0.0282	0.146	0.0366	0.218	X3,X4,X6
CN	0.1110	0.035	0.0208	0.073	0.1480	0.074	0.1827	0.086	0.1447	0.166	X5
VIS	0.1798	0.025	0.6095	0.004	0.8754	0.010	0.4803	0.049	0.2465	0.142	X3
PVN60	0.2874	0.016	0.0099	0.090	0.0700	0.097	0.0061	0.188	0.0076	0.268	X2,X8
PVN135	0.7255	0.002	0.0619	0.048	0.2190	0.062	0.0001	0.301	0.0001	0.433	X2,X8
Low-temperature cracking properties											
CT	0.2700	0.017	0.2242	0.021	0.0515	0.106	0.0103	0.174	0.0001	0.311	X1,X2,X7
TES	0.0001	0.205	0.0001	0.273	0.0001	0.317	0.0001	0.354	0.0001	0.432	X2,X7
S23	0.0032	0.116	0.0001	0.236	0.0001	0.334	0.0001	0.326	0.0001	0.411	X2,X7
S29	0.0099	0.090	0.0001	0.211	0.0001	0.319	0.0001	0.316	0.0001	0.467	X1,X2,X7,X8

Table 2. Regression Analyses between Physical Properties and TMA Parameters (n=80)

Dependent variables	Tg		Tsp		ML		MH		ALL 4 PARAMETERS		Selected variables from stepwise reg.
	P-value	R**2	P-value	R**2	P-value	R**2	P-value	R**2	P-value	R**2	
Rheological properties											
P5	0.0003	0.152	0.0001	0.228	0.0106	0.081	0.6021	0.004	0.0001	0.357	ALL
P25	0.0125	0.077	0.0001	0.207	0.0027	0.110	0.9885	0.000	0.0001	0.292	Tsp
P4	0.0016	0.121	0.0001	0.246	0.0057	0.094	0.8209	0.001	0.0001	0.340	ALL
VIS25	0.0037	0.103	0.0001	0.399	0.0003	0.157	0.7735	0.001	0.0001	0.474	Tsp
CF	0.9515	0.000	0.0001	0.249	0.0001	0.173	0.7922	0.001	0.0001	0.487	ALL
SI	0.9571	0.000	0.0001	0.249	0.0013	0.125	0.5032	0.006	0.0001	0.465	ALL
VIS60	0.2055	0.020	0.0001	0.297	0.0009	0.133	0.6978	0.002	0.0001	0.430	Tsp, ML, MH
VIS135	0.0520	0.048	0.0001	0.358	0.0001	0.173	0.7772	0.001	0.0001	0.508	Tsp, ML, MH
SP	0.0372	0.054	0.0001	0.336	0.0003	0.158	0.8249	0.001	0.0001	0.426	Tsp, ML, MH
Temperature susceptibility											
PR	0.5794	0.004	0.0004	0.150	0.0008	0.135	0.4413	0.008	0.0002	0.249	ALL
PI	0.1248	0.030	0.1208	0.031	0.3939	0.009	0.6061	0.003	0.0569	0.114	Tg, Tsp
CN	0.8330	0.001	0.0376	0.054	0.0960	0.035	0.6208	0.003	0.0497	0.118	Tsp
VTS	0.9091	0.000	0.5999	0.004	0.6046	0.003	0.8512	0.000	0.9374	0.011	None
PVN60	0.9802	0.000	0.0107	0.081	0.0413	0.052	0.7488	0.001	0.0083	0.165	Tsp
PVN135	0.9441	0.000	0.0970	0.035	0.2008	0.021	0.8359	0.001	0.2380	0.070	Tsp
Low-temperature cracking properties											
CT	0.0036	0.104	0.2035	0.021	0.9654	0.000	0.2546	0.017	0.0125	0.155	Tg, MH
TES	0.0016	0.120	0.0022	0.114	0.0216	0.066	0.8811	0.000	0.0008	0.221	Tg, Tsp
S23	0.0002	0.161	0.0001	0.280	0.0006	0.140	0.9183	0.000	0.0001	0.402	ALL
S29	0.0009	0.133	0.0001	0.211	0.0009	0.133	0.9954	0.000	0.0001	0.345	ALL

Table 3. Regression analyses: Physical Properties against TMA and HP-GPC Parameters (n=73)

Dependent Variables	TMA & HP-GPC parameters		Selected variables from stepwise reg.	
	P-value	R**2	TMA parameters	HP-GPC parameters
Rheological properties				
P5	0.0001	0.666	**Tsp**	**X2**,X6,**X7**
P25	0.0001	0.669	Tsp,ML,MH	**X4**,X6,**X7**
P4	0.0001	0.667	Tsp	**X2**,X4,X6,**X7**,X8
VIS25	0.0001	0.766	**Tsp**	X2,**X4**,X6,**X7**,MWT,PIDX
CF	0.0001	0.741	Tg,Tsp,**ML**,MH	**X2**
SI	0.0001	0.719	Tg,**Tsp**,ML,MH	**X2**
VIS60	0.0001	0.583	**Tsp**	X8
VIS135	0.0001	0.773	Tsp,ML,MH	X7
SP	0.0001	0.715	**Tsp**,ML,MH	**X1**,**X3**,**X6**,MWT
Temperature susceptibility				
PR	0.0001	0.636	Tsp	X2,**X4**,X5
PI	0.0517	0.309	Tg,Tsp	**X4**,PIDX
CN	0.2076	0.246	Tsp	X5
VTS	0.5121	0.187		X3
PVN60	0.0098	0.368		X2,X8
PVN135	0.0001	0.496		**X2**,**X8**
Low-temperature cracking properties				
CT	0.0008	0.438	Tg	X2,**X5**,**X7**,X8
TES	0.0001	0.564	Tg	X2,**X7**
S23	0.0001	0.655	**Tsp**,ML,MH	**X2**,X4,**X7**,PIDX
S29	0.0001	0.588	Tsp,ML,MH	X2,X5,**X7**

Bold face indicates significantly correlated variable.

Table 4. Critical Values for Performance Related Parameters

Parameter	Critical Value	Reference	Corresponding X2,%	Corresponding X7,%	Corresponding Tg,°C	Tsp,°C	ML,μm/°C
P4	>5	10	<18.5	>4.5	<-9.5	<32.9	<0.51
P25	>20	17	<18.0	>5.0	<-18.5	<31.0	<0.39
SI	<0.55	18	<18.1	>4.6		<36.0	<0.60
R&B SP	<65.5°C	17	<18.7	>4.6		<31.2	<0.45
VIS25	<2MPa·s	17	<18.2	>5.2	<-17.5	<28.0	<0.42
PVN60	>-1.3	5	>9.8	<13.6			
PVN135	>-1.0	19	>11.1	<12.7			
S23	>20ksi	20	<19.5	>3.7	<-17.0	<32.5	<0.47

Table 5. Proposed Trial Specification for Asphalt Cement

Test	AC-5	AC-10	AC-20
Original Asphalt:			
Viscosity @ 60 °C, poise[1]	500±100	1,000±200	2,000±400
Viscosity @ 135 °C, cSt, min[1]	175	250	300
Penetration @ 25 °C, min[1]	140	80	60
Flash point, °C, min[1]	177	219	232
Solubility in TCE, %, min[1]	99.0	99.0	99.0
Residue from TFOT:			
Viscosity @ 60 °C, poise, max[1]	2,000	4,000	8,000
Residue from Pressure-Oxidation, 46 hrs, 65 °C, and 20 atm:			
Viscosity @ 60 °C, poise, max	10,000	20,000	40,000
Penetration, 25/100/5, min	20	20	20
Penetration, 4/200/60, min	5	5	5
Penetration, 5/100/5, min	10	8	7
R&B softening point, °C, max	71	71	71
Stiffness, -23 °C, 10,000 sec, psi	20,000	20,000	20,000
Viscosity, 25 °C, megapoise, max	20	20	20
Shear susceptibility, max	0.55	0.55	0.55
X2 (HP-GPC), %, max	20	20	20
X7 (HP-GPC), %, min	5	5	5
Tg (TMA), °C, max	-20	-20	-20
Tsp (TMA), °C, max	28	28	28
ML (TMA), max	0.4	0.4	0.4

[1]AASHTO M226, Table 2

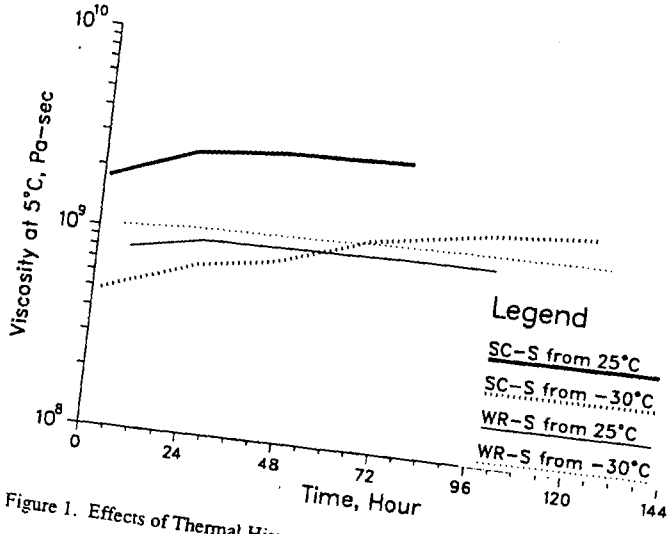

Figure 1. Effects of Thermal History on Viscosity at 5 °C for SC and WR asphalts

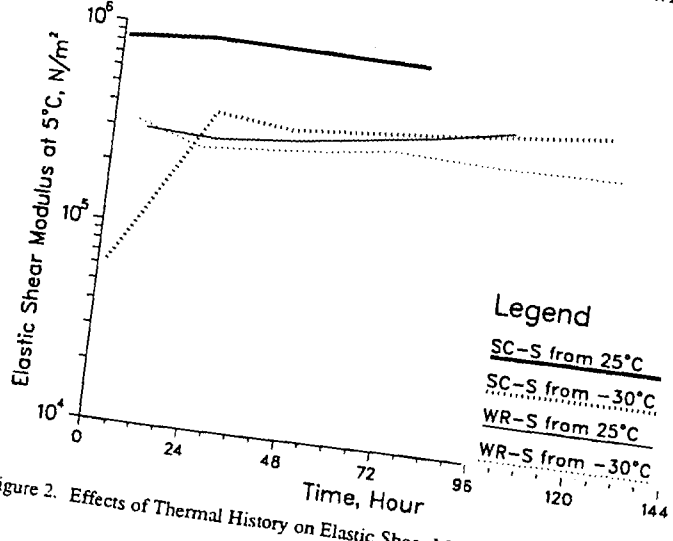

Figure 2. Effects of Thermal History on Elastic Shear Moduli at 5 °C for SC and WR asphalts

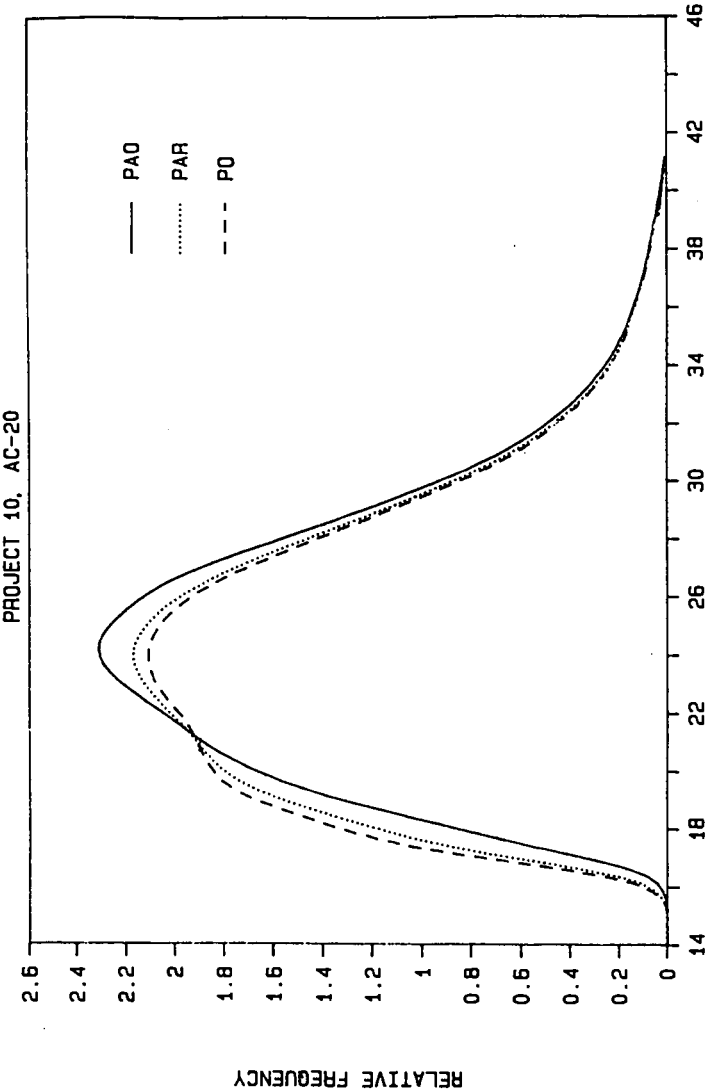

Figure 3. Effects of Aging on HP-GPC Chromatogram of Project 10 asphalt

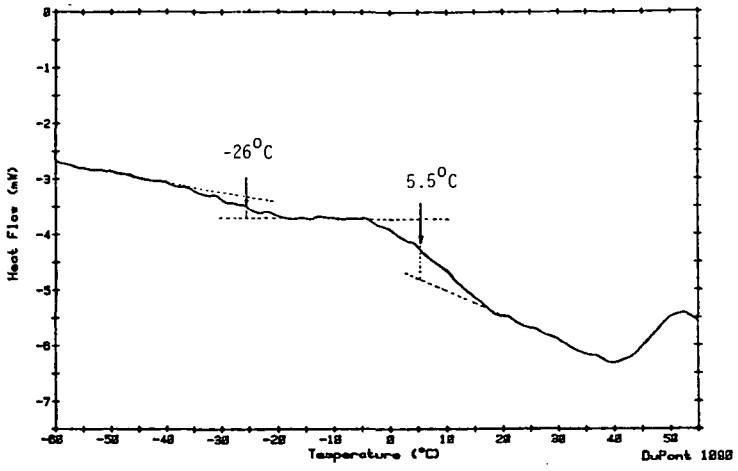

Figure 4. DSC thermogram of Asphalt B2975

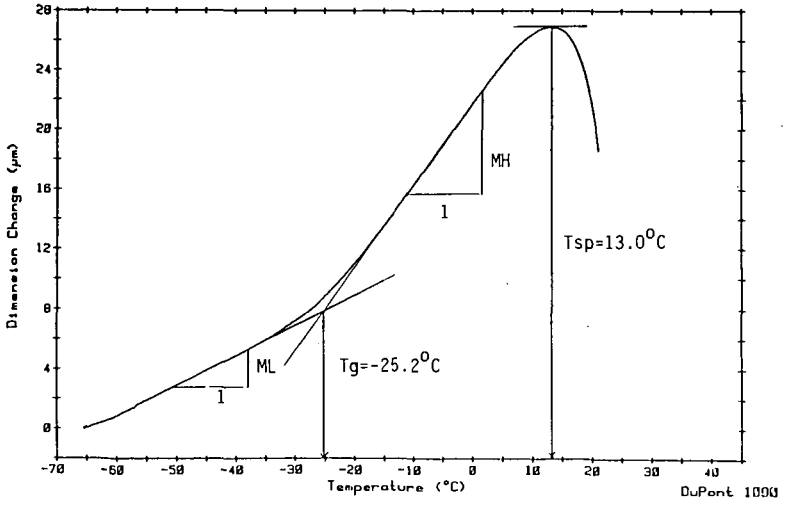

Figure 5. Typical TMA thermogram (K20-01-O)

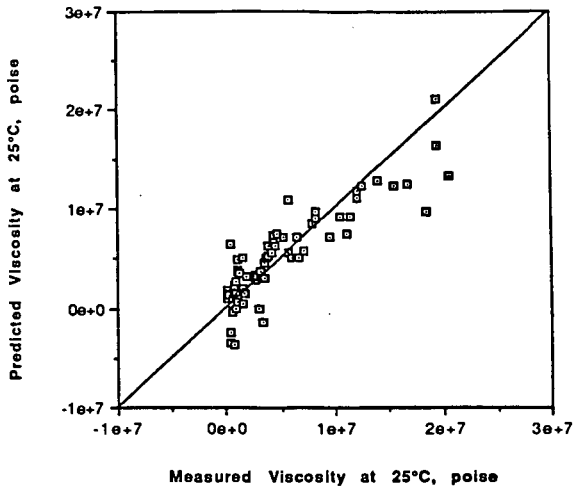

Figure 6. Measured Viscosity at 25 °C and Predicted from TMA and HP-GPC Parameters

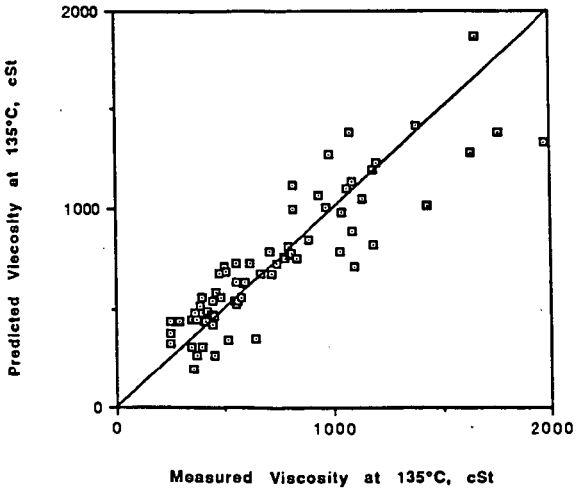

Figure 7. Measured Viscosity at 135 °C and Predicted from TMA and HP-GPC Parameters

RHEOLOGICAL ANALYSIS AND REINFORCEMENT EFFECTS OF POLYMER MODIFIED ASPHALT

William H. Daly, Ioan I. Negulescu and Zhaoyao Qiu(Chiu), Macromolecular Studies Group, Department of Chemistry, Louisiana State University, Baton Rouge, LA 70803-1804

Key Words: Asphalt/polymer blends, Dynamic rheology, creep

Introduction

Blends of polymeric materials with asphalt are complex and characteristically unique paving material systems. For any specific asphalt cement, (AC), the physical properties of the asphalt-polymer blend are affected by the amount of polymeric material added, its composition, its molecular weight, etc., but the most important variable may be the compatibility of the AC with the admixed polymer and the ability to enhance compatibility is critical to the commercial applications of reinforced ACs. Our research efforts are directed toward developing a simple method to estimate the compatibility of polymer additives with asphalt, to assess the phase structure of the asphalt-additive mixture, and to measure the blended polymer/asphalt performance relative to that of the pure asphalt matrix. Using dynamic testing techniques, we believe that a better assessment of asphalt cement performance can be obtained.

Polyethylene is a recyclable waste which is abundantly available either as virgin off spec material or from solid waste classification processes. Polyethylene is a useful asphalt modifier for increasing the low temperature fracture toughness of asphalt cements(1) and it may also confer additional pavement stability at elevated temperatures which would minimize rutting and distortion due to creep. Due to gross incompatibility, polyethylene/asphalt blends tend to separate when allowed to stand at elevated temperatures. We are exploring the potential for simple chemical modification of polyethylene to enhance its compatibility with asphalt. A low degree of chlorination may assure a favorable interaction with the polar components of asphalt. Further, the extent of chlorination can be utilized to vary the crystallinity of the polymer additive. The microstructure and morphology of chlorinated polyethylenes have been evaluated(2). In solution chlorination, attack occurs randomly along the chain and the resultant insertion of chlorine atoms distroys the crystallinity of the polymer.

Experimental

Materials used High density polyethylene (HDPE) was supplied by Allied Signal. A high melt index (MI = 25) sample with weight and number average molecular weights of 85,000 and 19,000 respectively was used as the substrate for chlorination as well as a standard for the polymer asphalt blends. Solution chlorination of HDPE was conducted in 1,1,2,2-tetrachloroethane (TCE) at 110° C(3); samples with 8.9 wt% and 15.2 wt% chlorine were used in this study. Asphalt samples from Southland, AC10, and Exxon, AC20, were used as the

continuous phase; detailed characterization of these samples is reported in the previous paper (4). The asphalt polymer blends were prepared by melting 5% polymer in asphalt at 150°C while stirring for 2 hours under N_2 atmosphere. The samples are identified as follows: ACD, Exxon Asphalt AC20; ACE, Southland Asphalt AC10; Asphalt blends: HDPE, High Density Polyethylene; CPEB, CPE with 8.9 wt% Cl content; CPEC, CPE with 15.2 wt% Cl content.

Fluorescence Reflection Microscopy The macrostructure of the asphalt polymer mixtures was examined using fluorescence reflection microscopy (FRM). The sample was fractured on dry ice and then the fracture surface was observed through a set of filtering lenses, where the asphalt phase appears dark yellow and the polymer phase bright. Figure 1 shows two FRM pictures of asphalt polymer blends. Clearly, the blends are two phase systems; the size of the CPE phase is larger than that of the HDPE phase for samples prepared under identical conditions.

DMA Bending Mode Measurements In a typical DMA experiment, an asphalt sample was heated to 150°C in a sand bath. The asphalt sample was then poured into a brass mold and kept at room temperature for at least an hour. The sample size was 50 mm long, 10 mm wide and 1.68 mm thick. The sample was run in bending mode at cooling rate of 1°C/min at the desired frequency. The Tg was identified as the temperature corresponding to the maxima of loss modular E" at each frequency.

Imposition of a larger strain (1 %) on the asphalt samples at 50 Hz in DMA experiments will induce cracking at a specific temperature during the cooling. The temperature, called cracking temperature (Tc), can be used to estimate the low temperature cracking resistance of asphalt or asphalt/polymer blends.

DMA Shearing Mode Measurements The shearing mode measurements were conducted at temperatures well above the glass transition temperature of asphalts and polymers employed. The samples were "sandwiched" between two parallel plates with size of 10 x 10 mm. Sample thickness was held to about 1.5mm, measured with a deviation of $\pm$0.05mm. Master curves were used with reference frequency of 20 Hz.

Constant Stress Creep Test The test was run at 5, 15, 25, 35°C, respectively, with Bohlin CS rheometer using a cone and plate mode. The stress applied was 590 Pa.

Results and Discussion

Low temperature cracking. The low temperature cracking test is quite sensitive to polymer/asphalt interactions. Since asphalt is a rather low molecular weight material, it becomes quite brittle at temperatures below its glass transition. In contrast, the Tg's of HDPE and CPE are greater than 30°C below the cracking temperatures of the blends. The amorphous regions of these polymers remain flexible while the crystalline phases provide tie points to limit chain reptation. Thus, these polymers should be effective impact modifiers. However, the extent of polymer contribution to blend properties depends upon the degree of compatibility with the asphalt matrix.

As can be seen in Table 1, the blends do indeed exhibit Tcs below the Tg of pure asphalt measured at the same frequency. We have shown that the Tc of pure asphalt falls above the corresponding Tg ( ) so the polymer component has improved the low temperature properties of the blends. Furthermore, CPE modified asphalts have lower Tcs than HDPE modified asphalts as might be expected from a more amorphous polymer with a higher degree of interaction with asphalt. Thus, our data indicate that CPE's are more compatible with asphalt than HDPE and are more effective in low temperature reinforcement.

Our fluorescence reflection microscopy observations confirm previous reports [5,6] that there are basically two phases existent in asphalt-polymer blends, an asphalt rich phase and a polymer rich phase. As fact of matter, the hetero-phased systems are advantageous from a practical of point of view; the dispersed polymer rich phases are expected to improve the toughness of brittle asphalt at low temperature and reinforce asphalt at high temperatures [7-9]. Since the polymers are not completely miscible in the asphalt continuous phase, their presence does not increase the melt viscosity of the blends excessively; asphalt cements prepared from these blends should flow smoothly and coat the aggregate efficiently.

The enhanced compatibility of CPE in asphalt can be attributed to a change in the polymer polarity as well as changes in morphology stemming from the reduced crystallinity. In crystalline polymers like HDPE, interaction with solvents and reagents is limited to the readily accessible amorphous regions. In HDPE, these regions are composed of -CH_2- segments more compatible with the saturates in asphalt. One would expect selective extraction of the saturates from the asphalt matrix by HDPE; this process would disrupt the balance of components in asphalt mixtures and promote phase separation.

Although chlorination of HDPE was conducted in solution, analysis of the chlorine distribution in the chains indicates that chlorination is not perfectly random. Runs of unreacted methylene groups that can crystallize remain. Chlorinated methylene groups do not enter the crystallites so the amorphous region contains a higher chlorine content than that measured in bulk samples. Thus, the amorphous regions are substantially more polar, and the presence of chlorine atoms on the polyolefin chain will improve the compatibility of the polymer with aromatic components and functional groups containing heteroatoms, such as, N, S, O, in asphalt. It was reported [10-13] that the CH_2/COO ratio was an important factor controlling the miscibility of blends prepared from a series of aliphatic polyester with polyvinylchloride; polymers with a higher polarity were more miscible. The polar components of asphalt would have a greater affinity for the amorphous regions of CPE and one would expect a corresponding increase in the compatibility of these polymers with asphalt. Introduction of chlorine adjusts the interaction parameters to reduce single component extraction thus the delicate equilibrium among the asphalt components is maintained.

Dynamic rheology. Rheological measurements under oscillating conditions yield the dynamic mechanical properties of polymers, i.e. the storage modulus, G', the loss modulus, G", and a mechanical damping or internal friction, tan δ. The storage modulus reflects the internal stiffness of a material under dynamic loading conditions; the corresponding stress response is in phase with the applied strain. The loss modulus is the viscous, damped response of the material; the corresponding stress is out of phase with the applied stain. This phase lag results from the time necessary for molecular rearrangements and is associated with relaxation phenomena. In studies of the response of a material to vibrational forces, stress, strain, frequency and temperature are the key variables. When a material is subjected to cyclical stress under conditions analogous to those encountered in the intended applications, the data reflect both short-term and long-term responses to the stress conditions. If time-temperature superposition can be applied, dynamic data obtained at short time intervals at high temperature can be transformed to yield long loading time data relevant to thermal cracking. (14)

On a molecular basis, the magnitude of G' depends on the nature of the conformation rearrangements can take place within the period of the deformation [15]. Examination of plots of logG' versus either temperature or frequency (figure 2) reveals that the slope of the curve for ACE-HDPE is very close to that for ACE. In another words, adding HDPE to ACE simply induces a parallel shift of the logG' curves toward high temperature or low frequency. The presence of HDPE particles results in the development of partially separated regions in the asphalt matrix, which are characterized by a higher rigidity than in the bulk asphalt. A contributing factor to both the parallel shift and the slight difference between slopes of the two curves is the selective adsorption of asphalt components by HDPE. Adsorption of the saturates by HDPE enriches the asphalt phase with aromatics resins and asphaltenes and creates a more rigid continuous phase. The dynamic mechanical response of ACE-HDPE is mainly from the continuous asphalt phase that is indirectly affected by the presence of HDPE.

Compared with that of ACE-HDPE, slopes of logG' curves of ACE-CPE blends decrease and become more linear (figure 3). Asphalt is much more temperature sensitive or frequency sensitive than the polymer additives employed. The decrease in temperature sensitivity exhibited by the blends may imply that the polymer rich phase is more and more directly involved in responding to the dynamic mechanical load. The effect is particularly pronounced is the higher temperature regimes. Introduction of chlorine atoms enhances compatibility between the polymer additives and asphalt, thus the volume of the polymer rich phase will be increased due to improved 'solubility' in the asphalt A morphological conversion from a particle filled matrix (HDPE blend) to a three dimensional network may occur in CPE blends.

Creep. Creep tests (figures 4-7) illustrate a pronounced difference between HDPE and CPE blends. At 35°C the presence of HDPE did not change the creep behavior significantly. Further one can distinguish between the degrees

of chlorination in the two CPE samples; the more amorphous samples were more resistant to creep.

Acknowledgement:

Support for this work was provided by Louisiana Transportation Research Center.

References

1. P. Jew and R. T. Woodhams, *Asphalt Paving Technology*, **55**, 541 (1986).
2. B. H. Chang, R. Ziegler and A. Hiltner, *Polym. Eng. Sci.* **28**, 1167 (1988) and references cited therein.
3. Zhaoyao Qiu *Thesis* Louisiana State University, p50, 1991
4. W.H. Daly and Zhaoyao Qiu, Fuel Chemistry Division Preprints, 1992.
5 B. Brule; Y. Brion and A. Tanguy, *Asphalt Paving Technology,* **57**, 41-64, (1988).
6. C. Lenoble, *Prepr. - Am. Chem. Soc., Div. Pet. Chem.*, **35(3)**, 541-49, (1990).
7. C. B. Bucknall and W. W. Stevens, *J. Material. Sci.*, **15**, 2950, (1980).
8. C. B. Bucknall and C. J. Page, *J. Material. Sci.*, **17**, 808, (1982).
9. P. Juliano, *Polymer Eng. Sci.*, **24**, 1359, (1984).
10. M. Aubin and R. E. Prud'homme, *Macromolecules*, **13**, 365, (1980).
11. M. Aubin and R. E. Prud'homme, *Polym. Eng. Sci.* **24**, 350, (1984).
12. M. Aubin; Y. Bedard; M. F. Morrissette and R. E. Prud'homme, *J. Polym. Sci., Polym. Phys. Ed*, **21**, 233, (1983).
13. J. E. Harris; D. R. Paul and J. W. Balow, *Polym. Eng. Sci.*, **23**, 676, (1983).
14. H. S. Pink, R. E. Merz and D. S. Bosniack, Asphalt Paving Tech. **49**, 64 (1980).
15. R. B. Bird; R. C. Armstrong and O. Hassager, *Dynamics of polymeric liquids, Volume 1, Fluid Mechnics*, 2nd Edition, John Wiley & Sons, Inc., New York, 1987.

Table 1. Glass Transition Temperature (Tg) from E" and Cracking Temperature (Tc) of Concerned Asphalts, Polymers and Asphalt-polymer Blends

Sample	1 Hz	10 Hz	50 Hz	Tb
ACE	-32.2 C	-26.6 C	-22.5 C	-20 C
ACD	-14.9 C	-9.9 C	-4.1 C	-5 C
CPEB	-12.7 C	-7.9 C	-5.7 C	
CPEC	-15.2 C	-12.4 C	-9.4 C	
ACE-HDPE	-30.3 C	-25.0 C	-20.5 C	-23 C
ACE-CPEB	-31.9 C	-26.3 C	-21.6 C	-28 C
ACE-CPEC	-31.8 C	-25.7 C	-21.4 C	-31 C
ACD-HDPE	-14.3 C	-8.5 C	-3.7 C	-7 C
ACD-CPEB	-16.9 C	-10.8 C	-6.0 C	-8 C
ACD-CPEC	-16.6 C	-10.4 C	-6.7 C	-10 C

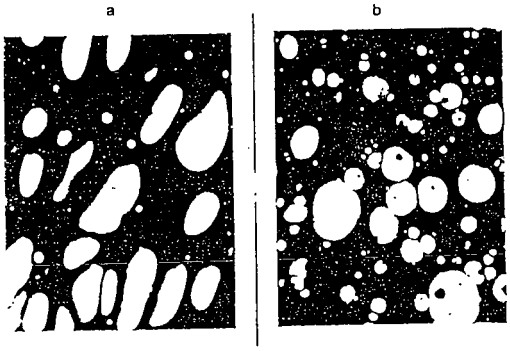

Figure 1 Pictures of fluorescence reflection microscopy. (a) 5% CPEC in ACD. (b) 5% HDPE in ACD.

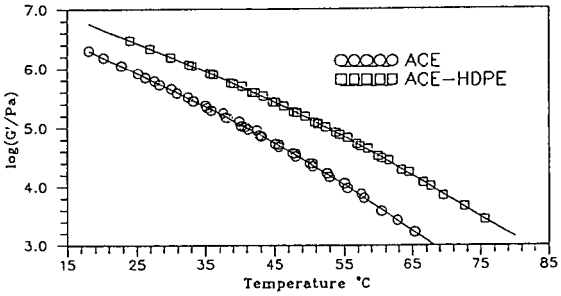

Figure 2 Plot of logG' versus temperature.

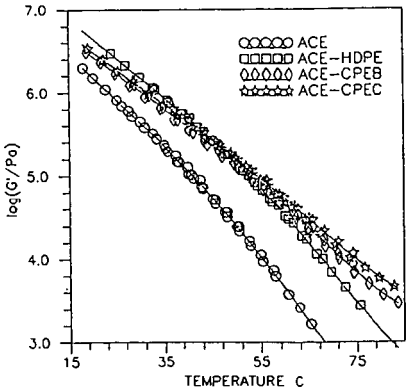

Figure 3 Plot of logG' versus temperature for ACE, ACE-HDPE, ACE-CPEB and ACE-CPEC.

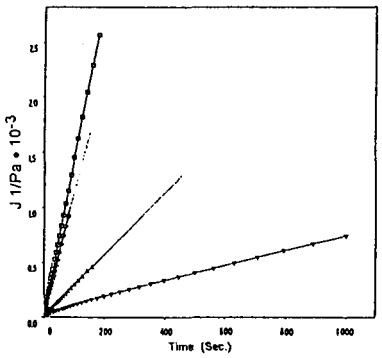

Figure 4 Constant stress creep curves at 35°C (from top to bottom: ACD, ACD-HDPE, ACD-CPEB, ACD-CPEC)

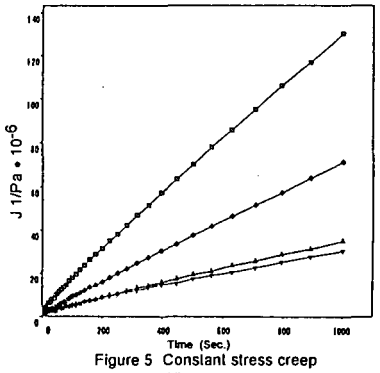

Figure 5 Constant stress creep curves at 15°C (from top to bottom: ACD, ACD-HDPE, ACD-CPEB, ACD-CPEC)

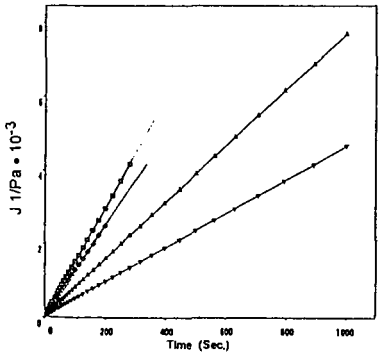

Figure 6 Constant stress creep curves at 35°C (from top to bottom: ACE, ACE-HDPE, ACE-CPEB, ACE-CPEC)

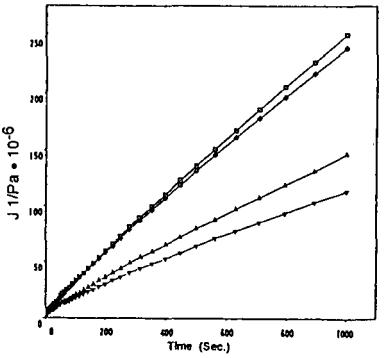

Figure 7 Constant stress creep curves at 15°C (from top to bottom: ACE, ACE-HDPE, ACE-CPEB, ACE-CPEC)

In Situ Measurement of Water at the Asphalt/Siliceous Aggregate Interface

Tinh Nguyen, Eric Byrd, and Dale Bentz

Building Materials Division
National Institute of Standards and Technology
Gaithersburg, MD 20899

Abstract

Water at the asphalt/aggregate interface is the major contributor to the debonding of asphalt from mineral aggregates (stripping). This paper describes a spectroscopic technique to detect and measure in situ water at the interface between an asphalt and a siliceous aggregate, and the application of the technique to studies of several asphalts. The technique employs Fourier transform infrared (FTIR) spectroscopy in the multiple internal reflection (MIR) mode. An asphalt layer of any thickness is coated on an SiO_2-covered Si internal reflection element (IRE) and a water chamber is attached to the asphalt-coated substrate. Spectra are taken automatically at specified time intervals without disturbance of the specimens. In the study, water at the asphalt/aggregate interface for five Strategic Highway Research Program (SHRP) core asphalts (AAC-1, AAD-1, AAG-1, AAK-1 and AAM-1) of about 60 μm thick on an SiO_2-Si substrate was measured using the technique. The amount and thickness of the water layer at the asphalt/siliceous aggregate interface were determined based on internal reflection spectroscopy theory, the water concentration-intensity calibration curve obtained using a series of H_2O/D_2O mixtures, and the water uptake of the asphalts. The results indicated that the thickness of the water layer at the asphalt/siliceous aggregate interface increased as time of exposure increased. Water adsorption characteristics at the asphalt/SiO_2-Si substrate interface were different for the five asphalts. The technique should be useful for evaluating asphalt/siliceous aggregate mixtures in terms of water diffusion, water susceptibility, effectiveness of antistripping agents, and effects of aggregate surface contamination on water stripping.

Keywords: asphalt/aggregate interface, *in situ*, water

INTRODUCTION

The debonding of asphalt from mineral aggregates in the presence of water (stripping) "has been observed at times ever since asphalt paving came into existence" (1). Since stripping was first recognized as a problem, many studies have been devoted to the search for a solution to this problem. Still, stripping continues to occur in many areas. Whether asphalts fail prematurely or in the range of the expected service life, they require large replacement costs that could probably be reduced through development of effective methods for measuring the effects of water on the stripping of asphalt from an aggregate and for evaluating the effectiveness of antistripping agents. A major technical barrier to overcoming the problem of stripping is the lack of a technique for measuring water at the asphalt/aggregate interface. Measuring water at bonded interfaces has been the subject of much interest, not only in the asphalt pavement area, but also in many areas involving a polymer film on a substrate, such as in the fields of coatings, adhesives, and fiber composites. However, until recent research at the National Institute of Standards and Technology (NIST) that led to a technique for measuring water *in situ* at the coating/metal interface (2-4), there has been no suitable technique available. The main objective

of this study was to develop a technique for measurement of water *in situ* at the interface between asphalt and a model siliceous aggregate.

The technique developed for studying water *in situ* at the asphalt/siliceous aggregate interface is based on Fourier transform infrared - multiple internal reflection (FTIR-MIR) spectroscopy, commonly known as FTIR-ATR (attenuated total reflection) spectroscopy. The theory and principles of FTIR-MIR are well understood (5). The application of this technique for measuring *in situ* (2) and quantifying (4) water at the interface between a polymer and a substrate has been described.

EXPERIMENTAL

The model siliceous aggregate used in this study was a 50x10x3mm, spectroscopic grade, SiO_2-covered Si internal reflection element (IRE). The asphalts were five of the Strategic Highway Research Program (SHRP) core asphalts: AAC-1, AAD-1, AAG-1, AAK-1, and AAM-1. Asphalts were heated to 60°C in air and applied on the model aggregate using a "drawdown" technique. The thickness of the asphalt films on the model aggregate was 63 ± 15 μm. A water chamber was attached to the asphalt-coated aggregate and water was introduced into the chamber. Figure 1 illustrates the specimen configuration and experimental setup. At specified time intervals, FTIR-MIR spectra were taken automatically without realignment of the instrument accessory and without disturbance of the specimens. Difference spectra between the water-exposed and unexposed asphalt-coated aggregate specimens as a function of exposure times were recorded. All spectra were the result of 32 coadditions and were collected at 4 cm^{-1} resolution throughout the 1200-4000 cm^{-1} range. Unpolarized light at an incident angle of 45° was used. Quantitative analyses were performed using the peak height method. Since this was an *in situ* measurement, no random errors due to specimen changing, spectrometer and environmental chamber conditions, and optical alignments were introduced in the measurement. Thus, any changes in the spectra were a direct result of water entering the asphalt/aggregate specimen. Further, because asphalt was directly applied to the IRE, errors resulting from variations in contact between the asphalt and the IRE were avoided.

To translate FTIR information to the amount and thickness of the water layer at the asphalt/aggregate interface, an FTIR-MIR intensity-concentration calibration curve for water was established and the amount of water absorbed in the asphalt was determined. The calibration curve was established by an FTIR-MIR analysis of water at eight different concentrations in D_2O. The amount of water absorbed in the asphalt was determined using the gravimetric method and 63-μm asphalt films on thin aluminum plates. The asphalt-coated aluminum plates (three replicates for each asphalt) were immersed in distilled water, taken out, blotted, and weighed at desired intervals up to 310 hours; the amount of water gained was expressed in percent by mass of the original asphalt. Complete experimental details are given in Reference 6

RESULTS

Figure 2 shows typical FTIR-MIR difference spectra of an asphalt/siliceous aggregate specimen exposed to water at different times. The intensities of the water bands (e.g. OH stretching near 3400 cm^{-1}) increased while those of the asphalt bands (e.g. CH band at 2922 cm^{-1}) decreased,

as a function of time of exposure. (The water bands were verified by the FTIR-MIR spectrum of the liquid water in contact with the asphalt-free siliceous aggregate.) The intensity-time plots of water (e.g. Figure 3) revealed that the increases and decreases were rapid initially, then slowed down. These results indicated that the technique is effective for detecting *in situ* water taken up by an asphalt-coated siliceous aggregate system. The effects of water on the asphalt-coated siliceous aggregate were different for the five asphalts. The intensities of the water bands of the AAD-1 asphalt increased substantially over the first 45 hours then levelled off, while those of the other asphalts increased more slowly (than AAD-1) but continued to increase even after much longer times.

The water detected in the asphalt/aggregate specimen was the sum of water absorbed in the asphalt within the FTIR-MIR probing depth and of the water at the asphalt/aggregate interface. This may be expressed mathematically as:

$$C_w(t) = A(t)[1-x] + x \quad [1]$$

$$x = l(t)/d_p(t) \quad [2]$$

$$d_p(t) = 0.243 - 0.018x \quad [3]$$

where $d_p(t)$, in μm, is the penetration depth of the evanescent wave in the samples as a function of exposure time, t; d_p was calculated based on the internal reflection spectroscopy as presented in detail in References 4 and 6 for polymer/substrate and asphalt/siliceous aggregate systems, respectively. $C_w(t)$ is the mass fraction of water within d_p; this quantity was derived from the results in Figure 3 and the calibration curve. A(t) is the mass fraction of water absorbed in the asphalts within d_p thickness as a function of time; A(t) was determined from the water absorption experiment. x is the thickness fraction of d_p occupied by the water layer at the asphalt/aggregate interface and l(t), in μm, is the thickness of the water layer at the asphalt/aggregate interface as a function of time. Equation 3 accounts for the change of d_p due to a replacement of asphalt (d_p = 0.243 μm) by water (d_p = 0.225 μm) during exposure.

Equations 1, 2, and 3 allowed the calculation of the amount and thickness of the water layer at the asphalt/model aggregate interface. A computer spreadsheet was designed to obtain the thickness, l(t), of the water layer at the asphalt/siliceous aggregate interface. The results are presented in Figure 4 for five SHRP asphalts. The thickness values were calculated assuming that water was uniformly distributed on the entire surface area of the specimen. The mass of water at the asphalt/aggregate interface was determined by multiplying the thickness by the surface area within the chamber walls (329 mm^2) and by a water density of 1 Mg/m^3. Alternatively, the mass can be determined first, then converted to a thickness value. The results showed that the thickness of the water layer at the asphalt/model aggregate interface varied with exposure times and with the asphalt types. For example, after 50 hours immersion, AAD-1 had a 85 nm-thick water layer, while AAC-1, AAG-1, AAK-1, and AAM-1 had thicknesses ranging from 20 to 28 nm after the same period. The thickness of the water layer of AAD-1 reached a plateau value after 50 hours, but that of the other asphalts continued to increase for some time.

CONCLUSIONS

A sensitive technique for measuring water *in situ* at the asphalt/model siliceous aggregate interface has been developed. The technique can detect and also quantify the water at the asphalt/siliceous aggregate interface. The technique will be valuable for understanding the water susceptibility of asphalt/siliceous aggregate mixtures. The technique is unique in providing information on the transport of liquid water through an asphalt layer of any thickness attached to an aggregate (6). Such information should be useful for predicting the performance of asphalt and asphalt/aggregate mixtures in service. The technique should therefore be useful for predicting water susceptibility and studying the effects of the aggregate, contamination of the aggregate, antistripping agents, and the asphalt on the water susceptibility of asphalt/siliceous aggregate mixtures. Further, the technique should be useful for measuring organic or inorganic materials, such as oil, lime, etc., *in situ* at the asphalt/aggregate interface. Similarly, it may also be useful for measuring the transport properties of water, organic, and inorganic materials through a layer of asphalt/aggregate mixture or concrete on a substrate. It is anticipated that the technique will have a wide range of applications in highway technology.

ACKNOWLEDGEMENTS

The research described herein was supported by the Innovations Deserving Exploratory Analysis (IDEA) Program of the Strategic Highway Research Program (SHRP), a unit of the National Research Council.

REFERENCES

1. P. Hubbard, Adhesion of Asphalt to Aggregate in the Presence of Water, Proceedings, Highway Research Board, 1938, Vol. 18, Part I, p. 238.
2 T. Nguyen, E. Byrd, and C. Lin, A Spectroscopic Technique for *In Situ* Measurements of Water at the Coating/Metal Interface, J. Adhesion Sci. Technol., 5, 697 (1991).
3. T. Nguyen, E. Byrd, C. Lin, and D. Bentz, A Novel Technique for Measurement of Water at the Interface between a Metal and an Opaque Polymeric Film, Advanced Composite Materials, 19, 1051 (1991).
4. T. Nguyen, E. Byrd, and D. Bentz, Quantifying Water at the Coating/Substrate Interface, Proc. Am. Chem. Soc., Polymeric Materials Sci. Eng., Vol. 66, p. 414, 1992.
5. N. J. Harrick, Internal Reflection Spectroscopy, Harrick Scientific Corporation, N. Y., 2nd ed., 1979.
6. T. Nguyen, E. Byrd, D. Bentz, and J. Seiler, Development of a Technique for *In Situ* Measurement of Water at the Asphalt/Model Siliceous Aggregate Interface, National Institute of Standards and Technology NISTIR No 4783, April 1992.

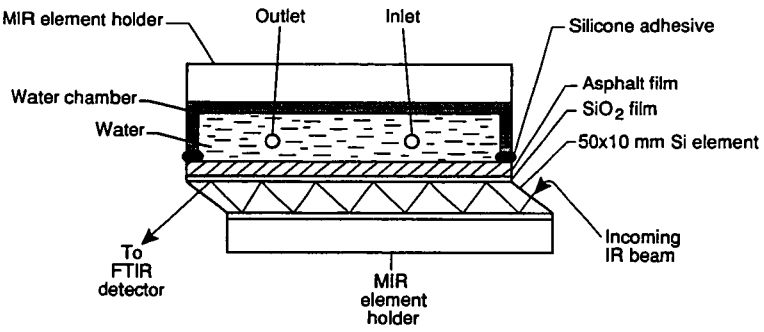

Figure 1. Specimen configuration and experimental setup for *in situ* measurement of water at the asphalt/siliceous aggregate interface.

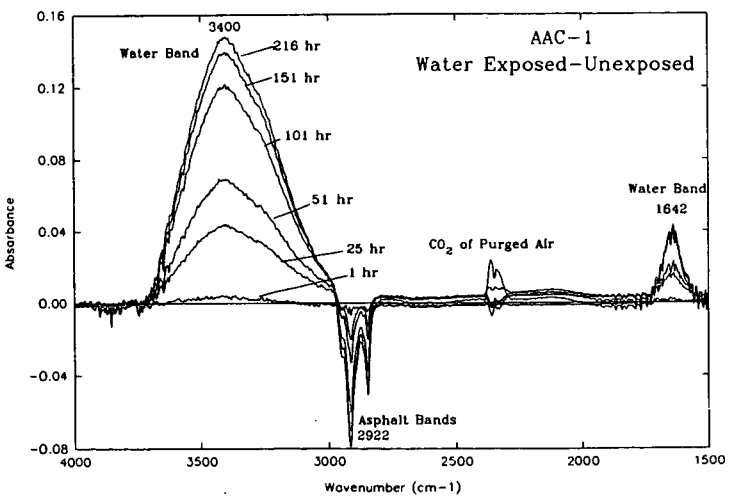

Figure 2. Typical FTIR-MIR difference spectra (water exposed - unexposed) of an asphalt/siliceous aggregate specimen for different exposure times in water.

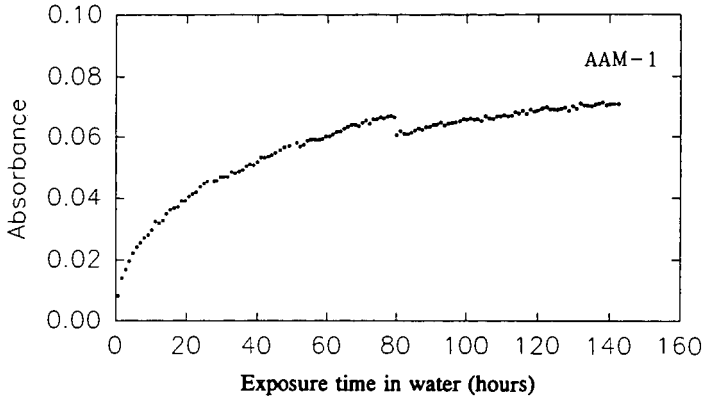

Figure 3. A typical water OH stretching intensity/time plot of an asphalt/siliceous aggregate specimen exposure to water. (Each dot represents one data point.)

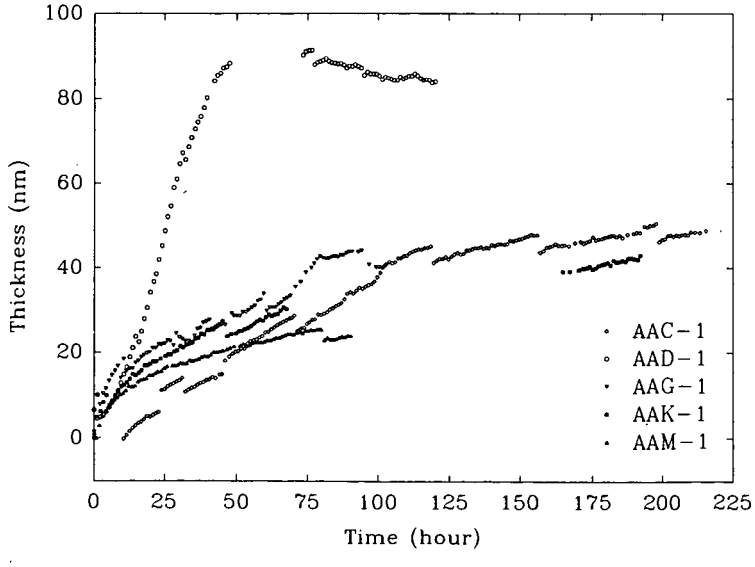

Figure 4. Thickness of the water layer at the asphalt/siliceous aggregate interface for five SHRP asphalts.

ASPHALT-AGGREGATE INTERACTIONS AND MECHANISMS FOR WATER STRIPPING

M. E. Labib, David Sarnoff Research Center, Princeton, NJ 08540

Keywords: asphalt-aggregate; donor-acceptor; water stripping

ABSTRACT

The surface chemical properties of four types of aggregates were measured by electrokinetic and spectroscopic techniques. The isoelectric points of aggregates ranged from 2.3 for granites to 9.3 for limestones. Zeta potential - pH curves were measured for four types of asphalts where the isoelectric points depended on the origin of the crude. Interaction diagrams between several aggregate and asphalt types were constructed and used to predict the extent of aggregate-asphalt adhesion. The contribution of electron donor-acceptor interaction to adhesion will be discussed. The reaction of water soluble ions leaching out from the aggregate surface with the carboxylic acids of asphalts is a major variable affecting adhesion and water stripping in pavements. Surface complexation of aggregate with asphalt species and the dissolution kinetics of such complexes are viewed as an important mechanisms for water stripping.

INTRODUCTION

The strength of the adhesion bond between aggregates and asphalts determines the performance of pavement. For acceptable performance, this adhesion bond must withstand the presence of water for prolonged periods of time. Pavement failure at the aggregate-asphalt interface due to water is termed "water stripping." The donor-acceptor interactions between aggregate and asphalt surfaces determine the extent of their adhesion in pavement. The effect of water on the aggregate-asphalt chemical bonding is expected to influence the water stripping performance.

For solid surfaces such as aggregates, the donor-acceptor surface properties may be divided into proton and electron transfer contributions [1]. Proton transfer surface properties are normally estimated from electrokinetic properties as a function of pH [2]. Electron transfer properties are determined by measuring the zeta potential of the solid particles in nonaqueous liquids of known donor or acceptor properties [2,3].

For asphalts, the proton transfer donor-acceptor surface properties can be determined from electrokinetic measurements of their emulsions as a function of pH. A technique was developed to prepare a stable asphalt emulsion that does not alter the intrinsic surface properties of the asphalt [4]. The electron transfer donor-acceptor properties were measured by FTIR techniques. This was done by measuring the frequency shift of the carbonyl mode in the presence of probe solvents. The above technique was developed for polymer matrices to predict their adhesion properties and performance in composites [5].

In this paper, we describe how the surface chemistry of aggregates and asphalts determines the propensity of interaction - which in turn dictates the extent of their

adhesion. The stability of aggregate-asphalt chemical bonding in the presence of water is discussed on the basis of detailed knowledge of surface chemistry. Mechanisms for water stripping are proposed. The results of this research demonstrate that knowledge of aggregate and asphalt surface properties is needed to construct pavement with better performance and service life.

EXPERIMENTAL PROCEDURES

Materials: Tables I and II summarize the properties of several types of aggregates and asphalts, respectively. The aggregates range from granites to limestones - which cover a wide range of donor-acceptor (acid-base) properties. The asphalts represent the main types and were recommended by the Strategic Highway Research Program (SHRP).

Procedures: The zeta potential of aggregates was measured by the acoustophoresis technique using the Pen Kem System-7000. The nonaqueous zeta potential of aggregate particles was calculated from mobility values measured by the Doppler-shift electrophoresis technique using the Malvern Zetasizer II. Details of the experimental techniques are described elsewhere [2,3]. The zeta potential of aqueous asphalt emulsions was measured by the Doppler-shift electrophoresis technique. The emulsion was stabilized with a peroxide-free nonionic surfactant [4]. The frequency shift of asphalt carbonyl mode due to probe solvents was measured by FTIR using the procedure developed by Fowkes et al [5]. Energy scale conversions were made according to Gutmann [6], Labib and Williams [2] and Fowkes et al [7].

RESULTS AND DISCUSSION:

The results and discussion of this work are presented in several sections. Proton and electron transfer donor -acceptor surface properties of aggregates and asphalts are presented in section I and II. Development of the interaction diagrams of some aggregate-asphalt pairs is given in section III. The last section IV discusses mechanisms of water stripping in pavement.

I. Proton and Electron Transfer Surface Chemistry of Aggregates

1. Proton Transfer Properties of Aggregates and Asphalts: The acid-base properties of aggregates were measured by the electrophoresis technique and expressed as zeta potential - pH curves. Figure 1 shows the electrokinetic properties of the four aggregate types defined in Table I. The isoelectric points ranged from 2.3 for quartz-based granite to 9.3 for calcite-based limestone. Apparently the two limestones RC and RD have different surface compositions, as indicated by their isoelectric points.

An important property of the aggregate surface is its stability towards dissolution in water. Table III summarizes the pH and specific conductivity of various aggregates after several soaking cycles. The results indicate that the surface of aggregates slowly dissolves upon exposure to water and that the pH of the medium near the interface is basic (pH >10.0). This was the case for all aggregate types including the quartz-based RJ. This finding is important to the

understanding of the pH conditions present at the aggregate-asphalt interface under wet conditions.

2. Electron Transfer Surface Chemistry of Aggregates: Figure 2 presents the donor-acceptor surface properties of the four types of aggregates. This diagram was constructed from the zeta potential - donicity results of the aggregates in organic solvents, as described by Labib et al [3]. The energy scale used in Figure 2 is based on converting the Gutmann acceptor number to an energy scale using the results of Fowkes et al [7]. The RJ granite exhibited strong acceptor properties while the RD limestone was the strongest donor aggregate. Clay aggregate (RL) has both donor and acceptor surface sites.

II. Proton and Electron Transfer Donor-Acceptor Surface Properties of Asphalts

1. Proton Transfer Properties of Asphalts: Figure 3 presents the zeta potential - pH curves for the four asphalts described in Table II. The measurements were made using an asphalt emulsion stabilized with peroxide-free nonionic surfactant. The asphalts had acid isoelectric points with the exception of non-marine origin AAG which was amphoteric. The results indicate that the surface charge of the asphalts is mainly due to carboxyl functionalities. There is evidence of hydroxyl group contribution to the surface chemistry of asphalts as evidenced by the increase in zeta potential at pH >9.0.

2. Electron Transfer Surface Properties of Asphalts: In the present context, the asphalt was treated as the matrix component of the pavement composite. The electron donor-acceptor properties are determined from the frequency shift of the carbonyl mode of asphalt solutions in probe solvents. The frequency shifts of asphalts carbonyl mode due to chloroform referenced to a cast film and to an asphalt solution in toluene are summarized in Table IV. A higher frequency shift in chloroform indicates stronger base properties of carbonyl functions of asphalts. Data for PMMA and polycarbonate are listed for comparison. It should be noted that the results of Table IV are of oxidized asphalts. We found oxidation to be essential to formation the electron donor groups in asphalts at reasonable concentration.

III. Interaction Diagrams Based on Proton Transfer Surface Properties:

1. Examples of Proton Transfer Interaction Diagrams:

a. Interaction of a Granite Aggregate with Asphalts:: Figure 4 is an interaction diagram for quartz-based RJ granite and four asphalt types. The figure shows that the surfaces of the aggregate and asphalt are both negatively charged at pH >3.0. This indicates that under dry conditions (pH 7.0), the propensity of adhesion between asphalt and aggregate is low. At pH 10.0, such as that encountered in the presence of water (Table III), the surfaces of aggregate and asphalt are strongly negative. This is expected to lead to repulsion and therefore water stripping. In actual performance evaluations, RJ was found to be a "stripper" with most asphalt types. The main source of adhesion expected in this case is due to electron transfer donor-acceptor interaction between acceptor sites on the granite and electron donor groups of asphalts.

b. Interaction of a Limestone Aggregate with Asphalts: Figure 5 is an interaction diagram for calcite-based RD limestone and four asphalt types. In this case, the surfaces of asphalt and aggregates have opposite polarities at pH 7.0 (proposed condition for the dry state). The interaction in the presence of water at pH 10.0 is small or zero. In actual performance tests, the RD limestone has been found to be a good performer with respect to water stripping.
Similar interaction diagrams can be constructed with the different aggregate-asphalt pairs. This technique was found to be valuable in predicting the performance of several asphalt -aggregate pairs.

2. Electron Transfer Donor-Acceptor Contribution to Asphalt-Aggregate Adhesion:

The contribution of electron transfer donor-acceptor interaction between aggregates and asphalts is viewed to be essential to their adhesion in some cases. Asphalts, especially after initial oxidation, have been found to contain aprotic electron donor groups such as carbonyl, sulfoxide, ether and lactone. The interaction of these donor groups is likely to take place with aggregate surfaces having acceptor properties. The bonding of asphalts with granite (RJ) and clay (RL) aggregates may be due in major part to the electron donor-acceptor interaction. The oxidation of asphalt surface is essential to the development of the above aprotic donor groups which in turn controls the bonding with aggregates. The donor-acceptor character of aggregates (Figure 2) and the frequency shift data of asphalts (Table IV) provide guidelines for predicting the extent of this contribution to bonding.

IV. Mechanisms of Water Stripping:

Water stripping in asphalt pavement results from the failure of the asphalt-aggregate adhesion bond due to the presence of water. The location of this failure (in the interface region) is crucial to understanding the mechanisms of water stripping. The following is a list of major mechanisms that are expected to lead to water stripping:

1. Weak Adhesion Bond - Lack of Bonding Sites on Aggregate Surface: The adhesion bond may be weak due to the lack of intrinsic chemical interaction between the aggregate and asphalt - as described for the case of granite (RJ) and asphalts. The remaining electron donor-acceptor bonding between aggregate and asphalt can be weakened or even reversed by water. This is a known failure mechanism in other material systems [8].
2. Naturally Emulsifiable Asphalt Leading to Unstable Adhesion: Due to their composition or balance of constituents, some asphalts are unstable in water and tend to form stable emulsions. This was the case for AAG which was amphoteric in character. This asphalt type is expected to form unstable interface with aggregates in the presence of water. This has been found to cause water stripping [9].
3 Soluble Cations Forming Displaceable Soap at Aggregate-Asphalt Interface: Most aggregates contain a large concentration of soluble ions that are leachable in water (Table III). These ions are known to form soaps (with asphalt caboxylic acids) at asphalt-aggregate interface. These soaps are displaceable and can cause

water stripping. Evidence is present to support better performance of experimental pavements made with thoroughly washed and dried aggregates [9].
4. Aggregates with Weak Boundary Layers: It has been demonstrated by Podoll [10] that the location of failure of some asphalt-aggregate pairs occurs in the aggregate side of the bond. The responsible weak boundary layer may be intrinsic to the aggregate or can be developed by surface complexation/dissolution, as described below.
5. Dissolution of Aggregate-Asphalt Surface Complexes: The exterior surface layers of aggregate may be weakened due to the formation of complexes between the aggregate surface sites and asphalt surface groups. These complexes are known to dissociate and dissolve from the aggregate surface. These concepts are developed by Stumm and are recognized in the literature [11,12].

For different asphalt-aggregate pairs, a combination of mechanisms may explain differences in pavement performance. The results of this work would guide us in selecting proper aggregates and asphalts for various climatic regions and in the design of adhesion promoters and anti-stripping agents, when necessary.

ACKNOWLEDGMENT:

The support of the Strategic Highway Research Program is gratefully acknowledged. The Author would to acknowledge the assistance of P.J. Zanzucchi for the FTIR work and other Sarnoff Staff who made this work complete. The author would also like to express gratitude to Dr. J. F. Branthaver of WRI for his valuable discussions, especially with respect to the geochemical aspects of this work.

REFERENCES:

[1] Labib, M.E., "The Origin of Surface Charge of Particles Suspended in Organic Liquids," Colloids and Surfaces, **29**, 293 (1988).
[2] Labib. M.E., et al.,"An Experimental Comparison Between the Aqueous pH Scale and the Electron Donicity Scale," Colloid & Polymer Science, **264**, 533 (1986).
[3] Labib, M.E., et al., "The Use of Zeta Potential in Organic Solvents to Determine The Donor-Acceptor Properties of Solid Surfaces." J. Colloid Interface Science, **97**, 356 (1984).
[4] Labib, M.E., in Preparation.
[5] Fowkes, F.M. et al., "Acid-Base Complexes of Polymers," J. Polymer Science, **22**, 547 (1984).
[6] Gutmann, V., "The Donor-Acceptor Approach to Molecular Interactions," Plenum Press, New York (1878).
[7] Fowkes, F.M., et al., "Spectral Shifts in Acid-Base Chemistry. 1. Van der Waals Contributions to Acceptor Numbers," J. Am. Chem, Soc., **112**, 3259 (1990).
[8] Labib, et al., "The Effect of Moisture on the Charge at the interface Between Solids and Organic Liquids," J. Colloid Interface Science, **115**, 330 (1987).
[9] Ensley, K., and H. Plancher of WRI, Private Communication (1991).
[10] Podoll, R.T., et al., SHRP Final Report (1991).
[11] Stumm, W., et al., "The Role of Surface Coordination in Precipitation and Dissolution of Mineral Phases," Croatica Chemica Acta, **56**, 593 (1983).

TABLE I

Composition and Description of Core Aggregates*

Aggregate Properties	RJ Mountain Gravel Conglomerate	RL Gulf Coast Gravel	RC Limestone (McAdams Limestone)	RD Limestone (Genstar Stone Prod.)
X-ray Diffraction-Major Minerals	Quartz, Potassium Cyanide Albite, Sodium Acetate	Quartz, Calcite Albite	Calcite, Dolomite Quartz	Calcite, Dolomite Quartz
Major Oxides, %:				
Silicon Dioxide	63.98	61.27	11.79	14.84
Aluminum Oxide	14.60	5.95	1.955	1.46
Ferric Oxide	4.54	3.77	0.96	0.89
Calcium Oxide	6.09	20.25	35.05	33.71
Magnesium Oxide	1.52	2.49	11.76	11.43
Sulfur Trioxide	0.10	0.15	0.48	0.34
Sodium Oxide	1.67	0.48	0.21	0.08
Potassium Oxide	3.31	1.41	0.51	2.00
Titanium Oxide	0.41	0.88	0.18	0.21
Phosphorus Pentoxide	0.11	0.02	<0.01	<0.01
Manganic Oxide	0.13	0.04	0.03	0.08
Loss on Ignition	3.54	13.29	37.64	34.64

*Source of Data: Southern Laboratories and SHRP Materials Reference Library

TABLE II

ASPHALT ORIGINS AND PROPERTIES

Sample, MRL Code	AAA-1	AAD-1	AAD-2	AAG-1	AAG-2	AAM-1	AAM-2
Crude (Origin)	Lloydmaste	Californi	Coastal	California	Valley	West Texas	Intermediate
Component Analysis, %							
Asphaltenes, (n-heptane)	18.3	23	21.3	5.8	5.1	3.9	4.0
Asphaltenes, (iso-octane)	3.4	3.4		3.3			
Polar Aromatics	37.3	41.3	40.1	51.2	51.0	50.3	50.0
Napthene Aromatics	31.8	25.1	26.7	32.5	35.3	41.9	41.3
Saturates	10.6	8.6	10.0	8.5	8.6	1.9	3.0
Elemental Analysis							
C, %	84.2	81.6		85.6		86.8	
H, %	10.5	10.6		10.5		11.2	
O,%	0.6	0.9		1.1		0.5	
Nitrogen, %	0.5	0.9	0.9	1.1	1.1	0.6	0.5
Sulfur, %	7.3	8.6	8.3	1.3	2.9	1.2	1.9
Viscosity, Prior to Oxidation	864	1055	600	1862	1056	1992	924
Viscosity, After Oxidation for 140F, poise	1901	3420	1715	3253	1761	3947	1816
Ratio	2.2	3.24	2.86	1.75	1.69	1.98	1.96

TABLE III

pH and Specific conductance (μ Scm^{-1}) of Core Aggregates Slurries* Upon repeated soaking and decanting cycles.

	RJ		RL		RC		RD	
	pH	μs cm^{-1}	pH	μS cm^{-1}	pH	μ S cm^{-1}	pH	μ S cm^{-1}
cycle I 1 hr. soak	9.6	75	9.5	113	9.0	143	9.1	125
cycle II 1 hr. soak	9.4	41	9.4	70	8.1	56	9.2	60
cycle III 1 hr. soak	9.3	37	9.4	61	9.1	46	9.3	49
cycle IV 1 hr. soak	9.5	33	9.6	54	9.1	45	9.5	44
cycle V 12 hrs. soak	9.3	36	9.4	56	9.5	42	9.5	42

* SLURRIES CONSISTED OF 4 GRAMS OF GROUND AGGREGATES IN 25 ML OF WATER.

TABLE IV

SHIFT OF THE CARBONYL MODE, cm^{-1} DUE TO THE LEWIS ACID, CHLOROFORM

Oxidized SHRP Sample	Reference Material Cast Film	Reference Material in Toluene
AAA-1	-1.8	-9.0
AAD-1	-3.0	-8.5
AAG-1	-2.3	-6.4
AAM-1	-3.7	-7.1
PMMA	-2.4	-5.5
PCarb*	-4.5	

PCarb*, poly(carbonate), a reference material for study.

FIGURE 1

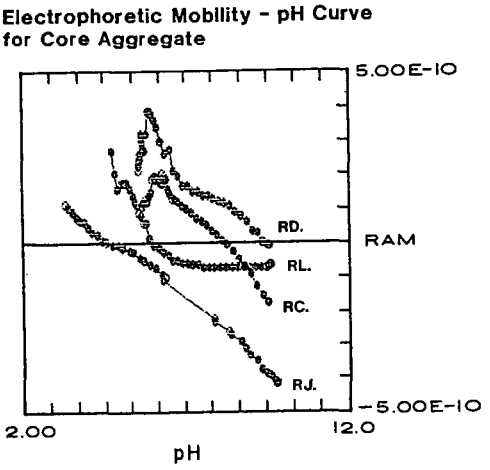

FIGURE 2

The Donor-Acceptor Character of the Four Core Aggregates. They are Arranged Top-to-Bottom According to their Relative Strength, as Judged by the Values of Zeta Potential in Various Liquids of the Donicity Series.

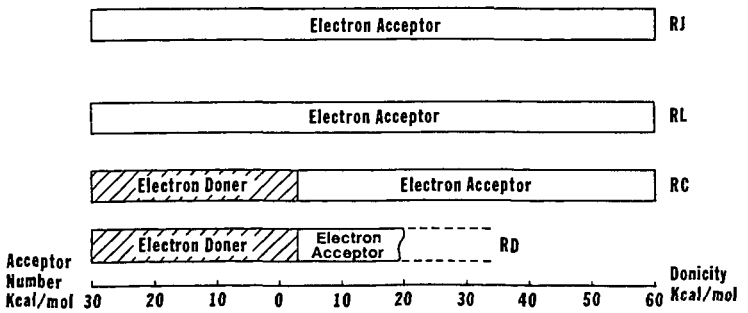

FIGURE 3: ZETA POTENTIAL - pH CURVES FOR AAA-1, AAD-1, AAG-1 AND AAM-1 CORE ASPHALTS.

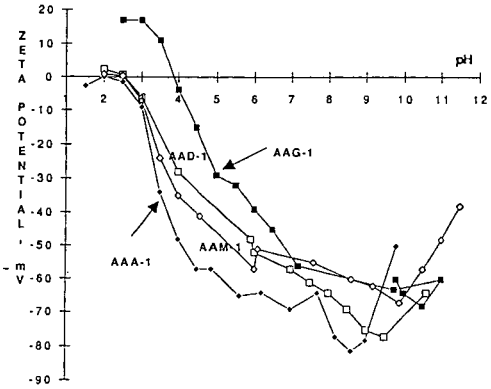

FIGURE 4
INTERACTION DIAGRAMS OF GRANITE AGGREGATE (RJ) WITH SEVERAL ASPHALTS

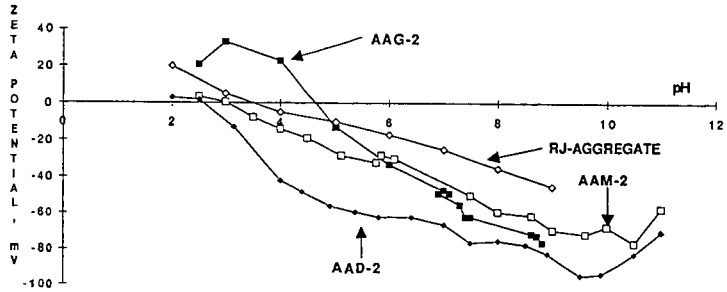

FIGURE 5
INTERACTION DIAGRAMS OF LIMESTONE AGGREGATE (RD) WITH SEVERAL ASPHALTS

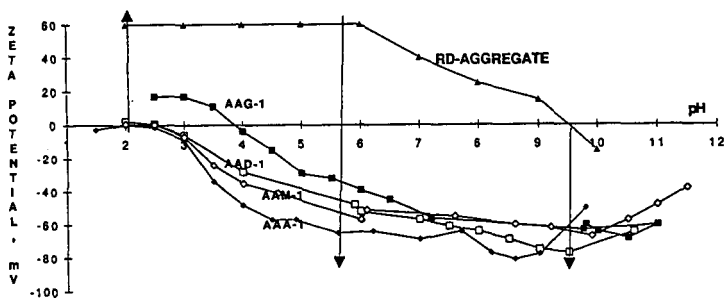

EFFECT OF AGGREGATE MODIFICATION BY ORGANOSILANE COUPLING AGENTS ON THE ADSORPTION BEHAVIOR OF ASPHALT MODELS AND ASPHALT

Lynn M. Perry and Christine W. Curtis
Chemical Engineering Department
Auburn University, AL 36849-5127

ABSTRACT

The effect of modifying aggregate surfaces by organosilane coupling agents on the adsorption and desorption behavior of asphalt models and asphalt was investigated. The organosilane coupling agents used were hydrocarbon silane of C_8 chain length, thiol silane, and amino silane. These agents were coupled to aggregates composed of limestone and gravel. The adsorption and desorption behaviors of asphalt models and asphalt were determined on treated aggregates and compared to their behaviors on untreated aggregate. The amount of bonding enhancement of the treated versus the untreated aggregate, which is a measure of the comparative resistivity of the asphalt-aggregate interfacial bond to water, caused by treating aggregate with organosilane agents was determined. Highly specific interactions were observed between pairs of asphalt models or asphalts and the organosilane treated aggregate. The highly specific behavior was dependent upon the chemistry of the model or asphalt as well as the chemistry of the silane coupling agent.

INTRODUCTION

Asphalt-aggregate interfacial interactions are important in the adhesion of asphalt to aggregate. At the interface, the first layer of asphalt must adhere to the aggregate for the adhesive binding action to occur that is required to maintain an asphalt pavement. This adhesive binding must hold through all the stresses that are applied to the asphalt pavement. These stresses include the effect of traffic, changes in daily and seasonal temperature, and the attriting force of water. All of these stresses attack the adhesive forces that hold the asphalt to the aggregate and, hence, the pavement together. These forces include the cohesive forces within the asphalt cement and within the aggregate in addition to the adhesive forces between asphalt and aggregate.

Organosilanes have been used to pretreat aggregate to promote water resistivity between the asphalt and the silane treated aggregate. Divito et al. (1982) compared the efficacy of one organosilane agent and two commercial amine antistripping agents for increasing the water resistivity of three aggregates from different sources. Silane treatment of aggregates showed increased water resistivity at the adhesive bond compared to aggregate treatment with two amine antistripping agents. Graf (1986) showed that diaminosilane produced increased hydrophobic bonding between crushed glass and asphalts. Hence, from this background, the present study for evaluating the potential of organosilane compounds for enhanced, durable bonding was undertaken.

The research presented is focused upon modifying aggregate in order to enhance adhesion between asphalt and aggregate. Aggregates were modified by using organosilane coupling agents with different chemical functional groups, hydrocarbon of C_8 chain length, thiol and amino groups. These silane functional groups were chosen as modifers for aggregates composed of

granite, limestone, and gravel to increase wetting of the aggregate surface, promote adhesion, and resist water. To evaluate the effect of the surface coupled organosilane agent, the adsorption and desorption behaviors of asphalt models and asphalts were measured on the silane-treated aggregate. The adsorption behavior was measured by adsorbing the asphalt models and asphalt from organic solution and developing an isotherm of their behavior. The desorption behavior was determined by adding water at adsorption equilibrium to the asphalt model or asphalt-aggregate system. The amount of bonding enhancement between the asphalt model or asphalt and the silane-treated versus the untreated aggregate provided a measure of the comparative resistivity to water rendered by treating the aggregate with organosilane coupling agents.

EXPERIMENTAL

Materials. The asphalt model compounds used for this study were benzoic acid, 1-naphthol, phenanthridine, and phenylsulfoxide, all of which were obtained from Aldrich with purities of 99+%. The asphalts (AAD-1, AAK-1, and AAM-1) used were obtained from the Strategic Highway Research Program's (SHRP) Material Reference Library (MRL). These asphalts came from different sources and were different viscosity grades.

Preparation of Organosilane Aggregate. Three aggregates, obtained from the SHRP MRL, were used for this study: RC-limestone, RJ-gravel, and RL-gravel. The aggregates, sized to -40+80 mesh, were contacted with 100 ml of 1%, by volume, silane solution for three minutes, filtered, and dried in a vacuum oven at 70°C for 48 hours. The solvent used for the hydrocarbon silane solution was 95%/5% ethanol/water while the thiol silane was prepared using water adjusted to a pH of 4.5. The amino silane was prepared as a water stable solution by the manufacturer, HULS.

Adsorption and Desorption Experiments. The adsorption of the asphalt models onto the aggregate was performed by adding varying amounts of aggregate, ranging from 1 to 10 g, into 20 ml of cyclohexane solutions containing 100 mg/l of asphalt model. The samples were agitated for one hour using an orbital shaker and then allowed to settle overnight. Agitation was repeated the next day, followed by one hour of settling. The solution was filtered through a 0.22 μm filter and was analyzed by UV-visible spectroscopy at the wavelength of maximum absorbance of the model compound (Curtis et al., 1991). The adsorption of the asphalt was performed in the same manner except that asphalt solutions, 100 ppm, were prepared in toluene and analyzed at 450 nm.

The desorption experiments for both the asphalt models and the asphalts were conducted similarly. Water introduced at an equivalent volume to the solvent was added into the system after the adsorption step was completed; the amount desorbed was monitored after 48 hours. Both the organic and aqueous phases were monitored for the desorbed material. Increases in the amount of model component or asphalt present in the solvent after the desorption equilibrium had been established were reported as the amount of material desorbed.

The concentrations of the asphalt model or asphalt present in solution after adsorption and desorption were monitored by UV-visible spectroscopy and the amount of model or asphalt adsorbed or the amount of either desorbed was calculated. Adsorption isotherms were developed for asphalt models in combination with silane treated aggregates and natural aggregates. The resulting data were treated by Langmuir analyses and by averaging experimental results on two points of the isotherm data. The relative rankings of both treatments of data for amounts of material adsorbed onto aggregate surface were nearly identical. Thus, all data for the

investigations reported herein, asphalt models and asphalts combined with silane-treated and untreated aggretages, are reported using the experimental average of data obtained from the adsorption isotherms. Surface amounts of material adsorbed were calculated for each system. Desorption experiments were performed at a selected point on the isotherms; the amount desorbed was compared to that of corresponding asphalt model- or asphalt-aggregate systems comprised of natural aggregate.

RESULTS AND DISCUSSION

Adsorption and Desorption of Asphalt Model Compounds on Organosilane Treated Aggregates. Asphalt model compounds of benzoic acid, 1-naphthol, phenanthridine and phenylsulfoxide were adsorbed from cyclohexane solution onto silane-treated and natural aggregates. The mass of asphalt model adsorbed onto all aggregates was determined by UV-visible spectroscopy at a wavelength of maximum absorbance for the adsorbing asphalt model (Curtis et al., 1991). The amount of each specific asphalt model adsorbed onto the silane-treated aggregates was compared to the amount adsorbed on the natural aggregate and has been reported in Table I. Positive signs indicate adsorbed masses increased with organosilane treatment while negative signs indicate adsorption of the asphalt model occurred to a greater extent on the natural aggregate, and thus, indicating organosilane treatment did not increase bonding between asphalt model and aggregate. Water was added to the adsorption system at equilibrium to determine the extent of debonding of asphalt model. The mass of asphalt model adsorbed was determined at adsorption equilibrium, and after desorption equilibrium was attained. The difference in amount of asphalt model adsorbed prior to water addition and after desorption equilibrium is reported as hydrophobic bonding enhancement in Table II. Positive signs on Table II indicate enhanced hydrophobic bonding as a consequence of organosilane treatment while negative signs indicate decreased hydrophobic bonding with organosilane treatment.

Adsorption of Asphalt Models. Adsorption behaviors were observed to be specific for the different combinations of silane coupling agent, the asphalt model compound, and the aggregate examined. Three organosilane agents, hydrocarbon, thiol, and amino, were used to treat the surface of three selected aggregates, one limestone and two gravels, that are commonly used in road pavements. The adsorption behavior of organic compounds, containing functional groups that are representative of those in asphalt, on silane-treated aggregates was compared to the adsorption behavior of the same organic compound on natural aggregate. This comparison has been reported in Table I as percent change in adsorption amount for each asphalt model/treated aggregate combination.

Few silane-treated aggregate/asphalt model combinations showed increased adsorption of asphalt models in comparison to adsorption amounts produced on the natural aggregate. Adsorption masses of benzoic acid and phenanthridine on hydrocarbon-treated RC-limestone increased to 20-34% with approximate error of $\pm 10\%$. Thiol-treated RC-limestone exhibited an increase in adsorption amount of benzoic acid, $25\% \pm 13\%$, compared to its adsorption on the natural aggregate. Additionally, increased adsorption, $32\% \pm 23\%$, of phenanthridine was observed for thiol-treated RC-limestone. Adsorption amounts for all other combinations of asphalt models and all silane-treated aggregates showed no change or decreased adsorption amounts compared to adsorption on the natural aggregate.

Most thiol treatments of RC-limestone and RJ-gravel resulted in greater decreases in adsorption amounts of phenysulfoxide, 1-naphthol, and phenanthridine, by nearly a factor of 2,

than those observed for these same models on thiol-treated RL-gravel. Amino-treated RJ-gravel and RL-gravel yielded large decreases, greater than 50%, in adsorbed amounts of all models, except for benzoic acid. Phenylsulfoxide presented little or no change in adsorption mass with hydrocarbon-treated RC-limestone, hydrocarbon-treated RL-gravel, and thiol-treated RL-gravel. Additionally, benzoic acid showed little or no change in adsorption mass for hydrocarbon-treated RL-gravel, thiol-treated RJ-gravel, and amino-treated RC-limestone.

For most of the systems, the propagated error associated with increases or decreases in adsorption mass of asphalt models for treated aggregates was dominated by the aggregate rather than the asphalt model or the silane treatment. This suggests that the chemical composition of the aggregate is the dominant factor for adhesion and subsequent durabilitiy for asphalt road pavements. Propagated error associated with organosilane treated RC-limestone adsorption masses of asphalt models were roughly 10%. Propagated error for treated RL-gravel ranged from 10-30%, and for RJ-gravel ranged from 20-48%.

Desorption and Bonding Enhancements. The desorption amounts of asphalt models from the silane-treated aggregates were system specific with the type of silane coupling agent and aggregate being influential in the desorption behavior. Silane treatments of nearly all aggregates resulted in enhanced hydrophobic bonding, i.e., less desorption of the asphalt models with the silane-treated aggregate than with the natural aggregates. Most of the treated aggregates retained more of the adsorbed model compounds in the presence of water, thus, indicating more durable bonding with less sensitivity to water. Hence, desorption percents were observed to be less with silane-treated aggregates than those observed for the natural aggregates.

A few combinations of asphalt models and silane-treated aggregates showed that silane treatments yielded no advantage in hydrophobic bonding. All silane treatments of RC-limestone in combination with 1-naphthol exhibited no change in hydrophobic bonding as compared to natural aggregates. Lack of change in hydrophobic bonding was also observed for all organosilane treatments of RJ-gravel in combination with phenylsulfoxide. Thiol-treated RC-limestone combined with phenylsulfoxide and thiol-treated RL-gravel combined with phenanthridine or benzoic acid indicated little or no change in percent desorptions with silane treatment as compared to those obtained for the same systems in combination with natural aggregates. Amino treatment of RC-limestone aggregate was especially deleterious for hydrophobic bonding of 1-naphthol which suggested that pairing asphalts with high phenolic content with amino-treated RC-limestone should be avoided.

Adsorption and Desorption of Asphalt on Organosilane Treated Aggregates. The SHRP MRL asphalts AAD-1, AAK-1, and AAM-1 were adsorbed from toluene solution onto silane treated and natural aggregates, RC-limestone, RJ-gravel, and RL-gravel. Changes in the amount of asphalt adsorbed on treated aggregates were monitored at 450 nm and compared to asphalt adsorbed onto natural aggregates as reported in Table I. At adsorption equilibrium, water was added to the system to determine the sensitivity of the adhesive bond to water. Any debonding of adsorbed asphalt from the silane-treated aggregates was compared to that observed for natural aggregates and reported as percent bonding enhancement. The bonding enhancement for the silane-treated aggregate for retaining adsorbed asphalt in the presence of water is given as a comparison of the percent desorbed from the silane-treated aggregate to the percent desorbed from the natural aggregate as reported in Table II. Whenever the percent desorbed was greater for the natural aggregate than for the silane-treated aggregate, bonding enhancement occurred as indicated by the positive sign in Table II.

Adsorption of Asphalt on Organosilane Treated Aggregates. Hydrocarbon treatment of RC-limestone, RJ-gravel, and RL-gravel resulted in increased adsorption mass for only one combination, hydrocarbon-treated RJ-gravel/AAK-1 asphalt, 50%±20%. All other combinations of hydrocarbon-treated RC-limestone and hydrocarbon-treated RJ-gravel presented virtually no change in adsorption mass of AAD-1 and AAM-1 asphalts as compared to those observed for the natural aggregates. Decreases in adsorption masses were observed for hydrocarbon-treated RL-gravel in combination with AAD-1 and AAM-1 asphalts.

Thiol-treated RC-limestone yielded little or no increase in adsorption mass for the three asphalts tested. Significant decreases, 60%±12-18%, in adsorption mass of AAM-1 asphalt on thiol-treated RJ-gravel and thiol-treated RL-gravel were observed. AAD-1 asphalt also showed decreased, 28-38%±12%, adsorption mass for these same two thiol-treated aggregates. In contrast, a substantial increase in adsorption mass, 186%±43%, was observed for AAK-1 asphalt on thiol-treated RJ-gravel.

Amino treatment of RC-limestone and RL-gravel produced no change in adsorption mass of AAD-1 asphalt. No changes were observed in adsorption mass of AAK-1 asphalt on amino-treated RC-limestone or for AAM-1 asphalt mass on amino-treated RL-gravel in comparsion to the adsorption mass obtained on the natural aggregates. Increased, 58-87%±41-48%, adsorption masses were noted for AAK-1 asphalt on both amino-treated gravels, while decreased, 27-68%±6-44%, respectively, adsorption masses were observed for the amino-treated RC-limestone and RJ-gravel aggregates.

In terms of increased adsorption of asphalt mass obtained on organosilane treated aggregates, as compared to asphalt mass obtained on natural aggregates, the data in Table I clearly show that AAK-1 asphalt adsorption was substantially enhanced by all organosilane treatements of RJ-gravel aggregate. Also, little or no enhancement in adsorption mass of any of the asphalts investigated was observed for any organosilane treatments of RC-limestone when compared to natural aggregates.

Desorption and Hydrophobic Bonding Enhancements for Asphalts. The specificity of organosilane treated aggregates for individual asphalts are clearly observed in Table II, which presents the percent hydrophobic bonding enhancement for treated aggregates in combination with selected MRL asphalts. Not all combinations showed an enhancement in hydrophobic bonding. For instance, RC-limestone aggregate treated with hydrocarbon, thiol, or amino silanes presented little or no change in bonding with the presence of water. Amino-treated RC-limestone in combination with AAM-1 asphalt indicated a very slight enhancement, compared to natural aggregate, in hydrophobic bonding, 5.9%±4.3%, while hydrocarbon-treated RC-limestone paired with AAK-1 asphalt showed a decrease, 5.9%±1.6%, for hydrophobic bonding. All other combinations of organosilane treated RC-limestone and asphalts presented no change in hydrophobic bonding as a result of the pretreatments. Thus, it was concluded that hydrophobic bonding between RC-limestone and these asphalts would not be enhanced with organosilane treatment of the aggregate.

Silane treatment of RJ-gravel aggregate resulted in contrasting behaviors for hydrophobic bonding that were dependent on the asphalt type. Silane treated RJ-gravel combined with AAK-1 asphalt yielded decreased, 17-40%±5-7%, hydrophobic bonding compared to natural aggregate and AAK-1 asphalt, while, no change or an increase in hydrophobic bonding was observed for all silane treated RJ-gravel with AAD-1 and AAM-1 asphalts. Thiol-treated RJ-gravel/AAD-1 asphalt showed substantial hydrophobic bonding enhancement of 38%±9%. AAM-1 asphalt indicated improved resistance to debonding by water when combined with

hydrocarbon and amino treated RL-aggregate as evidenced by bond enhancements of 17%±6% and 29%±9%, respectively.

No change in hydrophobic bonding enhancement for AAK-1 asphalt was observed for organosilane treated RL-gravel aggregates in comparison to desorption of AAK-1 asphalt from natural RL-gravel. Hydrocarbon and amino-treated RL-gravel in combination with AAD-1 and AAM-1 asphalts produced slight increases in hydrophobic bonding. Thiol-treated RL-gravel aggregate in combination with these same two asphalts produced decreased bonding enhancements.

SUMMARY

For the combinations of silane-treated aggregates, asphalt models, and asphalts tested, there was no relationship observed between increased adsorption amounts and increased hydrophobic bonding in comparison to similar investigations involving natural aggregates. Although, increased adsorption mass for some asphalt models and a few asphalts was observed, increased adsorption mass did not translate into increased resistance to water. Differences were observed in the hydrophobic bonding with the type of organosilane treatment employed for specific aggregate/asphalt model or asphalt combinations. The following conclusions point to the specificity of the interactions between all components of the asphalt pavement.

- Silane treatment of RC-limestone provided no advantage for increased hydrophobicity.
- None of the silane agents tested in this work provided any enhancement for hydrophobic bonding of AAK-1 asphalt to the selected aggregates, RC-limestone, RJ-gravel, and RL-gravel.
- Thiol-treated RJ-gravel provided increased water resistivity for bonding of AAD-1 asphalt.
- Hydrocarbon and amino-treated RJ-gravel provided greater water resistivity for AAM-1 asphalt than did identical silane treatments of RL-gravel.
- Hydrocarbon and amino-treated RL-gravel yielded small hydrophobic bonding enhancements for AAD-1 and AAM-1 asphalts.

REFERENCES

1. Curtis, C.W., Terrel, R.L., Perry, L.M., Al-Swailmi, S., Brannan, C.J. "Importance of Asphalt-Aggregate Interactions in Adhesion," Journal of AAPT, 60, 1991, 476.
2. Divito, J.A. and Morris, G.R. Trans. Res. Rec. 843, 1982, 104-11.
3. Graf, P.E. "Factors Affecting Moisture Susceptibility of Asphalt Concrete Mixes," Presented at the Annual Meeting of Association of Asphalt Technologists, 1986.

ACKNOWLEDGEMENTS

The Strategic Highway Research Program (SHRP) is gratefully acknowledged for support and input into this research. Gratitude is also expressed to G.Shieh and G.Li for their contributions.

Table I. Percent Change[a] in Adsorption Amounts[b] of Asphalt Models and Asphalts on MRL Aggregates Treated With Organosilanes

Modifier Aggregate	Asphalt Models				Asphalts		
	Benzoic Acid	Phenylsulfoxide	1-Naphthol	Phenanthridine	AAD-1	AAK-1	AAM-1
Hydrocarbon							
RC-limestone	+20±11[c]	+10±11*	-23±8	+24±10	+3±47*	0	-5±34*
RJ-gravel	-26±22	-53±32	-42±10	-32±25	-17±30*	+50±20	+4±16*
RL-gravel	-14±16*	+7±41*	-16±10	+32±23	-13±9	0	-34±19
Thiol							
RC-limestone	+25±13	-31±8	-43±32	-67±12	-15±32*	-12±39*	-26±28*
RJ-gravel	+8±21*	-71±35	-65±14	-45±19	-28±12	+186±43	-60±12
RL-gravel	-21±15	+7±30*	-26±8	-18±13	-38±3	-18±20*	-62±18
Amino							
RC-limestone	+4±10*	-71±9	-63±7	-82±6	+2±45*	-16±41*	-68±44
RJ-gravel	-35±26	-89±38	-69±12	-89±22	+43±30	+87±48	-27±6
RL-gravel	-46±16	-73±30	-53±7	-63±16	+53±64*	+58±41	+6±35*

a. Percent Change = $\left(\frac{\text{Amount Adsorbed on Natural Aggregate - Amount Adsorbed on Treated Aggregate}}{\text{Amount Adsorbed Natural Aggregate}}\right) \times 100$

b. Adsorption Amounts: + Increased with Treatment
- Decreased with Treatment

c. Propagated Error, Percent

* Values were considered insignificant due to large propagated error.

Table II. Percent Bonding Enhancement[a] for Organosilane Treated Aggregates for Hydrophobic Asphalt-Aggregate Bonding

Aggregate Model/Asphalt	Percent Enhancement in Hydrophobic Bonding		
	Organosilane Treatments		
	Hydrocarbon	Thiol	Amino
RC-limestone			
Benzoic Acid	+23.2[b]±1.5[d]	+11.1±2.8	+14.3±1.6
Phenylsulfoxide	+48.7±3.2	-1.1±3.2*	+32.8±6.5
1-Naphthol	-2.7±5.6*	-18.0[c]±6.0	-119±6.8
Phenanthridine	+49.8±19.8	+24.2±6.5	+25.8±16.0
RJ-gravel			
Benzoic Acid	+192±3.0	+80.7±2.7	+119±4.7
Phenylsulfoxide	+9.5±10.1*	+15.8±18.6*	-1.4±16.4*
1-Naphthol	+192±15	+12.8±8.6	+93.2±2.8
Phenanthridine	+8.5±2.9	+29.4±2.9	+64.6±11.3
RL-gravel			
Benzoic Acid	+10.4±6.5	+11.7±14.0*	+23.9±1.7
Phenylsulfoxide	+13.9±6.3	-15.2±4.4	+15.8±4.8
1-Naphthol	+39.0±12.0	+10.3±8.4	+65.9±1.4
Phenanthridine	+22.0±13.3	-4.5±16.3*	+13.3±11.2
RC-limestone			
AAD-1	-19.5±20*	-14.4±20*	-8.1±20*
AAK-1	-5.9±1.6	-0.3±1.8*	+0.8±3.0*
AAM-1	+3.6±4.2*	-2.3±4.8*	+5.9±4.3
RJ-gravel			
AAD-1	-5.5±6.5*	+37.7±8.8	+5.3±8.1*
AAK-1	-40.4±4.9	-36.5±6.6	-17.2±6.7
AAM-1	+16.6±6.1	-1.0±4.8*	+28.8±8.6
RL-gravel			
AAD-1	+9.8±8.8	-14.9±8.6	+14.3±9.8
AAK-1	-2.7±14.0*	+2.8±14*	+6.2±14*
AAM-1	+8.0±1.5	-4.1±1.7	+14.5±4.0

a. Percent Bonding Enhancement = (% Desorption on Treated Aggregate - % Desorption on Natural Aggregate.
b. Increased Hydrophobic Bonding.
c. Decreased Hydrophobic Bonding.
d. Propagated Error, Percent.
* Values were considered insignificant due to large propagated error.

PROPERTIES OF ASPHALT FRACTIONS OBTAINED BY SUPERCRITICAL EXTRACTION WITH PENTANE AND CYCLOHEXANE

Howard B. Jemison, Kevin M. Lunsford, Richard R. Davison*,
Charles J. Glover, and Jerry A. Bullin
Texas A&M University, Department of Chemical Engineering
College Station, Texas 77843-3122

Keywords: Asphalt, Fractions, Supercritical, Extraction, Pentane, Cyclohexane

INTRODUCTION

Supercritical fractionation is particularly attractive for asphalt fractionation as it already is used commercially for this purpose. The system explored in this work, like commercial processing, does not provide the separating efficiency of supercritical chromatography, but it provides large fractions for further study.

In earlier work (1) three asphalts were fractionated with a combination of supercritical and room temperature separations. The first step was with supercritical pentane and split the asphalts into top (approximately 60%) and bottom (approximately 40%) fractions. The top 60% was subsequently separated into four fractions with supercritical pentane. The hard bottom 40% was separated into 4 fractions by precipitation from mixtures of varying ratios of pentane and cyclohexane at room temperature.

In this current work three asphalts and three reduced crude feeds were fractionated. However, all the separation was done supercritically using either cyclohexane or pentane.

SUPERCRITICAL FRACTIONATION

The operation of the Supercritical Unit has been described previously (1) but the conditions used in this study were different and are shown in Table 1. The three asphalts were first fractionated into four fractions using supercritical cyclohexane. These are fractions 8, 9, 10, and C1. Fraction C1 was fractionated with supercritical pentane into fractions 5, 6, 7, and P1. Fraction P1 was then fractionated with pentane into fractions 1-4. The reduced crudes were similarly fractionated with cyclohexane but the top material was only separated into four additional fractions with the lightest containing material that would normally be in vacuum gas oil. In each run (i.e., pass through the supercritical unit), the heaviest fraction was insoluble at the initial conditions, the next two fractions precipitated on increase in temperature while the lightest fraction was completely separated from the solvent by a reduction in pressure.

ASPHALT ANALYSIS

Infrared analysis was described previously (1). Corbett analyses were done using a modification of ASTM D4124 (2). Asphalts were aged in pressure oxygen vessels that were described by Lau et al. (3). The asphalt is deposited on aluminum trays in an approximately 1mm film to minimize diffusion effects. The vessels were operated at 300

psi (20.1 bar) oxygen pressure at 160°F (71.1°C), 180°F (82.2°C), and 200°F (93.3°C) for periods of time ranging from 2-28 days depending on the temperature.

Low shear rate limiting dynamic viscosities were measured on a Carri-Med 500 (CSL) Controlled Stress Rheometer using the oscillatory mode. The reported values represent the frequency/shear rate independent viscosities. For samples with viscosities greater than 500,000 poise at 60°C, the dynamic properties were measured at 95°C and shifted using time/temperature superposition as described by Ferry (4) to 60°C.

RESULTS

The fraction distributions are shown in Table I. For the three asphalts used, fraction C1, the top cyclohexane fraction, contains from 60 to 80% of the feed material. The percentages of fractions C1 plus 8 through 10 should add to 100, but do not because of difficulty making accurate material balances. For the reduced crudes, the C1 fraction percentages reported in Table I are probably too high because of possible incomplete cyclohexane removal. The top fractions for the asphalt are remarkably uniform in size, while for the reduced crudes they show the relatively large amount of vacuum gas oil in these feeds. The presence of this large amount of vacuum gas oil in the supercritical phase had a marked effect on the temperatures necessary to precipitate the remaining material as shown in Table I.

The Corbett analyses for the Coastal fractions are shown in Figure 1 and are combined with the fraction sizes from Table I to produce the distribution of the whole asphalt Corbett fractions among the supercritical fractions (Figure 2). Thus 37% of all saturates in the Coastal asphalt is in fraction 1, and 40% of the total asphaltenes is in fraction 9. In general the saturates concentrate in the light fractions and the asphaltenes in the heavy fractions. The aromatics are widely distributed with the naphthene aromatic concentration reaching a maximum in fraction 2 or 3, and the polar aromatic at about fraction 6, although with Texaco (not shown) fraction 8 is the highest and 6 is actually lower than 4, 5, or 7. Stegeman et al. (1, 5) has shown that the molecular size of the material increases markedly with fraction number for the supercritical fractions and the individual Corbett fractions.

There is an obvious discontinuity between fraction 7 (the heaviest pentane fraction) and 8 (the lightest cyclohexane fraction). The excess saturates in fraction 8 and asphaltenes in fraction 7 indicate a lower selectivity with cyclohexane. Fraction 7 is much harder than fraction 8 and fraction 6 is generally significantly harder than fraction 8 but not as hard as 7.

This discontinuity is also demonstrated in Figure 3. In this figure the fractions are ranked with respect to solubility by calculating a number (termed the fraction mean) for each fraction which represents the percent of the whole asphalt which is less soluble than the fraction. For example, a fraction representing the most soluble 10% would be plotted at 95%. The whole asphalts, covering the entire range from 0 to 100% are all plotted at 50%. This figure includes all asphalt fractions having viscosities equal or less that 10^5 poise at 60°C including the whole asphalts. A smooth set of data results except

for the only three cyclohexane fractions (all fractions 8) which are widely separated from the pentane fractions and form their own curve.

Fraction Aging: Figure 4 shows aging of the fractions in terms of carbonyl formation. Carbonyl area is defined on an arbitrary scale in terms of the infrared peak between wavenumbers of 1650 to 1820cm^{-1} (3, 6). These data for Fina asphalt aged at 93.3°C (200°F) show a phenomenon common to all the asphalts. There is an initial rapid increase in carbonyl area, for all but the lightest material, which increases sharply with fraction number. After this initial rapid rate, the rate decreases and becomes constant indefinitely. At 93.3°C this constant rate is almost the same for all fractions, although for the Coastal asphalt (not shown) the rate seemed to increase slightly with fraction number. In Figure 5 the same phenomenon is seen for Texaco. The initial jump is smaller than for Fina and there is more effect of fraction number, but again the rate appears to remain unchanged after a short initial period of rapid oxidation.

In Figure 6, the aging of Texaco asphalt and fractions 1 at 82.2°C is shown in terms of viscosity changes. After an initial rapid change as was seen on the carbonyl plots, the log of viscosity changes linearly with time for all fractions and the whole asphalts. This occurs for all fractions at all temperatures.

One of the most interesting and useful relations between chemical changes and changes in physical properties is the universal linear variation of asphalt log viscosity with growth in the carbonyl area (3, 7, 8). Figures 7 to 9 show that this applies to the asphalt fractions as well. All the aging data at all three temperatures are shown on these graphs. These viscosities are measured at 60°C, but a linear relation exists for viscosities measured at other temperatures as well (3). It has been found that the original unaged material may deviate from these lines.

The anomalous behavior of cyclohexane-separated fraction 8 is shown in Figure 9 where fraction 8 is seen to have lower viscosities as it ages than fraction 6. In general, one observes an increase in the sensitivity of the viscosity to carbonyl growth (hardening susceptibility) with increasing fraction number. The Coastal whole asphalt and fraction 8 appear particularly sensitive to carbonyl formation. This does not in itself assure rapid hardening as this also depends on the rate of carbonyl formation which is strongly affected by temperature.

ACKNOWLEDGEMENTS

Support for this work by the Texas Department of Transportation, Study 2-9-90-1249, in cooperation with the U.S. Department of Transportation, Federal Highway Administration, is gratefully acknowledged.

The Carri-Med Controlled Stress (CSL) Rheometer was manufactured by Carri-Med, Ltd., Dorking, Surrey, England, and distributed in North America by Carri-Med Americas, Inc., Twinsburg, Ohio.

LITERATURE CITED

1. Stegeman, J.R., Kyle, A.L., Burr, B.L., Jemison, H.B., Davison, R.R., Glover, C.J., and Bullin, J.A., *PREPRINTS, Div. of Petrol. Chem., ACS,* **35**(3), 431-439 (July 1990).
2. Thenoux, G., Bell, C.A., Wilson, J.E., Eakin, D., and Shroeder, M., "Experiences with the Corbett-Swarbrick Procedure for Separation of Asphalt into Four Generic Fractions," *Trans. Res. Rec.*, **1171**, 66-70 (1988).
3. Lau, C.K., Lunsford, K.M., Glover, C.J., Davison, R.R., and Bullin, J.A.,, *Trans. Res. Rec.*, in press.
4. Ferry, J.D., *Viscoelastic Properties of Polymers*, 3rd ed., John Wiley & Sons, New York, (1980).
5. Stegeman, J.R., Davison, R.R., Glover, C.J., and Bullin, J.A., *Proceedings of the International Symposium: Chemistry of Bitumens,* Rome, Italy, **1**, 336-381, June 5-8, 1991.
6. Jemison, H.B., Burr, B.L., Davison, R.R., Bullin, J.A., and Glover, C.J., *PREPRINTS, Div. of Petrol. Chem., ACS,* **35**(3), 490-495 (July 1990).
7. Martin, K.L., Davison, R.R., Glover, C.J., and Bullin, J.A., *Trans. Res. Rec.*, **1269**, 9-19 (1990).
8. Jemison, H. B., Davison, R. R., Glover, C. J., and Bullin, J. A., *Trans. Res. Rec.*, in press.

TABLE Ia
Supercritical Fractionation Data: Asphalt Fractions

Fraction	Solvent	T(°C)	P(bar)	Fraction Percentages		
				Coastal	Fina	Texaco
1	n-pentane	149	10.1	16	15	14
2	n-pentane	229	47.0	13	10	11
3	n-pentane	227	47.0	9	9	8
4	n-pentane	224	47.0	3	9	3
5	n-pentane	221	47.0	10	13	11
6	n-pentane	213	47.0	3	5	4
7	n-pentane	204	47.0	12	19	14
8	cyclohexane	307	47.0	19	17	17
9	cyclohexane	299	47.0	9	3	17
10	cyclohexane	288	47.0	6	2	3
P1	n-pentane	149	10.1	42	45	33
C1	cyclohexane	204	10.1	67	80	58

TABLE Ib
Supercritical Fractionation Data: Reduced Crude Fractions

Fraction	Solvent	T(°C)	P(bar)	Fraction Percentages		
				Coastal	Fina	Texaco
1	n-pentane	149	10.1	57	46	44
2	n-pentane	249	47.0	22	43	24
3	n-pentane	232	47.0	4	8	8
4	n-pentane	204	47.0	4	3	6
5	cyclohexane	324	47.0	11	13	13
6	cyclohexane	310	47.0	4	3	7
7	cyclohexane	299	47.0	2	1	3
C1	cyclohexane	204	10.1	88	89	79

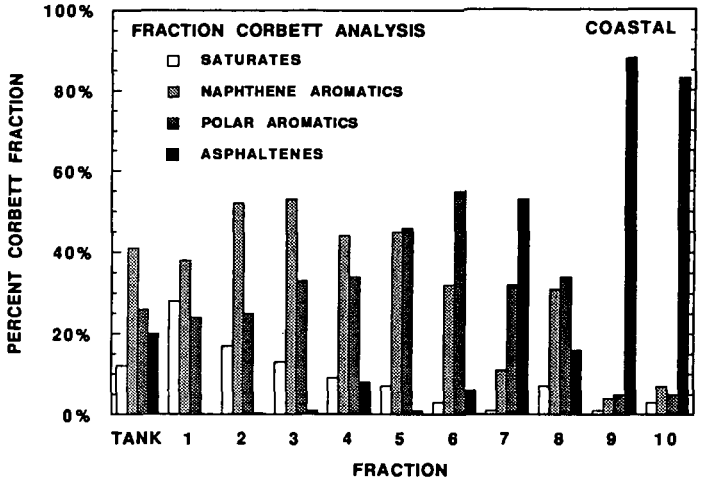

Figure 1: Corbett Analysis of the
Supercritical Fractions of the Coastal Asphalt

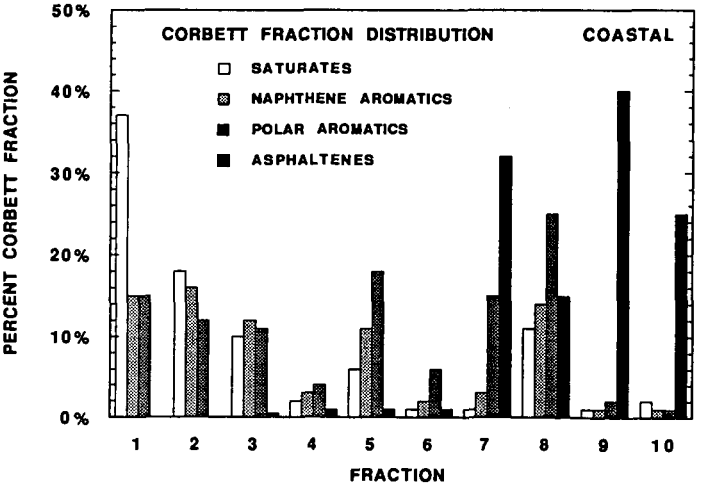

Figure 2: Distribution of the Whole Asphalt's Corbett Fractions
Among the Supercritical Fractions of the Coastal Asphalt

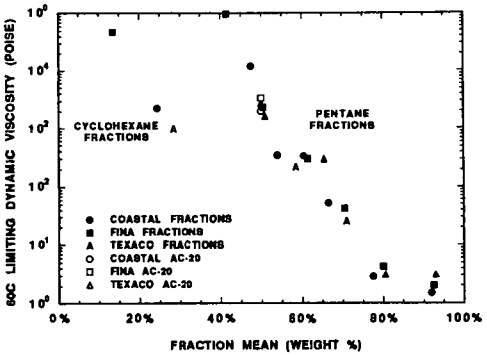

Figure 3: Viscosities of the Whole Asphalts and Their Supercritical Fractions

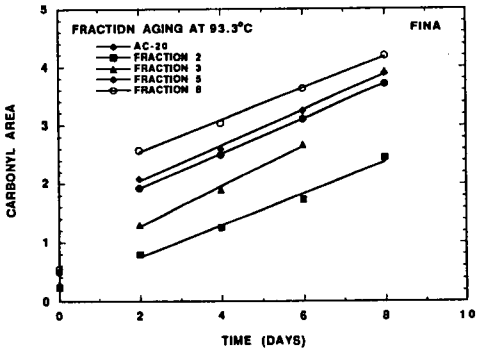

Figure 4: Carbonyl Growth with Time of the Fina Asphalt and Its Fractions Due to Aging at 93.3°C

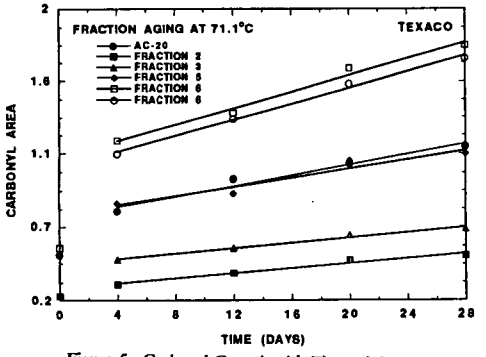

Figure 5: Carbonyl Growth with Time of the Texaco Asphalt and Its Fractions Due to Aging at 71.1°C

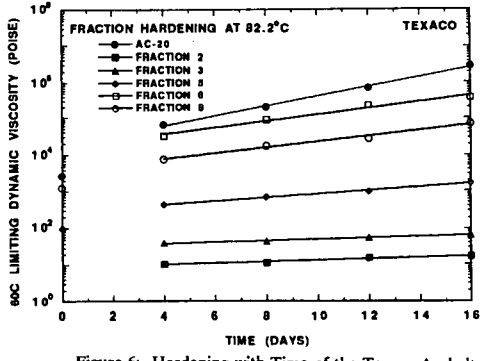

Figure 6: Hardening with Time of the Texaco Asphalt and Its Fractions Due to Aging at 82.1°C

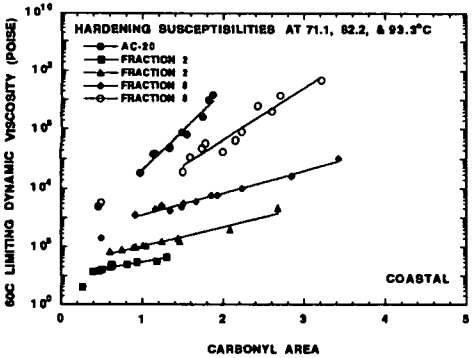

Figure 7: Hardening Susceptibilities of the Coastal Asphalt and Its Fractions at 71.1, 82.1, and 93.3°C

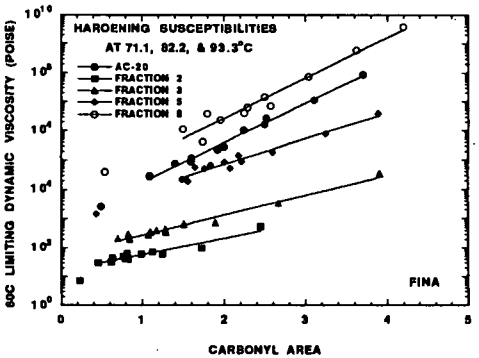

Figure 8: Hardening Susceptibilities of the Fina Asphalt and Its Fractions at 71.1, 82.1, and 93.3°C

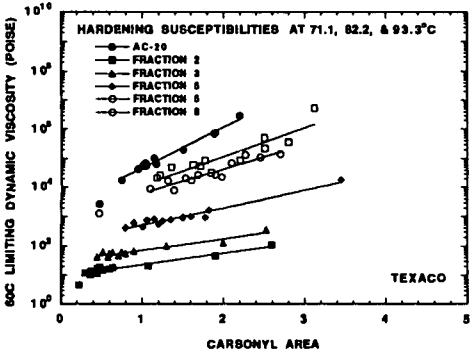

Figure 9: Hardening Susceptibilities of the Texaco Asphalt and Its Fractions at 71.1, 82.1, and 93.3°C

SYMPOSIUM ON CHEMISTRY OF ASPHALT AND ASPHALT-AGGREGATE MIXES
PRESENTED BEFORE THE DIVISION OF FUEL CHEMISTRY, INC.
AMERICAN CHEMISTRY SOCIETY
Washington, D.C. Meeting, August 23-28, 1992

The Effect of Composition of Distillable Fractions on the Rheological Temperature Susceptibility of Cold Lake Asphalt

H. Sawatzky, B. Farnand, J. Houde Jr., I. Clelland
Energy, Mines and Resources Canada, Energy Research Laboratories,
555 Booth St., Ottawa, Ontario, Canada K1A 0G1 (613) 996-7970

Introduction

In another presentation (1) we proposed a model to explain the mechanisms in asphalt whereby changes in viscosity due to changes in temperature are resisted. In this work the rheological temperature susceptibilities of Cold Lake asphalt have been studied as components are distilled from it and then replaced with various amounts of materials of diverse nature, as well as mixtures of these materials. The results are explained on the basis of the model previously proposed.

Experimental

Distillation

Figure 1 shows the distillation conditions and fraction yields obtained from the distillation of Cold Lake asphalt. The temperature of the asphalt in the distillation flask was not allowed to exceed 340°C to avoid pyrolysis. Figure 2 shows the change in penetration values of residue as distillation proceeds.

Rheological Temperature Susceptibilities

These susceptibilities were determined as penetration indices(2) from penetrations taken from 4°C to 40°C. The equation used to calculate the penetration index is given as:

$$PI=(20-500A)/(50A+1) \qquad 1)$$

where A is the slope obtained from the plot of logarithm (base 10) of the penetration in dmm with temperature in centigrade degrees.

Blending

The final distillation residue [+533°C] was blended with calculated amounts of the distillates to simulate the residues obtained when the distillation cuts were made. These blends and the blends obtained with other materials were thoroughly mixed at 135°C -150°C.

Blending Materials

Biomass Derived Oil (BDO)- This is a highly polar material, topped at 350°C, whose major functional groups consist largely of amides. It has nitrogen and oxygen contents of 4 wt % and 6 wt % respectively.

Mineral Oil (Min)- This oil was purchased from Fisher Scientific and consists of high boiling saturated hydrocarbons.

Hydrogenated Syncrude Gas Oil (H2Syn)- This gas oil consists predominantly of saturated aliphatic and naphthenic hydrocarbons with some aromatic hydrocarbons.

Waste Banbury Oil (Ban)- This high boiling oil is highly naphthenic and was used in the processing of rubber. It was obtained from Trent Rubber Services Inc.

Dutrex 776™ (Dut)- This Shell Oil product has a saturated hydrocarbon content of 24.4%, naphthenic-aromatics of 63.3% and polar components of 12.0%. It distils between 375°C and 580°C.

Shale Oil (Shale)- This was produced from New Brunswick oil sh le. These shale oils are known to have high contents of nitrogenous components.

Paraffinic Gas Oil (Para)- This was obtained from a waxy conventional crude oil.

Results and Discussion

The effect of distillation on the rheological temperature susceptibilities that are expressed in terms of "Penetration Index" [PI] are shown in Fig. 3, 4 and 5. As the distillation proceeds the PI of the residues increases. Also, the saturated hydrocarbon content of the distillates decreases and the polar components increase as shown in Table 1. Since the PI increases as materials are removed by distillation, it seems that components that are undesirable for low temperature susceptibility are being removed.

It is assumed that most of the distillate obtained from the Cold Lake asphalt originated from the continuous phase or uncomplexed material according to the model proposed earlier. Therefore, it would be expected that this phase became smaller as distillation proceeded. As there are temperature dependent equilibria of exchangeable components between the continuous and complexed phases and since the continuous phase decreases there should be a trend for the exchangeable components, in particular the more highly polar ones, to be forced into the complexes. This would leave a new fraction of less polar components in the exchangeable state which could be more responsive to temperature changes and result in greater resistance to viscosity changes. Also, the distillation changes the composition of the continuous phase (Table 1) and thereby changes the affinity of this phase for exchangeable components which favours greater responses to temperature changes.

Figure 5 plots PI vs the penetrations at 25°C of the various blends. The initial blends are designated by the suffix 1 and the subsequent blends designated by the suffix 2, i.e., Min1 and Min2. The curve on this plot represents the Cold Lake residues obtained during distillation and is used as a curve of reference in the subsequent figures.

As shown in Fig. 6, when the highly polar biomass derived oil [5%] was blended with the +533°C residue the PI fell below that of the reference curve

indicating that highly polar components are not desirable. This blend probably is quite complex, because some of the polar components of this oil might displace some of the original asphalt polar components from the micelles or complexes. The balance of affinities of the two phases for the interchangeable components becomes less favourable for resisting viscosity changes with changing temperatures. Therefore, it could be argued that the increase in PI during distillation is due to some decrease in undesired polar components.

The blend containing the first addition [5%] of the hydrogenated Syncrude (H2Syn1) had the highest PI, followed by that containing a similar amount of Banbury oil (Ban1) then that containing about 10% Dutrex (Dut1). A blend that contained a similar amount of mineral oil (Min1) and 10% of paraffinic oil (Para1) also had improved PI and the 5% shale oil blend (Shale1) can be considered neutral.

These trends change dramatically when twice the initial amount of these blending agents is added. The PI decreased in the blends containing Syncrude (H2Syn2), the Dutrex (Dut2) and paraffin (Para2). The PI of the Syncrude (H2Syn2) decreased by approximately 1.5 PI units. The PI of the Banbury oil blend (Ban2) also decreased, but still remains fairly high. The PI of the shale oil blend (Shale2), which was about the same as the +533°C residue, only decreased by as much as the reference curve during the increase in penetration. Therefore, it can be considered neutral again. It is quite remarkable that the PI of the blend containing the increased amount of mineral oil increased marginally.

When another increment of the mineral oil (13.26%) was added as shown in Fig. 7, a moderate decrease in the PI occurred due to an upset in the ratio of saturated hydrocarbon to aromatic plus naphthenic components. As shown in Fig. 8, when small amounts of the Syncrude gas oil were added to the mineral oil [~9%] containing blend, it appeared to have little effect. However, when added to a blend containing a larger amount there was significant positive effect, but when more was added the PI decreased although with the increased softening, this

decrease was similar to that in the reference curve. Similar results were obtained when Banbury oil was added to blends containing the mineral oil as shown in Fig. 9. In this case, a blend had a penetration similar to the starting Cold Lake asphalt but with a PI about 1.5 PI units higher.

It appears that replacing the distillates from the Cold Lake asphalt with the various blending agents modified the continuous phase and this affected the responses to temperature changes.

Conclusions

It has been shown that the composition of the distillable portion of asphalt can have a major effect on temperature susceptibility. Also, it has been shown that for Cold Lake asphalt, blending can increase the PI by at least 1.5 units. These effects can be explained on the basis of a proposed model. Work is continuing on the quantification of the model.

References

1. Sawatzky, H., Farnand, B., Houde, J. Jr. and Clelland, I., Div. of Petrol. Chem., ACS, Aug, 1992.

2. Pfeiffer, J.P. and van Doormaal, P.M., J. Inst. Petrol. Technol., 22, 414 (1936).

Table 1 - Component types in distillation fractions (%)*

	350 °C -448 °C	449 °C -482 °C	483 °C -497 °C	498 °C -529 °C	530 °C -533 °C
Saturates	34.4, 34.2	29.55, 29.86	28.04, 31.36	22.63, 22.91	18.58, 18.98, 19.81
avg.:	34.3	29.7	29.7	22.8	19.1
Naphthene-Aromatics I	27.78, 38.24	39.92, 40.79	43.30, 31.09	46.31, 41.08	41.90, 28.05, 29.85
avg.:	33.0	39.9	37.2	43.6	32.3
Naphthene-Aromatics II	27.28, 14.32	19.88, 17.91	16.08, 20.51	15.61, 21.21	16.82, 26.64, 31.23
avg.:	20.8	18.9	18.3	18.4	24.9
Polar Aromatics	5.75, 8.32	6.99, 7.53	9.21, 13.26	10.58, 10.87	13.78, 17.14, 10.67
avg.:	7.0	7.2	11.2	10.8	13.9
Loss	7.80, 4.91	3.67, 3.91	3.39, 3.78	4.87, 3.93	8.92, 9.19, 8.44
avg.:	4.9	3.8	3.6	4.4	8.9

* Modified ASTM D4124 procedure scaled down by a factor of 10.

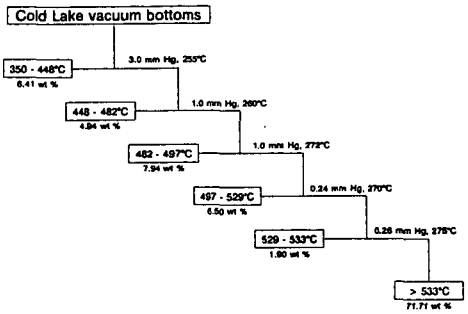

Fig 1 - Conditions and yields of vacuum distillation of Cold Lake vacuum bottoms

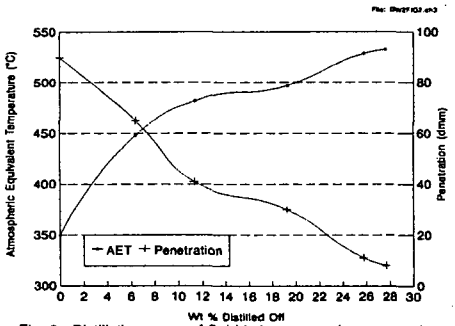

Fig. 2 - Distillation curve of Cold Lake vacuum bottoms and change in penetration of residue as distillation proceeds

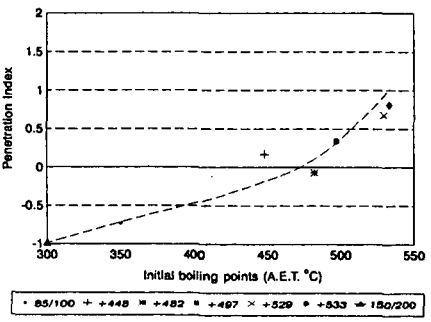

Fig. 3 - Penetration index vs Cold Lake vacuum bottoms 47-CL-89

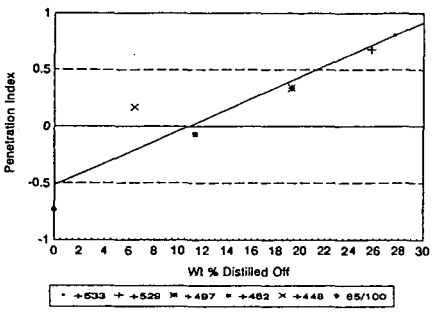

Fig. 4 - Penetration index vs wt % distilled off of Cold Lake vacuum bottoms

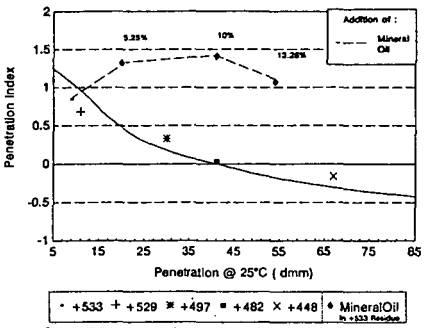

Fig. 7 - Penetration index vs penetration at 25°C of Cold Lake vacuum bottom blends

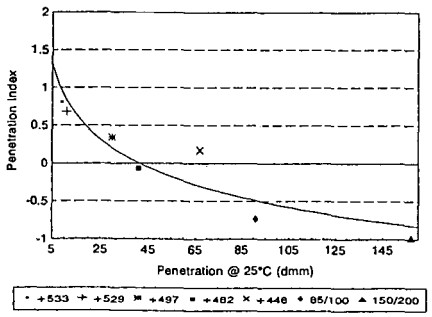

Fig. 5 - Penetration index vs penetration at 25°C of Cold Lake vacuum bottoms

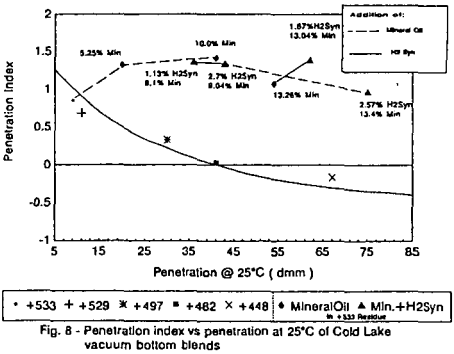

Fig. 8 - Penetration index vs penetration at 25°C of Cold Lake vacuum bottom blends

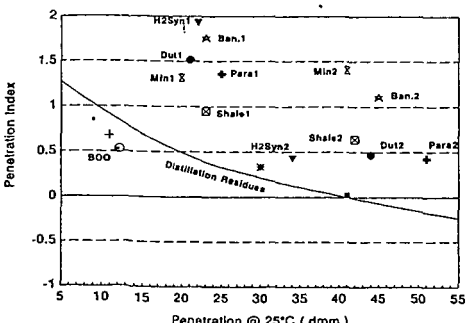

Fig. 6 - Penetration index vs penetration at 25°C of +533°C Cold Lake vacuum bottom blends

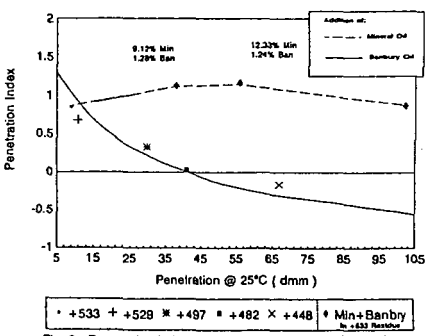

Fig. 9 - Penetration index vs penetration at 25°C of Cold Lake vacuum bottom blends

DEASPHALTING OF NON-CONVENTIONAL RESIDUES

S. Ng, E. Castellanos and B. Farnand

Energy Research Laboratories/CANMET
Energy, Mines and Resources Canada
555 Booth St., Ottawa, Ontario, Canada K1A OG1

INTRODUCTION

Mitchell and Speight[1] established a correlation between the weight of asphaltenes precipitated from Athabasca bitumen and the solubility parameter of the precipitating solvent. The polynuclear aromatic systems in asphaltenes isolated from Athabasca bitumen was also reported by Speight[2]. Recently, Kokal et al.[3] measured precipitation of asphaltenes in Canadian heavy oils by injecting light hydrocarbon gases, e.g., methane, propane, ethane/propane mixtures, and carbon dioxide at various temperatures and pressures. A thermodynamic model proposed by Hirshberg et al.[4] based on Flory-Huggins theory was used to correlate the experimental data and predict precipitate formation. The objective of this study was to evaluate the viability and processability of deasphalted oils (DAO) from Canadian non-conventional residues as feedstocks to produce transportation fuels. This paper only describes and compares the deasphalting characteristics of two vacuum tower bottoms (VTB) derived from Athabasca oil sand bitumen and Lloydminster heavy oil.

EXPERIMENTAL

The Athabasca VTB was obtained by distillation (ASTM D1160) of a coker feed (305°C+) from a commercial plant which produces synthetic crude from oil sand bitumen. The VTB (544°C+) constituted 63.5 wt % of the coker feed. Lloydminster VTB was obtained from an Eastern Canadian refinery that processes pipeline quality Lloydminster crude oil.

The equipment used for the deasphalting experiments is shown in Fig. 1. VTB was first dissolved in toluene (approximately 0.3 mL VTB/mL toluene). The blend was transferred to a double-ended sample cylinder (transfer vessel) which could withstand 500 psi pressure through mercury compression. The required amount of blend was transferred by mercury displacement to a detachable PVT cell which was held at 75°C. The PVT cell was removed from the system and attached to a vacuum line. Toluene was evaporated from the blend overnight. The PVT cell was restored to the deasphalting system. The volume of solvent required to give the desired solvent/VTB ratio was determined using Starling's tabulations[5]. This volume was added to the PVT cell, again using the mercury displacement technique. The cell was then brought to operating temperature and pressure, and the mixture was equilibrated by shaking for 1 h. The phases were allowed to separate for 3 h at equilibrium temperature and pressure.

The solvent-rich phase was removed at equilibrium pressure from the cell by mercury displacement and was collected in a tared flask which was chilled to prevent solvent loss (propane required a dry ice-acetone slurry, n-butane and n-pentane required dry ice, while an ice bath was sufficient for n-heptane). Toluene (50 mL) was added to the cell. After shaking for 20 min, the toluene

fraction was displaced from the cell using the mercury pump. This washing procedure was repeated four times. The weight of the solvent-rich phase was determined before the solvent was evaporated off and the weight of deasphalted oil determined. Toluene was also evaporated from the solvent-lean phase in order to determine the weight of residue. The weight of solvent in the solvent-lean phase was obtained by substracting the weight of solvent in the solvent-rich phase from the total weight of solvent added to the cell.

To complete the phase behaviour measurements, the concentrations of the oils, resins and asphaltenes in the solvent-rich and solvent-lean phases were required. The DAO and the residue were deasphalted using ASTM method D3279 and the recovered maltene fractions were then separated into oils and resins on an Attapulgus clay column. For this study, 33 g of clay was used to separate 1 g of maltenes dissolved in 10 mL of n-heptane. The oil was eluted from the column using 200 mL of n-heptane. Resins adsorbed by the column were then eluted using 70 mL of methylene chloride followed by 70 mL of 20% diethylether in methylene chloride. All solvents were finally evaporated off.

For both VTB's, most of the phase behaviour measurements were made over a wide range of solvent/VTB ratios using the following solvents and conditions:

Propane	75°C	465 psia
n-Butane	120°C	415 psia
n-Pentane	160°C	365 psia
n-Heptane	75°C	65 psia

Several measurements were made at other conditions. In all cases the system pressures were selected so that the solvent would be undersaturated by at least 50 psia (i.e., 50 psia above the bubble point) at the desired operating temperature to ensure that the systems would remain completely in the liquid phase.

The two VTB's were characterized using ASTM and other analytical methods.

RESULTS AND DISCUSSION

Table 1 gives the analyses of the two VTB's. It can be seen that the Athabasca VTB is significantly heavier than the Lloydminster. The Athabasca contains approximately one quarter more sulphur, nitrogen, asphalt (asphaltenes + resins), Conradson Carbon residue, and 1.5 times the Ni + V content. In addition, the Athabasca VTB has much higher softening point and viscosity. The gas chromatograph distillation (GCD) data indicate that the Athabasca sample has been cut a little heavier than the Lloydminster.

Comparison of the phase behaviour for solvent-VTB systems is facilitated by plotting the phase data on pseudo-ternary phase diagrams. Typical examples are shown in Fig. 2 and 3 for n-pentane/Athabasca and n-pentane/Lloydminster systems, respectively, at 160°C and 365 psia. The dotted dilution line connecting the pure solvent apex and VTB composition on the baseline serves to indicate (i) the solvent/VTB ratio; (ii) the ratio of solvent-rich and solvent-lean phases when used together with the individual tie-line in the immiscible region.

Variables that significantly affect the phase behaviour of the deasphalting process would be expected to influence both the quantity and quality of DAO produced. Using data from the phase behaviour measurements, these effects can be investigated and are summarized as follows:

A. **Effect of Solvent**

Table 2 compares data for the runs conducted at 75°C with a nominal volumetric solvent/VTB ratio of 9 for various solvents. The overall weight per cent of the original VTB recovered as deasphalted oil in the upper phase increased rapidly with higher carbon number of the solvent. This was accompanied by higher recoveries of (i) the oil fraction which reached about 90 wt % with n-heptane; (ii) the resin fraction and (iii) the asphaltene fraction with n-heptane. These observations accord with the conclusions of the Flory-Huggins liquid model, i.e., increasingly heavier solvents give smaller regions of immiscibility with shorter tie-lines and heavier deasphalted oils (greater resin and asphaltene contents).

In addition, between the two VTB's there was markedly better recovery of oil and resins from the Lloydminster over the Athabasca at equivalent conditions, especially with lighter solvents. This certainly reflects the differences in the VTB constituent fractions of the two oils and their influence on the phase behaviour.

B. **Effect of Temperature-Pressure**

These two variables could be combined so far as the pressure at any selected temperature was kept at least 50 psia above the solvent bubble pressure to maintain a liquid system. The effect of the temperature-pressure combination is presented in Table 3 for n-butane and n-pentane at a nominal volumetric solvent/VTB ratio of 9. It can be seen that the overall recovery of VTB as DAO was lower at higher temperature. For n-butane, the recovery of both oil and resin fractions was depressed at more severe operating conditions whereas for n-pentane the major effect was to lower the recovery of the resin fraction. The results concur with Flory-Huggins model which indicates an increase of disparity between solvent and solute as the temperature is raised. This leads to a larger region of immiscibility with a broader two-phase envelope and longer tie-lines on a pseudo-ternary representation.

It should also be noted from the results that the effect of the solvent predominated over that of the temperature-pressure combination. For n-pentane at the most severe conditions, recoveries exceeded those for n-butane at the lowest temperature. Also, the recoveries of Lloydminster VTB, both overall and for individual fractions, were better than those of Athabasca VTB at comparable operating conditions.

C. **Effect of Solvent/VTB Ratio**

Data for the deasphalted oil composition and weight per cent extracted as a function of solvent/VTB ratio are given in Table 4 for the n-pentane/Athabasca VTB system at 160°C and 365 psia. Over a range of ratio from 20 to 5.2, there was little change in either the composition or the extracted weight of the deasphalted oil. Only as the phase envelope started to close at the lower solvent/VTB ratios, a rapid increase occurred in the asphaltenes at the expense of the oil. The overall weight extracted also showed an increase at the low solvent/VTB ratio.

To conclude, deasphalting parameters such as solvent type, temperature, pressure and solvent/VTB ratio should be optimized to make deasphalting a viable process for subsequent fuel production. The qualities of the deasphalted oils produced from this study have been partially reported elsewhere[6]. The presence of asphaltenes, and to a lesser extent resins, in the DAO will certainly reduce its desirability as a fluid catalytic cracking (FCC) feed. This has been confirmed by microactivity tests (MAT) and kinetic riser simulations which indicate that propane and n-butane deasphalted heavy oil residues are acceptable feeds for FCC riser units provided the unit is flexible enough to permit considerable increase in the regenerator operating temperature[6]. Alternatively, the n-C4 to n-C7 DAO's can be diluted with conventional gas oils or hydrotreated to yield feedstocks acceptable to unmodified FCC units as suggested by Bousquet et al.[7]

References

(1) Mitchell, D.L. and Speight, J.G., Fuel 52, 149, 1973.

(2) Speight, J.G., PREPRINTS, Div. of Petrol. Chem., ACS, 31(4), 818, 1986.

(3) Kokal, S., Najman, J., Sayegh, S. and George, A., J. Can. Petrol. Tech., 31(4), 24, 1992.

(4) Hirshberg, A., De Jong, L.N.J., Schipper, B.A. and Meijer, J.G., SPE J., 34(3), 283, 1984.

(5) Starling, K.E., "Fluid Thermodynamic Properties for Light Petroleum Systems", Gulf Publishing Co., Houston, Texas, 1973.

(6) Pope, A.E. and Ng, S.H., Fuel, 69, 539, 1990.

(7) Bousquet, J. and Labourel, T., Oil & Gas J., 85(16), 62, 1987.

Table 1. Characteristics of Feedstocks

	Athabasca VTB	Lloydminster VTB
API Gravity	-0.7	6.3
Softening Point, °C	66	36
Pen @ 25°C, 0.1 mm	11	192
Viscosity @ 135°C, cSt	2002	205
Conradson Carbon, wt %	24.3	18.3
Total Nitrogen, ppm	6390	4964
Basic Nitrogen, ppm	1820	1352
Total Sulphur, wt %	5.9	4.5
Ni, ppm	130	84
V, ppm	310	189
Fe, ppm	470	510
Cu, ppm	0.8	0.1
Na, ppm	64	< 1
Oil Fraction, wt %	46.0	59.0
Resin Fraction, wt %	36.7	27.3
Asphaltenes (n-C7), wt %	17.3	13.7
Boiling Range by GCD, °C		
IBP	331	316
5%	507	429
10%	535	465
30%	-	554

Table 2. Effect of Solvent on Deasphalting

Nominal volumetric solvent/VTB ratio - 9, Temperature - 75°C

	Wt % Recovery of VTB Components as DAO			
Solvent	C3	n-C4	n-C5	n-C7
Pressure, psia	465	205	105	65
Athabasca				
Overall	11.6	47.1	66.0	80.5
Oil	22.2	74.8	85.5	89.6
Resins	3.7	34.4	72.5	95.0
Asphaltenes	0.1	0.3	0.4	25.6
Lloydminster				
Overall	27.3	64.5	77.1	
Oil	41.7	83.0	89.8	
Resins	9.8	56.7	88.1	
Asphaltenes	0.1	0.5	0.6	

Table 3. Effect of Temperature-Pressure on Deasphalting

Nominal volumetric solvent/VTB ratio - 9

	Wt % Recovery of VTB Components as DAO			
Solvent	n-C4		n-C5	
Temperature, °C	120	75	160	75
Pressure, psia	415	205	365	105
Athabasca				
Overall	39.2	47.1	58.4	66.0
Oil	65.5	74.8	85.7	85.5
Resins	24.6	34.4	51.4	72.5
Asphaltenes	0.2	0.3	0.7	0.4
Lloydminster				
Overall	56.9	64.5	71.7	77.1
Oil	76.1	83.0	93.9	89.8
Resins	43.8	56.7	59.4	88.1
Asphaltenes	0.4	0.5	0.5	0.6

Table 4.Effect of Solvent/VTB Ratio on Deasphalting

Athabasca VTB, n-Pentane, 160°C, 365 psia

	Wt %					
Solvent/VTB w/w	37.1	20.0	6.8	5.2	1.0	0.9
Oils	58.5	65.6	64.0	67.5	53.7	46.8
Resins	40.9	34.4	35.9	32.3	38.9	38.3
Asphaltenes	0.6	0.0	0.1	0.2	7.4	14.9
VTB Recovery	65.8	62.3	59.3	58.4	65.5	68.0

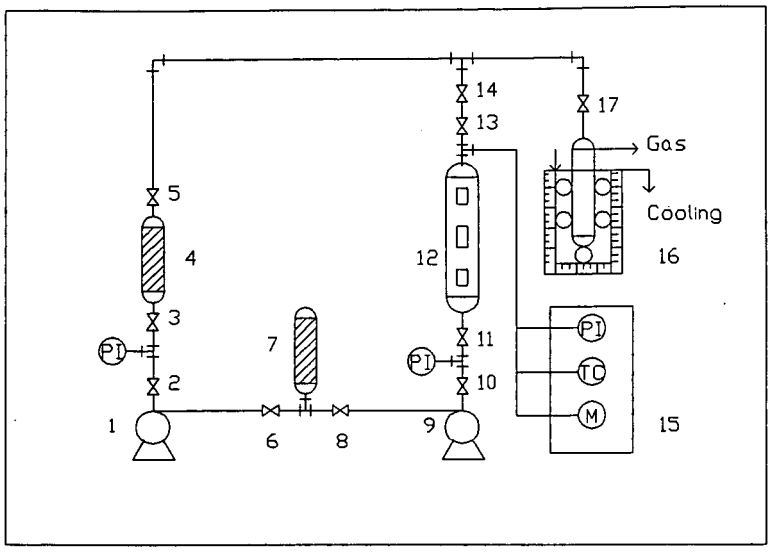

Fig. 1. Deasphalting System.

1: Sample pump.

2, 3, 5, 6, 8, 10, 11, 13, 14, 17: On-off valves.

4: Sample cylinder (transfer vessel).

7: Mercury reservoir.

9: Cell pump.

12: Three window PVT cell.

15: Controllers (pressure indicator, temperature control, motor control).

16: Solvent trap.

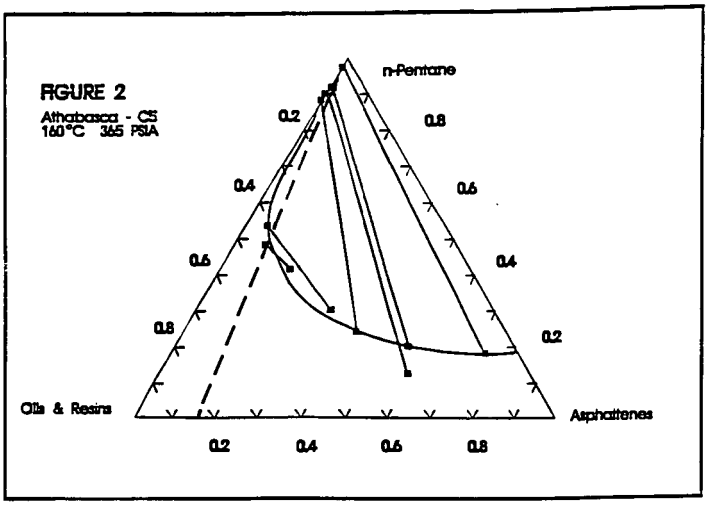
FIGURE 2
Athabasca - C5
160°C 365 PSIA
n-Pentane
Oils & Resins
Asphaltenes
0.2
0.4
0.6
0.8

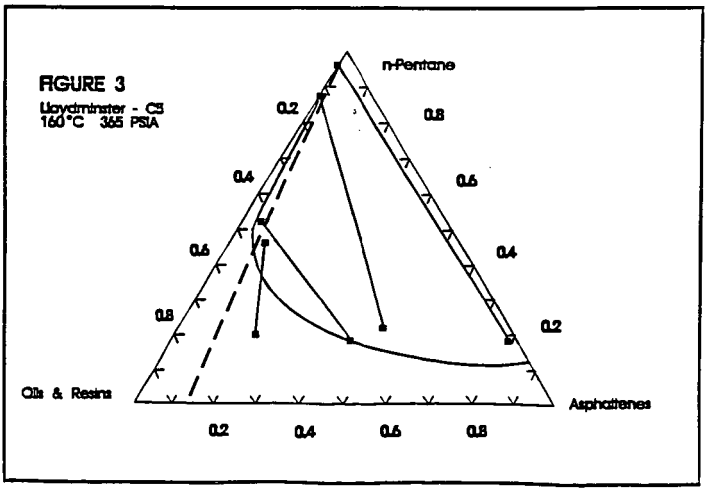
FIGURE 3
Lloydminster - C5
160°C 365 PSIA
n-Pentane
Oils & Resins
Asphaltenes
0.2
0.4
0.6
0.8

UTILIZATION OF CARBON DIOXIDE FROM FOSSIL FUEL - BURNING POWER PLANTS WITH BIOLOGICAL SYSTEMS

John R. Benemann and David M. Tillett*
1212 Kelley Ct., Pinole, California, 94564; * SeaAg, Inc.,
5220 Old Dixie Hwy., Ft. Pierce, Florida, 34946

Keywords: Global Warming, CO_2 mitigation; Microalgae

ABSTRACT

Currently available physical-chemical processes for CO_2 capture and disposal from fossil fuel-fired power plant flue-gases are very expensive. Biological systems for CO_2 utilization involve plant photosynthesis and conversion of the biomass produced to fuels that can substitute for fossil fuels. Photosynthesis by many plants increases with higher CO_2 levels suggesting that flue gas fertilized greenhouses or even flue gas dispersal into open plant stands could increase biomass production. However, such systems are neither effective nor practical. Only for submerged aquatic plants - microalgae, seaweeds, and some higher plants - does a high concentration of CO_2 as present in flue-gases, result in large increases in productivity. Microalgae have the potential for high productivities and ready conversion to gaseous and liquid fuels. A cost-analysis of such a process suggests that if high productivities are indeed achievable, overall costs could be much lower than currently available methods for CO_2 flue gas capture and disposal. Limitations are the relatively large land areas required, a maximal reduction in CO_2 outputs of only 25 to 30% of total emissions, and the relatively undeveloped state of this technology.

INTRODUCTION

Reducing CO_2 loads on the atmosphere is required to forestall potentially catastrophic consequences of the greenhouse effect. Although the possible consequences are highly uncertain, reducing the current and projected rise in CO_2 concentration appears to be a prudent course of action. Several European countries and Japan are proposing to reduce current levels of CO_2 emissions from fossil fuels by 20% to 25%. Natural processes already remove 50 to 60% of anthropogenic CO_2 emissions, thus a 25% reduction would actually slow atmospheric CO_2 increases by between 40% to 50%, assuming current conditions continue. This would significantly reduce the probabilities of the catastrophic consequences of the greenhouse effect (Benemann, 1992). Fossil fuel-burning power plants generate about 25% of all fossil fuel derived atmospheric CO_2 inputs. Thus they are a major target in plans to reduce CO_2 accumulation in the atmosphere.

Reducing the CO_2 outputs of fossil fuel-fired power plants could be accomplished through a number of methods, such as increasing efficiency in fossil fuel utilization, substitution of fossil fuels with energy sources that do not produce net CO_2 emissions, establishing remotely sited reforestation projects that would sequester CO_2 into standing biomass (Marland, 1988), and recovery and subsequent sequestration of CO_2 directly from flue (stack) gases of fossil fuel-burning power plants. The latter options, CO_2 sequestration from flue gases using presently available chemical scrubbing systems, appear to be much more expensive than the former. Recent cost-analysis of the costs of

CO_2 removal and concentration from stack gases suggests that this would essentially double current electricity costs, and the amount of fossil fuel used. This does not include ultimate disposal of the sequestrated CO_2 (in the ocean depths, depleted oil and gas wells) which add to costs and uncertainties (Herzog et al., 1991; Fluor Daniels, 1991).

BIOLOGICAL CO_2 MITIGATION OPTIONS

A variety of microbes utilize CO_2. But all, except for the microalgae, require some inorganic reducing agent (H_2, H_2S, NH_3, pyrites, etc.). Such substrates are unlikely to be available in the quantities required for CO_2 removal from power plants. If nuclear or solar (photovoltaics) electricity generation were to allow economical H_2 production, it could be plausibly converted to a C-based fuel using CO_2. The methanogenic bacteria are able to convert H_2 and CO_2 into CH_4. However, it is likely that methanol would be the preferred product, as it would be useable as a liquid fuel, favoring chemosynthetic processes. Thus, only photosynthetic processes based on water as the electron source for CO_2 reduction are likely applicable for CO_2 mitigation.

Photosynthetic processes are able to convert CO_2 into biomass, which can be used or in turn converted to biomass fuels that can replace fossil fuels, either for electricity production or in other sectors of the economy (e.g. transportation) (Benemann, 1980). Plant photosynthesis is already a major world-wide source of fuels, with biomass fuels representing about 15% of all primary energy consumption (Scurlock and Hall, 1987). Biomass fuels could displace a major fraction of current fossil fuel consumption, particularly if CO_2 mitigation were to become a policy and economic goal.

Biomass production takes place in the presence of atmospheric levels of CO_2, the concentrated CO_2 present in flue gases is not required. Nevertheless, it is well known that plants exhibit higher productivities under elevated levels of CO_2. In greenhouses, elevated levels of CO_2 are routinely used to increase plant production. The cultivation of algae, both the seaweeds and the smaller microalgae, requires an enriched source of CO_2, as the transport of CO_2 from the atmosphere into the growth ponds is not sufficient to support their growth. These possibilities were reviewed in the present evaluation of biological systems for direct utilization and mitigation of stack-gas CO_2 sources.

PHOTOSYNTHETIC PROCESSES FOR FLUE GAS CO_2 UTILIZATION

The use of higher plants, either in greenhouses or in the open air, for the utilization of flue gas CO_2 has been proposed (Bassham, 1977) but does not appear practical nor feasible. CO_2 fertilization can increase plant productivities by a significant factor (20 to 30% are typical enhancements, although higher values are reported, see Benemann, 1982, for references). However, comparisons with open air cultivation are not as favorable because of the reduction in light intensities in greenhouses due to glazing - which typically are in the same range as the CO_2 fertilization effects. Thus, overall, greenhouse agriculture is, in principle, not significantly more productivity than open air systems. However, greenhouse agriculture does exhibit high productivities (Wilson et al., 1992), but for other reasons: greater control over water supply and fertilizers, higher management inputs, and, of course, temperature control to overcome low temperatures in unfavorable climates. However, greenhouse crops cost typically over ten times more to produce than open air crops. Thus, greenhouses would not be a suitable method for biomass fuels production, the objective of any CO_2 mitigation program.

An alternative possibility would be to fertilize open air stands of plants (trees, row crops) with flue-gas CO_2, dispersed through distribution pipes. The major factors to consider are the effects of wind, turbulence, etc. on the dispersal plume and the effects of highly variable CO_2 concentrations on plant productivity. Experimental systems are being operated, to study the effects of CO_2 on natural stands (e.g. outside of greenhouses) in which dispersal is through distribution pipes which discharge CO_2 from various points in a stand, computer controlled to adjust for variations in wind direction, intensity, daytime, etc. In a large stand, encompassing many square miles, such systems may indeed achieve a relatively good dispersal. However, the incremental productivities, estimated at 20 to 30% from those observed without CO_2 supplementation, and most likely only half those, would not likely justify the extensive distribution piping and control systems required. Also, the actual utilization factor for the CO_2 is likely to be low. This preliminary analysis suggests that such a process could not be justified.

This leaves the submerged plants - microalgae, seaweeds and some higher plants - as the only biological systems which could benefit from the use of flue gas levels of CO_2 (typically about 10% by volume). The transfer of CO_2 from the atmosphere into a pond, assuming essentially zero CO_2 in the ponds, would only support 1 to 2 g of biomass production/m^2 per day, a small fraction (< 5%) of potential productivity. Energetically it is not feasible to supply CO_2 by bubbling air through the cultures, to provide CO_2 (Steinberg, 1991). Only a highly enriched source of CO_2, e.g. flue-gas, could supply submerged plants with the CO_2 required. Thus, among biological systems only submerged plants could make use of flue gas CO_2 sources.

SUBMERGED HIGHER PLANTS AND SEAWEEDS

Of the three alternatives - microalgae, seaweeds, and higher plants - the latter two have significant limitations. Higher submerged plants exhibit relatively low productivities, even under optimal conditions of nutrient and CO_2 supply (Murry and Benemann, 1980). The reasons for this is primarily due to hydrodynamic factors; it is difficult to get good water exchange in dense stands of such submerged plants. In water CO_2 diffusion is over 1,000 times slower than in air, and thus not only the transfer into the ponds but also from the water phase to the leaves is a major limitation in such systems. Creation of sufficient turbulence to overcome diffusion limitations does not appear practical.

Seaweeds exhibit relatively higher productivities than submerged higher plants, and have been produced commercially in near-shore, shallow ocean systems and have been considered for energy production (See Bird and Benson, 1987, for reviews). In such systems the C required is provided from seawater, and the relatively high water exchange in such open systems. Seawater, at pH 8.2 and 2.3 meq. l^{-1} alkalinity, contains almost 40 mg of available CO_2 (assuming an upper pH of about 10 for seaweed growth). A 1 m deep culture system thus would be able to support a production of about 20 g/m^2 of biomass (organic dry weight assuming 50% C), suggesting a once to twice a day water turn-over to supply the required C. Thus, seaweed culture, as currently practiced in near-shore environments, would not be limited by C, and would not require flue gas CO_2 injection.

In on-shore, shallow ponds, water exchange would become a limiting factor, depending on lift (head losses). From the above, it would require approximately 50,000 m^3 of seawater to supply the C required for one ton of biomass, which would make seawater an uneconomical source for this nutrient for on-shore systems. The advantages of on-shore,

vs. near-shore, cultivation is that a higher control over cultivation conditions is feasible, including predations, competing algae, diseases, etc. Also, other nutrients (N, P, Fe, etc.) can be supplied without the large losses experienced in near-shore farming techniques. And, perhaps most important, the losses experienced due to storms would be minimized. However, seaweed culture in open ponds has not been developed except on an experimental basis. The reason for this are the hydrodynamic constraints on such cultures: the rather dense seaweed cultures require considerable mixing and turbulence to allow effective transfer of nutrients (particularly CO_2) to the plants (Wheeler, 1988). Such mixing and turbulence requires considerable energy inputs, which would make such systems impractical, at least for the production of fuels. Although preliminary, this evaluation suggests that on-shore seaweed cultivation is not a favorable approach to flue gas CO_2 utilization. These mixing limitations do not apply to the smaller microalgae.

MICROALGAE FOR CO_2 MITIGATION

Microalgae culture technology has been developed for over 40 years (Burlew, 1953). The concept of using the CO_2 in power plant flue gases for producing microalgae and converting the biomass to fuel, was first studied over thirty years ago by Oswald and Golueke at the University of California Berkeley. They proposed using municipal sewage to grow algae in large open ponds into which flue gas would be injected, harvesting the biomass by settling, and digesting it to methane gas, which would be used by the power plant. The digester residues (containing the nutrients and residual organic and inorganic C) and water would be recycled, allowing system size expansion well beyond that feasible from the production of algae for waste water treatment alone. A laboratory-scale system, involving algae growth, digestion to methane, and recycle of the nutrients, was successfully demonstrated (Golueke and Oswald, 1959). A preliminary analysis concluded that with favorable assumptions this process could be economically competitive with nuclear power (Oswald and Golueke, 1960). This concept was further refined by Oswald and colleagues and others during the 1970's, with research sponsored in large part by the U.S. Department of Energy (U.S. DOE). Conceptual engineering designs and cost estimates (Benemann et al., 1982) supported the conclusion that, in principle, algal biomass cultivation in open ponds could be relatively inexpensive.

About a decade ago, the "Aquatic Species Program" (ASP), was initiated at the Solar Energy Research Institute (SERI, now NREL, National Renewable Energy Laboratory, a U.S. DOE facility). The ASP emphasized the development of algae systems for the production of liquid transportation fuels (specifically vegetable oils) (Neenan et al., 1986). This program, supported many basic research projects, including isolation of a large number of algal strains and investigation of biochemical and genetic aspects of lipid production in microalgae. Three outdoor algal production facilities were supported by the ASP, in California Hawaii and New Mexico. These outdoor projects, together with an updated engineering and cost feasibility analysis (Weissman and Goebel, 1987), and the considerable experience from commercial operations for microalgae production for food supplements (Benemann et al., 1987), and use of microalgae in waste water treatment (Oswald and Benemann, 1980), support the conclusion that, in principle, it is possible to produce microalgae in large-scale outdoor ponds at both high productivity and at relatively low cost. Microalgae are now being studied for CO_2 mitigation in the U.S. and Japan (Laws and Berning, 1991, Negoro et al., 1991, for examples). However, considerable R&D is still required and many aspects of this technology remain to be demonstrated, from species control and stability, to harvesting and algal processing.

COST ANALYSIS OF MICROALGAE CO_2 MITIGATION

Table 1 summarizes the overall cost estimates for a large-scale (appx. 1,000 ha) microalgae production system for liquid-fuels using flue gas CO_2 from a power plant. Using a "CO_2 mitigation credit" of \$16/tCO_2, fuel costs of about \$40/barrel are projected. These cost estimates are based on prior studies (Benemann et al., 1982; Weissman and Goebel, 1987), and reflect numerous favorable assumptions about both the engineering and biological aspects of such a system. For example, the individual growth ponds would be "raceway" designs, with a single central baffle and 10 ha in size, over ten times larger than any operated previously, and mixed with paddle wheels. For economy, the ponds would be earthwork construction without plastic liners, with a clay sealer to minimize percolation. The water source (such as seawater) must containing sufficient alkalinity to allow some CO_2 storage. CO_2 would be supplied via diffusers and sumps. Major design factors are the depth of the sumps (which determines transfer efficiency), the mixing velocities (typically 20 - 30 cm/sec), the number of carbonation stations (which depend on the CO_2 storage, pH range for operations and outgasing rates), the depth of the pond culture (typically 20 to 30 cm). These factors are interactive and must be optimized.

Many aspects of this process require R&D. Harvesting involves "bioflocculation", in which the algae spontaneously flocculate and sediment in settling ponds. Although a well known natural process which has been demonstrated in waste grown algae (Benemann et al., 1980), its applicability to large-scale systems needs to be demonstrated. The extraction and processing of the vegetable oils from the algal biomass was cost mated based on soybean processing as no relevant data for algal biomass is available. The algal oils would be produced by limiting the algal cultures for nitrogen, which has been demonstrated at the laboratory scale (Benemann and Tillett, 1987) but not yet in open ponds. The residue from the oil extraction would be fermented to produce methane gas.

Most important, in Table 1 two different productivities were assumed, about 109 and 219 metric tons/ha/yr, corresponding to about 5 and 10% solar energy conversion efficiencies, for favorable sites in the U.S.. The lower productivity is based on present experience. The higher productivity will require the development of algal strains that have a lower pigment content, allowing better overall light utilization in dense cultures (Benemann, 1990). If the higher productivities are indeed achievable, and the other assumptions on which this cost estimate is based are verified, then such a process could produce biomass fuels using flue gas CO_2, with a relatively modest CO_2 mitigation credit (\$16/t CO_2), within the range of those presently discussed (Lashoff and Tirpak, 1989).

A major constraint on such systems, besides the R&D issues, is the availability of sufficient land and water near the power plant. A 1,000 MWe power plant would require as few as 6,000 ha (Table 2). Also, only about 30% of the CO_2 emissions from the power plant could be captured, as the system would be sized to utilize most of the CO_2 produced during peak summer daytime utilization, wasting night and much of the winter CO_2 outputs. However, as pointed out in the introduction, such a rate of CO_2 capture would mitigate most of the potential adverse effects of CO_2 released from such a power plant. And the land area required is a small fraction, less than one tenth, that required for other biomass systems (tree farms). Perhaps most important, such systems would provide over 3 million barrels of fuel per year. Although much R&D is still needed, no insurmountable problems are apparent and no "breakthroughs" are required. Microalgae systems could become an affordable process for CO_2 removal from flue gases.

REFERENCES

Bassaham, J.A., in A. Mistui et al., eds., Biological Solar Energy Conversion, Academic Press, New York, p. 151 (1977).

Benemann, J.R., Plant and Soil, in press (1992).

Benemann, J.R., D.M.Tillett, and J.C. Weissman, Trends in Biotechnology, 5, 47 (1987).

Benemann, J.R., R.P. Goebel, J.C. Weissman, D.C. Augenstein. Microalgae as a Source of Liquid Fuels, Final Report U.S. Department of Energy, pp. 202 (1982).

Benemann, J.R., in Algal Biotechnology, in R.C. Cresswell, T.A.V. Rees, and N. Shah, eds., Longman, London pp. 317 (1990).

Benemann, J.R., B.L. Koopman, J.C. Weissman, D.E. Eisenberg and R.P. Goebel, in G. Shelef, and C.J. Soeder, eds., Algal Biomass, Elsevier, Amster., p. 457 (1980).

Benemann, J.R. Intl. Energy Journal, 1, 107 (1980).

Benemann, J.R., and D.M. Tillett, in D. Klass, ed., Symp. Proc. Energy from Biomass and Wastes XI, Institute of Gas Technology, Chicago, Ill. (1987).

Bird, K.T., and P.H Benson (eds.), Seaweed Cultivation for Renewable Resources, Elsevier, Amsterdam (1987).

Burlew, J., Algae Culture: From Laboratory to Pilot Plant, Carnegie Institute, Washington D.C. (1953).

Fluor Daniel, Inc., Engineering and Economic Evaluation of CO_2 Removal from Fossil-Fuel Power Plants, Electric Power Research Institute, Palo Alto, California, EPRI IE-7365 (1991).

Golueke, C.G., and W.J. Oswald, App. Microbiol., 7, 219 (1959).

Herzog, H., D. Golomb, and S. Zemba, Environmental Progress, 10, 64 (1991).

Lashof, D.A., and D.A. Tirpak, Policy Options for Stabilizing Global Climate, U.S. Environmental Protection Agency, Washington D.C., February (1989)

Laws, E.A., and J.L. Berning, Biotech. Bioeng., 37, 936 (1991).

Marland, G., The Prospect of Solving the CO_2 Problem Through Global Reforestation, Oak Ridge Associated Universities, Department of Energy, Washington D.C. DOE/NBB-0082 (1988)

Murry, M.A. and J.R. Benemann. in T.A. McClure and W.S. Lipinski, eds., Handbook of Biosolar Resources. C.R.C. Press, Boca Raton, FL., III, p. 407 (1981).

Neenan, B., et al., Fuels from Microalgae: Technology Status, Potential, and Research Requirements, Solar Energy Research Institute, Golden, Colorado, SERI SP-231-2550 (1986).

Negoro, M., N. Shioji, M. Miyamoto, and Y. Miura, Biochem. Biotech., 28/29, 877 (1991).

Oswald, W.J., and C.G. Golueke, in S. Pietro, ed., Biochemical and Photosynthetic Aspects of Energy Production, p. 59 (1980).

Oswald, W.J., and C.G. Golueke, Adv. Appl. Microbiol., 11, 223 (1960).

Scurlok, J.M.O. and D.O. Hall, Biomass 21: 75 (1990).

Steinberg, M., J. Lee, and S. Morris, An Assessment of CO_2 Greenhouse Gas Mitigation Technologies, Brookhaven National Lab., Upton, NY, BNL 46045 (1991).

Weissman, J.C., R.P. Goebel, and J.R. Benemann, Bioeng. Biotech., 31: 336-344 (1988).

Weissman, J. C. and R. P. Goebel, Design and Analysis of Pond Systems for the Purpose of Producing Fuels, Solar Energy Research Institute, Golden Colorado SERI/STR-231-2840 (1987).

Wheeler, W.N., Prog. in Phycological Res., 6, 23 (1988).

Wilson, J.W., D.W. Hand, and M.A. Hannah, J. Exp. Botany, 43, 363 (1992).

TABLE 1. MICROALGAE SYSTEM CAPITAL AND OPERATING COSTS

PRODUCTIVITY ASSUMED: Average Daily: (ash-free dry weight) Annual:	30 g/m^2/d 109 mt/ha/yr	60 g/m^2/d 219 mt/ha/yr
CAPITAL COSTS ($/ha):		
Ponds (earthworks, CO_2 sumps, mixing)	27,500	33,000
Harvesting (settling ponds, centrifuges)	12,500	17,000
System-wide Costs (water, CO_2 supply, etc.)	30,000	40,000
Processing (oil extraction, digestion)	10,000	20,000
Engineering, Contingencise (25% of above)	20,000	27,500
TOTAL CAPITAL COSTS ($/ha)	100,000	137,500
Capital Costs $/t-yr	920	630
Barrels of Oil/y (@ 3.5 bar./t)	380	760
CAPITAL COSTS $/Barrel/y	260	180
OPERATING COSTS ($/ha/yr):		
Power, nutrients, labor, overheads, etc.	10,000	15,500
Credit for methane	- 3,000	- 6,000
Net Operating Costs $/ha/yr	7,000	9,500
Net Operating Costs $/barrel oil	18	13
CO_2 Mitigation Credits ($16/t$CO_2$)	-10	-10
Annualized Capital Costs (0.2 x Capital)	52	36
TOTAL COSTS $/BARREL	60	39

TABLE 2. LAND REQUIREMENTS FOR ALGAE CO_2 UTILIZATION

Assumptions: 30% CO_2 average annual CO_2 utilization
1,000 MW power plant, 0.88 kgCO_2/kwh (Herzog et al., 1991).
Composition: 50% lipid, 25% carbohydrate, 25% protein.
Heat of Combustion: 7.5 Kcal/g (60% C in biomass).
Avg. Annual Solar Insolation: 500 Langleys, 45% visible.
Production: 1.05 x 10^6 mt/yr biomass; 3.7 x 10^6/yr barrels oil.

PRODUCTIVITY ASSUMPTIONS:		
Avg. Ash free dry weight g/m^2/d	30	60
Annual Productivity mt/ha/yr	109	219
Lipid fuels barrels/ha/yr	380	760
Solar Conversion Efficiency (appx.)	5	10
Fixation C mt/ha/yr	66	131
Fixation CO_2 mt/ha/yr	241	482
LAND AREA REQUIREMENTS:		
,000 Ha required growth ponds area	9.6	4.8
,000 Ha total area (ponds x 1.25)	12	6

that *T. denitrificans* may be readily cultured aerobically and anaerobically in batch and continuous reactors on gaseous H_2S under sulfide-limiting conditions. A microbial process for the removal of H_2S from gases have been proposed based on contact of the gas with a culture of *T. denitrificans* [3]. Sublette and Sylvester [3,4] have shown that sulfide concentrations as low as 100 to 200 μM inhibit the growth of the wild-type strain of *T. denitrificans* (ATCC 23642) on thiosulfate. Complete inhibition was observed at initial sulfide concentrations of 1 mM. However, a sulfide- and glutaraldehyde-resistant strain (strain F) of *T. denitrificans* has been isolated by enrichment from cultures of the wild-type [7]. This strain grows at inorganic sulfide concentrations in excess of 1000 μM and glutaraldehyde concentrations of 25 to 40 ppm. These concentrations are lethal to the wild-type.

T. denitrificans strain F has been successfully grown in co-culture with the sulfate-reducing bacterium, *Desulfovibrio desulfuricans*, both in liquid culture and through Berea sandstone cores without the accumulation of sulfide [8]. The presence of the sulfide-resistant strain F also controlled microbial sulfide production in an enrichment from an oil field brine. The effectiveness of strain F is due to its ability to grow and use sulfide at levels which are inhibitory to the wild-type strain of *T. denitrificans*.

The ability of *Thiobacillus denitrificans* strain F to control H_2S production in an experimental system using cores and formation water from a gas storage facility was investigated. Strain F and nitrate were added to nutrient amended formation water and injected into the core system. It is important to note that the objective was not to control the concentration of sulfate-reducing bacteria. Strain F does not inhibit the growth of sulfate-reducing bacteria; it simply removes the unwanted product of sulfate reduction, sulfide [8]. The test was therefore considered successful if the sulfide concentration of the effluent of the core treated with strain F was lower than that found before strain F treatment.

MATERIALS AND METHODS

Formation Water

Formation water was collected daily from well Davis-6 of the Northern Natural Gas Co. gas storage in Redfield, Iowa. The chemical composition of the water was as follows (in mg/L): iron (0.6), sulfide (9), chloride (420), sulfate (450), phosphate (1.8), hardness (960), alkalinity (660), and total dissolved solids (718).

Core System

The core system used in these experiments was assembled by Bioindustrial Technologies, Inc. (BTI, Grafton, NY) and was previously used to test the effectiveness of biocide formulations in controlling sulfide production by sulfate-reducing bacteria in the cores. BTI operated the core system with a feed of Davis-6 formation water for approximately ten weeks. Following the completion of the BTI studies, the core system was flushed with formation water at approximately 75 mL/hr in the treated core (see below) and at approximately 14 mL/hr in the control core for seven days before the experiments described here were initiated.

The core system contained cylindrical cores of St. Peter sandstone with dimensions of about 2.5 cm diameter and 7.5 cm length, each of which was mounted in polyvinyl chloride (PVC) tubing. Two sets of three cores each were connected in series using stainless steel tubing and compression fittings. Each set of cores had its own feed pump to inject fluids. The intake line of each core system had a course 5 μm membrane

filter to remove suspended solids (iron sulfides) from the fluid before injection into the cores. A sampling port was located at the inlet side of each core in the set. The porosity of the St. Peter sandstone was 30%. From the porosity of the cores and the volume of the tubing, the liquid volume of the core system was estimated to be 240 mL.

As noted above, one set of cores had previously been treated with biocides while the other set of core set served as the control. The injectivity of the control set of cores was much lower than that of the biocide treated set. Because of this, the flow rates of the two core sets were very different; the flow rate of the control core set was 14 mL/h while that of the treated core set was 75 mL/h. These were the maximum flow rates that could be obtained without leakage due to an excessive pressure. The hydraulic retention times were 3.2 and 16.7 h for the test and control cores systems, respectively.

Stock Cultures

Stock cultures of *Thiobacillus denitrificans* strain F were maintained anaerobically in thiosulfate medium described previously [4]. In this medium, thiosulfate is the energy source, nitrate is the terminal electron acceptor, bicarbonate is the source of carbon and ammonium ion is a source of reduced nitrogen. Stock cultures were transfered every 30 days and stored at 4°C until used.

Growth of Cells for Core Injection

T. denitrificans strain F cells were grown anaerobically in thiosulfate medium in 2-L cultures in a B. Braun Biostat M at 30°C and pH 7.0. The culture received a gas feed consisting of 30 mL/min of a gas mixture containing 5% CO_2, with the balance being N_2 to ensure that the culture did not become carbon limited. When the OD_{460} of the culture medium reached approximately 1.0 (about 10^9 cells/mL), the cells were harvestesd by centrifugation at 5000 x *g* and 25°C. The cells were then washed with 15 mM phosphate buffer, pH 7.0, and shipped as a wet pellet by overnight delivery service to the test site. Sufficient medium (without thiosulfate) was used to resuspend the pellet in a five-liter beaker so that the suspension was only slightly turbid. The viable cell concentration of the suspension was estimated by end-point dilution method using the above medium with thiosulfate. Because of the lack of facilities on site, medium that was injected into the core system was not sterilized.

Core Experiments

The objective of the first experiment (E1) was to determine whether indigenous microbial populations capable of oxidizing sulfide and using nitrate as the electron acceptor were present in the core system. Formation water supplemented with 40 mM sodium nitrate was injected into the test core set only for 24 h. Formation water with sodium nitrate was then injected into both sets of cores for another 24 h. After each 24 h period, a sample was collected from the sample port located upstream of the first core of each set and from the tubing exiting each core set. The samples were immediately analyzed to determine the concentrations of sulfide, sulfate-reducing bacteria, acid-producing bacteria, and strain F. The remainder of each sample was frozen and analyzed for nitrate, nitrite, sulfate, and sulfite at a later date.

In a second experiment (E2), *T. denitrificans* growth medium without thiosulfate was injected into each core set for 40 h to determine whether the addition of nutrients would stimulate the production of sulfide in the core system. Samples for chemical and microbiological analyses were taken after 24 and 40 h of medium injection.

In a third experiment (E3), the test core was inoculated with strain F to determine the effectiveness of this organism in preventing the production of sulfide in a continuous flow system. Approximately 10^5 viable cells/mL of strain F suspended in growth medium (without thiosulfate) was injected into the test set of cores for 6 h (about 0.5 L). This was followed by the injection of growth medium without thiosulfate for 24 h. This cell inoculation procedure was repeated once. During the inoculation procedure, growth medium without thiosulfate was injected into the control core set. Samples for chemical and microbiological analyses were taken every 24 h.

In a fourth experiment (E4), a mixture of growth medium and formation water starting with 90% (vol/vol) growth medium without thiosulfate and 10% (vol/vol) formation water with 40 mM sodium nitrate was injected into both sets of cores. Every 12 h, the fraction of formation water with nitrate injected into the core system was increased by 10% until only formation water with nitrate was injected into the core system. When the fraction of formation water injected into the core was 30, 60 and 80%, the test core was again treated with a cell suspension of strain F in growth medium without thiosulfate for a period of six hours, followed by a 6 h treatment of the appropriate combination of formation water with 40 mM sodium nitrate. When the percentage of formation water with nitrate reached 100%, the amended formation water (with 40 mM nitrate) was injected into both cores sets for 24 h. Samples for chemical and microbiological analyses were taken every 12 h.

During the time that 100% amended formation water was injected into the core systems, samples from both sets of cores contained a compound that interfered with the detection of sulfide. This suggested that a nutrient may be limiting the growth of strain F which would result in the incomplete oxidation of sulfide or the incomplete reduction of nitrate. Because of this problem and after receiving 100% amended formation water for 24 h, the test core was treated with growth medium (without thiosulfate) for 6 h and then with formation water with 10 mM sodium nitrate containing (in g/l) KH_2PO_4 (1.8), $MgSO_4 \cdot 7H_2O$ (0.4), NH_4Cl (0.5), $CaCl_2$ (0.03), $NaHCO_3$ (1.0). In experiment E5, this nutrient amended formation water with the lower nitrate concentration was injected into both sets of cores for 32 h, after which time the fluid flow to both sets of cores was stopped. After 12 h of incubation without fluid flow, the injection of nutrient-amended formation water with 10 mM nitrate was reinitiated. Samples for chemical and microbiological analyses were periodically taken during this treatment.

Twelve hours after fluid flow was reinitiated, the fluid injected into the control set of cores was changed to formation water without any nutrient or nitrate amendments. The core system was operated in this manner, i.e., with nutrient-amended formation water with 10 mM nitrate injected into the test set of cores and formation water only injected into the control set of cores for an additional 48 h.

Microbiological and Chemical Analyses

Concentrations of *T. denitrificans* strain F, sulfate-reducing bacteria, and acid-producing bacteria were estimated used the end-point dilution method. One milliliter of the sample was diluted in the respective growth medium. The inoculated bottles were then incubated at 30°C and checked for growth on a daily basis.

Strain F was enumerated using the growth medium given previously described [4]. Sulfate-reducing bacteria and acid-producing bacteria were enumerated using BTI-SRB medium and BTI-APB medium (Bioindustrial Technologies, Inc., Grafton, NY).

Samples were analyzed for sulfide immediately by the methylene blue method using Hach Chemical (Loveland, CO) field kits. Sulfate, nitrate, and nitrite were determined by high pressure liquid chromatography (HPLC) using anion exchange column and a conductivity detector as previously described [8].

RESULTS

The addition of nitrate alone to the formation water injected into the core systems resulted in lower effluent sulfide levels (Table I). Concomitant with the reduction of sulfide was the decrease in nitrate concentrations in the core effluent, suggesting the presence of indigenous microbial populations capable of oxidizing sulfide using nitrate as the electron acceptor. However, in an earlier study of microbial activities in the subsurface at this site, BTI did not identify any indigenous organisms capable of sulfide oxidation [9]. The addition of nitrate did not affect the numbers of sulfate-reducing bacteria and acid-producing bacteria. Strain F-like organisms were not detected in the core effluents. In the test core system, where the flow rates were about five times faster than the control core system, the sulfide levels were reduced by about 40%, while in the control core system sulfide levels were decreased by 98%. The efficacy of the nitrate treatment clearly depended on the residence time of the liquids in the core system. It is interesting to note that the sulfide levels in the influent and the effluent before treatments began were similar. This suggested that little or no sulfide production occurred within the core system. (No organic nutrients were added to the formation water to support the growth of sulfate-reducing bacteria). In earlier studies at this site, BTI personnel observed that a change in microbial activities occurred when nitrate was detected in the produced water [9]. These investigators found that nitrate can be used as an electron acceptor by the majority of the community members. As a consequence, a reduction in sulfide concentration in the formation water was observed when nitrate was present [9].

The injection of nutrients for *T. denitrificans* did not stimulate sulfide production in the core systems. Although the numbers of sulfate-reducing bacteria were not affected, the influent and the effluent sulfide levels were low when only medium was injected into the core systems. This again suggested that little or no sulfide production actually occurred within the core system. Significant numbers of strain F cells were detected in the first two cores of the test core system after the first treatment with strain F. The number of strain F cells increased with the subsequent treatment with cells followed with medium injection. Thus, cells of strain F were maintained in the test core system when growth medium was used.

Preliminary studies suggested that the formation water contained a compound inhibitory to the growth of strain F (data not shown). Therefore, as noted above, the fraction of formation water injected into the core was increased in steps in order to acclimate strain F (experiment E4). Relatively high concentrations of strain F were detected in samples of the effluent and from each intermediate sampling port even when the influent contained 80% formation water with nitrate. When the influent was 100% formation water with nitrate, the levels of strain F decreased, but complete washout of strain F was not obsesrved. During these experiments the effluent from the control core system contained a compound that interfered with the detection of sulfide. This problem plus the fact that the control core and the test core systems operated at different flow rates made definitive comparisons between the two cores systems difficult. However, throughout this period, the concentration of sulfide in the effluent of the test core system was consistently lower than the influent concentration. There was also a concomitant reduction in nitrate levels in the test core system suggesting that these two processes were linked. Interestingly, the sulfate concentrations in the effluent relative to the

influent concentration of the test core system increased after strain F inoculation. This was not observed in the control core system and suggested that strain F was oxidizing endogenous sulfur compounds (such as iron sulfides) that had accumulated in the core system. This would explain why the concentration of nitrate in the effluent of the test core system was much lower than expected if the sulfide present in the influent was the only source of electrons for nitrate reduction.

During this experiment, strain F was consistently detected in all cores of the test core system. This suggested that strain F was active and growing in the test core system. However, when the influent was shifted completely to formation water, the concentration of strain F in the test core system decreased substantially and interferences in effluent sulfide analyses were observed. This suggested that some essential nutrient may be limiting the growth of strain F which would result in the incomplete oxidation of sulfide or in the incomplete reduction of nitrate. In subsequent treatments, the concentration of nitrate was decreased from 40 mM to 10 mM and nutrients were added to the formation water as noted in the Materials and Methods section.

The treatment of the test core system with strain F and the subsequent injection of formation water with reduced nitrate concentration and nutrient amendments resulted in the reestablishment of strain F in the test core system. Concomitant with the increase in strain F was the disappearance of the interfering substance from the effluent of the test core. A reduction in sulfide concentration in the effluent compared to the influent concentrations in the test core was also observed. The levels of sulfide in the effluent of the test core compared to the influent concentration were reduced by 84 to 99%. There was a substantial reduction in the levels of nitrate and a substantial increase in the levels of sulfate in the effluent compared to the influent of the test core system. This suggests that, in the core system, strain F was oxidizing the sulfide present in the formation water to sulfate using nitrate as the electron acceptor. However, the amount of sulfate detected in the effluent of the test core system was much higher than that expected if strain F completely oxidized only the sulfide present in the formation water. As noted above, this suggests that strain F may have metabolized sulfur compounds that had accumulated within the core system. These sulfur compounds may have been iron sulfides or other sulfide precipitates which accumulated in the core sections during previous experiments. Strain F has been observed to utilize as an energy source iron sulfide precipitates produced by sulfate-reducing bacteria in media containing Fe^{3+} [8].

DISCUSSION

Several lines of evidence support the conclusion that treating the test core system with *Thiobacillus denitrificans* strain F, nitrate, and certain inorganic nutrients was effective in controlling sulfide production. After the strain F treatments, the effluent sulfide concentration in the test core system was 84 - 99% lower than the influent concentration. Also, after strain F treatment, the effluent sulfide concentration in the test core system was 90 to 99% lower than the effluent sulfide concentrations before the test began. And lastly, following strain F treatment the sulfide concentration in the test core effluent was 86 to 97% lower than when the test core system was treated with formation water plus 40 mM nitrate. Since the control core system had a much slower flow rate and samples from this core system contained compounds that interfered with the detection of sulfide, direct comparisons between the test and control systems are not possible. However, it is clear that less sulfide was detected in the effluent samples of the test core system after strain F treatment.

High concentrations of strain F were observed in the effluent and at each sampling port in the test core system after inoculation and injection of nutrient supplemented formation

water with 10 mM nitrate. This indicates that strain F was able to colonize the core system and successfully compete with the indigenous microbial populations over a long period of time. The growth of strain F in the core did not result in any significant increase in the pressure drop through the system. The presence of high levels of strain F at the time when effluent concentrations of sulfide and nitrate decreased, and sulfate increased suggests not only that strain F was maintained in the system, but that it was metabolically active. Strain F-like organisms were not detected in samples from the control core system suggesting that the changes observed in the test core system were the result of strain F treatment.

Concomitant with the reduction of sulfide in the effluent was a decrease in the effluent concentration of nitrate and an increase in the effluent concentration of sulfate in the test core system. These changes suggest that as sulfide was used, nitrate was reduced and sulfate was produced. Little or no change was observed in the effluent concentrations of sulfate and nitrate compared to the influent concentrations of these compounds in the control core system. Since the control core system was not inoculated with strain F and strain F-like organisms were not detected in the control core system, this suggests that the changes in the effluent concentrations of nitrate and sulfate observed in the test core system were the result of the activity of strain F.

The addition of nitrate alone to the formation water did result in the reduction of sulfide in the core system. This was most pronounced in the control core system where little or no sulfide was detected in the effluent after nitrate treatment. However, the effectiveness of this treatment is difficult to determine since the samples from the control core system contained a compound that interfered with detection of sulfide. In the test core system, the addition of nitrate alone was not as effective in reducing sulfide concentrations compared to that observed in the control core system. These data suggest that the efficacy of nitrate addition clearly depended on the retention time of liquids in the system. At the shorter retention times that occurred in the test core system, the addition of nitrate was not as effective in reducing sulfide concentrations as was the strain F treatment.

The fact that the effluent sulfate concentration of the test core system after strain F treatment was almost twice the influent core system suggests that sulfur-containing compounds had accumulated within the test core system and were being oxidized to sulfate by strain F. This would explain why the such a large decrease was observed in the effluent concentrations of nitrate after strain F treatment. One possible source of endogenous sulfur compounds may have been iron sulfide precipitates. Iron sulfide precipitates were clearly visible in the formation water and the tubing entering the core systems. Montgomery *et al* [8] showed that strain F can metabolize sulfide in the form of iron sulfide resulting in a clearing of the medium and removal of blackened areas in sandstone cores. Iron sulfide precipitates that form as a consequence of sulfide production can plug pores in porous rock and lead to the loss of injectivity. The fact that strain F is able to use these precipitates should increase the permeability and injectivity of oil and gas wells.

CONCLUSIONS

Once inoculated into the test core system, *Thiobacillus denitrificans* strain F was maintained for a long period of time. After inoculation with strain F, a 84 to 99% reduction in the sulfide levels in the effluent compared to the influent concentration of the test core system was observed. Effluent sulfide levels of the test core system were much lower than those observed before the test began or after treating the core with nitrate amended formation water. Concomitant increases in effluent sulfate levels and

decreases in effluent nitrate levels suggest that strain F metabolized sulfide to sulfate while using nitrate. These data will support the conclusion that strain F was metabolically active and effective in controlling the level of sulfide in the test core system.

ACKNOWLEDGEMENT

The authors wish to express their appreciation to Northern Natural Gas Co. and to Mr. Steven D. Thomas for access to the test site and use of laboratory facilities. We also wish to thank Mr. Rick Gomez of Northern Natural Gas co. for his assistance in the day to day operation of the core system. This work was funded by the Gas Research Institute (Chicago, IL) and ABB Environmental Services (Portland, ME).

REFERENCES

1. Orr, W. L. 1977. Geologic and geochemical controls on the distribution of hydrogen sulfide in natural gas. Advances in Organic Geochemistry 1975 (R. Campos and J. Goni, eds.), pp. 571-597, Enadimsa, Madrid, Spain.

2. Westlake, D. W. S. 1991. Microbial ecology of corrosion and reservoir souring, . Microbial Enhancement of Oil Recovery--Recent Advances. (E. C. Donaldson, ed.), pp. 257-263, Elsevier, Amsterdam.

3. Sublette, K. 1987. Aerobic oxidation of hydrogen sulfide by *Thiobacillus denitrificans*. Biotech. Bioeng. 29: 650-659.

4. Sublette, K. and Sylvester, N. D., 1987a. Oxidation of hydrogen sulfide by *Thiobacillus denitrificans*. Biotech. Bioeng. 29: 245-257.

5. Sublette, K. and Sylvester, N. D. 1987b. Oxidation of hydrogen sulfide by continuous cultures of *Thiobacillus denitrificans*. Biotech. Bioeng. 29: 753-758.

6. Sublette, K. and Sylvester, N. D., 1987c. Oxidation of hydrogen sulfide by mixed cultures of *Thiobacillus denitrificans*. Biotech. Bioeng. 29: 759-761.

7. Sublette, K. and Woolsey, M. E. 1989. Sulfide and glutaraldehyde resistant strains of *Thiobacillus denitrificans*. Biotech. Bioeng. 34: 565-569.

8. Montgomery, A. D., McInerney, M. J., and Sublette, K. 1990. Microbial control of the production of hydrogen sulfide by sulfate reducing bacteria. Biotech. Bioeng. 35: 533-539.

9. Dziewulski, David M., 1990. A Case Study of Biological Souring in a Gas Storage Field Operation, paper presented at the Third International Symposium on Gas, Oil, Coal and Environmental Biotechnology, New Orleans, LA (Dec. 3-5, 1990).

TABLE I. Summary of the effects of strain F inoculation and nitrate addition on sulfide production in test core system.

TREATMENT	EFFLUENT SULFIDE (μM)	CELL CONCENTRATIONS (CELLS/ML)		
		SRB	APB	STRAIN F
None	160	10^5	10^5	0
Nitrate	110	10^5	10^7	0
Nitrate, strain F, and nutrients	3-16	10^7	10^7	10^7

MICROBIAL CONTROL OF HYDROGEN SULFIDE PRODUCTION

Michael J. McInerney
Vishvesh K. Bhupathiraju
Department of Botany and Microbiology
University of Oklahoma
770 Van Vleet Oval
Norman, OK 73019

Kerry L. Sublette
Center for Environmental Research and Technology
University of Tulsa
600 S. College Ave.
Tulsa, OK 74104

Key words: souring, petroleum, natural gas, desulfurization

INTRODUCTION

Microbial Souring of Oil and Gas Reservoirs

Hydrogen sulfide is a toxic and corrosive gas that greatly increases the cost of recovery of oil and natural gas. A major mechanism for hydrogen sulfide production in petroleum/gas reservoirs below 80°C is microbial sulfide production [1]. Because of their diverse metabolic properties and widespread occurrence, sulfate-reducing bacteria were once thought to be only microorganisms responsible for microbially induced souring. However, sulfate reducers are not the only organisms found in oil/gas reservoirs that produce sulfide [2]. In fact, the most commonly detected sulfide-producing bacteria (such as *Shewanella putrefaciens*) do not use sulfate as an electron acceptor, but use other sulfur oxyanions. Thus, methods to detect or control souring based solely to the detection or control of sulfate-reducing bacteria may not be effective in actual field situations.

The detrimental activities of sulfide-producing bacteria can be controlled by the effective use of biocides. This type of remediation strategy is most successful in controlling unwanted activities in surface facilities. However, the control of these activities in the reservoir through the use of biocides is often difficult and expensive. Our approach is to manipulate the ecology of the system so that the terminal electron-accepting process is changed from sulfate reduction to nitrate reduction. Thus, even if sulfate reducers are present in the reservoir, the accumulation of the unwanted product of their metabolism, sulfide, is prevented. This is done by the addition of specialized strain of *Thiobacillus denitrificans* that can oxidize sulfide to sulfate by reducing nitrate to nitrogen gas.

Thiobacillus denitrificans

Thiobacillus denitrificans is an obligate autotroph and facultative anaerobe which can utilize reduced sulfur compounds as energy sources and oxidize them to sulfate. Under anaerobic conditions, nitrate is used as a terminal electron acceptor and is reduced to elemental nitrogen. Sublette and Sylvester [3-5] and Sublette [6] have demonstrated

CYTOCHROME P-450 OF *STREPTOMYCES GRISEUS* AND XENOBIOTIC METABOLISM

F. Sima Sariaslani*; M. K. Trower; M. Ramachandra; S. E. Buchholz; Ralph Stahl and C. A. Omer
Central Research & Development, E. I. duPont de Nemours & Co.,Wilmington, DE 19880-0228, USA
(Central Research & Development contribution # PP8247)

Keywords: cytochrome P-450; *Streptomyces griseus*; xenobiotic metabolism

INTRODUCTION

Streptomyces are aerobic prokaryotic microorganisms that are present in terrestrial and aquatic environments.[1] These organisms have long been exploited as producers of antibioitcs and enzymes. In addition, because of their remarkable versatility and metabolic capability *Streptomyces* are instrumental in the breakdown of organic matter in the environment and therefore in recycling carbon in nature.[1]

Streptomyces griseus

We have been studying the enzymatic system employed by *Streptomyces griseus* for oxidation of a diverse array of xenobiotics. We have shown that growth in a medium enriched with soybean flour induces a multicomponent cytochrome P-450 ($P\text{-}450_{soy}$) enzyme system in *S. griseus*.[2,3] $P\text{-}450_{soy}$ resembles its mammalian counterparts in its broad substrate specificity. The reactions performed by $P\text{-}450_{soy}$ include, but are not limited to, aromatic and alicyclic hydroxylations (biphenyl, phenol, benzene, chlorobenzene, Benzo(a)pyrene, cyclohexane), *O*-dealkylation (7-ethoxycoumarin), epoxidation (precocene II) and *N*-acetylation (aniline), and *N*-oxidation (pyridine).[4]

S. griseus cells enriched in $P\text{-}450_{soy}$ exhibit lack of stereo- and regioselectivity during camphor oxidation.[5,6] This is in contrast to camphor oxidation by $P\text{-}450_{cam}$ of *Pseudomonas putida* which shows a high degree of regio- and stereospecificity resulting in the production of 5-*exo*-hydroxycamphor as the sole reaction product.[5,7] The strict specificity of $P\text{-}450_{cam}$ has been attributed to the presence

of tyrosine-96 in the structure of this enzyme.[8,9] The major product formed during oxidation of camphor by *S. griseus* cells containing P-450$_{soy}$ is 6-*endo*-hydroxycamphor together with 5-*endo*-, 3-*endo*- and 5-*exo*-hydroxy derivatives as minor products.[6] Multiple hydroxycamphor product formation is also observed in reconstituted assays containing homogeneous preparations of P-450$_{soy}$.[10] Alignment of the amino acid sequence of P-450$_{soy}$ with the *P. putida* enzyme indicates that tyrosine-96 is not conserved in P-450$_{soy}$. We have proposed that lack of this residue in P-450$_{soy}$ contributes to its lack of specificity during camphor oxidation.[10]

In search for the other ancillary proteins of P-450$_{soy}$ system we have identified a soybean flour-inducible, 14,000 molecular weight 7Fe ferredoxin (*S. griseus* 7Fe ferredoxin) in crude extracts of *S. griseus*.[11] This ferredoxin couples electron flow between spinach ferredoxin reductase and cytochrome P-450$_{soy}$ for NADPH-dependent substrate oxidation. We have determined the primary structure of this ferredoxin and have shown that it contains a [3Fe-4S] and a [4Fe-4S] cluster.[12] The amino acid sequence of this protein, which consists of 105 amino acids with a calculated molecular weight of 12,291, shows high homology to the other reported 7Fe ferredoxins.[12]

We have recently isolated an FAD-containing and highly unstable soybean flour-inducible ferredoxin reductase (*S. griseus* ferredoxin reductase) from *S. griseus* crude extracts.[13] This 60,000 molecular weight protein requires the presence of 20% glycerol and 5mM dithiothreitol for stabilization. *S. griseus* ferredoxin reductase is an NADH-dependent flavoprotein which requires Mg^{2+} for *in vitro* activity. A consensus FAD binding sequence, which possesses a high degree of homology to the other FAD-containing ferredoxin reductases, starts at residue 7 of the N-terminus of this flavoprotein. In reconstituted assays, the *S. griseus* ferredoxin reductase can use a variety of ferredoxins such as *Clostridium pasteurianum* ferredoxin, spinach ferredoxin and adrenodoxin for coupling electron transfer from NADH to cytochrome P-450$_{soy}$. We have observed catalytic activities of 20-40 nmol product formed/min/mg P-450$_{soy}$ when the *S. griseus* 7Fe ferredoxin and the ferredoxin reductase were used in reconstituted assays.

P-450$_{soy}$ is encoded by *soyC* (CYP105D) gene. This gene encodes a 413 amino acid protein with a molecular weight of 45,400.[10] Five base pairs downstream of the stop codon of *soyC* is a translationally coupled open reading frame for a ferredoxin-like

protein of 6,600 molecular weight. The amino acid sequence of this ferredoxin-like protein is dissimilar to the soybean flour-inducible *S. griseus* 7Fe ferredoxin. Due to its proximity to the *soyC* gene we think that this open reading frame probably encodes the *in vivo* ancillary ferredoxin for P-450$_{soy}$ and have therefore named this gene *soyB*.

To date we have shown that a recombinant *S. lividans* strain which contains the *soyC,B* gene oxidizes 7-ethoxycoumarin and precocene II. We are currently investigating metabolism of a wide array of xenobiotics by this recombinant strain. In addition, we are involved in over-expression of *soyC,B* genes which would allow isolation and characterization of the *soyB* gene product.

We have exploited the broad substrate specificity of P-450$_{soy}$ and its resemblance to its mammalian counterparts to activate promutagenic chemicals.[14] In a modified version of the *Salmonella*/gene mutation (Ames) assay, *Salmonella typhimurium* strains TA98 and TA1538 were reverted by mutagenic metabolites that were produced by *S. griseus* cells enriched in cytochrome P-450$_{soy}$. Promutagens that were activated included a variety of aromatic amines (benzidine; 2,4-diaminotoluene; 4-chloro-2-nitroaniline), polycyclic aromatics (benzo(a)pyrene), and small aliphatics (chloropicrin).

In another test system we have used two genetically engineered strains of *S. griseus* which can activate promutagenic chemicals and detect the presence of their mutagenic metabolites.[15] One recombinant strain detects point mutations, while the other strain is sensitive to frame shift mutations. To our knowledge this is the first reported single-organism test system in which the enzymatic machinery for activation of promutagens has been linked to a detection system within the same organism.

We have been studying the feasibility of using artificial electron donors for transfer of reducing power from NADH to the P-450$_{soy}$ component. We have shown that, in reconstiuted assays, redox mediators such as phenazine methosulfate (PMS) and phenazine ethosulfate (PES) effectively replace the ferredoxin reductase and the ferredoxin and affect the NADH-dependent substrate oxidation by P-450$_{soy}$.[16] We have shown reduction of P-450$_{soy}$, O-dealkylation of 7-ethoxycoumarin and epxodiation of precocene II by the NADH/PMS/ or NADH/PMS/P-450$_{soy}$ system.[16]

As summarized above, P-450$_{soy}$ of *Streptomyces griseus* mimics its mammalian counterparts in its broad substrate specificity

and the ability to activate promutagenic chemicals. Biochemical and molecular studies are currently underway to unravel the mechanism of the action of P-450$_{soy}$ and the nature of the active site of this interesting enzyme.

References

1. **Goodfellow, M., Williams, S. T. and Mordarski, M.,** Actinomycetes in Biotechnology, Academic Press, N. Y. 1988.
2. **Sariaslani, F. S.,** Microbial cytochromes P-450 and xenobiotic metabolism, Adv. Appl. Microbiol., 36, 133, 1991.
3. **Trower, M. K., Sariaslani, F. S., and O'Keefe, D. P.,** Purification and characterization of a soybean flour-inducible cytochrome P-450 in *Streptomyces griseus*, J. Bacteriol., 171, 1781, 1989.
4. **Trower, M. K., Sariaslani, F. S., and Kitson, F. G.,** Xenobiotic oxidation by cytochrome P-450-enriched extracts of *Streptomyces griseus*, Biochem. Biophys. Res. Commun., 157, 417, 1989.
5. **White, R. E, McCarthy, M., Egeberg, K. D. and Sligar, S. G.,** Regioselectivity in the cytochromes P-450: Control by protein constraints and chemical reactivities, Arch. Biochem. Biophys., 228, 493, 1984.
6. **Sariaslani, F. S., McGee, L. R., Trower, M. K., and Kitson, F. G.,** Lack of regio- and stereospecificity in oxidation of (+) camphor by *Streptomyces griseus* enriched in cytochrome P-450$_{soy}$. Biochem. Biophys. Res. Commun., 170, 456, 1990.
7. **Sligar, S. G., and Murray, R. I.,** Cytochrome P-450$_{cam}$, and other bacterial P-450 enzymes, in *Cytochrome P-450*, Ortiz de Montellano, P. R. Ed., Plenum Press, New York, 1986, chap. 12.
8. **Atkins, W. M., and Sligar, S. G.,** The roles of active site hydrogen bonding in cytochrome P-450$_{cam}$ as revealed by site directed mutagenesis, J. Biol. Chem., 263, 18842, 1988.
9. **Atkins, W. M., and Sligar, S. G.,** Molecular recognition in cytochrome P-450: Alteration of regioselective alkane hydroxylation via protein engineering, J. Am. Chem. Soc., 111, 2715, 1989.
10. **Trower, M. K., Lenstra, R., Omer, C. A., Buchholz, S. E., and Sariaslani, F. S.,** Cloning and nucleotide sequence determination of the genes encoding cytochrome P-450$_{soy}$ (*soyC*) and ferredoxin$_{soy}$ (*soyB*) from *Streptomyces griseus*, submitted.

11. **Trower, M. K., Emptage, M., and Sariaslani, F. S.,** Purification and characterization of a 7Fe ferredoxin from *Streptomyces griseus*, Biochim. Biophys. Acta, 1037, 281, 1990.
12. **Trower, M. K., Marshall, J. E., Doleman, M. S., Emptage, M. H., and Sariaslani, F. S.,** Primary structure of a 7Fe ferredoxin from *Streptomyces griseus*, Biochim. Biophys. Acta, 1037, 290, 1990.
13. **Ramachandra, M. Seetharam, R., Emptage, M. H., and Sariaslani, F. S.,** Purification and characterization of a soybean flour-inducible ferredoxin reductase of *Streptomyces griseus*, J. Bacteriol., 173, 7106, 1991.
14. **Sariaslani, F. S., and Stahl. R. G.,** Activation of promutagenic chemicals by *Streptomyces griseus* containing P-450_{soy}, Biochem. Biophys. Res. Commun., 166, 743, 1990.
15. **Buchholz, S. E., Omer, C. A., Viitanen, P. V., Sariaslani, F. S. and Stahl Jr. R. G.,** Activation and detection of (pro)mutagenic chemicals using recombinant strains of *Streptomyces griseus*, Appl. Biochem. Biotechnol., (in press).
16. **Ramachandra, M. Rajan, J., Emptage, M. H., and Sariaslani, F. S.,** Replacement of ancillary electron transport protein componenets of cytochrome P-450_{soy} system of *Streptomyces griseus* with artificial electron donors, Annual Meeting of American Society for Microbiology, May 1992, New Orleans.

BIOMIMETIC CATALYSTS: APPLICATION OF COORDINATING COMPLEXES CONTAINING AN ASYMMETRIC COORDINATING LIGAND

M.W. Droege; J.H. Satcher, Jr.; R.A. Reibold; T.J.R. Weakely[1], L. Chauffe[2], and B.E. Watkins

Lawrence Livermore National Laboratory, PO Box 808, Livermore, CA., 94550; [1]Dept of Chemistry-University of Oregon, Eugene, OR., 97403, [2]Dept. of Chemistry, Cal State Hayward, Hayward, CA. 94542

Keywords: Catalysts, binuclear complex, methane monooxygenase

INTRODUCTION

The catalytic conversion of methane from natural gas into a readily transportable liquid fuel is a research area that is currently attracting considerable attention. This is a difficult transformation from a thermodynamic viewpoint since methane is a relatively unreactive substance and chemicals derived from methane are substantially more reactive than methane itself. Thus, no industrial process to date has been able to convert methane to liquid products in high yield.

One of the more studied process is the oxidative coupling of methane to higher hydrocarbons and olefins. To date no laboratory processes have come close to a yield necessary for an economically viable process. Modeling studies suggest that a theoretical ceiling in overall yield exists as the rate constant of a catalyst is increased[1]. The rate constant of the catalyst must be sufficient to overwhelm the non-specific gas phase reactions but low enough to prevent over oxidation. In theory this limits the yield to about 35%.

Because of this perceived limitation in heterogeneous catalysts, we undertook a program to take advantage of the selectivity already known to exist in a bacterial enzyme system. A group of aerobic soil/water bacteria called methanotrophs can efficiently and selectively utilize methane as the sole source of energy and carbon for cellular growth.[2] The first reaction in this metabolic pathway is the conversion of methane to methanol and is catalyzed by the enzyme methane monooxygenase[3] (MMO). (Figure 1) Of the many liquid products available directly from methane, methanol is one of the more technologically important. It can be easily converted to liquid hydrocarbon transportation fuels, used directly as a liquid fuel itself, or serve as a feed stock for fine chemicals production.

Microorganisms can produce MMO in two distinct forms: a membrane-bound particulate form or a discrete soluble form. The soluble form contains an oxygenase subunit, whose active site includes a binuclear iron center.[4,5,6] The

complete details of the structure of the active site are not known. However, the general description of the iron site in the soluble form is a binuclear cluster containing some type of μ-oxo ligand between the iron atoms. The remaining ligands (derived from adjacent amino acid residues) coordinate to the metals through nitrogen or oxygen and the Fe-Fe distance is 3.4 Å. The best description of the amino acids coordinating the binuclear iron center is surmised by the close amino acid sequence homology between MMO and ribonucleotide reductase[7], an enzyme containing a binuclear iron center whose X-ray crystal structure has been determined[8].

Compared to the soluble form of MMO the particulate form is poorly characterized and is thought to contain copper at the active site. This form is also active in methane oxidation in the biological system, and may be selectively produced by manipulating the bacterial growth conditions.[9]

Our work centers on the characterization of the structure/activity relationships of the particulate form of MMO and synthesis and characterization of inorganic/organic chemical models of MMO (both particulate and soluble). We have focused on the synthesis of an asymmetrical, binuclear chelating ligand possessing an alkoxo group that can serve as a bridging μ-oxo ligand. The advantage of such a ligand system is twofold: (a) metal complexes of an asymmetric binuclear ligand will provide coordinate unsaturation at only one metal resulting in focused substrate reactivity at that site and (b) a single ligand with binuclear coordination provides a more robust environment for metal oxidation state changes and accompanying chemical reactions. These complexes are being evaluated for their ability to oxidize methane and other hydrocarbons.

EXPERIMENTAL

The synthesis of the chelating ligand HMeL obtained by a five step procedure in ~35% overall yield is outlined in Scheme 1. Mono and binuclear copper complexes of HMeL were prepared by dissolving 100 or 200 mole% of cupric perchlorate with 100 mole% HMeL and sodium acetate in methanol, as shown in Scheme 2. The crude materials were recrystallized by vapor diffusion of ethyl ether in acetonitrile and chemically characterized, including single crystal X-ray crystal structure[10].

Catalytic reactivity was determined under atmospheric pressure and ambient temperature. Cyclohexane as the hydrocarbon substrate, hydrogen peroxide the oxidant, and a metal complex were employed in ratios of 1000:100:1 respectively with final catalyst concentration 9.0×10^{-4}M. $Cu(BF_4)_2$, $Cu[HMeL][ClO_4]_2$, or $[Cu_2\text{-MeL-OAc}][ClO_4]_2$ (4.5×10^{-5} moles) were dissolved in acetonitrile and placed Fisher-Porter reaction bottle. A mixture of cyclohexane (4.5×10^{-2} moles) and 30% hydrogen peroxide (4.5×10^{-3} moles) in acetonitrile was added to the catalyst solution with vigorous stirring at T=0. Aliquots (1mL) were removed periodically and a portion was analyzed by GC/MS for

cyclohexanol/cyclohexanone content with the remainder being titrated with a standard solution of potassium permanganate to determine hydrogen peroxide conversion.

RESULTS

Scheme 1 shows the synthetic route for the prototype binuclear chelating ligand, HMeL. Elemental analysis and NMR studies confirm the composition and structure of the ligand. It possesses a hydroxyl functionality that could serve as a bridging alkoxo group and aliphatic and aromatic nitrogen coordination groups (benzimidazole). We expected that one metal ion would be coordinated by one aliphatic nitrogen and two imidazole nitrogens and bridged by the hydroxy group to another metal coordinated by one aliphatic nitrogen and one imidazole nitrogen. This structure establishes a basis for coordinate asymmetry. Additional ligands to fulfill the coordination requirements of the metals would be available from the solvent or by the addition of acetate.

HMeL will readily binds to one mole of Cu(II) to produce a mononuclear complex (Scheme 2). Addition of two moles of copper does not alter the resulting product, as formation of the mononuclear complex appears to be independent of copper concentration. Addition of 200 mole% of copper to HMeL in the presence of 200 mole% of acetate gives rise to a binuclear complex. One mole of the acetate is necessary to fulfill the coordination requirements of Cu(II) and he other to act as a Lewis base to assist in removing the hydroxyl proton on HMeL. The mononuclear complex may be readily converted to the binuclear complex by the addition of copper and acetate. This suggests the possibility that asymmetric binuclear complexes may be generated with different metals in specific positions.

One coordination site at one copper center of the binuclear Cu(II) complex is available to bind with extraneous ligands. This was shown by forming a stable complex between the binuclear Cu(II) complex and azide ion, whose structure was confirmed by solving the X-ray crystal structure. We expect that in a catalytic system that the vacant coordination site will be available to bind and activate oxygen, hydrogen peroxide, or other oxidizing agents.

These complexes were evaluated for their ability to oxidize cyclohexane and to disproportionate hydrogen peroxide and compared to unchelated Cu(II) under the same conditions. The results are presented in Table 1. Neither the unchelated Cu(II) or the mononuclear complex is capable of either disproportionating hydrogen peroxide or oxidizing cyclohexane. However, the binuclear Cu(II) complex is capable of oxidizing cyclohexane to a mixture of cyclohexanol and cyclohexanone, as well as disproportionating hydrogen peroxide. It is not clear if only the vacant binding (peroxide binding) site in sufficient for peroxide activation or if the coupled copper ions possess unique redox properties. These data show the proof-of-principal that these coordinately

asymmetric complexes will function as biomimetic catalysts and that they have the ability to oxidize hydrocarbons.

CONCLUSIONS

Our catalyst development effort has gone one full cycle in the design, synthesis and evaluation of a binuclear, coordinately-asymmetric coordination complex. Unchelated and a mononuclear copper complex do not show catalytic properties to activate hydrogen peroxide or to oxidize cyclohexane. However, the binuclear copper complex tested was capable of activation hydrogen peroxide and the presumed oxo-copper intermediate was able to oxidize cyclohexane. We are using this ligand as a starting point to synthesize new catalysts/ligands. Specifically, complexes with other metals (iron) and complexes with additional ligand groups and with varying oxygen to nitrogen contact atoms will be prepared.

REFERENCES

1. Hair, L.M., Pitz, W.J.; Droege, M.W.; and Westbrook, C.K. Preprint, ACS National Meeting, April 6-10, 1992, San Francisco, CA
2. Dalton, H. Adv. Appl. Microbiol. 1980, 26, 71-87.
3. (a) Woodland, M.P.; Dalton, H. J. Biol. Chem. 1984, 259, 53-59. (b) Green, J.; Dalton, H. J. Biol. Chem. 1985, 260, 15795-15801. (c) Fox, B.G.; Froland, W.A.; Dege, J.E.; Lipscomb, J.D. J. Biol. Chem. 1989, 264, 10023-10033.
4. (a) Woodland, M.P.; Patil, D.S.; Cammack, R.; Dalton, H. Biochim. Biophys. Acta 1986, 873, 237-242. (b) Fox, B.G.; Surerus, K.K.; Munck, E.; Lipscomb, J.D. J. Biol. Chem. 1988, 263, 10553-10556.
5. Prince, R.C.; George, G.N.; Savas, J.C.; Cramer, S.P.; Patel, R.N. Biochim. Biophys. Acta 1988, 952, 220-229.
6. DeWitt, J.G.; Bentsen, J.G.; Rosenzweig, A.C.; Hedman, B.; Green, J.; Pilkington, S.; Papaefthymiou, G.C.; Dalton, H.; Hodgson, K.O.; Lippard, S.J. J. Am. Chem. Soc. 1992, 113, 9219-9235.
7. Pilkington, S.J.; Salmond, G.P.C.; Murrell; Dalton, H. FEMS Microbology Letters 1990, 72, 345-348.
8. Nordlund, P.; Sjöberg, B.-M.; Eklund, H. Nature 1990, 345, 593-598.
9. (a)Stanley, S.H.; Prior, S.D.; Leak, D.J.; Dalton, J. Biotechnol. Lett. 1983, 5, 487. (b) Park, S., Hanna, M.L., Taylor, R.T., Droege, M.W. Biotechnology and Bioengineering 1991, 38, 423-433.
10. Droege, M.W.; Satcher, J.H.; Reibold, R.A.; Weaklely, T.J.R. Preprint, ACS National Meeting, April 6-10, 1992, San Francisco, CA

ACKNOWLEDGEMENTS

Work performed under the auspices of the US Department of Energy by the Lawrence Livermore National Laboratory under contract No. W-7405-ENG-48

Table 1. Oxidation of Cyclohexane

Complex	% H_2O_2 Converted	Products	Turnover
$Cu(BF_4)_2 \cdot 6\ H_2O$	0 (24 hrs)	--	--
$[CuMEL][ClO_4]_2$	0 (48 hrs)	--	--
$[Cu_2MELOAc][ClO_4]_2$	40 (48 hrs)	cyclohexanol cyclohexanone	3

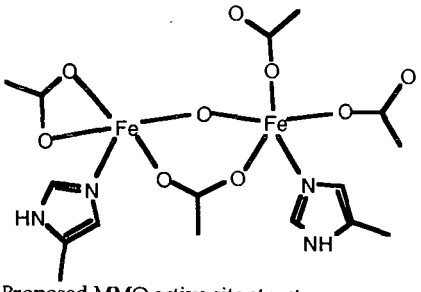

Proposed MMO active site structure

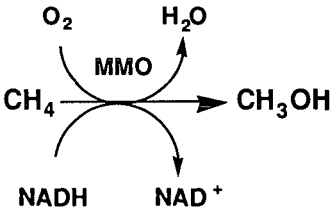

MMO Function

Figure 1. Structure/Function of MMO enzyme

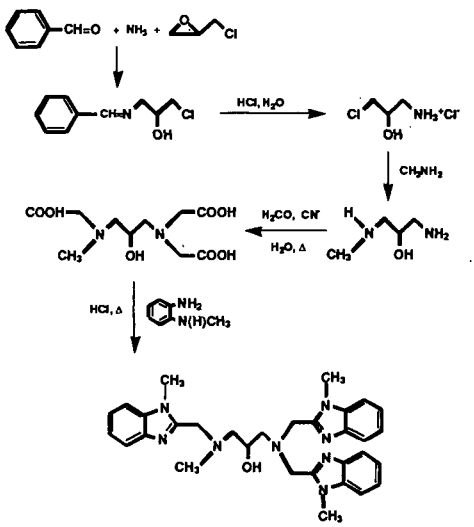

Scheme 1. Synthesis of HMeL

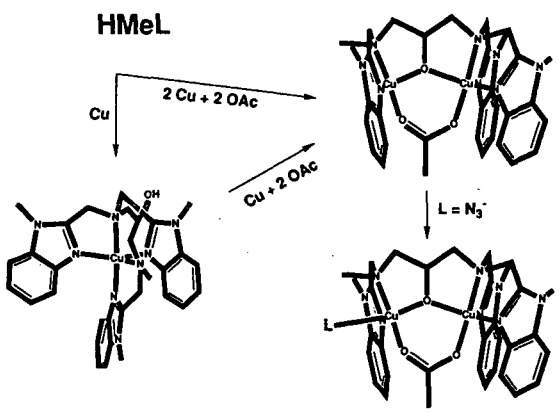

Scheme 2. Copper Chelation by HMeL

ELECTRICAL ENHANCEMENT OF BIOCIDE ACTION FOR IMPROVED BIOFOULING AND BIOCORROSION CONTROL

S.A. Blenkinsopp, C.P. Anderson, A.E. Khoury*, J.W. Costerton
NSERC Biofilm Group, Biological Sciences, University of Calgary, Calgary, AB, Canada; *Urology Division, Hospital for Sick Children, University of Toronto, Toronto, Ontario, Canada

Keywords: Biocide, Bioelectric, Biofilm

ABSTRACT

Attached microbial communities or biofilms cause a significant proportion of the fouling and corrosion problems faced by industry. Unfortunately, bacteria within the exopolysaccharide matrix of a biofilm are very well protected from antimicrobial agents such as biocides. Biofilm bacteria are generally resistant to 50 to 500 times the biocide concentration sufficient to kill planktonic or free-floating cells of the same species. We have recently discovered that the application of a low strength electric field/current density can enhance the efficacy of three common industrial biocides to such an extent that biofilm bacteria are killed at biocide concentrations lower than the planktonic minimum inhibitory concentration (MIC). This enhancement of biocide efficacy in the presence of an electric field/current density is known as the "bioelectric effect". By exploiting this effect it may be possible to significantly reduce biocide levels and their impact on the environment, without sacrificing their performance.

INTRODUCTION

Microorganisms are commonly found attached to surfaces in aqueous industrial systems. When these attached or sessile microorganisms produce a blanketing layer of exopolysaccharide, they are termed a "biofilm" (3, 9). These biofilms are often responsible for the fouling (7, 11, 13) and corrosion (1, 2, 4, 5, 6, 18) problems faced by industry. It is also widely acknowledged that biofilms within water distribution systems may act as reservoirs for pathogenic bacteria (eg. *Legionella pneumophila*) that pose a threat to the general population (16, 17, 19).

In industrial systems, microorganisms may be found as free-floating or planktonic cells, which are quite susceptible to the action of killing agents. However, when these cells attach to surfaces and form biofilms, their resistance to biocides increases quite markedly (12, 15, 19). The practical consequence to this resistance is that it is absolutely essential to sample not only a bulk water sample to ensure planktonic cell kill, but also to sample the pipeline wall to ensure that the attached population has been eradicated. Unless this protocol is followed, the pipeline will be continuously re-inoculated by cells from the more resistant biofilm population.

Even with the above protocol in place, satisfactory control of biofilm populations may not be achievable if the costs of the necessary biocide applications are not economically feasible. Recent studies in the medical section of our laboratory have found that

antibiotics work more effectively when applied against biofilms in a low strength electric field/current density (10). We have discovered that the efficacy of the three common industrial biocides tested to date can similarly be dramatically enhanced against biofilm bacteria, when applied in the presence of a low strength electric field/current density.

In this paper, we will present representative findings for the biocide glutaraldehyde against an environmental *Pseudomonas aeruginosa* biofilm.

METHODS

Biofilms were grown by flowing an environmental isolate of *Pseudomonas aeruginosa* in M-56 nutrient medium (8) through parallel perspex chambers which contained sampling studs of known diameter (0.5 cm^2). These perspex chambers are called modified Robbins devices (MRDs)(14). One MRD was a non-electrified control and the other was electrified by connecting it, where stated, to a 3 V DC power source. Polarity was altered every 64 s, so that the electrodes alternated as anode and cathode.

The first experiment was performed to determine the effect of the electric field/current density on an established biofilm population. After a 24 h colonization period in the absence of an electric field/current density, the inoculum flask was replaced by one containing the nutrient medium M-56, and one MRD was electrified.

The second experiment was performed to determine whether biocide effectiveness was enhanced in the presence of an electric field/current density. The experimental protocol was identical, with the exception that the inoculum flask was replaced after a 24 h colonization period with one containing 5 ppm glutaraldehyde in M-56 nutrient medium.

Studs were sampled in duplicate from each device over the 24 h period following electrification. After sonication to remove the attached cells from the studs, the suspension was plated onto ½ Brain Heart Infusion plates. Results are reported as CFU/cm^2 after 48 h at 37°C.

RESULTS

The electric field/current density was of such a low strength that it did not have a significant effect on the established biofilm bacterial population when exposed in the absence of biocide. Viable cell counts were very similar between the control and electrified MRDs (Fig. 1).

Glutaraldehyde effectiveness was dramatically enhanced in the presence of the electric field/current density. The established biofilm bacterial population was killed within 24 hours (Fig. 2). This result was in sharp contrast to the non-electrified control, in which the level of glutaraldehyde employed had very little effect on the biofilm population over 24 hours (Fig. 2).

DISCUSSION

It is quite clear from these results that the biocidal action of glutaraldehyde can be significantly enhanced when applied in a low strength electric field/current density. It is also quite significant that this kill was achieved when using a glutaraldehyde concentration of only 5 ppm. This concentration is insufficient to kill the more sensitive planktonic bacterial cells.

This work and similar results from the two other common industrial biocides tested to date indicate that it may be possible to use this "bioelectric effect" to reduce the levels of biocide currently used, without sacrificing their effectiveness. This technology may be particularly attractive to industry if there are environmental impact concerns over the biocide concentrations employed at present. Further experiments are in progress to elucidate the mechanism of the effect.

ACKNOWLEDGMENTS

We wish to thank B.D. Ellis and K. Lam for technical support. Petrolite Corporation (Calgary, Alberta) supplied the biocides tested.

REFERENCES

1) Angell, P., and A. H. L. Chamberlain, Int. Biodeterior. 27, 135 (1991).

2) Beech, I. B., and C. C. Gaylarde, Int. Biodeterior. 27, 95 (1991).

3) Blenkinsopp, S. A. and J. W. Costerton, Trends in Biotechnology 9, 138 (1991).

4) Bondonno, A., A. Von Holy, and A. A. W. Baecker, Int. Biodeterior. 25, 285 (1989).

5) Bremer, P. J., and G. G. Geesey, Appl. Environ. Microbiol. 57, 1956 (1991).

6) Bryant, R. D., W. Jansen, J. Boivin, E. J. Laishley, and J. W. Costerton, Appl. Environ. Microbiol. 57, 2804 (1991).

7) Bryers, J. D., and W. G. Characklis, Water Res. 15, 483 (1981).

8) Carlton, B. C. and B. J. Brown. *In*: P. Gerhardt, R. G. E. Murray, R. N. Costilow, E. W. Nester, W. A. Wood, N. R. Krieg and G. Briggs Phillips (ed.), Manual of Methods for General Bacteriology. American Society for Microbiology, Washington, D.C., p. 222 (1981).

9) Costerton, J. W., K. -J. Cheng, G. G. Geesey, T. I. Ladd, J. C. Nickel, M. Dasgupta, and T. J. Marrie, Annu. Rev. Microbiol. 41, 435 (1987).

10) Costerton, J. W. and A. E. Khoury. Unpublished data.

11) Lappin-Scott, H. M. and J. W. Costerton, Biofouling 1, 323 (1989).

12) LeChevallier, M. W., C. D. Cawthon, and R. G. Lee, Appl. Environ. Microbiol. 54, 2492 (1988).

13) McCoy, W. F., J. D. Bryers, J. Robbins and J. W. Costerton, Can. J. Microbiol. 27, 910 (1981).

14) Nickel, J. C., I. Ruseska, J. B. Wright, and J. W. Costerton, Antimicrob. Agents Chemother. 27, 619 (1985).

15) Ruseska, I., J. Robbins, J. W. Costerton, and E. S. Lashen, Oil and Gas J. March 8, 253 (1982).

16) Schofield, G. M. & R. Locci, J. Appl. Bacteriol. 58, 151 (1985).

17) Timbury, M. C., J. R. Donaldson, A. C. McCartney, R. J. Fallon, J. D. Sleigh, D. Lyon, G. V. Orange, D. R. Baird, J. Winter, and T. S. Wilson, J. Hyg. 97, 393 (1986).

18) Walker, J. T., A. B. Dowsett, P. J. L. Dennis, and C. W. Keevil, Int. Biodeterior. 27, 121 (1991).

19) Wright, J. B., I. Ruseska, M. A. Athar, S. Corbett, and J. W. Costerton, Infect. Control Hosp. Epidemiol. 10, 408 (1989).

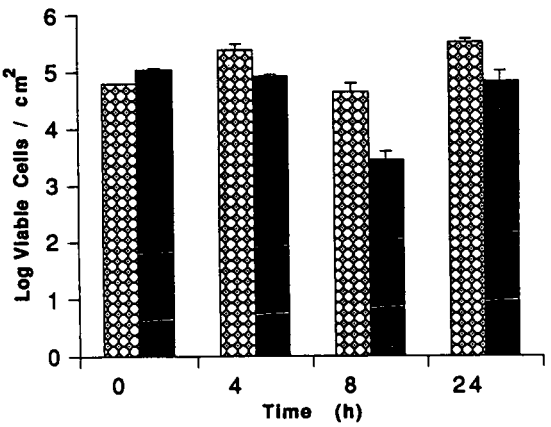

Figure 1 The effect of a low strength electric field/current density on an established *Pseudomonas aeruginosa* biofilm population. The control and electrified modified Robbins devices are represented by patterned and solid bars, respectively. (Mean ± 1 SE, n=2).

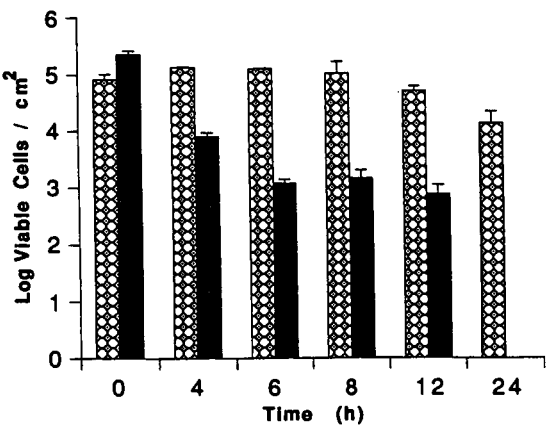

Figure 2 The effect of 5 ppm glutaraldehyde against an established *Pseudomonas aeruginosa* biofilm population in the absence (pattern) and presence (solid) of a low strength electric field/current density. (Mean ± 1 SE, n=2).